Conceptual Study of a Micrometeoroid Deep Space Satellite

FINAL REPORT

Vol. III

Orbital Mechanics

Power Supply and Distribution

Vehicle Design

Thermal Control

Attitude Sensing and Determination

MARTIN

Conceptual Study of a Micrometeoroid Deep Space Satellite

FINAL REPORT

Vol. III

Orbital Mechanics

Power Supply and Distribution

Vehicle Design

Thermal Control

Attitude Sensing and Determination

Edward C. Weissmann
Study Director

January 1965

ER 13700-III

Submitted to the NASA Langley Research Center in compliance with Contract No. NAS 1-4162.

MARTIN
BALTIMORE DIVISION
BALTIMORE, MARYLAND 21203

CONTENTS

		Page
I.	Orbital Mechanics--Flight Plan, Launch Vehicle, and Orbit Selection	I-1
	A. Conclusions and Recommendations	I-1
	B. Technical Discussion	I-2
II.	Power Supply and Distribution	II-1
	A. Conclusions and Recommendations	II-2
	B. Technical Discussion	II-4
	C. References	II-30
III.	Vehicle Design	III-1
	A. Conclusions and Recommendations	III-1
	B. Technical Discussion	III-5
	C. References	III-122
	Appendix III-1--Means of Packaging and Deploying State-of-the-Art Capacitance-Type Micrometeoroid Detectors	III-1-1
IV.	Thermal Control	IV-1
	A. Conclusions and Recommendations	IV-1
	B. Technical Discussion	IV-6
	Appendix IV-1	IV-36
V.	Attitude Sensing and Determination	V-1
	A. Recommended System and Conclusions	V-10
	B. Study Results	V-36
	C. References	V-86

I. ORBITAL MECHANICS

William J. Pragluski
Robert G. Salinger

I. ORBITAL MECHANICS--FLIGHT PLAN, LAUNCH VEHICLE, AND ORBIT SELECTION

The objective of the Micrometeoroid Deep Space Satellite (MDSS) is to investigate the micrometeoroid density in cislunar space. The most desirable orbit is one which has a long lifetime of up to one year, and yet has an apogee altitude approaching lunar distances. Unlike most other satellite missions, such an orbit must come under the strong influence of the moon. Over the satellite lifetime, the high ellipticity of the orbit makes it vulnerable to long term soli-lunar perturbations of large magnitude.

The purpose of this study was to demonstrate the practicality of achieving orbits satisfying the mission objectives, developing a conceptual spacecraft design capable of obtaining the required data, and matching the spacecraft to one of three launch vehicle combinations: the Atlas/X-259, the Atlas/Agena, and the Saturn C-1B. These requirements have been satisfied.

A. CONCLUSIONS AND RECOMMENDATIONS

The baseline orbit used throughout the study was one with a perigee altitude of 200 naut mi and an apogee altitude of 150,000 naut mi (symbolized as 200 x 150K naut mi, hereafter). The evaluation of orbit stability, launch vehicle performance and injection accuracy, and orbit lifetime criteria have substantiated this selection within the study guidelines. Since the mean lunar distance is 207,750 naut mi, the desirability of having orbits with even higher apogee altitudes is apparent. Although such orbits are feasible, they should be considered as special purpose missions which require considerably more detailed planning.

The launch vehicle selected was the Atlas/Agena. This launch vehicle provides excellent performance for the spacecraft developed during the study. In particular, the restart capability of the Agena allows flexibility in selecting the ascent technique. Making use of this factor results in a payload margin for the design spacecraft of over 50%.

The nominal ascent technique selected is the direct ascent. This technique is one in which the rocket motors are burned continuously from liftoff to final injection, interrupted only by staging sequences. The payload margin (relative to 3σ launch vehicle performance) is over 15% for this technique. The greater payload margin is achieved by using the indirect ascent which makes use of the Agena restart capability.

B. TECHNICAL DISCUSSION

1. Launch Vehicle Performance Characteristics

As stated previously, the launch vehicles considered were the Atlas (SLV-3)/X-259, the Atlas (SLV-3)/Agena D, and the Saturn C-1B. The stage characteristics and rocket motor performance characteristics for each of these launch vehicles are presented in Appendix II-1. It also includes detailed descriptions of the methods of analysis and several of the tradeoff studies performed as part of this study. However, only summary data of these studies are presented here.

The direct ascent and indirect ascent techniques used are illustrated in Fig. I-1. The direct ascent assumes continuous burning from liftoff to final injection, interrupted only by the staging sequences. The indirect ascent assumes a burn-coast-burn type of ascent. Here, a distinction must be made between the Atlas/X-259 and Atlas/Agena. The Agena, having a restart capability, can be used in part during the initial burning period. After shutdown, the Agena plus spacecraft can coast to the final injection altitude where the remaining Agena propellant is consumed to achieve the desired injection velocity. The ascent profile used assumes first burnout at 90 naut mi, followed by a Hohmann transfer-type coast to the desired final injection altitude.

The X-259, a solid rocket motor, does not have restart or shutdown capabilities. With this launch vehicle, the coasting period must start at Atlas burnout with the X-259 ignition taking place after the coasting period. This arrangement does not allow the efficient Hohmann transfer-type coast and results in considerably shorter coast times and downrange distances. The performance numbers presented here (and in Appendix I-1) all assume the use of the project fire attitude control system between Atlas burnout and X-259 ignition.

The payload capability of the Atlas/X-259 and Atlas/Agena launch vehicles is summarized in Fig. I-2 for both the direct and indirect ascent techniques. The curves represent nominal performance, but the correction for 3σ performance is noted on the figure. The design spacecraft weight (for the Agena shroud) is 696 lb. With the Atlas/Agena nominal payload capability of 1015 lb (855 lb 3σ) for the direct ascent and 1258 lb (1098 lb 3σ) for the indirect ascent, considerable weight growth is allowable. The suggested ascent technique for the design spacecraft is the direct technique. This results in a more straightforward operational procedure, does not require Agena shutdown and restart, and, as is shown later, a more accurate injection. Relaxation toward the indirect technique can be made should the spacecraft have an unusually large weight growth.

The Saturn C-1B data are not included in Fig. I-2. The use of a two-stage vehicle to reach injection velocities of over 35,000 fps is quite

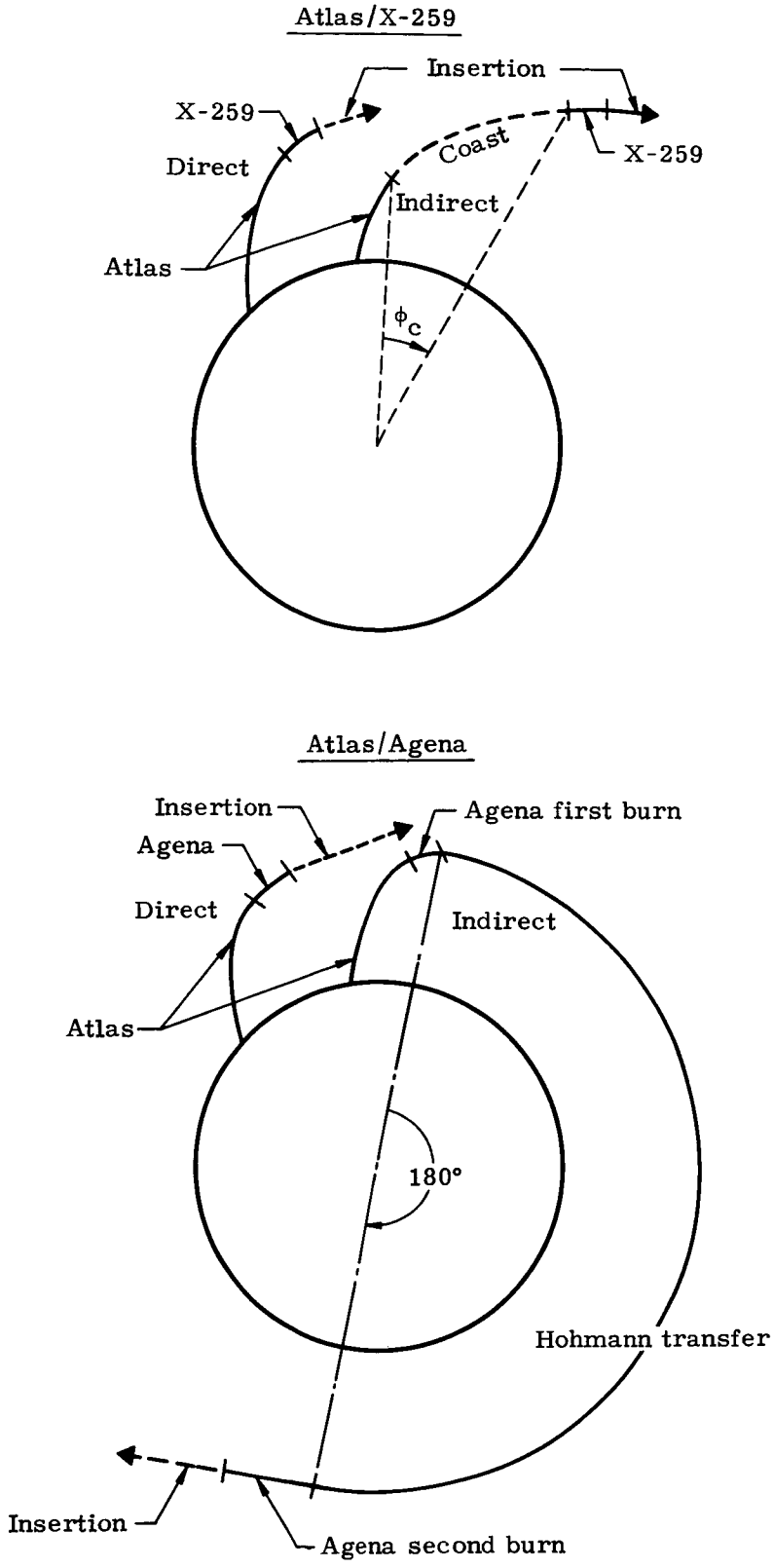

Fig. I-1. Ascent Techniques

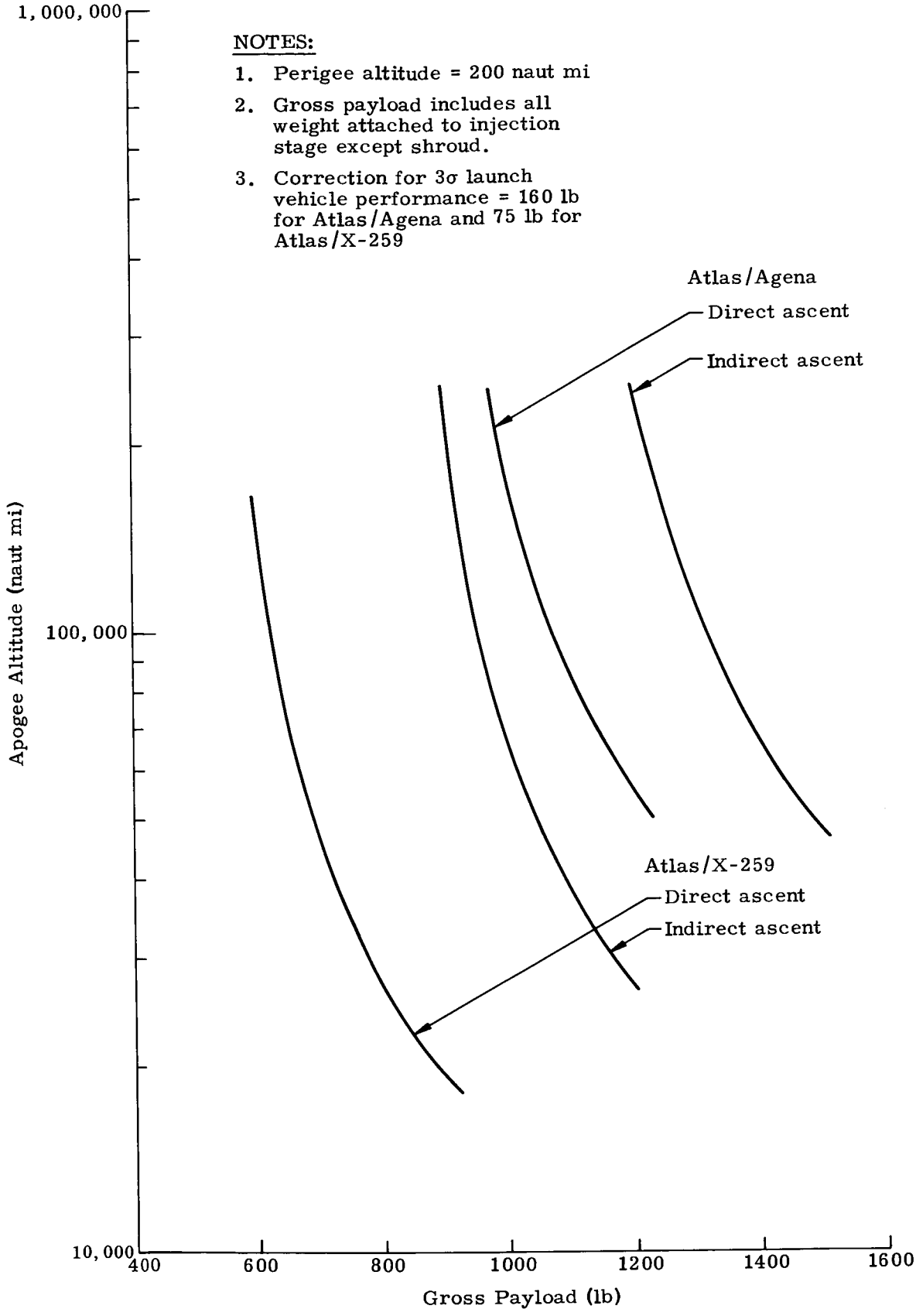

Fig. I-2. Nominal Launch Vehicle Payload Capability

inefficient. This, in fact, turned out to be the case for the Saturn C-1B. The performance capability of the two-stage launch vehicle, presented in Appendix I-1, demonstrates the impracticality of the Saturn C-1B without an additional upper stage for this mission.

The desire to get maximum performance from the launch vehicle usually leads to specifying as low an injection altitude as possible. The injection altitude selected for this mission (on the basis of orbit stability) is 200 naut mi, although it could be reduced to 175 naut mi or lower if necessary. The payload variation for the Atlas/X-259 and Atlas/Agena as a function of injection altitude is summarized in Fig. I-3. As can be seen, the payload is fairly insensitive to injection altitude for the indirect ascent technique, but highly sensitive for the direct ascent technique. Therefore, the use of the direct ascent technique requires the injection altitude to be as low as is practical. If any significant improvement in the overall mission could be gained by going to much higher injection altitudes, the indirect ascent technique would be required.

These launch vehicle performance characteristics, plus others which relate to the orbital stability study, are integrated with the other studies in the following sections.

2. Orbit Stability and Lifetime Criteria

The principal factors to be considered in the orbit selection are experiment requirements, orbit stability, and aerodynamic effects on the orbit lifetime. Secondary considerations include spacecraft subsystem constraints such as eclipse time effects on electrical power generation and thermal control.

Detailed discussion of experiment requirements has been presented in Volume II, Chapter I. Some of the important conclusions are reiterated. The experiment requires a highly elliptical orbit with the perigee near earth and the apogee as close to lunar distance as is practical. The orbit orientation, relative to the earth-moon-sun system, might be fixed to gather data near the earth-moon system libration points or try to investigate the hypothesized lens effect. Finally, the investigation will be carried out with orbits close to the ecliptic or moon's orbital plane.

Most of these experiment requirements can be easily met with the proposed configuration. The limiting factor is the orbit stability. The nominal mission requires an orbit lifetime of 6 mo to 1 yr to obtain a statistically significant amount of data with the most adverse micrometeoroid density model assumed in this study. Over this long period

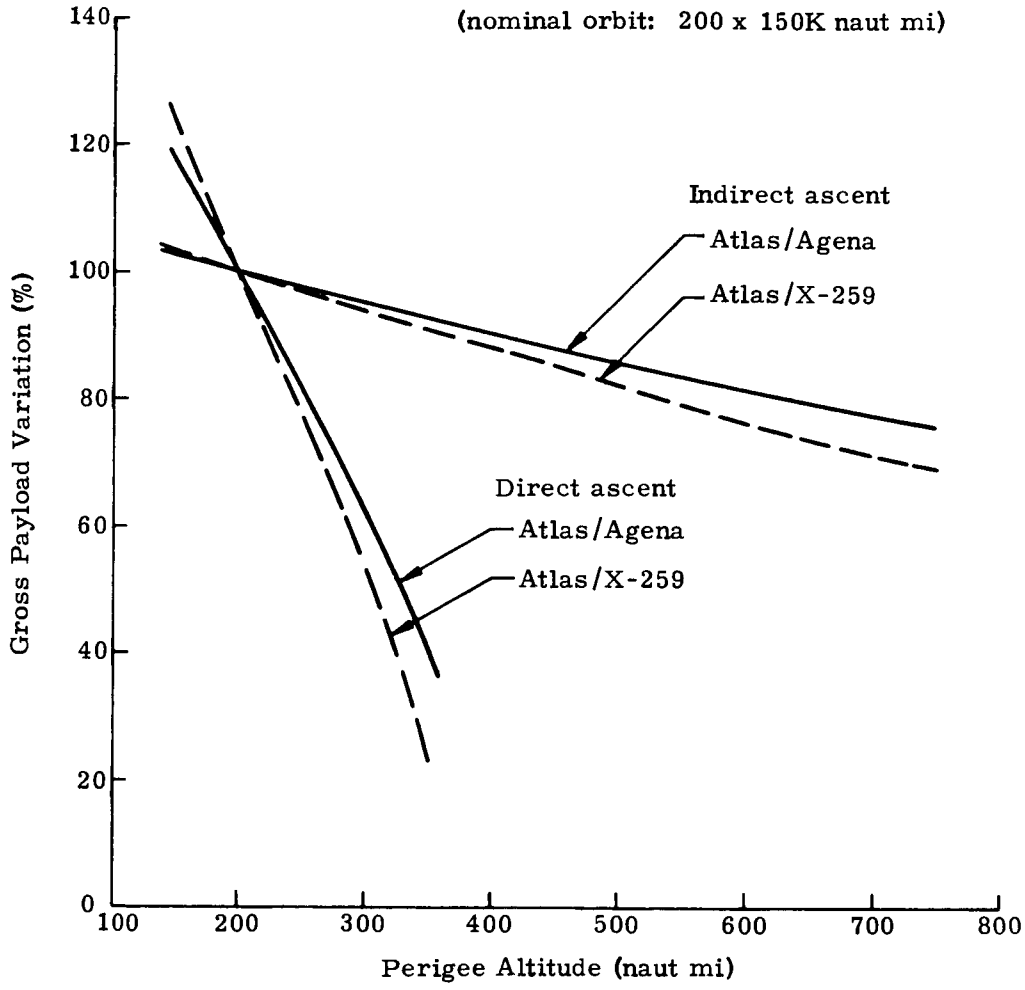

Fig. I-3. Payload Variation with Injection Altitude

of time, both the sun and moon will have significant effects on the orbit. The possible variations in perigee altitude over a year can be separated into a periodic and secular variation due to the sun and moon. Maximum changes which can be expected for an orbit with a 200 naut mi perigee and variable apogee are illustrated in Fig. I-4. As can be seen, the potential perturbations, particularly the combined solar and lunar secular perturbations, are considerably greater than any practical injection altitude. Typical perigee time histories for a 200 x 153K naut mi orbit are shown in Fig. I-5 for launches on 21 July 1964, and various injection times.

The dependence on injection time on any given launch date is quite apparent. This leads to the concept of the launch window map which displays the allowable launch times for each possible launch date. An example for this orbit is shown on Fig. I-6 which gives the allowable injection times for launches between July 1964, and July 1965. The orbit stability criteria for this map is that the perigee height does not drop below 125 naut mi at any time for a year. Thus, ample launch opportunity exists for the conditions assumed for this orbit.

The ragged nature of the map is due to the lunar periodic perturbations. The data shown in Fig. I-6 also shows a window calculated with the lunar secular terms included, but lunar periodic terms neglected. The regular nature of this map allows more straightforward analysis of the effect of various injection conditions such as injection altitude, injection point position, and apogee altitude. Integrating the allowable launch time per day over a year and dividing by the number of days yields an average launch time tolerance per day. Although the actual launch window maps are presented and discussed in detail in Appendix I-2, only the average launch time tolerance will be used to reflect the effect of injection parameters.

The most important parameter in establishing a stable orbit is to have the correct argument of perigee. This is obtained by controlling the ascent range angle (central angle measured at the center of the earth between the radius vectors pointing at the launch point and injection point). A typical daily launch time tolerance as a function of ascent range angle is shown in Fig. I-7. These data illustrate the advantages of short range or very long range ascents. Ascent range angles around 80 to 120 deg give effectively no launch window when considering all other factors. The figure also illustrates the relative insensitivity of the launch window to apogee radius.

The effect of orbit perigee, apogee, and orbit inclination on the daily launch time tolerance is shown in Fig. I-8. Again, the relatively small effect of apogee radius on the launch window size due to the long period soli-lunar perturbations is illustrated. The most significant changes are realized by perigee and inclination variations. This conclusion is somewhat modified, however, when considering the effect of short period lunar effects. These effects become increasingly significant for apogee radii greater than 165,000 naut mi. This is discussed in more detail below.

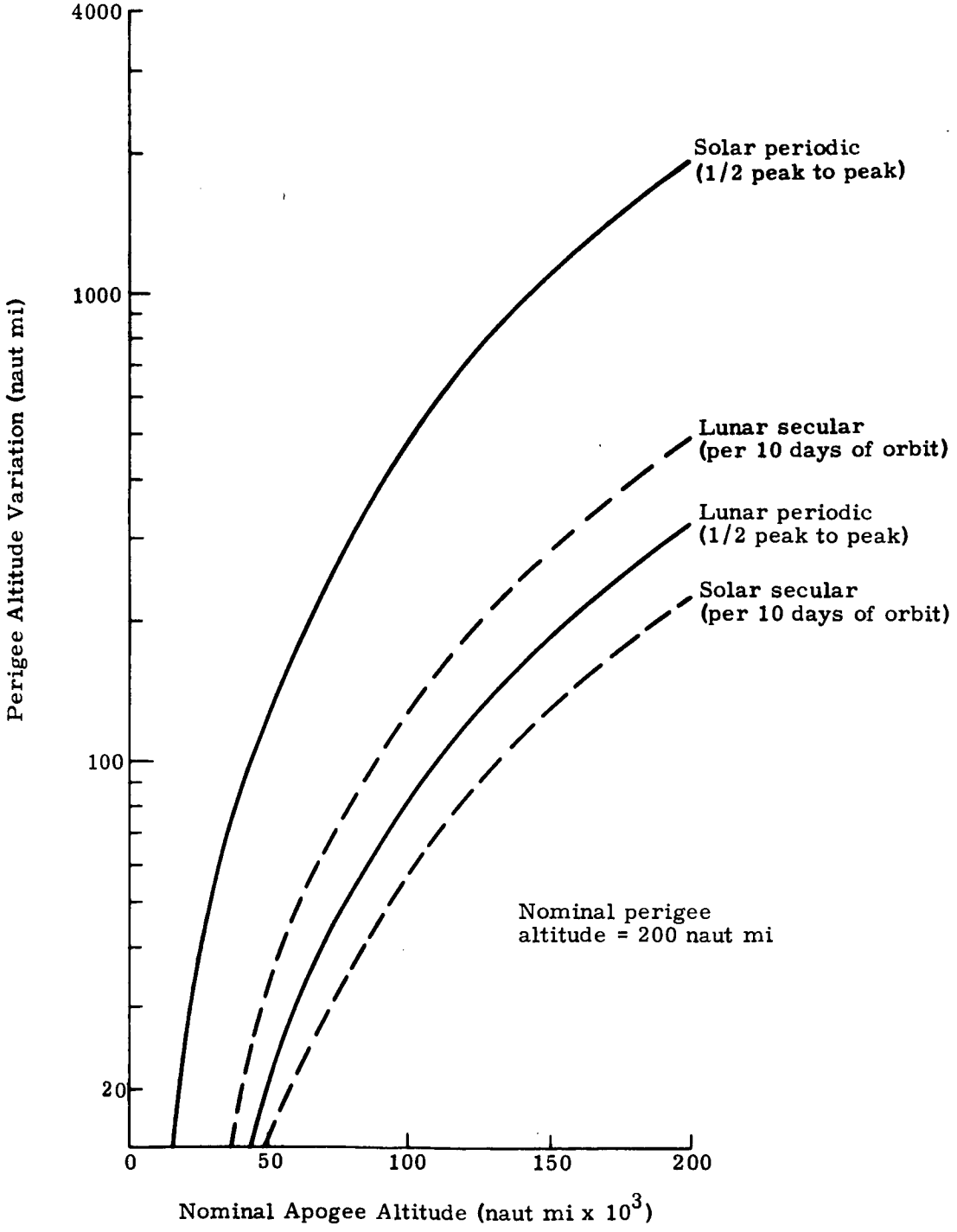

Fig. I-4. Maximum Long Period Soli-lunar Perturbations on Orbit Perigee Altitude

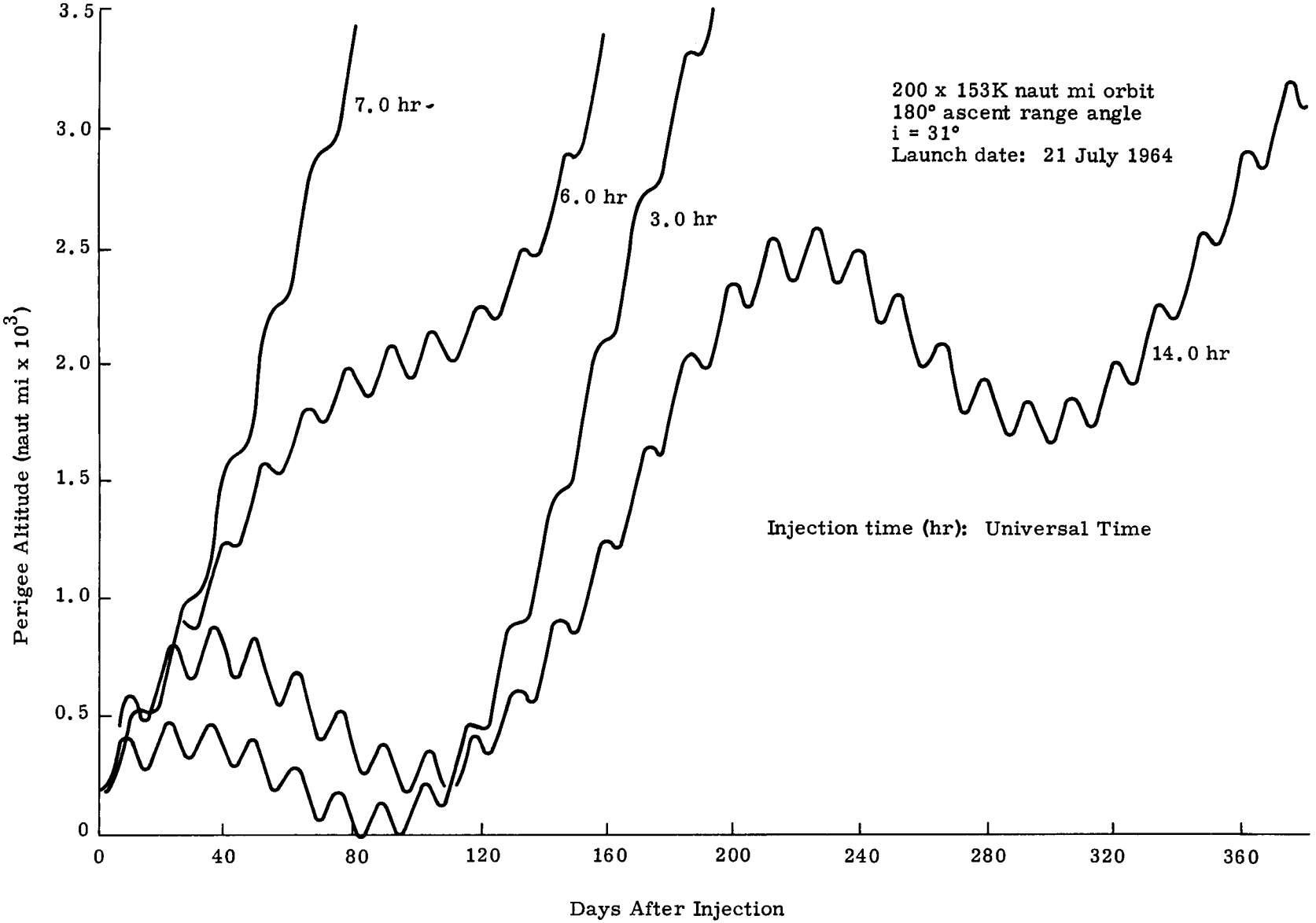

Fig. I-5. Soli-lunar Perturbations on Perigee Altitude

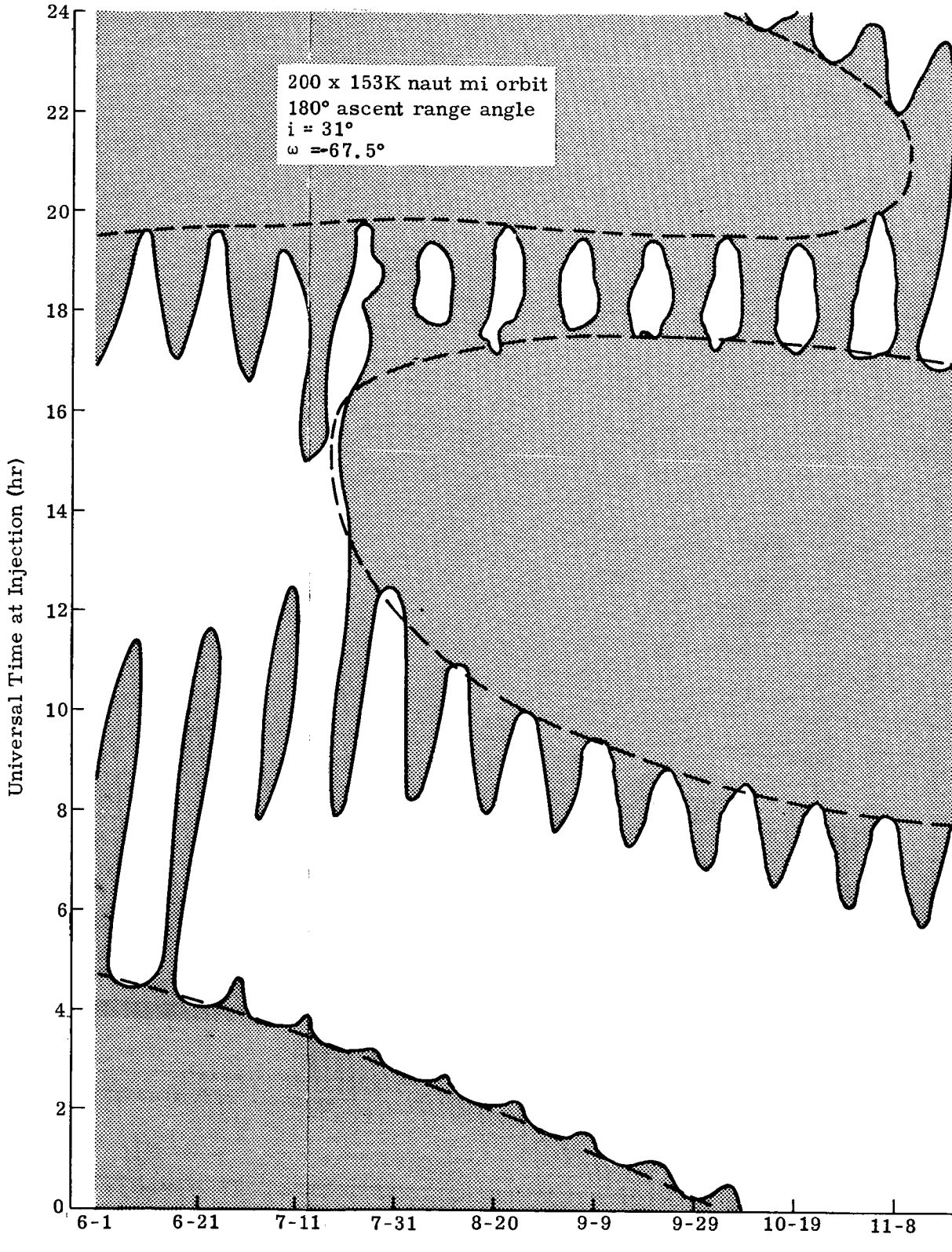
200 x 153K naut mi orbit
180° ascent range angle
i = 31°
ω = -67.5°
Universal Time at Injection (hr)
24
22
20
18
16
14
12
10
8
6
4
2
0
6-1
6-21
7-11
7-31
8-20
9-9
9-29
10-19
11-8

La

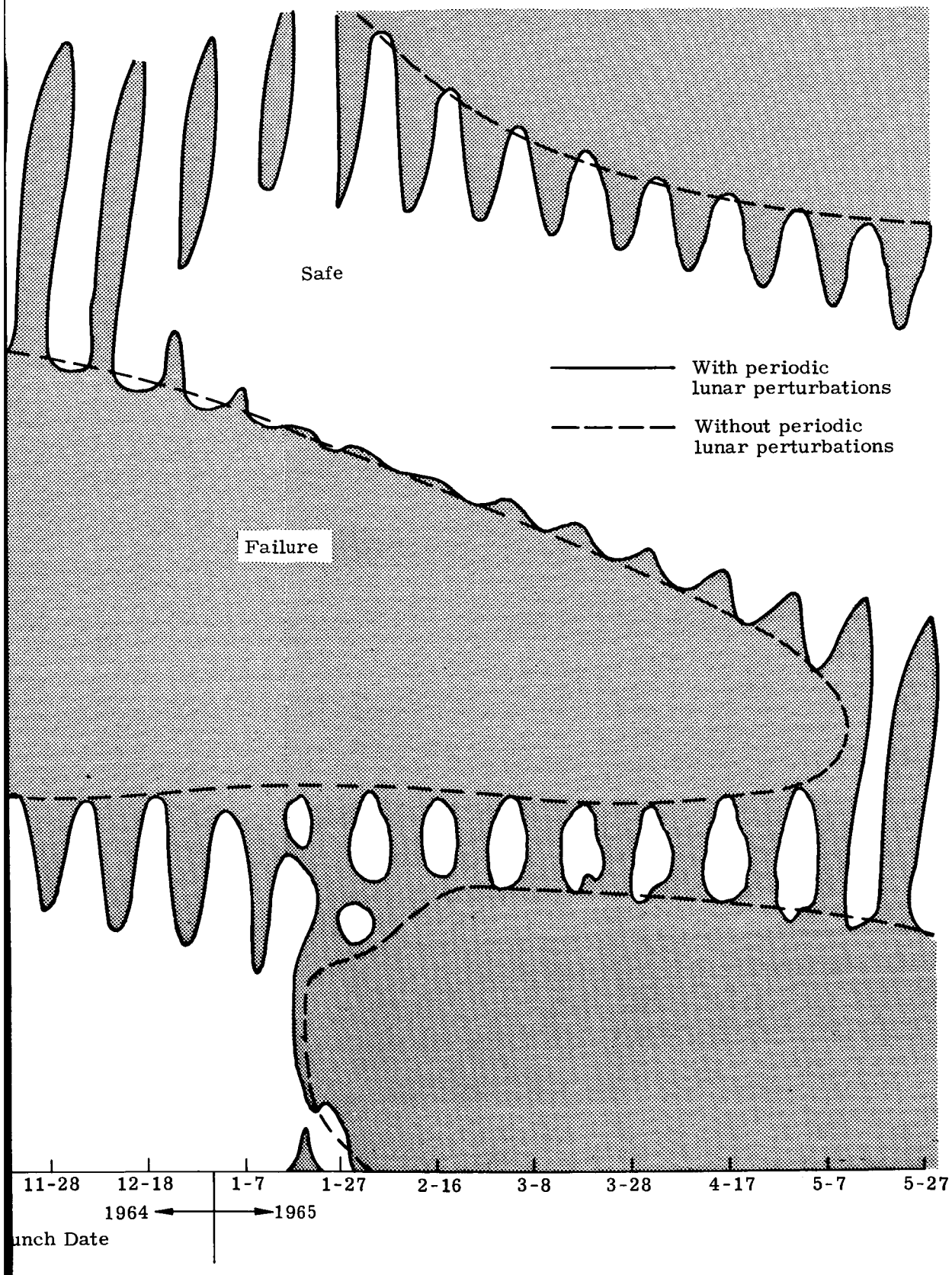

Fig. I-6. Launch Window

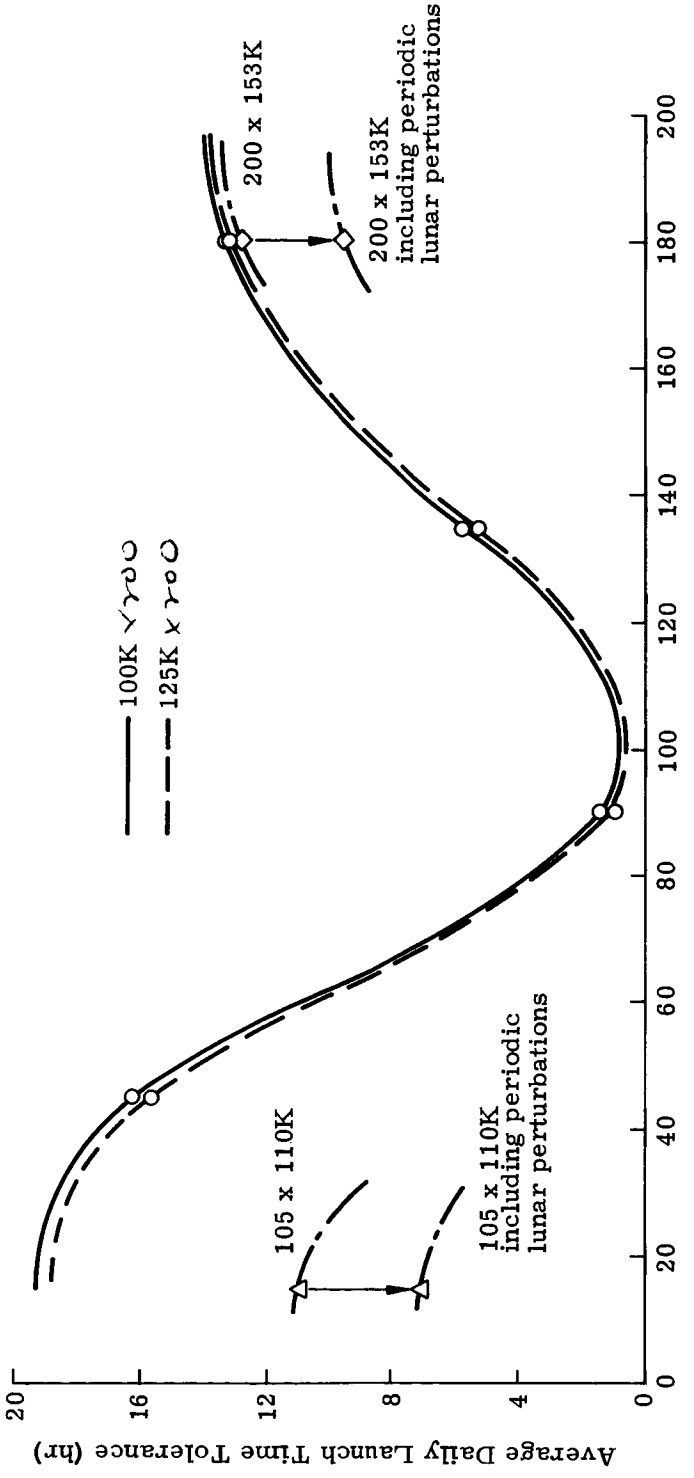

Fig. I-7. Effect of Ascent Range Angle on Launch Window Size

The selection of a minimum perigee altitude from an orbit stability viewpoint requires consideration of both the type of data shown in Figs. I-7 and I-8 (which do not include the effect of lunar periodic perturbations except for the special points shown in Fig. I-7) plus the data shown in Fig. I-4. The lunar periodic perturbation must decrease the effective launch time tolerance more for low initial perigee altitudes than for higher ones. In Fig. I-7, two examples are shown; one for an orbit of 105 x 110K naut mi which experiences a 36% reduction, and one for an orbit of 200 x 153K naut mi which experiences a 26% reduction. The data in Fig. I-4 shows a periodic lunar perturbation of 190 naut mi (maximum) for the 200 x 153K naut mi orbit. Figure I-5 shows an effective amplitude of approximately 90 naut mi for the same orbit for the nonmaximum conditions which actually existed. If the initial perigee altitude were increased to 580 naut mi, the resultant reduction in effective daily launch time tolerance would have been lowered from 26 to approximately 12% (or about 1.5 hr). The gain in launch window does not seem to be worth the payload decrease (launch vehicle performance) and 200 naut mi appears to be a good compromise. This discussion is carried out in more depth in Appendix I-2.

The final consideration in the orbital parameter selection is the effect of the atmosphere on the orbit. The main effect of atmospheric drag is a potentially rapid decrease in apogee altitude (neglecting the thermal control problems). The effect of initial apogee and perigee altitudes on apogee decay rate is shown in Fig. I-9 for a ballistic coefficient, $B = \left(\frac{C_D A}{2m}\right)$, of one. The actual spacecraft ballistic coefficient will lie between 10 and 15 (13.8 for the nominal design) resulting in a maximum decay rate of less than 25 naut mi per orbit for the nominal 200 x 150K naut mi orbit. Over a year, this would amount to less than 1500 naut mi, a negligible drop. Even this drop in apogee will not be experienced due to atmospheric effects because of the large increases in perigee altitudes that must be experienced (Fig. I-5). The method of analysis and more detailed discussion of atmospheric effects is given in Appendix I-3.

3. Orbit Tracking and Communications Coverage

The highly elliptical orbits required for this mission have spacecraft angular velocities greater than the earth's rotational speed near perigee and less than the earth's rotational speed near apogee. The break-even point occurs when the spacecraft is about 20K naut mi from earth. In this altitude range, the spacecraft appears to be moving directly away or towards a ground-fixed observer. At higher altitudes, the spacecraft appears to be slowly regressing (westerly

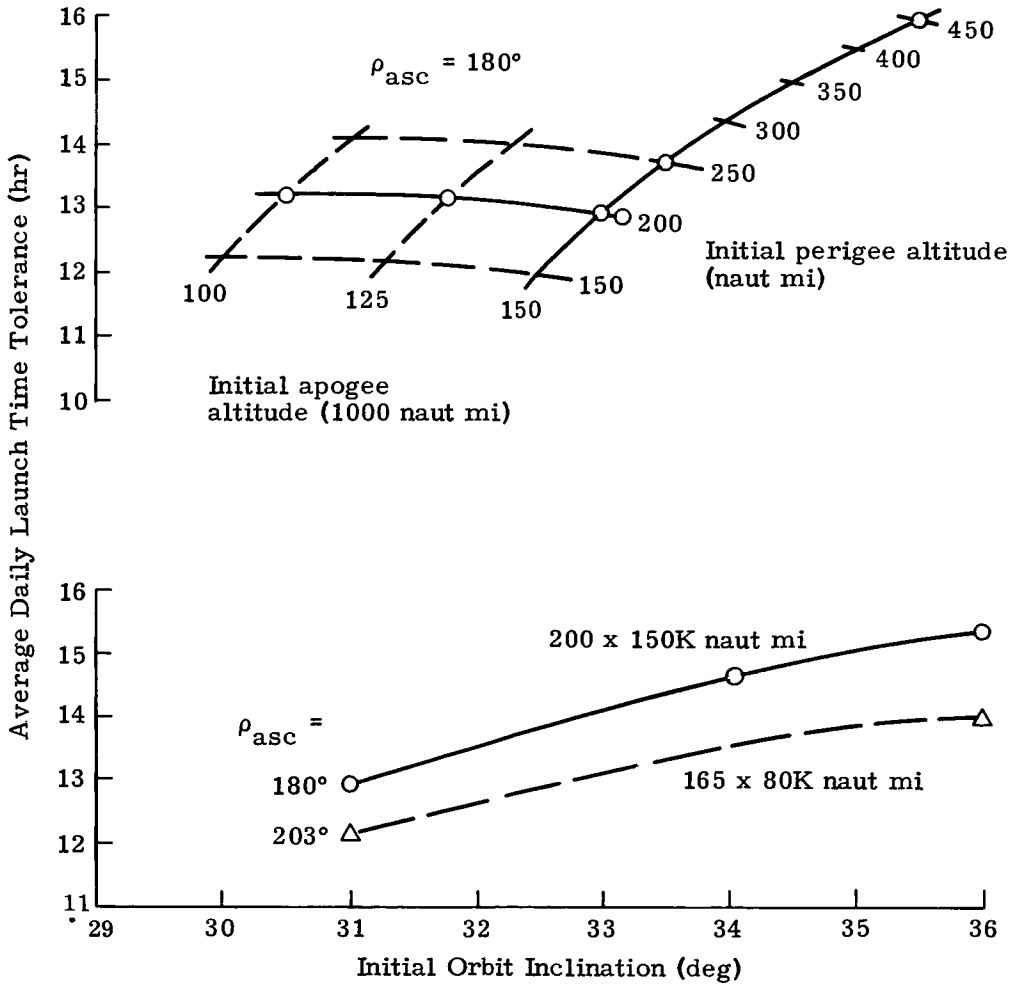

Fig. I-8. Effect of Orbit Perigee, Apogee, and Inclination on Launch Window Size

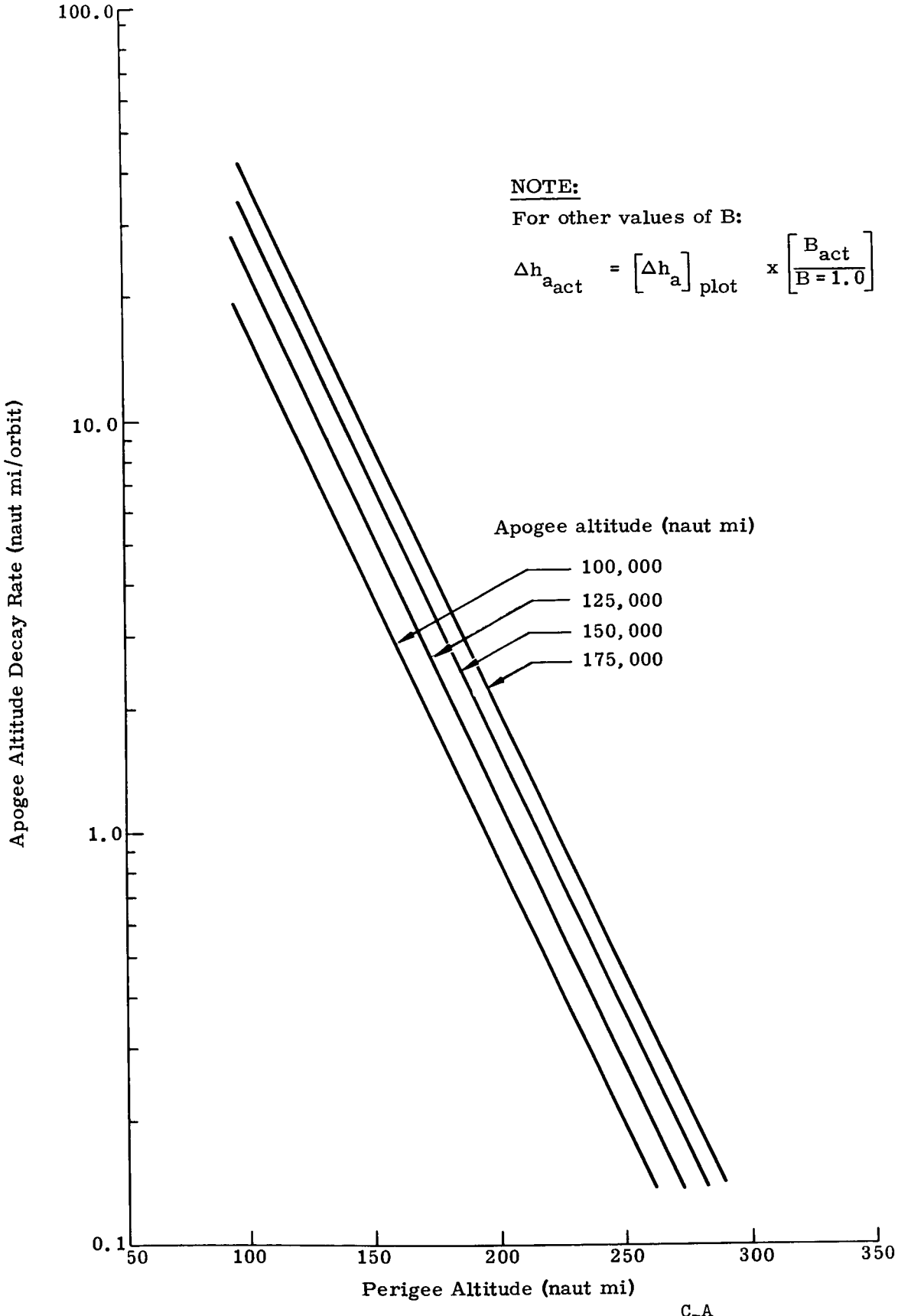

Fig. I-9. Drag Effect on Apogee Altitude, $B = \frac{C_D A}{2m} = 1{:}0$

motion). Near perigee, the spacecraft has a high speed relative to the ground in the easterly direction.

The selection of launch vehicle and ascent techniques plays an important part in establishing the ground track of the orbit and the spacecraft position relative to available tracking/communication stations. The short range (direct) ascents result in the injection point (and perigee) at northern latitudes as high as the latitude of Cape Kennedy. The spacecraft at apogee will have a ground track at the corresponding southern latitude. The opposite situation occurs for the Atlas/Agena launched spacecraft using the indirect ascent (Hohmann transfer). Here the injection point is in the southern latitudes; apogee in the northern latitudes. The Atlas/X-259 indirect ascent (short coast) lies between these two extremes with both the apogee and perigee located in the vicinity of the equator.

The significance of these characteristics is illustrated in Figs. I-10a and b. The first track corresponds to the long range type ascent, the second to the medium range type ascent. The long range ascent (Fig. I-10a) is characterized by a band of tracks at a northern latitude (spacecraft near apogee) with a large loop beneath as the spacecraft approaches perigee. The inverse of this is true for the short range ascents (i.e., turn the world upside down). The medium range ascents (Fig. I-10b) have the band of tracks near the equator with a figure eight type of loop straddling north and south of the equator.

The time ticks indicated on the ground tracks show the high relative speed when the spacecraft is near perigee. In effect, tracking or communications when the spacecraft is less than 5000 naut mi from earth will be uncertain and, at best, will only be possible for several minutes. On the other hand, when the spacecraft is in the 10K to 30K naut mi region from earth, a single station will generally be able to communicate with the spacecraft for over 3 hr and have little change in tracking azimuth and elevation. Above 75K naut mi, any station which can see the spacecraft will be able to communicate with it for several hours as it slowly drifts westerly from horizon to horizon.

Referring once again to Fig. I-10a, the spacecraft is in the 10K to 30K naut mi region where the ground track changes direction from east to west (or vice versa). This occurs near zero latitude. Thus, with the long range ascent, stations in the equatorial and northern latitudes will have the most tracking and communications coverage. The inverse is true for the direct-type ascents (any launch vehicle). The medium range ascent will result in equatorial stations seeing the spacecraft in the 75K naut mi and up ranges with northern stations picking up the spacecraft in the 10K to 30K naut mi range as the spacecraft approaches perigee and southern stations seeing it as it leaves this perigee. In all cases, as long as the orbital inclination is not much greater than

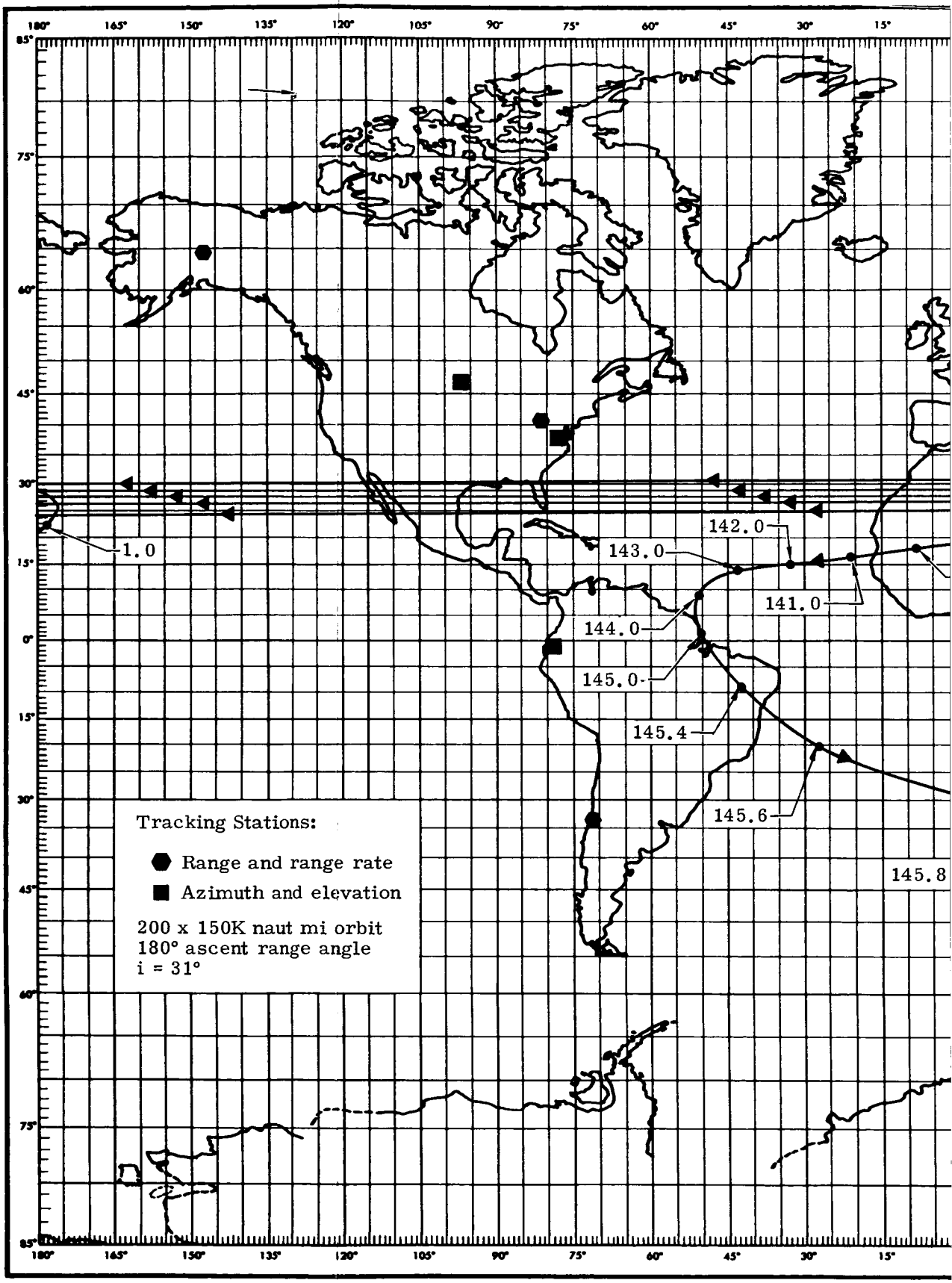
180° 165° 150° 135° 120° 105° 90° 75° 60° 45° 30° 15°
85° 75° 60° 45° 30° 15° 0° 15° 30° 45° 60° 75° 85°
1.0
142.0
143.0
141.0
144.0
145.0
145.4
145.6
145.8
Tracking Stations:
Range and range rate
Azimuth and elevation
200 x 150K naut mi orbit
180° ascent range angle
i = 31°

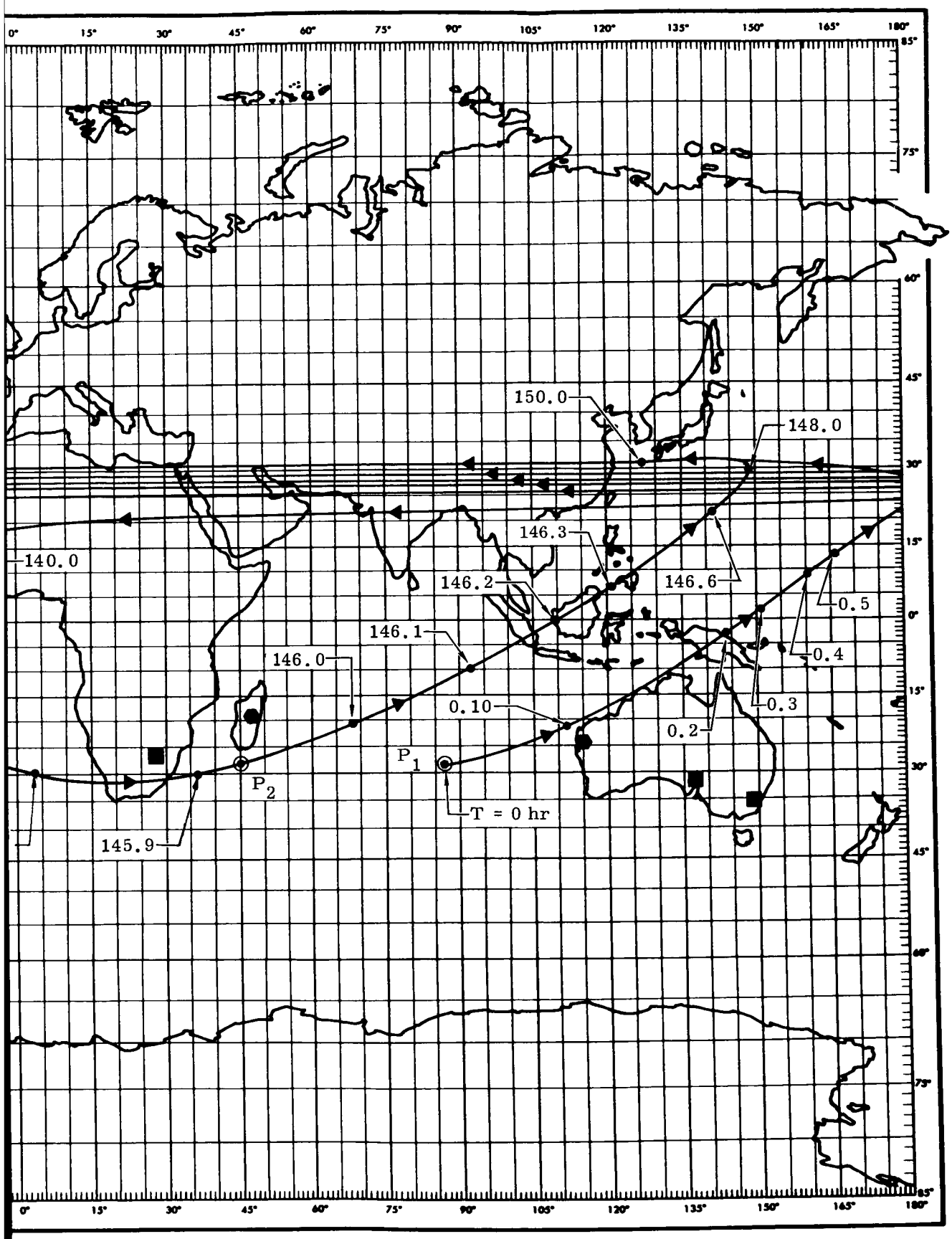

Fig. I-10a. Typical Ground Trace

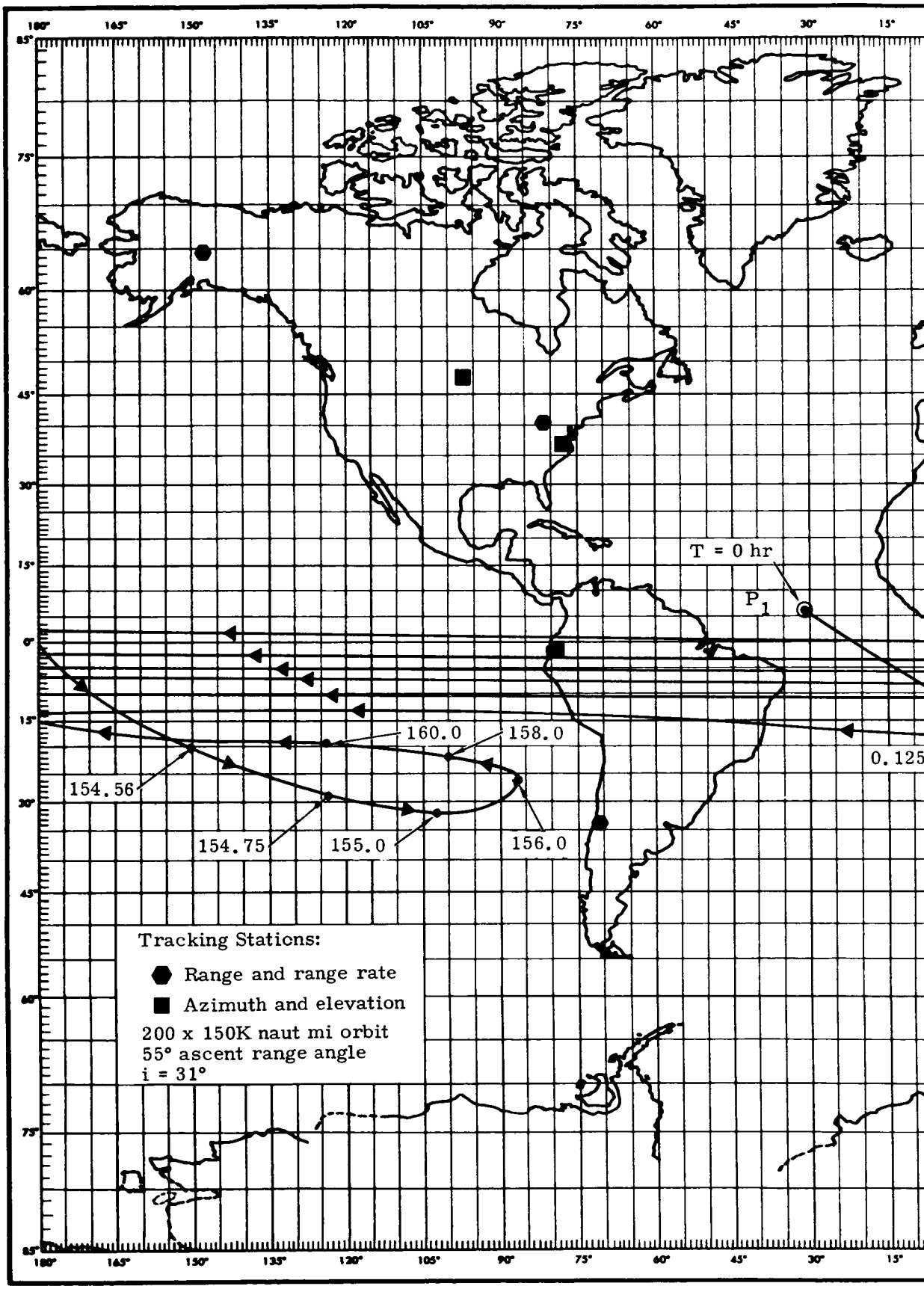
T = 0 hr
P_1
160.0
158.0
154.56
154.75
155.0
156.0
0.125
Tracking Stations:
Range and range rate
Azimuth and elevation
200 x 150K naut mi orbit
55° ascent range angle
i = 31°

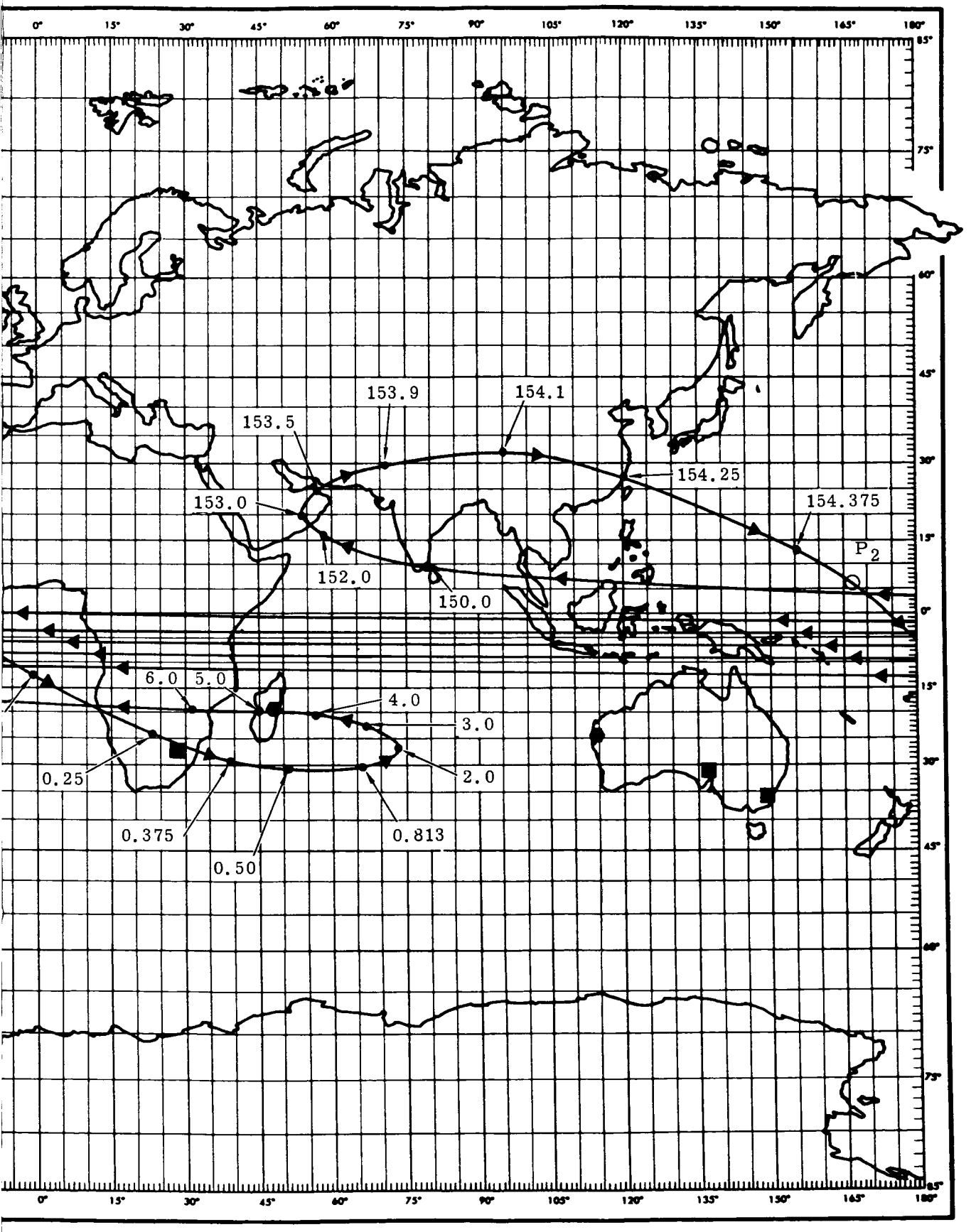

Fig. I-10b. Typical Ground Trace

~~the spacecraft approaches perigee and southern stations seeing it as it leaves this perigee. In all cases, as long as the orbital inclination is not much greater than~~ 30 deg, excellent tracking and communications coverage will be available. An example of potential coverage for the long range ascent, for range and range rate stations, and azimuth and elevation stations is shown in Fig. I-11.

The allowable tracking coverage is more than adequate to establish a good orbit ephemeris within the first half of the orbit. The one sigma position uncertainty will be well under a mile using range and range rate data and less than 10 mi for azimuth and elevation data only. A detailed orbit ephemeris accuracy as a function of type and amount of tracking data is presented in Appendix I-4. A typical example, showing only the one sigma uncertainty in the orbit semi-major axis, is shown in Fig. I-12. For the R&RR data, it was assumed that no tracking data could be taken when the spacecraft distance was over 100K naut mi. As can be seen, the azimuth and elevation data are most effective near perigee. The R&RR data are always effective.

4. Launch Vehicle and Orbit Selection

The data presented summarizes the studies performed in the areas of launch vehicle performance, orbit stability and lifetime, and tracking and communications coverage. Considerably more detailed data and analysis backing up the summary data appear in Appendices I-1 through I-4. Elsewhere in this report, the selected spacecraft configuration and subsystems are presented.

Preliminary configuration studies showed that the spacecraft on top of either the Atlas/X-259 or Atlas/Agena would be size limited by the shroud rather than weight limited by launch vehicle performance capability. Since an X-259 configured spacecraft or Agena configured spacecraft could be propelled to near escape speed by selecting the optimum ascent technique and injection altitude, orbit selection, as such, was not directly included in the selection of launch vehicle. The X-259 configured spacecraft was found to have lower probability of mission success (see Progress Report No. 2, ER 13603-2). This was largely a result of the effect of impulse uncertainty in the X-259 rocket motor and its effect on apogee altitude selection and 3σ variation. In addition, use of the direct ascent with Atlas/X-259 requires a low injection altitude (below 150 naut mi), which is undesirable. Use of the indirect ascent technique results in ascent range angles which are most adverse relative to orbit stability. On these bases, emphasis was placed on the Agena configured spacecraft. The subsequent discussion illustrates the above conclusions in more detail.

The design configuration has a gross payload weight of 696 lb. Comparison with the Atlas/Agena payload capability (Fig. I-2) shows that considerable weight growth margin is available even for the direct ascent technique regardless of injection altitude or desired nominal apogee

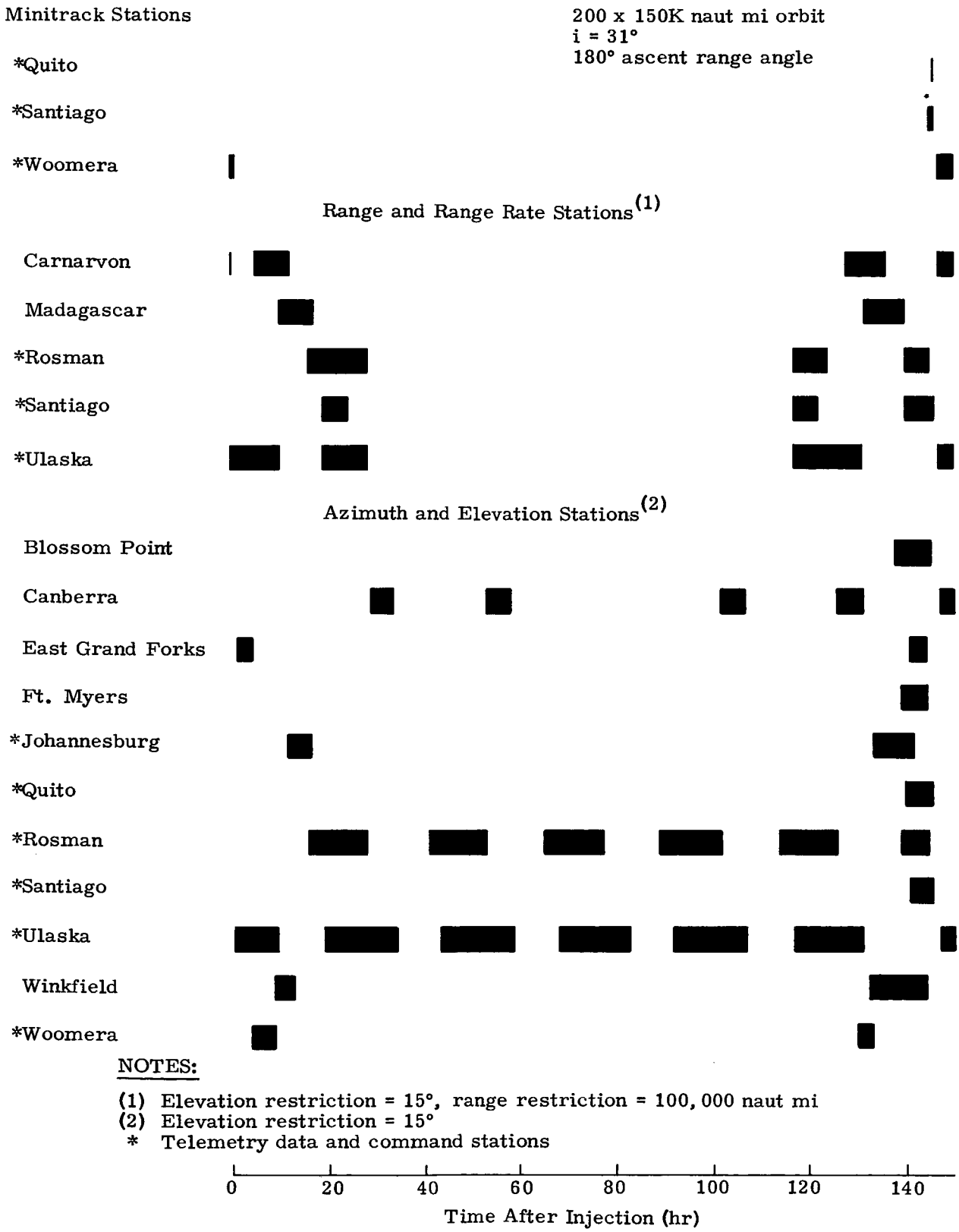

Fig. I-11. Possible Tracking and Communication Coverage

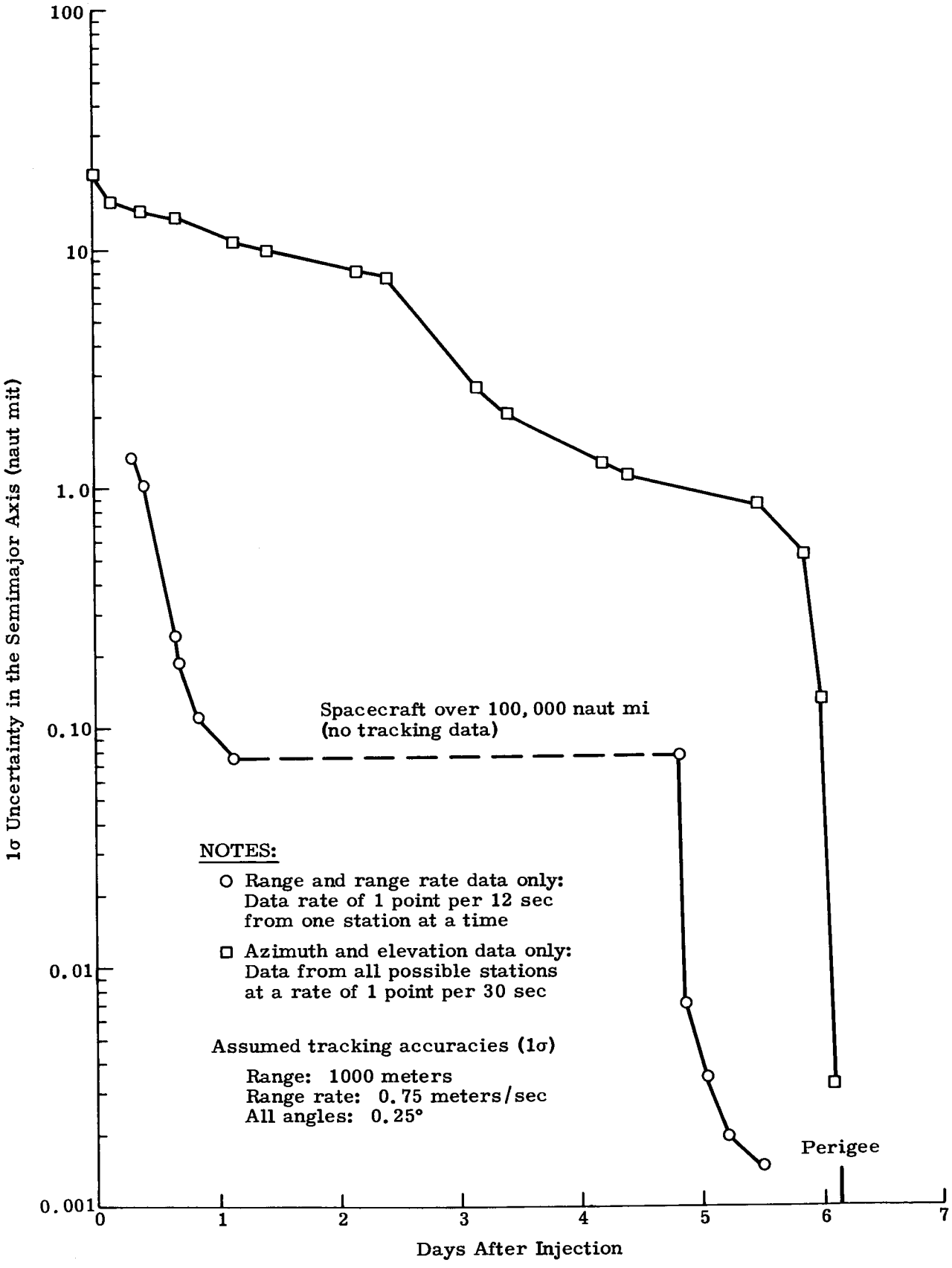

Fig. I-12. Typical Orbit Ephemeris Accuracy

altitude. Thus, the selection between the direct or indirect type ascents had to be made on another set of criteria such as operational simplicity, orbit stability, launch window, and effect of ascent guidance accuracy.

Operational simplicity certainly suggests the direct as opposed to indirect ascent technique. By using the direct approach, restart capability in the Agena is not required, nor is the attitude control system required over the 45-min coast period. The time from liftoff to injection is much shorter, thus improving the probability of successful injection.

The orbit stability and launch window criteria for the Atlas/Agena is primarily sensitive to the nominal injection point position, the direct ascent resulting in the injection point being 23.6 deg downrange from the launch point. The indirect ascent results in the injection approximately 180 to 200 deg downrange from the launch point. Reference to Fig. I-7 shows that both are quite acceptable, with the direct ascent showing a slight advantage.

It should be pointed out that the Atlas/X-259 indirect ascent results in an injection point 86 deg downrange from the launch point. This, in fact, would be totally unacceptable from an orbit stability viewpoint (Fig. I-7) since no effective launch window is available. This could be rectified by shaping the ascent trajectory at the expense of payload penalty and operational simplicity. The Atlas/X-259 direct ascent does not suffer from the adverse downrange position of the injection point (quite the contrary, in fact), but is incapable of achieving injection altitudes much higher than 150 naut mi. This compromises its effectiveness to some degree, but certainly does not eliminate it. The higher injection altitude does require greater pitch rates during the sustainer burning period, however.

Finally, the question of the effect of ascent guidance accuracy must be investigated. The nominal orbit will have injection velocities less than 500 fps below escape speed. Thus, 500 fps is the difference between achieving an orbit with an apogee of 150K naut mi and infinity. This illustrates the sensitivity of the orbit to injection velocity accuracy. The effect of ascent guidance accuracy on the nominal apogee radius is shown in Fig. I-13 for both the Atlas/X-259 and Atlas/Agena launch vehicles. The assumed ascent guidance accuracies plus the analysis techniques are described in detail in Appendix I-5. It should be mentioned, however, that the X-259 3σ total impulse uncertainty was assumed to be 1%. Although this is rather nominal for solid rocket motors, it could be worse for the standard motor or be made better by obtaining specially loaded motors. Needless to say, the X-259 motor performance is the primary difference between the Atlas/X-259 and Atlas/Agena data shown in Fig. I-13.

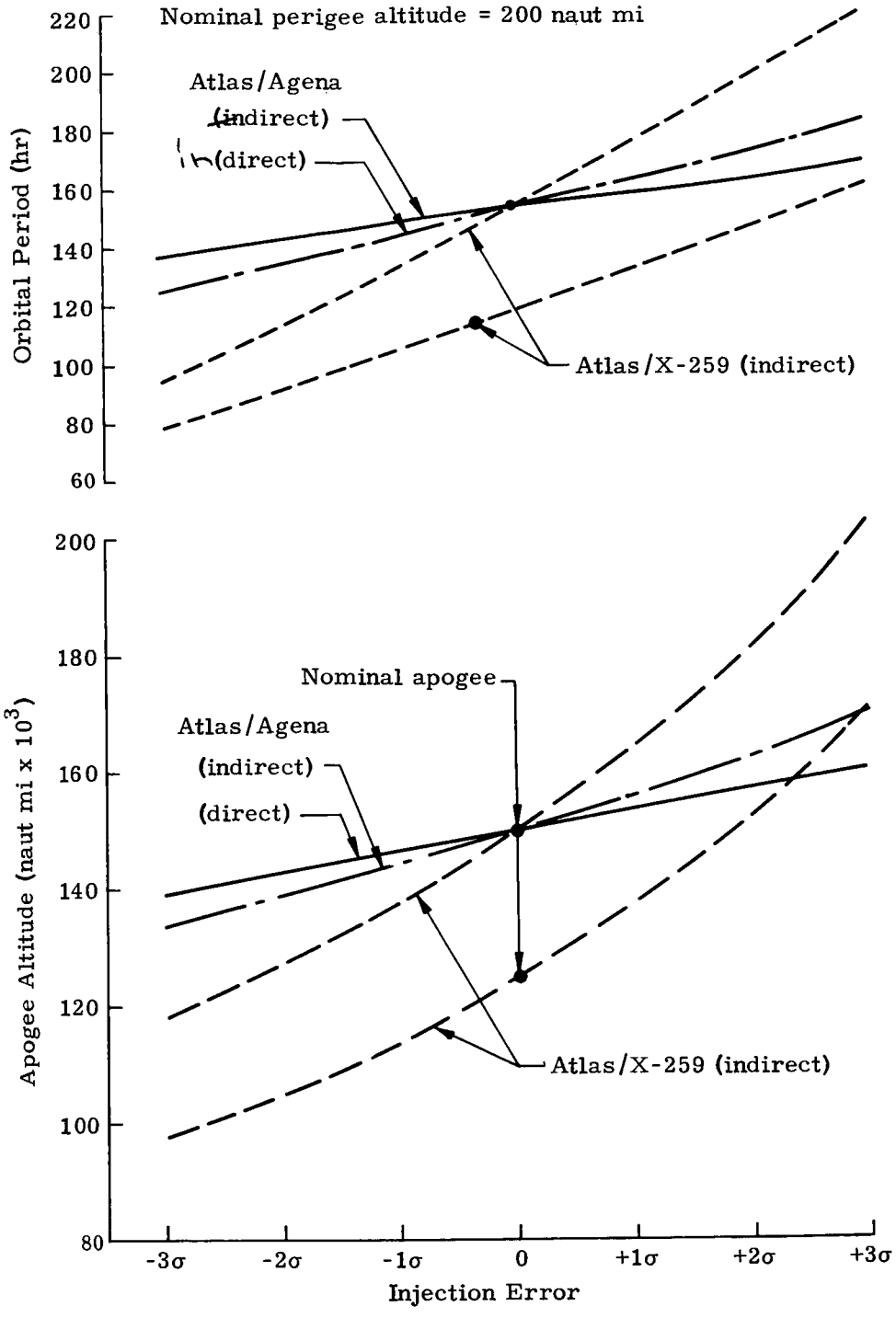

Fig. I-13. Effect of Injection Errors on Orbital Parameters

The significance of the injection accuracy cannot be fully appreciated until the reasons for the orbit selection are presented. More will be provided after discussing the orbit selection process.

The mission objectives call for an orbit with as high an apogee as is practical and, for early micrometeoroid density investigations at least, be near the ecliptic plane. The latter requirement cannot help but be satisfied. It is not possible to get appreciably far away from the ecliptic relative to Astronomical Unit (AU) distances and still satisfy the basic mission guidelines of staying in a stable earth orbit. The primary emphasis, then, is to define a practical upper limit to the apogee altitude while still ensuring the required orbital lifetime of 6 mo to 1 yr.

The data shown for orbit stability and launch windows (Figs. I-4 through I-8) included the long term periodic and secular perturbations of the sun and moon plus the secular perturbations caused by earth oblateness. To this must be added the short term (or single orbit) perturbation which the moon can supply. This can occur any time the moon is at its closest point to the orbit when the spacecraft reaches apogee (or roughly every 28 days). This effect starts being felt any time the apogee gets over 130K naut mi and reaches serious proportions for an apogee radii over 170K naut mi. At 170K naut mi, for example, the perigee altitude can be changed as much as 3000 naut mi up or 2000 naut mi down in a single orbit with an increase in apogee altitude of up to 7000 naut mi. A change of this magnitude is predictable for the first orbit, but, because of the orbital period uncertainties shown in Fig. I-13, could not be accurately predicted for later orbits. Thus, the available launch window would have to be reduced to ensure at least a long period increase of over 2000 naut mi by the end of the first lunar month plus the possible failure at the end of 6 mo when the solar periodic perturbation tends to return the perigee to its near injection altitude level. On this basis, the practical upper limit on apogee altitude should be in the 160K to 165K naut mi region, somewhat lower than the 170K naut mi example, to reduce the possible single orbit perturbations, particularly if the close spacecraft-to-moon encounter occurs when the moon is near its orbital perigee. The question of short period lunar effects is presented in more detail in Appendix I-2.

Referring, once again, to Fig. I-13, it is apparent that the nominal apogee radius should be approximately 150K naut mi for the Atlas/Agena launched spacecraft and 125K naut mi for the Atlas/X-259 launched spacecraft. The potentially wide range of apogee altitudes which might result from the X-259 injection accuracy, coupled with the low nominal apogee radius (and potentially lower -3σ apogee) were some of the factors which led to the conclusion of lower probability of satisfactorily achieving the mission objectives with this launch vehicle.

On the basis of this analysis, the nominal launch vehicle selected was the Atlas/Agena using the direct ascent technique. The nominal orbit is the 200 x 150K naut mi orbit inclined 31 to 33 deg to the equatorial plane.

Although the analysis suggests an upper limit on the nominal apogee radius, this is not to say higher apogee missions cannot be flown as special purpose missions after the initial data are satisfactorily obtained. It is possible to obtain limited launch windows for orbits with apogee radii as great as 190K naut mi by either selecting orbital periods and orientations which avoid close spacecraft-to-moon encounters or purposely using the moon to get very large perigee altitude increases (10K to 15K naut mi) on the first orbit coupled with large secular soli-lunar perturbations. Such missions require separate mission planning in considerable detail, however, and were not within the scope of this task.

5. Flight Profile

The planning of a specific mission must start within the framework of a launch window covering a long period of time (6 mo to 1 yr). Such a window must reflect not only the orbit lifetime requirements (as shown), but also spacecraft subsystem and experiment constraints. With this preliminary data, the task of coordinating mission requirements, and the availability of the launch vehicle, launch pad, and tracking network,can proceed.

An example of such a window (without lunar periodic perturbations) is shown in Fig. I-14. The window reflects not only the orbit lifetime constraints, but also subsystem constraints such as maximum eclipse time for electrical power generation or thermal control. In both cases, the design spacecraft can tolerate 4 hr per orbit with ample margin. A typical eclipse time per orbit over the first 200 days of the mission is shown in Fig. I-15 for launches on 1 October 1964 and various injection times. One launch time, 8 hr (UT), has a single spike of 6 hr eclipse with no other eclipse during the year. Although this falls outside the boundary shown in Fig. I-14, it could, in fact, be tolerated. This does indicate that subsystem constraints on a launch window are subject to judgment if other conditions make launching at a given time important.

Another potential simplifying feature which could be designed into the electrical power and thermal control subsystems is a restriction on spin axis orientation to the sun. This is not the case for the design spacecraft (which tumbles rather than spins), but such a design constraint could be made. By ensuring high orbit inclination to the ecliptic, the number of solar cells required would have been reduced. An example of such a constraint is also illustrated on the launch window (Fig. I-14).

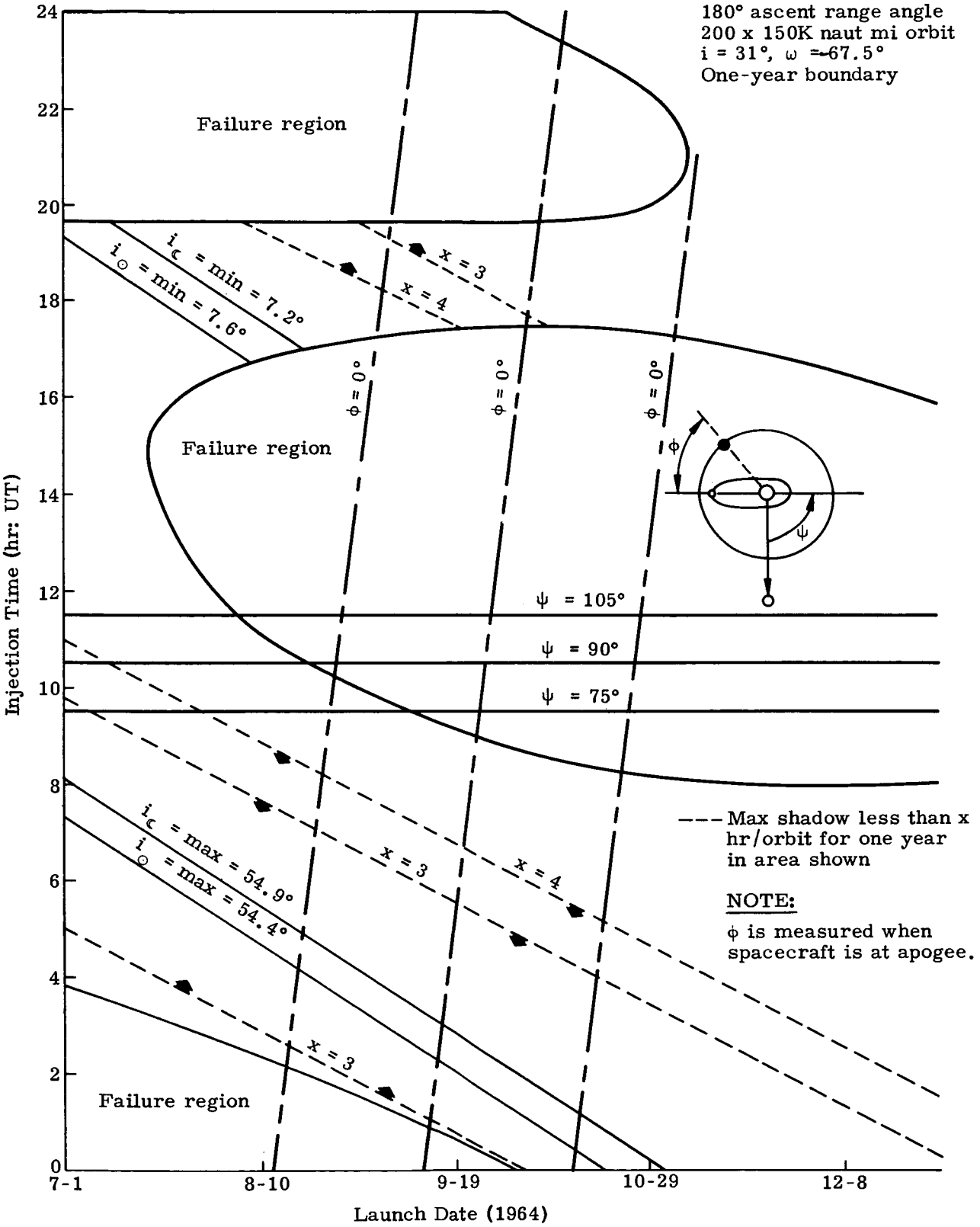

Fig. I-14. Launch Window

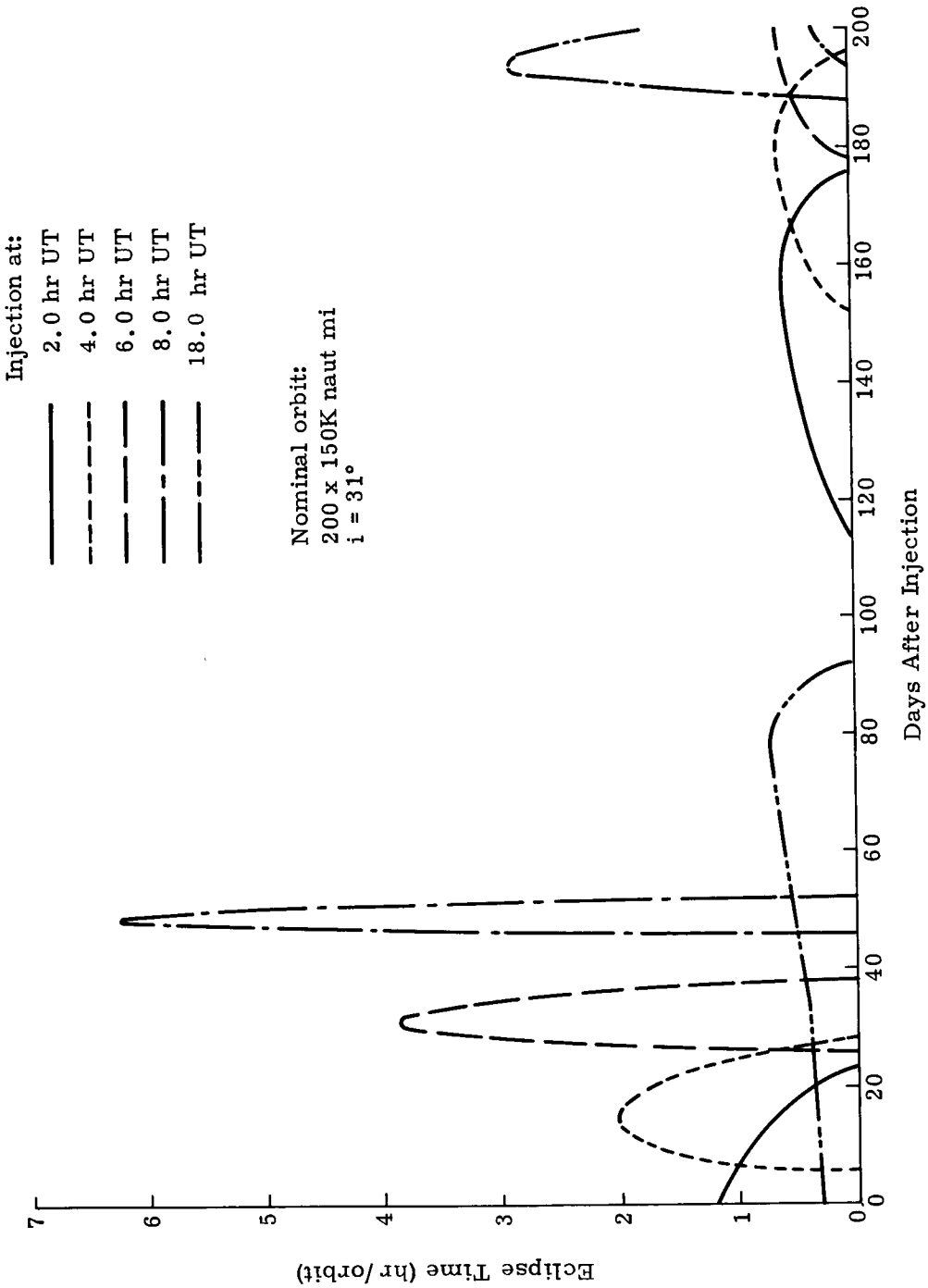

Fig. I-15. Eclipse Time History (inject epoch = 10/1/64)

Possible, but not probable, experiment constraints could be orbit orientation to the earth-sun or earth-moon lines. The former might be used to investigate the so called lens effect. The latter might be used to investigate the variation in micrometeoroid density as a function of moon position relative to earth. Typical constraints such as these are also illustrated in Fig. I-14.

Once the detailed launch window is fixed and the actual launch period is set, the detailed Flight Operations Manual must be formulated. This can best be presented by example. However, two generalizations have been made in the interest of brevity. First, only those functions peculiar to the Micrometeoroid Deep Space Satellite vehicle itself are emphasized. Items relative to the launch vehicle and prelaunch checkout have been purposely minimized. Second, even items relative to the satellite are not covered in complete detail where the detailed information is available in other sections of this report.

The flight operations manual will list the functions (or actions) required by ground personnel during the course of the mission to ensure success. These functions include both normal actions as a function of time as well as reactions to emergencies arising from malfunction onboard the spacecraft. An example of such a manual is presented in Table I-1.

The functions described in the table indicate the simplicity built into the conceptual design presented in this report. In normal operation, the number of commands which will be sent from the ground are minimal and include, primarily, only those required for range and range rate tracking and data playback. All spacecraft operations through launch are automatically programmed with both a primary deployment timer initiated at Agena separation and a backup timer initiated at liftoff. The primary transmitter is linked directly to the solar cells and starts operating as soon as the cells become active after paddle deployment. The secondary transmitter works directly off the battery until the solar cells become activated. Ground commands are not required for these operations.

The sequence shown in Table I-1 is only carried up to the Orbital Operations Phase. A detailed description of the orbital operations relative to communication and data readout is presented in Vol. I, Chapter II.

TABLE I-1

Typical Flight Operations Manual

Time	Altitude (naut mi)	Function or Event	Ground Station Coverage
Prelaunch Phase			
Continuous	0	Monitor system status	
-10 min		Initiate final systems check. Readout. Real time housekeeping data.	
-1.5 min		Switch to internal power	
-2.0 sec		Engine light-up	
-1.5 sec		Initiate backup deployment timer; switch over to telemetry deployment format transmission mode.	
-1.0 sec		Separate umbilical	
Launch Phase			
0	0	Liftoff; initiate launch vehicle tracking	Cape Kennedy
132 sec	33	BECO	
133 sec		Booster engine separation	
280 sec	118	SECO and shroud separation. Monitor antenna erection	
316 sec	137	VECO	
317 sec		Sustainer separation	
371 sec	161	Agena ignition	Antigua
614 sec	200	Agena cutoff	

TABLE I-1 (continued)

Time	Altitude (naut mi)	Function or Event	Ground Station Coverage
Orbit Insertion Phase			
616 sec		Agena separation	
630 sec	215	Restraining bands blown; deployment sequence initiated	
0.5 hr	1500	Verify completion of deployment sequence; initiate azimuth elevation tracking; monitor data	Johannesburg
0.7 hr	4000	Command R&RR beacon on; initiate R&RR tracking	Madagascar
1.0 hr	7000	Terminate R&RR tracking	Madagascar
		Monitor switch-over from deployment mode to telemetry data mode	Johannesburg
Orbital operations phase			
NOTE: This phase covered in detail in Section III			

II. POWER SUPPLY AND DISTRIBUTION

E. Warren Colehower

II. POWER SUPPLY AND DISTRIBUTION

1. Constraints and Design Philosophies

Concept development and the subsequent design of a solar array/battery power system has followed the requirements defined in the statement of work for the MDSS relative to the use of an Atlas/Agena launch vehicle.

The selected orbit, with a nominal apogee of less than 160,000 naut mi, results in the vehicle being in sunlight approximately 99-3/4% of the time, regardless of time of injection. Approximately 62% of the launch windows that permit a 1-yr orbital lifetime will result in orbits having a maximum of 4 hr of earth shade. The capacity of the battery has been selected to furnish the full requirements of the system for 4 hr at a depth of discharge not exceeding 60 to 70%. Thus, the power requirements during the shorter boost phase (ascent) period during launch and cislunar orbital injection are met with adequate reserve capability.

The power supply and distribution system has been designed to be compatible with the telecommunication system (described in Volume II, Chapter II). Solar array capacity has been determined so that two data transmitters may be operated continuously, thus providing high reliability, and the greatest possible operational flexibility.

Each of the two continuously operating data transmitters is furnished power from separate power systems. One of the systems is supported by a battery, the other, without a battery, operates only when in sunlight (99-3/4% of the time).

The solar cell arrays have been located on the deployed vehicle so that sufficient power is available independent of vehicle attitude.

2. Power Requirements

The continuous loads of the primary system (for daytime transmission of penetration counts) and the secondary system (continuous transmission of penetration counts or transmission of stored data on command) require 26.20 and 37.42 w, respectively. Reserve, losses and battery charging when added to the continuous requirements result in a 28-v d-c requirement of 31.20 and 47.55 w, respectively from a solar array or 37.61 and 54.48 w from radioisotope-thermoelectric generators, if used. These requirements are based on the use of 28-v d-c transmitters. The requirements are slightly higher if a 50-v d-c input transmitter is used. Since the transmitters consume 75% of the system power required, minimum voltage conversion and maximum reliability will be realized if the power system voltage is selected to match the input voltage requirements of the transmitters. Intermittent loads for both systems and shade period requirements of the solar cell system have been included in the respective battery charging requirements.

Subsequent to the completion of the design of the finalized power systems, a more efficient 28-v d-c transmitter has been located. Its use would reduce the vehicle power requirements to about 3/4 of the aforestated values.

A. CONCLUSIONS AND RECOMMENDATIONS

1. Power Source Selection

The application of four space proven SNAP-9A radioisotope (Pu-238)-thermoelectric units to this mission has been compared with the use of an N/P silicon solar cell system. For this mission, with the satellite being almost continuously in sunlight, the solar cell system would be approximately 42 lb lighter than the isotope system, even including a 34.5-lb battery. Since both systems would be of comparable reliability, and since the isotope system does not offer any outstanding features for this particular mission, the lighter weight, nonradiative solar cell system has been selected.

Although all results shown in this report are based on the use of a nickel-cadmium battery, the use of a silver-cadmium battery should not be disregarded. More operational and laboratory test experience is available on the nickel-cadmium battery; however, the silver-cadmium cell offers a weight advantage and its low rate charge and discharge characteristics are most appropriate to this mission.

2. Selected System Description

Two solar cell systems have been selected, one applicable to transmitters requiring a 28-v d-c input and the second for transmitters requiring 50-v d-c input. The basic bus voltage of each system is the same as the transmitter voltage input.

Table II-1 is a summary of the characteristics of these alternative systems. Each has a separate primary and secondary power system containing identical continuous loads, reserve (installed growth), and line losses from the bus to the equipment. The primary systems contain a simple voltage regulator consisting of zener diodes. The secondary systems contain a high efficiency (95%) pulse width modulation type voltage regulator of redundant solid-state devices, capable of maintaining the bus voltage within 1% of the desired setting. Multiple voltages required in the secondary system are obtained from redundant converters powered from the ±1% bus. In the 28-v d-c system, the high voltage requirement (50 v) of the capacitor sensors is furnished by voltage boosters. The battery is charged at a constant current by a charge limiter at a 300-hr rate, thus returning the energy taken by the bus during shade periods and by intermittent loads that exceed the capacity of the array.

TABLE II-1
Final Power Supply Comparison Summary

Item	Notes	Transmitter and System Voltage			
		28-v/d-c		50-v/d-c	
		Primary	Secondary	Primary	Secondary
Continuous loads*		26.20	37.42	26.20	37.42
Reserve	~10%	2.54	3.98	2.54	3.98
Losses--lines to equipment	~3-1/2%	1.01	1.46	1.01	1.46
--voltage regulator	Primary 1 ma/zener Secondary eff = 95%	0.84	1.83	0.93	1.83
--converters	25% of load	0.46	1.25	1.01	3.02
--boosters	22/50 x 25% of load	0.15	0.15	--	--
Battery charging	37 ma/22 ma total	--	1.30	--	1.36
Charge limiter loss	η = 89.5%/86%	--	0.16	--	0.22
System watts required from array		31.20	47.55	31.69	49.29
Vehicle watts required from array		78.75		80.98	
Array					
Installed capacity, watts		31.2	54.0	31.9	53.5
Installed growth (including reserve), watts		2.54	10.43	2.75	8.2
Available unused array area, watts		18.8		18.8	
Minimum average number of illuminated strings		20	28	12	16
Number of 1 x 2 cm cells/string		81	100	138	173
Minimum array voltage		30	37	51	64
Battery					
Typical discharge, w-hr			50		50
Maximum discharge, w-hr			214		223
a-hr			7.1		4.2
Total installed battery capacity, w-hr			360		318
a-hr			12		2 x 3
Constant charge rate, ma			37		2 x 11
hr			325		273
Weight, lb			34.5		41

*Intermittent loads included in battery charging.

Power system growth capability of 42% has been provided by two means, by installing a small excess capacity and by provision on the structural areas reserved for solar cell arrays for the addition of more series strings of cells to either the primary or secondary section of each array area. Contrary to present trends, the smaller solar cells (1 x 2 cm) are recommended in order to preclude excessive loss of power in the event one string becomes inoperative.

Standard capacity nickel-cadmium cells have been selected, 12 and 3 amp-hr, respectively, for the two secondary systems. A 4-hr discharge will use only 59% or 70% of the battery capacity, respectively.

Power system reliability and vehicle reliability are enhanced by the provision of two independent power supplies. The primary system has a simple and reliable method for voltage regulation and for furnishing the low voltage needs. All its loads are directly connected, and a battery has been excluded. The secondary system contains redundant voltage regulation and conversion, and equipments are fused when redundant. Fortunately, the weights entailed by these facets that create a highly reliable power supply have been permitted by the payload capability of the Atlas (SLV-3)-Agena D launch vehicle and the efficient design in other vehicle systems.

3. Recommendations

For purposes of standardization and for a more flexible design, it is recommended that a transmitter requiring an input voltage of 28 v d-c be used.

It is recommended that the development and test of hermetically sealed silver-cadmium cells, applicable to this mission, be actively encouraged.

B. TECHNICAL DISCUSSION

1. Constraints, Requirements and Ground Rules

The design of the power system has been constrained by the booster and power supply requirements of the MDSS conceptual study statement of work. The power system developed herein has been based on the use of an Atlas-Agena launch vehicle only. The requirement to study the feasibility of an N/P silicon solar cell, nickel-cadmium battery power supply system and the requirement to study the feasibility of other power supply systems have been satisfied.

The selected orbit imposes constraints on the electric power system. For a deployable solar cell system, the duration of the shade period will determine the battery size if the watt-hr for the maximum shade period is greater than that for the launch to deployment period. Data on earth shadow characteristics for the first 200 days (4800 hr) after injection is summarized in the following table for 5 typical times of injection.

Time of Injection (UT)	Total Shade in First 4800 Hours (hr)	Longest Shade (hr)	Orbits Shaded in First 29 (quantity)
2.0	6.44	1.05	13
4.0	8.36	1.95	11
6.0	7.45	3.75	5
8.0	6.25	6.25	1
18.0	11.1	2.85	17

From the table it may be concluded that, under worst conditions, the total shade duration is less than 1/4% of the total mission duration, the longest shade period exceeds 6 hr, and the longer shade periods occur less frequently. The longer shade periods occur on orbits having a greater perigee sensitivity, as shown in Volume III, Chapter I. Typical injection times over a 180-day period may be grouped as

Unusable--mission life less than 1 yr	45%
Marginally usable and shaded more than 4 hr	21%
Usable and shaded less than 4 hr	34%

Of the injection times that permit a 1-yr orbital lifetime (the latter two items above), 62% have an earth shade of less than 4 hr. Similarly, it can be shown that the longer earth shade periods occur on orbits of subminimal duration. A maximum shade period of 4 hr has been accepted as a power system constraint for study purposes.

Since sunlight is available for at least 99-3/4% of the mission, battery charging could be accomplished at a very slow rate, thus requiring a minimum of array power. The effect of constraining battery charging to low rates is discussed in Section B2.

Micrometeoroid penetration and impact data acquired could be telemetered to the earth, including data repetition, on a part-time transmission basis. The average power required by the transmitter would be considerably less than that required by continuously operated transmitters. However, to improve the reliability of data communication

and to provide flexibility in the duration of data transmission, the power supply has been designed to the constraint of furnishing power to one transmitter continuously, day or night, and to a second transmitter, during daytime only (99-3/4% of the time).

The configuration of a vehicle having large deployed areas inherently determines and, at the same time, simplifies the configuration of an applicable solar array. If the solar array can be included in the capacitor sensor panels, the deployment of the panels will also result in the deployment of the solar array, thus improving mission reliability. For structural simplicity and to avoid shadowing the capacitance sensors, the solar array must be coplanar with the sensor panels. Thus, part of the array may be shadowed by the "wings" of the spacecraft containing other parts of the array and the capacitor sensors.

Solar array area determination has considered both spinning and tumbling vehicles. None of the systems onboard the spacecraft require attitude control, only attitude sensing. The smallest possible array would have to be solar oriented, thus requiring the addition of an attitude control system. The additional system would reduce mission reliability. Since we are considering a mission duration of 1 yr, the smallest array for a spinning vehicle would require that its spin axis be perpendicular to the ecliptic. The Agena could accomplish reorientation after injection and prior to spinup; however, these additional requirements imposed on the Agena would reduce mission reliability, compared to a randomly oriented vehicle. Theoretically, the solar cell area of a tumbling vehicle compared to a spinning vehicle is only $4/\pi$ or 27% greater (sphere versus a cylinder). In the case of a cubic array, the ratio would approach 6/4 or 50% greater.

In order to provide maximum mission reliability and a more adaptive power system, an omnidirectional solar array has been accepted as a design constraint, thus providing adequate power independent of vehicle orientation.

2. Preliminary Design Considerations

a. Transmission duty cycle

Prior to making the decision to provide dual continuous transmission, Table II-2 was prepared to evaluate the effects of transmission duty cycle. This figure shows the vehicle power requirements estimated at that time. The miscellaneous equipment values of 2 and 7 w represent the average power required by all onboard equipment except transmitter and battery for a minimal and nominal design, respectively. These values have since proved to be underestimated; however, the total array watts reveal the gross effect that a 2-hr per 144-hr transmission duty cycle has on the array area, weight and cost. The difference

TABLE II-2

Transmission Duty Cycle Effect

Number of Transmitters in Use at Any One Time		Continuous Daytime Orbital Transmission Only			1.4% Duty Cycle Transmission 2 hr/144		
		1	2	3	1	1	
Watts**	Transmitter (6 watts radiated)	24	48	72	0.33	0.33	
	Misc equipment	2	7	7	2	7	
	Battery charging	0.5	1.1	1.1	0.5	1.1	
	Total--at single bus	26.5	57.1	80.1	2.83	8.43	100
	Total--array	159	343	481	17	51	600
Array	Total cell area (sq ft)	19.5	41.8	58.7	2.08	6.1	73.3
	lb/sq ft cell area	0.63	0.63	0.63	0.36	0.36	0.63
	Total weight (lb)	12.3	26.3	37.0	0.75	2.2	46.1
Battery	Rated capacity (a-hr)	<1	1	1	3*	3*	
	Weight (lb)	3	4-1/2	4-1/2	10	10	
Array cost/vehicle ($)		66,000	140,000	200,000	7000	21,000	250,000
Number of solar array sections		1	2	3	1	2/2	
Total power required from array		26.5	65.2	96.3	2.83	8.8	

Assumed total cell area equals 6 times required solar intercept
8.2 w/sq ft
0.36 lb/sq ft--cells only, one side
0.54 lb/sq ft--paddle structure
} 0.36 + 0.54 + 0.36 = 1.26 lb/sq ft for two-sided panel
Max: 4-hr shade (no transmission)
Avg: 1-hr shade
No transmission during ascent except as noted

*Includes capability of 1-hr transmission in shade or ascent.
**Estimated values, exclude losses.

between "watts-total-array" and "total power required from array" results from the provision made in the system to furnish the miscellaneous equipment and battery charging from any one of the number of solar array sections specified. In deference to the array size, cost and weight savings offered by a limited transmission duty cycle, transmission reliability and transmitter thermal cycling requirements have determined the need for continuous transmission by all active transmitters.

b. Battery low charge rates

In contrast to batteries used in low altitude earth orbiting vehicles, the battery in this application will not be subjected to the problems of rapid charging. Instead, it may encounter slow charge problems, especially if charging is spread over the 140-hr minimum sunlight period. A given number of watt-hours may be returned to the battery at a lower wattage if the charging hours are kept at a maximum. Consequently, minimum power is required of the solar array if charging is accomplished at the low rate.

Gulton Industries have reported (Fig. II-1 curve, Gulton M0475) that their VO-6HS cells lose capacity at charge rates slower than the 12-hr rate. For example, Fig. II-1 shows that only 50% rated amp-hr capacity would be available after charging at the 60-hr rate. Charging was accomplished with a total input of 145% of rated amp-hr capacity. The net battery amp-hr efficiency, therefore, was 34.5%.

The Martin Company has tested (Ref. II-1) nickel-cadmium vented cells of various manufacturers in the 3-, 5- and 8-amp-hr sizes at 350- to 1100-hr charging rates. At room temperature after charging 21 cells for 240 hr at the 350- to 570-hr rate, 67% of the rated amp-hr capacity had been inserted. When discharged at a 2-hr rate, the average capacity available was 51% of rated capacity, resulting in an average charge efficiency of 76%. By extrapolating the 67% and a 47% and 20% insertion to 130% (representative overcharge), pessimistically the available capacity would approximate 66% of rated capacity, as shown by the square point in Fig. II-1. The resultant amp-hr efficiency would be 51% at a 350- to 570-hr charge rate. At -20° F the amp-hr charge efficiencies approached 100%.

A Martin-built, radioisotope powered data telemetry package (Ref. II-2), buried in Axel Heiberg Island (Arctic), has operated for more than 3 yr. Each year the 11 amp-hr battery has been removed and tested for available capacity. Each of the three successive batteries used was fully charged after one year of operation. Although the depth of discharge is only 1.2% of rated capacity, the amp-hr charge efficiency is 68%. Battery temperature remains between the limits of 40° and 80° F. This operation is shown in Fig. II-1 at the 96-hr charge rate.

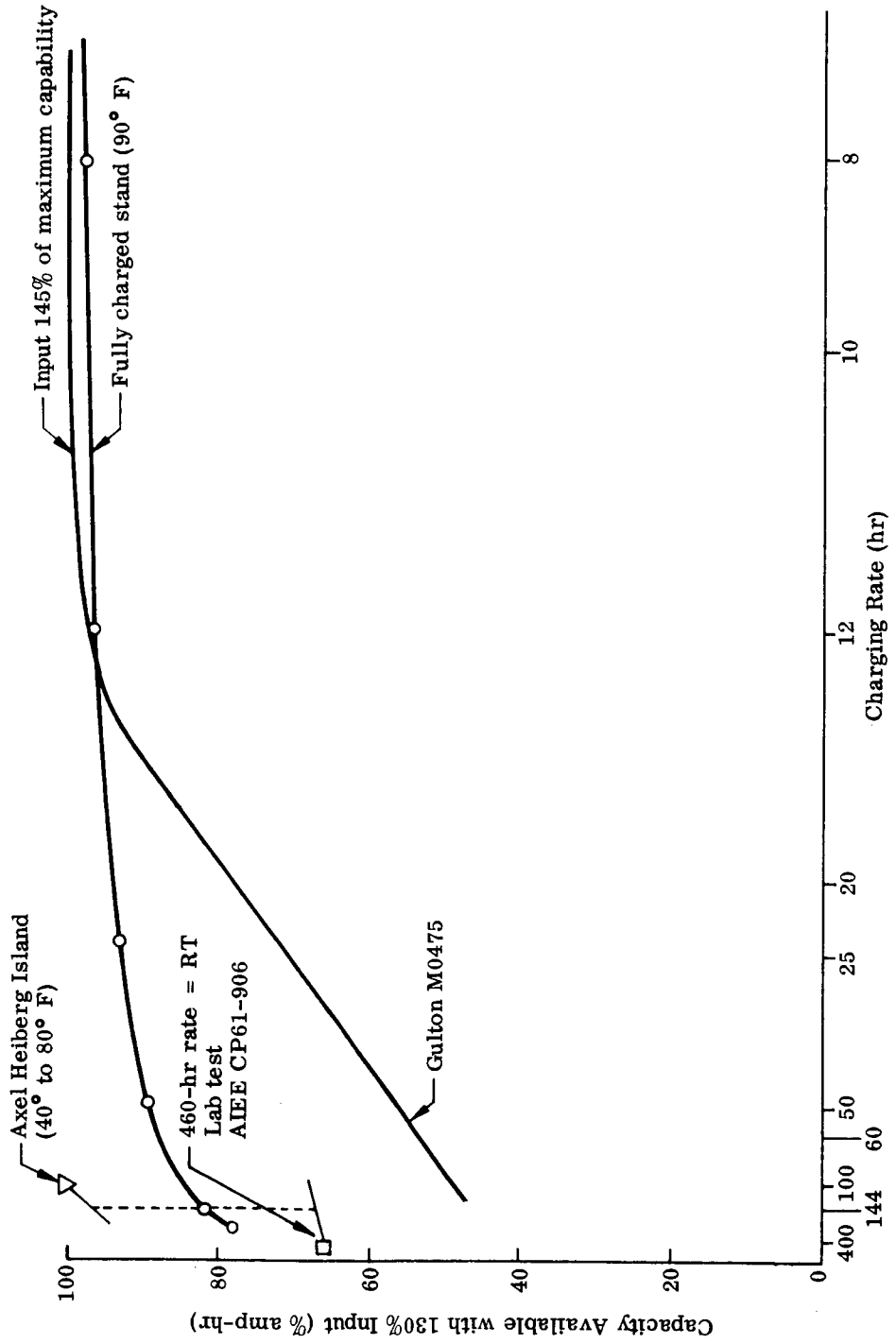

Fig. II-1. Nickel-Cadmium Battery Charge Rate and Stand Characteristics

From these three sources of information, it can be seen that a nickel-cadmium battery when applied to the MDSS orbit conditions should furnish between 70 and 95% of rated capacity if battery temperature does not exceed 80° F.

In view of the ability to charge at very low rates, and considering the probability that the battery could be continuously charged for upward to 140 days, charge current control has been incorporated. The proposed charge limiter would be a constant current device set at a value such that after a maximum discharge sufficient amp-hr would be returned to the battery to cover the next shade period and the succeeding system overload experienced during the first part of the charging interval. After a maximum shade of 4 hr, 2.4 hr of shade will be experienced on the next orbit followed by 5 hr at "full attitude read-in" power levels. Battery rated capacity has been determined by permitting only a 60 to 80% maximum depth of discharge at any time and selecting amp-hr sizes previously used on other satellites. The maximum charge rate therefore need only return upward to 46% of rated capacity. A hermetically sealed nickel-cadmium battery at 80° F can be overcharged continuously at the 10-hr rate. The charge limiter safely restricts the charging current to a 300-hr rate.

c. Distribution system characteristics

In order to provide high reliability of data transmission, three independent transmitters have been employed: Transmitters 1 and 2 are operating continuously, while Transmitter 3 is on standby as a redundant unit for Transmitter 2. To maintain a consistent philosophy, the power supplies for the active transmitters and their respective signal conditioners and data format generators have been furnished power from two independent portions of the solar array. These components are shown on an early concept of a 28-v d-c power and distribution system, Fig. II-2. The daytime transmitter and its 50-v booster (if required) receive power from the primary array, while Transmitter 2 or 3 receives power from the secondary array or the nickel-cadmium battery. The daytime Transmitter in the primary system is not supported by a battery, since array power is available at least 99-3/4% of the time. The primary data processing subsystem receives power from the secondary system battery via the dual feed bus during shade periods. The addition of a battery to the primary bus would reduce the reliability of the primary system 99-3/4% of the time and would improve primary system reliability only 1/4% of the time.

The dual feed bus also feeds one of the two command receivers. During the early phases of the study, it was assumed that commands would be required prior to deployment and that the battery would feed a minimum of loads during ascent, e.g., only two command receivers and a beacon transmitter. Since then the battery has been increased

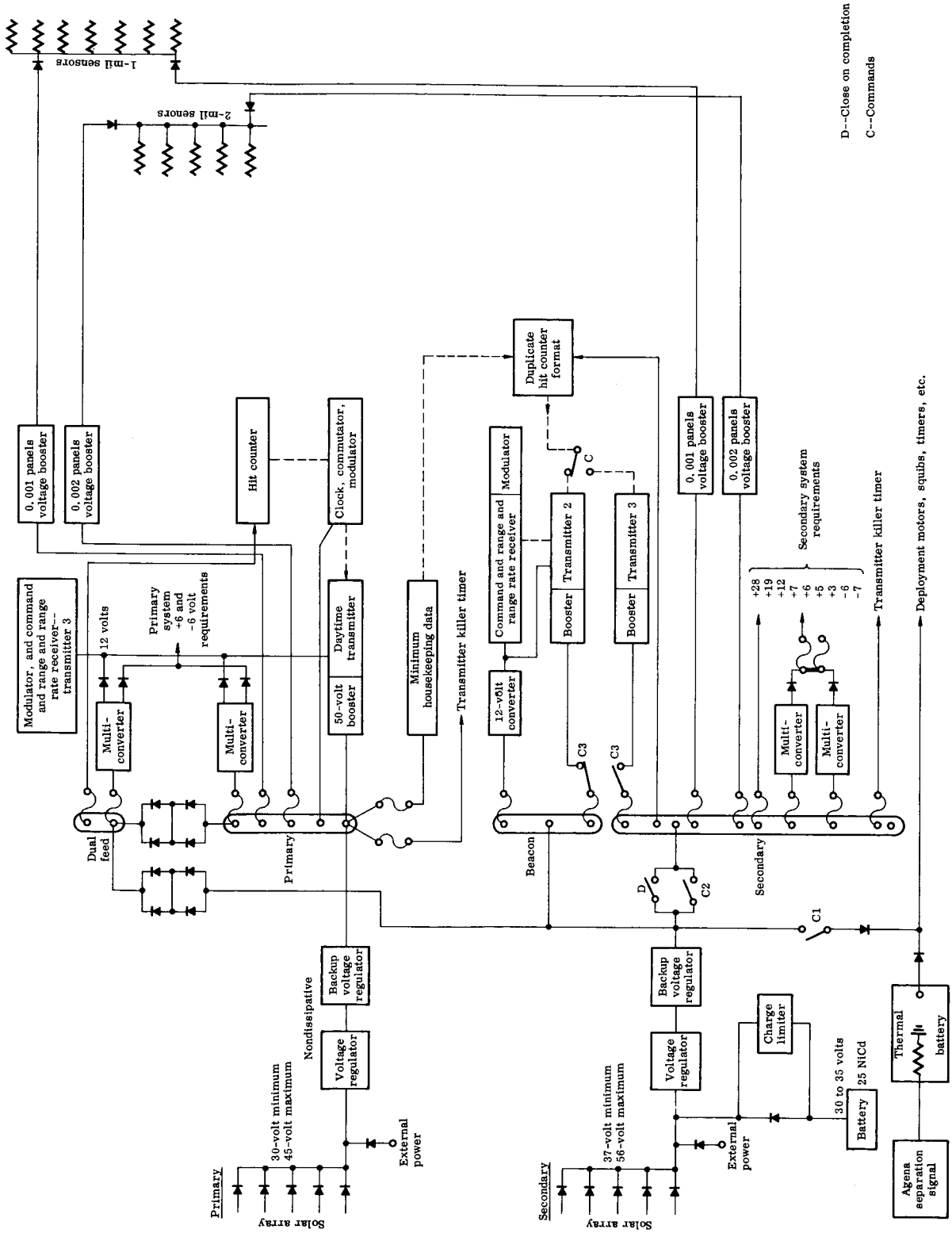

Fig. II-2. Preliminary 28-Volt Power System Using 50-Volt Transmitter

in size to power the entire secondary system during ascent, thus eliminating two functions (C and D of Fig. II-2). Since vehicle weight is not critical, the improvement in reliability was worth the battery weight increase.

In order to be assured of penetration counts from the capacitor sensor panels during sunlight and/or shadow, all the panels of one gauge are energized by either of two redundant voltage boosters (charge generators), both independently powered from the two power systems. This arrangement is repeated for all the panels of the other gauge. Intersystem damage is minimized by isolating the two power feeds by diodes.

d. Voltage conversion

On Fig. II-2, a partial attempt was made to integrate the multivoltage requirements. Multiconverters for each power system, redundant to each other, had their respective output windings isolated from each other by means of double diodes. These diodes in turn back up the diodes in the rectifier section of each converter. All outputs feeding multiple nonvital loads or redundant loads would be fused so as to limit the damage caused by equipment failure. Note that all loads on the dual feed bus are fused, whereas single item loads on the primary bus, such as the daytime transmitter, are not fused.

Subsequent load analyses are summarized in Table II-3. The continuous loads for the respective system buses and for the dual feed bus are shown for a 28-v d-c system using a 50-v transmitter. Under the 50/12-v d-c system, the 50-v loads have been separated from the total requirements; the 12-v columns include all loads not requiring 50 v. Adding the corresponding conversion, line and regulation losses, battery charging, etc., to the two types of distribution systems (28- and 50/12-v d-c systems) reveals that the total power required of the 50/12-v d-c system be 10% less than that of the 28-v d-c system (using a 50-v d-c transmitter). The difference is caused by lesser conversion losses in the latter system. A review of Fig. II-3 reveals a simpler voltage distribution system, but a more complex battery system.

e. Battery quantity

For the 28-v d-c system, a single, 25-cell, nickel-cadmium battery was provided (Fig. II-2). Since the higher voltage system (Fig. II-3) requires nearly twice as many cells in series, redundant 38-v batteries were provided in series with a single 14-v battery. Thus, the reliability of the battery system in the 50/12-v system (with 44 series cells partially redundant) and the 28-v d-c system (with 25 nonredundant series cells) would be approximately equal. When multiple batteries were used (Fig. II-3), each was provided with its own charge limiter.

TABLE II-3

Preliminary Power Supply Comparison Summary Using 50-Volt Transmitter

		28 v d-c System		50/12 v d-c System			
				Primary		Secondary	
	Notes	Primary	Secondary	50 v	12 v	50 v	12 v
Continuous loads*--system bus only		24.61	30.68	23.00	1.61	23.0	7.68
--dual feed bus		1.78	1.78	1.35	0.43	1.35	0.43
Losses--12-volt converter	η = 80%	0.32	0.46	--	--	--	--
--multiconverter	η = 80%	0.16	1.54	--	0.16	--	1.54
--22-volt booster	η = 91%	2.68	2.68	--	--	--	--
--equipment line	4%	1.18	1.50	0.97	0.09	0.97	0.39
--voltage regulator (pair)	5%	1.48	1.86	1.22	0.11	1.22	0.48
Unknown loads (including conversion)	10 to 12%	2.79	4.59	2.26	0.30	2.85	1.14
Battery charging		--	1.72	--	--	0.58	1.07
Battery charger limiter losses		--	0.19	--	--	0.13	0.17
Total system watts		35.0	47.0	28.80	2.70	30.10	12.90
Total watts from array		35	47	20.5	11	21.5	21.5
		82		74.5			
Minimum array voltage		30	37	38	14	47	19
Total battery capacity: amp-hr		--	8.05	--	--	2.21	9.86
w-hr		--	242	--	--	71	118
Battery constant charge rate: ma		--	49	--	--	10	73

*Intermittent loads included in battery charging.

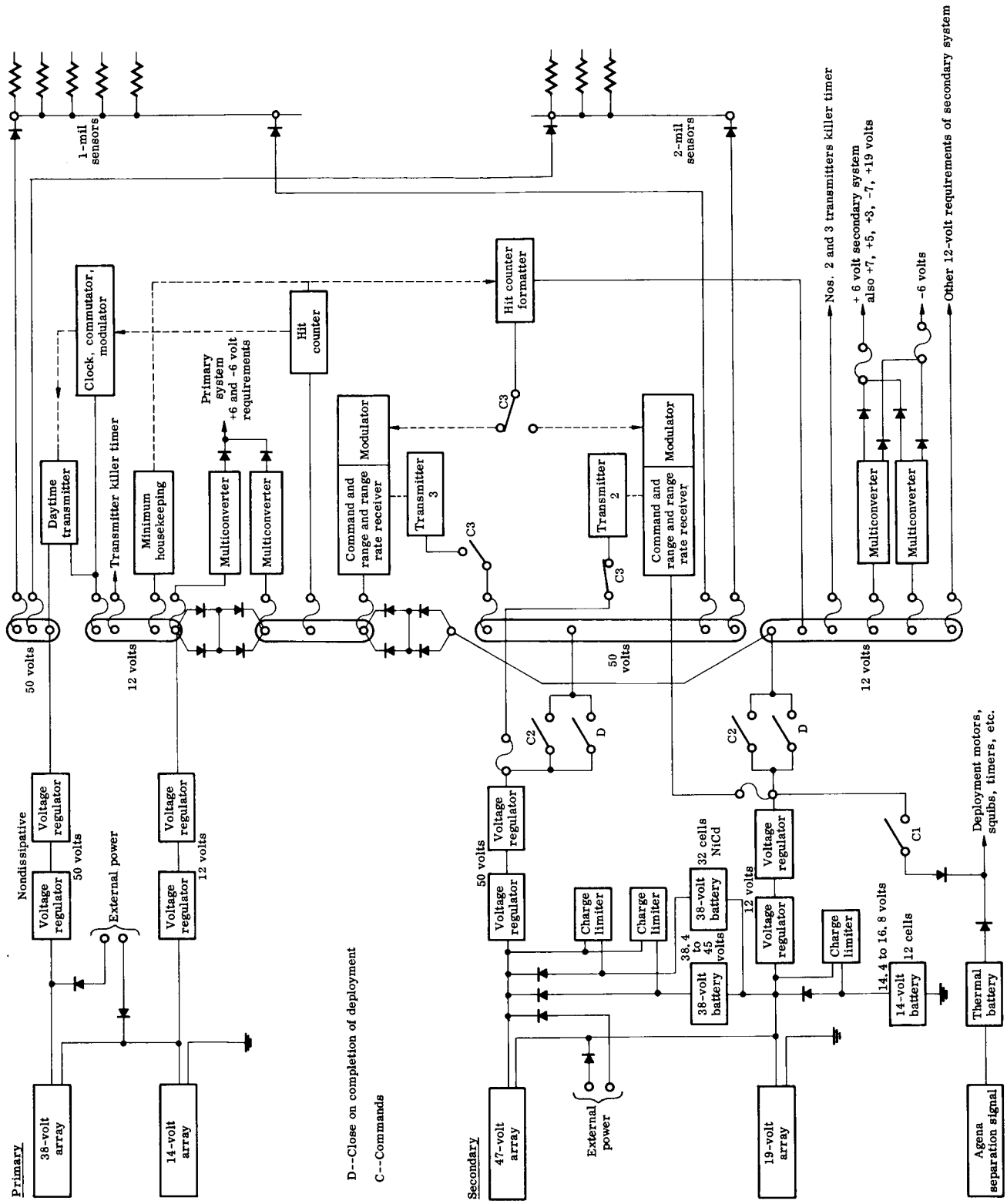

Fig. II-3. Preliminary 50/12-Volt Power System Using 50-Volt Transmitter

f. Voltage regulation

The efficiency of series or shunt voltage regulators is poor when excess power is available. They also present a thermal dissipation problem when the excess power is not used. Pulse width regulators have a much higher efficiency under all load conditions and do not require the dissipation of excess power not required by the system. These nondissipative-type regulators, however, are more complex than a simple zener shunt and require backup functions in order to duplicate the reliability of the simpler regulator. The filter sections need not be duplicated, only the solid-state devices. The distribution diagrams of this report show dual regulators to represent this backup feature.

As shown in Figs. II-2 and II-3, the voltage regulators are in full-time use, day and night, and therefore maintain the bus voltage within 1% when either the array or battery or both are in use. The number of cells in the batteries has been selected to produce approximately 2 v more than the bus voltage desired when the batteries are under load and 80% discharged. Part of the 2-v drop is across the battery discharge diode and part across the voltage regulator. The greater portion across the voltage regulator is not a power loss since the regulator causes a current transformation. Thus, when the battery is fully charged and its voltage is high, the battery current will be less than the load current.

The voltage regulator is capable of accepting a maximum voltage 50% greater than the minimum. This condition could be approached when the array re-enters sunlight after being shaded for 4 hr.

g. Solar array

On all secondary systems, the minimum voltage of the array has been selected to be 2 v higher than the maximum battery charging voltage required, the latter being 1.40 v/cell. At the 300-hr charge rate, a maximum of 1.40 v/cell will permit safe overcharge for batteries at a temperature as low as 0° F. The 2-v drop is required by the charge limiter for current sensing.

The minimum array voltage occurs when the array is at maximum temperature and when the solar cells have been degraded 5% by radiation damage at the end of the mission. At that time, vehicle motion is assured; consequently, the solar cells may reach only 43° C. Under these end-of-mission conditions, the voltage of each N/P solar cell under load will be 0.37 v. The number of cells in each string has been selected on this basis. The radiation damage power degradation allowance of 5% for these N/P solar cells with 6-mil microsheet coverslip is equivalent to an 8% degradation for P/N cells with 12-mil coverslip. IMP-A, using P/N cells and a 12-mil coverslip, experienced minor damage during the first two months in a similar orbit. Therefore, the 5% allowance is pessimistic, even for a 6-mil coverslip.

h. Deployment requirements

Deployment will be initiated by a signal from the Agena just prior to separation. Figures II-2 and II-3 show a thermal battery initiated by this signal. The thermal battery provides a reliable and independent source of power to fire squibs that release hold-down devices to operate deployment timers and to power the capacitor sensor panel deployment motors. In the event this power source fails to operate, a command could close switch C1, thereby independently obtaining power from the secondary system battery which is isolated from the thermal battery by diodes.

In an effort to reduce the number of command functions, the final distribution system now replaces the latter link by a second thermal battery initiated by a timer. The timer would be set to energize the second battery later than normal Agena separation but prior to secondary battery depletion. The latter restraint should also consider shadow period duration immediately subsequent to deployment.

3. Finalized Solar Cell System Description

a. Load requirements

The final system design has been based on the loads shown in Table II-4. Initially, the 6-w VHF transmitter required 24-w input at 50-v d-c. However, since then a 6-w transponder which accepts 28-v d-c has been located. The transmitters are shown as accepting either 50 or 28 v. Since the power required by the transmitters is more than 3/4 of the total vehicle power requirements, transmitter voltage selection greatly influences system generation voltage selection. Two final solar cell power systems are presented, one for 50-v transmitters and a second for 28-v transmitters.

The power required by the capacitor sensors is duplicated on both power supplies since they can obtain power from either system. The wattage values assume that 10% of the panels are permanently shorted and that they draw 1 ma each.

The attitude sensing and diagnostic loads are intermittent and are shown on a subsequent schedule. The primary system signal conditioner and data formatting units (counters) appear in both systems since they can obtain power from either system.

b. Voltage requirements

The loads shown in Table II-4 have been grouped and rearranged to produce Table II-5. The latter shows the total continuous (average) power required of the primary and secondary systems at various volt-

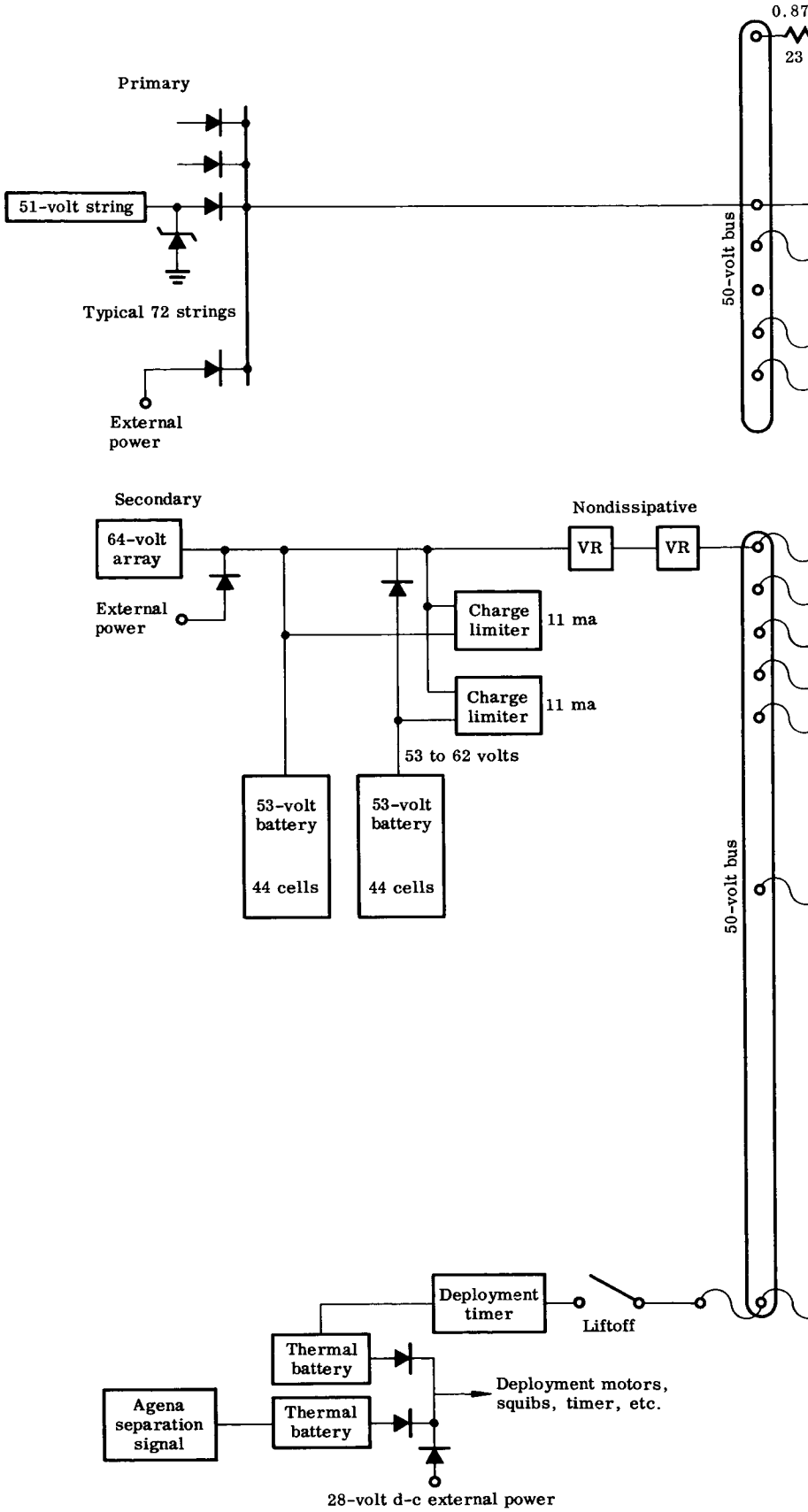
0.87
23
Primary
51-volt string
Typical 72 strings
External power
50-volt bus
Secondary
Nondissipative
64-volt array
VR
VR
External power
Charge limiter
11 ma
Charge limiter
11 ma
53 to 62 volts
53-volt battery
44 cells
53-volt battery
44 cells
50-volt bus
Deployment timer
Liftoff
Thermal battery
Deployment motors, squibs, timer, etc.
Agena separation signal
Thermal battery
28-volt d-c external power

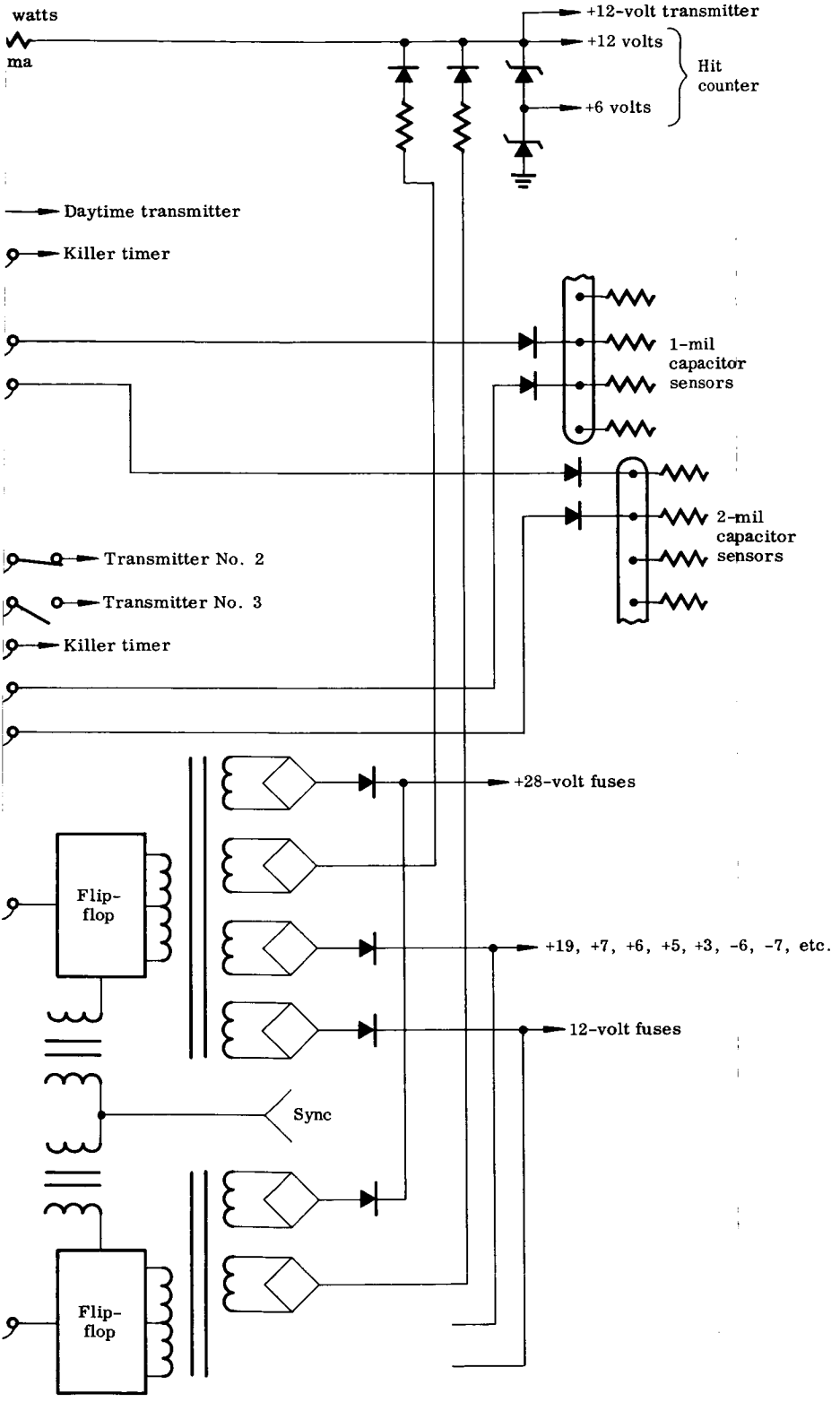

Fig. II-4. Final Power System Using 50-Volt Transmitter

TABLE II-4
Electric Loads--Final

Primary Power Supply

Equipment	Voltage	Watts per Unit	Units in Use at One Time	Continuous
Hit count transmitter	50 or 28 12	24.0 0.10	1 1	24.0 0.10
Subcarrier oscillator and modulator	12	0.10	1	0.10
Penetration detection unit	6	0.08	1	0.08*
Counters	6, -6	0.14	1 ps	0.14
Clock, commutator, formatter	6, -6	0.51/0.46	1	0.46
1-mil capacitance sensors	>50	1 ma (max)	120 ps	0.60
2-mil capacitance sensors	>50	1 ma (max)	144 ps	0.75
Killer timer	12 or 28	0.05	1	0.05

Secondary Power Supply

Equipment	Voltage	Watts per Unit	Units in Use at One Time	Continuous
VHF transmitter	50 or 28 12	24 0.1	1 1	24.00 0.10
Range, range rate and command receiver	12	0.17/0.16	2	0.32
Subcarrier oscillator	12	0.1	1	0.10
Command decoder	19 or 12	3.5/0.005	2	0.02
Command logic	12 or 28	4/0.005	1	0.01
Penetration direction and area detection unit	6	2.69/0.67	1	0.67*
1-mil capacitance sensors	>50	1 ma (max)	120 ps	0.60
2-mil capacitance sensors	>50	1 ma (max)	144 ps	0.75
Exotech sensors	12 or 28	7 w total	36 pairs	7
Capacitance and Exotech data unit	6, -6	2.37/1.01	1	1.01
Mariner gauges	12, 3, -7	0.2	3	0.60
Velocity gauges	12, 7	0.45/0.18	2	0.36
Mariner and velocity data unit	6, -6	1.72/1.56	1	1.56
Magnetometer	28	2	3/3	--
Solar aspect and earth sensors	12 or 28	1.0+0.5	6/6+5/5	--
Attitude data unit: hourly full	6, -6 6, -6	1.31/0.76 1.28/0.76	1 1	-- --
Diagnostic system	8 voltages	5/1	1	--
Diagnostic data unit: critical full	6, -6 6, -6	1.7/0 4.17/0	1 1	-- --
Memory units	6, -6	0.22/0.02	3/3	0.02
Killer timer	12 or 28	0.05	1	0.05
Master clock and divider	6, -6	0.33/0.32	1	0.32
Primary system counters	6, -6	0.14	1 ps	0.14
Memory system overflow	6, -6	0.47/0.46	1	0.46

*These late additions not included in subsequent totals.

TABLE II-5
Voltage Requirements--Final Loads

Load \ Voltage Required	Primary System (watts)					Secondary System (watts)						
	50 or More	50 or 28	28 or 12	12	+6 -6	50 or More	50 or 28	28 or 12	12	+6 -6	Misc	
VHF transmitter		24.00		0.10			24.00		0.10			
Range and range rate receiver									0.32			
Subcarrier oscillator				0.10					0.10			
Command decoder									0.02			
Command logic								0.01				
								(0.05)				(ascent only)
Timers--deployment and transmission		**	0.05				**	0.05				
Mariner and velocity gauges									0.58	1.56	0.38	
Attitude: hourly								(1.50)		(0.76)		3 min/hr store*
full								(3.50)		(0.76)		5 hr/orb store*
Diagnostic: deploy												
critical										(1.70)	(1.0)	1/3 sec/24 hr store*
full										(4.17)	(5.0)	1 hr/orb R.O.*
Capacitance and Exotech: counters					0.14					0.14 0.42		
other	1.35				0.17	1.35		7.00		0.59		
										(0.18) 0.48		2.53 hr/orb full R.O.*
Memory and overflow												
Master clock and divider					0.29					0.32		
Total, continuous	1.35	24.00	0.05	0.20	0.60	1.35	24.00	7.06	1.12	3.51	0.38	No losses
Total, nonsimultaneous maximum			Same			1.35	24.00	10.56	1.12	7.68	5.38	
				26.20					37.42			

*Alternate conditions, only one at a time.
**Timers may use 12, 28 or 50 volts.

ages. Intermittent loads and their duty cycle are also shown. The "total, nonsimultaneous maximum" values are shown in order to size voltage converters. The total continuous load on the secondary system of 37.42 w does not include intermittent loads or conversion, line, etc., losses. The intermittent loads will be included under battery charging. From this summary it will be noted that the greatest requirement is for 50 or 28 v, the second greatest for 28 or 12 v and the residue is minor. Consequently, in order to minimize voltage conversion losses and to improve reliability, the generated voltage should match the greatest load, the transmitters. If the transmitters require 50-v d-c, the 28- or 12-v requirements may as well be 12 v and join the other 12-v requirements. The preliminary 50/12-v power system (Fig. II-3) would still be appropriate; however, the generation and storage of two voltages complicate the system. The description of a 50-v system follows. If the transmitters require 28-v d-c, the 28- or 12-v requirements could be supplied 28 v, and a 28-v d-c system would be most appropriate. The description of such a system follows.

c. Power system using 50-v d-c transmitter

Distribution system. A final power system block diagram, shown in Fig. II-4, is applicable if 50-v d-c transmitters are used. It is further assumed that the capacitor sensor panels require 50-v d-c. This system is simpler than the 50/12-v system (Fig. II-3) since only one voltage need be generated, stored, regulated and distributed. Other voltages are obtained by conversion. Other refinements have been included which will be discussed in subsequent paragraphs. The ability of the primary system penetration counters and the capacitor sensors to obtain power from either system has been retained. The same circuit protection philosophy also has been retained.

Voltage regulation. Secondary system voltage regulation is identical to that described in paragraph B2f, that is, a pulse width modulation device, including backup of the solid-state circuitry, regulates the array and/or battery output. It has a net efficiency of 95% when the array is at minimum voltage, minimum power and will regulate the bus voltage within ±1%.

The primary system voltage regulator has been replaced by 72 small zener diodes, a minimum of 12 in use at one time. A nondissipative-type regulator is not required in the primary system since it does not include a battery. The array is the only source of power and it has only one minimum voltage at which it can be clamped. An array/battery system has a minimum voltage for both power sources. Clamping would have to be done at the greater voltage and the difference between these minima would produce an undesirable bus voltage variance.

The multiple zeners are located at the array upstream of the blocking diodes for two reasons: a shorted zener causes the loss of only one string and the excess power can be more readily dissipated at the array than in the equipment module.

Batteries and charge limiters. Two batteries and their respective charge limiters and discharge diodes have been included in order to provide reliability comparable to one 30-v battery. Shade periods of 4-hr duration have a low probability of occurrence; most shade periods will be of less than 1-hr duration. Redundancy of full capacity would cost approximately 40 lb, therefore the maximum discharge requirement has been divided between the two batteries. Either battery can supply power during most shade periods.

The pair of batteries has been sized to supply the entire secondary system for a period of 4 hr plus the full attitude read-in requirements for 5 hr (Table II-5) without exceeding a 70% depth of discharge. Each battery is composed of 44 hermetically sealed nickel-cadmium cells of 3 amp-hr capacity and each weighs approximately 20 lb.

The charge limiter is composed of a 6-v zener reference controlling a transistor which maintains battery charge current at 11 ma. When the charge limiter is applied to the 64-v array, 112 mw will be lost in each limiter, each battery receiving 680 mw, resulting in a net efficiency of 86%. At this low power level, efficiency improvement by using a more complex device is unwarranted.

The charge current setting has been determined by the method explained in Section B2, namely, the return of 2.4 hr of full bus load plus 5 hr of full attitude read-in over that portion of the sunlight cycle wherein charging may be accomplished (127/144 hr). Since only 46% of rated battery capacity is being returned and this is a maximum case, battery amp-hr efficiency has been assumed to approach 100% at a w-hr efficiency of 86% (53/62 v).

Voltage conversion. Requirements for voltages other than 50 v in the secondary system are supplied by either of two redundant multiconverters. In order to avoid spurious a-c signals onboard, the free-running flip/flops of the two converters can be synchronized by pulses from a frequency divider operated from the secondary system master oscillator. Each converter input is fused to provide protection to the 50-v bus in the event of an internally faulted converted. All output circuits will be fused or otherwise protected by current limiters downstream from the diodes used to isolate each converter. Intermittent loads would be powered from separate windings so as to minimize voltage variations of the continuous loads.

The power required in the primary system at +12 and +6 v is small; consequently complex converters are not desired. Figure II-4 shows these requirements regulated by zener diodes powered from the 50-v bus through a resistor. This simple and reliable regulation and conversion scheme although only 19% efficient causes only 1.01 w to be wasted. Further efficiency improvement at the expense of reliability is unwarranted.

Power from the two secondary system converters is fed to the two 6-v zeners through separate isolation diodes and regulation current limiting resistors. Thus the primary hit counter can receive power through 3 routes from two independent power sources and the battery.

Deployment power. Deployment will be initiated by a signal from the Agena just prior to separation. This signal ignites a thermal battery which independently of the spacecraft battery furnishes power to fire squibs that release hold down devices, to operate deployment timers, and to power the capacitor sensor panel deployment motors. A back-up thermal battery is initiated by a timer set to energize the second battery later than the normal Agena separation but prior to depletion of the secondary system battery. These identical thermal batteries reliably supply 2 amp at 28-v d-c for 30 sec and are capable of 5-amp pulses shortly after initiation. Each would weigh 0.44 lb.

Solar array. The outboard portion of each of the 12 capacitor sensor panels includes a 12-1/2 x 36-1/2 x 1/2 in. section of aluminum honeycomb with both sides reserved for solar cells. The honeycomb substrate weighs 0.42 psf. Of these 24 areas, 4 face each of the 6 orthogonal directions. Referring to Fig. II-5, if the sun illuminates the vehicle such that $\gamma = 90°$, four cell areas are constantly illuminated as θ varies. If the vehicle is oriented such that $\gamma = 0$, the number of areas illuminated will depend on the sun angle θ. Between 34.5° and 39.6° mutual shadowing occurs. Over an interval of less than 3°, less than 4 areas are illuminated; however, if the vehicle is rotating in this mode the average number of areas will be 4.3. It appears that the worst composite view angle, where less than 4 areas are illuminated is a narrow angle and since vehicle tumbling is assured (Volume III, Chapter V), a minimum of 4 areas can safely be used as an average design criteria.

In calculating the number of N/P solar cells required in each of the systems the following factors were used:

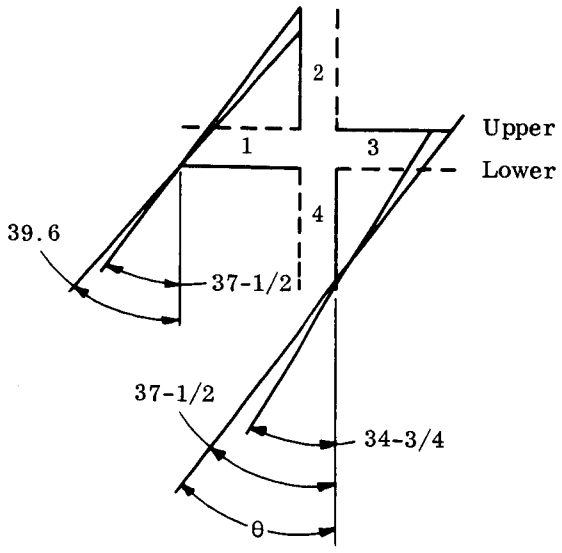

γ --out of plane of paper in 2-4 direction

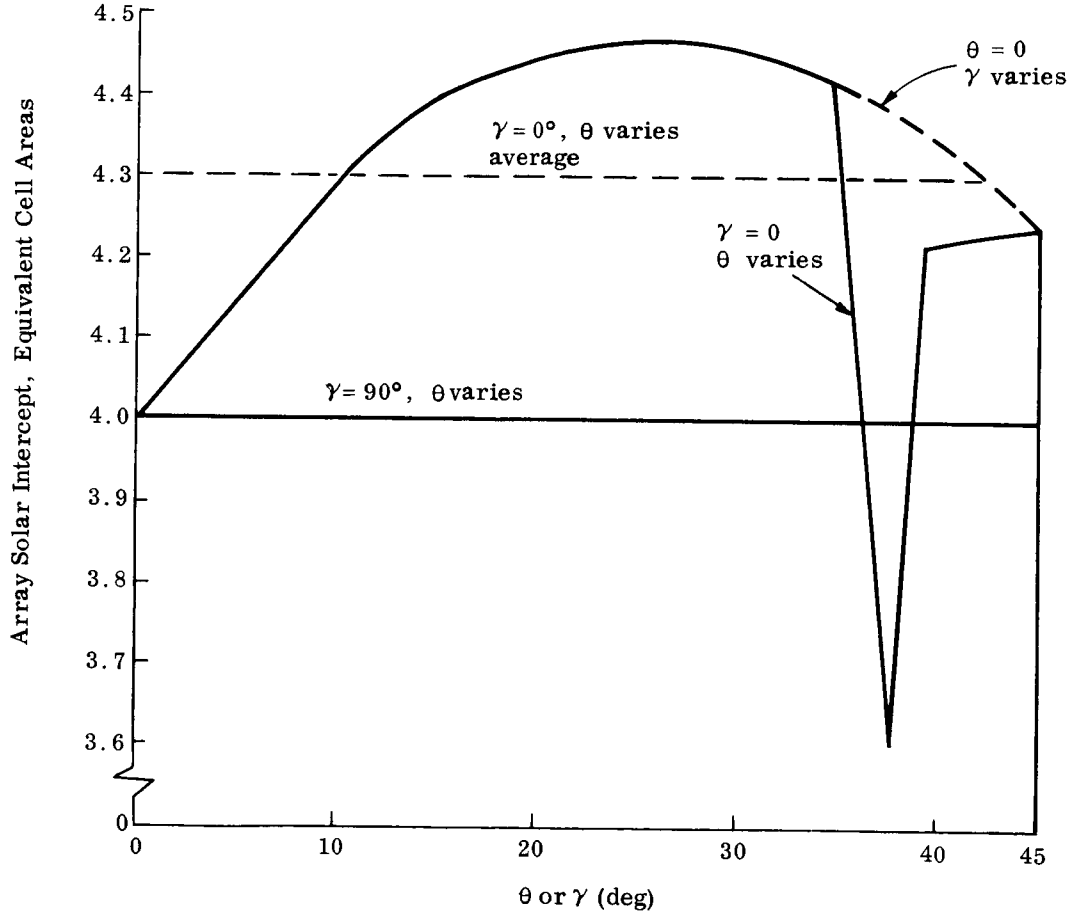

Fig. II-5. Solar Array Solar Intercept

Filter loss factor	0.92
Manufacturing and mismatch factor	0.95
Blocking diode factor	0.965
Array wiring loss factor	0.98
Vehicle at 1.03 AU and tolerance of standards	0.95
Active/panel area	0.853
Radiation damage factor	0.95
Maximum temperature 43° C	0.94
N/P silicon cell efficiency (10 ohm-cm)	0.105

The product of these factors 0.063 at 130 w/ft^2 yields 8.2 array w/ft^2 of panel. Each 3.17 ft^2 area will produce at least 26 w. Assuming that 1 x 2 cm cells installed flat occupy 92% of the panel area (active/cell area = 0.93), 1350 cells can be installed on each area, thus producing an equivalent of 19.25 mw/ 1 x 2 cm cell.

A value of 0.37 v/cell has been selected as a compromise to provide maximum power after radiation damage has occured (Ref II-3). As shown in Table II-1, for the 50-v system, 138 cells will compose one string in the primary system, 173 in the secondary. They will produce 2.66 and 3.34 w/string, respectively. To satisfy the total system watts of Table II-1, at least 11.9 and 14.75 strings/vehicle must be illuminated. Since a minimum of 4 areas will be illuminated at one time, 3 and 4 strings/area, respectively, will satisfy this requirement.

The installed growth per system, including the reserve of Table II-1 is 2.75 w and 8.2 w. Each area has a capacity of 1350 cells but the above 7 strings of 1106 cells will occupy only 82% of the available cell area. Thus the installed growth, reserve and unused array area provide a growth capability of 30 w from the present requirement of 74.46 w excluding reserve. A minimum of 11.9 and 14.75 strings of series cells which satisfy the requirements of the primary and secondary systems respectively necessitate the use of 1 x 2 cm solar cells. The use of 2 x 2 cm cells would improve reliability by requiring less interconnections, and would reduce vehicle cost. However, the attendant halving of the number of strings, under the worst conditions (vehicle spin about the longitudinal axis) would reduce power output by 17% if one of those six strings in the primary system were lost. The loss of one string of 1 x 2 cm cells, under these conditions, causes the loss of only 8% power.

d. Power system using 28-v d-c transmitter

Distribution system. The final power system block diagram, shown in Fig. II-6 is applicable if 28-v d-c transmitters are used. Since the voltage required by the capacitor sensors is higher than the bus voltage, voltage boosters (charge generators) have been provided. These devices are more efficient than converters since the latter must transform the entire power requirement. Although a capacitor bus voltage of 50-v d-c has been assumed for this system, the voltage boosters provide more latitude in voltage selection than the 50-v system described in Section B3 which did not contain voltage boosters.

Improvement features of Fig. II-4 have been included in Fig. II-6, modified to accommodate the lower bus voltage (28 v d-c). Subsequent paragraphs delineate only those features differing from the 50-v version.

Voltage regulation. The secondary system redundant pulse width modulated voltage regulator is the same type of device as used in the 50-v system except for the lower output voltage and corresponding input voltage range. Primary system voltage clamping is still accomplished by zener diodes except that 120 are used herein. The lower voltage system requires more parallel strings with fewer cells in each series string to produce 78.75 w for the 28-v system instead of 80.98 w for the 50-v system (Table II-1).

Battery and charge limiter. The battery consists of 25 hermetically sealed, nickel-cadmium cells of 12 amp-hr capacity and weighs approximately 34.5 lb. The capacity was selected using the design concepts outlined in Section B-3; however, in this case the maximum discharge depth is only 59%. The charge limiter operating at a constant current of 37 ma returns 2.4 hr of full bus load plus 5 hr of full attitude read-in load, the same concept as used in paragraphs B-2 (c) and B-3 (c). In 127 hr of sunlight at the 37 ma rate, 39% of rated capacity is returned. The amp-hr efficiency has been assumed to approach 100% at this low percentage of return and the w-hr efficiency has been assumed to be 86% (30/35 v).

The charge limiter adapted to the 37-v source will have a loss of 157 mw while supplying 1300 mw to the battery. The efficiency of the charge limiter therefore is 89.5%.

Voltage conversion. Multiple voltages required in both systems are produced in the same manner as for the 50-v system (Section B-3). The primary system regulation and conversion method for the +6- and +12-v requirements is 34% efficient. Only 0.46 w is wasted in the resistor and zeners.

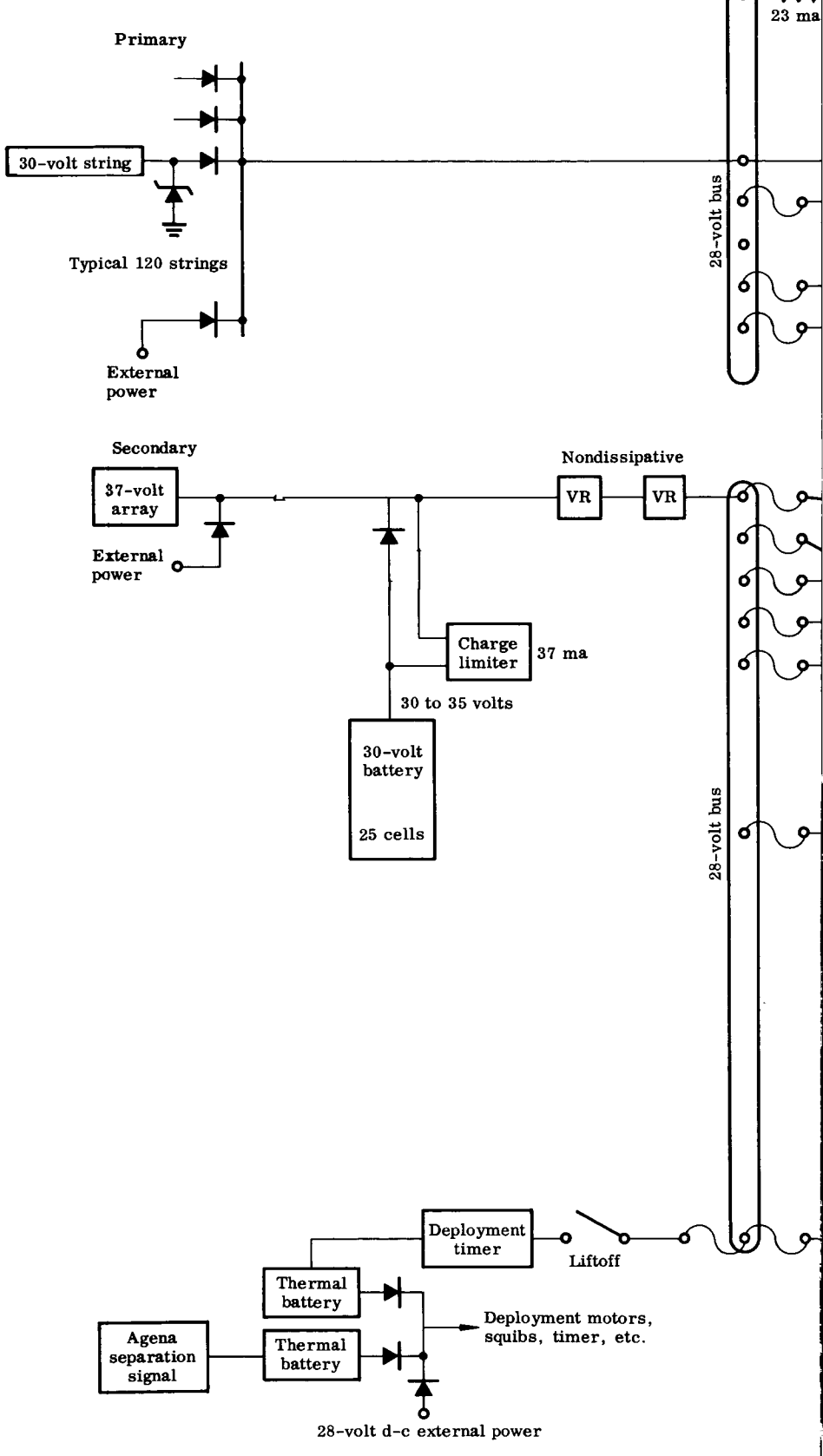
0.32 wa
23 ma
Primary
30-volt string
Typical 120 strings
External power
28-volt bus
Secondary
37-volt array
External power
Nondissipative
VR
VR
Charge limiter
37 ma
30 to 35 volts
30-volt battery
25 cells
28-volt bus
Deployment timer
Liftoff
Thermal battery
Thermal battery
Agena separation signal
Deployment motors, squibs, timer, etc.
28-volt d-c external power

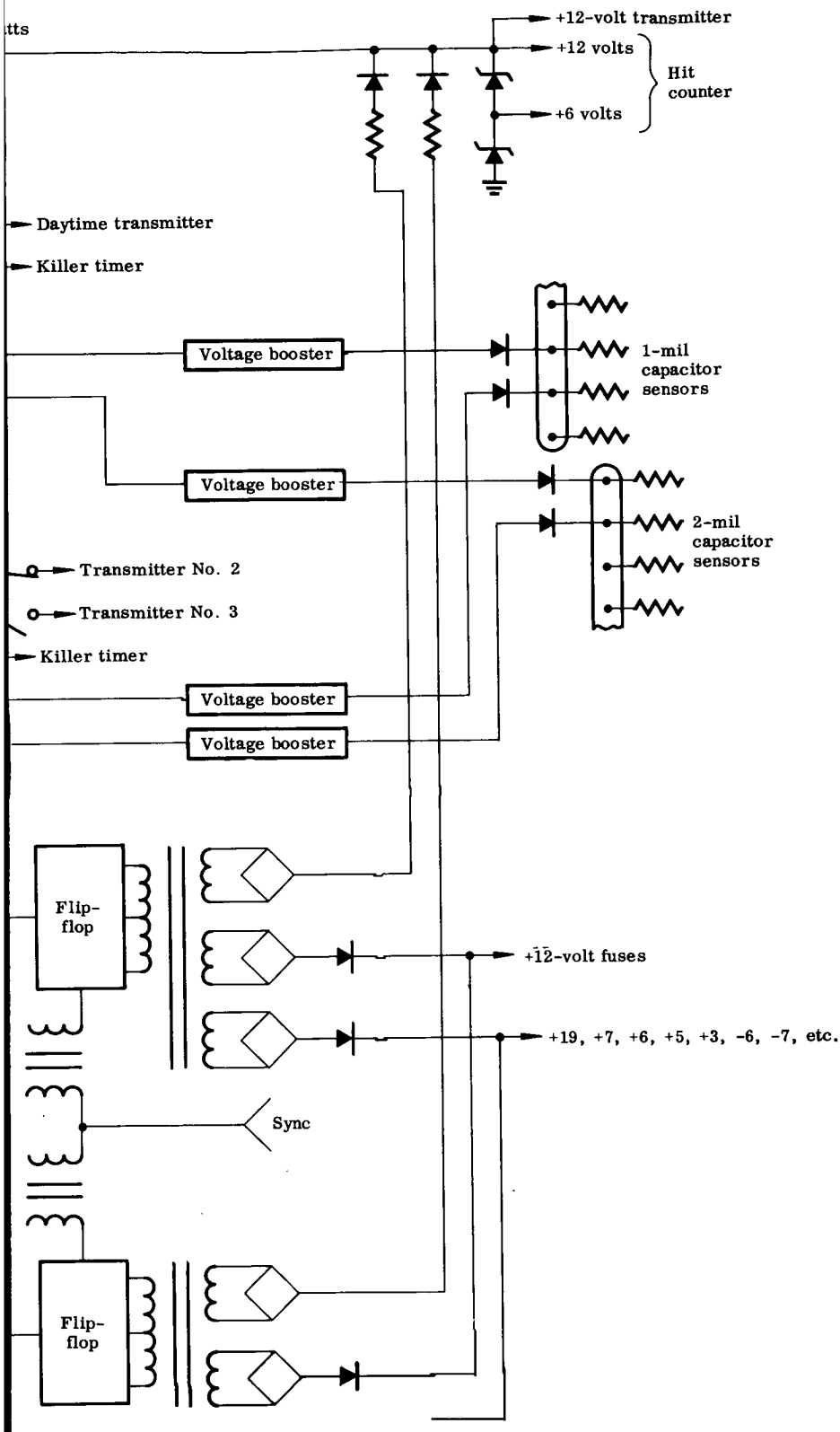

Fig. II-6. Final Power System Using 28-Volt Transmitter

Deployment power. This system is identical to that described in Section B-3 except that the deployment timer operates from a 28-v bus.

Solar array. The solar array panel construction and installation, the solar cell power loss factors and output voltage per cell are the same for the 28-v system as for the 50-v system (see Section B3).

As shown in Table II-1 for the 28-v system, 81 cells in series will compose one string in the primary system (30/0.37) and 100 (37/0.37) for the secondary system. Each string will produce 1.56 and 1.925 w, respectively. At least 20 and 24.7 strings, respectively, must be illuminated. Since a minimum of 4 areas will be illuminated at one time (Section B3), 5 and 7 strings per area are required.

The installed growth per system, including the reserve of Table II-1 is 2.54 and 10.43 w. The aforementioned 12 strings of 1105 cells per area occupy only 82% of the available cell area. Thus the growth, reserve and unused array area provide a growth capability of 32 watts from the present requirement of 72.73 watts (excluding reserve).

The loss of one illuminated string under the worst conditions, with the vehicle spinning about its longitudinal axis, would reduce the power output by 5% (one in 20 strings). If 2 x 2 cm cells are used, the loss of one string would cause the loss of 10% power. Consequently, in this application 1 x 2 cm cells are recommended.

4. Power System Selection and Conclusions

a. Solar cell versus radioisotope

To effectively compare the application of these two power generation methods to the micrometeoroid deep space satellite, the total power required of both types of generators must be determined and identical bus system voltages used. The 28-v d-c system is preferred to the 50-v d-c system, since it is simpler, more conventional, and an existing 28-v transmitter has recently been located. Therefore, the solar cell system to be used for comparison purposes is the 28-v system described in Section B3 and summarized in Table II-1.

Using the same continuous loads of Table II-1, two radioisotope-thermoelectric systems would have to furnish the following losses and total loads.

Item	Notes	Watts Primary	Watts Secondary
Continuous loads *		26.20	37.42
Reserve	~10%	2.54	3.98
Losses - lines to equip	~3-1/2%	1.01	1.46
- converters	eff = 80%	7.49	10.71
- voltage regul	~1%	0.37	0.52
Battery charging			0.20
Charge limiter loss			0.19
Total watts at power source		37.61	54.48

* Intermittent loads included in battery charging

Comparing these values with those of Table II-1, it will be noted that the first 3 items are identical; however, conversion losses are much greater since practically all loads require the 6-volt output of the thermoelectrics to be converted to the end usage voltage. Voltage regulator loss is shown for the end of mission since the zener's clamp under this condition will draw about 1 ma. Battery charging is much lower since the continuously available power source also handles the shade period requirements. The battery, therefore, need only furnish the overload requirements, approximating 15 w-hr. One 5-lb battery should suffice.

The SNAP-9A power supply fueled with Pu-238 has been space proved on a DOD satellite. This unit with all six fuel capsules installed produces 27 w for 27 lb. It is representative of radioisotope-thermoelectric generators that could be applied to the 1-yr mission of this vehicle. By using only 5 fuel capsules, 20 w is produced for 25.7 lb. The power requirements of the primary and secondary systems could be met by the use of two SNAP-9A units in each system, the primary system units being only 5/6 fueled.

The portions of a SNAP-9A system and a solar cell system that differ are compared in the following table.

	Radioisotope		Solar Cell	
	Primary	Secondary	Primary	Secondary
Power source (watts)	40	54	31.2	54.0
(lb)	51.4	54.0	16.6	23.4
Battery (lb)		5.0		34.5
Converters (lb)	4.0	6.0	Negl	3.0
Total Weight (lb)	54.4	65.0	16.6	60.9
	119.4		77.5	

The isotope system inherently does provide continuous primary system data transmission during sunlight and/or shade without dependence on a battery. Throughout the early part of the mission, even the secondary system overloads could be handled by the excess power available from the isotope generator. During this period, the secondary system would not be dependent on its battery.

The solar cell system, space proved on many vehicles, in this application does not require its own deployment mechanism; it is structurally combined with the prime sensor which must be deployed. Since the vehicle is in sunlight 99-3/4% of the time, the battery is relegated to secondary importance.

The radioisotope system, in this application of almost continuous sunlight, does not offer a weight advantage nor operational advantage over the solar cell system. The primary advantage of the isotope system, continuity of power in sunlight or shade, is overshadowed by the weight and nonradiative advantages offered by the solar cell system. The solar cell systems summarized in Table II-1 have therefore been selected.

b. Nickel-cadmium versus silver-cadmium

The statement of work for the MDSS Conceptual Study required that nickel-cadmium batteries complement the N/P silicon solar cell system. As a consequence, energy storage devices described herein are of the nickel-cadmium type. It is realized that more operational and laboratory knowledge has been gained on the nickel-cadmium battery than on others; however, there are many favorable attributes of the Ag-Cd cells applicable to this mission.

Nickel-cadmium cells are most applicable to low altitude orbits for long mission periods where 3-hr charge rates and 1.5-hr discharge rates to a 1/3 depth of discharge are repeated upwards to 6000 times per year, a total of 9000 hr of discharge. On this mission, a 300-hr charge rate is used; maximum discharges occur at the 6-hr rate and

may total only 20-hr of discharge per year. The low charge and discharge rate and the low cycle life required of this mission are most adaptable to the Ag-Cd type of cell. In addition, Ag-Cd cells have almost a 100% amp-hr efficiency even at the 300-hr charge rate; they would be lighter and they are nonmagnetic (no nickel). It is recommended that the development and test of hermetically sealed Ag-Cd cells, applicable to this mission, be strongly encouraged by the NASA.

C. REFERENCES

II-1 "Problems in the Selection and Testing of Nickel-Cadmium Batteries for Satellites," Albrecht, F., Paper No. CP61-906, AIEE Aero-Space Transportation Conference, Philadelphia, June, 1961.

II-2 "Data Telemetry Package Powered by Strontium-90 Fueled Generator," Martin Company Report MND-SR 2615, Sept 1961.

II-3 "The Electrical Characteristics of Irriadiated Silicon Solar Cells as a Function of Temperature," NASA Goddard Report X636-64-135, March 30, 1964.

III. VEHICLE DESIGN

Robert W. Halli
John J. Heindl
Samuel D. Hall
Albert G. McCall
M. Francis Taylor

III. VEHICLE DESIGN

This portion of the study was devoted to determining feasible configurations for a micrometeoroid deep space satellite for a cislunar mission. Boosters considered were the Atlas-Agena, Atlas-X 259, and Saturn 1B. Performance evaluations eliminated the Atlas-X 259 and Saturn 1B, although concepts compatible with them were developed in the early phase of the study. The recommended configuration (Fig. III-1) is described in detail in Section B1. It is known as the "Z" configuration, its weight in orbit is 696 lb, and it can be launched by direct injection into cislunar orbit by an Atlas-Agena. Development of its features is described in Section B3 and the substantiating analyses are included in Section B4.

A. CONCLUSIONS AND RECOMMENDATIONS

The design and analyses efforts expended have demonstrated the feasibility of the proposed design. The weight and volume of the satellite are within the payload capability of the Atlas-Agena for direct injection into cislunar orbit. The structure can be manufactured from available materials using existing tooling and methods.

The structural arrangement is suitable for the accelerations and vibrations of launch, separation and deployment loads, and the space environment. Temperature effects in space should be minimized by the satellite's tubular frame work structure and the spring suspension of its capacitor sensors.

An outline of the features of the design is given below, followed by recommendations for the application of future effort.

1. Configuration Design Features

(1) Launch vehicle: Atlas-Agena

(2) Agena long fairing heat shield and its separation system.

(3) Satellite weight: 696 lb in orbit

(4) Experiment sensors:

Capacitor sensor area: 39 sq ft 0.001-in. aluminum target

503 sq ft 0.002-in. aluminum target

Velocity gages: 2

Mariner gages: 3

Infrared flash detectors (Exotech sensors): 72 (2 as backup in each capacitor sensor bay)

(5) Attitude sensors:

Magnetometers: 2

Sun sensors: 5

Earth sensors: 5

(6) Solar cell area: 70 sq ft

(7) Antennas: 2 omnidirectional (1 turnstile 1 unsymmetrical disc cone) No deployment except for automatic spring deployment of 1 segment of the turnstile.

(8) Systems module: Removable from support bulkhead
Removable covers on top and bottom
Three shelves, 2 of which are removable
Center and upper shelf accessible on launch pad

(9) Spacecraft-booster separation system:

V-band clamp explosively separated at 2 places and retained on adaptor.

(10) Adaptor: Machined "I" ring

(11) "Z" configuration:

4 "Z" arms present effectively equal meteoroid intercept areas regardless of viewing angle.

Omnidirectional exposure of solar cells.

4 movable arms deployed independently 90° by torsion springs governed by planetary gear reduced DC motors.

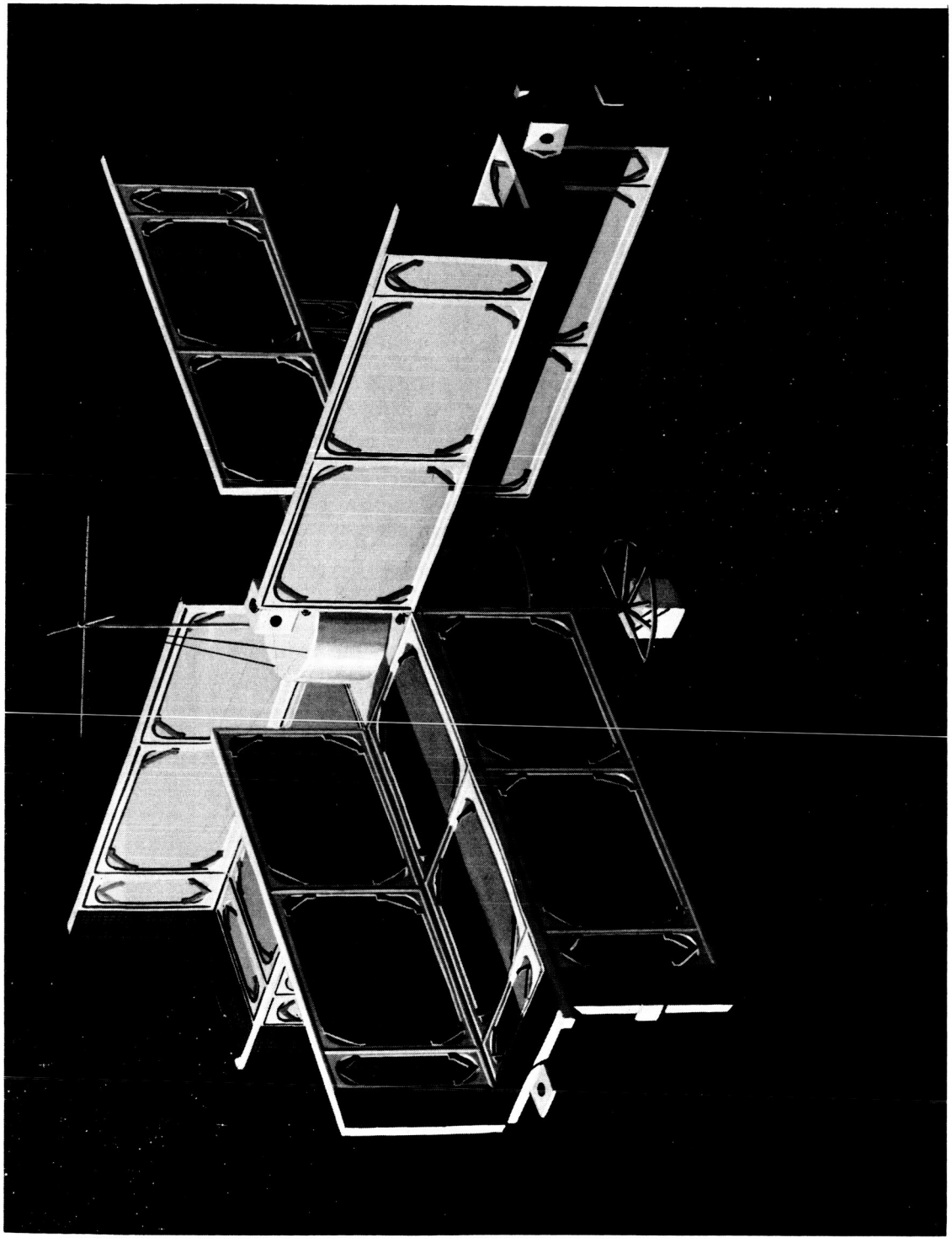

Fig. III-1. Micrometeoroid Deep Space Satellite

4 movable planes, one per arm, deploy independently--90° using similar system to that of arms.

Ratchet locks control position of movable arms and planes throughout travel.

Deployment of arms and planes begins automatically with cutting two nylon retaining straps.

Spacecraft packaged in heat shield has volume available for future growth, either in sensor area or added propulsion for extended missions.

Spring mounted segmented capacitor sensor panels minimize structural weight, eliminate possible radiation shorts through elimination of sensor backup, facilitate Exotech sensor installation, and are less sensitive to temperature change.

No attitude stabilization system is required.

2. Recommendations

As a result of the study the following items are selected as the more important ones requiring further analysis and/or development testing.

Spring suspended segmented capacitor. This recommended design has many desirable features and is applicable to the present capacitor as well as those under development. Additional analysis and development testing is needed to obtain design data. Tests would be conducted on the effects of spring load, panel thickness, and size on the ability of the panel to withstand launch vehicle noise and vibration in conjunction with decrease in air density during launch.

Backup capacitor designs. Other designs for mounting panels should be evaluated in case unforeseen difficulties arise in the development of the spring panel. One of these, presented in Section B4, has the sensor bonded to an auxiliary frame which is mounted in the satellite arm structure. Development testing similar to that for spring suspension is required.

Mounting and deployment of satellite. The method of supporting the systems module, which requires that the satellite arms be load-carrying and structurally integral during launch, should be tested to demonstrate structural stiffness and initiation of deployment. Release of the arms for deployment, accomplished by cutting nylon straps, should be tested. Although considerable effort during the conceptual study did not result in the design of a completely satisfactory mechanical release in lieu of the nylon straps, additional effort could be spent investigating this area.

B. TECHNICAL DISCUSSION

1. Vehicle Description

In the course of the study, many configurations and structural arrangements were investigated which were applicable to one or more of the boosters considered. Some of these are discussed in Section 3. The configuration recommended as being most efficient for the cislunar mission is shown (deployed) in orbit in Figs. III-1 and III-2. The launch vehicle is the Atlas (SLV-3)/Agena D.

A distinctive characteristic of the design is the arrangement of the capacitance sensor panels in four arms of "Z" cross section to provide three dimensional space coverage. Solar cell panels are also incorporated in these arms to allow generation of electrical power independent of the vehicle attitude. Seventy square feet of solar cell area is shown. These features are obtained while retaining simplicity of arm and panel deployment. Each arm and panel is independent of all other arms and panels, and requires only 90° of travel for full deployment. The arms are mounted from the sides of the square bulkhead which supports the systems module. In orbit the satellite weighs 696 pounds, well within the capability of Atlas (SLV-3)/Agena D for direct injection into cislunar orbit. It has a span of 290 in. and a basic height of 76 in., exclusive of antennas and sensors. During launch, the folded vehicle is contained within the payload envelope for the Atlas-Agena long fairing. The only deployable item other than the capacitance sensor panels is one segment of the turnstile antenna which is spring loaded and partially deployed against the heat shield, deploying fully as the heat shield is separated. The turnstile antenna mounted on top of the equipment module and the cone disc antenna on the bottom of the equipment module provide omnidirectional coverage required by the random tumbling of the spacecraft in orbit.

Onboard sensors include 39 square feet of 0.001-inch aluminum target capacitor sensor panel, 503 square feet of 0.002-inch aluminum target capacitor sensor panel, two velocity gages, three Mariner gages and 72 Exotech sensors (two in each capacitor sensor bay).

The vehicle contains no attitude control equipment; attitude is determined on the ground from telemetered data collected by five sun sensors, five earth sensors and two magnetometers.

a. Structural arrangement

The structural framework of the vehicle consists of the four "Z" arms which extend radially, one from each side of the square bulkhead in which the systems module is mounted. In the launch configuration, these arms fold together to form a hollow rectangular box shape (~44 in. square and 131 in. high) with the bulkhead which supports the module and from which the arms are deployed at the forward or upper end (Fig. III-3).

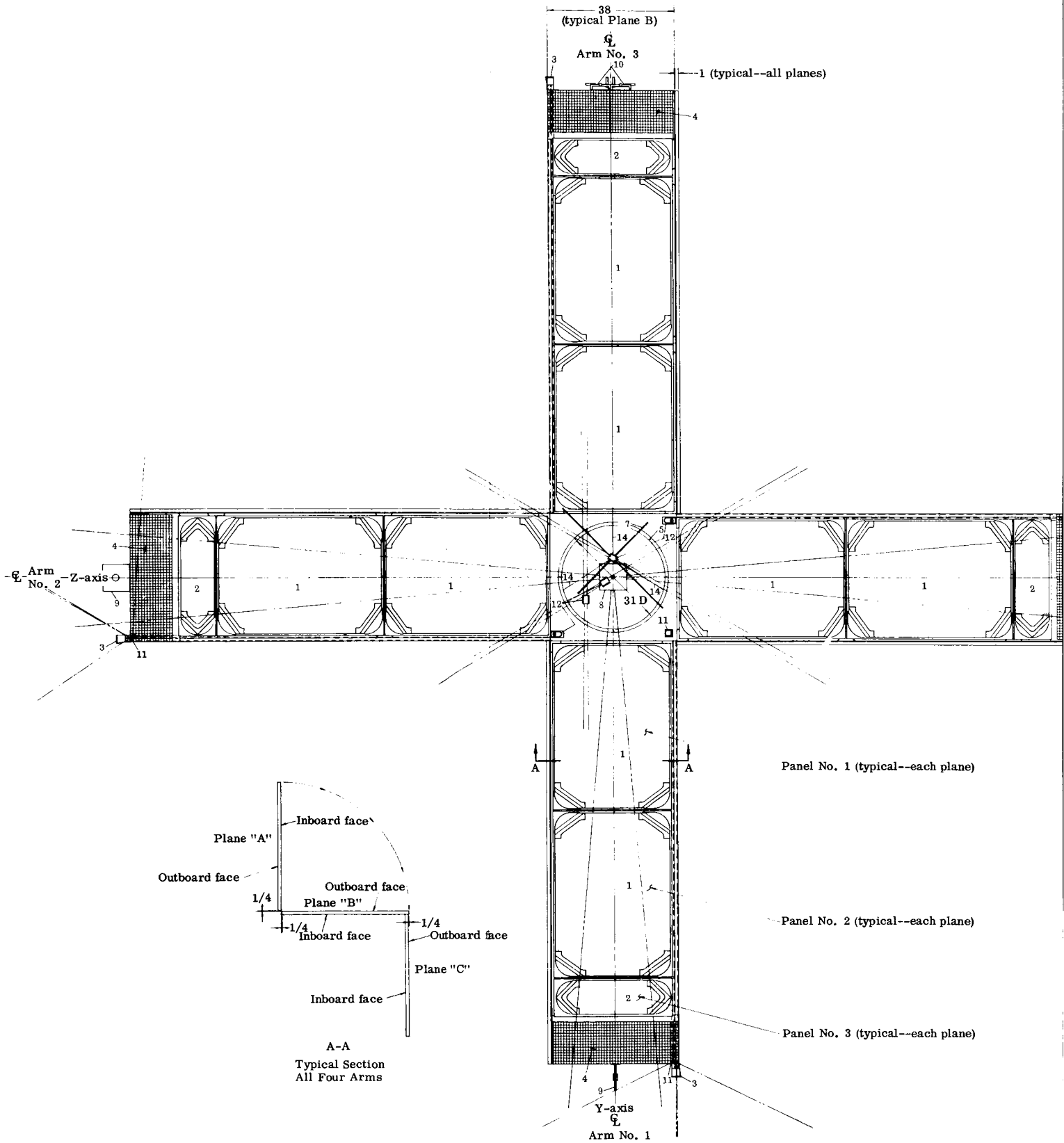
38
(typical Plane B)
℄ Arm No. 3
1 (typical--all planes)
℄ Arm No. 2
Z-axis
31 D
A
A
Panel No. 1 (typical--each plane)
Panel No. 2 (typical--each plane)
Panel No. 3 (typical--each plane)
Y-axis
℄ Arm No. 1
Plane "A"
Inboard face
Outboard face
Plane "B"
Outboard face
Inboard face
Plane "C"
Outboard face
Inboard face
1/4
1/4
1/4
A-A
Typical Section
All Four Arms

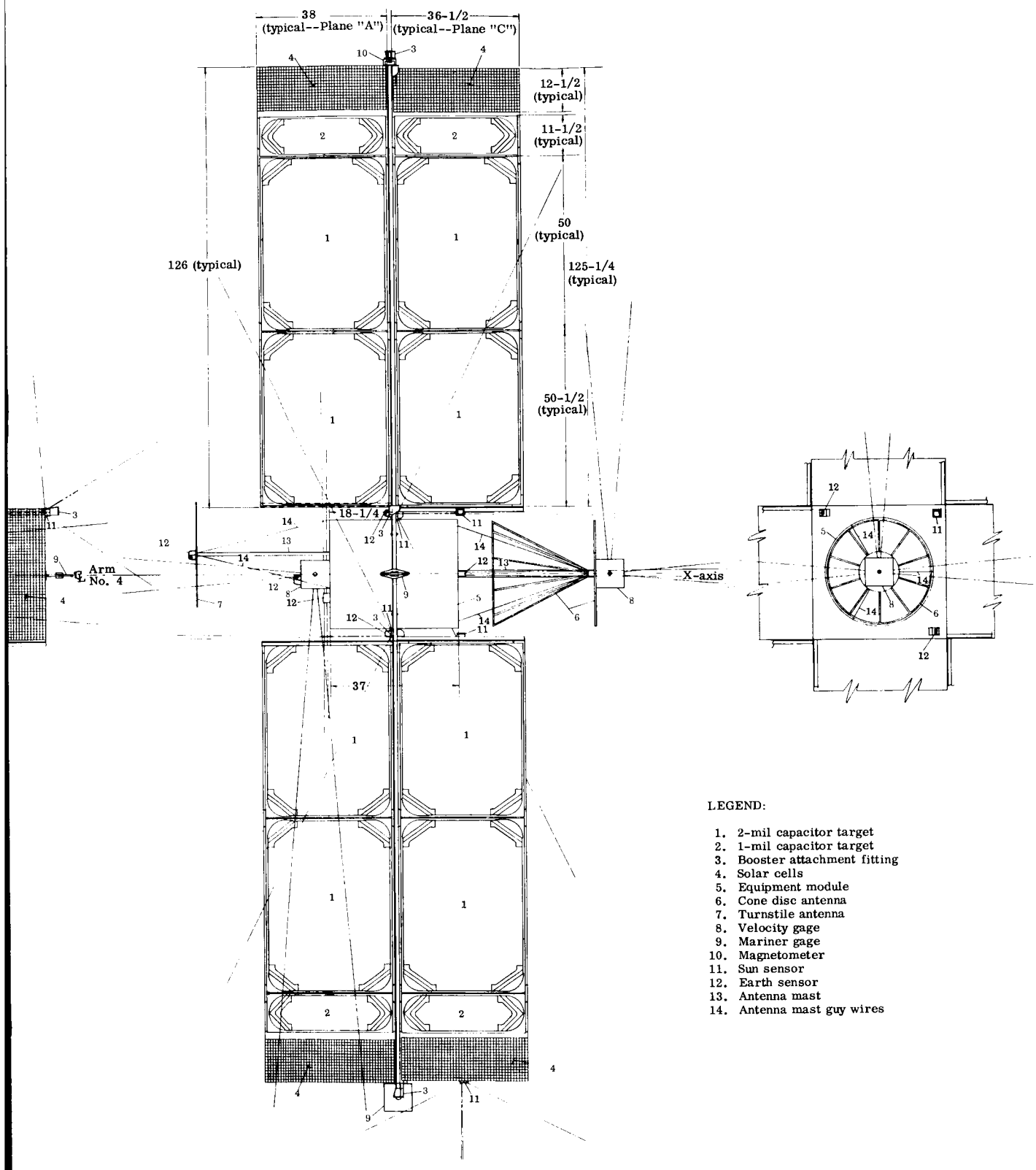

LEGEND:

1. 2-mil capacitor target
2. 1-mil capacitor target
3. Booster attachment fitting
4. Solar cells
5. Equipment module
6. Cone disc antenna
7. Turnstile antenna
8. Velocity gage
9. Mariner gage
10. Magnetometer
11. Sun sensor
12. Earth sensor
13. Antenna mast
14. Antenna mast guy wires

Fig. III-2. MDSS General Arrangement

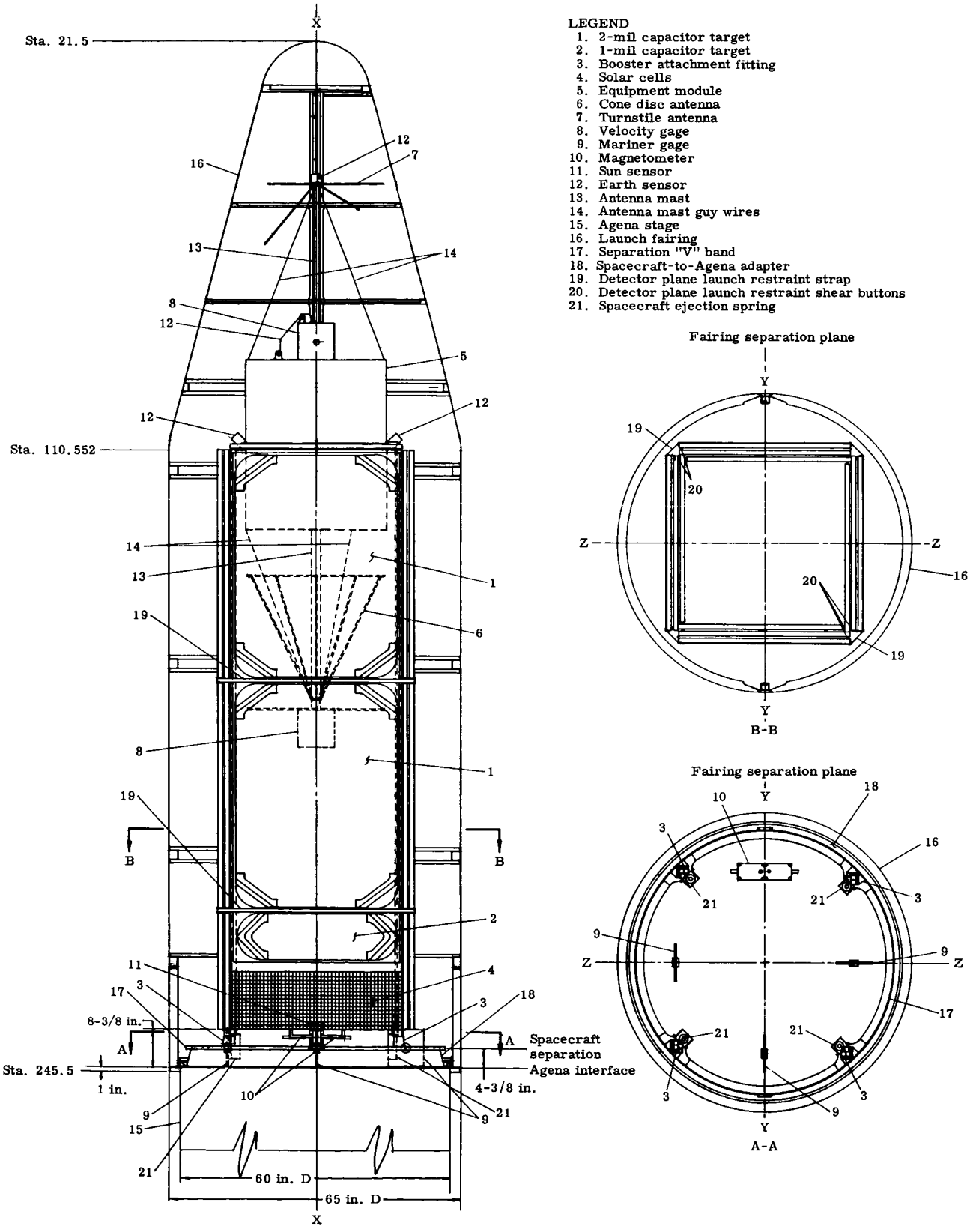

Fig. III-3. MDSS Launch Arrangement--Atlas-Agena Launched

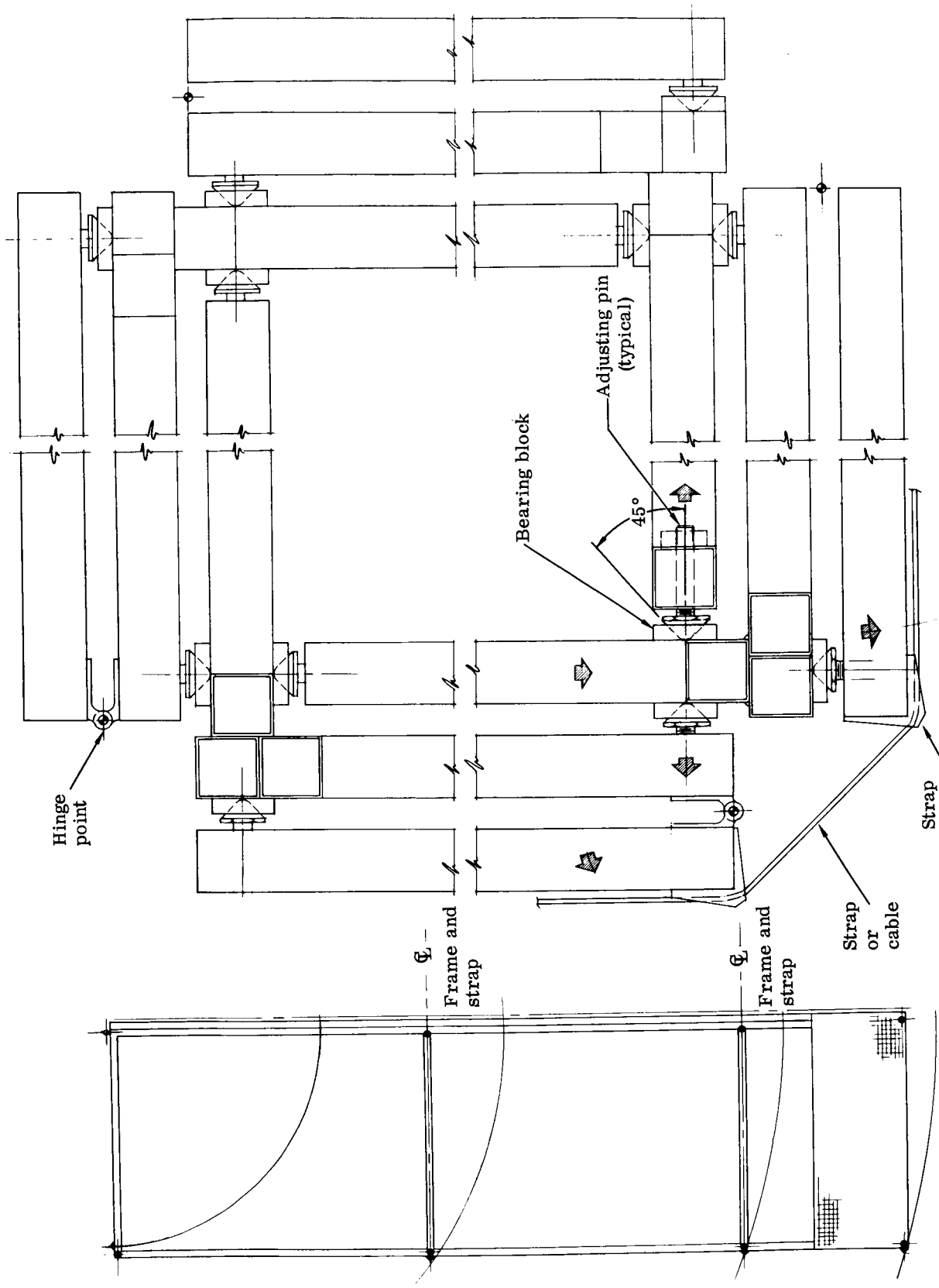

Fig. III-4. Typical Section at Strap Frames

Each corner of this box is the intersection of the two fixed perpendicular planes in each arm and forms the vertical load carrying column. The lower end of the column terminates in the fitting that attaches the spacecraft to the adapter. Two methods of attachment and separation, V-band clamp and tension bolts with shrouded explosive nuts, are discussed later.

The four "Z" arms are essentially the same. They have one-inch square aluminum tubing edge and cross members secured at the corners and intersections by aluminum plate gussets fastened by blind rivets. The two fixed perpendicular planes share a reinforced edge member at their intersection, and the folding plane of each arm which is the outboard plane at launch, is attached to the free edge of one of the perpendicular panels by piano hinge segments. For the launch environment, the folded arms are interconnected by conical shear buttons located at the plane edge and cross members, and are held in place to form a rigid box assembly by two nylon straps at the intermediate cross members (Fig. III-4).

The four arms are connected by piano hinge segments to the central support bulkhead which is square and consists of one-inch thick aluminum honeycomb construction with aluminum edge members.

The arms and folding panels are deployed by means of torsion springs and electric motors, and are held in position by ratchet-type locks as discussed later.

The equipment module is mounted centrally in the support bulkhead and is attached to it by a flange on the center shelf.

b. Capacitor panel installation

Capacitor sensors (Fig. III-5) consist of a 5052-H19 aluminum face, laminated mylar film dielectric, and vapor deposited copper. Thirty-nine square feet of 0.001-inch aluminum target is provided in 24 panels--2 panels back-to-back in each of the 12 planes. Each of these 24 panels has the copper divided into 5 segments so that 120 separate targets are available. A total of 503 square feet of 0.003-inch aluminum target is provided in 48 panels--2 pair of back-to-back panels in each of the 12 planes. Each of these 48 panels has 3 segments so that there are 144 of these targets (Fig. III-2). The installed panel weight of the 0.001-inch targets is 0.59 lb/sq ft; the 0.002-inch targets are 0.62 lb/sq ft (Table III-1). Sensor panels are installed in the structural plane frames by means of tension springs attached to the frame gussets at each corner.

An opaque mylar light block, 0.001 inch thick, covers the gap between the sensor panels and the structural frame and is secured by Hartwell Manufacturing Company "Velcro" closure strips bonded to the

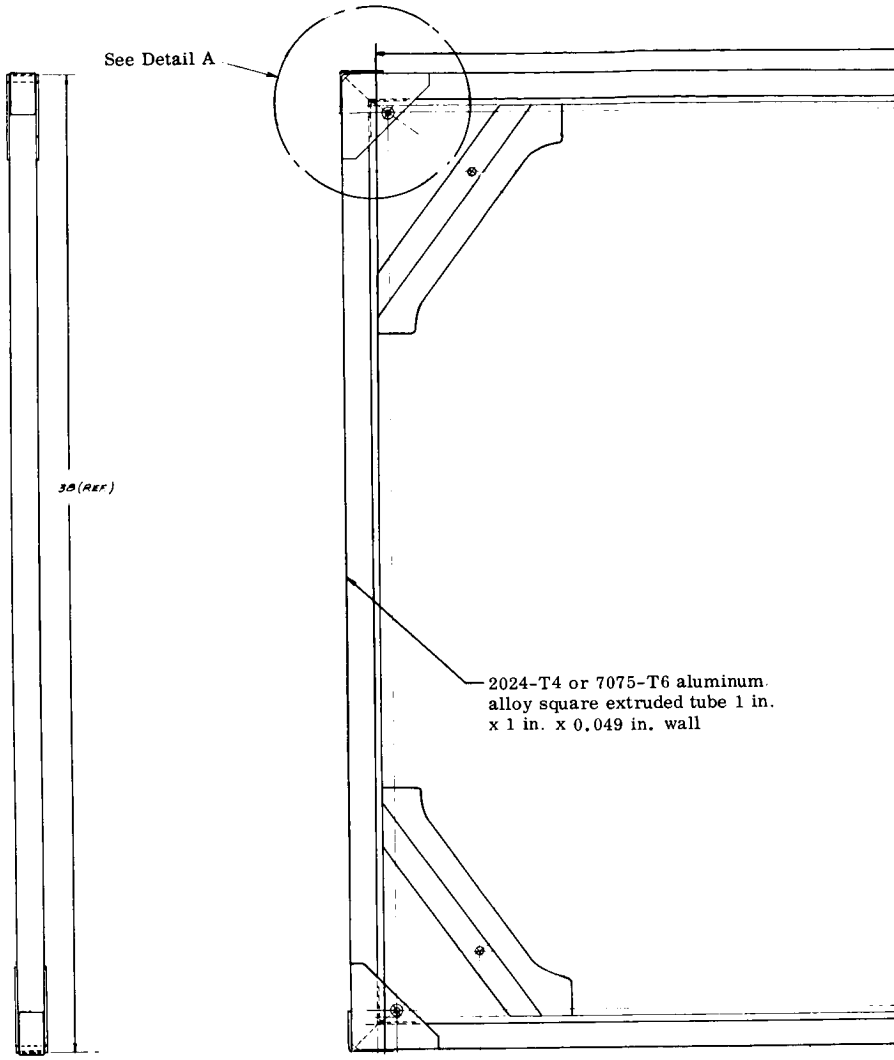
See Detail A
39 (REF)
2024-T4 or 7075-T6 aluminum alloy square extruded tube 1 in. x 1 in. x 0.049 in. wall

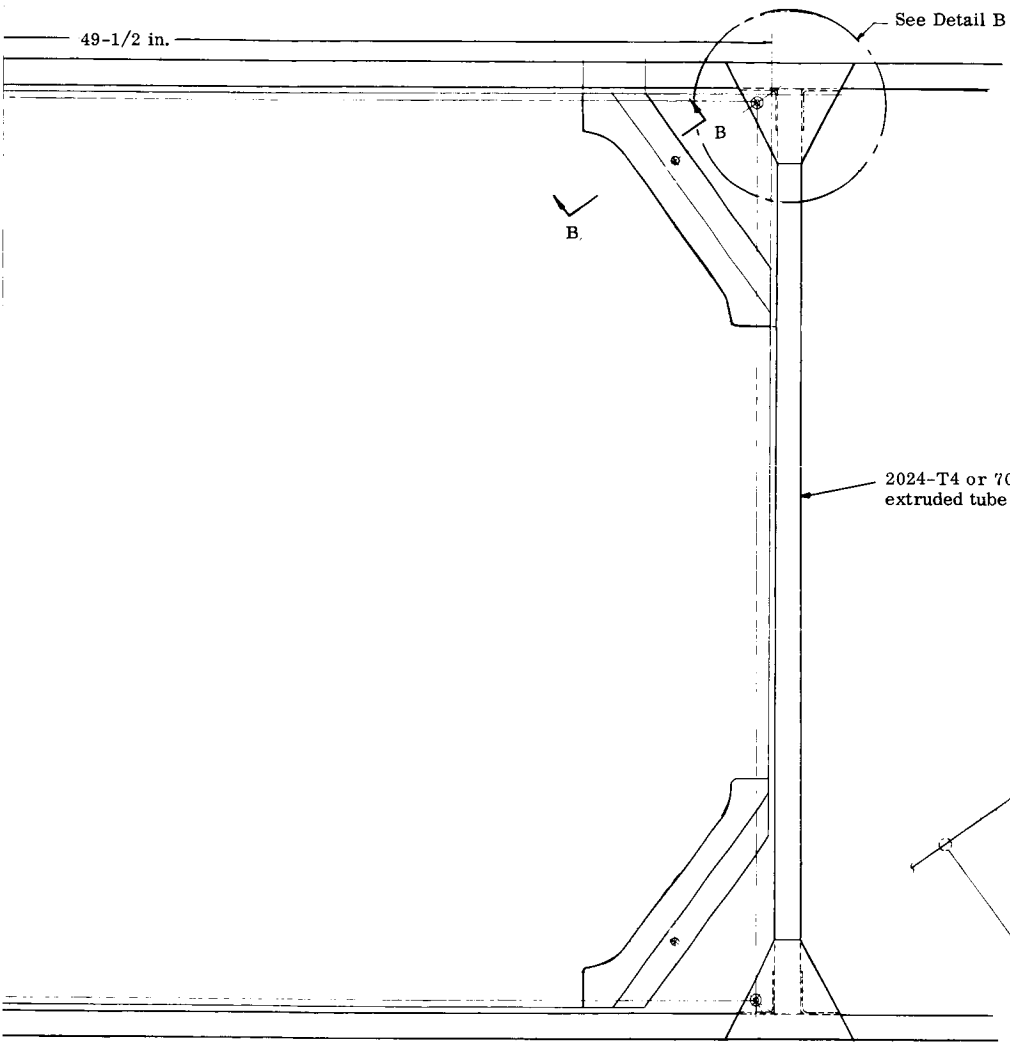
49-1/2 in.
See Detail B
B
B
2024-T4 or 7075-T6 aluminum alloy square
extruded tube 1 in. x 1 in. x 0.049 in. wall

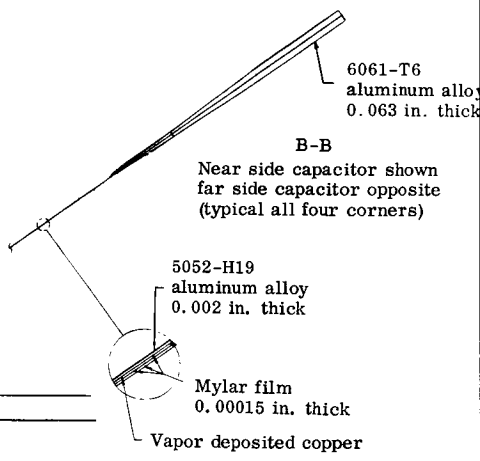
6061-T6
aluminum allo
0.063 in. thick
B-B
Near side capacitor shown
far side capacitor opposite
(typical all four corners)
5052-H19
aluminum alloy
0.002 in. thick
Mylar film
0.00015 in. thick
Vapor deposited copper

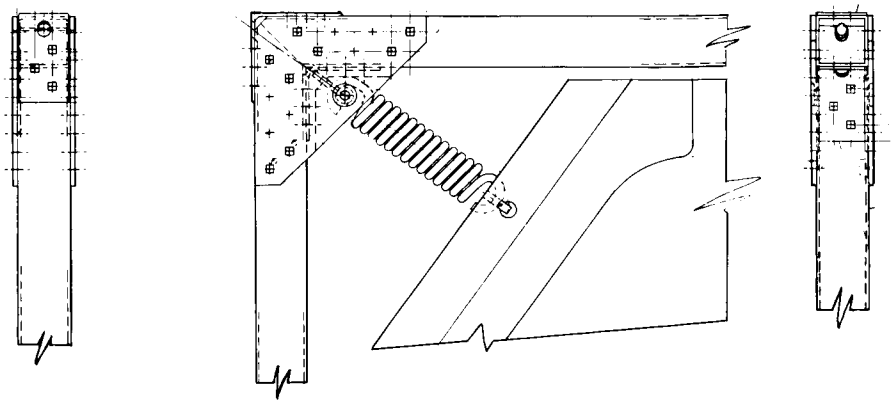

Detail A

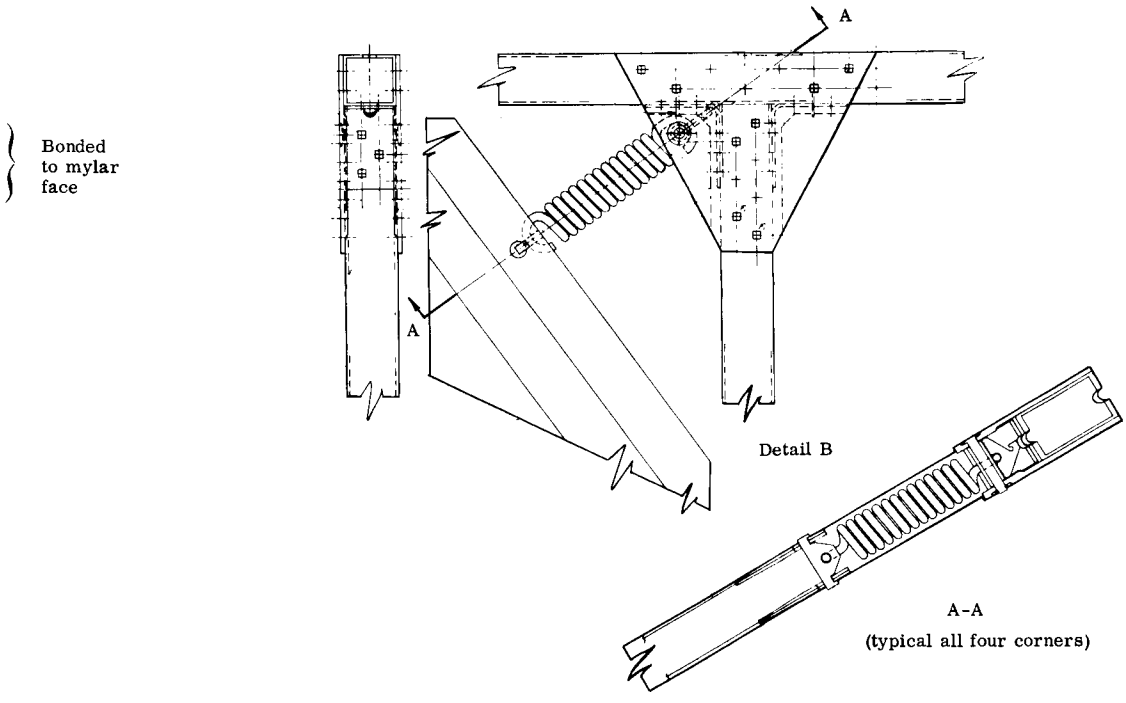

Fig. III-5. Capacitance Sensor Panel; Structural Details Only

TABLE III-1

	Unit Weight (lb/sq ft)
Bonded 0.002 aluminum, Mylar and adhesives (one assembly)	0.0325
Reinforcement at corners	0.0727
One reinforcement, bonded assembly	0.1052
Frame assembly	0.4050
Installed two-sided capacitor panel with 0.002 target	0.6154
Bonded 0.001 aluminum, Mylar and adhesives (one assembly)	0.0191
Reinforcement at corners	0.0727
One reinforcement, bonded assembly	0.0918
Frame assembly	0.4050
Installed two-sided capacitor panel with 0.001 target	0.5886

frame and light block for quick installation or removal (Fig. III-6).

This method of installation facilitates use of the Exotech sensor as a backup, as well as requiring a minimum amount of support structure. It also eliminates the need for foam backup of the sensor and. therefore, may improve the reliability and accuracy of the capacitor sensor. A detailed investigation has been made to determine the feasibility of tooling and installing such thin panels; procedures developed as follows.

Capacitor panels, when received from the subcontractor, will be complete, including the light shield material around the edge. Each pair of panels will be received in the shipping and handling frame (Fig. III-7), which holds them in the proper relationship to each other, for mounting in the spacecraft structure.

With the structural plane, into which the panels are to be mounted, supported vertically and with the long axis horizontal, the two upper installation tools are positioned (Fig. III-8) on the frame edge. The wing nuts on the rods with wire loop ends, in these tools, are backed off to the ends of the rods. At these two locations the springs with the spring end fittings attached are hooked to the wire loops on the tool rods (Figs. III-5 and III-8). The capacitor panels are now positioned in the frame using the handling and shipping tool. The spring fittings on the panel end of the spring are hooked into the two holes provided for this purpose in the panel corner doublers. The wing nuts on the tool rods are now tightened until the panels hang from them roughly centered in the frame. The two lower edge springs, with their end fittings attached are hooked in the lower corners of the panels, the two lower edge installation tools are positioned on the frame and hooked to the spring end fittings, and the wing nuts tightened to hold these tools in place. The shipping and handling frame is removed from the capacitor panels, and the four wing nuts are tightened alternately a little at a time until the tubes on the spring end fittings are lined up with the holes in the frame corner gussets. The clevis pins are inserted through them and the snap rings applied to the pin ends. The wing nuts are backed off and the four installation tools removed. The Velcro edge on the mylar light shield material, around the edges of the capacitor panels, is pressed against its mating strips around the frame (Fig. III-6) and the installation is complete.

c. Solar cell installation

Solar cells are mounted on both sides of a substrate structure. This structure is brazed aluminum honeycomb one inch thick, 13 inches wide and extends the full width of each of the 12 planes. Seventy square feet of solar cell area is shown (Fig. III-2).

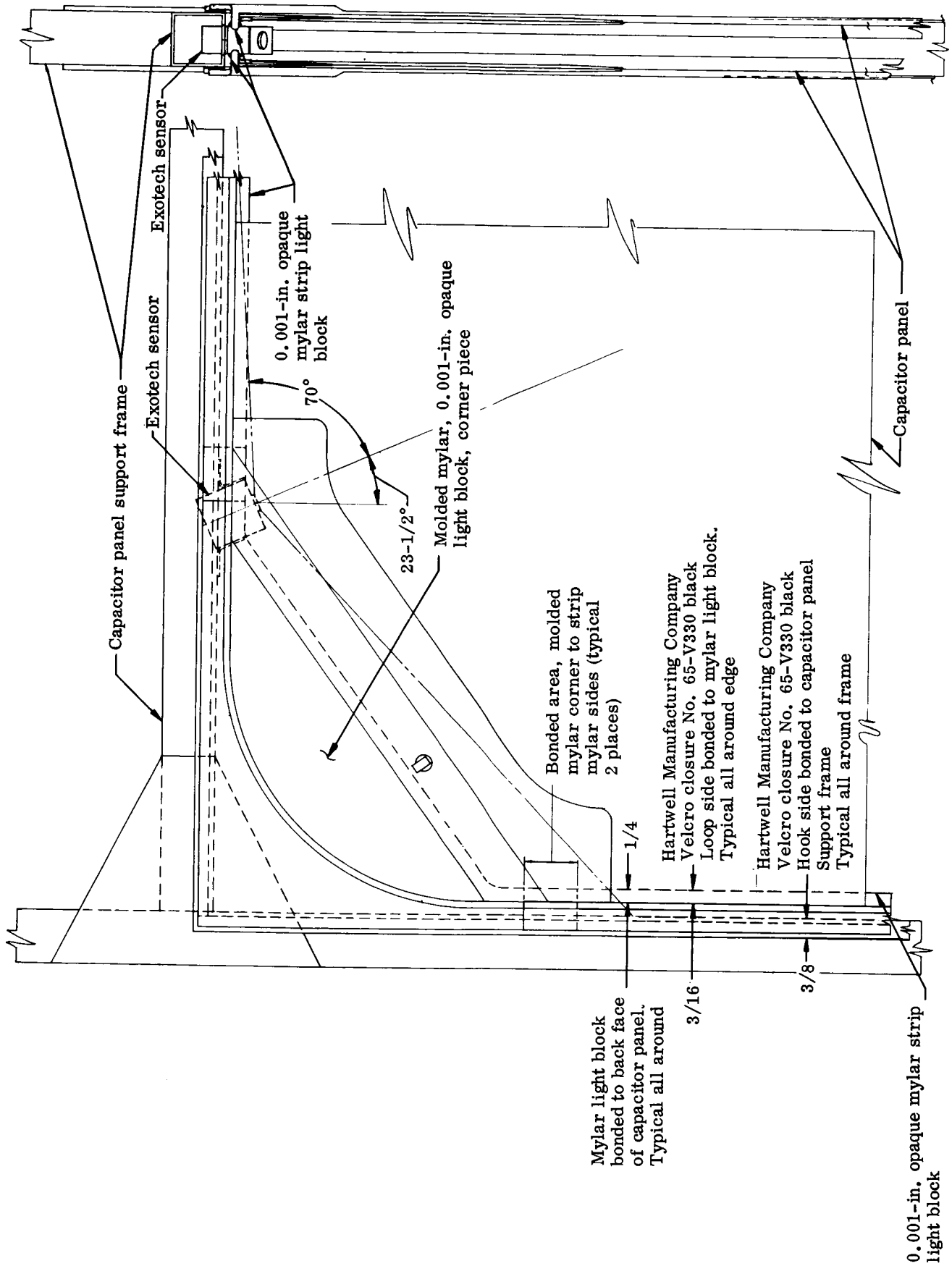

Fig. III-6. Capacitor Panel, Exotech Sensor and Light Block Arrangement

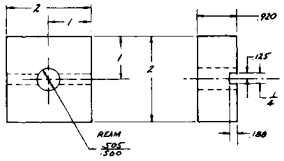

DETAIL - 15
PLASTIC, LAMINATED SHEET COTTON-BASE, PHENOLIC MIL-P-15035 TY. FBM 2" THK.

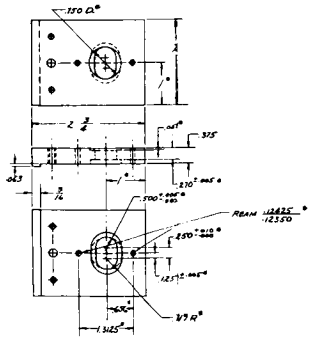

DETAIL - 13 & - 5
PLASTIC, LAMINATED SHEET COTTON-BASE, PHENOLIC MIL-P-15035 TY FBM 1/8 THK.
* IN-13 ONLY

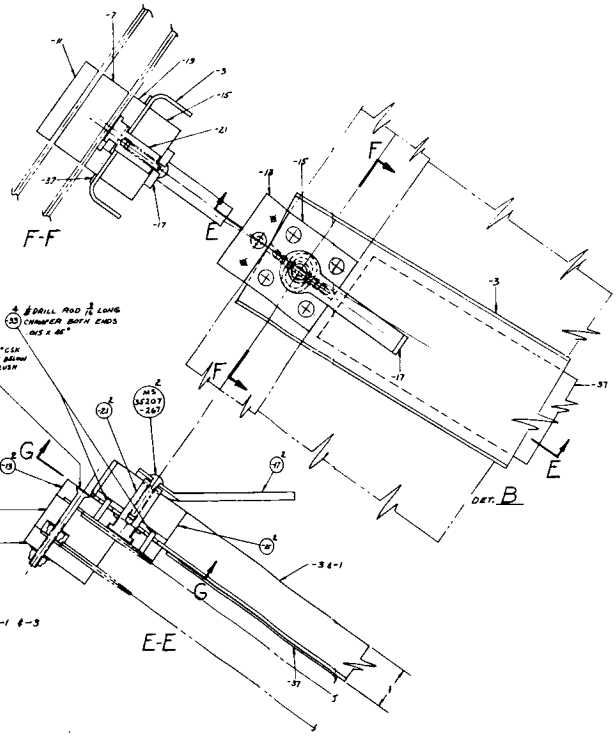

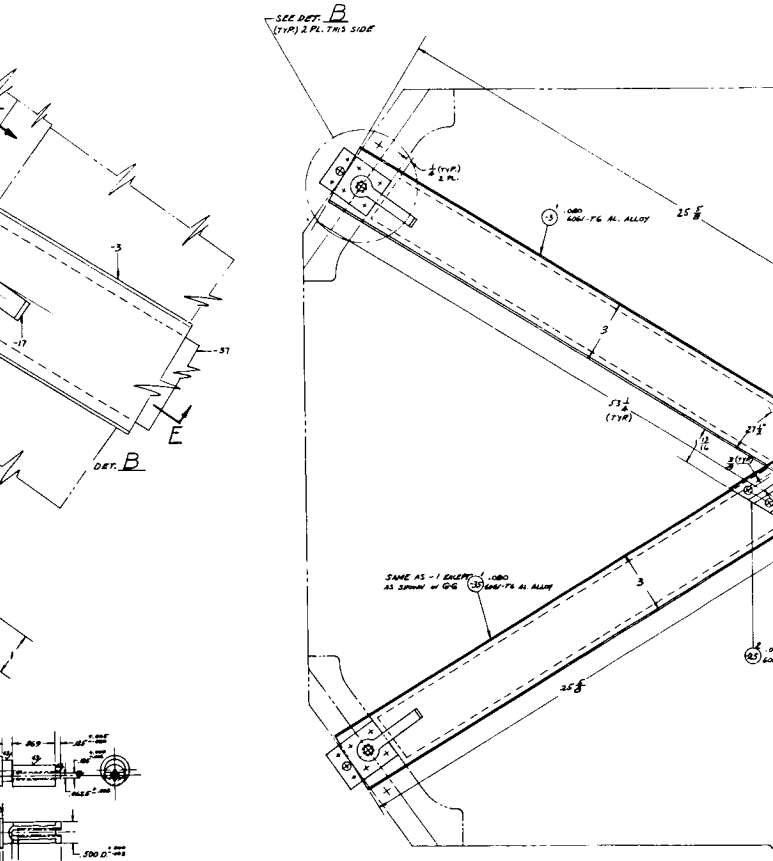

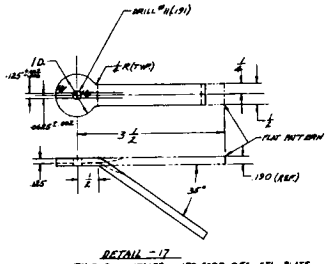

DETAIL - 17
TY. 302 ANNEALED .190 CORR. RES. STL. PLATE CHAMFER OUTLINE EDGES 1/32 x 45°
UNLESS NOTED

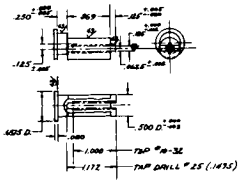

DETAIL - 21
TY. 303 COND. A. ANNEALED CORR. RES. STL. BAR
UNLESS NOTED

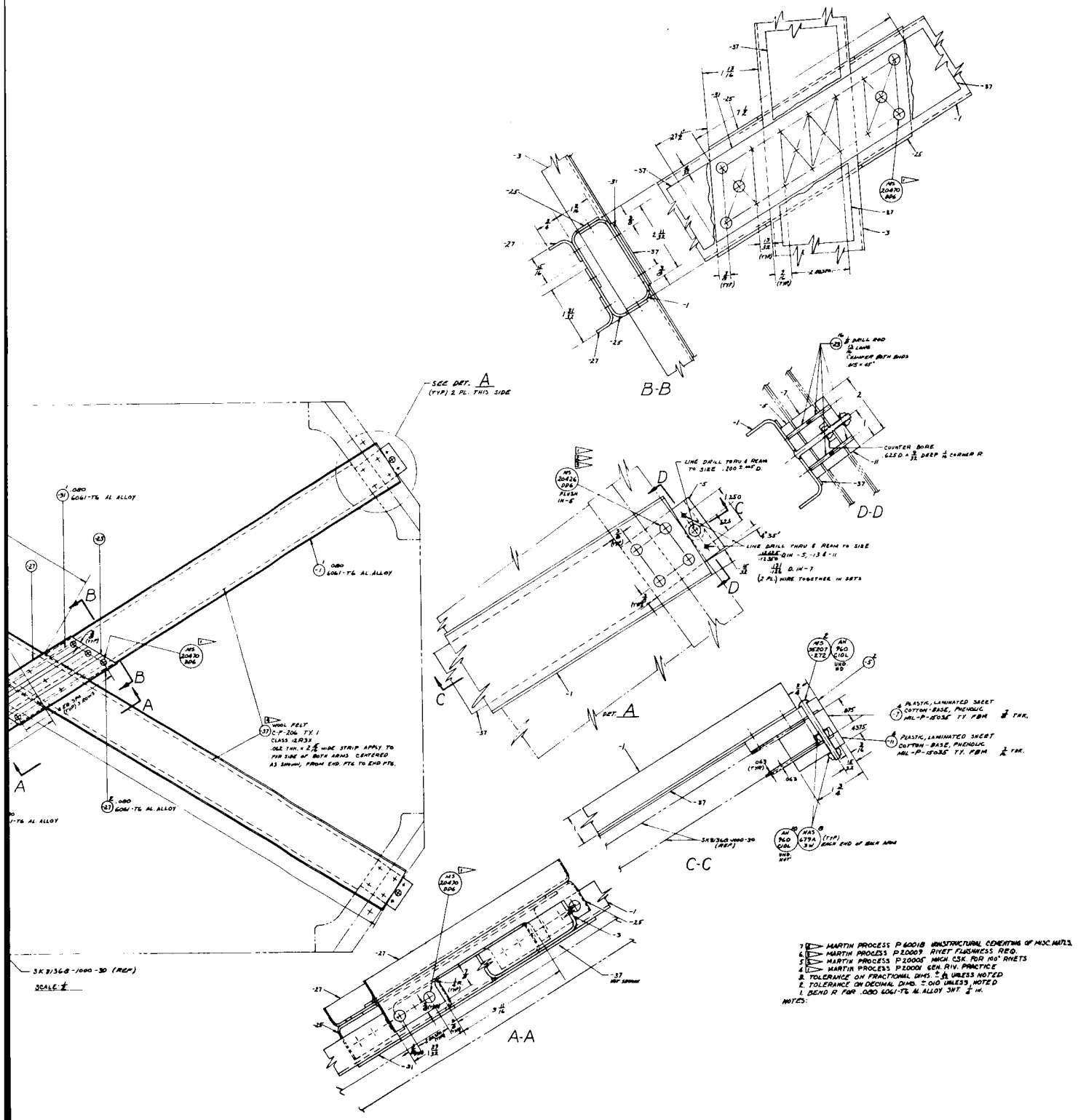

Fig. III-7. Sensor Test Sheet Handling and Shipping Frame

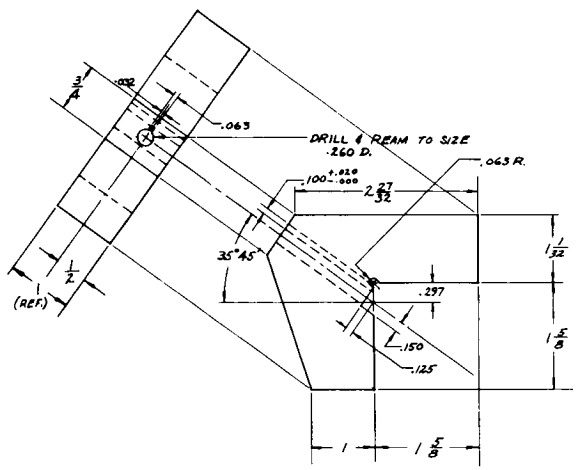

DETAIL - 3
PLASTIC, LAMINATED SHEET
COTTON-BASE, PHENOLIC
MIL-P-15035 TY. FBM 1" THK.

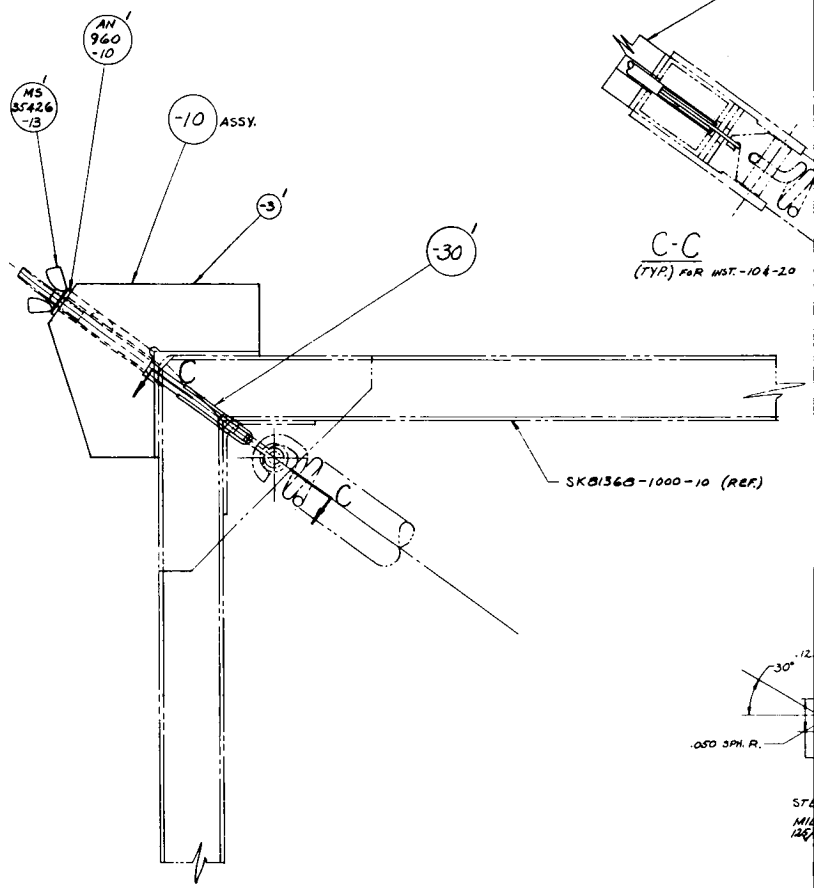

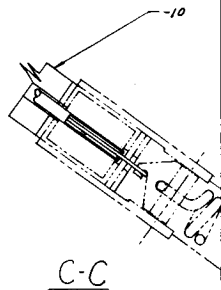

C-C
(TYP.) FOR MST.-10 & -20

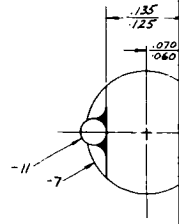

A-A
SCALE 10:1

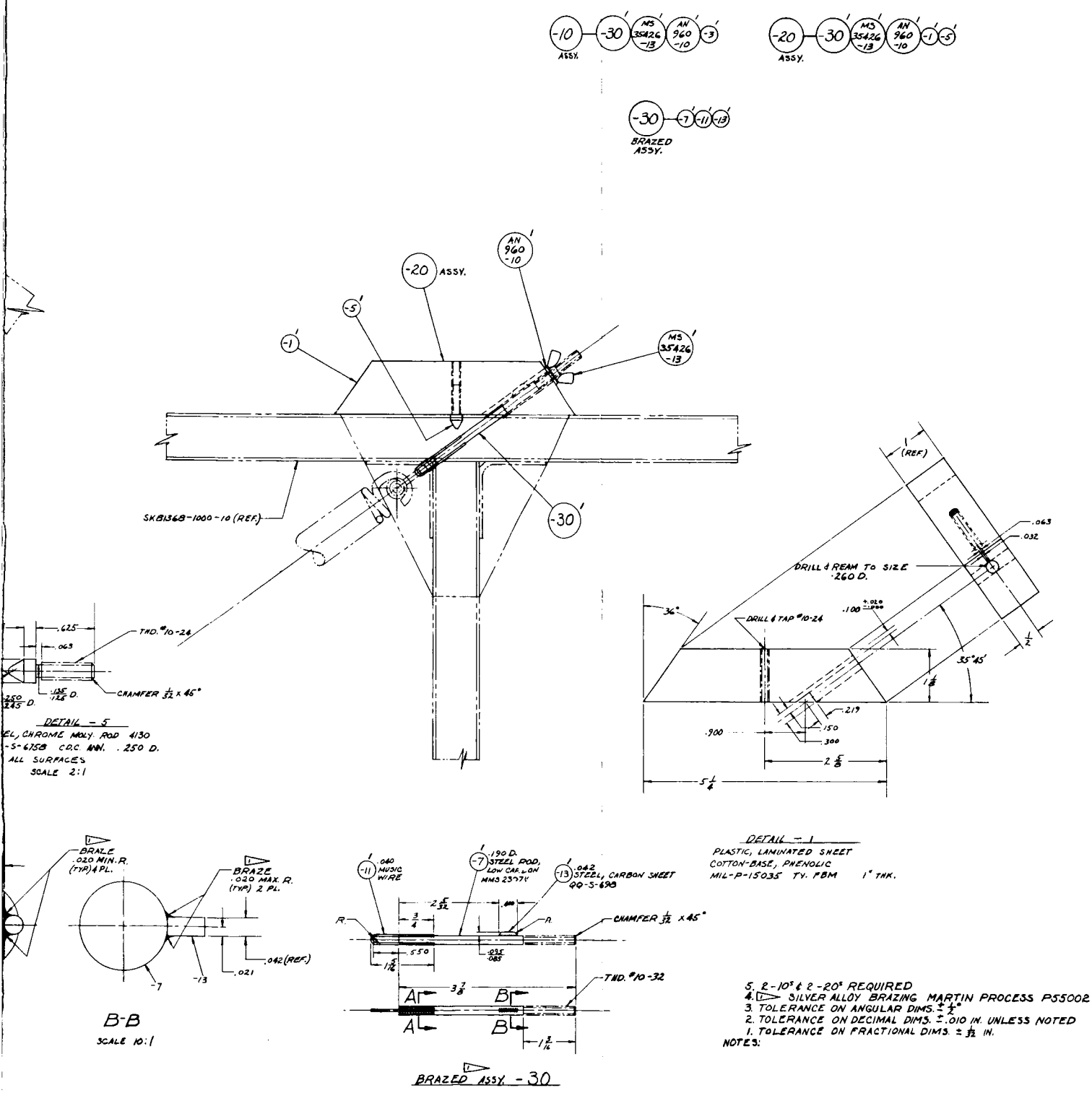

Fig. III-8. Capacitor Sensor Installation Tools

Brazed honeycomb will provide a good thermal path from the cells facing the sun to the cells on the opposite side, thus keeping the cells facing the sun from overheating.

The brazing process contemplated is a fluxless aluminum braze that has been tested at the Martin Company with excellent results.

The edge members of these panels are bent-up "Z" sections, with the protruding flanges all on the same face of the panel and extending one inch beyond the edge. The complete panel, after solar cell application, is attached to the square tubing frame by machine screws through its edge member flanges.

d. Systems module (Fig. III-9)

This unit houses the electronic nerve center of the satellite and provides the thermal environment and structural mounting for its components. It is 31 inches in diameter and 37 inches high.

The housing structure consists of three one-inch thick circular shelves and a two-piece cylindrical outer cover, all constructed of bonded aluminum honeycomb sandwich material.

The central shelf has a flange around its periphery extending beyond the outer cylinder wall by approximately 1.0 inch, used to mount the equipment module on the central honeycomb bulkhead of the spacecraft. The other two shelves are supported from the central shelf by four sheet-aluminum brackets, to which they are fastened by four screws. These shelves are slightly smaller than the inside diameter of the cover.

The two part cover is constructed of 0.25-inch thick honeycomb, with half of the cylindrical length on either side of the central shelf.

Thermal radiators for the transmitters are aluminum plates built into the side wall of the covers and thermally isolated from the surrounding honeycomb. Each one replaces the honeycomb of the side wall for ten inches of height and 14.5 inches of periphery. There are three of these radiators, one on the upper cover and two diametrically opposite on the lower cover. The one on the upper cover is centered 90° to those on the lower cover.

The covers are attached by radial screws through the edge adjacent to the central shelf to the auxiliary shelf support brackets and the angle strips between them.

Subsystems components housed in this module are mounted on the shelves-on both sides of the central shelf and one side of the two auxiliary shelves. Bonded inserts in the honeycomb are used to attach these units.

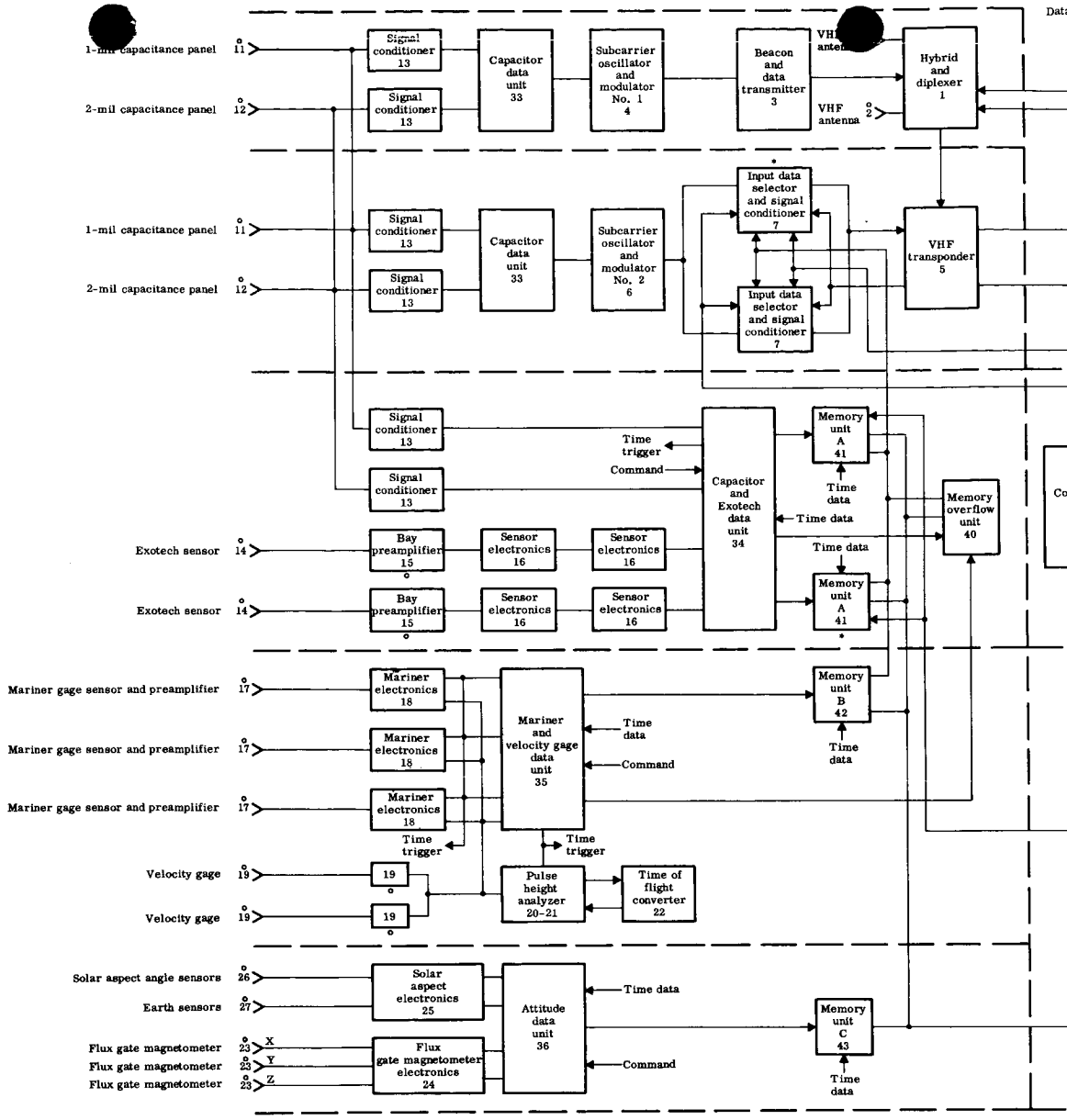
1-mil capacitance panel 11
2-mil capacitance panel 12
Signal conditioner 13
Capacitor data unit 33
Subcarrier oscillator and modulator No. 1 4
Beacon and data transmitter 3
VHF antenna 2
Hybrid and diplexer 1
Subcarrier oscillator and modulator No. 2 6
Input data selector and signal conditioner 7
VHF transponder 5
Time trigger
Command
Capacitor and Exotech data unit 34
Memory unit A 41
Time data
Memory overflow unit 40
Exotech sensor 14
Bay preamplifier 15
Sensor electronics 16
Mariner gage sensor and preamplifier 17
Mariner electronics 18
Mariner and velocity gage data unit 35
Memory unit B 42
Velocity gage 19
Pulse height analyzer 20-21
Time of flight converter 22
Solar aspect angle sensors 26
Earth sensors 27
Solar aspect electronics 25
Attitude data unit 36
Flux gate magnetometer 23
Flux gate magnetometer electronics 24
Memory unit C 43

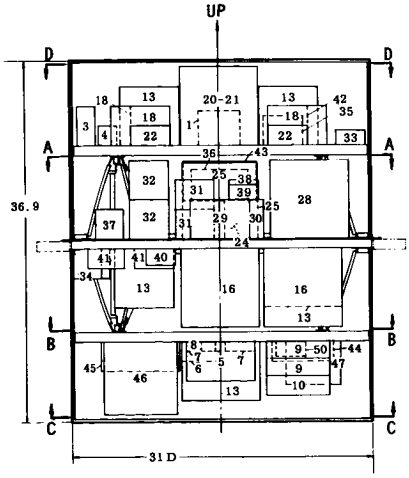
UP
D
A
B
C
36.9
31 D

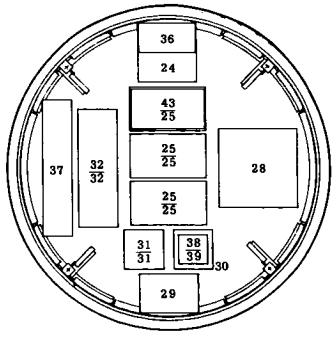
A-A

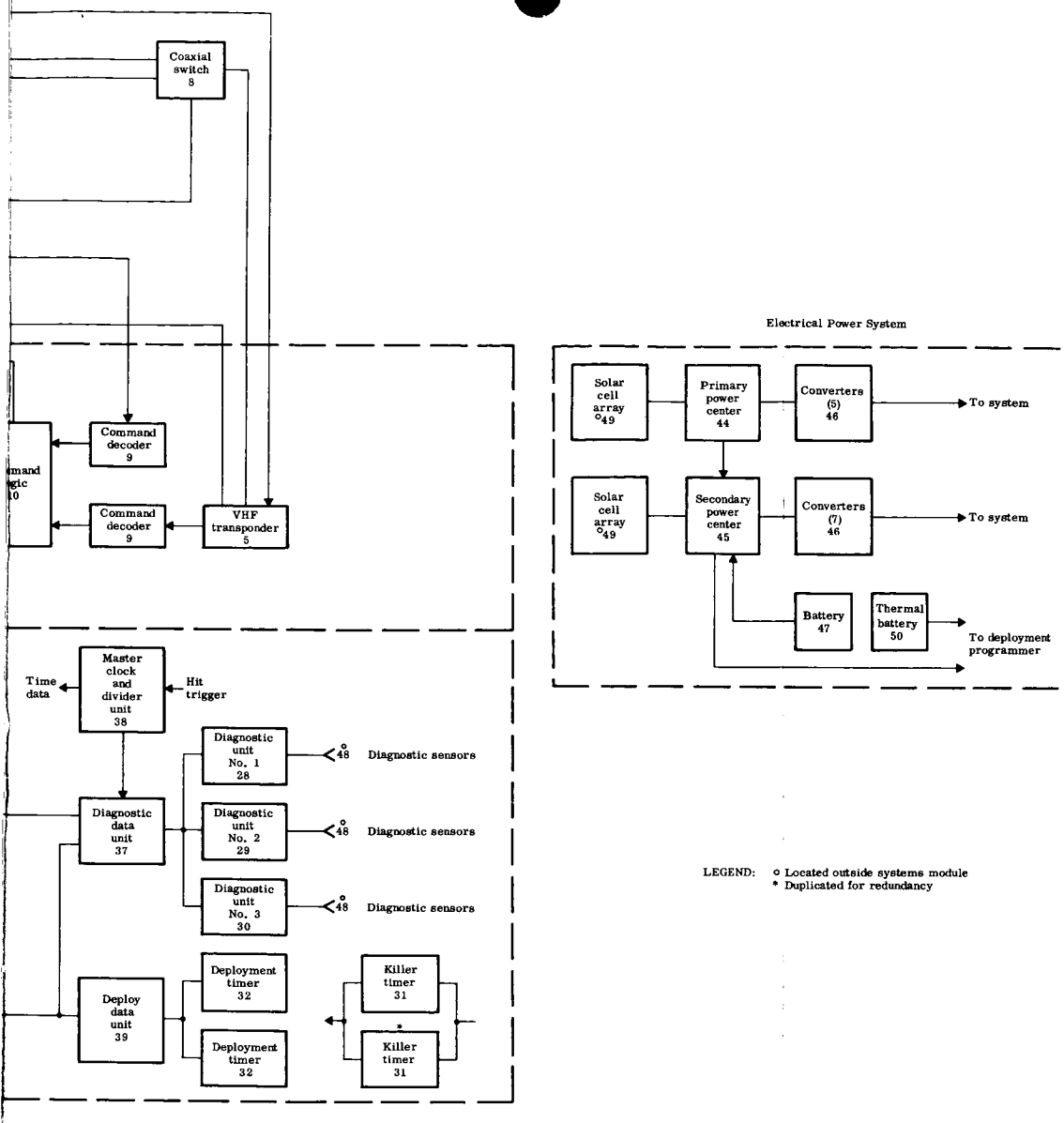

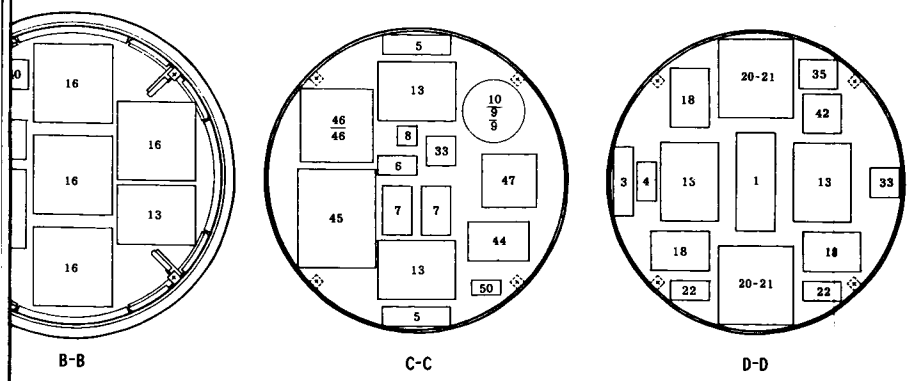

Fig. III-9. Systems Module Arrangement

Of late, minor changes have been made to the system:

(1) An additional subcarrier oscillator No. 2 has been added (Fig. III-9, Item 6).

(2) Exotech sensor electronics units (Fig. III-9, Item 16) were reduced in quantity from four to two.

(3) The pair of signal conditioners (Fig. III-9, Item 13) between capacitance panels and the capacitor and Exotech data unit have been deleted.

(4) An additional three-axis magnetometer is provided, along with its electronics unit (Fig. III-9, Items 23 and 24).

These changes have not been incorporated in Fig. III-9.

In the schematic diagram on Fig. III-9 certain groupings of components are shown by dotted lines. These groupings comprise subassemblies which may be assembled and checked out independently. It will be noted that these groupings have been maintained on the module shelves, simplifying the assembly and checkout operation and minimizing interconnection wiring requirements.

e. Antenna installation

This spacecraft has two antennas, mounted on the end covers of the equipment module, which provide omni coverage (Fig. III-2).

One of these antennas is a turnstile type mounted on top of a mast that extends 38 inches above the module upper cover. The mast is one-inch outside diameter aluminum tubing, braced with three guy wires from its top to the edge of the cover. This mast is off center on the cover by 5-3/4 inches, along the Y-Y axis, toward the No. 3 arm to keep the antenna out of the field of view of the velocity gage.

The other antenna is an unsymmetrical disc type, mounted from the opposite end of the equipment module cover. It is also on a 38-inch mast braced by three guy wires. This mast, however, is two-inch diameter aluminum tubing due to the greater weight of equipment that it must support. This mast is centered on the lower module cover.

Two legs of the turnstile antenna (those nearest the No. 3 arm of the vehicle) will be spring hinged at their inner ends. When the launch fairing is placed around the spacecraft, these two antenna legs are bent down and their outer ends rest against bumper blocks on the fairing inner surface (Fig. III-3), springing into place at fairing separation.

The cone disc antenna is easily contained within the hollow "box" formed by the folded "Z" arms at launch and, therefore, requires no deployment.

f. Attitude sensing equipment

The configuration and installation of the sensors for this system are discussed herein, and their locations are shown in Fig. III-2. The sensors used include magnetometers, sun sensors and earth sensors. The attitude sensing system is discussed in Chapter V.

Magnetometer. Two magnetometers are required per spacecraft: one high-level and one low-level unit. Each magnetometer has three sensor heads, each approximately 0.7 inch in diameter by 3.0 inches long. These heads are positioned on a 6.0- by 3.5-inch platform so that their longitudinal axes are mutually perpendicular and the spacing between heads is sufficient to minimize mutual sensing interference. The platform has four mounting legs, each approximately 1.5 inches long, located at the four corners of the platform.

The magnetometers must be located and installed such as to minimize vehicle magnetic effects. The two instruments are mounted end to end, on the outboard edge of Arm No. 3 of the spacecraft, in the center of the "B" plane. The planes of the mounting platforms are perpendicular to the "B" plane with the long axis of the platforms aligned parallel to the end edge of the "B" plane. One sensor head axis on each unit is on this platform axis, one is pointed parallel to the arm axis and the third is perpendicular to the "B" plane.

Thus, the magnetometers are far removed from the vehicle magnetic influences and exposed to space environment to the greatest extent possible without the use of booms (Fig. III-2).

Sun sensor. The sun sensor detector head is packaged in a 2.25-inch square by 0.5-inch thick housing. It has two viewing slits about 1.25 inches long, arranged perpendicular to each other near and parallel to two adjacent edges of one of the square faces. Each slit has a fan shaped field of view that equals the slit length in thickness and is ± 64° from a perpendicular to the detector head face, about the slit axis. Five of these sensors are required. Three of them are arranged 120° apart, coplanar or in parallel planes and the other two are 180° apart, looking perpendicular to the plane of the first three.

These units are mounted on three adjacent arms of the satellite and on the central square bulkhead. The three arm-mounted units are centered on the outboard ends of plane "C" on Arms 1, 2 and 4. The unit on Arm 1 has its viewing axis parallel to the arm axis; the units on Arms 2 and 4 have their viewing axes 30° off their respective arm axis

in the direction away from Arm 1. The slits are oriented parallel and perpendicular to the "C" plane and corresponding slits in these three units are parallel. The sensors mounted in the central square bulkhead are located on diagonally opposite corners. Their viewing axes are 180° apart and their slits are parallel to the edges of the central bulkhead and to each other. These sensors have unobstructed fields of view.

Earth sensor. This sensor is housed in a 2.0-inch square by 2.5-inch long case. It has a 0.75-inch diameter aperture, in both square faces. The angular field of view, centered on the axis of these apertures, is 1.0°. Five of these instruments are required: three have their viewing axes 120° apart, coplanar or in parallel planes and the other two are 90° apart, each inclined 45° to the plane of the initial three. The axes of the latter two sensors are also in a plane, or are parallel to a plane perpendicular to the axis of one of the initial three sensors.

One of these sensors is mounted on top of the equipment module upper cover with its viewing axis parallel to the vehicle Y-Y axis. It is offset from the center of the cover toward Arm 2. Another is mounted atop the velocity gage, which is centered on the same equipment module cover. Its axis is 30° to the spacecraft Z-Z axis so as to pass across the edge of Arms 2 and 4 in plane "C." A third sensor is located on top of the turnstile antenna at its center. Its axis is also 30° to the spacecraft Z-Z axis, 60° from the previous sensor axis. These sensors axes lie in planes parallel to the spacecraft Y-Z plane. Two additional sensors are located in the spacecraft central bulkhead structure. Their axes are perpendicular to each other, 45° to the vehicle Y-Z plane and lie in planes parallel to the vehicle X-Z plane. They are mounted in cutouts in this structure at diagonally opposite corners, opposite the corners containing the sun sensors. These earth sensors have an unobstructed field of view.

g. Experiment sensors

Installation of the velocity gages, Mariner gages and Exotech sensors is shown in Fig. III-2 and discussed herein. Installation of the capacitor panel is discussed in Section III-1b. The sensors and their operation are discussed in Volume II.

Velocity gage. This unit is packaged in an 8.0-inch cube, having four ports for micrometeoroid entry (Fig. III-10).

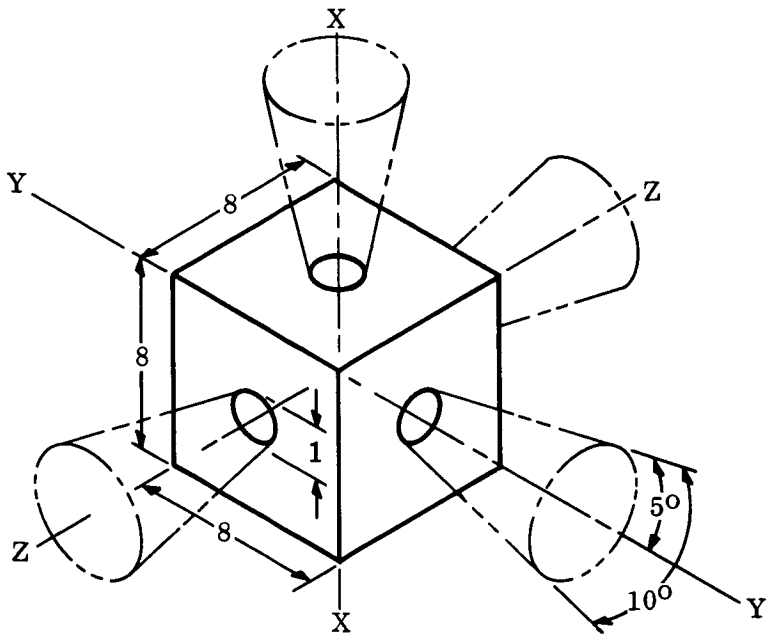

Fig. III-10.

Two of these instruments are required per vehicle, and are arranged so that their Z-Z axes are parallel and the corresponding ports in the X-Y plane are 180^{o} apart.

One of the instruments is centered on the systems module's upper cover, the other is mounted on the outer surface of the disc of the cone disc antenna. The X-X port axes are coincident with the longitudinal X-X axis of the spacecraft and Z-Z and Y-Y ports are in the Z-X and Y-X planes of the satellite. This arrangement aligns the port axes with the satellite arms and provides unobstructed acceptance angles for the viewing ports. (It is realized that mounting this instrument on the antenna may lead to RF problems. Further analysis would be required to definitely ascertain the feasibility of mounting the velocity gage in such a manner.)

Mariner gage. This unit is an 8.0-inch square plate, less than 0.25 inch thick. A small microphone is mounted in the center of one of the square faces. Three of these units are required per satellite and arranged so that their faces are mutually perpendicular. They should be located on the vehicle so as to have the best possible view of the surrounding environment.

One instrument is mounted off the outboard edge of each of three of the spacecraft's arms, in the center of the "B" plane (Fig. III-2). When the vehicle is deployed, the instruments have a relatively unobstructed field of view and are mutually perpendicular.

Exotech sensor (infrared flash detector). The sensor is housed in a 1.0 x 1.0 x 0.5-inch container, along with its preamplifier. The 0.312-inch diameter (approximate) sensor element is located in one of the 1.0 x 0.5-inch faces. The sensor element has a 140° conical field of view. Two sensors are required within each capacitor detector panel bay.

In the presently considered capacitor sensor panels without baffles, these units are mounted between the capacitors on the narrow end of each panel frame, near the corners, so that their viewing axis is approximately along the panel diagonal. The sensor elements face each other across the bay, providing maximum coverage of the panel.

h. Deployment and separation systems

Deployment sequence. Deployment of the spacecraft is shown in Fig. III-11. Shroud separation occurs early in the boost phase, at the time that dynamic pressure has decreased to zero. This shroud is the flight proven Douglas long fairing design, originally developed for the Nimbus program. It is constructed in two halves and made of a fiber glass honeycomb shell stiffened by aluminum "hat" section rings. It will use its proven separation system. Spacecraft separation from the Agena upper stage occurs immediately after Agena burnout, and is accomplished by the release of a V-band tension strap, that clamps the four spacecraft fittings to the Agena adapter ring. The spacecraft is pushed away by the action of four compression springs near these same fittings. The V-band is released by means of two diametrically opposed squib-actuated adjustable links, used to apply the initial tension. The V-band halves, after release, are retained by lanyards to the adapter ring and, therefore, stay with the Agena stage.

Release and unfolding of the spacecraft arms and planes occurs shortly after Agena separation. It is accomplished by cutting the two nylon web straps that bind the arms of the spacecraft together during boost, allowing the torsion springs and gear motor drives at the hinge axes to begin rotating their respective structures toward their final deployed position. The nylon web tension straps are cut by squib-actuated devices, near diametrically opposite corners of the folded vehicle. There are two of these straps, one near the Agena end and one approximately in the middle of the spacecraft. There are no free metallic or hard dense parts released in this operation, only the cut nylon web straps (Fig. III-12).

The sensor planes of the vehicle are locked in the deployed position by a ratchet segment at the hinge line. This device prevents any reversal of the unfolding process at any point in the travel. The deployment and locking mechanism is discussed in detail later.

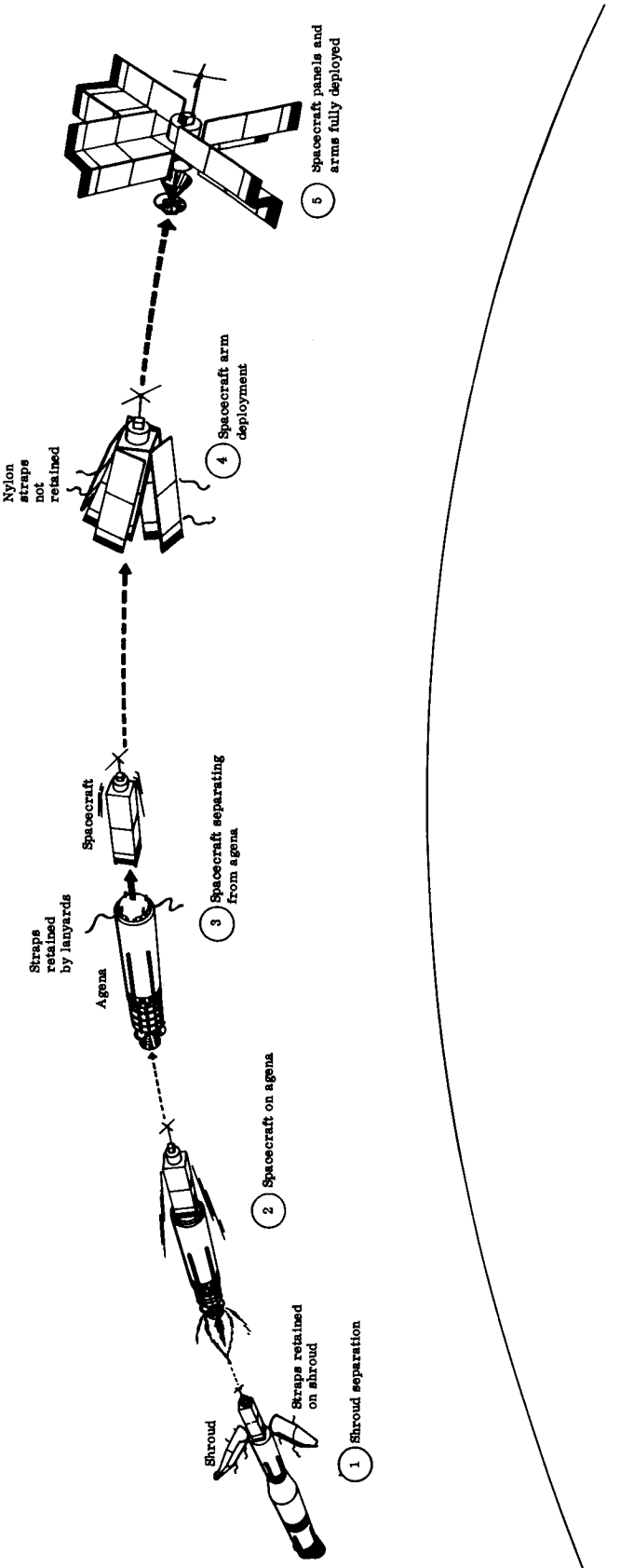

Fig. III-11. Separation Sequence

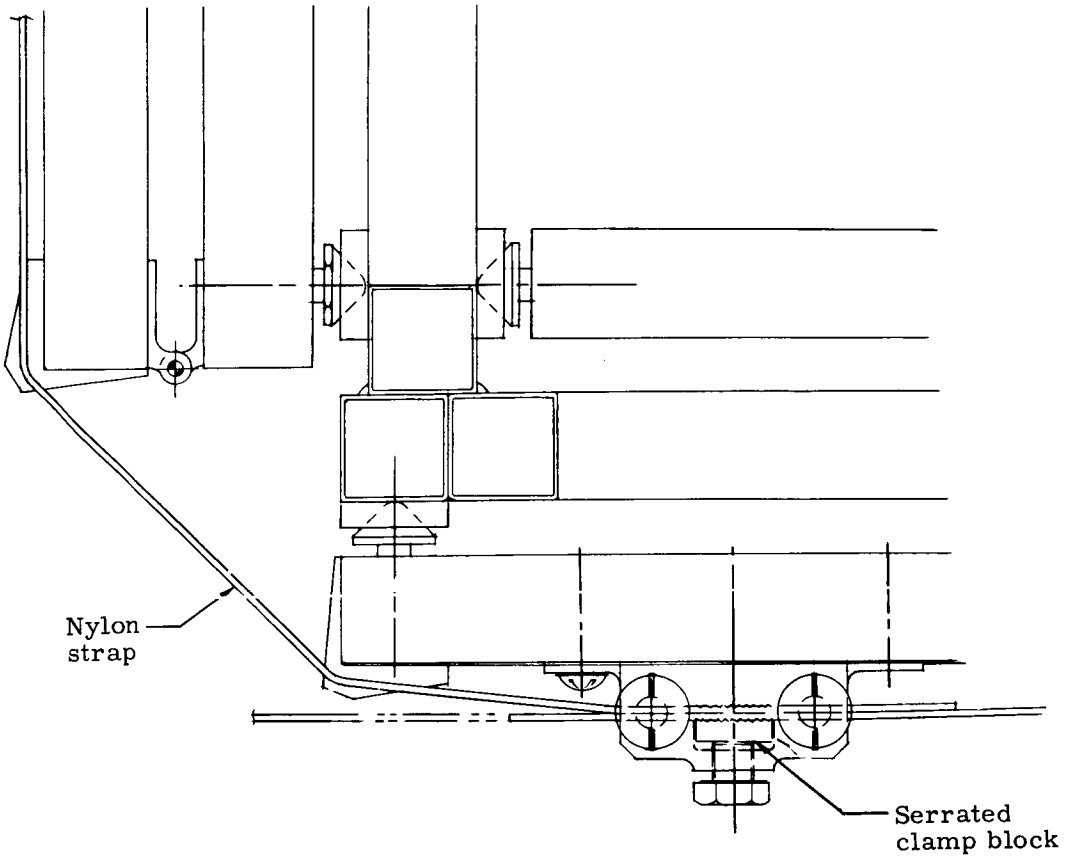

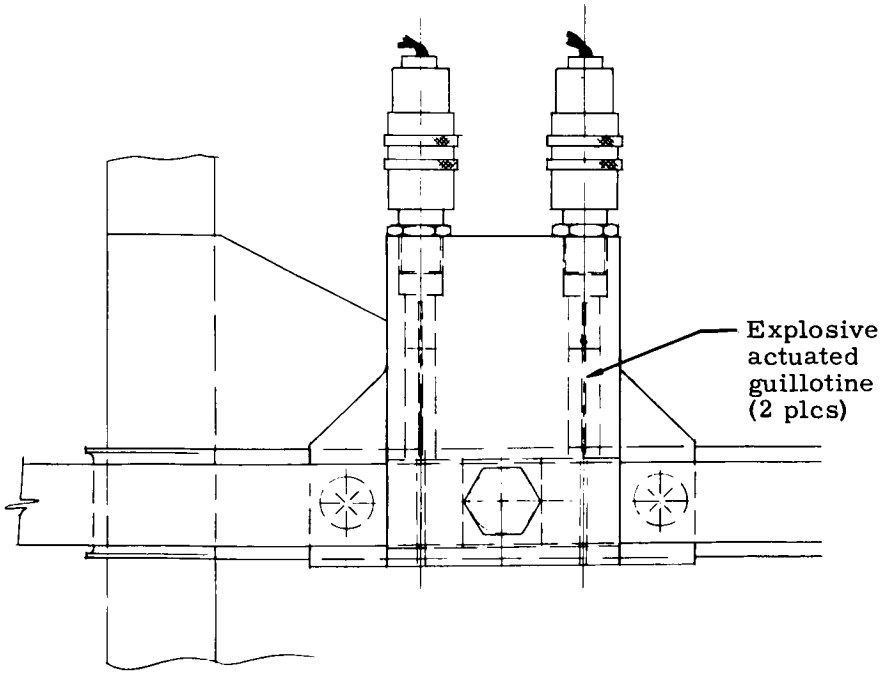

Fig. III-12. Nylon Strap Cutters

Spacecraft mounting and separation. The separation plane between the spacecraft and the Agena is 4-3/8 inches above the Agena interface frame. The space between these two locations is occupied by the spacecraft mounting adapter (Fig. III-13).

The adapter is a turned aluminum ring with flanges top and bottom so that the section is a sloped "I." The diameter of the sloped web at the Agena side is 57 inches and is 55 inches at the separation plane. The web of this ring is perforated all around by two-inch lightening holes.

The flange at the Agena side is match drilled to the Agena interface frame for the Agena attachment bolts. The mating of the spacecraft with the booster takes place at this surface. The male V-section ring to which the launch fairing is mounted via its mating V-groove ring can be made integral with this flange.

The flange at the separation plane has the male V-ring for the separation V-band clamp as an integral part. The upper half of this ring is machined away locally at the location of the four spacecraft mounting fittings which include this piece as part of their mounting fittings. A short shear and alignment pin is located in the center of each of these areas, for positioning the spacecraft and to react the loads that can not be reacted by the V-band clamp.

Just inboard of each of the four mounting fittings is the separation spring, the axis of which is parallel to the longitudinal axis of the spacecraft. It is supported at its lower end by a "hat" section fitting that is attached to the inner wall and upper flange of the adapter ring and it reacts against a fitting that is nested in the corner formed by the two perpendicular fixed planes of each detector array arm. This reaction surface is located 3-1/2 inches above the separation plane. Each of these springs has a spring rate of 119 lb/in., the installed loads is 297 pounds, the compressed length is 5.1 inches and the extended length is 7.6 inches. These springs impart a relative velocity between the payload and the Agena of four feet per second. They are made of 0.250-inch diameter music wire, and their outside diameter is 1.75 inches. The springs are retained on the adapter after payload separation by a rod through the center. The lower end of this rod contacts the bottom face of the spring support fitting when the spring is fully extended. This rod is also used to compress the spring and hold it while the spacecraft is installed.

The V-band clamp, for payload separation, is a flat steel band with intermittent aluminum, V-groove ring segments attached. It is in two halves, with a mechanically adjustable, explosively released tensioning device at each juncture. Both halves of this band are retained on the adapter by light tension springs, that accelerate its removal at separation.

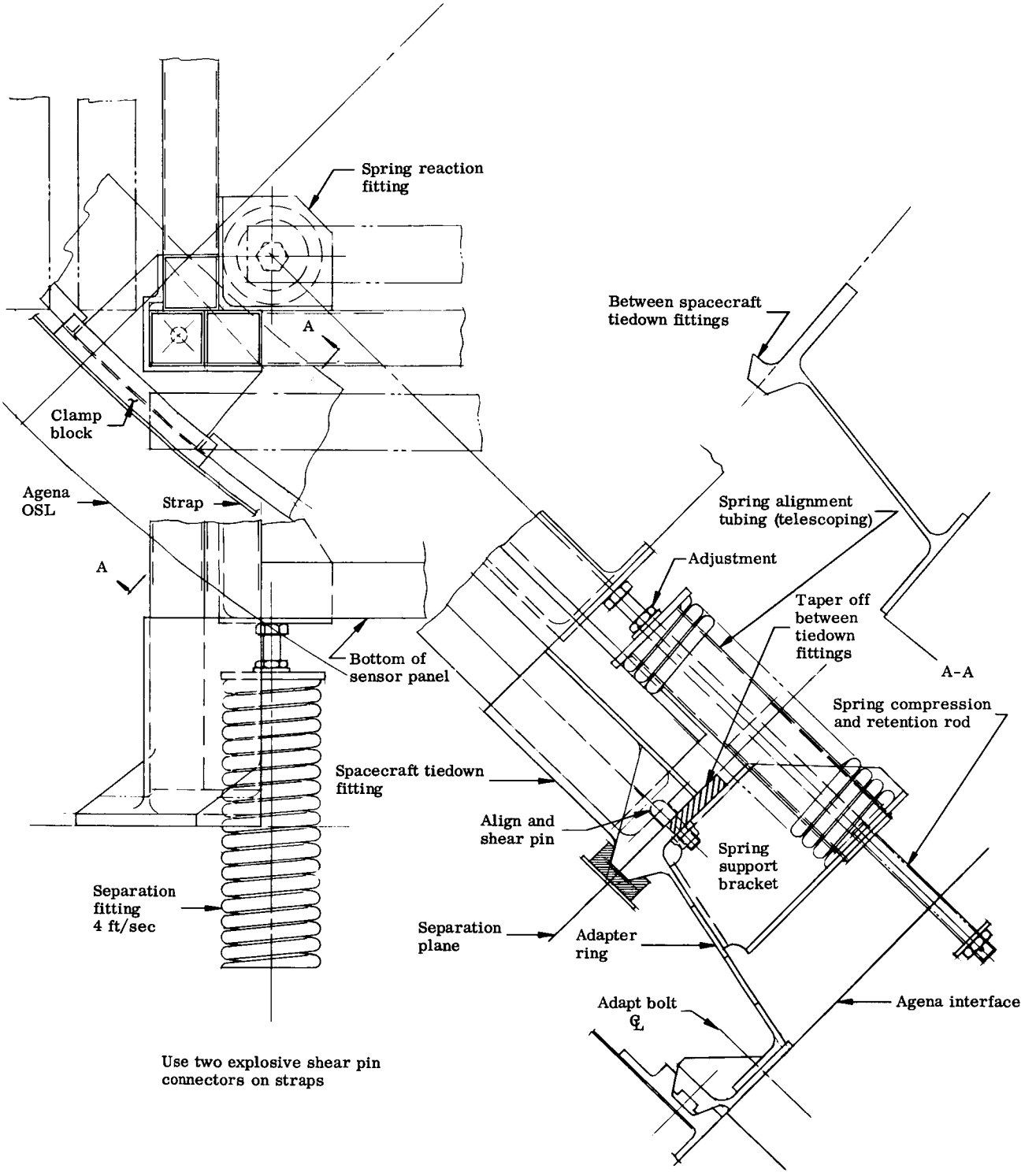

Fig. III-13. MDSS Zee Deployment Bolt--Strap Separation

Another separation system using shrouded explosive nuts on tension bolts was investigated (Fig. III-14). It is similar to the system described above in all respects except that the tension bolts replace the V-band clamp. It appears equally feasible.

Arm and plane deployment. When the nylon retaining straps are cut, the movable arms and planes of the spacecraft are free to deploy, independent of each other. Since the deploying mechanisms are the same, the rate of each arm and plane deployment should be similar, but it is not necessary that they be synchronized or sequenced.

The basic mode of deployment is similar for both the arm and its movable plane. The operating mechanism for each consists of torsion springs, and a Globe Industries, Inc. Type SS planetary gear reduced dc motor, fitted with a disc clutch (Fig. III-15). In normal operation, the torsion springs provide the energy for deployment, and the motor, with the clutch slipping, serves as a speed governor. If, due to a malfunction, increased torque is required, the motor will supply it up to the slipping torque of the clutch. In the case of a malfunction in which the motor does not receive electrical power, the springs will drive the motor in reverse through the gearing and the motor will still serve as a speed governor. The clutch is provided so that if the gearing becomes inoperative, the springs will slip the clutch as they deploy the panels. Operational curves are shown in Figs. III-16 and III-17 for the mechanisms described above. In the earlier phases of the study, deployment without the use of a clutch was considered. Curves showing the operation of a movable plane with the motor operating and with the motor inoperative are included in Figs. III-18 and III-19. These curves represent preliminary studies and are not necessarily consistent, since different springs and motors are used. Additional effort would be required prior to the selection of a deployment system for the operational vehicle.

Work to date shows that the systems indicated are feasible; however, some testing is necessary for determining the proper spring and clutch characteristics.

Arms and movable planes are provided with a one-direction latch, a ratchet, which is self-energizing against the folding motion and prevents any reversal during deployment. This latch keeps the arms and planes under control at all times so that they will be in a locked position even if some malfunction should prevent complete deployment (Fig. III-15). Dashpot deceleration techniques are not considered necessary.

Since deployment occurs shortly after launch, lubrication problems occasioned by the space environment are not serious. Distilled F-50 silicone oil may be used for lubrication of the motor reduction gear train. Hinge bearings can be bushed with reinforced Teflon bushings to

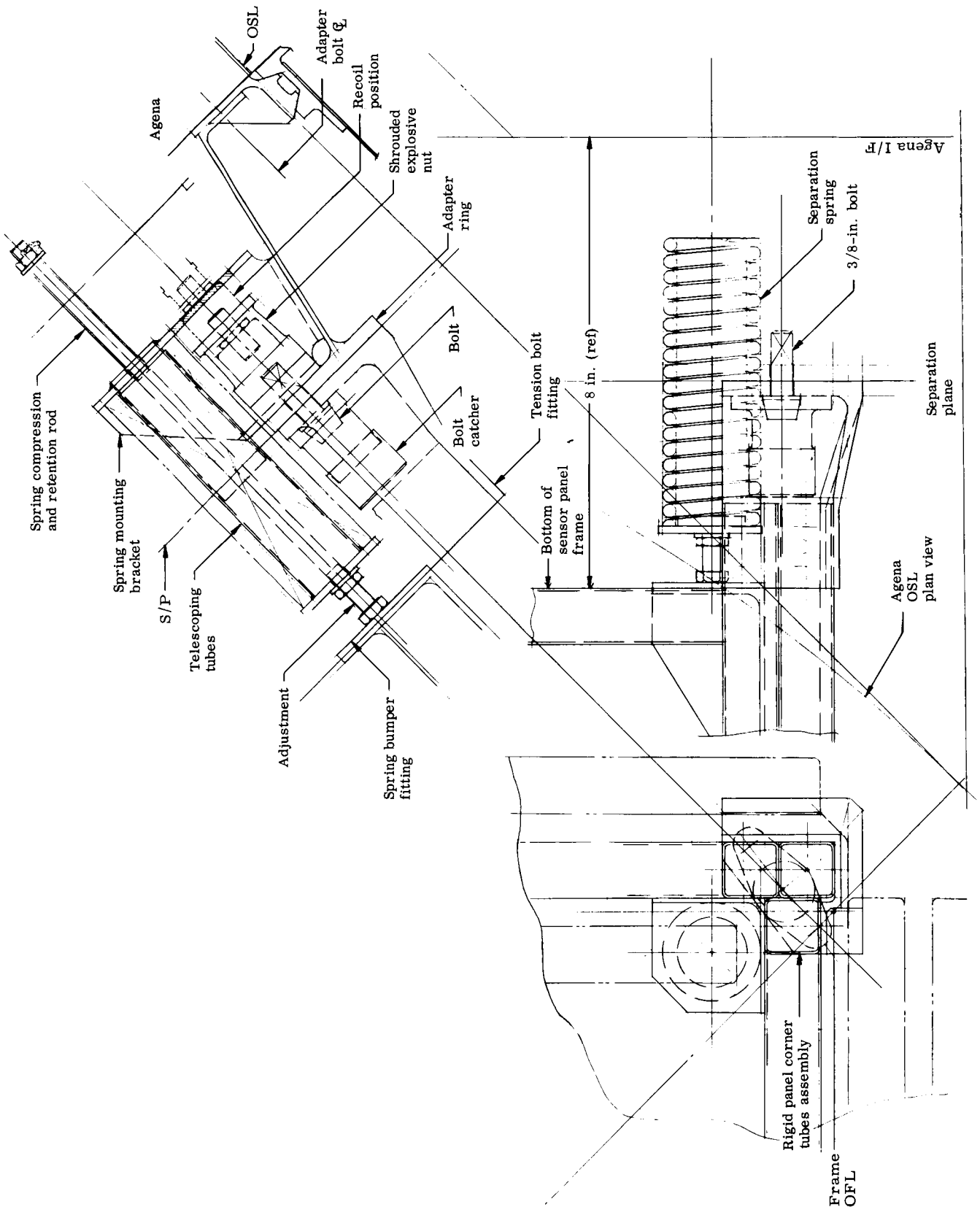

Fig. III-14. Spacecraft Attachment to Adapter No. 3--Bolt Type

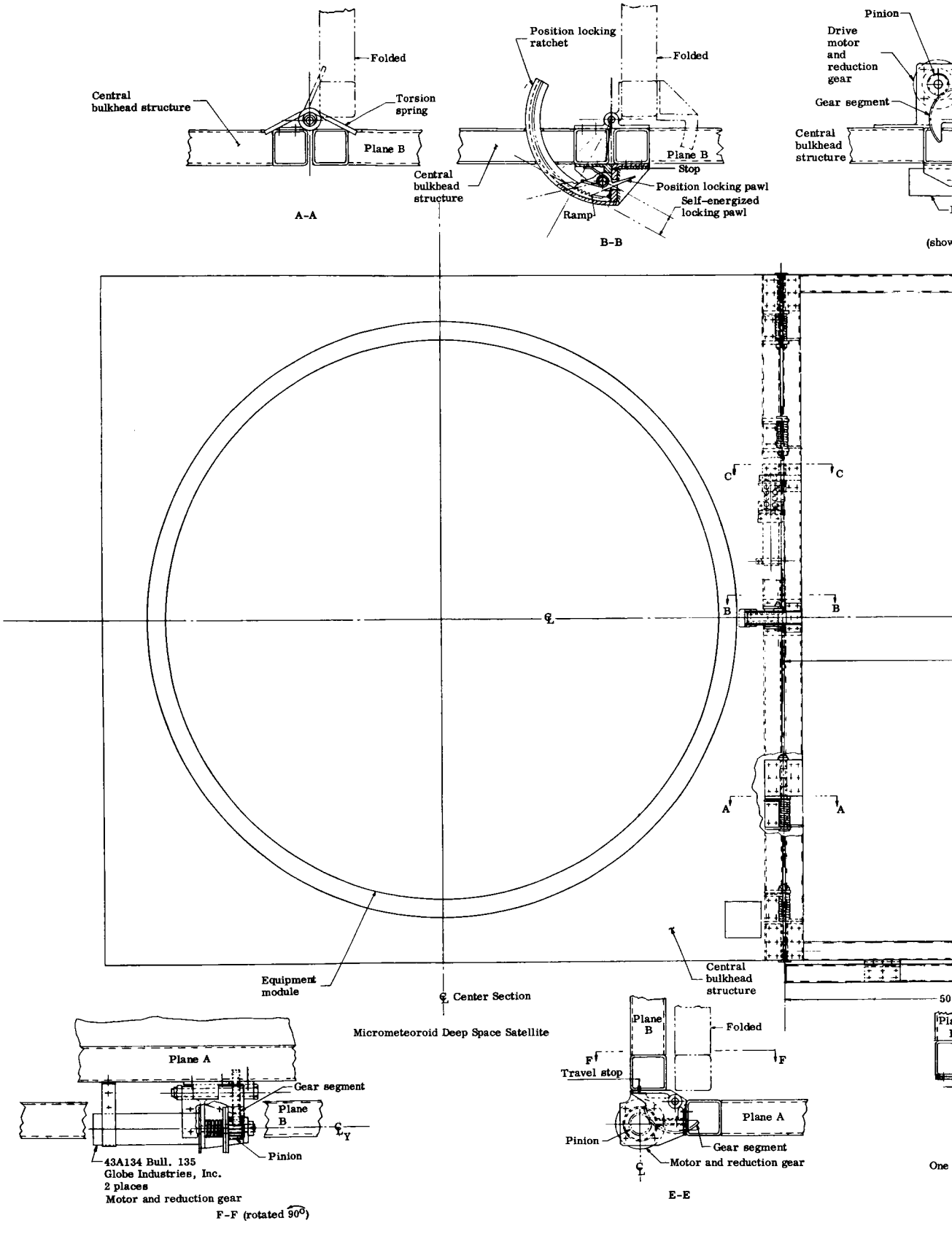
Folded
Central bulkhead structure
Torsion spring
Plane B
A-A
Position locking ratchet
Folded
Plane B
Stop
Central bulkhead structure
Position locking pawl
Self-energized locking pawl
Ramp
B-B
Pinion
Drive motor and reduction gear
Gear segment
Central bulkhead structure
(show
C
C
B
B
A
A
Equipment module
Central bulkhead structure
Micrometeoroid Deep Space Satellite
Center Section
Plane A
Gear segment
Plane B
Pinion
43A134 Bull. 135
Globe Industries, Inc.
2 places
Motor and reduction gear
F-F (rotated 90°)
Plane B
Folded
F
Travel stop
F
Plane A
Pinion
Gear segment
Motor and reduction gear
E-E

ER

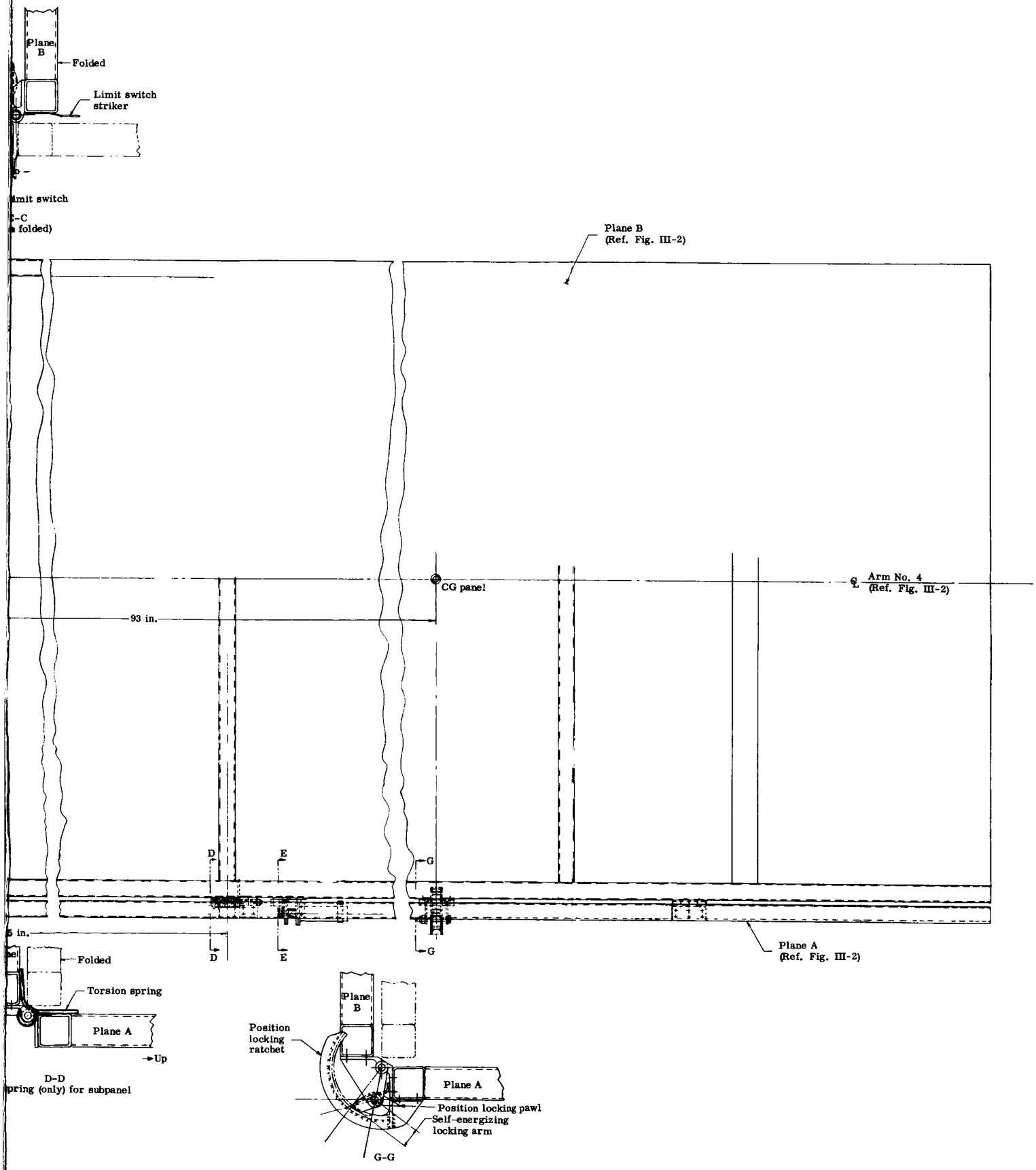

Fig. III-15. Micrometeoroid Deep Space Satellite Unfolding Mechanism

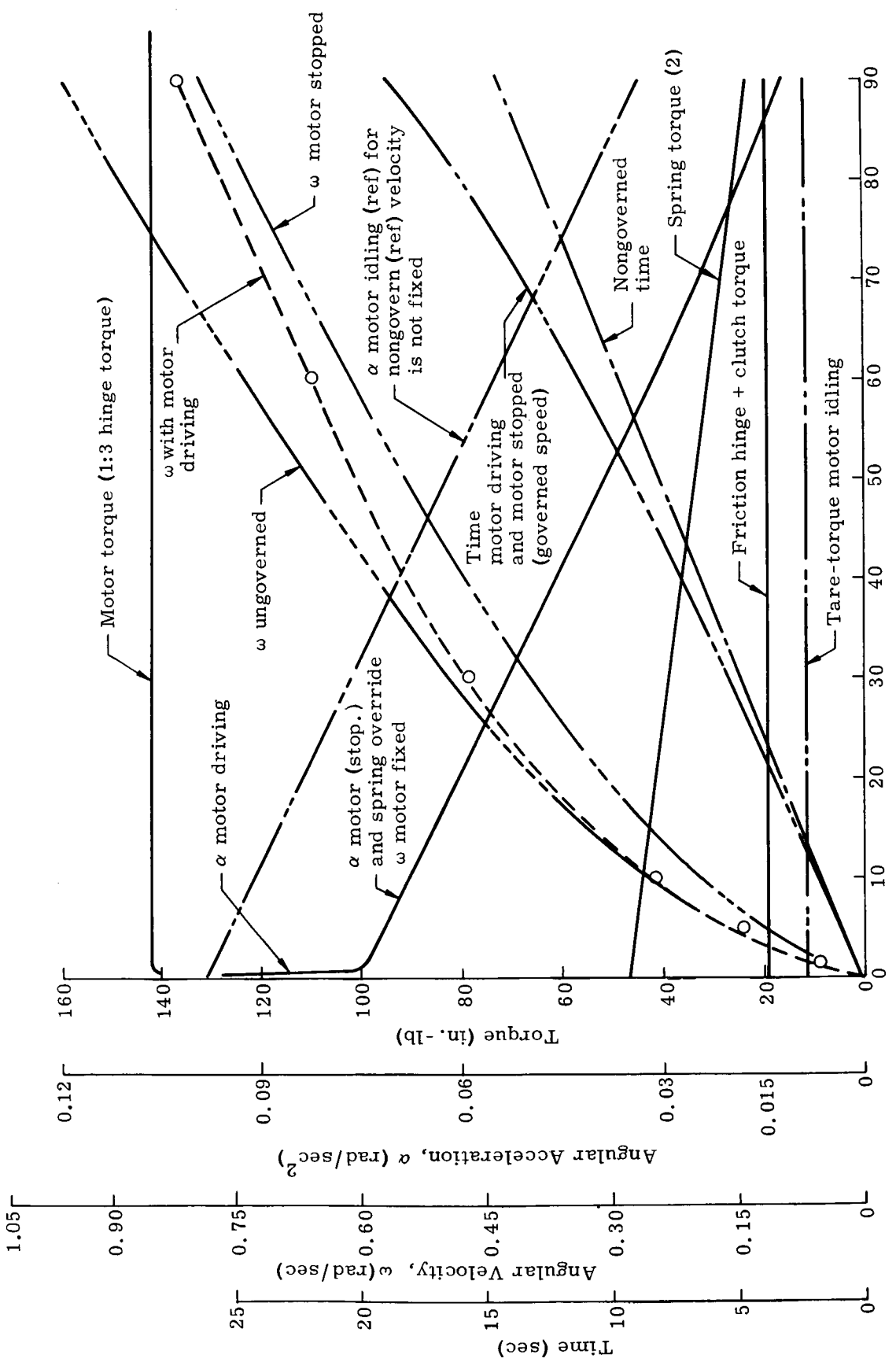

Fig. III-16. Subpanel Opening

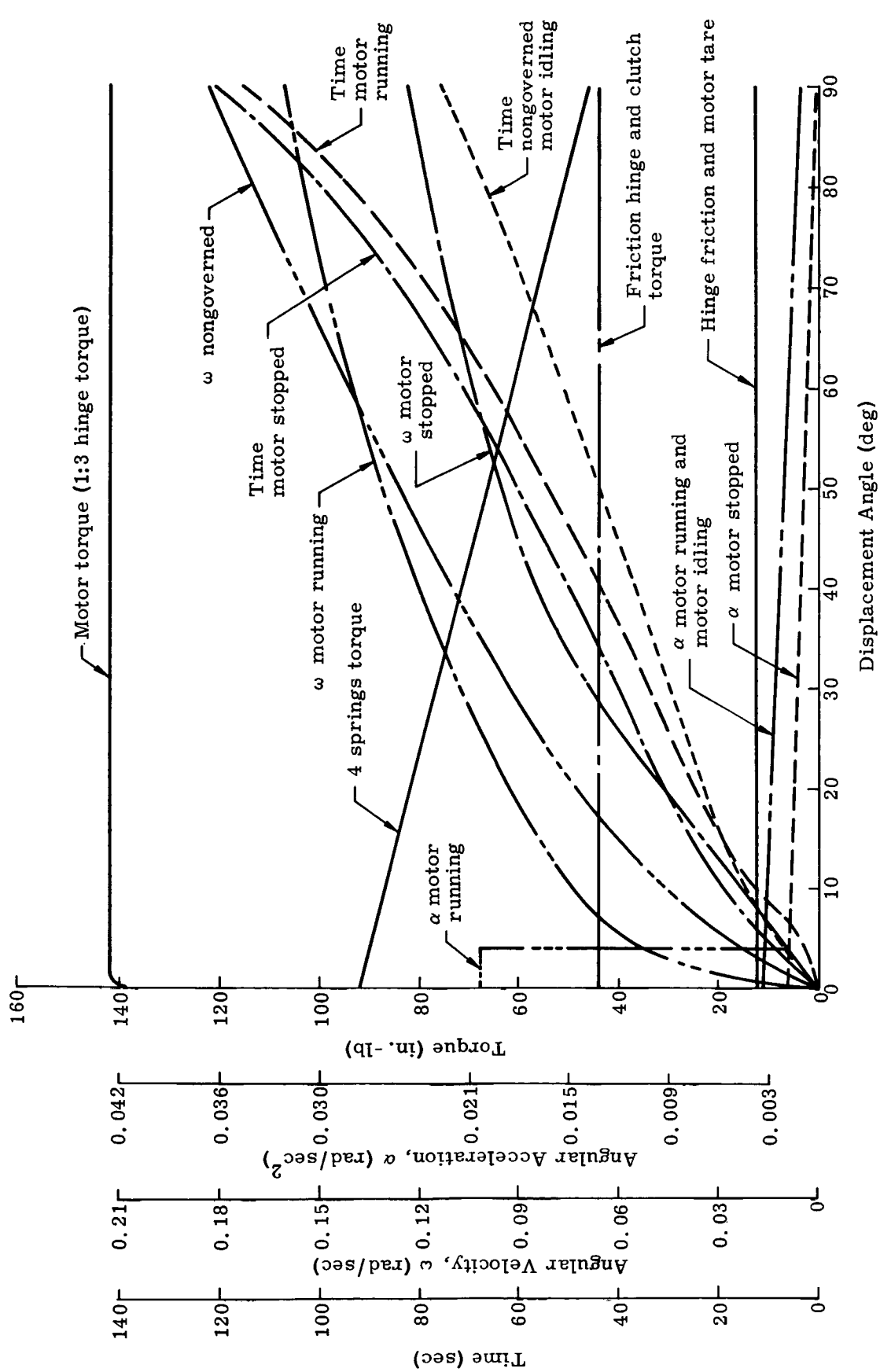

Fig. III-17. Main Panel Assembly Unfolding

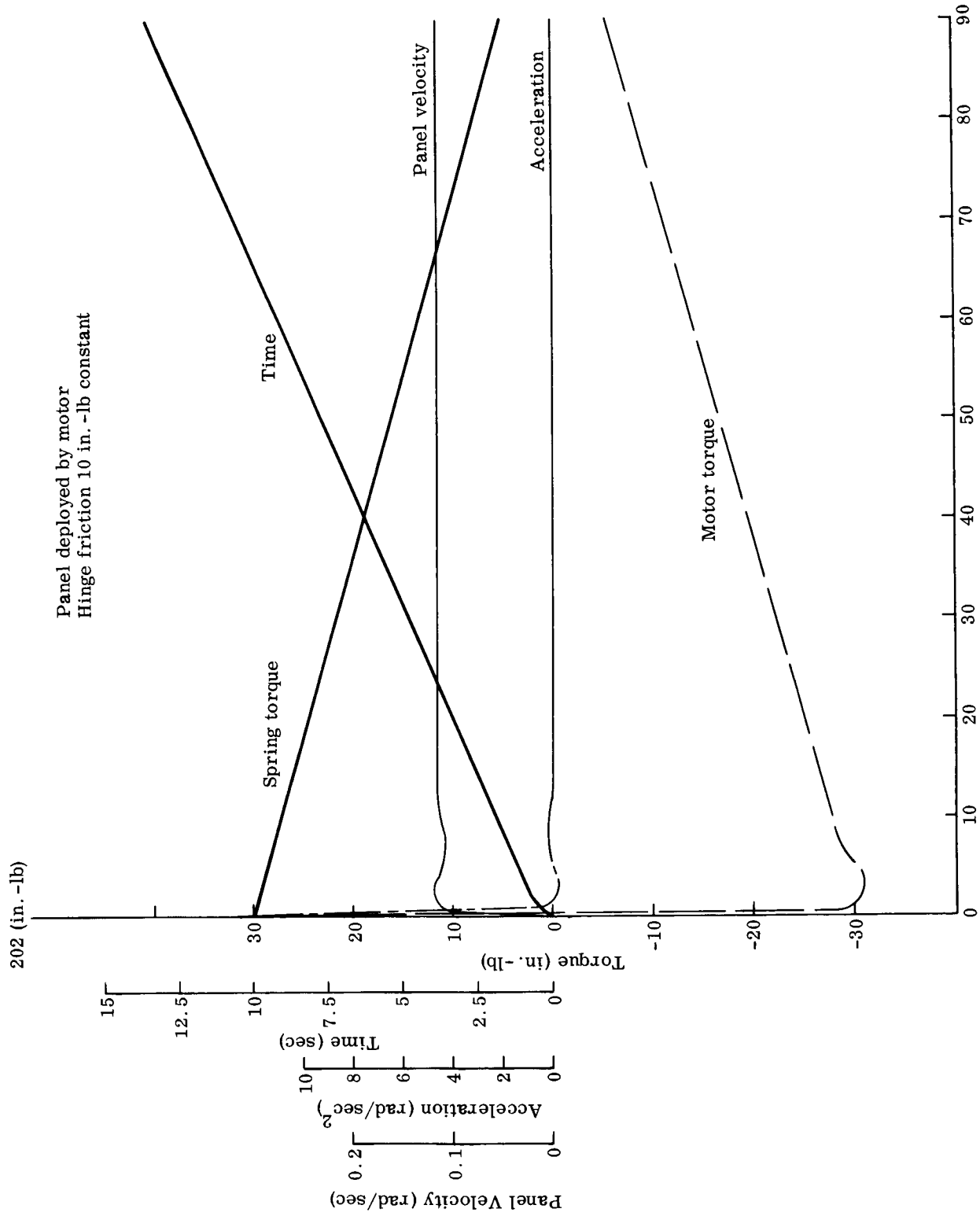

Fig. III-18. Single Panel Deployment--Motor Operating

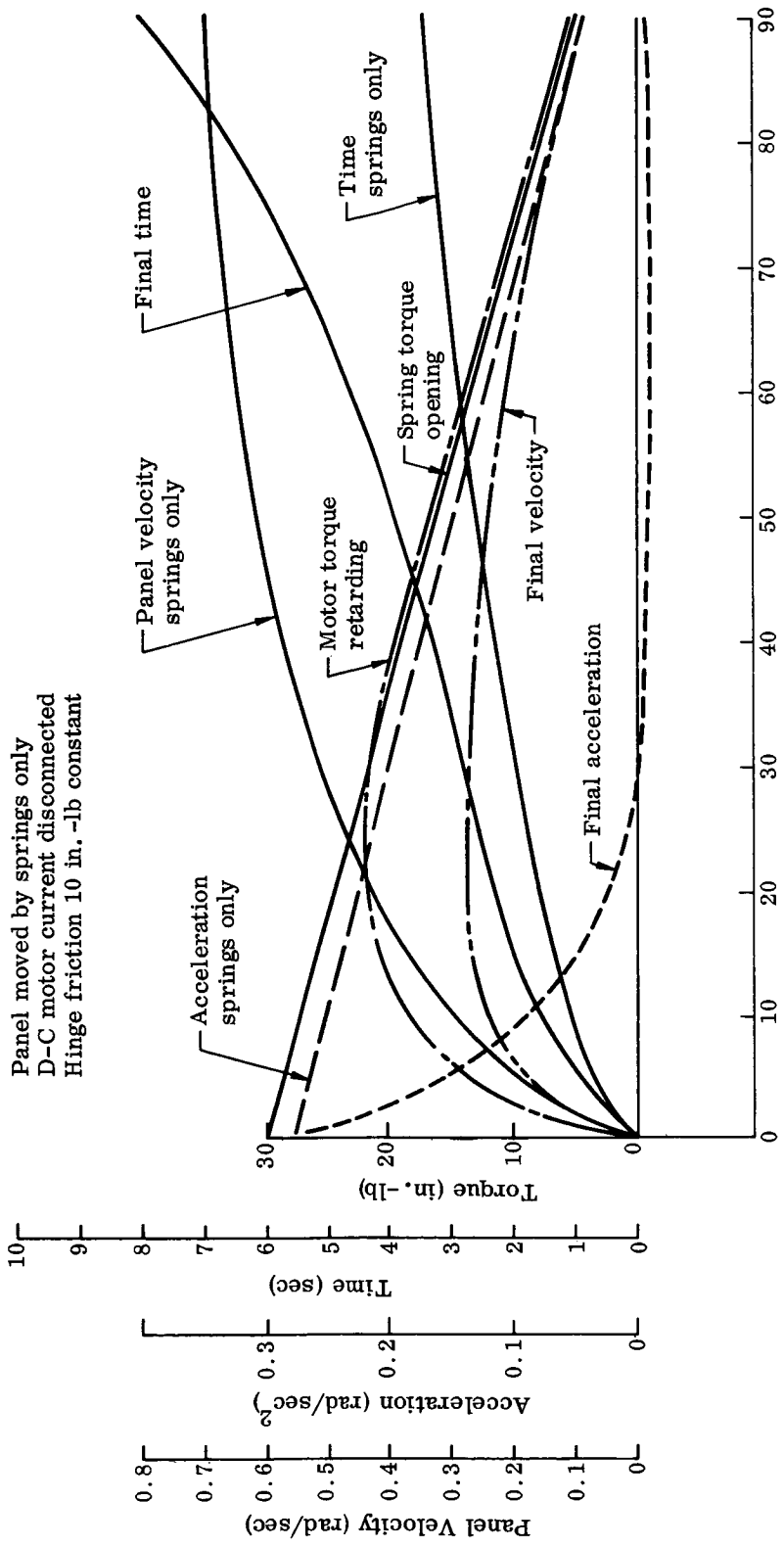

Fig. III-19. Single Panel Deployment--Motor Not Operating

reduce friction and to avoid the possibility of vacuum welding of materials in the hinges.

A brief discussion of the analysis made and of the curves plotted in Figs. III-16 and III-17 follows. It will be noted that the arms deploy somewhat slower than the movable panels due to their greater mass and the longer radius to their center of mass; however, time for deployment is not critical. Motion of the systems module and its support structure counteracting the motion of the arms was considered in determining stop loads but was not significant. The momentum imparted to the spacecraft as movement of the movable planes is stopped will cause the spacecraft to start a slow spin.

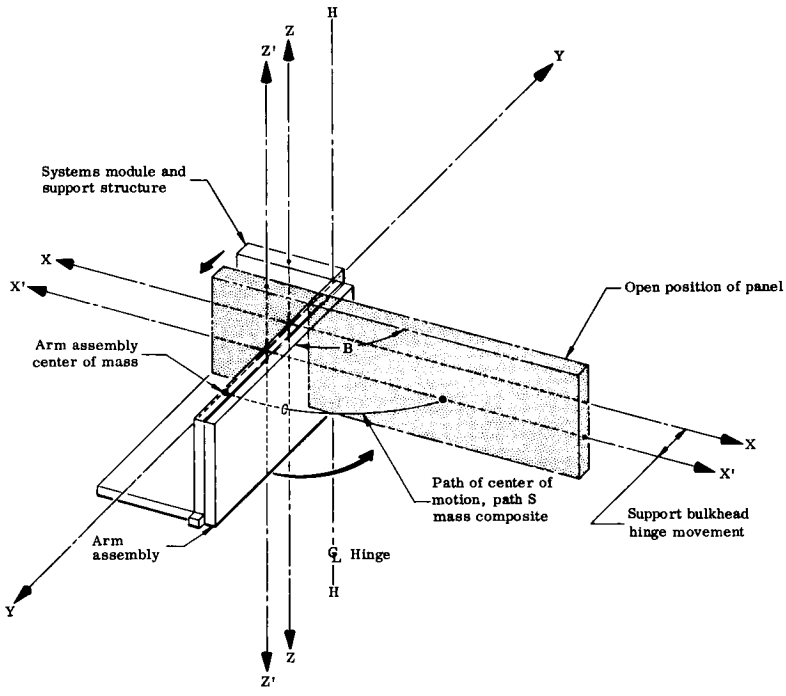

Fig. III-20.

Figure III-20 shows the general schematic for a typical arm assembly. The systems module and support structure weighs approximately 349 lb, M_c.

The arm assembly weighs 83 lb, M_p, and occurs at four hinge locations. Total weight is 332 lb.

Path S defines the composite result of relative motion of arm cg during opening.

Angle B is the angle generated by arm opening in the X-Y plane. r is the distance from cg to H-H, hinge line axis.

$\left(\frac{\partial S}{\partial t}\right)_c$ = path of arm holding support structure stationary

$\left(\frac{\partial S}{\partial t}\right)_p$ = path of arm holding arm stationary

A balance of momentum along Y-Y axis is:

$$4\, M_p \cos B \left(\frac{\partial S}{\partial t}\right)_c = M_c \left(\frac{\partial S}{\partial t}\right)_p \cos B + \Delta M_p\, \omega_{X_0}\, K \sin B$$

where $\Delta M_p\, \omega_{X_0} K \sin B$ results from rotation of the arm about its center of percussion by motion of $\left(\frac{\partial S}{\partial t}\right)_p$; $K\, \omega_{X_0} \sin B$ is linear velocity in the Y-Y direction of the hinge pin centerline. ΔM_p is the mass resulting from the concept $M_p = \frac{I_p}{r^2}$ approximately when $\left(\frac{\partial S}{\partial t}\right)_p$ occurs. The $I_{H\text{-}H}$ is equal to zero, $I_p + M_p r^2 = I_{H\text{-}H} = 0$

The shape of the "S" curve is closely approximated to be an ellipse due to the cg of the arm moving outward a distance equal to r while the support structure motion and the arm cg motion in the Y-Y direction are sharing r according to their mass inertia ratio. Then arm velocity is 6°/sec, angle θ for ω_{X_0} is very nearly 3°, and ΔM_p = 8.25 lb.

The r dimension is then shared:

$$r - b = \frac{r}{2} \times \frac{M_p\, V_P}{\left(M_c + \Delta M_p\right) r_c}$$

$$r - b = \frac{93}{2} \times \frac{332}{349 + 4\,(8.25)} = 33.00$$

b = 5 ft (approximately)

Ellipse equation $\frac{x^2}{a^2} + \frac{y^2}{G^2} = 1$

$$y = \frac{b}{a}\sqrt{a^2 - x^2}$$

In polar coordinates involving time

$$x = r \cos\theta \quad \frac{dx}{dt} = -r \sin\theta \frac{d\theta}{dt}$$

$$y = \frac{b}{a} (a^2 - r^2 \cos^2\theta)^{1/2} \text{ and } r = a$$

$$dy = \frac{b \cos\theta \sin\theta}{(1 - \cos^2\theta)^{1/2}} \frac{d\theta}{dt}$$

$$\left(\frac{ds}{dt}\right)^2 = \left(\frac{dx}{dt}\right)^2 + \left(\frac{dy}{dt}\right)^2 \quad \left(\frac{d\theta}{dt}\right) = \omega$$

$$\frac{ds}{dt} = \omega a \sin\theta \left[1 + \frac{b^2 \cos^2\theta}{a^2(1 - \cos^2\theta}\right]$$

Maximum velocity of panel occurs when

$$\theta = 90° \quad \cos\theta = 0 \quad \sin\theta = 1$$

$$\frac{ds}{dt} = \omega a$$

At the point of contact of the arm and stops on the support structure, the linear velocity of the arm cg produces a magnified load on the arm hinges equal to the retarding impulse. The drawing indicates the magnification factor to be $\frac{93}{1.3} = 71.5$.

If time, t, is taken as 0.05 sec, the force on the hinge is Ft = $(\omega_2 - \omega_a)M$. The hinge momentum forces involved when ω_2 is taken as 0.16 (Fig. III-17), the force from $\Delta M_p \omega_{x_0} K \sin B = \frac{I_{xx}}{r^2} \cdot V_{Y-Y'}$

$\frac{8.25 \times 0.16 \times 7.75}{32.2 \quad 0.05}$ = 6.36 lb added to the hinge arm-swing stop force on the hinge line = $0.16 \times 7.75 \times \frac{83}{32.2} \times 71.5 \times \frac{1}{0.05}$ = 4,560 lb (force). Within the accuracy of this study, the hinge force can be taken as $F = \frac{\omega 2}{t}$ from the curve. Figure III-17, arm assembly unfolding, is plotted from kinematic equations

$$\omega_t = \omega_0 + \alpha t$$

$$\theta = \omega_0 t + 1/2\ \alpha t^2$$

$$t = \sqrt{\frac{2\theta}{\alpha}}$$

Average values were used for incremental angle θ, arm travel 0° to 5°, 10° to 30°, 60° and 90°. Torque loads average for these increments were modified by torque values of friction and tare for the moving parts. Velocity and time were plotted according to increment accumulations; i.e.,

$$\omega = \omega_0 + \frac{d\omega}{dt} \quad \Delta t$$

and time = $\frac{2\Delta\theta}{\alpha}$ 1/2

The arm assembly is driven by four springs and the total torque value per increment of angular displacement appears on Fig. III-17. There is a Globe Industries, Inc. Type SS planetary gear reduced dc motor, fitted with a disc clutch, also operating on the hinge line of the panel. This motor was selected as part number 43A134 to provide a slow governed speed of 0.0542 rad/sec (3.1°). In the event such a motor and gear box should receive a direct hit from a micrometeoroid or become inoperative for any reason, the friction disc clutch was added to ensure arm motion from the springs. The clutch must slip to be effective, resulting in an arm acceleration which allows increasing angular velocity throughout the travel.

The curves show tradeoff values. Angular velocity is plotted for springs operating against hinge friction torque and motor assembly

idling with 6.56 in.-lb maximum tare. For the idling condition, the motor is nongoverned, to show possible maximum angular velocity. Motor running and motor stopped or jammed angular velocity curves are separated by a value of ω, generated from high initial acceleration and constant governed motor angular velocity of 0.0542 rad/sec. The slipping clutch and hinge friction provide damping to the spring torque effort on the arm assembly.

Time curves for these operations are included to show relative values but short time periods are not really necessary in the deployment of the array.

Movable plane opening. The plane opening creates the "Z" cross-section from the L-shaped stored arm configuration. The moment of inertia about the hinge line = $I_{H\text{-}H_p} = I_{H\text{-}H_x} + I_{H\text{-}H_y}$

$$I_{H\text{-}H_x} = I_{x_o} + r_1^{\,2} M$$

$$I_{H\text{-}H_y} = I_{y_o} + r_2^{\,2} M$$

$$I_{H\text{-}H_p} = \frac{11561.3}{32.2} = 362 \text{ lb-in}^2$$

The actuating springs provide torque loading in the unfolding direction as shown on Fig. III-16. A similar reduction gear motor drive is used with a clutch designed to slip at 15 in.-lb hinge torque. The hinge friction is estimated to be 4.6 in.-lb torque averaged over the travel. The motor drive torque is 426 in.-lb, governed to 0.0542 rad/sec plane hinge velocity. All component values are referred to the hinge line rotational kinematics.

Three conditions were calculated using the same method as used for the arm deployment. The total time (19.43 sec) for opening with motor stopped compares with 19.54 sec with motor running and therefore only one curve was plotted for these time parameters. The nongoverned motor time does not appear to be so much slower but that a governed motor assembly could be eliminated except for the increased load on stops and loss of motor capability to assist the springs in case of malfunction.

The ungoverned maximum angular velocity, ω, equals 0.9615 rad/sec compared with 0.8206 for the governed motor, an increase of 17%. The normal hinge load for the motor driving condition is obtained from

$Ft = (\omega_2 - \omega_1)M$, where t may be taken as 0.02 sec.

$$F = \frac{0.8206}{0.02} \times \frac{19}{1} \times \frac{83}{32.2}$$

$F = 2013.0$ lb

The maximum ungoverned motor hinge load would be 1.17 x 2013 = 2355 lb.

Umbilical. The only umbilical contemplated for this spacecraft is one at the payload-Agena separation plane. The Agena half of this connector will be located on the adapter ring adjacent to one of the spacecraft support fittings. The spacecraft half, will be mounted on this fitting and the wires from the connector to the equipment module will be routed through the structural tubing of the panel.

The Agena half of this connector will be jettisoned just prior to payload separation, but will be retained on the adapter.

2. Weight Summary

	(lb)	(lb)
Structure, center		85.0
Cylinder	75.0	
Arm support	10.0	
Power supply		122.1
Solar cells	44.4	
NiCd battery (2)	32.0	
Thermal battery (2)	0.9	
Voltage regulator	1.3	
Converters (2 sets)	3.3	
Charger limiter	0.2	
Miscellaneous circuitry wiring	40.0	
Instrumentation and secondary sensors		170.4
Signal conditioning units (4)	18.0	
Exotech sensors and preamplifiers (72)	7.2	
Exotech electronics (2)	4.0	
Mariner gage and preamplifier (3)	1.5	
Mariner electronics (6)	12.0	
Velocity gage (2)	8.0	
Velocity gage electronics (4)	16.0	
Time of flight converter (2)	3.0	
Fluxgate magnetometer		
6 heads, 4 electronics	15.0	

	(lb)	(lb)
Diagnostic system 1	4.0	
Diagnostic system 2	3.0	
Diagnostic system 3	2.0	
Diagnostic system sensors (40)	4.0	
Killer timer (2)	1.0	
Deployment timer (2)	1.0	
Capacitance panel test (2)	1.0	
Panel charge generator (4)	1.0	
Capacitor data unit (2)	0.5	
Exotech data unit	0.6	
Mariner data unit (2)	1.2	
Diagnostic data unit	1.2	
Master clock and divider unit (2)	0.2	
Deployment data unit	0.1	
Memory overflow unit	0.1	
Memory unit A (2)	0.4	
Memory unit B (2)	3.6	
Memory unit C	3.5	
Solar aspect electronics (2)	7.0	
Solar aspect sensors (5)	1.3	
Earth sensor unit (2)	1.0	
Aspect data unit (2)	2.0	
Installation and circuitry	46.0	
Communications		41.8
Hybrid and diplexer assembly	2.8	
Beacon and data transmitter	1.5	
VHF transponder (2)	5.4	
Command decoder (2)	5.0	
Command logic	3.0	
Subcarrier oscillator and modulator 1 and 2	0.6	
Imput data selector and signal conditioner	0.6	
Coaxial switch	0.2	
VHG antenna (2)	6.0	
Installation and circuitry	16.7	
Separation		15.0
Environmental control		10.0
Capacitor sensors		251.3
Supporting structure	140.8	
Light shields	10.0	
Hinges and mechanism	24.6	
Panel stops	4.0	
Bonded sensors (0.002)	67.0	
Bonded sensors (0.001)	4.9	
Total spacecraft weight		695.6
Agena adapter		22.4
Spacecraft straps		5.0
Total Agena payload		723.0

3. Configuration Development Studies

In this section, a brief summary will be given of the various stages by which the design described in Section B1 was developed. Some of the various configurations, capacitor sensor panel designs and methods of securing and deploying the spacecraft that were investigated will be outlined.

a. Configuration

Configurations were developed for the Atlas-Agena and Atlas-X-259 boosters that were compatible with the Atlas long fairing heat shield. The Saturn 1B configurations were contained in a truncated cone payload envelope 336 in. high, 156 in. in diameter at the top and 260 in. in diameter at the bottom.

Atlas configurations. During the study in which the proposal which resulted in this contract was prepared, the configuration shown in Fig. III-21 was developed. It was compatible both with the Atlas-Agena and Atlas-X-295 boosters, and featured four sets of three panels each. Each set was rotated 90° in deployment and had two movable panels which were then deployed 180°. The resultant configuration was essentially a flat plate. Panels were mounted from the bulkhead that supported the systems module and were non-load carrying. The corners of the movable panels were trimmed to provide necessary clearance. The X-259 configuration which had the systems module at the top required a long adapter and required that the sets of panels be deployed 90° prior to separation. In the early phases of the study, effort was directed toward obtaining maximum capacitor sensor area. Since the present configuration filled all available space between the heat shield and the X-259, effort was then concentrated on the Atlas-Agena configuration where additional volume was available under the fairing. When the "Z" configuration was conceived, the maximum sensor area available on the X-259 was found to increase from 592 to 680 sq ft (Fig. III-22), but since performance tradeoff studies showed that the Atlas-X-259 booster was not as good as the Atlas-Agena, no further work was done on the Atlas-X-259 configuration.

In developing the Atlas-Agena configuration, and additional panel was first added to each set on the proposal configuration, folded 180° into the now empty center of the folded configuration. This increased the available area from 592 to 702 sq ft, and when the similar panel was added to the "Z", the area increased to 790 sq ft. The "Z" configuration, conceived first by rotating the movable panels only 90° instead of 180°, was basically intended to provide a three-dimensional sensor surface. When investigated, it had many additional advantages:

(1) It eliminated the need for the clearance trim cut on the movable panels and thereby increased available area.

(2) It reduced deployment requirements of the movable panels from 180° to 90°.

(3) It permitted two of the panels in each set to be built integral, thereby eliminating four hinge lines and mechanisms and making it possible to design the panels to support the spacecraft.

The above permitted the systems module to be mounted on top which greatly simplified antenna installation, improved serviceability of the systems module,and permitted additional increase in available sensor area (Fig. III-23). Total available sensor area (Fig. III 23) increased from 664 to 752 sq ft when the adapter was shortened so that the systems module became tangent to the separation plane. With the systems module located on top and the adapter made as short as practical, the area increased to 790 sq ft. Further area increases (Fig. III-23) were realized by adding additional "Z" panels to each of the sets and stowing them in the volume formerly filled by the X-259 motor (Fig. III-24). This is not investigated further because the "Z" configuration provided adequate target areas of 0.001-in. and 0.002-in. aluminum without the added complexity of deployment. It should be noted that sensor areas mentioned above are the maximum available, whereas those given in Section B1 are net after allowing for structure, installation, solar cell area, etc. They are satisfactory for comparisons only. This describes briefly the steps taken from the proposal configuration (Fig. III-21) to the study configuration (Fig. III 2).

Saturn configurations. Before the performance of the two-stage Saturn 1B was known to be unsatisfactory, emphasis was spent in determining the maximum capacitor sensor area that could be contained within the Saturn 1B heat shield. Areas from 6088 to 9328 sq ft were obtained on configurations such as: flat plate, "Z," multiwinged and parasol (Fig. III-22). The "Z" configuration, shown deployed and within the heat shield in Fig. III-25, had approximately 7000 sq ft of sensor area. The layout of spring mounted sensors in a typical panel is shown in Fig. III-26. Since the heat shield was so large, an octagonal shaped sensor panel that required no deployment was investigated (Fig. III-27). Its maximum available area was 1640 sq ft, including the end bulkheads. The Atlas-Agena, areas mentioned here are the maximum available, which include structure, sensor installation, solar cells, etc. The numbers shown above are satisfactory for comparisons only. Upon determination that the Saturn 1B was not suitable for this mission, the effort was terminated.

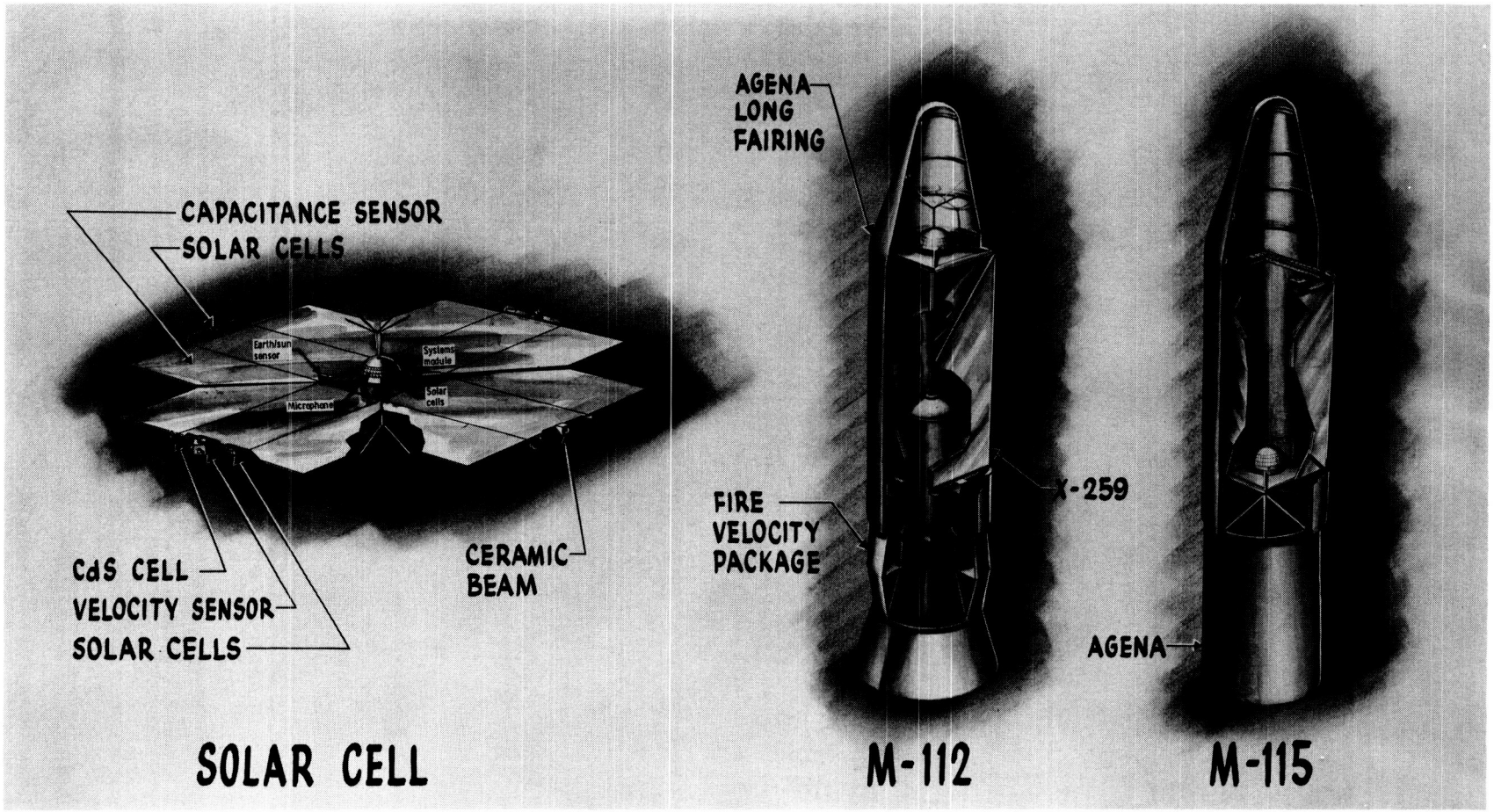

Fig. III-21. Proposal Configurations

PANEL	CONFIGURATION	BOOSTER	MAX SENSOR AREA AVAIL (SQ FT) NO WT LIMI-TATION (BOTH SIDES OF PANEL)
M-112	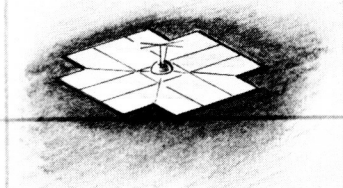	ATLAS-X259	592
M-115		ATLAS-AGENA	592
M-115 MODIFIED	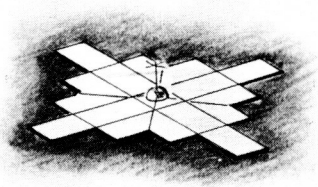	ATLAS-AGENA	702
AX-1	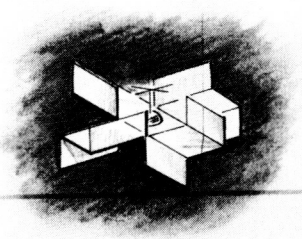	ATLAS X259	680
AA-1		ATLAS-AGENA	680

PANEL	CONFIGURATION	BOOSTER	MAX SENSOR AREA AVAIL (SQ FT) NO WT LIMI-TATION (BOTH SIDES OF PANEL)
AA-1 MODIFIED	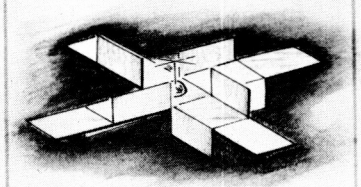	ATLAS-AGENA	790
S-1	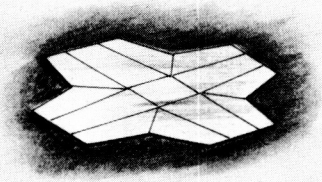	SATURN 1B	6088
S-2	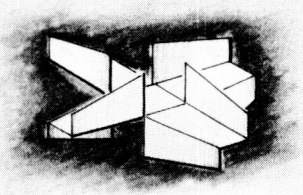	SATURN 1B	6984
S-3	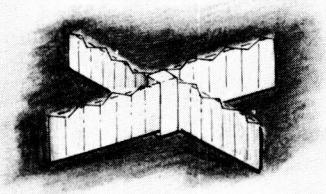	SATURN 1B	8000
S-4	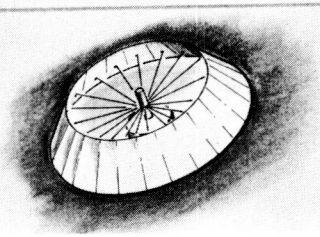	SATURN 1B	9328

Fig. III-22. Configuration Booster Combinations

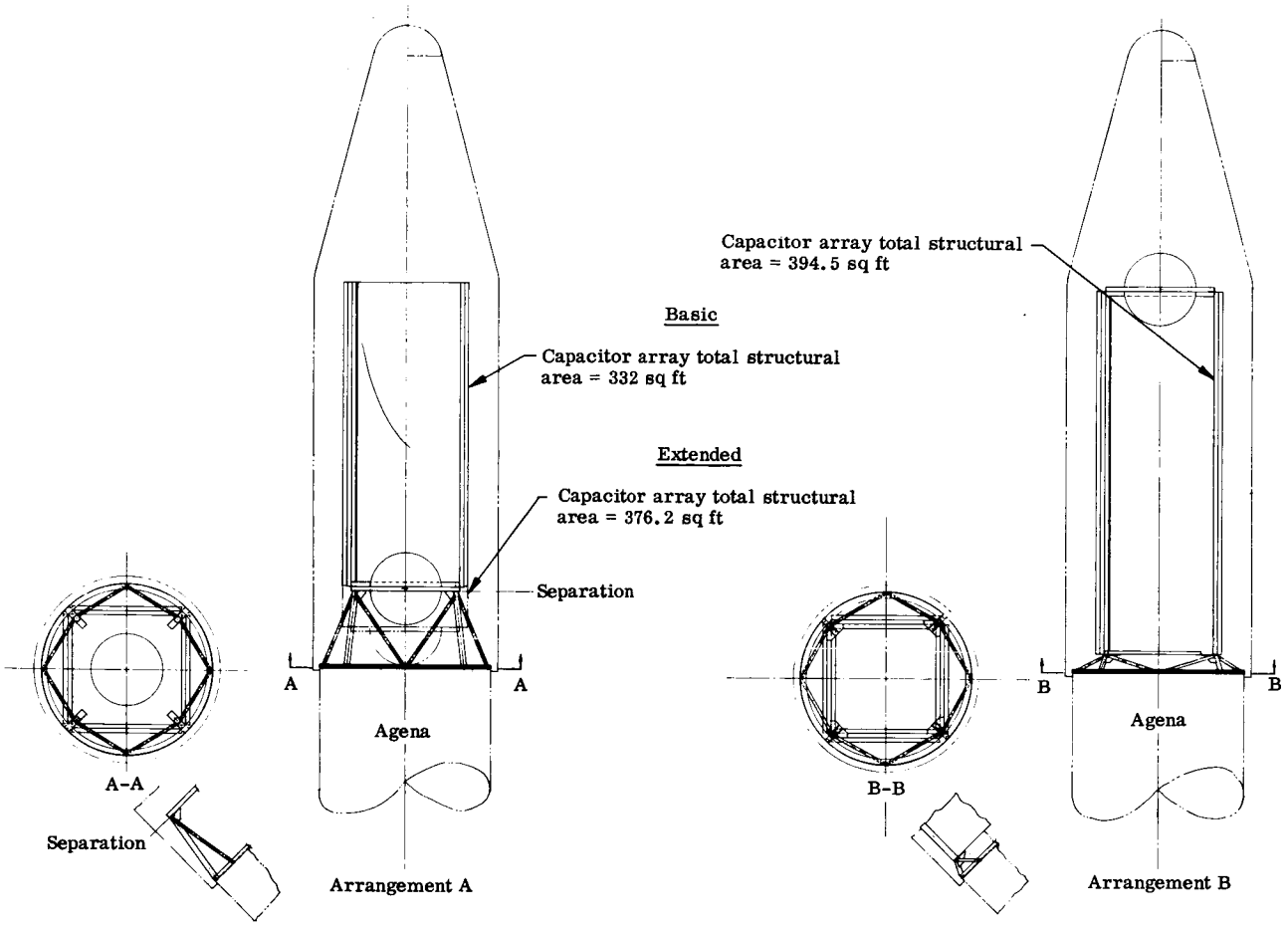

Atlas-Agena Configuration	Structural Area (sq ft)	Gross Sensor Area (sq ft)
(1) Progress Report Configuration AA-1 (mounted as shown for M 115)	332	664 (680)
(2) AA-1 with equipment module tangent to separation plane and panel array extended accordingly	376	752
(3) AA-1 mounted on short adapter with equipment module on top extending into nose cone taper	395	790
(1) With added Z's extended	591	1182
(2) With added Z's extended	658	1316
(3) With added Z's extended	691	1382

Fig. III-23. Comparison of Capacitor Array Areas

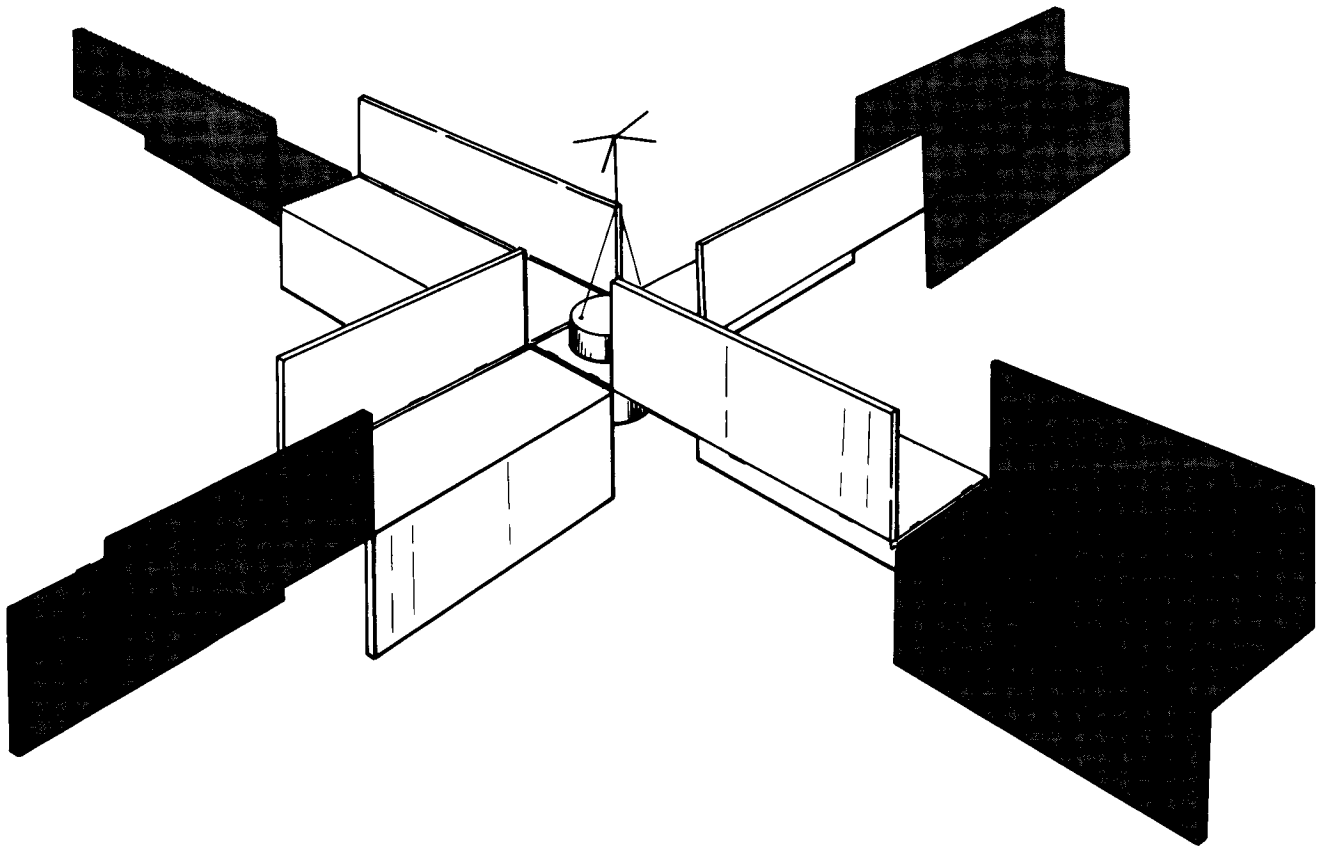

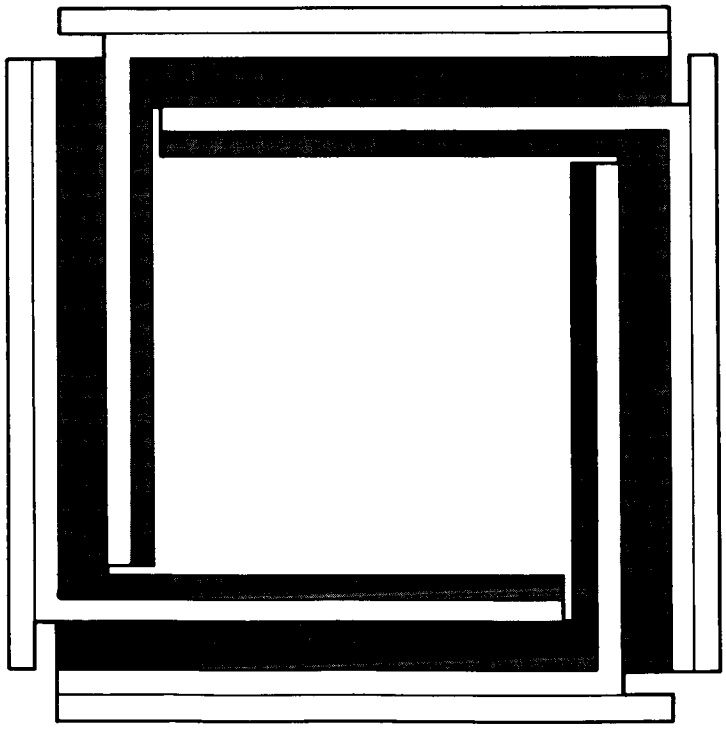

Fig. III-24. Panel Growth Potential

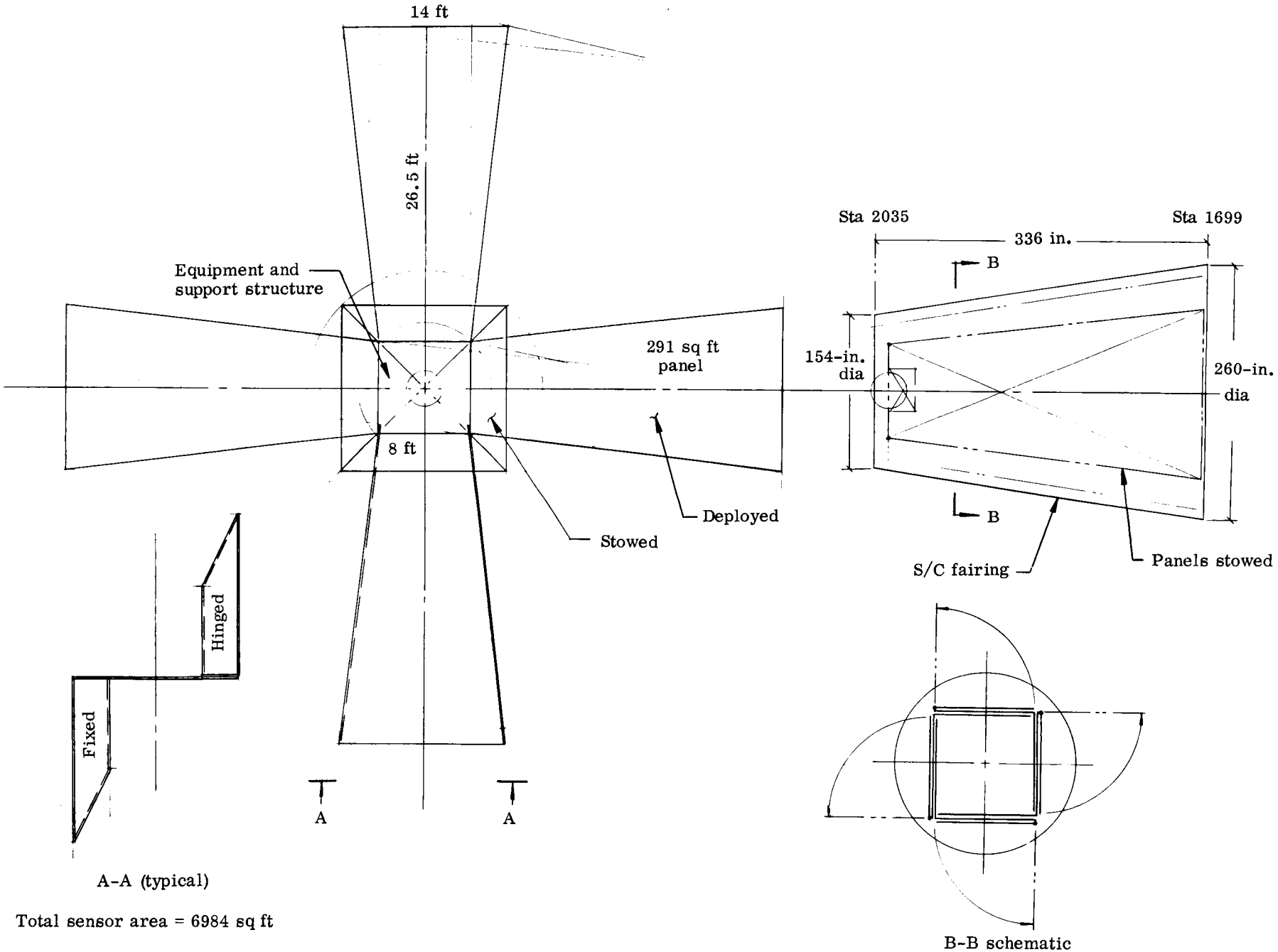

Fig. III-25. Saturn 1B

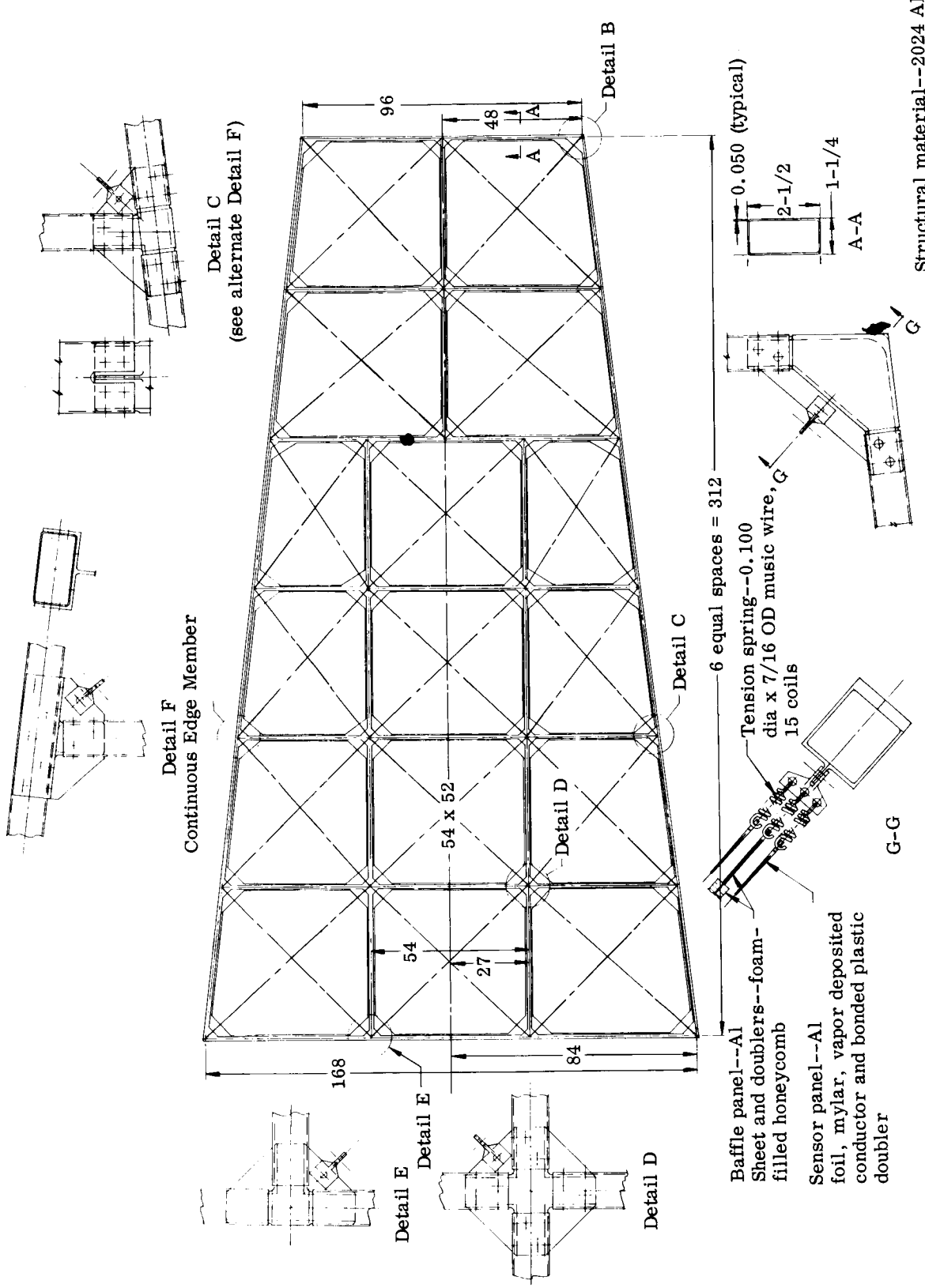

Fig. III-26. Saturn 1B Trapezoidal Panel--Zee Configuration

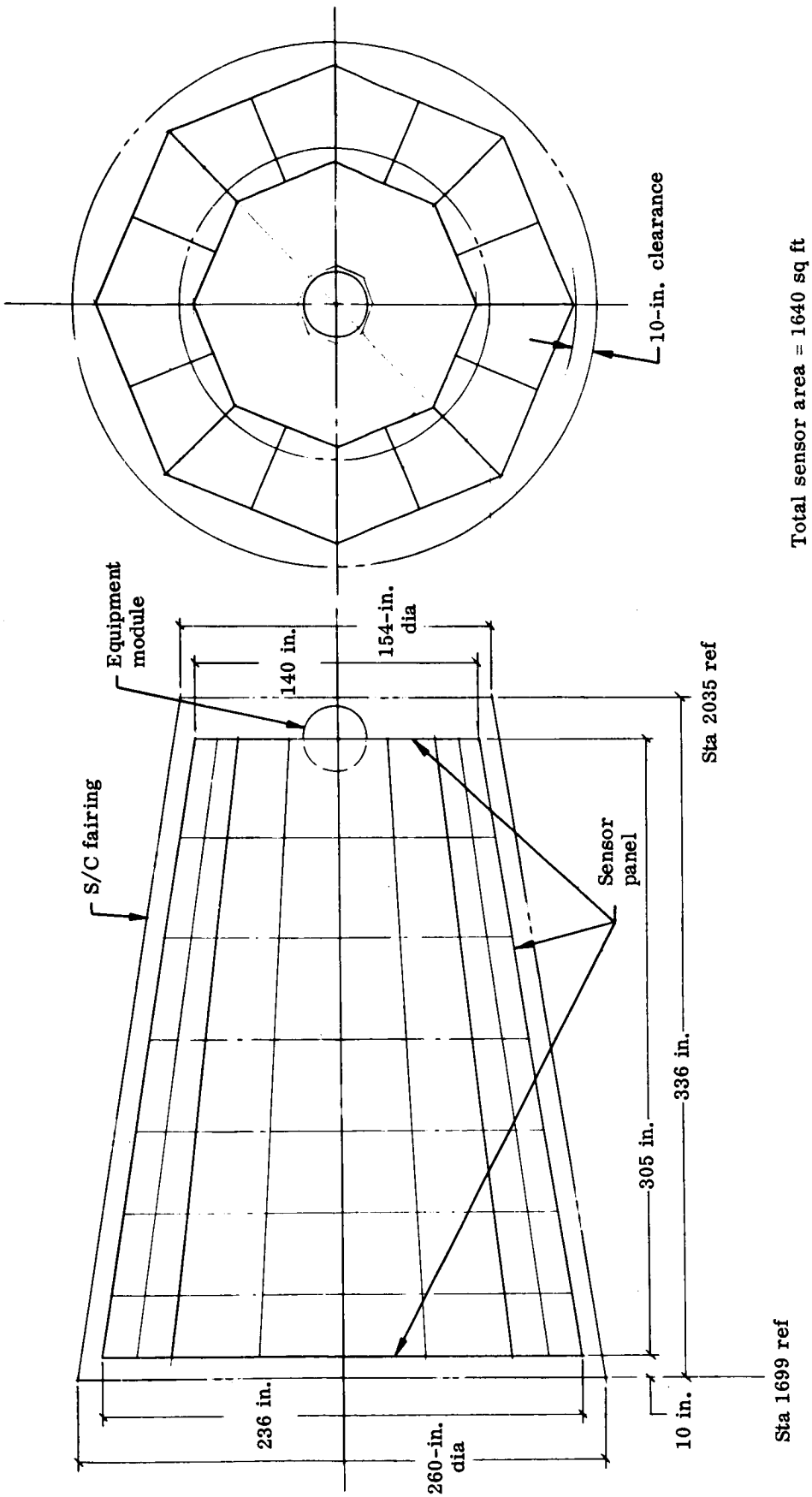

Total sensor area = 1640 sq ft

Fig. III-27. Saturn 1B Octagonal Configuration

b. Sensor panel design

One of the design requirements for the spacecraft was that it provide as much sensor area as possible. To achieve this, the lighest method of supporting the sensor panels was sought. An idea advanced in the Lunar Orbiter Study was applied here. This was to spring mount the sensors and baffles in a tubular space frame. Figure III-30 shows a typical installation of a panel and various baffle designs. Baffles were sized from a meteoroid penetration study which is summarized in Fig. III-31. A dynamic analysis revealed that the sensor suspension would not be critical but that the spring baffle panels would require additional study due to their mass. At this time, the idea of segmenting the sensors was developed. Statistical analyses showed that only a small percentage of the sensors would be shorted, and this could be tolerated. Therefore, it became possible to save additional weight through removal of the baffles. Removal of the baffles also facilitated installation of the Exotech sensor to serve as a backup to the capacitor. This required light shielding of the panel, which is accomplished by an opaque mylar light block. This is the installation described in Section B1. The capacitor shown consists of an aluminum target, mylar dielectric, and vapor-deposited copper because this type is available. New capacitors using other dielectric and capacitance plates can readily be adapted as they are developed.

An alternate capacitor sensor mounting (Fig. III-32) was devised to supplement the spring-mounted panel if it posed any problems in development. Capacitors are bonded to an auxiliary frame which is mounted in the spacecraft planes. This design is discussed further in Section B4.

Pressurized sensors were also considered and an installation of pressure tubes is shown in Fig. III-33 in a "Z" configuration. This is a modification of the pressure sensors used in the Explorer series. Both sides of the 2-in. sensor tubes are exposed and ~600 sq ft of area is thereby obtained. Another feasible method of providing a pressurized sensor is by using a sealed honeycomb panel whose faces are the target. These designs are discussed in Section 3.4.1.4 and in Section 3.2.1 of Chapter I, Vol. II.

Consideration was also given to multilayer capacitor sensors and to bumper-type sensors, and some details of their design are given in

Volume II, Chapter I. These designs were not pursued at this time, since they involved development programs for evaluation and calibration.

A weight comparison of the sensors studied is given in Table III-2.

TABLE III-2

Sensor	Target	Progress Report No. 2 Unit Weight (lb/sq ft)	Current Unit Weight (lb/sq ft)
Capacitor without baffle	0.002 Al	0.059	0.065
Capacitor with baffle	0.002 Al	0.295	Not detailed
Pressurized cylinders	0.001 BeCu	0.286	
Pressurized honeycomb	0.001 BeCu	0.273	
Framing and installation		0.330	0.405

Table III-2 shows the current, more detailed, design unit weights compared to those shown in Progress Report No. 2 (ER 13603-2, dated October 1964). As shown, the average unit weight of a typical manufactured panel will have corner reinforcements added to the above midpanel unit weights as follows:

Capacitor without baffle (two assemblies)	0.065
Corner reinforcements (two assemblies)	0.145
Framing and installation (1)	0.405
Total	0.615

While other sensors have not been detailed to the same extent as the capacitor without baffle, the unit weight trends may be estimated by comparison with the data from Progress Report No. 2.

c. Securing and deployment

The spacecraft design described in Section B1 requires that the structural framework of the sensor arms and movable planes be secured during launch so that they are structurally integral. Several methods were investigated before the one shown in Fig. III-4 was developed.

Using the motion of the panels as an aid, tapered pins--first without and then with pin-pullers--were tried and rejected. It was felt that the tapered pins would tend to bind due to temperature change, and that they required too many pin pullers to be sufficiently reliable.

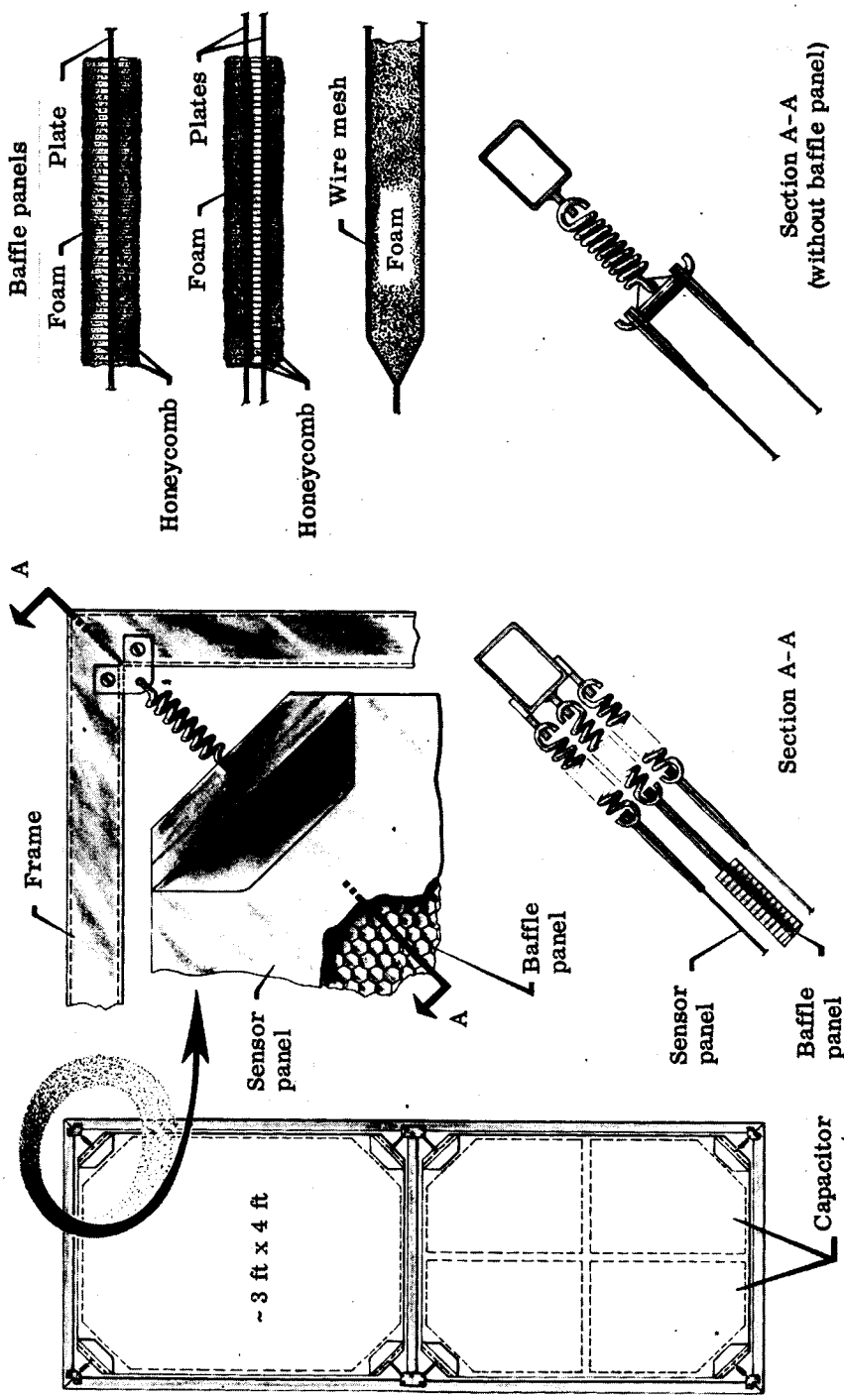

Fig. III-30. - Proposed Capacitor Sensors

Design No. 1

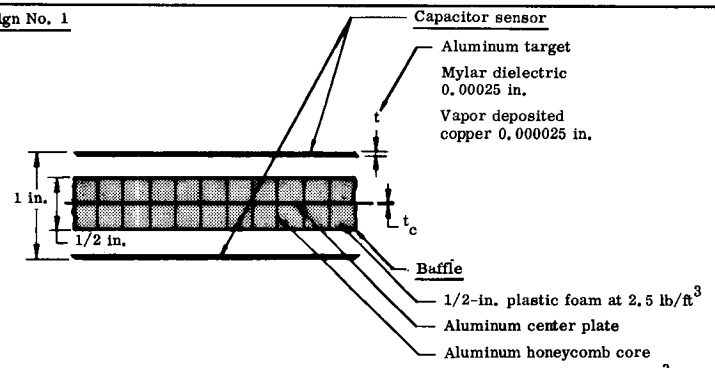

Design No. 2

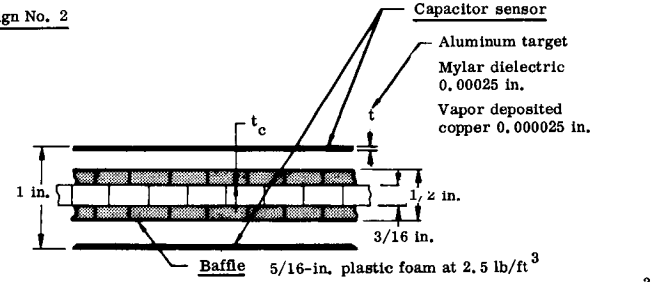

Design No. 3

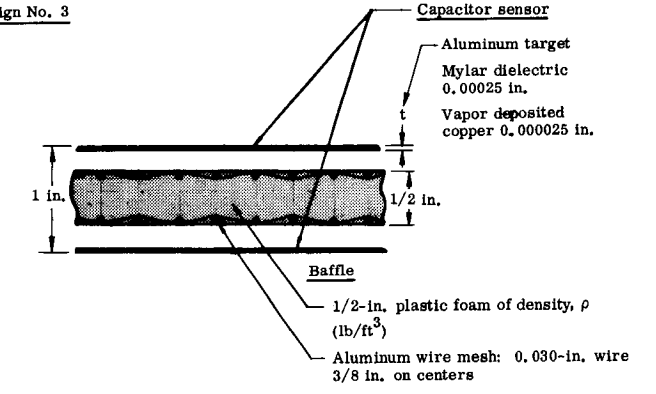

Baffle Design	Target Thickness t (in.)	Probability of Penetration 0.01	0.005	0.002	0.001 (Recommended for design purposes)
Design No. 1	0.001	0.003*	0.003*	0.003*	0.003*
	0.002	0.003*	0.003*	0.003*	0.0031
	0.003	0.003*	0.003*	0.0047	0.0078
	0.004	0.003*	0.0043	0.0084	0.0125
	0.005	0.0039	0.0070	0.0120	0.0176
	* 0.003 in. minimum practicable for structural reasons				Values of t_c, center plate thickness
Design No. 2	0.001	0.002**	0.002**	0.002**	0.002**
	0.002	0.002**	0.002**	0.002	0.0028
	0.003	0.002**	0.002	0.0037	0.0051
	0.004	0.002**	0.0035	0.0055	0.0074
	0.005	0.002**	0.0049	0.0073	0.0097
	** 0.002 in. minimum practicable for structural reasons				Values of t_c, sandwich face thickness
Design No. 3	0.001	0.32	1.15	1.56	1.93
	0.002	0.58	2.10	2.85	3.86
	0.003	1.12	3.06	4.14	5.11
	0.004	1.24	4.00	5.41	6.65
	0.005	1.39	4.95	6.61	8.29
					Values of ρ, foam density (lb/ft^3)

Fig. III-31. Probability of Micrometeoroid Penetration of Sensor and Baffle

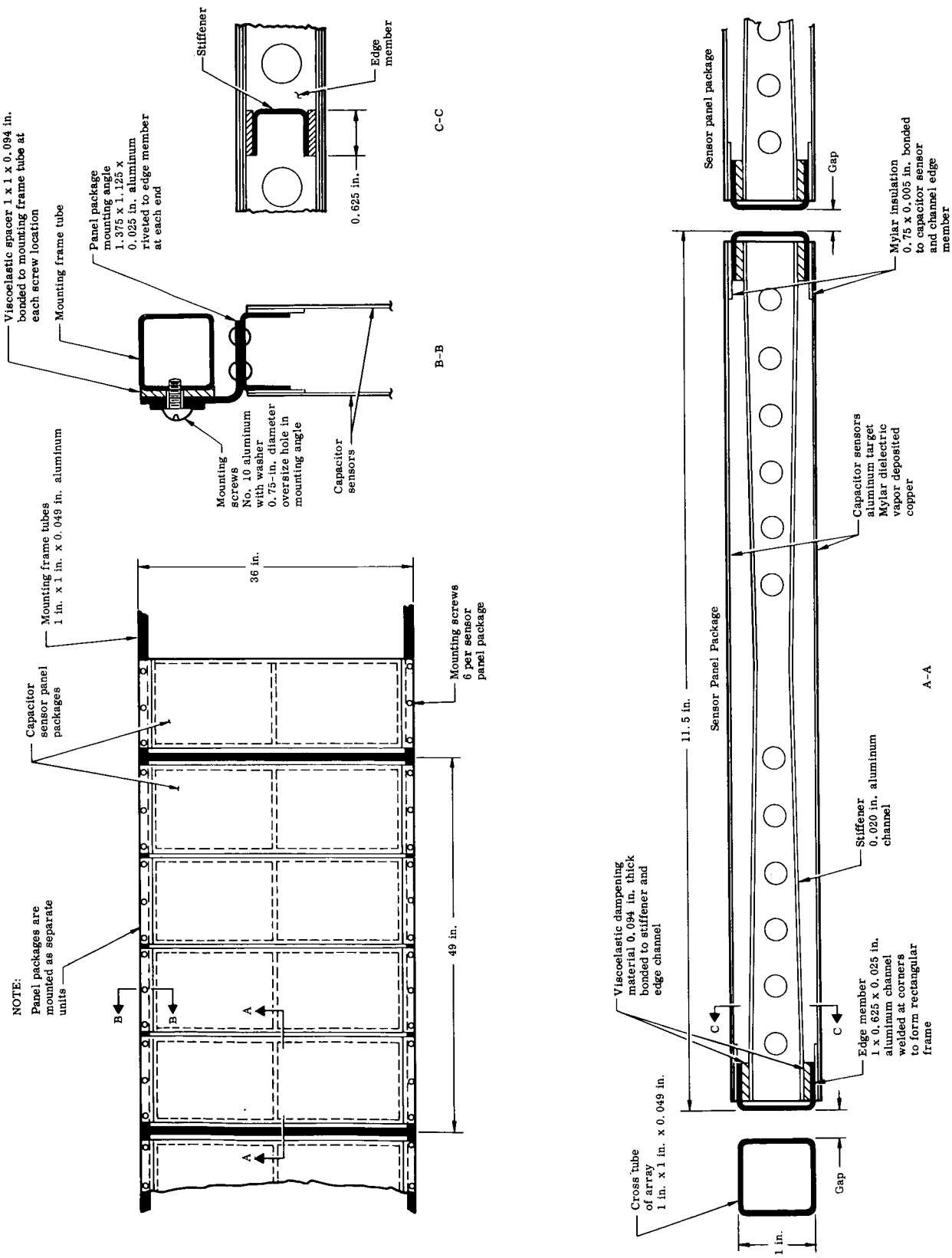

Fig. III-32. Alternate Capacitor Sensor Mounting

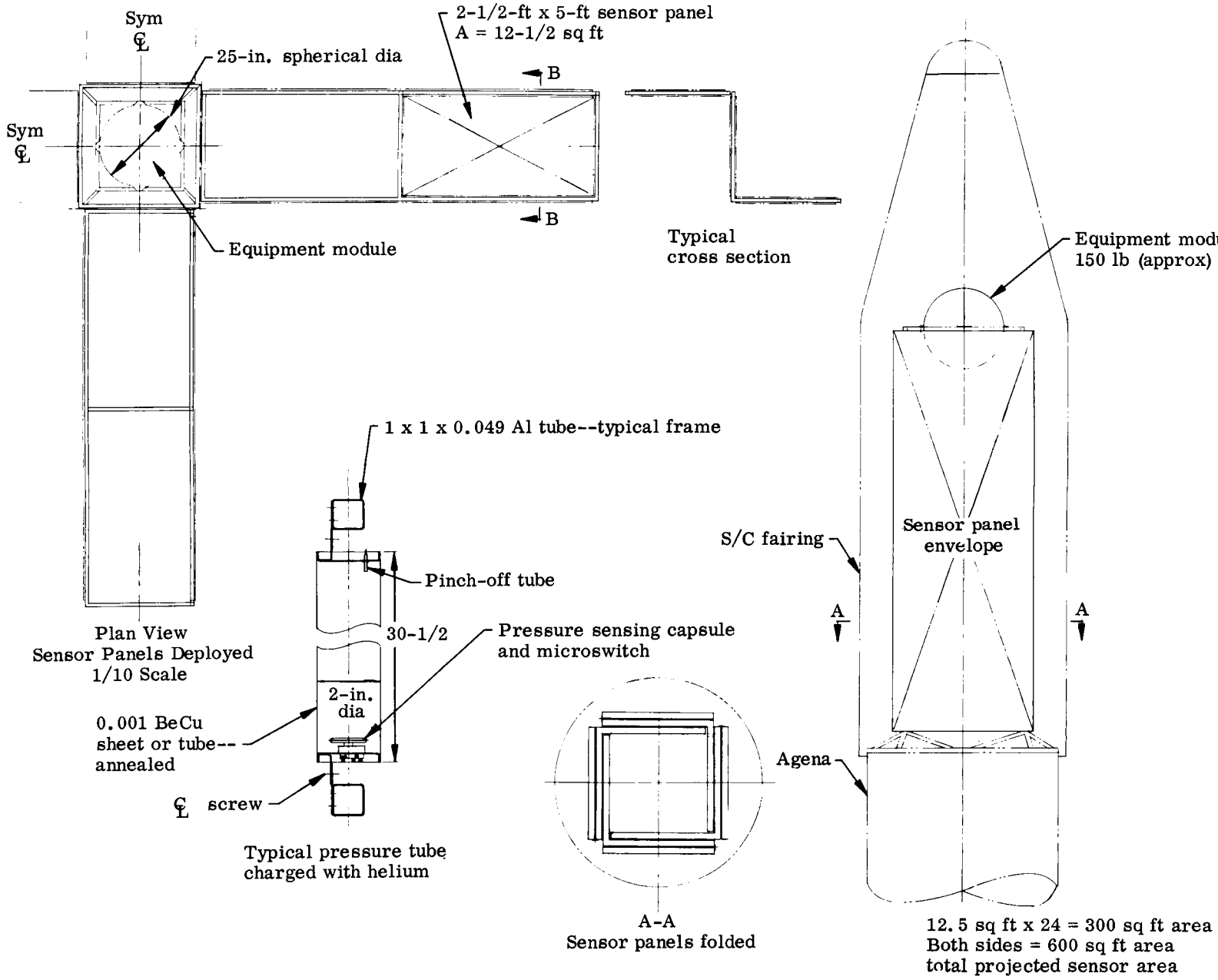

Fig. III-33. Zee Configuration, Pressurized Cylinder Sensors--Agena

Tapered blocks were laid out so that the effect of temperature change in the longitudinal direction of the panels could be minimized. These were incorporated with a center truss structure to support the satellite, since the blocks could not carry load in the longitudinal direction. However, the center truss complicated deployment of the satellite because clearance between the arms and the truss became critical, even if the satellite areas were extended before separation (Fig. III-34).

Development of the 90° conical shear buttons solved the problem of shear transfer of load between panels but left the problem of holding the panels together to make the shear transfer effective. Mechanical methods of accomplishing this were explored without obtaining completely satisfactory solutions. The most promising system devised uses nylon straps and buttons as discussed in Section B1. Other methods investigated involved shear pins and explosive separation (Figs. III-35 and III-36).

4. Structural Design and Analyses

a. Design criteria

The following criteria are proposed for the design and testing of a micrometeoroid deep space satellite using the Atlas (SLV-3)/Agena D as a launch vehicle. The criteria are based on the technical guideline of the NASA statement of work for the conceptual study of the micrometeoroid satellite (Refs. III-1, III-2 and III-3).

(1) Suitable experiments shall be provided to meet the following objectives, in order of relative importance:

   (a) Penetration rate variation with distance from earth.

   (b) Impact rate variation with distance from earth.

   (c) Mass distribution in the same environment.

   (d) Velocity distribution in the same environment.

(2) The orbit shall be a highly eccentric, earth-centered orbit. Orbit perigee height shall be compatible with a one-year lifetime. Orbit apogee height shall be selected such that micrometeoroid data may be reliably extrapolated to the moon, and to allow orbit stability for one year. The nominal orbit apogee which satisfies these requirements is approximately 147,000 naut mi.

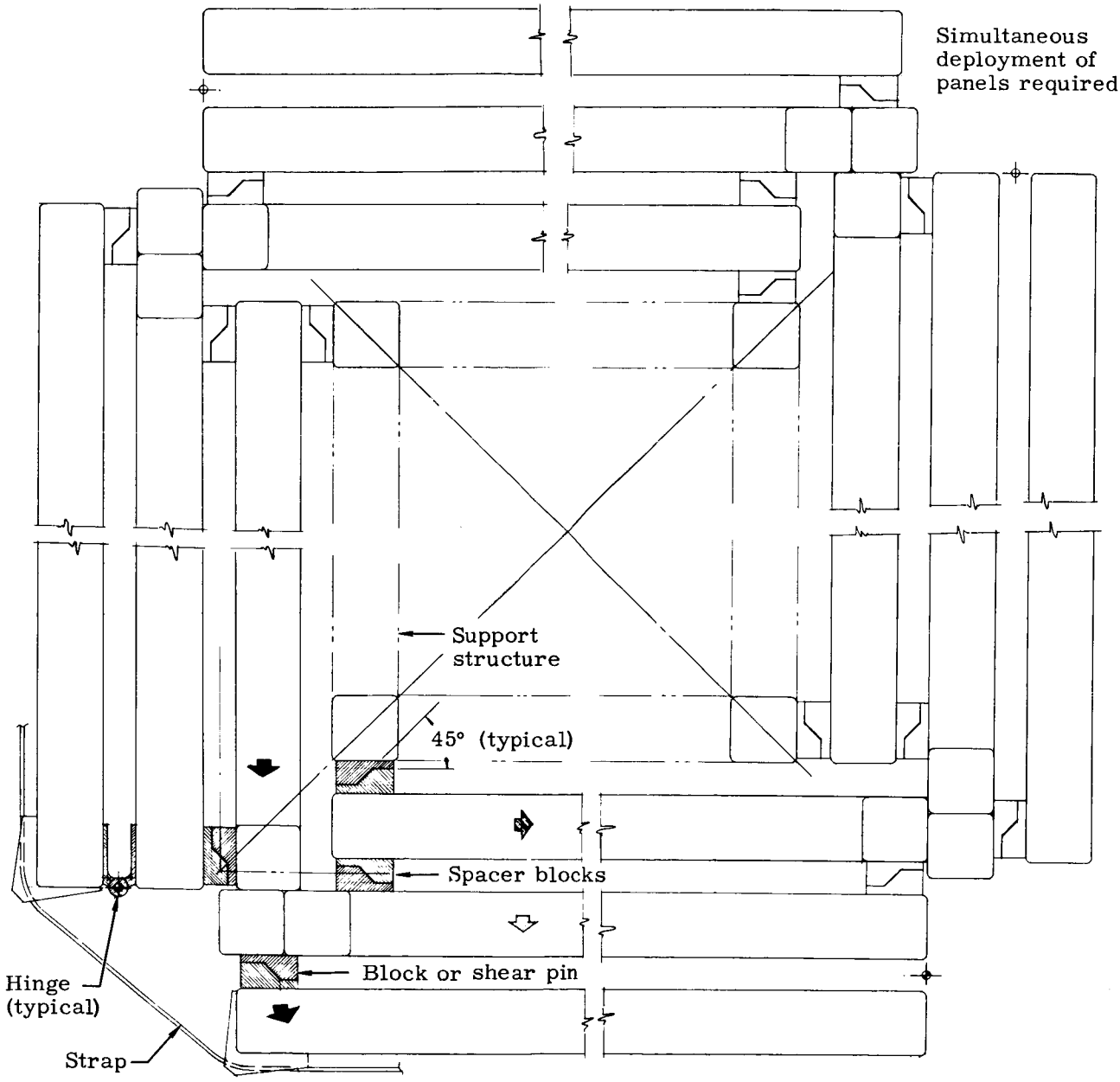

Fig. III-34. Center Structure Basic Zee Configuration

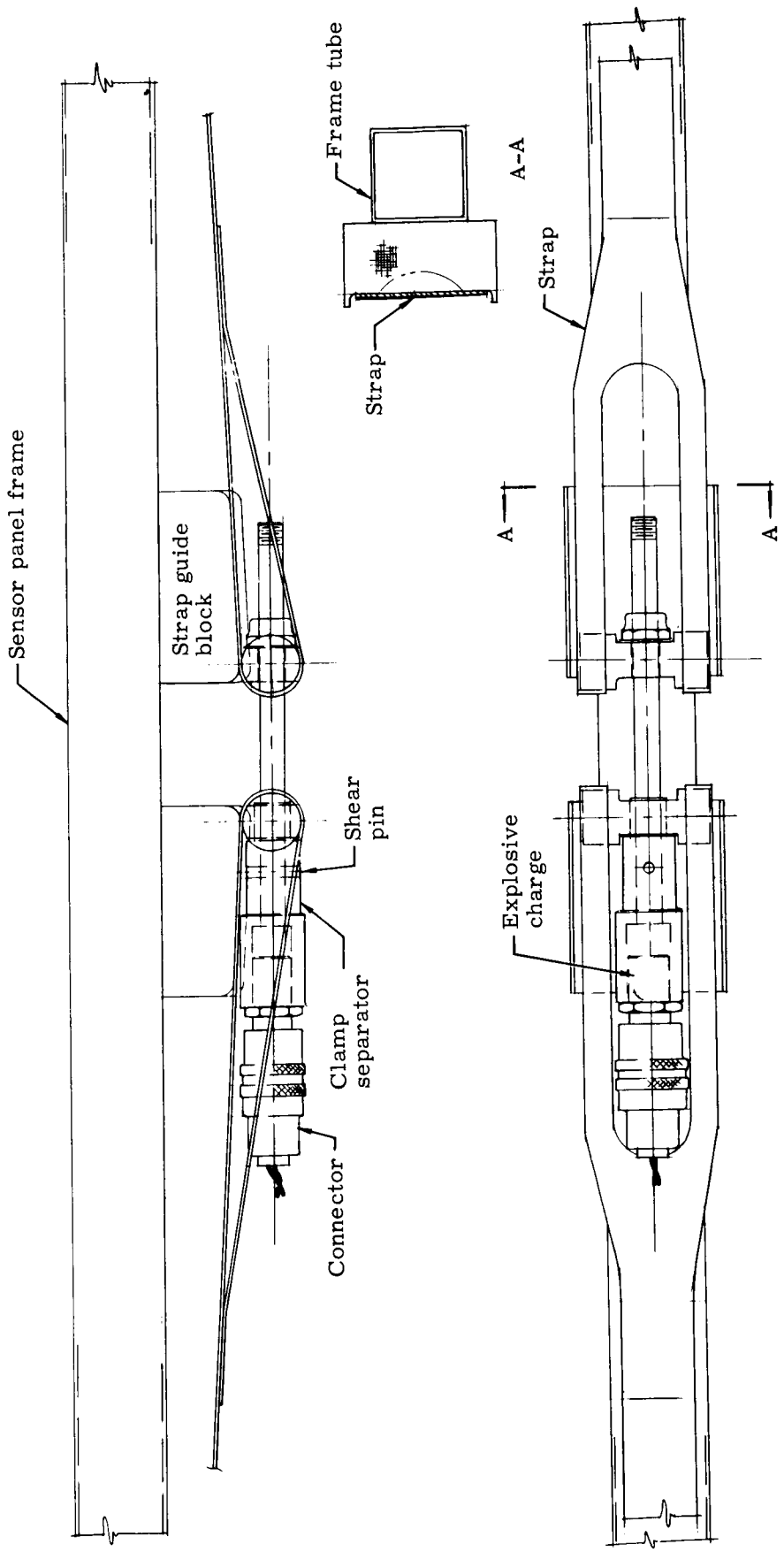

Fig. III-35. Explosive Strap Separator

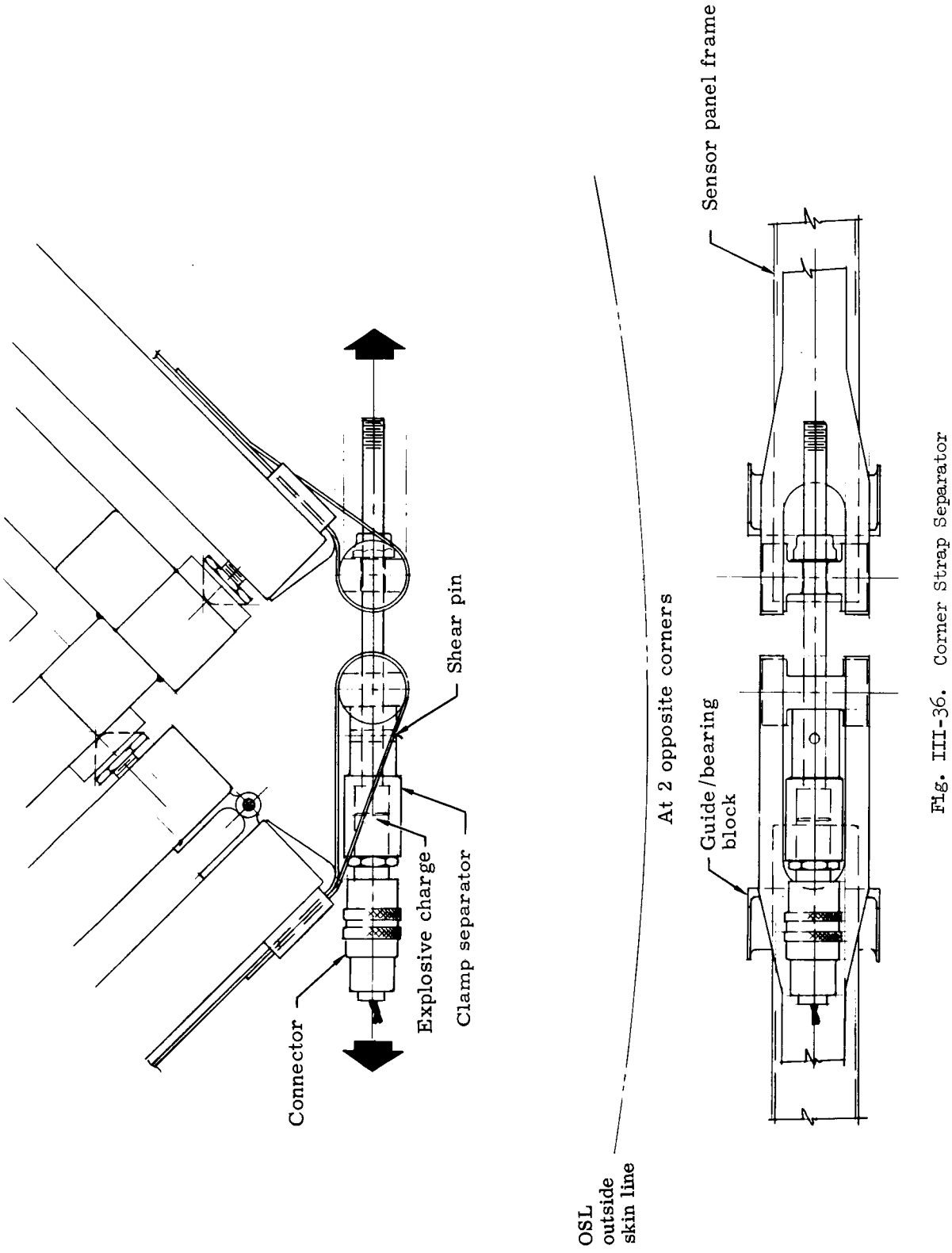

Fig. III-36. Corner Strap Separator

(3) The launch vehicle for the satellite shall be the Atlas (SLV-3)/Agena D.

(4) The reliability design goal for mission completion (1 yr in orbit with satisfactory operation of all systems) shall be 0.85.

(5) (a) Shock. Satellite equipment (for items of 75 lb or less) shall be designed to withstand an ascent shock acceleration of 30 half sine pulse with eight milliseconds maximum duration in all three directions.

(b) Acceleration. The satellite and its systems shall be designed for the following accelerations:

Flight Phase	Longitudinal Axis		Lateral and Normal Axes	
	Design Limit (g)	Design Ultimate (g)	Design Limit (g)	Design Ultimate (g)
Atlas Boost	11.0	15.0	±2.0	±2.5
Agena	9.0	11.5	±2.0	±2.5

No yielding or deflection of the spacecraft structure and its system components which will adversely affect satisfactory operation shall occur at 110% of design limit loads. No failure of the structure or the components shall occur at design ultimate accelerations.

Accelerations associated with ground handling of the satellite shall not exceed the above flight accelerations.

(c) Vibration. The satellite and its systems shall be designed for the following launch phase vibration levels:

Sinusoidal		Random	
Frequency Range (cps)	Amplitude (*)	Density (g^2/cps)	Rms Acceleration (g)
5 to 14	0.50 in.		
14 to 400	5 g	0.05	4.4
400 to 2000	7.5 g	0.12	13.9

(*) g = zero to peak acceleration
in.= peak-to-peak amplitude

(d) Noise. The satellite and its systems shall be capable of satisfactory operation after being subjected to a noise level of 145 decibels.

(e) Ground temperature and humidity. The satellite and its systems shall be designed to withstand ambient ground temperatures ranging from 20° to 160° F in a humidity of 95% at sea level pressure.

(f) Aerodynamic heating during ascent. Satellite systems shall be capable of satisfactory operation after exposure to the effect of ascent aerodynamic heating transmitted through the launch vehicle heat shield.

(g) Space environment. Satellite systems shall be capable of satisfactory performance for one year while subjected to the space environment associated with its orbit trajectory:

(i) Vacuum. Extreme vacuum equal to 10^{-12} torr.

(ii) Solar radiation. Solar flare protons based on NASA-ARC model. Solar wind plasma flux equal to 1.2×10^{3} per square centimeter per second (1 to 2 mev). Solar electromagnetic radiation of X-rays through infrared based on modified Johnson spectrum in ultraviolet and X-ray bands.

(iii) Cosmic radiation. Based on modified Winckler curve (0.5 gev).

(iv) Meteroid flux and penetration. The flux model for near earth meteoroid environment is:

$$\text{Log } N = -1.34 \text{ Log } m - 13.95$$

where N = flux in number of impacts per square meter per second

m = meteoroid mass (gin)

the penetration equation is:

$$P = K (mv)^{1/3}$$

where P = thickness of the thin target (in.)

m = meteoroid mass (gm)

V = meteoroid velocity (km per second) (taken as 22.0 for design purposes

K = constant

= 0.102 for aluminum targets

= 0.051 for beryllium-copper and stainless steel targets

The meteoroid penetration sensors shall be sized by using a power law flux-distance variation assuming the near earth flux is reduced to 1/100 at the moon.

b. Sensor design concepts and analysis

One of the prime requirements for the micrometeoroid satellite is that is must provide large areas of penetration sensors. This section of the report will present several design concepts for the sensors and an evaluation of them. Problems of mounting the sensors on the satellite will be discussed and conceptual designs will be shown. Finally, a recommended design for use on an Atlas(SLV-3)/Agena D satellite will be given.

(1) Sensor concepts

Rigid sandwich capacitors (Fig. III-37). The capacitor-type sensors are adhesively bonded to a thin layer of flexible plastic which is then bonded to a thicker piece of rigid plastic foam. The foam serves two purposes: it acts as a meteoroid and target spray baffle and it gives rigidity to the panel. As shown in Fig. III-36, the thickness of the panel will be about one inch. Flexible foam is used to allow for differential thermal expansion of the targets.

This design can be made structurally self-supporting and mounted in a framework, a definite advantage. On the other hand, there is a possibility that the plastic foam material may build up an electrical charge due to space radiation effects. This electrical charge may cause spurious discharges of the capacitor sensor, giving false signals of meteoroid penetration.

Thin sheet capacitor (Fig. III-38). The sensors are capacitor types, consisting of the foil target material, mylar dielectric and a vapor-deposited conductor. Mounting of large areas of these sensors which have target faces of a few thousandths of an inch requires some ingenuity in design to withstand the launch and space environments.

One method of mounting the sensors is by using four springs, one

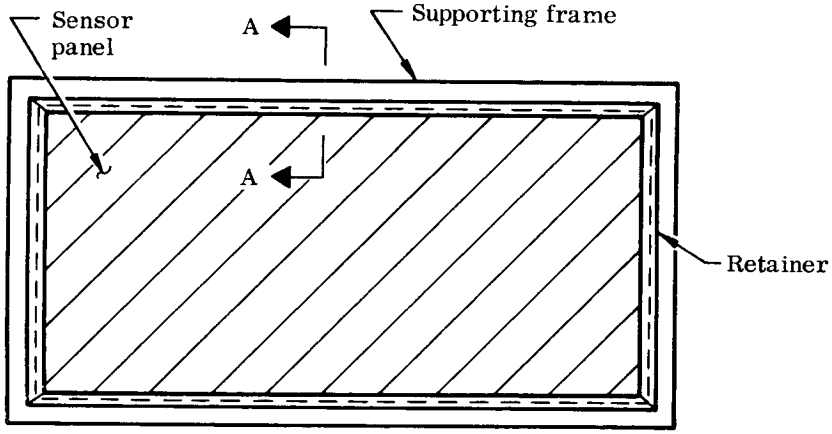

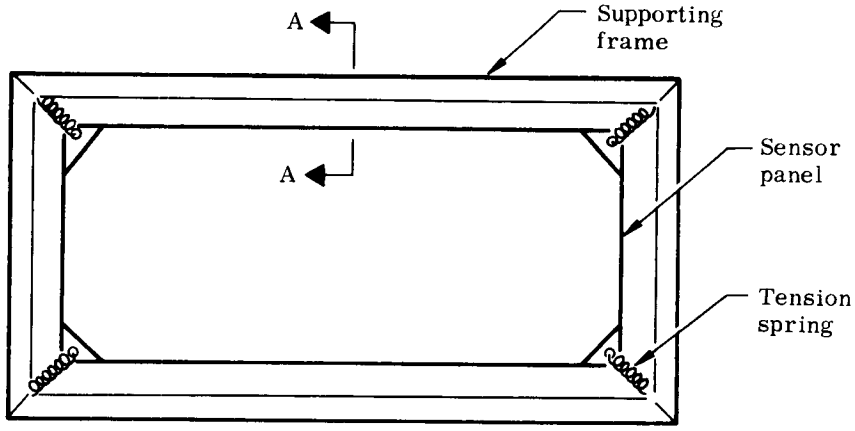

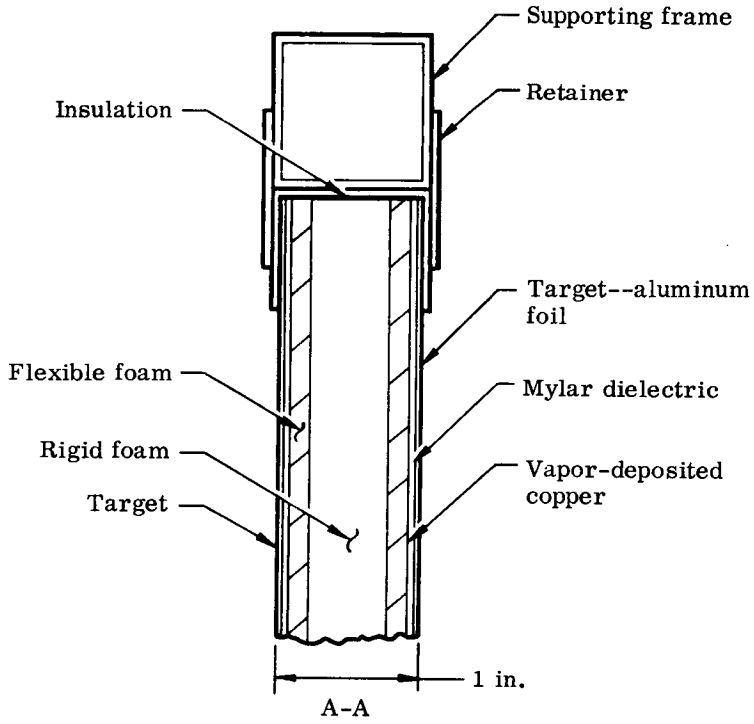

Fig. III-37. Rigid Sandwich Capacitor Sensor

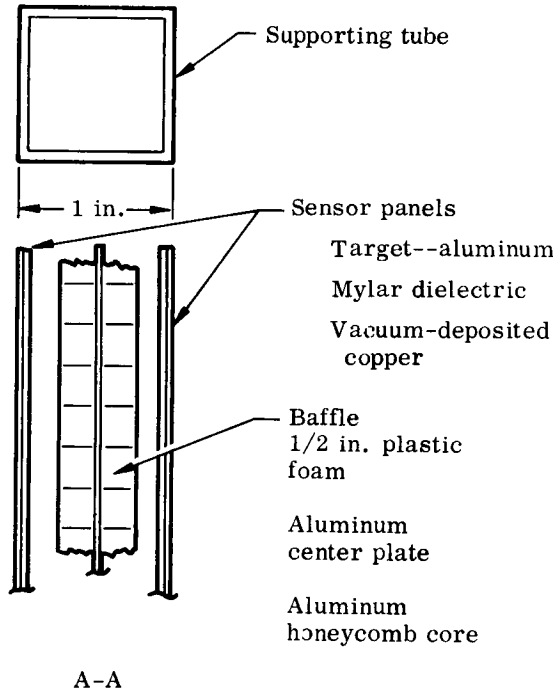

Fig. III-38. Thin Sheet Capacitor

at each corner of a rectangular panel (Fig. III-38). The springs are connected to corner doublers on the sensor panels and to the tubular structural framework. The preloaded springs induce tension in the sensor panels. By varying the initial spring load, the vibration response of the panel can be controlled within some limits. The springs also allow for the contraction and expansion of the sensor panel due to temperature changes.

The spray baffle is located between the two capacitors and, depending on the design of the baffle, can also be spring mounted. Detail design considerations for baffles are given later.

Multilayer flexible capacitor. Another form of sensor is the multilayer flexible capacitor shown in Fig. III-39. This type of capacitor is adapted to high density packaging for use on inflatable satellite designs. Mounting of this sensor in the form of large flat panels could be accomplished by spring-loading the corners similar to the method shown in Fig. III-38.

Pressurized cells. Penetration sensors using pressurized cans have been successfully used on the Explorer XVI and XXIII satellites. The size and shape of the micrometeoroid deep space satellite requires the use of pressurized cylindrical tubes for the sensors (Fig. III-40). The main disadvantage of pressurized penetration sensors is that effective sensor area is lost with each penetration. This can be overcome by using a large number of individual sensors incurring a corresponding weight increase due to the additional tubes, pressure transducers, wiring and data handling equipment.

(2) Study analysis

Spring-loaded thin sheet capacitor. Early in the program it became evident that large areas of thin sensor capacitors would be needed to obtain the required penetration data. One of the most promising designs is that shown in Fig. III-30. This design has the rectangular-shaped thin sensors mounted in a structural frame by means of four springs, one at each corner. The baffle is located between the two sensors and is also mounted by the four-spring method. The following paragraphs present some of the design analyses made during the study.

Stress and dynamic analysis. Mounting of the sensor panels by use of springs at the corners has the advantages of:

(1) Providing a means of keeping the panels flat and, at the same time, a means of controlling panel vibration.

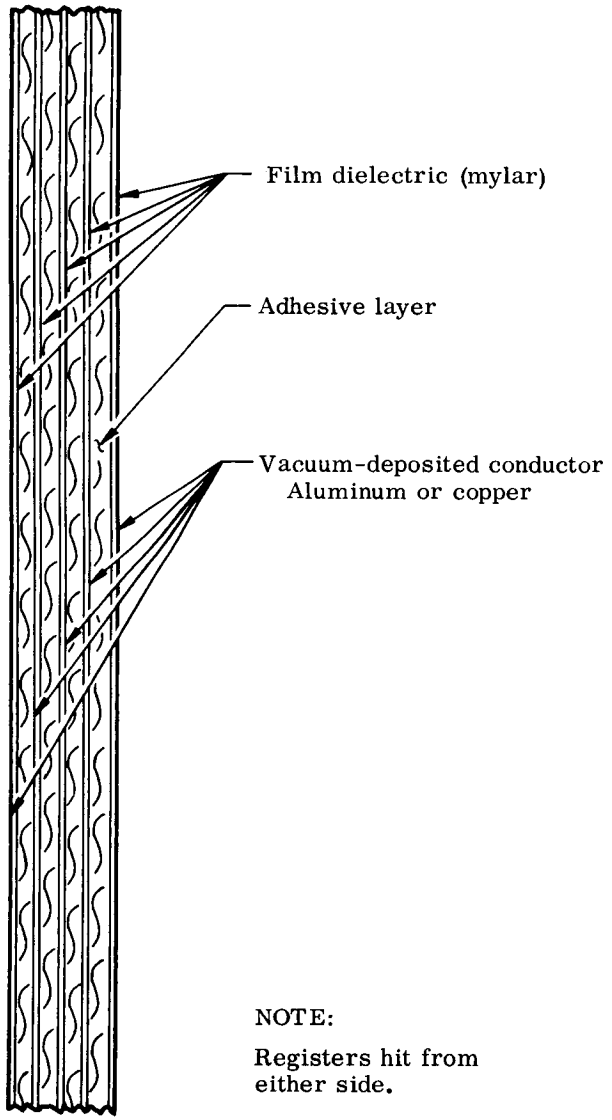

Fig. III-39. Multilayer Flexible Capacitors

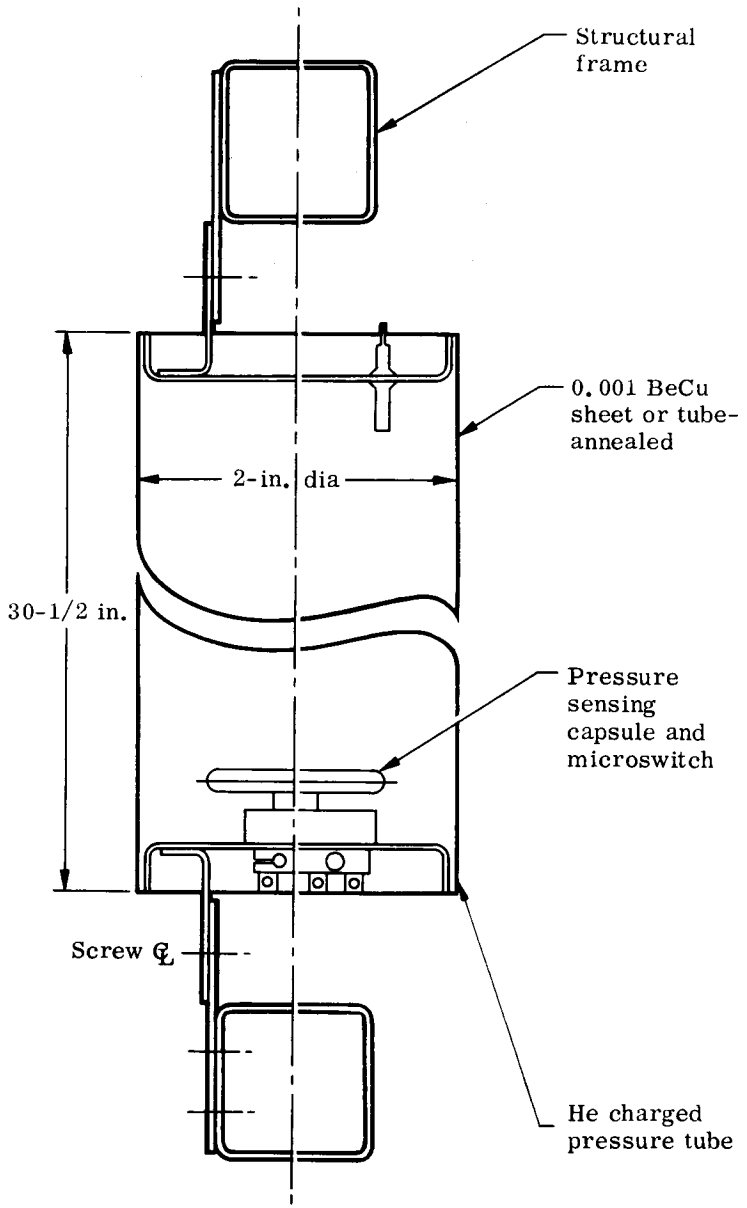

Fig. III-40. Pressurized Sensor--Cylindrical Tube Design

(2) Allowing the panel to expand and contract with respect to the frame due to temperature differentials.

The stress distribution in a thin sheet loaded at the corners is complex. Radial stresses at the corners are high but diminish rapidly with distance from the corner. An investigation was made of the radial stress distribution using the methods of Osgood (Ref. III-4), and applying the methods to a square plate loaded at the corners.

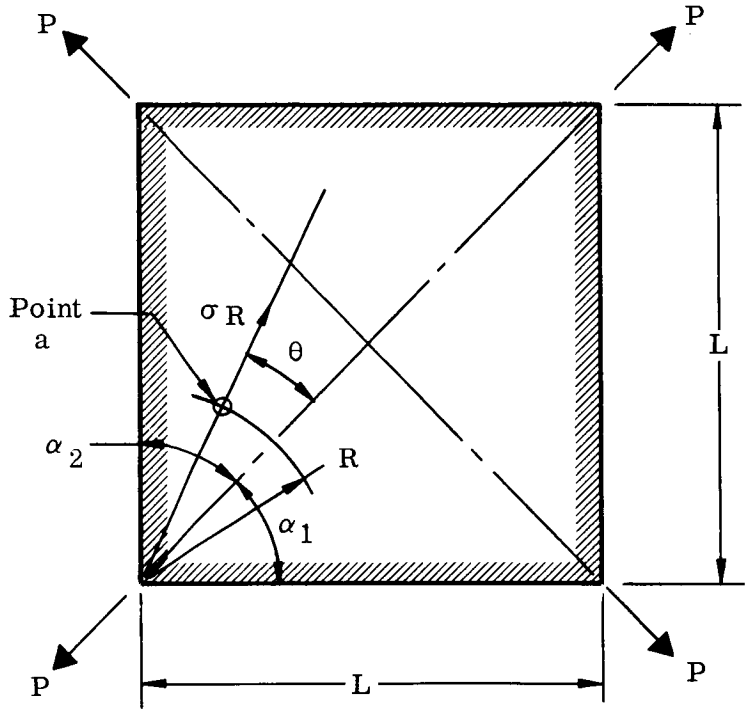

Let σ_R = radial stress at a

R = radial distance from corner

P = load at corner

t = plate thickness

L = side of square plate

From Ref. III-4, it can be shown that

$$\sigma_R = \frac{P\cos\theta}{Rt\,(\alpha + \sin\alpha\cos\alpha)} \quad \text{(III-1)}$$

Where for a square plate loaded diagonally

$\alpha_1 = \alpha_2 = 45°$, $\alpha = 45°$

Fig. III-41. Corner Loaded Plate

For $\alpha = 45°$ (or 0.785 rad), $\sin\alpha = 0.707$ and $\cos\alpha = 0.707$.

Substituting in Equation III-1,

$$\sigma_R = \frac{P\cos\theta}{Rt\,(0.785 + 0.707 \times 0.707)} = \frac{P\cos\theta}{1.285\,Rt} \quad \text{(III-2)}$$

Values of $\frac{\sigma_R t}{P}$ for various values of R and θ are given in Table III-3.

TABLE III-3

$\frac{\sigma_R t}{P}$ for Values of R and θ

R (in.)	$\sigma_R t/P$ θ = 0°	θ = 15°	θ = 30°	θ = 45°
0.1	0.779	0.753	0.675	0.551
0.5	0.1559	0.1504	0.135	0.1102
0.10	0.0779	0.0753	0.0675	0.0551
0.20	0.03895	0.0376	0.03375	0.02755
0.30	0.02593	0.02505	0.02250	0.01837
0.40	0.01448	0.0188	0.01688	0.01378

Earlier in the study, it was found that a panel size of approximately 3 x 4 ft met the design requirements for an 0.002-in. sensor as far as stress, vibration and mounting. Based on this, an analysis was made of the corner stress distribution in an 0.002-in. thick, 40-in. square aluminum sheet, loaded at the four corners by 100-lb loads.

By using the data of Table III-3, with P = 100 lb and t = 0.002 in., the values of radial stress, σ_R, for values of R and θ can be found as shown in Tables III-4 and III-5.

TABLE III-4

σ_R for Values of R and θ for P = 100 lb and t = 0.002 in.

R (in.)	σ_R (psi) θ = 0°	θ = 15°	θ = 30°	θ = 45°
1	38,950	37,650	33,750	27,550
5	7,795	7,520	6,750	5,551
10	3,895	3,765	3,375	2,775

Table III-4 (continued)

R (in.)	θ = 0°	θ = 15°	θ = 30°	θ = 45°
20	1,998	1,880	1,687	1,387
30	1,297	1,252	1,125	920
40	999	940	844	694

TABLE III-5

Values of R for Constant Values of σ_R

R (psi)	R (in.) θ = 0°	θ = 15°	θ = 30°	θ = 45°
40,000	0.974	0.940	0.843	0.688
30,000	1.298	1.251	1.122	0.918
20,000	1.942	1.880	1.688	1.378
15,000	2.595	2.510	2.245	1.838
10,000	3.885	3.760	3.350	2.751
8,000	4.860	4.700	4.220	3.44
6,000	6.480	6.270	5.61	4.59
4,000	9.740	9.40	8.42	6.88
2,000	19.42	18.80	16.88	13.78
1,000	38.85	37.60	33.50	27.51

The data of Table III-5 for the radial stresses is plotted in the form of contours in Fig. III-42. Points of significance indicated in the figure are:

(1) Very high radial stresses occur at small distances from the corners and, therefore, doubler plates are required to distribute the spring load into the thin sheet.

(2) Stresses at the center and midpoint of the edges are relatively low and, hence, the sheet may have a low frequency of vibration.

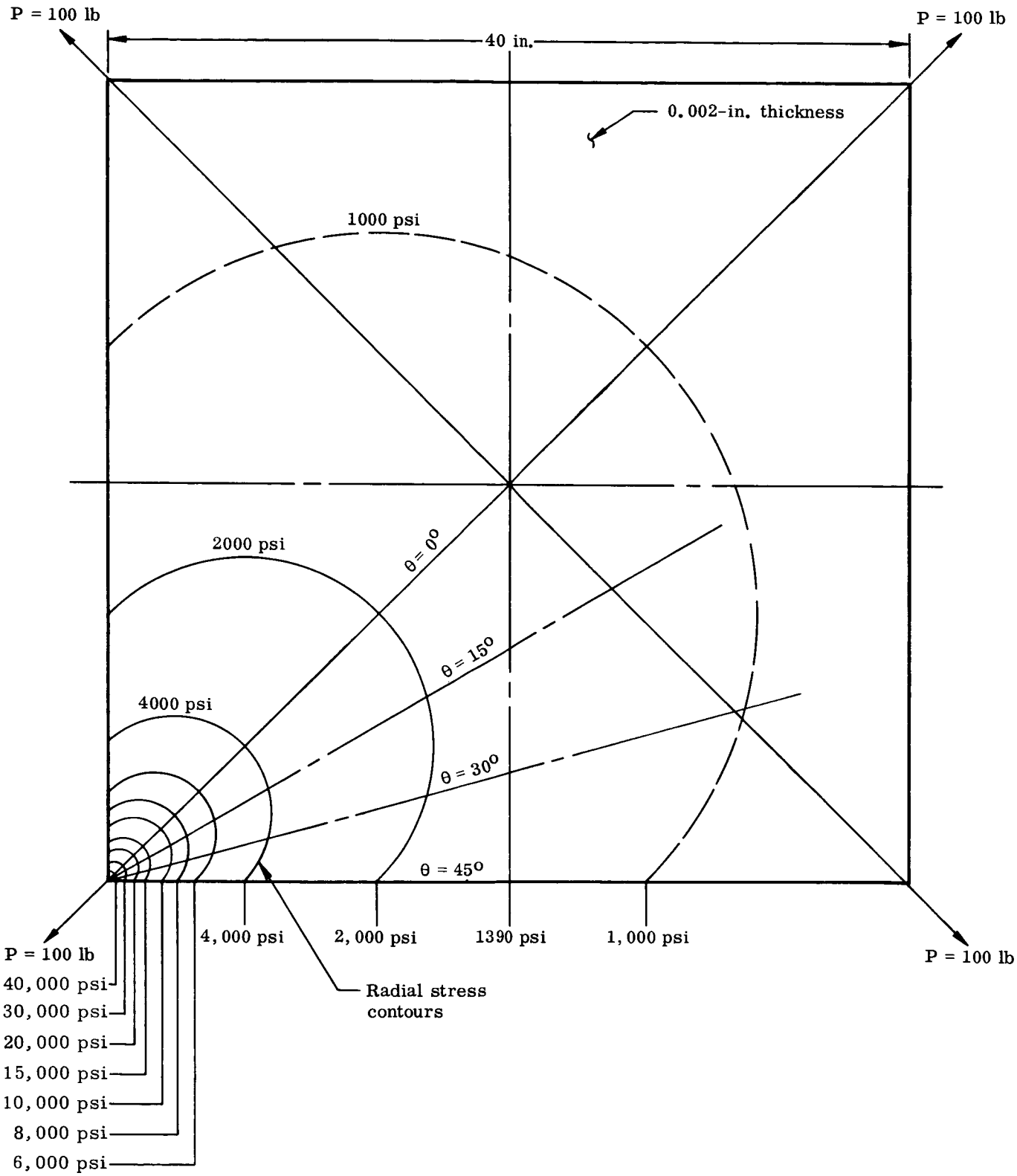

Fig. III-42. Stresses in a Corner Loaded Square Panel

(3) The stress pattern in the sheet at its center area is complex due to the overlapping of the stress effects of the four corner loads.

The doubler size should be as small as possible since it reduces the effective area of the sensor. An estimate of the size of the doubler can be made:

Assume the 0.002-in. sheet is of 5052-H19 which is a high-strength aluminum foil with ultimate strength of 42,000 psi and a yield strength of 35,000 psi.

Further assume that due to fatigue considerations and stress concentrations at the end of the doubler, the maximum stress on the 0.002-in. sheet must be limited to 1/4 x 42,000 or 10,500 psi.

From Table III-5 and Fig. III-42, it can be seen that the doubler should extend at least 3.9 in. from the corner apex as measured along the diagonal ($\theta = 0°$). This size doubler appears reasonable in respect to loss of effective sensor area.

Vibration characteristics of a spring-loaded thin plate of rectangular shape are complex. The in-plane vibrations can possibly be handled by conventional methods if the sheet is kept taut. The out-of-plane vibration is complex due to the varying stress level in the sheet, its light weight and extreme flexibility, and the mass of the springs.

An approximate method was used to obtain some idea of the effect of spring load and vibration frequency by treating the plate as equivalent to a thin strip loaded uniformly in tension. The vibration frequency of a simply supported thin strip of low flexibility is given by:

$$n = \frac{1}{2L}\sqrt{\frac{T}{m}}$$

where n = vibration frequency (cps)

L = length (ft)

T = tension (lb)

m = mass per unit length $\left(\frac{lb/g}{ft}\right)$

g = 32.2 (ft/sec^2)

For an 0.002-in. aluminum strip of one-inch width, the weight per foot = (1 x 0.002 x 0.101) x 12 = 0.00242 lb

and the mass per foot = $\frac{0.00242}{32.2} = 75.2 \times 10^{-6}$

$$\therefore \quad n = \frac{1}{2L} \sqrt{\frac{T}{75.2 \times 10^{-6}}} = \frac{10^3}{2 \times 8.69\ L} \sqrt{T}$$

$$n = \frac{57.7}{L} \sqrt{T} \qquad \text{(III-3)}$$

For the panel shown in Fig. III- , where L = 3.33 ft (40 in.) and assuming average stress in 0.002 in. sheet of 1500 psi, the tension load on a 1-in. strip = 1 x 0.002 x 1500 = 3.0 lb.

Using Equation 3, the vibration frequency is:

$$n = \frac{57.7}{3.33} \sqrt{3.0} = 30 \text{ cps}$$

This frequency is relatively low in magnitude but, because of the damping effect of the air mass surrounding the panels, the dynamic response is probably not great. However, during the launch phase the air mass effect decreases with increasing altitude while the vibration input amplitude may remain the same. It is felt that a development test program must be undertaken to evaluate this design as soon as possible. An R&D effort is now under way at the Martin Company to establish analytical methods of obtaining the dynamic response of the spring-loaded panels. A test panel of 0.0015 in. aluminum of 19 x 25 which is approximately one-half size of the proposed Atlas-Agena satellite panel has been built and preliminary vibration tests are under way.

The dynamics aspects of the spring-mounted thin panels and their mounting requires further effort before a hardware design phase can be started. Alternative designs must be explored. One such design is considered in the following (see para b).

Baffle design. One of the early requirements in the study was that a baffle would be required between the two sensors as shown in Fig. III-30. The purpose of this baffle is to prevent the spray debris from the meteoroid penetration of one sensor from impacting on the back side of the other sensor, causing a permanent short-circuit of the sensor and destroying its effectiveness.

An analysis was made to determine the configuration and sizes of various baffle designs. In making this analysis, requirements set up were:

(1) The baffle must provide suitable stopping power for the spray debris .

(2) The baffle must have electrical continuity with the sensor mounting frame to bleed off any electrostatic changes.

(3) No bumper effect of the sensor target would be assumed. This would be conservative in establishing baffle sizes.

(4) Sensor spacing is one inch, baffle thickness is one-half inch.

Three design concepts were investigated using plastic foam and various metallic frameworks. Sizes and foam densities were established to provide various probabilities of no penetration of one sensor plus the baffle. It was decided that a design level of one in one-thousand probability of penetration of sensor plus baffle would be adequate.

The detail analysis is given in the following sections. Results are summarized in Fig. III-31 for the three baffle design concepts.

Structural mounting of the baffle between the two sensors can possibly be achieved by spring-mounting at the corners as previously discussed for the sensor mounting. Mounting of the baffles needs further stress analyses and dynamic investigation.

Proposed Design No. 1.

Equivalent thickness in terms of aluminum

Sensor Target Mylar Copper

$$t_S = t + 0.00025 \times \frac{0.05}{0.101} + 0.000025 \times \frac{0.322}{0.101}$$

$$t_S = t + 0.00021$$

(Density ratio)

Baffle (Center plate, Foam)

$$t_B = t_C + \frac{1}{2} \text{ inch} \times \frac{2.5}{174}$$

$$= t_C + 0.0072$$

Sensor + baffle*

$$t_T = t_S + t_B = t + 0.00021 + t_C + 0.0072$$

$$\therefore t_T = t + t_C + 0.00741$$

$$\text{or } t_C = t_T - t - 0.00741$$

*No bumper effect of target

Flux-penetration variation

$$N = \left(\frac{9.65 \times 10^{-5}}{P}\right)^{4.02}$$

N = flux (no. per sq meter/sec)
P = penetration (in.)

$$\therefore N_S = \left(\frac{9.65 \times 10^{-5}}{t_S}\right)^{4.02}$$ for sensor

$$\text{and } N_T = \left(\frac{9.65 \times 10^{-5}}{t_T}\right)^{4.02}$$ for sensor plus baffle

$$\frac{N_T}{N_S} = \left(\frac{t_S}{t_T}\right)^{4.02} \quad \text{or} \quad \frac{t_T}{t_S} = \left(\frac{N_S}{N_T}\right)^{\frac{1}{4.02}}$$

Ratio of penetrations through sensor plus baffle to sensor penetration

$\frac{N_T}{N_S}$	$\frac{N_S}{N_T}$	$\log \frac{N_S}{N_T}$	$\frac{1}{4.02} \times \log \frac{N_S}{N_T}$	$\frac{t_T}{t_S}$
0.50	2	0.30103	0.07488	1.189
0.10	10	1.0	0.24876	1.766
0.05	20	1.30103	0.32364	2.107
0.01	100	2.0	0.49751	3.145
0.005	200	2.30103	0.57240	3.736
0.002	500	2.69877	0.67139	4.692
0.001	1000	3.0	0.74627	5.575

		t_C for N_T/N_S =		Recommended for design	
t	t_S	0.01	0.005	0.001	0.002
0.001	0.00121			-0.0017	
0.002	0.00221	-0.0024	-0.00116	0.0031	0.00097
0.003	0.00321	-0.0004	0.00158	0.0078	0.00468
0.004	0.00421	+0.0018	0.00429	0.0125	0.00837
0.005	0.00521	+0.0039	0.00704	0.0176	0.01202

NOTE: Minus value of t_C indicates no center plate required.

Proposed Design No. 2

Equivalent thickness in terms of aluminum

Sensor Target Mylar Copper

$$t_S = t + 0.00025 \times \frac{0.05}{0.101} + 0.000025 \times \frac{0.322}{0.101}$$

$$t_S = t + 0.00021$$

Baffle Faces Foam

$$t_B = 2\,t_C + \frac{5}{16}\ \text{inch} \times \frac{2.5}{174}$$

$$= 2\,t_C + 0.00448$$

Sensor plus baffle*

$$t_T = t + 0.00021 + 2\,t_C + 0.00448$$

$$= t + 2\,t_C + 0.00469$$

*No bumper effect of target

		t_C							
		$\frac{N_T}{N_S} = 0.01$		0.005		0.002		Recommended for design 0.001	
t	t_S	t_T	t_C	t_T	t_C	t_T	t_C	t_T	t_C
0.001	0.00121	0.00214	-0.0018	0.00451	-0.0006	0.00569	0	0.00675	0.00053
0.002	0.00221	0.00390	-0.0014	0.00825	0.00078	0.01038	0.00185	0.0123	0.00281
0.003	0.00321	0.00566	-0.001	0.0120	0.00216	0.0151	0.0037	0.0179	0.00511
0.004	0.00421	0.00742	-0.00063	0.0157	0.00351	0.01975	0.00553	0.0234	0.00736
0.005	0.00521	0.0092	-0.00025	0.01946	0.00489	0.0242	0.00725	0.0290	0.00966

NOTE: Minus value for t_C indicates no thickness required as part of baffle to stop meteoroid.

Proposed Design No. 3.

Equivalent thickness in terms of aluminum

Sensor Target Mylar Copper

$$t_S = t + 0.00025 \times \frac{0.05}{0.101} + 0.000025 \times \frac{0.322}{0.101}$$

$$= t + 0.00021$$

Baffle Foam Foam density (lb/cu ft)

$$t_B = \frac{1}{2} \times \frac{\rho}{174} = \frac{\rho}{348}$$

Aluminum density (lb/cu ft)

Sensor + baffle*

$$t_T = t_S + t_B = t + 0.00021 + \frac{\rho}{348}$$

*No bumper effect of target

				Foam Density ρ (lb/cu ft)					
		$\frac{N_T}{N_S} = 0.01$		0.005		0.002		Recommended for design 0.001	
t	t_S	t_T	ρ	t_T	ρ	t_T	ρ	t_T	ρ
0.001	0.00121	0.00214	0.324	0.00451	1.149	0.00569	1.56	0.00675	1.93
0.002	0.00221	0.00390	0.582	0.00825	2.10	0.01038	2.85	0.0123	3.86
0.003	0.00321	0.00566	1.118	0.0120	3.062	0.0151	4.14	0.0179	5.11
0.004	0.00421	0.00742	1.238	0.0157	4.00	0.01975	5.41	0.0234	6.65
0.005	0.00521	0.0092	1.392	0.01946	4.95	0.0242	6.61	0.0290	8.29

Segmentation. The design and mounting of the baffle shown in Fig. III-30 and discussed previously will be a problem. Moreover, the baffle will be heavy and extensive as compared to the sensor panels. Thus, elimination of the baffle is desirable.

With this in mind, the idea of using a segmented capacitor sensor was conceived. The proposed design is shown in Fig. III-43. The target sheet is one piece over the full size of the sensor panel. However, the vacuum-deposited conductor is segmented into small rectangular areas. Any short circuit of the small segments by spray debris causes only a small proportion of the sensor effective area to be lost.

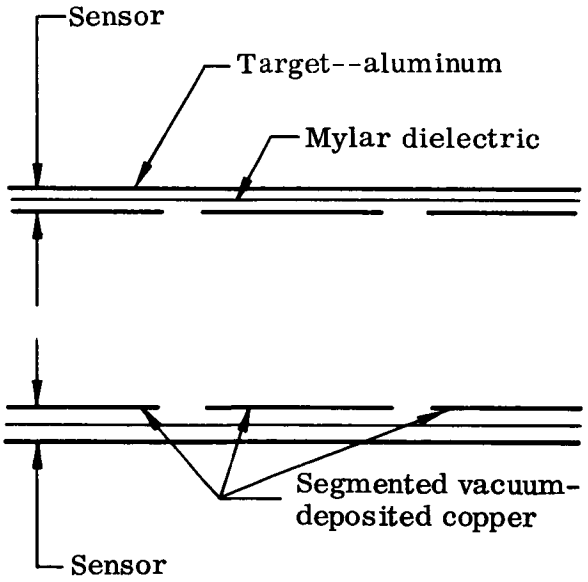

Fig. III-43. Segmented Capacitor

By proper selection of the number and area of segments relative to the total sensor area, the loss of effective area can be controlled. The statistical analysis to determine the number of segments is presented in Volume IV. The segmentation of the sensor does lead to additional electrical wiring, but this appears to be offset by less weight, less cost and, possibly, less structural problems if the baffle is not used.

(b) Alternate sensor design

While the spring-loaded design described in the preceding sections appears feasible, an alternative sensor design was investigated during the study (Fig. III-32). It consists of two thin sensor panels adhesively bonded to a rectangular metal frame. The size of the panel shown in the figure is 11-1/2 in. x 36 in., which is about as large as practicable. No baffle is shown, since segmented capacitor sensors would be used.

The preliminary analysis of the panel follows. A weight estimate indicates the weight per square foot of exposed sensor area to be 0.201 pound. This weight includes the 0.002-in. target and sensor, and the mounting frame provisions. Although heavier than the spring-loaded design, the alternative design warrants further consideration.

Weight estimate of the 11-1/2-in. x 36-in. package

		(lb)
0.002-in. target	$2 \times 0.002 \times 11.25 \times 33 \times 0.101$	= 0.160
0.005-in. mylar	$2 \times 0.005 \times 2 \times [10.5 + 32.5] \times 0.055$	= 0.047
0.025-in. edge channel	$0.025 \times (1 + \frac{5}{8} + \frac{5}{8}) \times 2 \times [11.5 + 33] \times 0.101$	= 0.506
0.020-in. stiff. channel	$0.020 \times (0.6 + \frac{5}{8} + \frac{5}{8}) \times 11.25 \times 0.101$	= 0.042
0.032-in. mounting angle	$0.032 \times (1\text{-}1/8 + 1\text{-}3/8) \times 11.5 \times 2 \times 0.101$	= 0.186
0.093-in. visco-elastic	$4 \times 0.093 \times \frac{5}{8} \times \frac{1}{2} \times 0.065$	= 0.008
0.093-in. spacer	$6 \times 0.093 \times 1 \times 1 \times 0.065$	= 0.036
3/4-in. diameter washer	$6 \times 0.040 \times (\frac{\pi}{4} \times \overline{0.75}^2) \times 0.101$	= 0.011
No. 10 mounting screws	6×0.002	= 0.012
0.00015-in. mylar dielectric (3 layers)	$2 \times 3 \times 0.00015 \times 11.25 \times 33 \times 0.055$	= 0.018

		(lb)
0.000025-in. vacuum deposited copper	2 x 0.000025 x 11.25 x 33 x 0.321	= 0.006
	Total	= 1.032

Weight/sq ft of exposed sensor structural area = $\frac{1.032}{11.25 \times 33/144}$ =

$\frac{1.032}{2.580}$ = 0.402 lb.

Weight/sq ft of exposed sensor area = 0.201 lb.

Stress analysis

Design accelerations

Vertical = 15.0 g ultimate down
Lateral = ±2.7 g ultimate down
Normal = ±2.7 g ultimate down
} Launch phase

Check of 0.025-in. edge channel

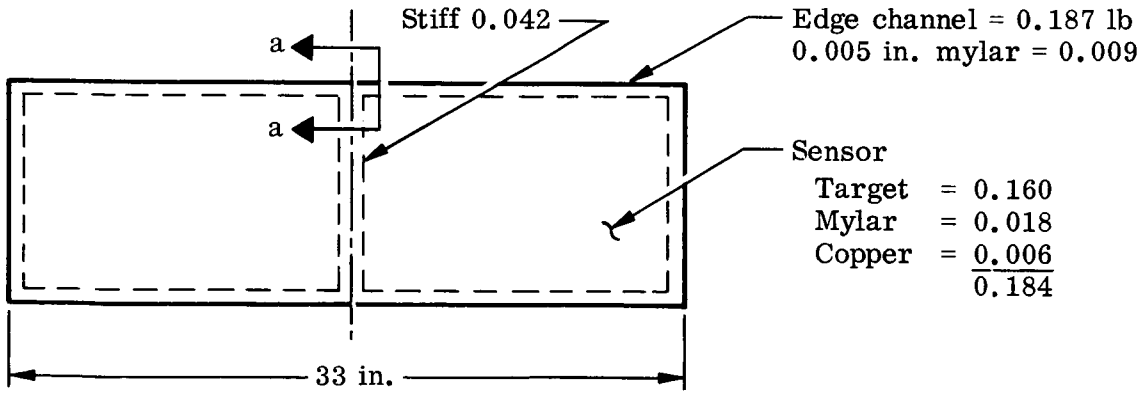

Weight per inch on edge member = $\frac{0.187 + 0.009 + 0.184 \text{ x* } 2 + \frac{0.042}{2}}{33}$

$= \frac{0.585}{33}$ = 0.0177 lb/in.

*Full weight of both sensors is taken by one channel

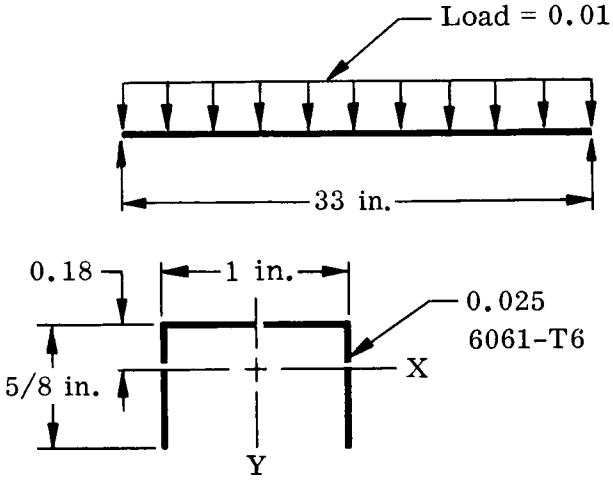

$$\text{Max mom.} = \frac{w\ell^2}{8}$$

$$M = \frac{0.266 \times 33^2}{8} = 36.7 \text{ lb-in.}$$

$\zeta_y = 0.322 \qquad A = 0.053$

$I_y = 0.0055 \text{ in.}^4$

$$fa = \frac{+36.7 \times 0.445}{0.0055} = +2770 \text{ lb/in.}^2$$

$Ftu = 42{,}000 \text{ lb/in.}^2$

Vibration analysis. Vibration frequency of edge channel about Y-Y axis

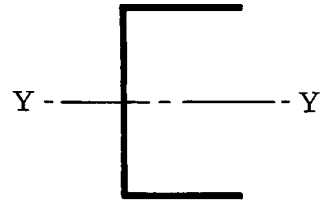

Total weight per channel $= 0.187 + 0.009 + \frac{2 \times 0.184}{2} + \frac{0.042}{2} = 0.401$ lb

Channel length = 33 in. = 2.75 ft

$I_Y = 0.00988 \text{ in.}^4 = 4.77 \times 10^{-7} \text{ ft}^4$

$w = \frac{0.401}{33} \times 12 = 0.146$ lb/ft

$E = 10.5 \times 10^6 \text{ psi} = 1.511 \times 10^9 \text{ lb/sq ft}$

$g = 32.2 \text{ ft/sec}^2$

$$\text{Frequency } n = \frac{\pi}{2} \times \frac{1}{\ell^2} \quad \frac{E I g}{w}$$

$$n = \frac{\pi}{2} \times \frac{1}{(2.75)^2} \sqrt{\frac{1.511 \times 10^9 \times 4.77 \times 10^{-7} \times 32.2}{0.146}}$$

$$= \frac{\pi}{2} \times \frac{1}{7.55} \sqrt{15.91 \times 10^4}$$

$n = 83$ cps

(3) Stress analyses

Various stress analyses were made during the study to justify the structural design of the satellite and to establish a firm basis for estimating the weight. Load paths, sizes of members and materials to be used in the design were established for the various proposed configurations. The following analyses cover some of the more important structural design aspects.

(a) Design loads

The structural design criteria given earlier for the Atlas-Agena launch vehicle were used to derive the loads acting on the satellite. The design accelerations are given below:

Design Accelerations

	Limit	Yield	Ultimate
Longitudinal	11.0	12.1	15.0
Lateral	±2.0	±2.2	±2.7
Normal	±2.0	±2.2	±2.7

No yielding of the structure components shall occur at the yield accelerations and no failure shall occur at the ultimate accelerations. For design purposes, the longitudinal, lateral and normal accelerations were assumed to act simultaneously.

For structural design, the weight of the satellite was assumed to be 800 pounds; near the upper limit of the Atlas-Agena payload capability. This weight was divided as follows:

Structural Design Weight Estimate

Equipment module	150
Lower support truss adapter	25
Sensor array	625
Total	800 lb

The present estimated weight of the Atlas-Agena meteoroid satellite is 723 pounds, which is lower than the structural design weight of 800 pounds on which the structural analysis was based.

(b) Adapters

Early in the study, two configurations of the satellite were investigated. One (Fig. III-44) had the equipment module located at the lower end at which the satellite was attached to the adapter. The other

(Fig. III-45) has the equipment module at the upper end with the lower end of the sensor array attached to the adapter. The latter was eventually selected as the recommended design since it provided more sensor area, better antenna installation, facilitated equipment module installation and maintenance and, incidentally, simplified the adapter used to attach the satellite to the booster.

The early adapters investigated were trusses and the analyses for the above configurations are included in the following pages. The configuration selected permitted the satellite to be located within 4 inches of the booster. This eliminated the necessity of a welded truss and channel ring, since it permitted use of a one-piece machined conical ring (Fig. III-46).

The satellite is attached to the adapter at four points. Two feasible designs have been investigated. One design uses four tension bolts with an explosive nut at each point; the other a V-band clamp which secures the four corner fittings as shown in Fig. III-46.

Configuration 1 analysis of support truss

Loads on truss at Points A, B, C and D

Vertical load = (625 + 150) x 15.0 = 11,600 lb ultimate

Normal load = (625 + 150) x 2.7 = ±2090 lb ultimate

Lateral = (625 + 150) x 2.7 = ±2090 lb ultimate

Moment (both lateral and normal directions) = (625 x 2.7 = 1690 lb) x (81.5 - 28 = 53.5 in.) = ±88,900 lb-in. ultimate

Since normal and lateral loads can act in any horizontal direction, they will be combined with the vertical load to give the most critical loads on sensor array attachment Points A, B, C, D

$$\text{Due to vertical load} = -\frac{11,600}{4} = -2900 \text{ lb}$$

Due to combined normal and lateral loads

$$= \pm \frac{\sqrt{(1690^2 + 1690^2}}{49.5} \times 53.5 \text{ in.}$$

$$= \pm \frac{2\,390 \times 53.5}{49.5} = \pm 2585 \text{ lb}$$

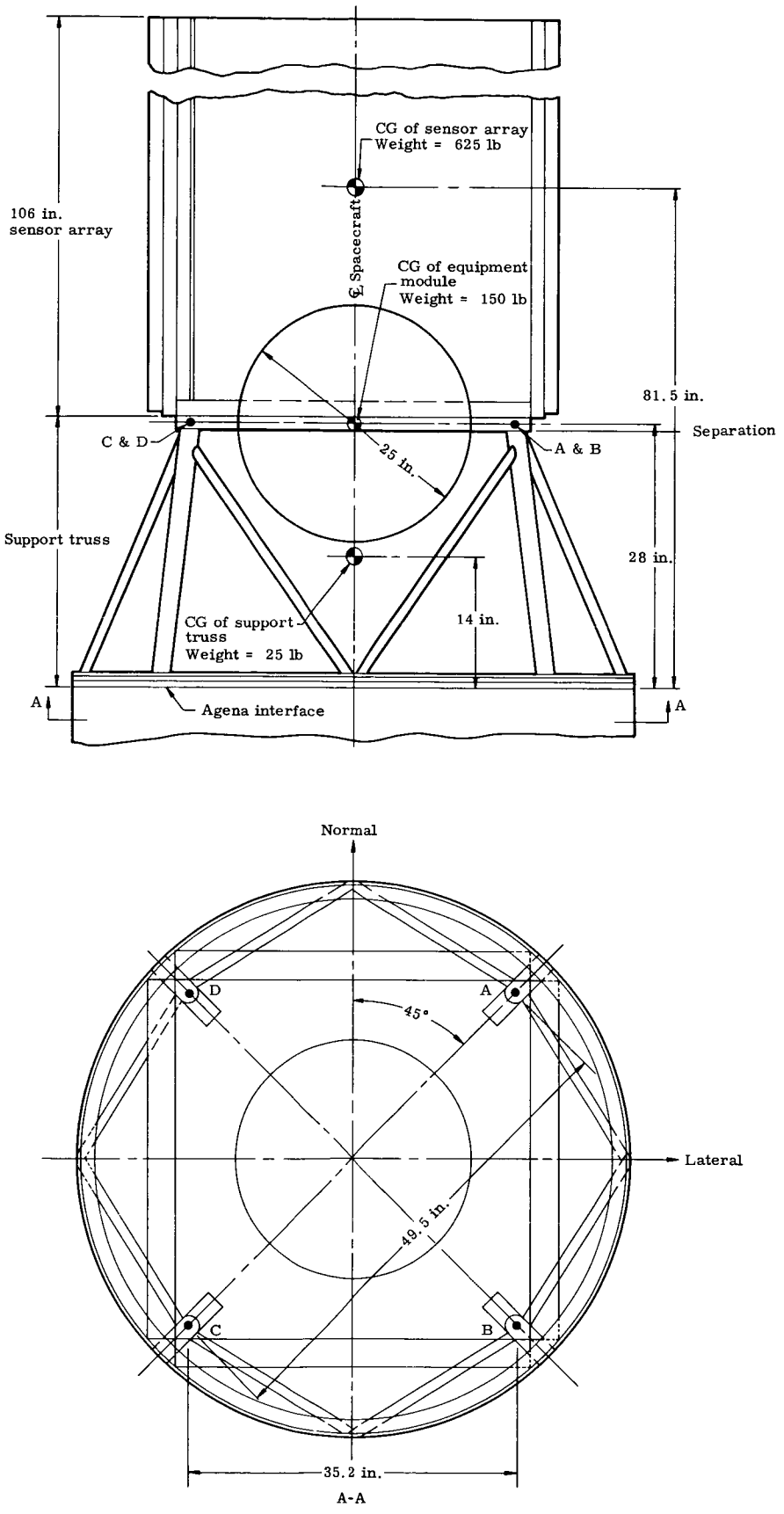

Fig. III-44. Spacecraft Adapter--Model 1

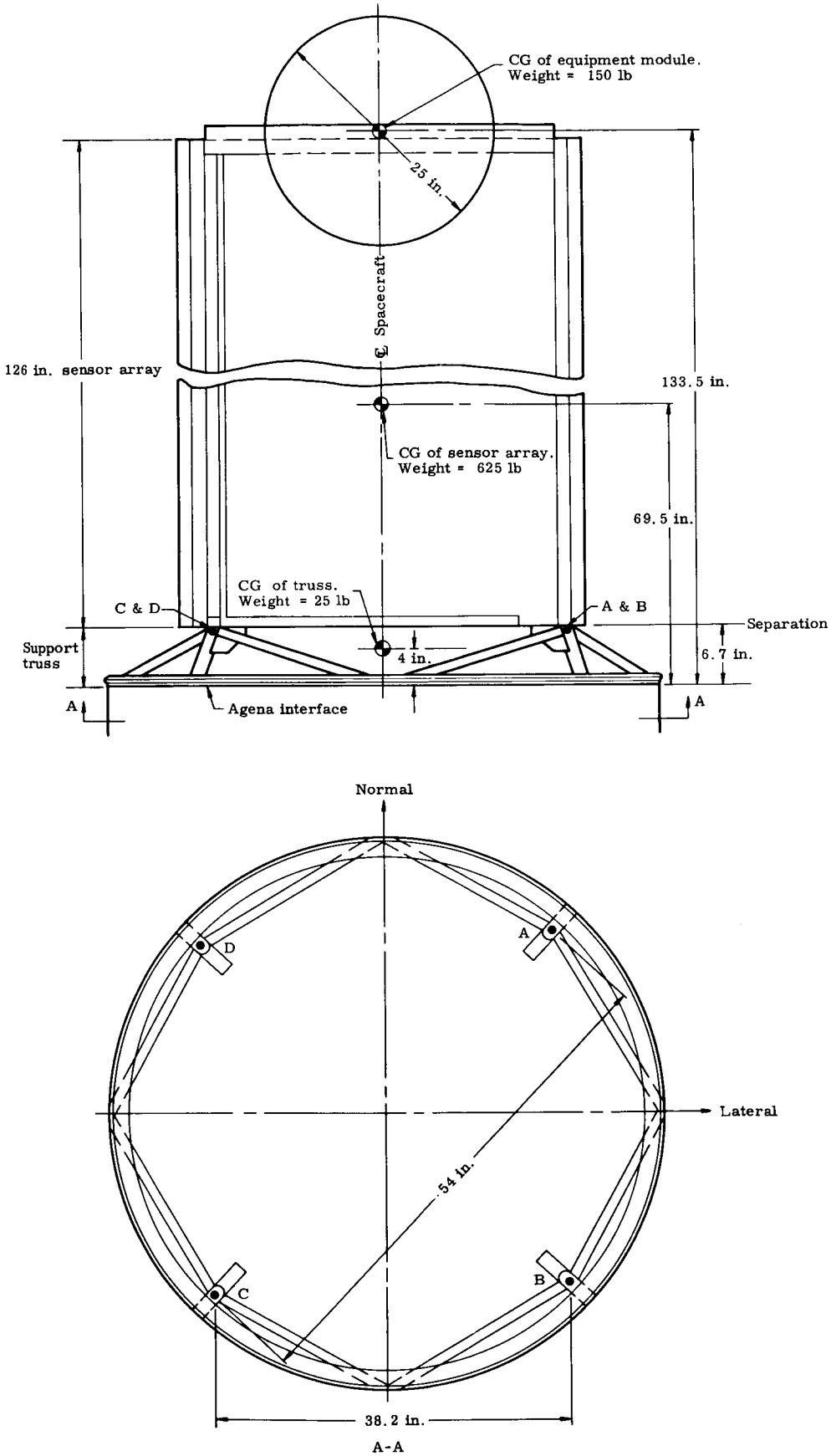

Fig. III-45. Spacecraft Adapter--Model 2

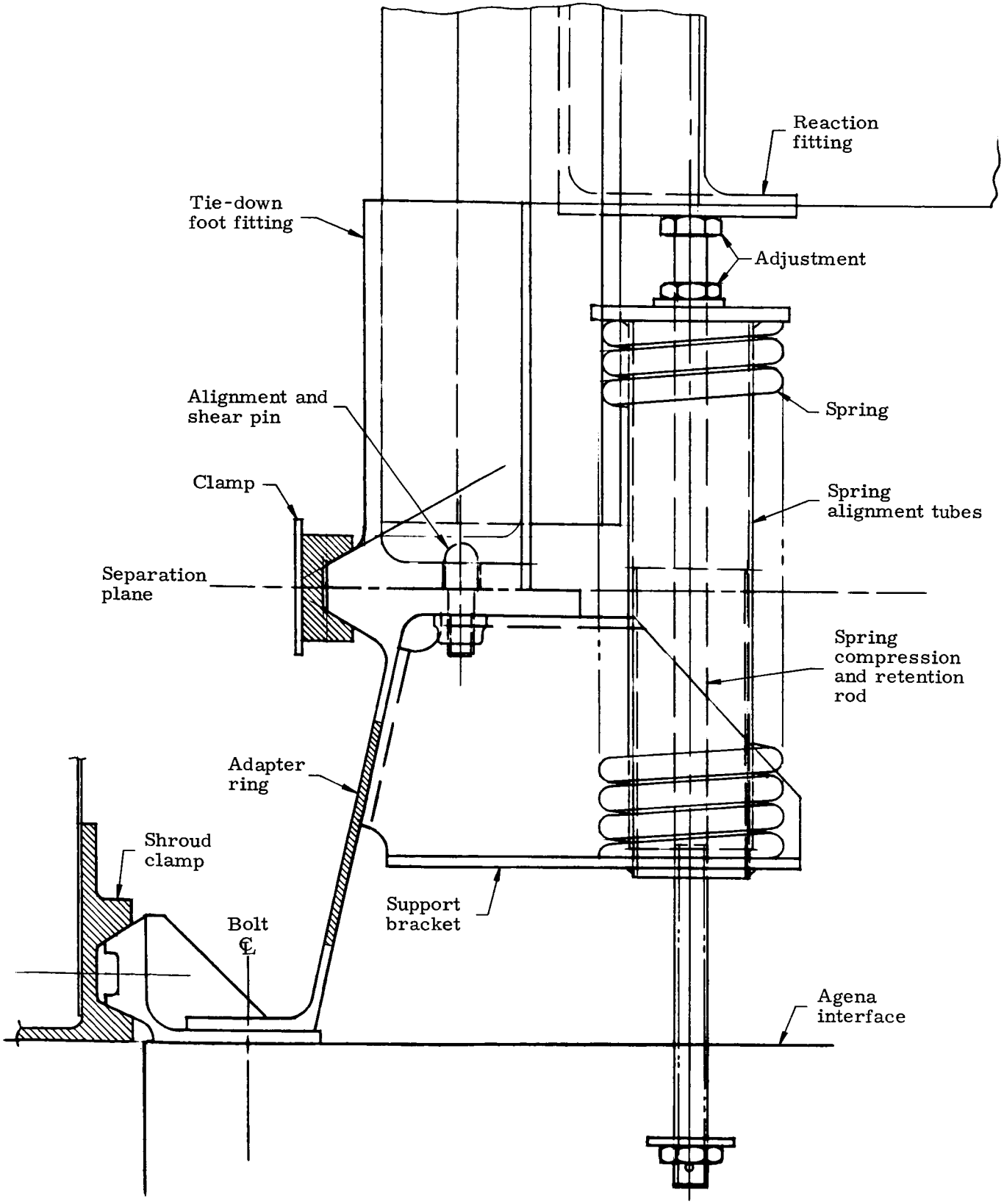

Fig. III-46. S/C to Adapter Attachment

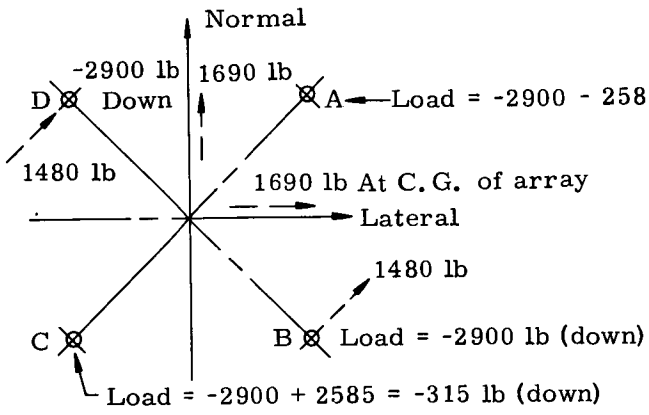

Shear = $\sqrt{2090^2 + 2090^2}$ = 2960 lb
at plane of truss

Assume this load is reacted at B and D

Configuration I
Support Truss Analysis

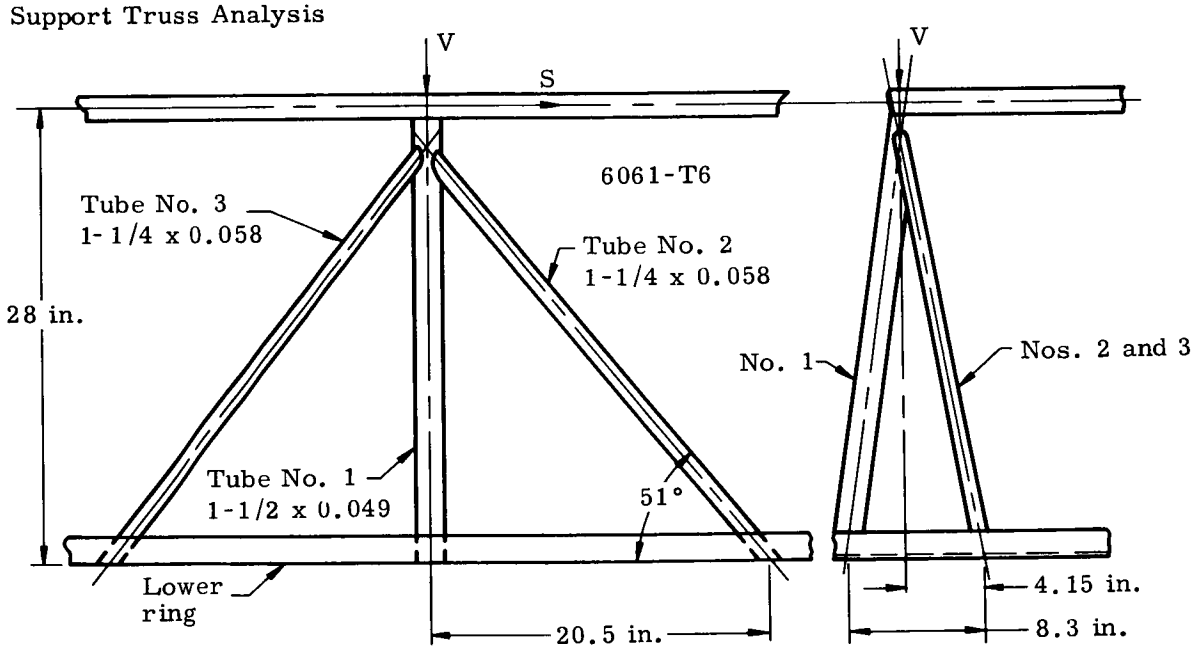

Load condition 1

V = -5400 lb down

Load condition 2

V = -2900 lb down

S = 1480 lb side

Condition 1

Tube No. 1

Load = 5400 x 0.90 = -4860 lb (assume 90% of "V" acts on tube)

Try 1-1/2 x 0.049 6061-T6

$A = 0.2234 \text{ in.}^2$ $L/\rho = \frac{28}{0.513} = 54.5$ $F_{COL} = 23{,}000 \text{ lb/in.}^2$

$\rho = 0.513$ in.

$\frac{P}{A} = \frac{4860}{0.2234} = 21{,}600$ lb

Tubes 2 and 3

$$\text{Load} = -5400 \times \frac{4.15}{8.3} \times \frac{1}{2} \times \frac{1}{\sin 51^\circ} = -1740 \text{ lb ult}$$
$$0.777$$

Try 1 x 0.058 in. 6061-T6

$A = 0.1716 \text{ in.}^2$ $L = 34$ in. $L/\rho = 34/0.3337 = 102$

$\rho = 0.3337$

$F_{COL} = 10{,}000$ psi

$\frac{P}{A} = \frac{1740}{0.1716} = 10{,}100$ lb

Condition 2

V = -2900 lb S = 1480 lb

Load in tube No. 2 (or tube No. 3) = $-2900 \times \frac{4.15}{8.3} \times \frac{1}{\underset{0.777}{\sin 51^\circ}} \times \frac{1}{2} - \frac{1480}{2} \times \frac{1}{\underset{0.629}{\cos 51^\circ}}$ =

$$-934 - 1497 = -2431 \text{ lb ult}$$

Try 1-1/4 x 0.058 6061-T6

A = 0.2172 L = 34 in. $L/\rho = \frac{34}{0.422} = 81.9$

$\rho = 0.422$ $F_{COL} = 16{,}000$ psi

$\frac{P}{A} = \frac{2431}{2172} = 11{,}200$ psi

Lower ring. All vertical loads from truss tubes are assumed to be reacted by Agena structure (therefore, there is no bending in ring normal to its plane). However there is bending in plane of ring.

Condition 1

Load in tubes 2 and 3 = -1740 lb

Horizontal composition = $-1740 \times \underset{0.629}{\cos 51^\circ}$

$$= -1095 \text{ lb}$$

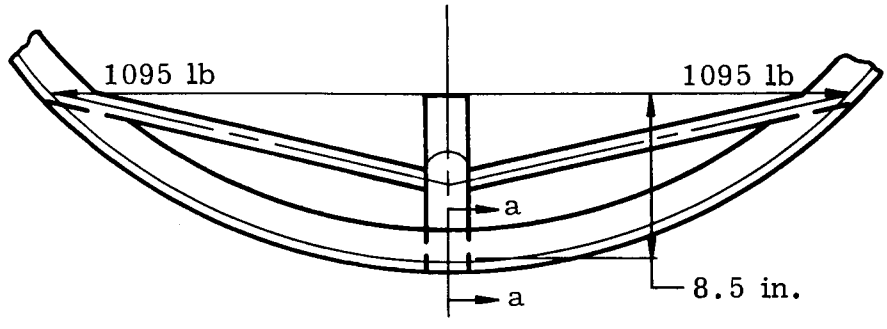

Section a-a (on ring)

P = 1095 lb tension

M = 1095 x 8.5 = 9300 lb-in.

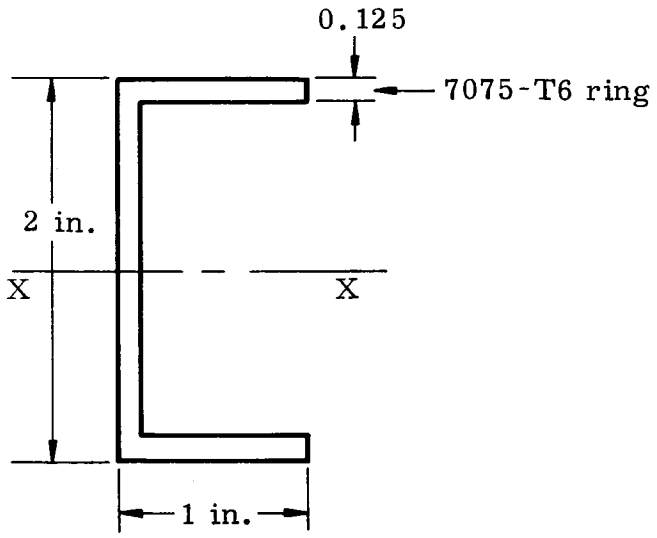

$$A = 2 \times 0.875 \times 0.125 + 2 \times 0.125$$

$$= 0.469 \text{ in.}^2$$

$$I_x = \frac{1 \times \overline{2}^3}{12} - \frac{0.875 \times \overline{1.75}^3}{12}$$

$$= 0.277 \text{ in.}^4$$

$$f_t = \frac{1095}{0.469} = +2{,}330 \text{ psi}$$

$$f_b = \frac{9300 \times 1}{0.277} = \pm 33{,}600 \text{ in.}$$

$$\text{Total} = \begin{cases} +35{,}930 \text{ in.} \\ -31{,}270 \text{ in.} \end{cases}$$

$$b/t = \frac{1}{0.125} = 8 \quad F_{CR} = 59{,}000 \text{ psi}$$

Configuration 2 support truss

Loads at Points A, B, C and D

Vertical load = (625 + 150) x 15.0 = 11,600 lb ultimate

Normal load = (625 + 150) x 2.7 = ±2090 lb ultimate

Lateral load = (625 + 150) x 2.7 = ±2.090 lb ultimate

Moment (both lateral and normal directions) = (625 x 2.7 x 62.6) + (150 x 2.7 x 126.8) = 105,500 + 51,300 = ±156,800 lb-in.

Loads at attachment points

Due to vertical load = $-\frac{11{,}600}{4}$ = -2900 lb

Due to combined normal = $\pm \frac{156{,}800 \times \sqrt{2}}{54}$ = ±4100 lb

Shear = $\sqrt{\overline{2090}^2 + \overline{2090}^2}$ = ±2960 lb

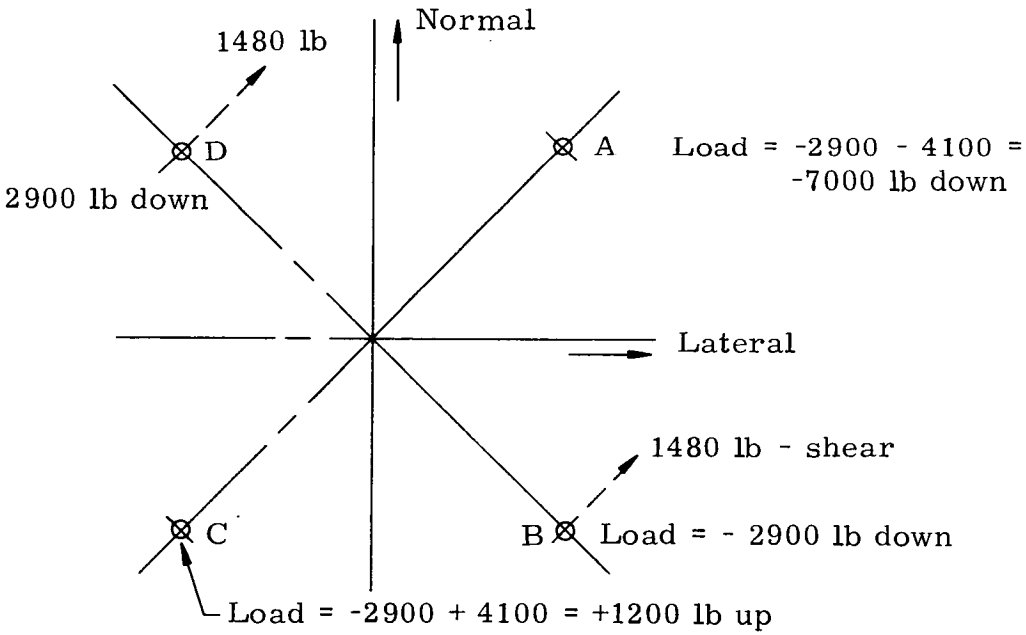
Normal
1480 lb
D
2900 lb down
A
Load = -2900 - 4100 =
-7000 lb down
Lateral
1480 lb - shear
C
B
Load = - 2900 lb down
Load = -2900 + 4100 = +1200 lb up

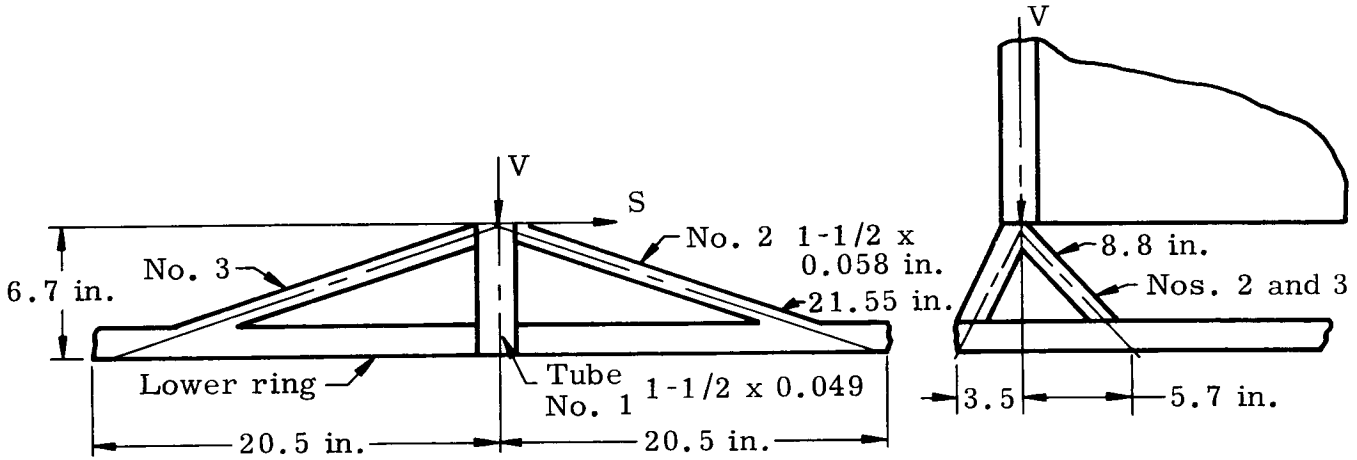
V
S
No. 3
6.7 in.
No. 2 1-1/2 x
0.058 in.
21.55 in.
Lower ring
Tube
No. 1
1-1/2 x 0.049
20.5 in.
20.5 in.
V
8.8 in.
Nos. 2 and 3
3.5
5.7 in.

Load Condition 1

V = -7000 lb ultimate

Tube No. 1

Assume to carry 90% of "V" = 0.90 x 7000 = -6300 lb

L = 7.0 in.

6061-T6 A = 0.2234 $L/e = \frac{7.0}{0.513} = 13.7$

$1\frac{1}{2}$ x 0.049 $\rho = 0.513$ $F_{col} = 36,000$

$\frac{P}{A} = \frac{6300}{0.2234} = 28,200$ lb/in.^{2}

Tube No. 2 $= -7000 \times \frac{3.5}{9.2} \times \frac{21.55}{6.7} \times \frac{8.8}{5.7} \times \frac{1}{2} = -6600$ lb

Load Condition 2

V = -2900 lb S = 1480 lb

Tube No. 2

Load $= -6600 \times \frac{2900}{7000} - \frac{1480}{2} \times \frac{21.55}{20.5} \times \frac{22.3}{20.5} = -2730 - 845 = -3575$ lb

Max load = -6600 lb Condition 1

L = 22.6 in. $L/e = \frac{22.6}{0.513} = 44.1$

$1\frac{1}{2}$ x 0.049 = 6061-T6 $F_{col} = 27,500$ psi

$\frac{P}{A} = \frac{6600}{0.2234} = 29,600$ lb/in.^{2}

Use $1\frac{1}{2}$ x 0.058 in. A = 0.262

Configuration 2

Lower ring

Condition 1

Load in tube No. 2 = -6600 lb

Horizontal component = $-6600 \times \frac{20.5}{21.5} \times \frac{20.5}{22.5} = -5880$ lb

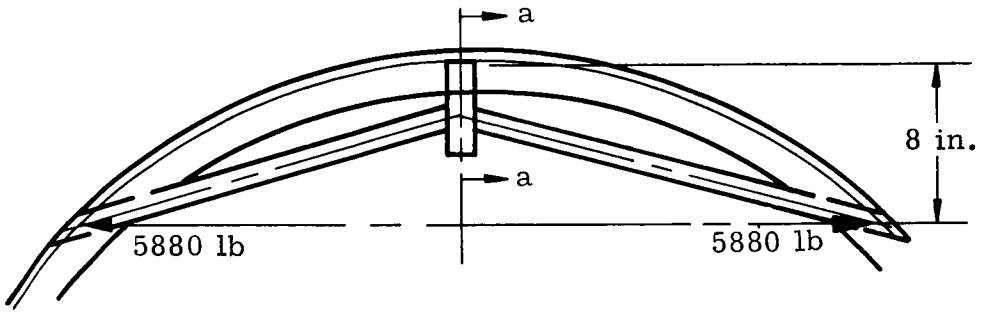

Section a-a

Tension = +5880 lb

Momentum = 5880 x 8.0 = 47,000 lb-in.

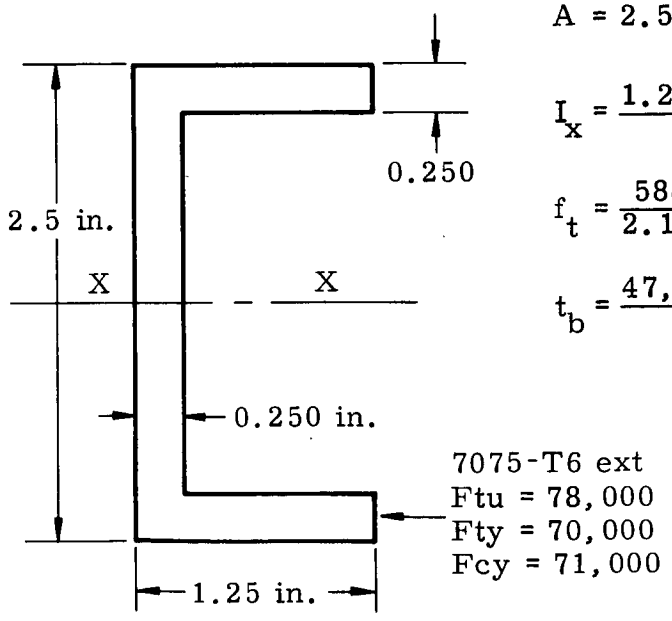

$A = 2.5 \times 1.25 - 2 \times 1.0 = 2.125$ in.^{2}

$I_x = \frac{1.25 \times \overline{2.5}^3}{12} - \frac{1 \times \overline{2}^3}{12} = 0.945$ in.^{4}

$f_t = \frac{5880}{2.125} = +2760$ lb/in.^{2}

$t_b = \frac{47,000 \times 1.25}{0.945} = \frac{\pm 62,200 \text{ in.}}{+64,960 \text{ in.}}$
$-59,440$ lb/in.^{2}

(c) Sensor and mounting frames

The proposed configuration (Fig. III-2) consists of a mounting platform for the systems module and four deployable sensor arrays. These arrays consist of three sides which form a "Z" configuration when fully deployed. Two of the sides are fixed 90° with respect to each other. The third side is hinged to one of the other sides and folds out to 90°.

Overall structural analysis. Each of these sides consists of a tubular rectangular frame of 125-in. length and 36-in. width. The main frame has cross-members which form smaller rectangular panels (Fig. III-47). The spring-loaded sensor panels are mounted within these smaller rectangular panels.

All the inertia loads developed at launch on the satellite are carried by the tubular framework of the sensor arrays in their folded position. To form a rigid structure of the arrays to carry the axial and lateral shear loads at launch, it was found necessary to provide 90° conical shear pins at all frame joints between panels as discussed earlier. These shear pins provide a means to transfer loads from one panel to another and also from one array to another. They interlock all panels and arrays together with the aid of the straps in the undeployed configuration to form an open box-type structure. This structure is closed at the top end by the systems module platform. At the lower end, the loads from the satellite are taken out by four fittings attached to fixed-corner members of the arrays. These corner members distribute the load from the fittings into the array framework.

A stress analysis of this structural framework follows.

The material of the tubular members was originally chosen as 6061-T6 aluminum alloy, since it was felt that the framework would be of welded construction. However, it was found that a riveted or bolted assembly might be more advantageous and easier to manufacture. For this type of construction, the high strength alloys of 2014-T6 and 7075-T6 could be used with some weight reduction.

It is pointed out that there are some minor discrepancies in dimensions of the sensor mounting panels between those used in the stress analysis and the final drawings given elsewhere in the report. This is due to changes in configuration as the study moved along. However, the analysis is accurate enough to apply to the final configuration, since the analysis is based on a satellite weight of 800 lb compared to a final weight of 723 lb.

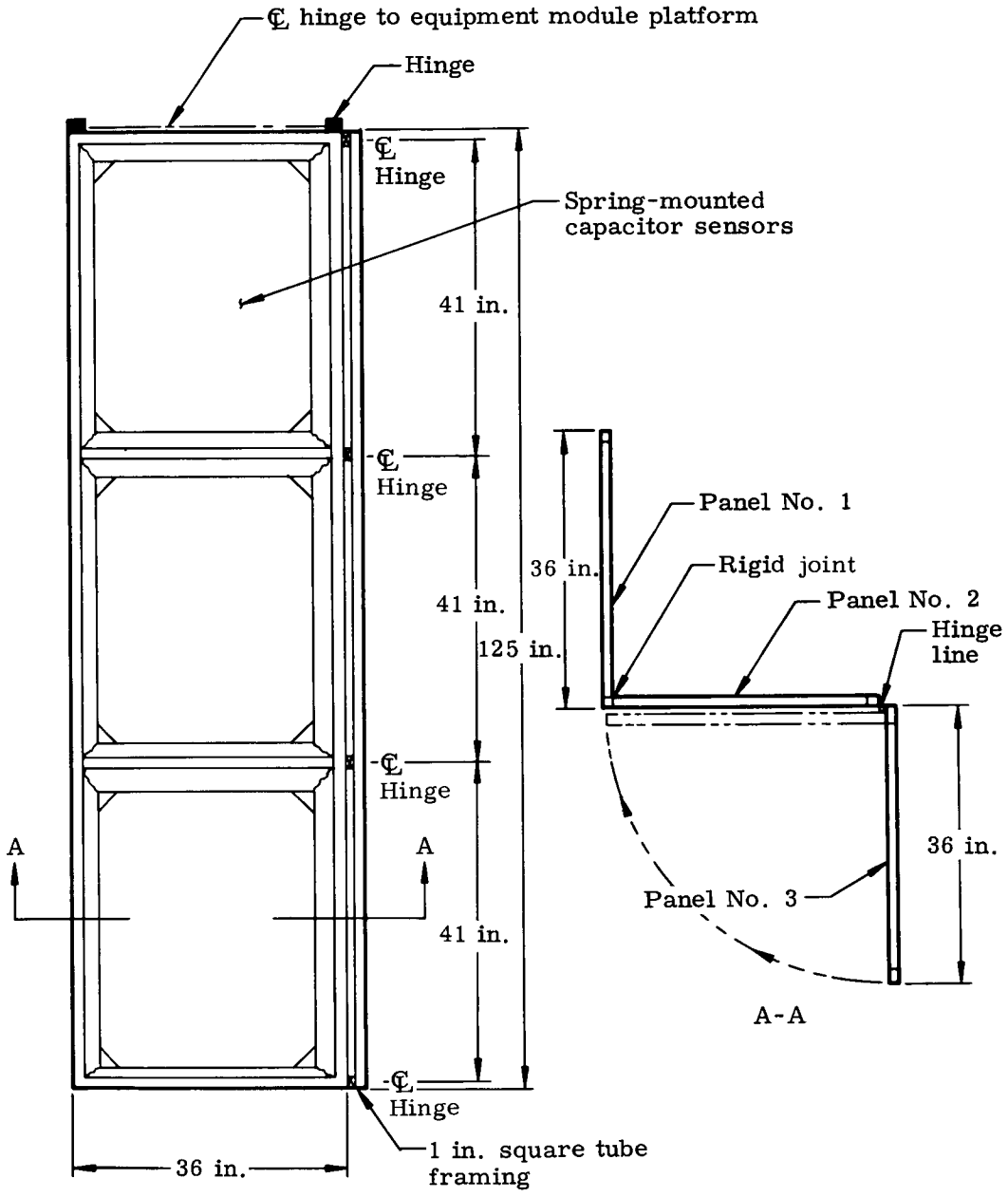

Fig. III-47. Structural Frame and Sensor Mounting

Atlas-Agena Configuration

Sensor area	= 690 sq ft (actual)
Structural area	= 376 sq ft (12 panels)
Estimated weight	= 625 lb wt/panel = $\frac{625}{12}$ = 52 lb
Equipment module	= 150 lb (located at top of array)
Lower support truss	= 25 lb
Sensor array	= 625 lb
	800 lb total spacecraft

Design accelerations

	Limit	Ultimate
Longitudinal	11.0	15.0
Lateral	±2.0	±2.7
Normal	±2.0 ↑ No yielding at 1.10 times these values	±2.7 ↑ No failure at these values

Analysis of Panel No. 3 (flip-out)

Weight = 52 lb

Vertical load = 52 x 15 = 780 lb ultimate down

Lateral load = 52 x 2.7 = ±140.5 ultimate
Normal load = 52 x 2.7 = ±140.5 ultimate
} Any horizontal direction resultant = $\sqrt{2}$ x 140.5 = 199 lb

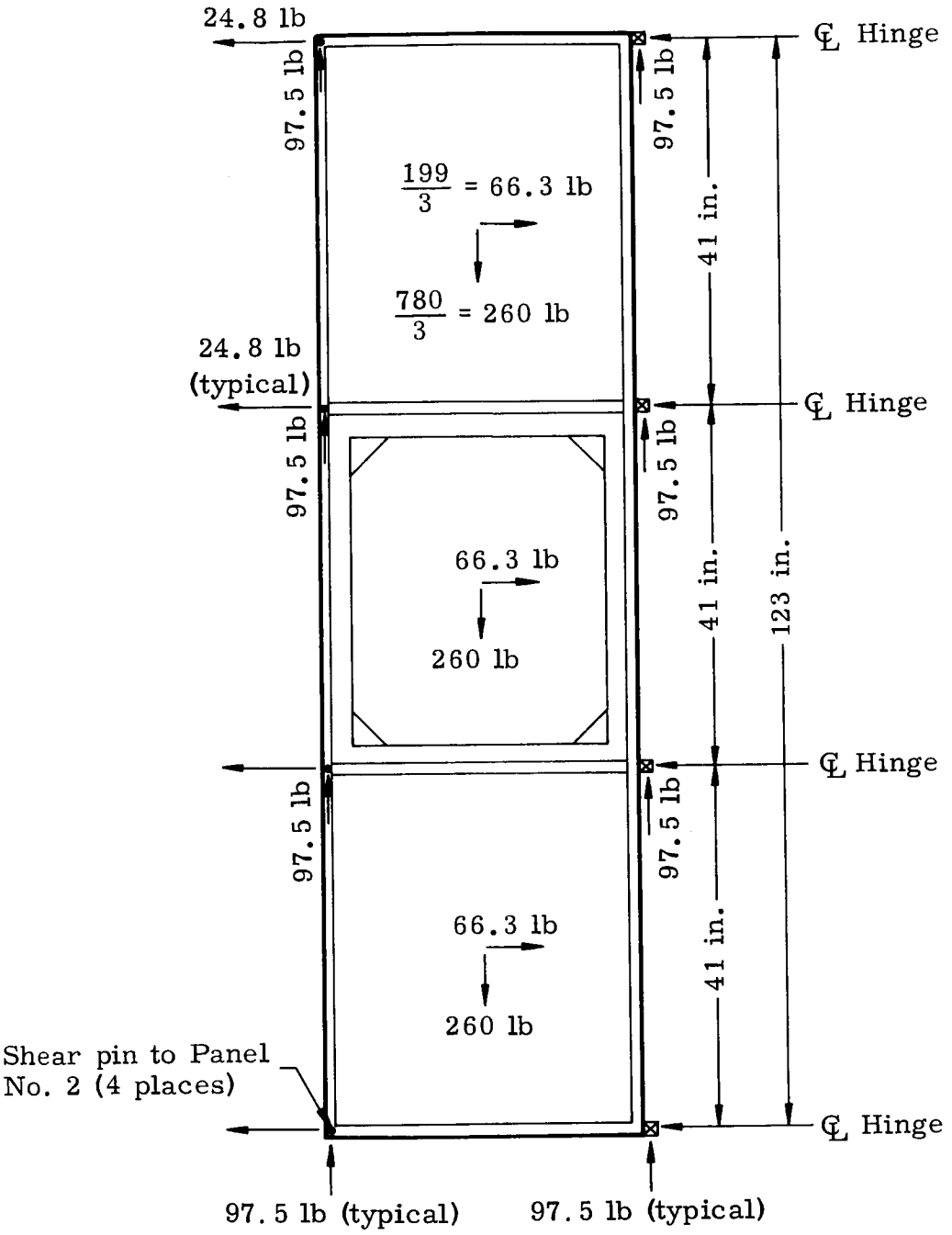

Assumptions. Vertical load of 780 lb is reacted equally at four hinge points and four shear pins. Side load is reacted at same points.

Since the sensors are spring mounted, sensor inertia loads get into the frame at the corners. The location of the shear pins and the hinges at the corners result in little axial load in the tubes other than that due to initial spring tension.

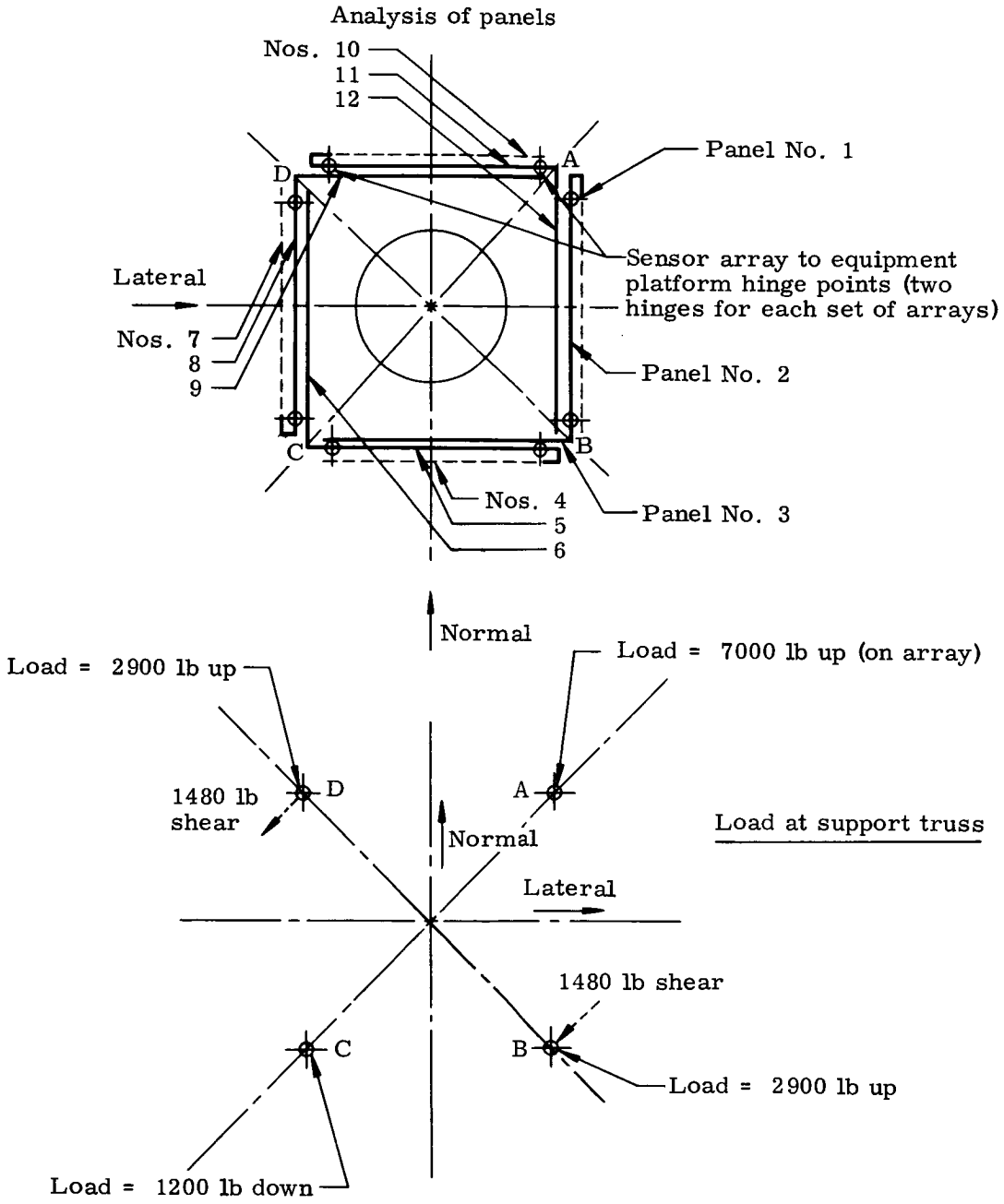
Analysis of panels
Nos. 10
11
12
Panel No. 1
A
D
Sensor array to equipment platform hinge points (two hinges for each set of arrays)
Lateral
Nos. 7
8
9
Panel No. 2
C
B
Nos. 4
5
6
Panel No. 3
Normal
Load = 2900 lb up
Load = 7000 lb up (on array)
1480 lb shear
D
A
Normal
Load at support truss
Lateral
1480 lb shear
C
B
Load = 2900 lb up
Load = 1200 lb down

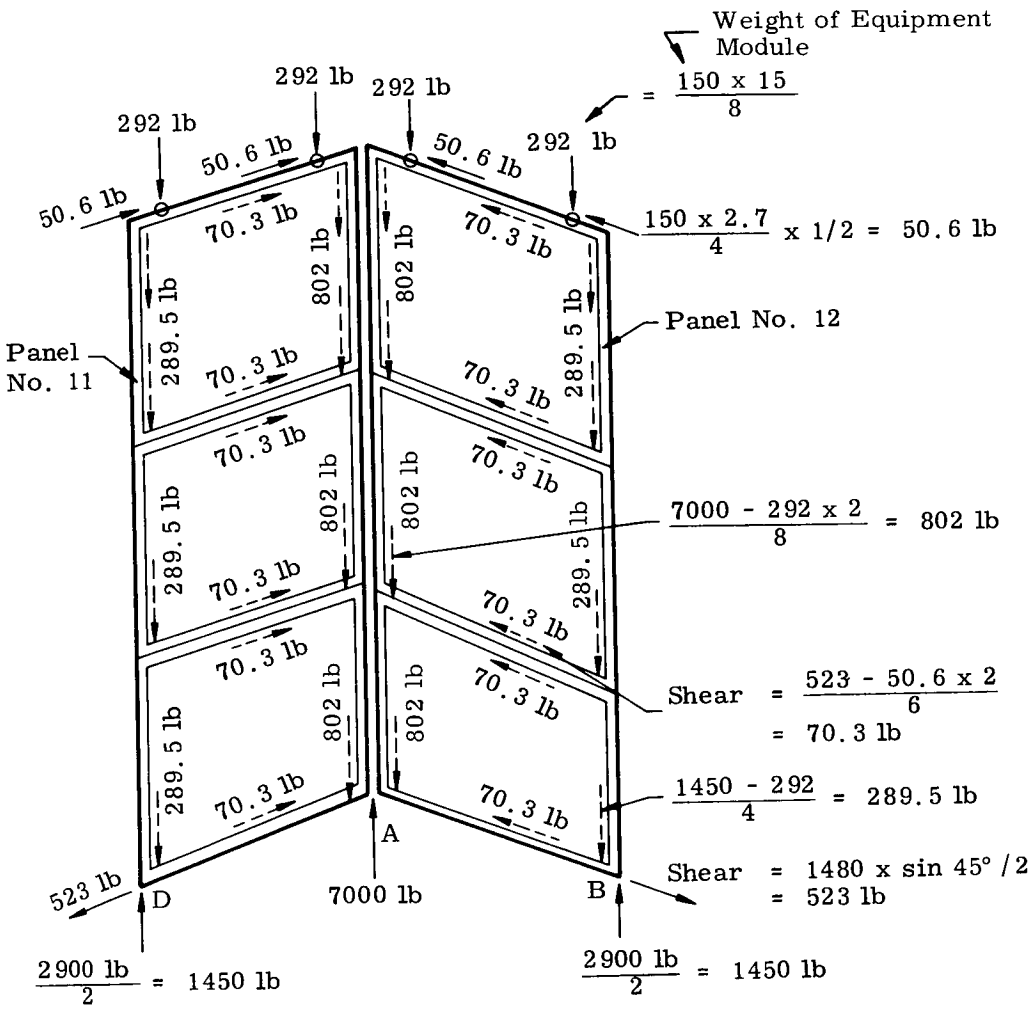
Weight of Equipment Module
= 150 x 15 / 8
292 lb
292 lb
292 lb
50.6 lb
50.6 lb
50.6 lb
150 x 2.7 / 4 x 1/2 = 50.6 lb
Panel No. 12
Panel No. 11
70.3 lb
802 lb
289.5 lb
7000 - 292 x 2 / 8 = 802 lb
Shear = 523 - 50.6 x 2 / 6 = 70.3 lb
1450 - 292 / 4 = 289.5 lb
Shear = 1480 x sin 45° / 2 = 523 lb
523 lb
D
A
7000 lb
B
2900 lb / 2 = 1450 lb
2900 lb / 2 = 1450 lb

Bending due to shear loads

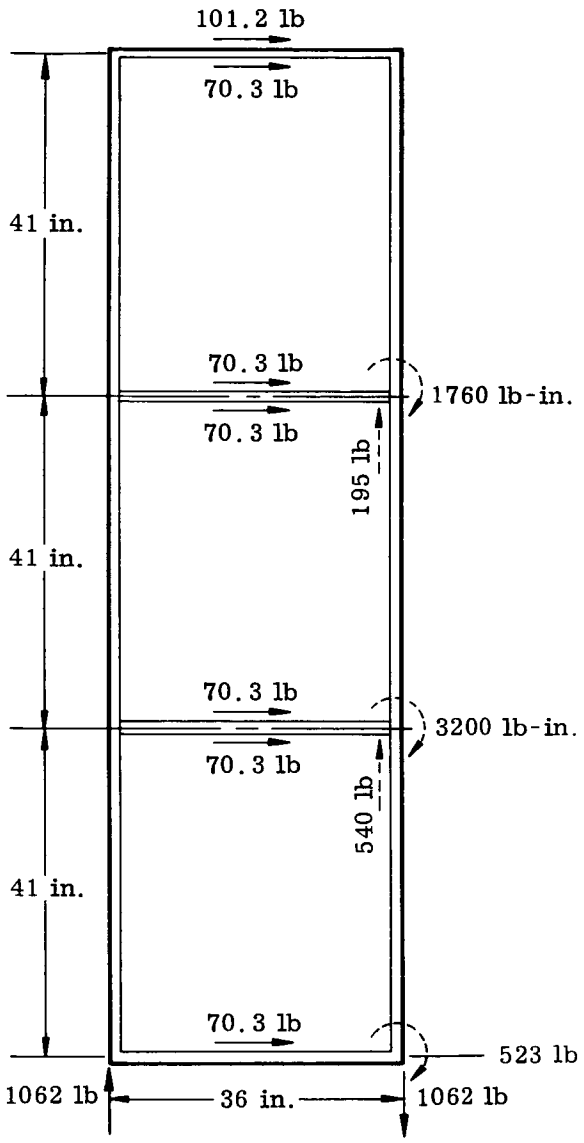

101.2 x 123	=	12,480 lb-in.
70.3 x 123	=	8,610
140.6 x 82.0	=	11,510
140.6 x 41.0	=	5,760
		38,360 lb

$$\text{Couple load} = \frac{38,360}{36} = 1,062 \text{ lb}$$

NOTE:
1/3 of these corner moments is reacted by bending in edge members of each panel

101.2	=	101.2 lb
70.3	=	70.3
70.3 x 4	=	281.2
		452.7 lb

$$4640 \text{ lb-in.} = 452.7 \times \frac{41}{4}$$

Bending due to shear loads in a rectangular bay

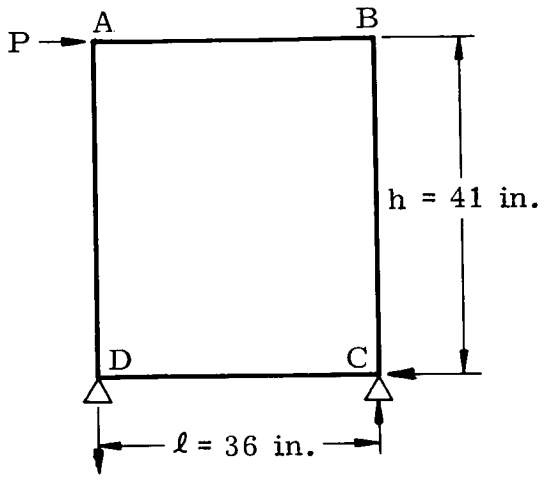

$$I_{AB} = I_{DC} \qquad I_{AD} = I_{BC}$$

$$K = \frac{I_{AB}}{\ell} \qquad n = \frac{Kh}{I_{AD}} = \frac{h}{\ell} \times \frac{I_{AB}}{I_{AD}}$$

$$p = \frac{K\ell}{I_{DC}} = \frac{I_{AB}}{I_{DC}}$$

$$B = 6n + p + 1 = \frac{6h}{\ell} \times \frac{I_{AB}}{I_{AD}} + \frac{I_{AB}}{I_{DC}} + 1$$

If I of all members are equal

$$n = \frac{h}{\ell} \qquad p = 1 \qquad B = \frac{6h}{\ell} + 1 + 1 = 2\left(\frac{3h}{\ell} + 1\right)$$

$$M_{AB} = -M_{BC} = \frac{Ph}{2} \times \frac{3n + p}{B}$$

$$= \frac{Ph}{2} \times \frac{\frac{3h}{\ell} + 1}{2\left(\frac{3h}{\ell} + 1\right)} = \frac{Ph}{4}$$

$$M_{CD} = -M_{DA} = \frac{Ph}{4}$$

Corner member at "A"

Corner member at "A"

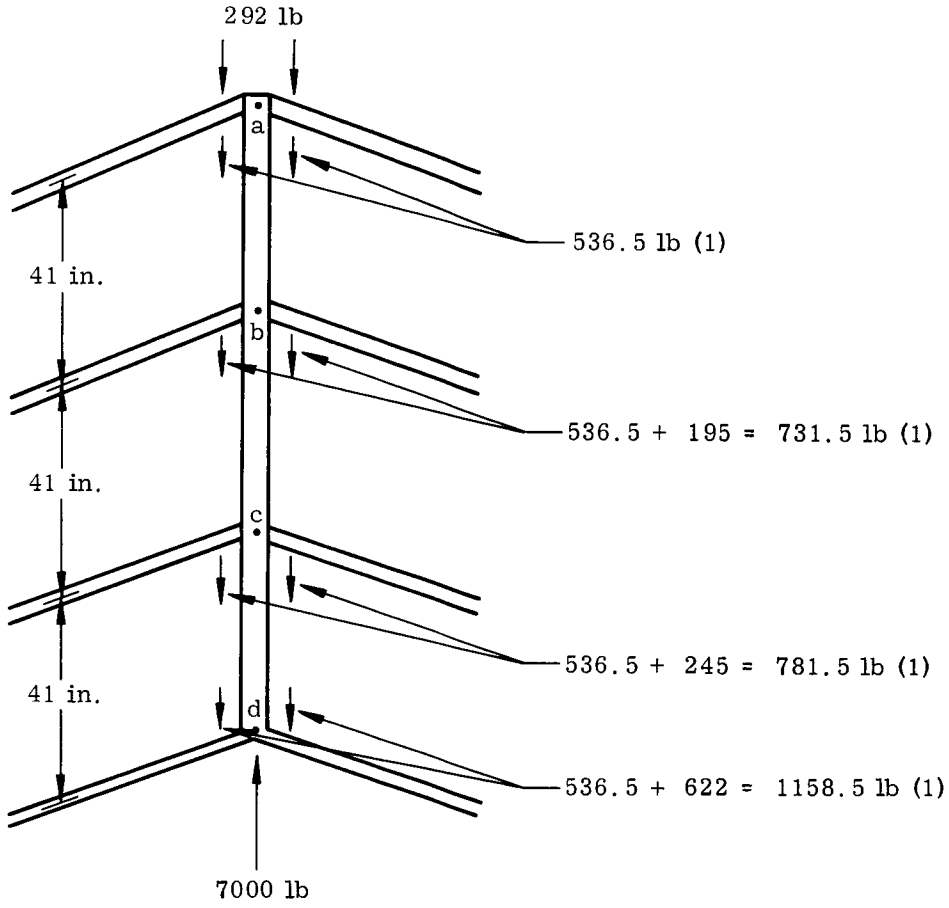

NOTE:

(1) Due to vert load $= \frac{7000 - 292 \times 2 - 1062 \times 2}{8}$

$= \frac{4292}{8} = 536.5$ lb

Loads and moments

Point "a" Load = 2 (292 + 536.5) = -1657 lb

Moment = $\frac{1760}{3}$ x 2 = 830 lb-in.

Point "b" Load = -1657 - 2 (731.5) = -3100 lb

Moment = $\frac{3200}{3}$ x 2 = 1510 lb-in.

Point "c" Load = -3100 - 2 (781.5) = -4663 lb

Moment = $\frac{4640}{3}$ x 2 = 2200 lb-in.

Point "d" Load = -4663 - 2 (1158.5) = -6980 lb--below point d

= -4663 lb (above point d)

Moment = 2200 lb-in. Checks 7000 lb reaction

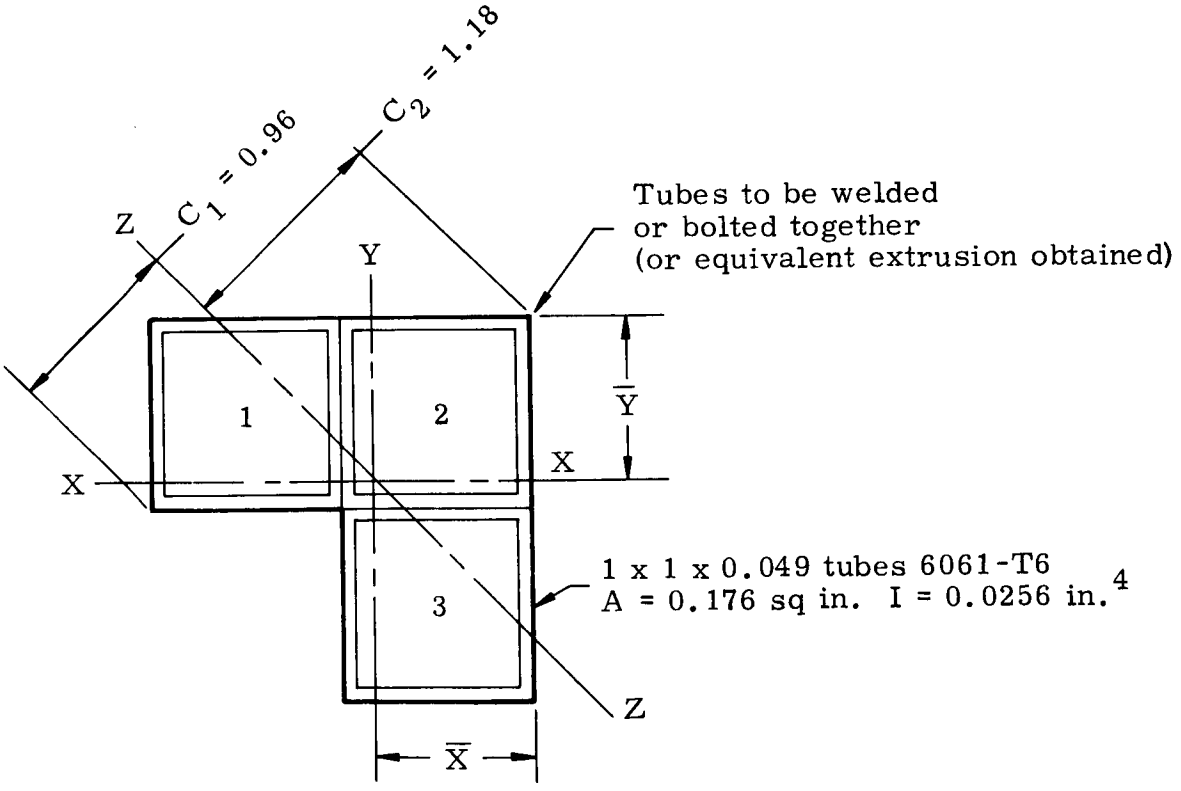

Item	A	x	A_x	A_x^2	I_0
1	0.176	1.50	0.264	0.396	0.0256
2	0.176	0.50	0.088	0.044	0.0256
3	0.176	0.50	0.088	0.044	0.0256
	0.528		0.440	0.484	0.0768

$\bar{x} = \frac{0.440}{0.528} = 0.835$ in. $\quad \bar{y} = 0.835$ in.

$I_y = 0.484 + 0.0768 - 0.528 \times 0.835^2 = 0.294$ in.^{4}

$I_x = 0.294$

$I_z = 0.294 \times 0.707^2 + 0.294 \times 0.707^2 = 0.293$ in.^{4}

$\rho_z = \sqrt{\frac{0.293}{0.528}} = 0.745$

At Point d

Load = -4663 lb[above point (d) M_z = 2200 lb-in.]

Load = -7000 lb[below point (d) M_z = 0]

A = 0.528 $\quad f_c = \frac{4663}{0.528} = 8820$ lb/in.^{2}

I_z = 0.293

C_1 = 0.96 $\quad L'/\rho = \frac{41}{0.745} = 55 \quad F_{col} = 24,000$ lb/in.^{2} (6061-T6)

C_2 = 1.18 $\quad F_{col} = 27,500$ lb/in.^{2} (2024-T3)

ρ_z = 0.745 $\quad f_b = \frac{2200 \times 1.18}{0.293} = 8880$ lb/in.^{2}

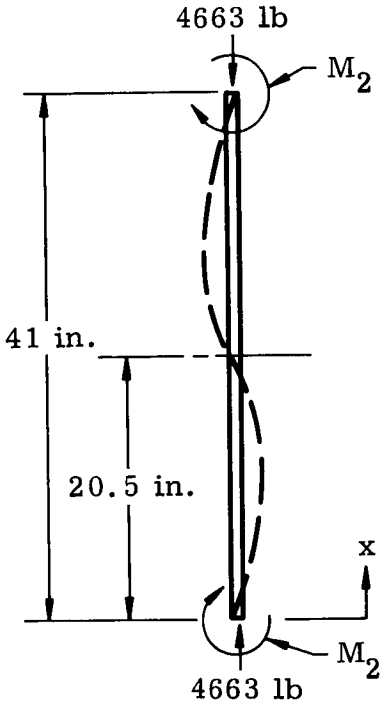

Beam-column analysis

$$J = \sqrt{\frac{EI}{P}} = \sqrt{\frac{10.5 \times 10^6 \times 0.293}{4663}}$$

$J = 25.7$ in.

$$U = \frac{\ell}{J} = \frac{20.5}{25.7} = 0.799$$

$\sin U = 0.717$

$\cos U = 0.696$

$$\text{Maximum moment} = \frac{M}{\cos \frac{x}{J}}$$

$$x = J \arctan \left(\frac{-M \cos U}{M \sin U} \right)$$

$x = 25.7 \tan^{-1} (-1.03)$

$x = 25.7 \times 2.34 = 60.2$ in. since $x > \ell$

Maximum moment = M = 2200 lb - in.
at x = 0

$$\text{Maximum moment} = \frac{2200}{\cos \frac{20.55}{25.7}} = \frac{2200}{0.697} = 3150 \text{ lb-in.}$$

$$f_b = \frac{3150 \times 1.18}{1293} = 12,700 \text{ lb/in.}^2$$

Beam column

For 6061-T6

F_{tU} = 42,000

F_{cM} = 35,000

F_{col} = 24,000

F_{cr} = 35,000 at corners

f_c = 8820

f_b = 12,700

$$R_c = \frac{8820}{24,000} = 0.368$$

$$R_b = \frac{12,700}{35,000} = \frac{0.363}{0.731}$$

$$MS = \frac{1}{0.731} - 1 = +0.37$$

Maximum deflection at x = 0

$$Y = \frac{1}{P}\left[M - M \times \frac{x}{\ell} + M \cos U \frac{\sin \frac{x}{J}}{\sin U} - M \cos \frac{x}{J}\right]$$

$\frac{x}{\ell} = \frac{0}{20.5} = 0$ $\qquad$ $\cos U = 0.696$

$P = 4663$ lb $\qquad$ $\sin \frac{x}{J} = \sin \frac{0}{25.7} = 0$

$M = 2200$ lb-in. $\qquad$ $\sin U = 0.717$

$\cos \frac{x}{J} = 1$

$$y = \frac{1}{4663}\left[2200 - 2200 \times 0 + 2200 \times \frac{0.696 \times 0}{0.717} - 2200 \times 1.0\right]$$

$$y = \frac{1}{4663}\left[2200 - 2200\right] = 0 \text{ (as it should be at } x = 0)$$

Sensor structural analysis. Mounting the thin rectangular capacitor sensors by springs at each corner appears most promising. The following stress analyses were made to establish feasibility of the design and to establish sizes for weight estimates.

The analyses include selection of the mounting spring and its loads, design of the mounting frame for loads from diagonal springs, and detail design of the corner doublers on the sensor through which the spring load is distributed into the thin target plate of the sensor.

Figure III-48 shows the configuration (also see Fig. III-5) for which the analysis was made. Two sensor panels with 0.002-in. aluminum targets are mounted by four springs within a 38 in. by 52 in. rectangular

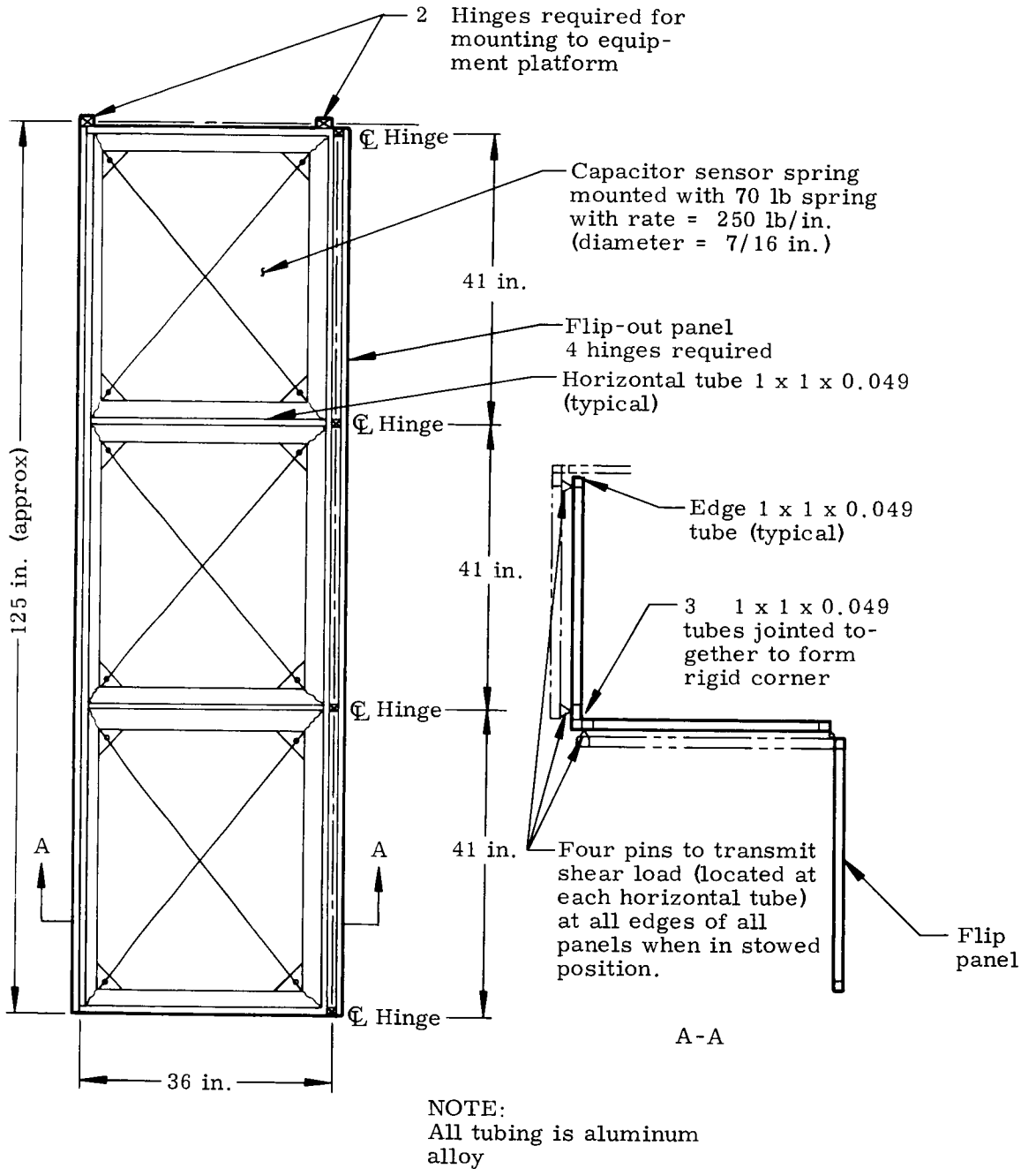

NOTE:
All tubing is aluminum alloy

Structural Requirements for Zee Configuration

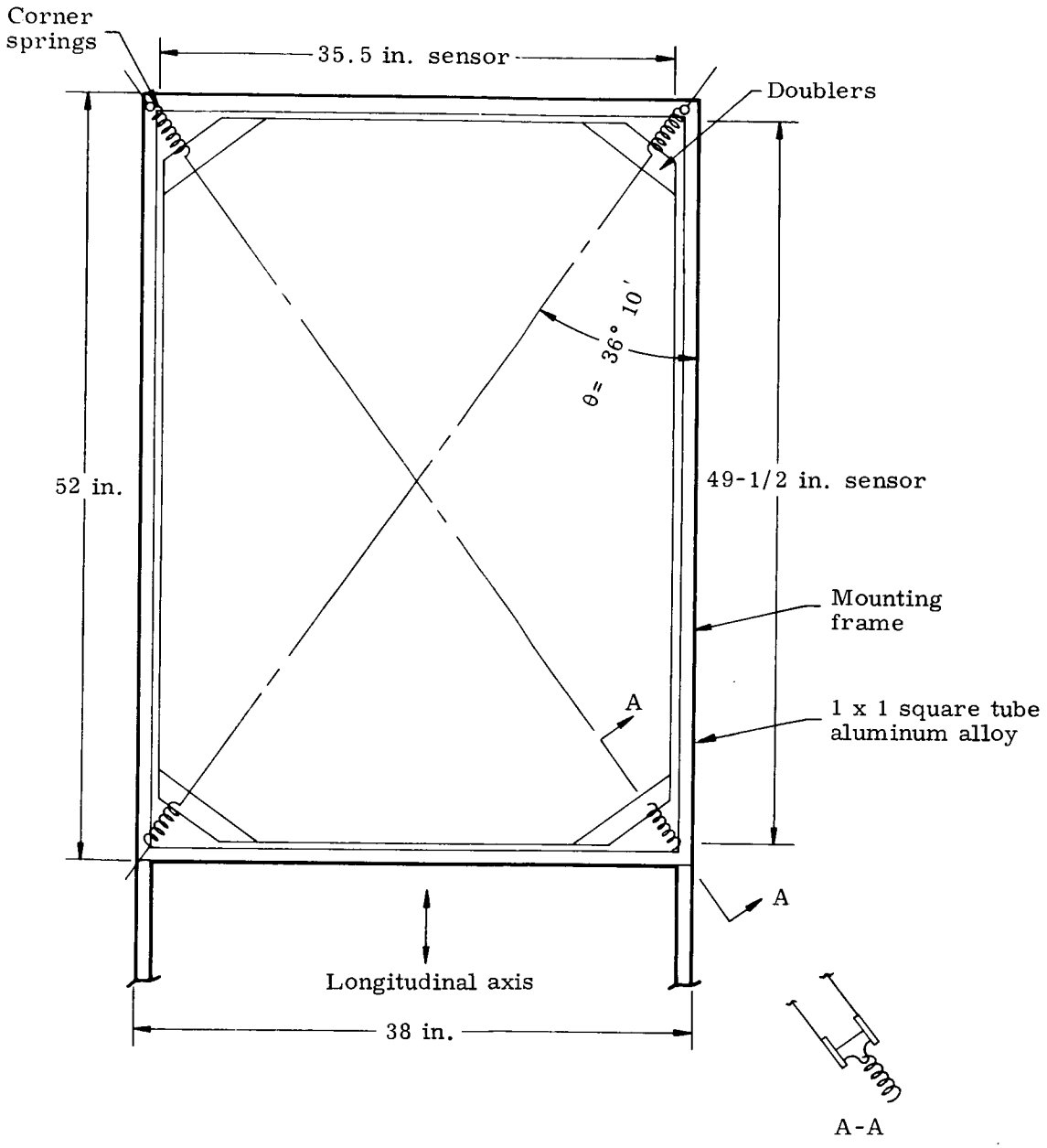

Fig. III-48. Sensor Panel Configuration

tubular frame. The spring load was based on reacting inertia loads with a dynamic magnification factor included and keeping enough tension in the sensors to meet vibration requirements.

The mounting frame is analyzed for the loads from diagonally opposite springs. Such a loading condition causes large bending moments as well as axial loads on the frame. This loading can occur if any spring breaks or is not properly attached during installation of the sensor in the frame.

The design of the doublers needed to carry the spring load into the thin target is also included in the analysis. The doubler must be capable of spreading the spring load into the target without overstressing the material when the panel is subjected to the launch vehicle vibration and the thermal expansion and contraction in space. The design of the spring-loaded sensor panel will require further analysis mainly in the dynamic area. Test programs will need to be run to prove out the designs and, possibly, to obtain design data. Since the spring-loaded design is lightweight and analyses made to date indicate no major disadvantages, the concept is recommended for further evaluation for the MDSS.

The stress analysis has shown that the target material should be a high strength aluminum alloy foil such as 5052-H19 which has a yield strength of 35,000 psi. If lower strength alloys are used, the size of the doublers would need to be larger, reducing available sensor area. Figure III-49 shows one concept for the doublers.

Required spring load

Weight of panel

0.002-in. aluminum target = 0.002 x 144 x 0.101 = 0.0291 lb/sq ft

0.00025-in. mylar = 0.00025 x 144 x 0.060 = 0.0022 lb/sq ft

0.000025-in. copper = 0.000025 x 144 x 0.322 = 0.0012 lb/sq ft

0.0325 lb/sq ft

Size (35.5 in. x 49.5 in.) ÷ 144 = 12.2 sq ft

Weight of one sensor = 0.0325 x 12.2 = 0.396 lb

Weight of two sensors = 0.396 x 2 = 0.792 lb

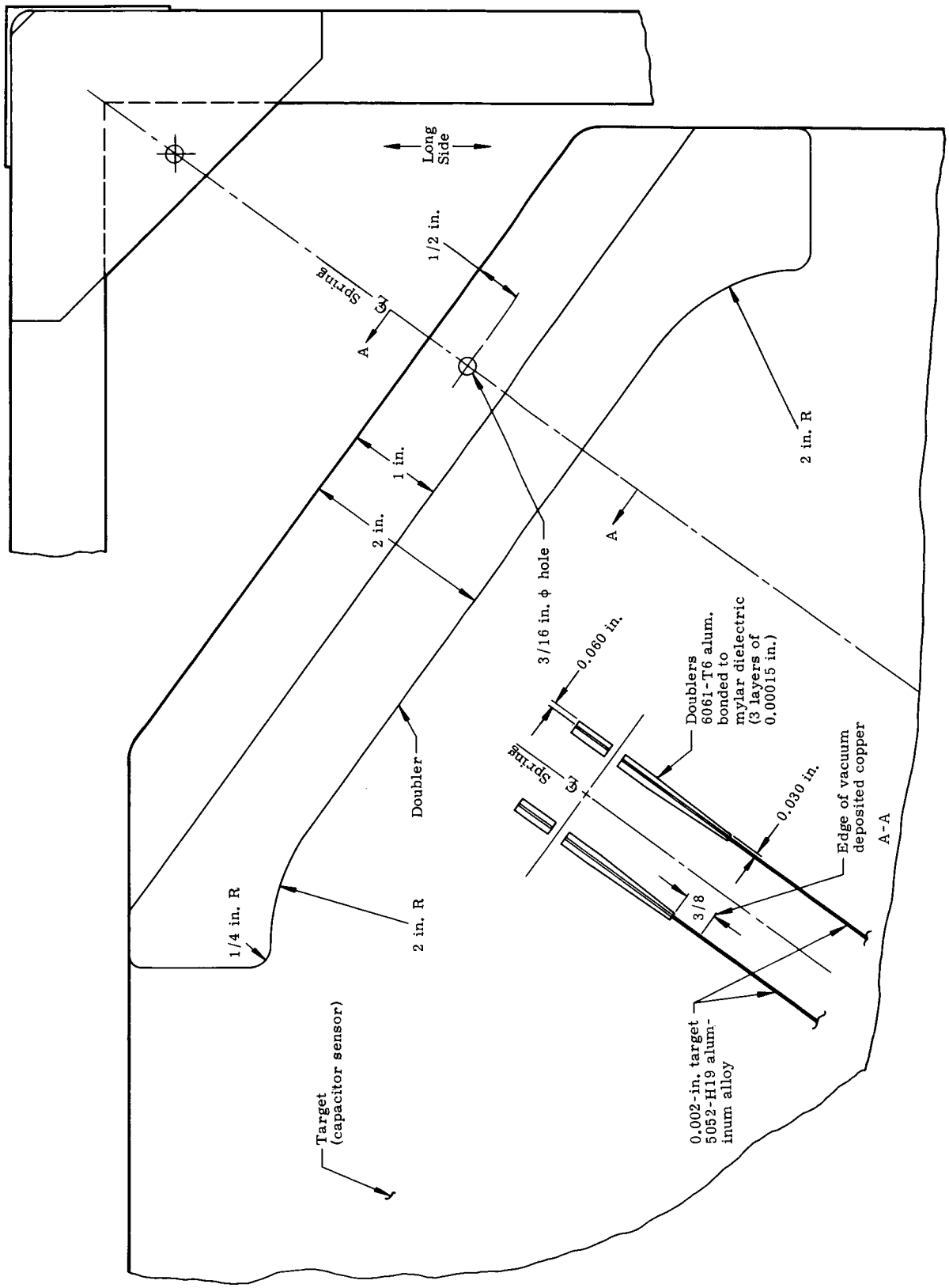

Fig. III-49. Capacitor Sensor Panel Corner Design

Maximum axial load factor = 75 g (from dynamics analysis)

Total load = 0.792 x 75 = 59.4 lb for 2 sensors

$$\text{Load/spring} = \frac{59.4}{2} \times \frac{1}{\cos \theta} = 36.8 \text{ lb}$$

2 springs (1 per corner)

Installed spring load must be equal to this load or greater

$\theta = 36° 10'$

$\sin \theta = 0.5901$

$\cos \theta = 0.8070$

$\tan \theta = 0.7310$

Spring rate = 250 lb/in. or greater

Design criteria for spring

Installed load = 100 lb (min), 125 lb (max)

Yield load of spring = 125 x 1.5 = 187.5 lb

Spring rate = 250 lb/in.

Maximum OD = $\frac{7}{8}$ in.

Spring design

Try $\frac{13}{16}$ in. OD spring 0.162-in. music wire

F_{st} = 112,000 lb/sq in. torsional yield

Load = 183 lb at 100,000 psi

Rate = 3581 lb/in. per coil

$$\text{Allowable load} = 183 \times \frac{112,000}{100,000} = 205 \text{ lb}$$

For rate of 250 lb/in., try 14 coils

$\therefore$ Rate = $\frac{3581}{14}$ = 256 lb/in.

Coil, solid length = 14 x 0.162 = 2.27 in.

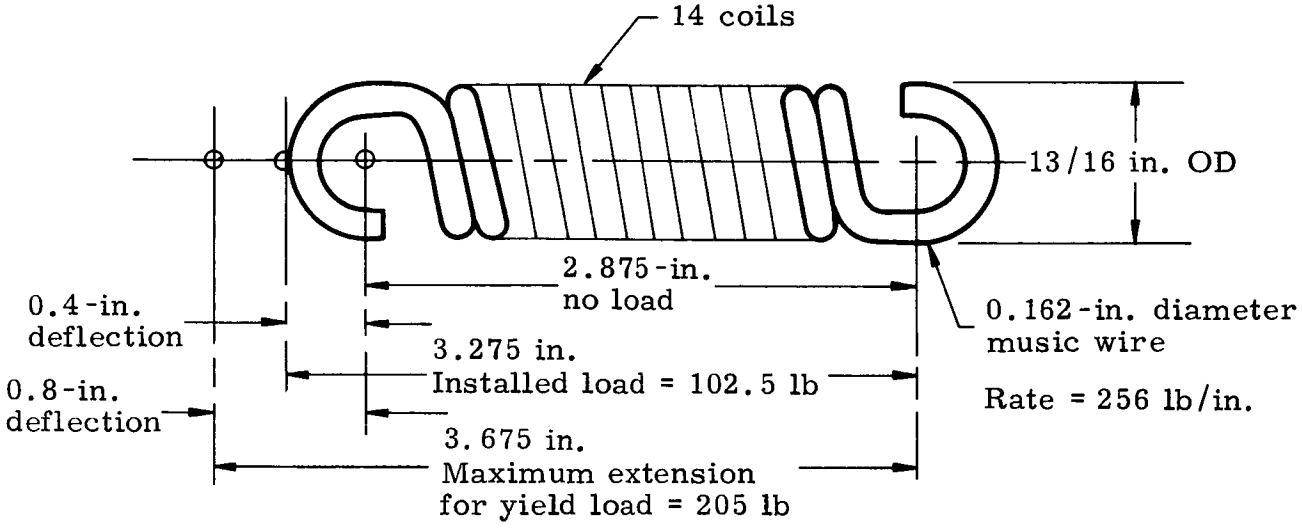

Frame design. Design frame for no yielding at spring load = 1.10 x 205 lb = 226 lb and for no failure at 1.35 x 205 = 277 lb for diagonal opposite spring loads.

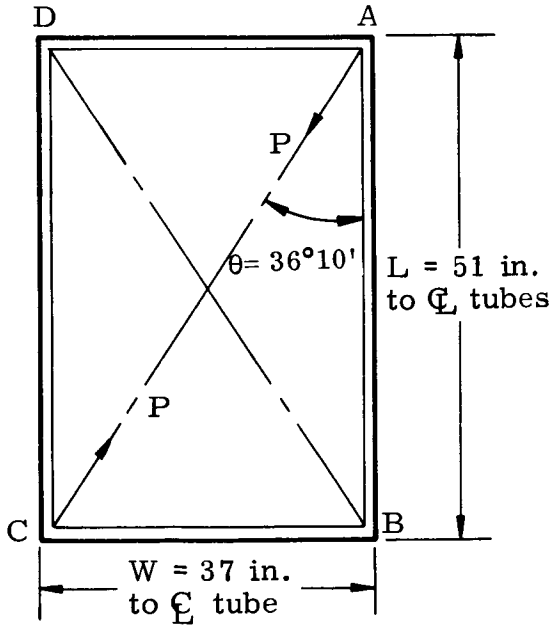

P = 226 lb yield

= 277 lb ultimate

Moment at corners

$$M = \frac{P \times L \times W}{4\sqrt{L^2 + W^2}}$$

$$M = \frac{P \times 51 \times 37}{4 \times \sqrt{51^2 + 37^2}} = 7.45\ P$$

$\therefore$ M = 7.45 x 226 = 1685 lb yield

or 7.45 x 277 = 2065 lb ultimate

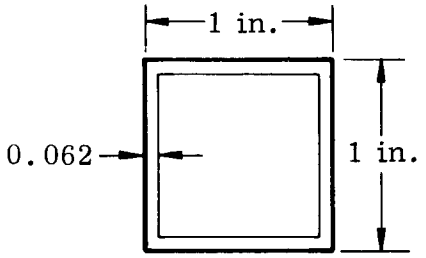

Axial load in AB = P x cos θ =
P x 0.807 = 183 lb yield and
224 lb ultimate

Try 6061-T6 extruded tubing

F_{tU} = 38,000 F_{BRY} = 56,000 psi

F_{ty} = 35,000 F_{beu} = 80,000

F_{cy} = 35,000

F_{su} = 24,000

$A = 0.220 \text{ in.}^2$

$I = 0.031 \text{ in.}^4$

$\rho = 0.376$ in.

In plane bending and axial load

Yield	Ultimate
P = 183 lb	P = 224 lb
M = 1685 lb-in.	M = 2065 lb-in.
$f_c = \frac{-183}{0.220} = -833 \text{ lb/in.}^2$	$f_c = \frac{-224}{0.220} = -1020 \text{ lb/in.}^2$
$f_b = \pm\frac{1685 \times 0.5}{0.031} = \pm 27{,}200 \text{ lb/in.}^2$	$f_b = \frac{\pm 2065 \times 0.5}{0.031} = \pm 33{,}400$
$f_c + f_b = -28{,}033 \text{ lb/in.}^2$	$f_c + f_b = -34{,}420 \text{ lb/in.}^2$
$MS = \frac{35{,}000}{28{,}033} - 1 = \underline{+0.25}$	$b/t = \frac{1}{0.062} = 16.2$ both edges fixed
	$F_{cr} = 35{,}000 \text{ lb/in.}^2 \ (=F_{cy})$
	$MS = \frac{35{,}000}{34{,}420} - 1 = \underline{+0.018}$

Check for beam-column effect

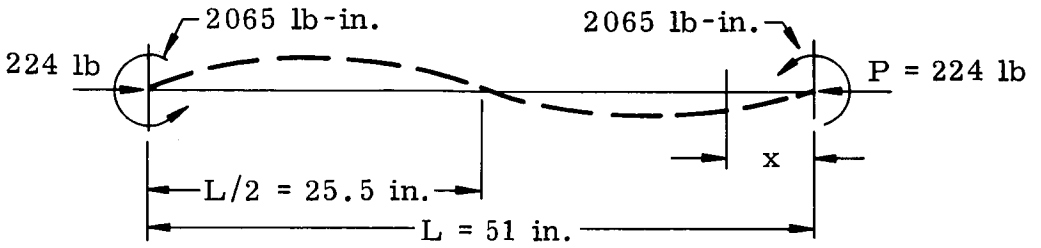

Maximum moment at $x = j \arctan \left[- \frac{M \cos U}{M \sin U} \right]$

$x = j \arctan (-\cot U)$

$$j = \sqrt{\frac{EI}{P}} = \sqrt{\frac{10.5 \times 10^6 \times 0.031}{224}} = 38.0$$

$$U = L'/j = \frac{25.5}{38.0} = 0.671 \qquad \cot U = 1.262$$

$x = 38.0 \arctan (-1.262) = 38.0 \times 2.24 = 85$

Since x is >L' = L/2 = 25.5 in. (max; moment is at x = 0 and = 2065 lb-in.)

Column check (out-of-plane bowing)

$P = 224$ lb

$$L/\rho = \frac{51}{0.376} = 135.8$$

$F_{col} = 5800$ lb/sq in.

$$\frac{P}{A} = \frac{224}{0.220} = -1020 \text{ lb/sq in.}$$

Check of frame tube

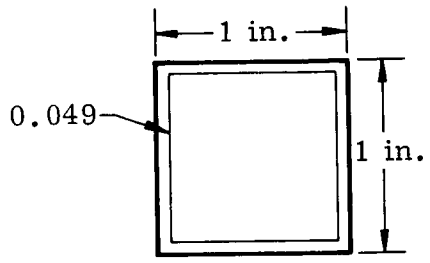

2014-T6 aluminum alloy extruded tubing

Ftu = 60,000 psi
Fty = 53,000 psi
Fcy = 55,000 psi
Fsu = 35,000 psi

$A = 0.176 \text{ in.}^2$

$I = 0.0256 \text{ in.}^4$

$\rho = 0.3813 \text{ in.}$

Since,

$$\left.\begin{array}{l} P = -224 \text{ lb} \\ M = 2065 \text{ in.} \end{array}\right\} \text{ ultimate}$$

$$f_c = \frac{-224}{0.176} = -1270 \text{ lb/sq in.}$$

$$f_b = \frac{2065 \times 0.5}{0.0256} = \frac{\pm 40,400}{-41,670 \text{ lb/sq in.}} \\ +39,130 \text{ lb/sq in.}$$

$$b/t = \frac{1}{0.049} = 20.4 \qquad F_{cr} = 55,000 \text{ lb/sq in. (for both edges fixed)}$$

$$MS = \frac{55,000}{41,670} - 1 = \underline{+0.32}$$

Frame design

Corner connection

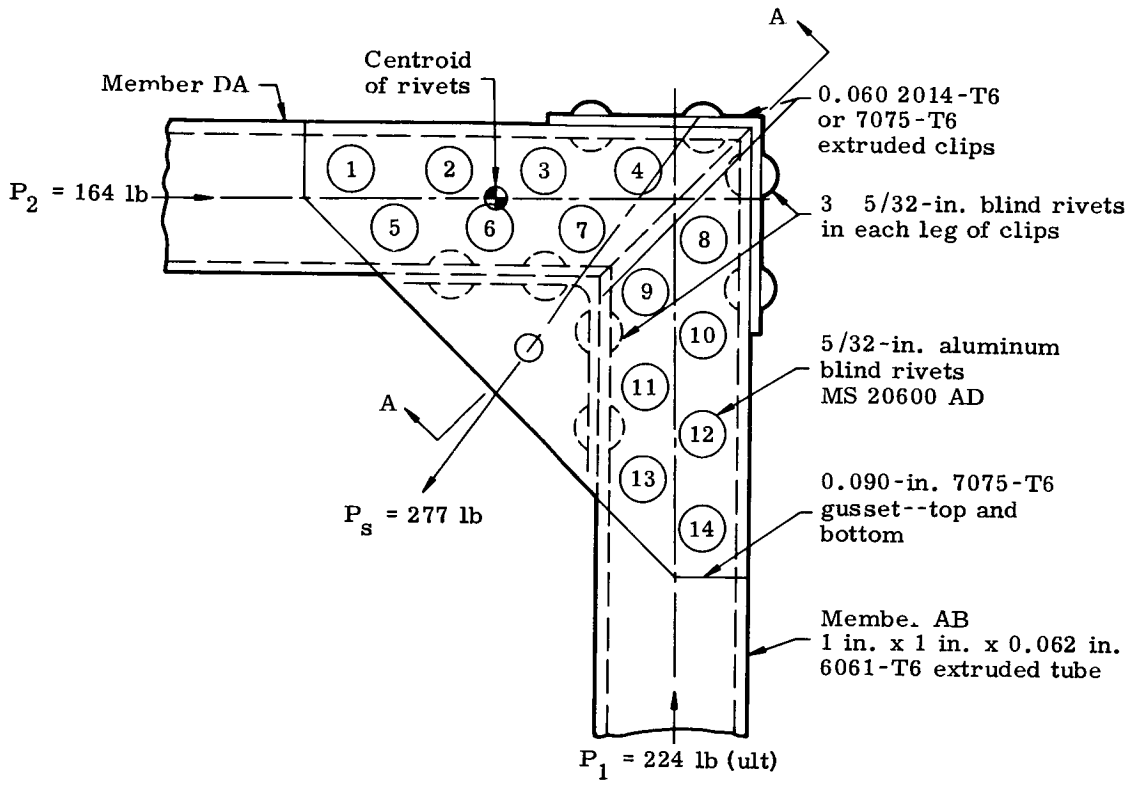

Corner moment = 2065 lb-in.

Rivet	Distance from Centroid = d	d^2
1	0.98	0.96
2	0.37	0.137
3	0.37	0.137
4	0.98	0.96
5	0.70	0.49
6	0.20	0.04
7	0.61	0.37
		3.094

Load on rivet No. 1 = $\frac{224}{2 \times 7}$ +

$\frac{2065 \times 0.98}{3.094 \times 2}$ = 16 + 327 = 343 lb

Use 5/32 in. aluminum blind rivet
SS = 596 lb[bearing on 0.062 6061-T6 = 0.062 x 5/32 x 56,000 = 541 lb]

Gusset--Section A-A

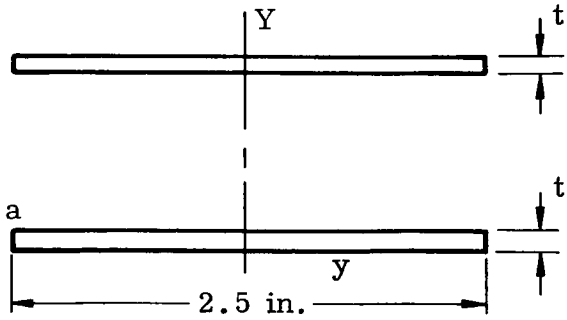

Try

$$t = 0.090 \qquad I_y = 2 \times \frac{0.090 \times \overline{2.5}^3}{12} = 0.234 \text{ in.}^4$$

At Point "a"

$$f = \frac{\pm 2065 \times 1.25}{0.234} = \pm 11,000 \text{ lb/in.}^2$$

Allowable column stress between rivets 5 and 13

$$\ell = 2.4$$

$$\rho = 0.289 \times 0.090 = 0.026 \text{ in.}$$

$$\frac{\ell}{\rho} = \frac{2.4}{0.026} = 92.5 \qquad F_{col} = 12,000 \text{ lb/sq in.}$$

Corner design

Stress in 0.002-in. target

Assume shaded areas "a" and "b" react the spring load by tension on the 0.002-in. target

$$\text{Maximum stress} = \frac{\text{Load/target}}{1.5 \times 0.002} = \frac{166/2}{1.5 \times 0.002} = 27,700 \text{ lb/sq in.}$$

$$F_{ty} = 35,000$$

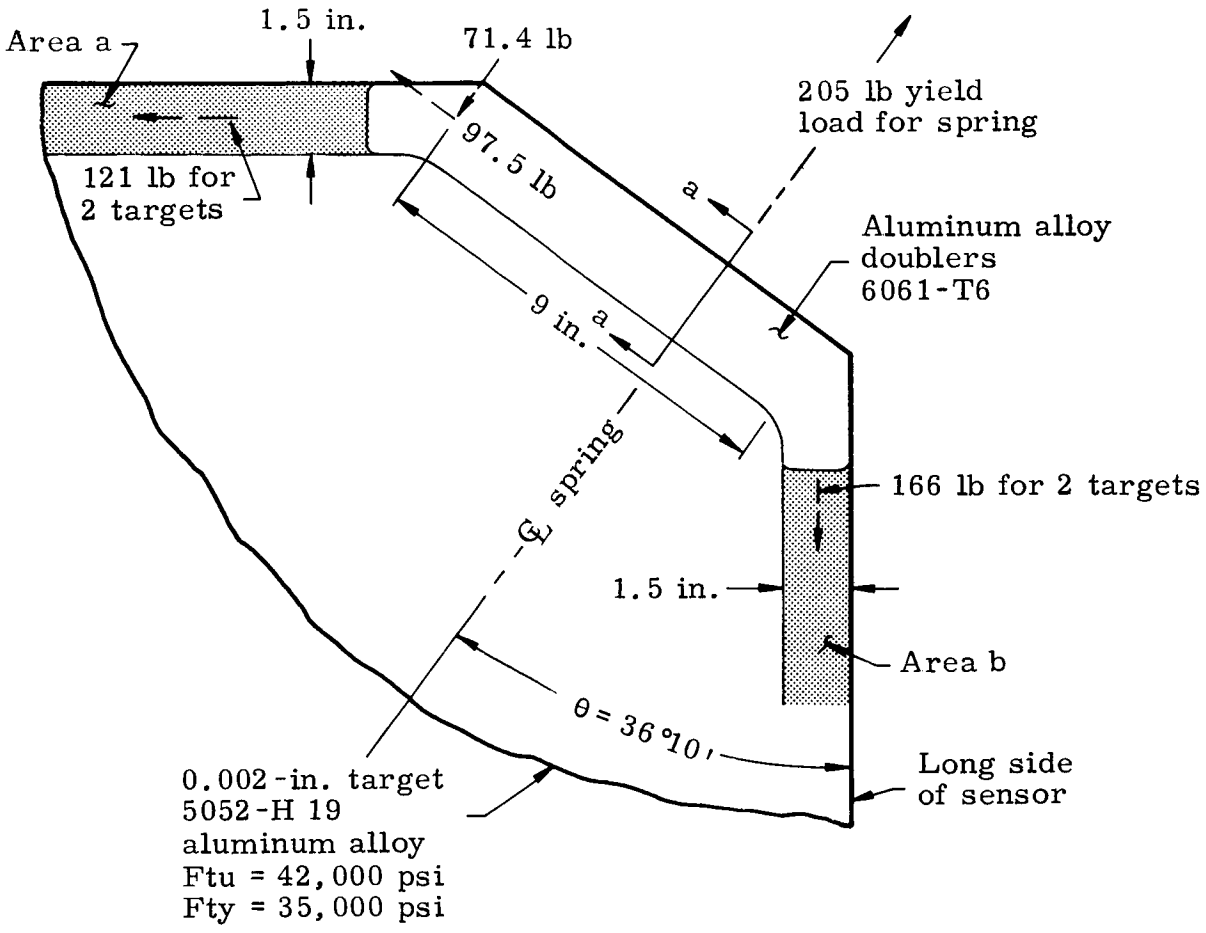

Section a-a on doubler

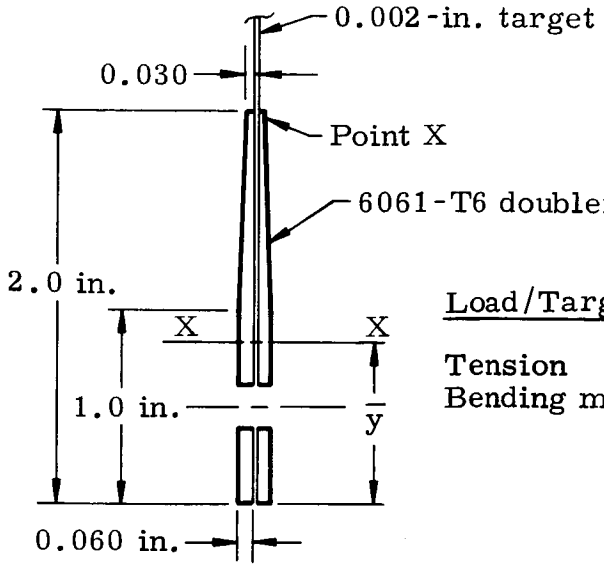

Load/Target

Tension = 97.5 lb/2 = 48.75
Bending mom = 71.4 x 6.4/2 = 228 lb-in.

Item	A	y	A_y	A_y^2	I_0
2 x 0.030	0.060	1.0	0.060	0.060	0.0203
1 x 0.030	0.030	0.5	0.015	0.0075	0.0025
	0.090		0.075	0.0675	0.0228

$$\bar{y} = \frac{0.075}{0.090} = 0.8333$$

Total A = 0.090 x 2 = 0.018 sq in.

Total $I_x = 2\,(0.0675 + 0.0228 - 0.090 \times \overline{0.833}^2)$

$= 2\,(0.0903 - 0.0624) = 0.0558$ in.^{4}

At Point x

$$f = + \frac{48.75}{0.018} - \frac{228 \times 1.167}{0.0558} = + 2700 - 4780$$

f = - 2080 lb/sq in.

Average stress (at Point x) over 2-in. span = 1/2 x - 2080 lb/sq in. = - 1040 lb/sq in.

Assume $\rho = 0.289\,(0.030 + 0.030) = 0.01738$ in.

$\therefore L'/\rho = \frac{9}{0.01738} = 518$

Euler column formula $F_{col} = \pi^2\, E/(L/\rho)^2$

$\therefore F_{col} = \pi^2 \times 10.5 \times 10^6 \times \frac{1}{(518)^2} = 3960$ lb/sq in.

which exceeds average stress of - 1040 lb/sq in.

$\therefore$ Lateral buckling of doublers is not likely for the assumed conditions.

(d) Separation system

The spacecraft must be separated from the Agena launch vehicle after burnout. Enough separation velocity must be provided so that the spacecraft is not overtaken by the Agena stage.

The design separation velocity was taken as 4.0 fps. The actual separation forces are provided by four springs located between the spacecraft and the adapter. The following analysis was made to determine the size of the separation springs.

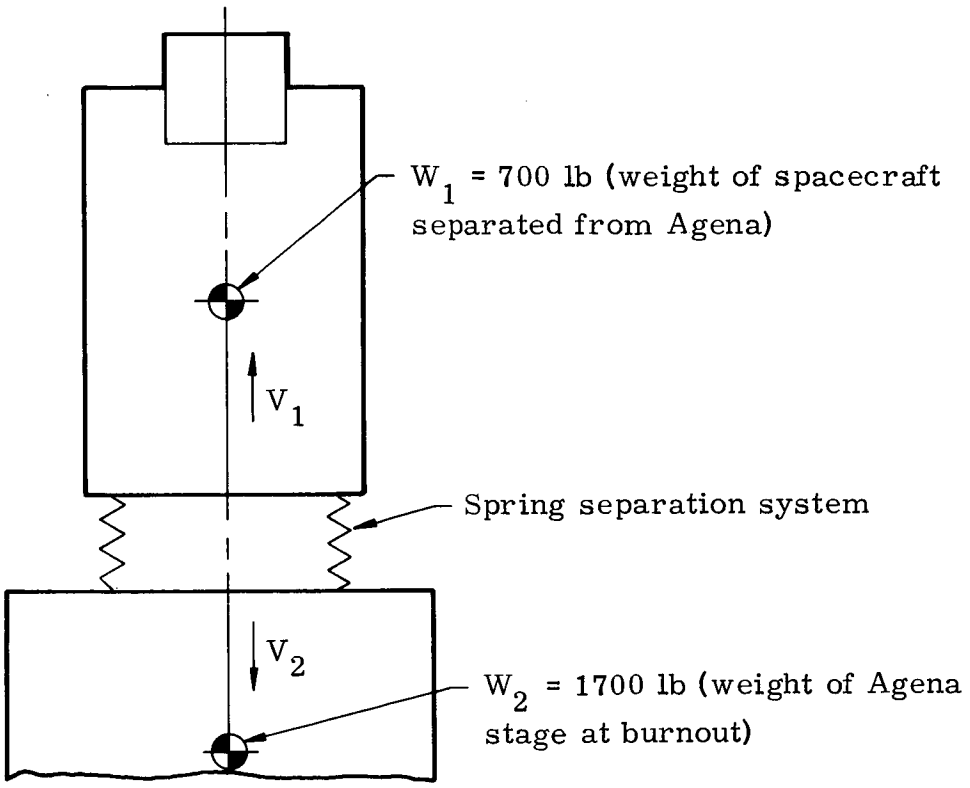

Let E = energy obtained from springs during separation (ft-lb)

M_1 = mass of spacecraft (slugs)

M_2 = mass of Agena (slugs)

V_1 = velocity of spacecraft (fps)

V_2 = velocity of Agena (fps)

$$M_1 = \frac{W_1}{g} = \frac{700}{32.2} = 21.85 \qquad M_2 = \frac{W_2}{g} = \frac{1700}{32.2} = 52.8$$

Energy balance

$$E = \frac{1}{2} M_1 V_1^2 + \frac{1}{2} M_2 V_2^2$$

Assuming that $M_1 V_1 = M_2 V_2$

$$V_2 = \frac{M_1}{M_2} V_1 = \frac{21.85}{52.8} V_1 = 0.412 V_1$$

since

$$V_1 + V_2 = 4$$

$$V_1 + 0.412\ V_1 = 4$$

or

$$V_1 = 2.83 \text{ fps}$$

and

$$V_2 = 1.17 \text{ fps}$$

Thus

$$E = \frac{1}{2} \times 21.85 \times (2.83)^2 + \frac{1}{2} \times 52.8 \times (1.17)^2$$

$$E = 87.5 + 36.2$$

$$\therefore E = 123.7 \text{ ft-lb}$$

Each of the four springs must provide 1/4 of this energy or 1/4 x 123.7 = 31.0 ft-lb.

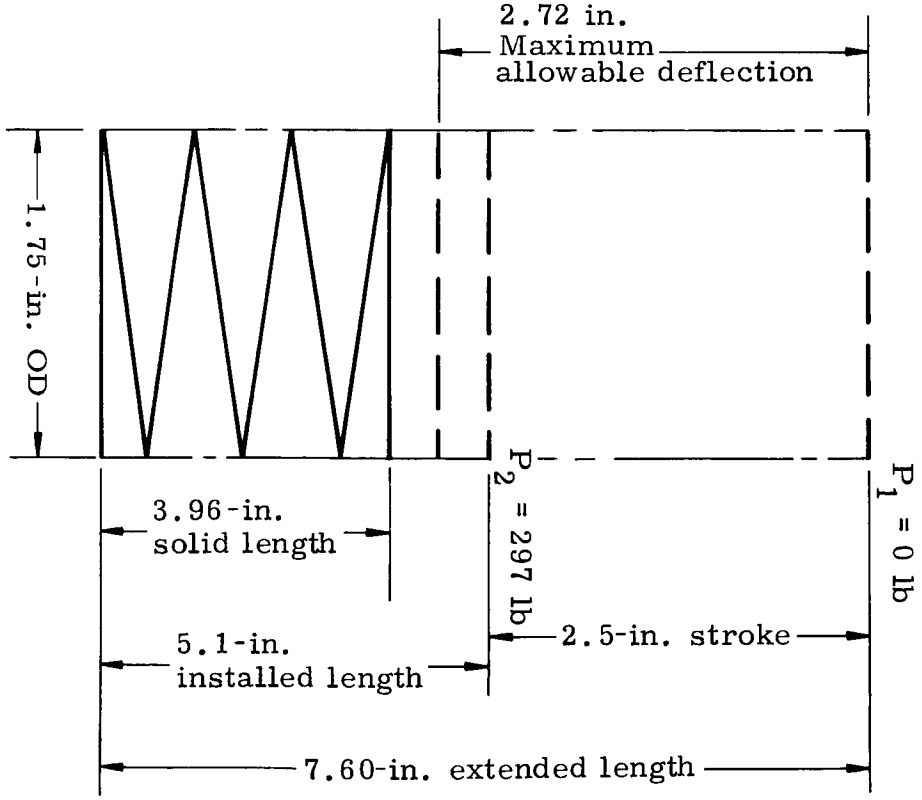

To keep the spring size to a minimum, the separating travel was limited to 2.5 in. and the spring outside diameter to 1.75 in.

Wire diameter = 0.250 in.
Material: music wire
Allowance T_{sy} = 99,000 psi

OD = 1.75 in.

Allowable load = $328 \times \frac{99,000}{100,000}$ = 324 lb

Rate/coil = 1667 lb/in.

Required energy in 2.5-in. stroke = 31 ft-lb

$$\cdot \frac{1}{2}(P_2 - P_1) \times 2.5 = 31 \times 12$$

$$\frac{1}{2}(P_2 - 0) \times 2.5 = 372$$

or P_2 = 297 lb. (This is required load at 2.5-in. deflection.)

Required rate = $\frac{P_2 - P_1}{2.5} = \frac{297 - 0}{2.5}$ =

119 lb/in.

Required number of active coils = $\frac{1667}{119} = 14$

Extended length = 7.6 in.

Installed length = 7.6 - 2.5 = 5.1 in.

Total coils = 14 + 2 = 16

Solid length = $(16 - \frac{1}{2})(0.250 + 0.005) = 3.96$ in.

Allowable deflection = $\frac{324}{119} = 2.72$ in.

This preliminary effort provided information for feasibility layout of the separation system. Much additional work would be done to determine the trajectory and motion characteristics of the spacecraft and launch vehicle at separation.

C. REFERENCES

III-1. NASA Statement of Work, "Conceptual Study of a Micrometeoroid Deep Space Satellite," 25 June 1959.

III-2. "General Environmental Specification for Equipment of the Agena and Associated Payload," Lockheed Report LMSC 6117D, 13 November 1962.

III-3. "Solar Probe Study, Volume V, Vehicle Design," Martin Report ER 13110-V, August 1963.

III-4. Osgood, W. M., "A Theory of Flexure for Beams with Non-parellel Extreme Fibers," Journal of Applied Mechanics, September 1939, p A-122.

APPENDIX III-1

MEANS OF PACKAGING AND DEPLOYING STATE-OF-THE-ART CAPACITANCE-TYPE MICROMETEOROID DETECTORS

Final Report

Martin Marietta P. O. No. 459056

Prepared For

SPACE VEHICLES DIVISION
MARTIN MARIETTA CORPORATION
BALTIMORE, MARYLAND

by the

G. T. SCHJELDAHL COMPANY
Northfield, Minnesota

November 9, 1964

PREPARED BY:

S. J. Stenlund, Project Engineer

Don Roiseland, Project Engineer

APPROVED BY:

F. H. Bratton, Vice President and Director of Research

E. A. Basquin, Reports Editor

ABSTRACT

This study of micrometeoroid detectors was centered on present state-of-the-art concepts which would permit measurements of infrequent penetrations of large particles. A device to perform this function requires large areas of thick detectors because of the low frequency of expected hits. This requires that detector panels be mounted on either side of bulky impenetrable spacers to avoid duplication of register. This requirement led to a study of compressible spacers suitable for efficient storage prior to deployment. Sensor deployment methods were studied which were reliable, lightweight and occupy little space.

I. INTRODUCTION

The G. T. Schjeldahl Company has been asked to describe methods for storing and deploying state-of-the-art, capacitance-gage micrometeoroid detectors allowing maximum sensor area with minimum weight associated with storage and deployment structures. Three concepts for achieving this end are presented. First, sensors can be stored by simply stacking one on top of the other. Second, the volume of a stack can be reduced by replacing a unit's conventional hard core with a compressible one with the stack held under compression. Third, sensors can be interconnected via flexible ribbons and deployed in a plane by De Havilland booms or space inflatables which hold the ribbons in weak tension.

II. SUMMARY

Martin-Marietta Corporation has asked the Schjeldahl Company for recommendations of methods of deploying capacitance gage micrometeoroid detectors in connection with a "Conceptual Study for a Micrometeoroid Deep Space Satellite" being performed by Martin. Schjeldahl was asked because it is manufacturing thick plate capacitance gage detectors, has manufactured flexible metalized plastic film detectors, and because of its experience with space inflatables which might be used in deploying such capacitors.

Two facts have been of overriding significance in the work which follows. First, a workable capacitance gage sensor is desired; the thick plate sensors being made are thought to be workable. Second, the main objective of a deep space probe is to insure that the micrometeoroid hazard to manned spacecraft going between the earth and the moon has been correctly allowed for. The direct and presumably most effective way of evaluating the hazard is to deploy structural materials which simulate spaceship coverage as closely as possible, say 40-50 mils of aluminum alloy, and note puncturing of this material. Hence, to reduce extrapolation it is desirable to deploy as thick a capacitance gage as possible (6-8 mils); noting only if the plate has been punctured. It appears that flexible

paraglider material is not of as much interest as thick plate capacitance gage detectors. The suggestions which follow are limited to the fabrication, storage, and deployment of such thick plate detectors.

In the initial portions of this work it was thought that detectors of a more novel nature would be of interest. Ideas along these lines were discarded for work on the more conventional type. In Appendix II are cataloged some of the concepts which were briefly considered.

The first two columns of Figure 1, supplied by Martin, give for a target plate thickness t the target area A which must be deployed for a successful experiment. To realize the largest target thickness t one must exploit every feasible means for reducing the weight and volume of both sensor units and storage-deployment apparatus.

The conventional method of storing and deploying thick plate detectors mounts each unit independently in a frame. Each unit then serves as one "window" of a multi-windowed frame. The frames are stacked one beside the other and during deployment are positioned edge to edge by suitable rigging to form a

plane. The concept for storing capacitors presented here dispenses with the frames, sensor units being stacked directly one on top of the other. Compressive forces applied to the stack give it mechanical rigidity. Such pressure could electrically short out a capacitor, damage a unit's thermal balance layer, or crush its core. Tests to pressures of 300 lb/in^2 have not compromised a capacitor's electrical integrity. Compressive forces strong enough to keep a sensor from sliding against its neighbor will be relied upon to prevent damage to the thermal balance layer. Scratches occurring during stack assembly are thought to be of cosmetic importance only. The question of damage to the foam core is dealt with below.

It is desirable to reduce the volume of a stack of sensor units like that considered above. The method for doing this considered here replaces semi-rigid foam cores with elastic compressible ones. The core no longer serves as a structural member. It is assumed that the ability of such a core to prevent debris from a micrometeoroid puncturing one capacitor from from impinging on the opposite capacitor must equal that of a

conventional core. It is also assumed here that any finely divided core material one inch thick having a density of 4 lb/ft^3 is equivalent in stopping power to a conventional core.

The question still remains whether a compressible core can be found which retains its springiness under sustained compression and temperature. Loss of springiness tends to destroy the rigidity of a stack as well as cause deployment problems. The most promising core worked with to date consists of a stack of 185 sheets of crinkled 1/4-mil Mylar. The Mylar is aluminized on both sides to minimize charge build-up in the core due to Van Allen radiation. A stack of sensor units having such a core can be reduced to about 1/5 its uncompressed volume by a pressure of 1 lb/in^2.

Having minimized storage structures and introduced a compressible core, the problem of deploying a stack of such units remains. One method considered involves positioning the units on a plane like squares on a quilt. Adjacent sensors are connected together at their corners via flexible ribbons. The "quilt" is folded up and put under compression. Two means for deploying the stack are considered. The first uses De Havilland type booms, the second a space inflatable. The particular inflatable considered is a torus which, when deployed, surrounds the sensor blanket and pulls on it keeping the ribbon interconnections under weak

tension. The torus would be made of strain rigidizing material so that upon inflatant loss it would continue to act as a weak structural member.

The suggestions given above will allow one to dispense with a large fraction of the weight and volume associated with conventional storage and deployment apparatus. The use of a compressible core allows one to realize the weight lifting capabilities of present-day boosters.

the stack are thought to be of cosmetic importance only.

Having "solved" the mechanical problem by relying on compressive forces large enough to do the job, the problem remains of whether such forces will destroy the integrity of the capacitor. Tests show that a capacitor can stand large compressive forces without injury. The tests were performed on a modified capacitor having a compressible core. The reason for requiring a compressible core is that such a configuration allows several times as many sensors to be stored per unit volume than is possible with the sensor units of Section A.

Experience with 6- by 9-inch single layer Mylar dielectric capacitors constructed for NASA Langley indicated that pressure applied to the copper surface could short out the capacitor. To test whether pressure exerted on a trilaminate capacitor having a compressible core shorted the capacitor out, the following procedure was employed. Approximately forty 2- by 3-inch sheets of 1/4-mil Mylar were individually crumpled, spread out, and assembled into a pile. A trilaminate capacitor with no adhesive covering the copper was cleared at 250 volts. The capacitor was inserted into a hydraulic press the stack of crumpled Mylar being placed between the copper and one face of the press. A pressure

of 3800 lb/sq in was held for 30 seconds, the pressure released, and low voltage applied across the capacitor. No current flow was detected. The voltage was raised to 250 volts. No shorts, i.e., capacitor discharges, were observed. The procedure was repeated again except for holding the applied pressure of 3800 lb/sq in for 10 minutes. The same results were obtained. An ohmmeter placed across the capacitor while the dielectric was under pressure gave no indication of a short. A second trilaminate capacitor, this one having its copper face covered by the adhesive used to protect the copper from attack during application of the thermal balance layer, was subjected to a 30-second pressure test with no subsequent shorting.

It appears feasible to construct a capacitor pair having a compressible core and subject this unit to very high compressive forces without destroying the electrical integrity of the capacitor. This assumes that high voltage is not applied to the capacitor while the pressure is being applied. That shorting would arise in such a procedure is doubtful on the basis of the following test. A trilaminate capacitor having no adhesive over the copper was subjected to 250 volts. In this state it proved possible to scratch the copper surface lightly with a razor blade without causing the capacitor to

discharge. (Removing the voltage from the capacitor, pushing a corner of a razor blade through the dielectric, removing the razor blade, and applying low voltage across the capacitor did not always yield an indication of a shorted capacitor. This means that the switch concept mentioned in a previous report may not be directly workable.)

In using a compressible core, it is thought that edge bands of some flexible material would be used to hold the capacitor plates from separating from each other by more than an inch. The model of Figure 2 has edge bands of 2-mil Mylar aluminized on their outside surface. Thermal balance is not a problem since even though the A/E of the aluminizing is very high, the effective A/E is approximately the A of the aluminizing divided by the E of the inside surface, here Mylar. Infrared energy radiated to the core from the edge band is transferred to the capacitor panels and radiated to space via the sensors thermal balance coating. The expansive characteristics of the core are selected so that large area capacitors, separated by an inch at their edges, do not bow further apart than this at their centers. Another requirement on the core is that it exhibit a stopping power for micrometeoroid debris equivalent to or greater than that of the conventional foam core met in Section A. In what follows

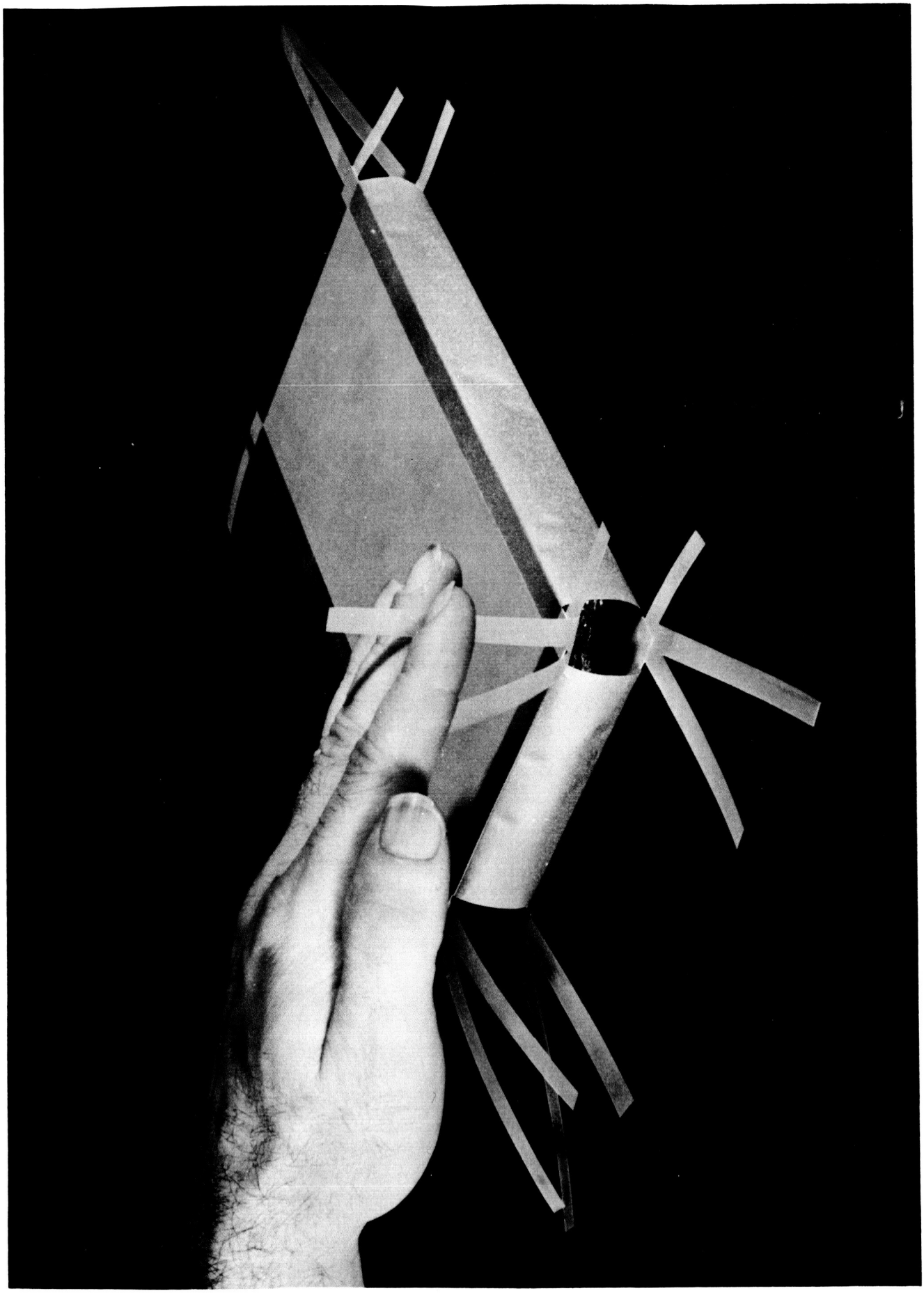

FIGURE 2 COMPRESSIBLE CORE SENSOR
ER 13700-III

it is assumed that any finely divided core one inch thick having a density of 4 lb/cu in is equivalent in stopping power to the conventional core. Figure 3 shows the volume saving possible with a compressible core.

Two types of compressible cores were worked with; Scott polyurethane open cell foam having 100 cells per inch and a density of about 2 lb/cu ft, and a stack of crinkled Mylar sheets. Figure 4 indicates the foam compresses to 1/4 its initial height at a pressure of about 1.0 lb/sq in. Figure 5 shows the rather slow rate of expansion of the foam after release of 1.0 lb/sq in pressure applied for 25 hours at room temperature. Note that the core continued to contract during this 25-hour period. A foam core, pressed to 1/4 its volume, and held at 167 F for four hours fails to expand appreciably when the pressure is removed. Foam can only be useful, therefore, if it is kept near room temperature in its compressed state. A foam core having a density of 4.0 lb/cu ft would be expected to compress to 1/2 its thickness at 1.0 lb/sq in, thereby allowing only two sensor units to be stored in the volume occupied by one conventional unit.

A crumpled Mylar core can yield a packing factor of about five at an applied pressure of 1.0 lb/sq in as compared with two for the foam. It exhibits the same type of relaxation

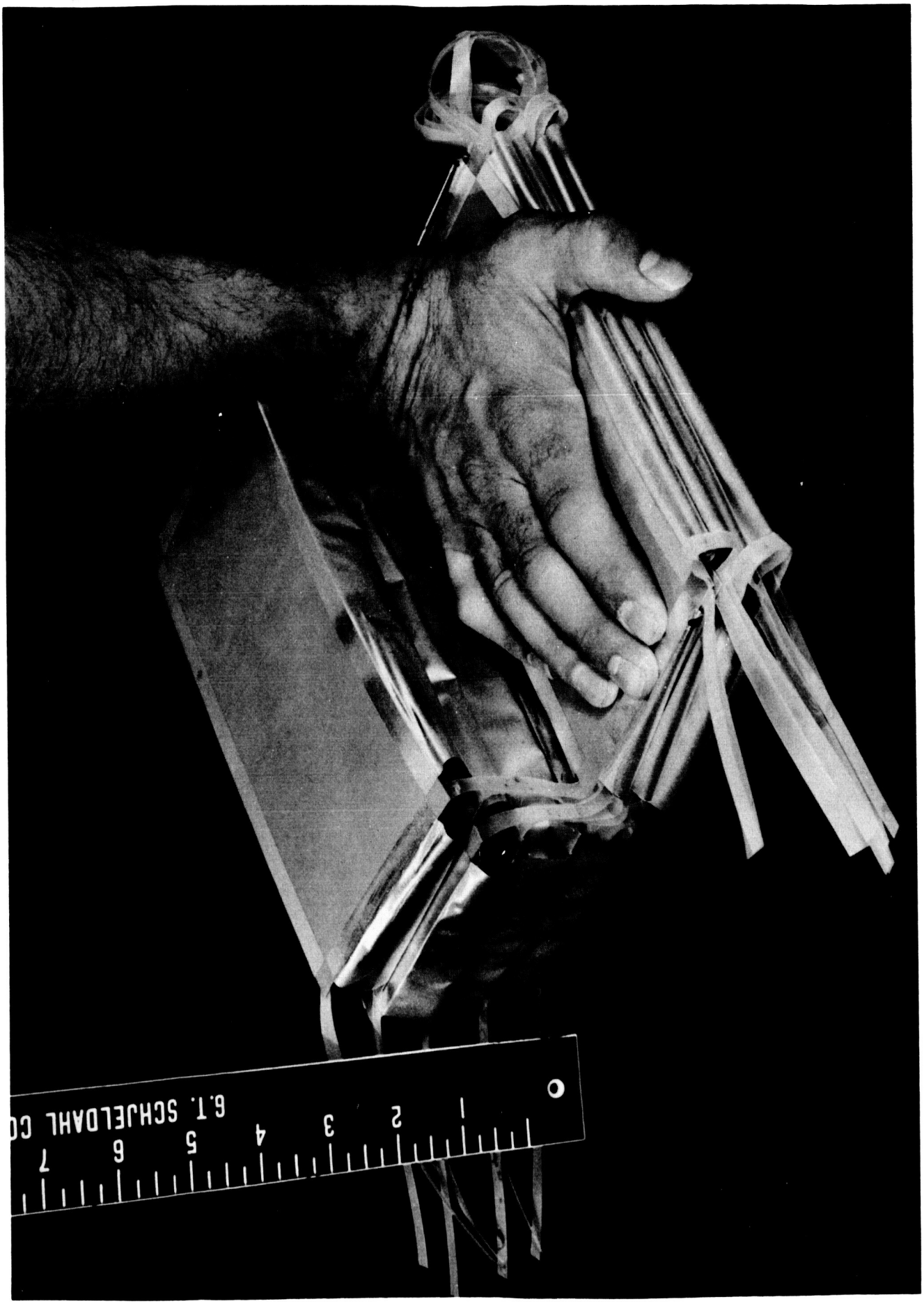

FIGURE 3 EIGHT UNIT SENSOR STACK
ER 13700-III

Fig. 4

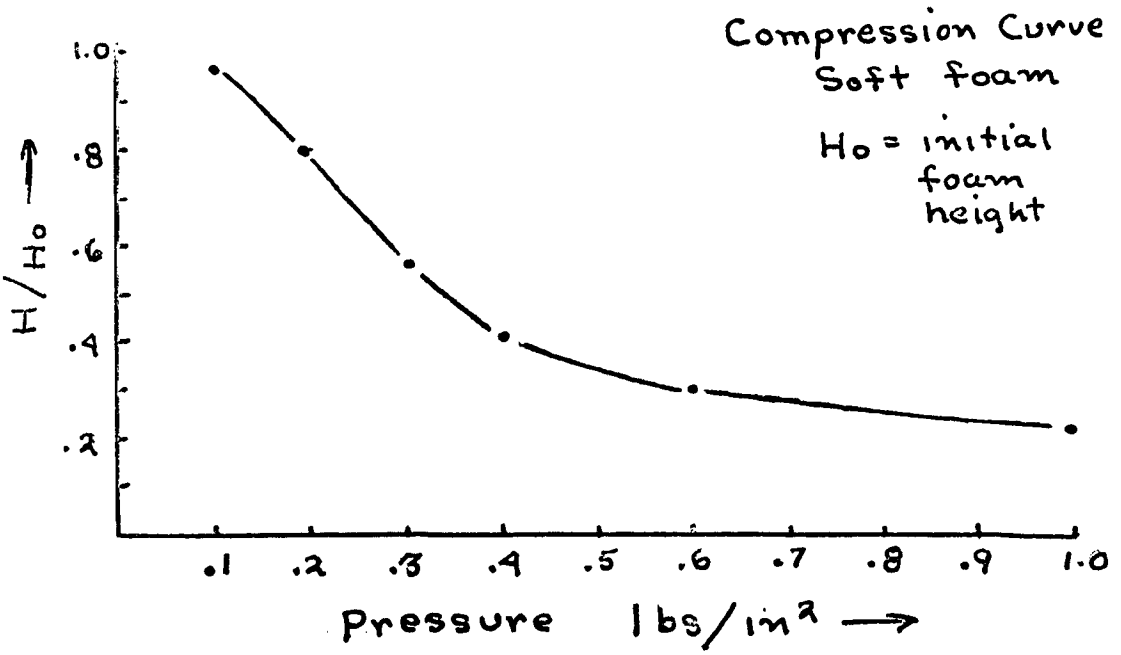
Compression Curve
Soft foam
Ho = initial foam height
1.0
.8
.6
.4
.2
H/Ho
.1
.2
.3
.4
.5
.6
.7
.8
.9
1.0
Pressure lbs/in²

Fig. 5

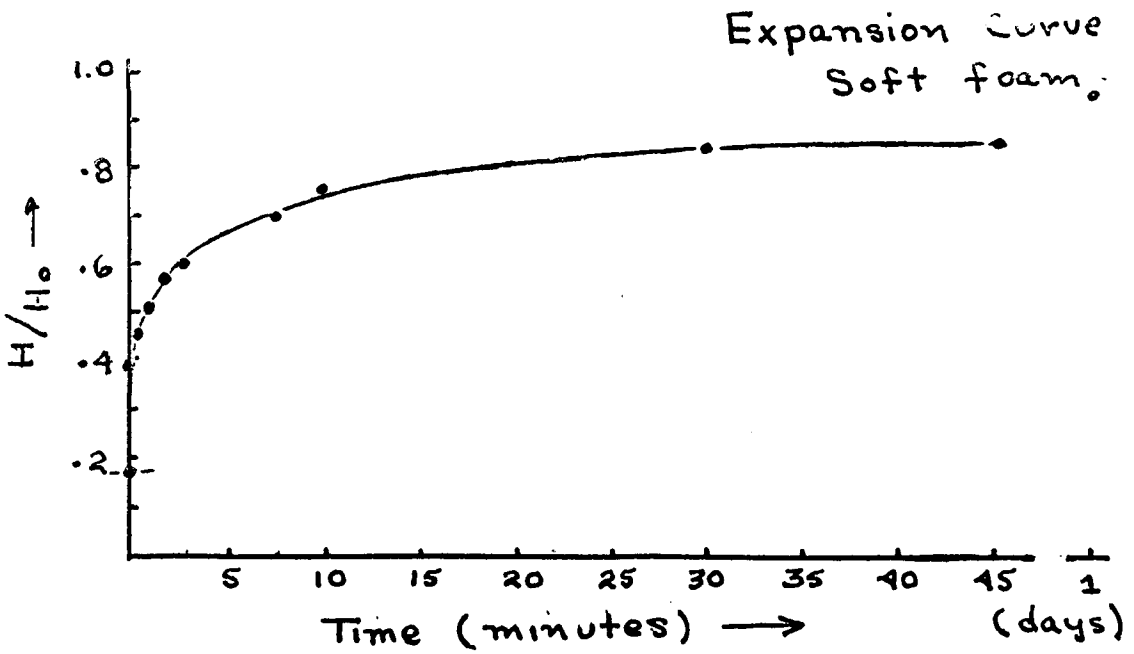
Expansion Curve
Soft foam.
1.0
.8
.6
.4
.2
H/Ho
5
10
15
20
25
30
35
40
45
1
Time (minutes)
(days)

as the foam but to a lesser degree. One hundred and eight-five 1/4-mil Mylar sheets are individually crumpled, unfolded, and then assembled into a stack. (When the stack is compressed to a height of one inch, the material's average density is 4 lb/cu ft.) Figure 6, curve A gives the height of such a stack versus pressure. Curve B is for the same stack after having been subjected to 200 lb/sq in, 400 lb/sq in, and 600 lb/sq in for 30 seconds each. Curves C and D, corresponding to A and B respectively are for a 46-sheet stack made of 1-mil crinkled Mylar. Curves B and D show that 1.0 lb/sq in yields a stack about 3/16-in high, therefore about five compressible core units can be put in the same volume as one conventional unit.

Relaxation takes place in a compressed Mylar stack. Subjecting the stack associated with curve B of Figure 1 to 800 lb/sq in for 13 minutes gave a stack which could be compressed to 3/16-in with 0.6 lb/sq in. Holding the stack at 3/32-inch thickness for 148 hours allowed the stack to be compressed to 3/16-in thickness with only 0.2 lb/sq in. The stack yielding curve D of Figure 6 requires about 1.0 lb/sq in to compress it to 3/16-inch thickness. Holding this stack at 3/16-inch and subjecting it to 130 F for 48 hours yields a stack requiring only 0.2 lb/sq in to compress it to 3/16-inch.

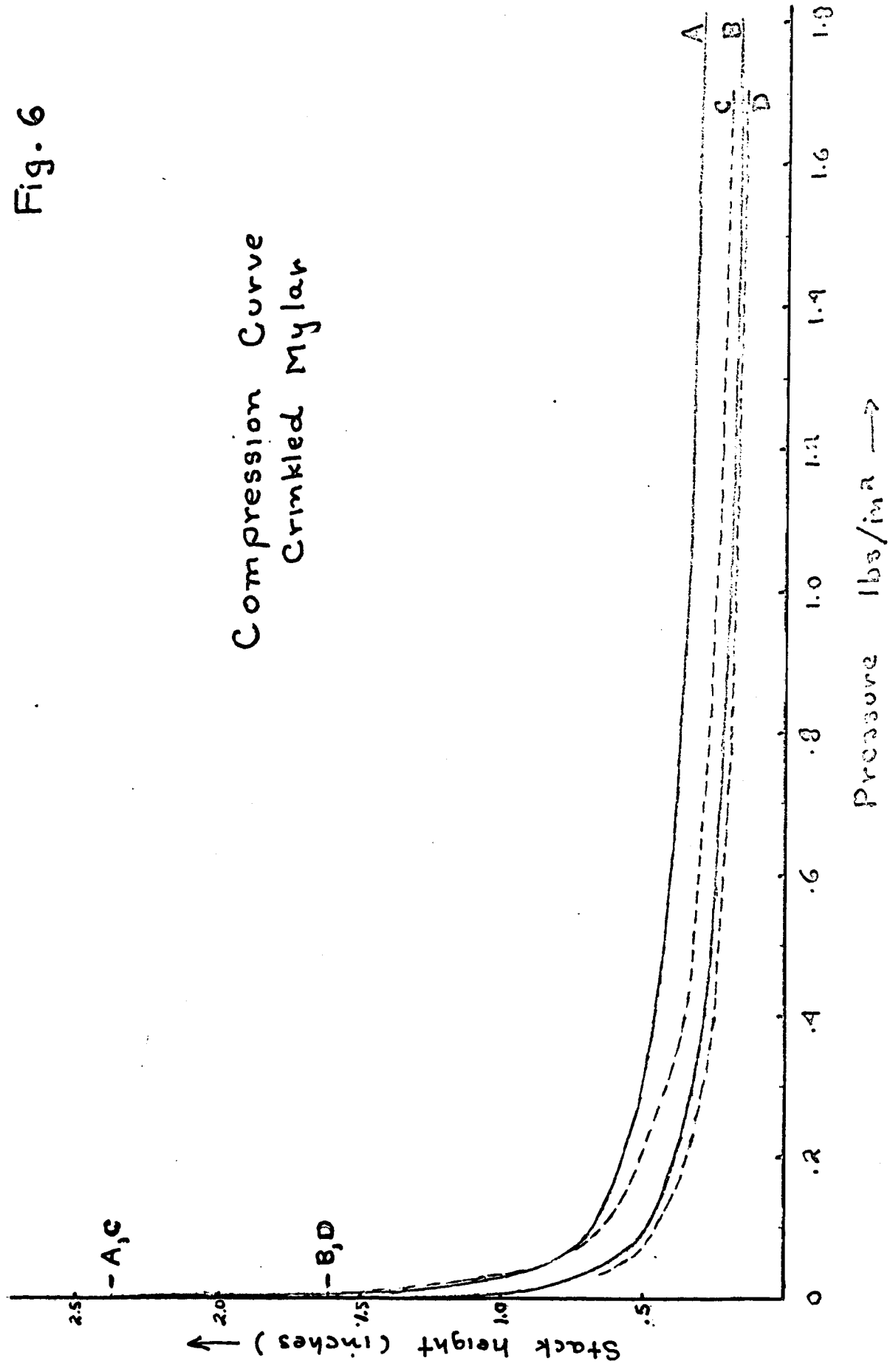

FIGURE 6 CRINKLED MYLAR CORE DATA ER 13700-III

An advantage of a Mylar core is the possibility of using Mylar which has been aluminized on both sides. Aluminizing minimizes blocking at high pressure and high temperature. Grounding one sheet of such a core would probably eliminate any charge build up in the core. If it does not, the problem can be eliminated by forming the core out of a single sheet of aluminized Mylar and grounding it at some point. A Mylar core springs back relatively quickly to its equilibrium position upon pressure release.

B. Deployment

The method considered here for deploying the stack of sensors discussed in Section C involves connecting sensors together via ribbon hinges and deploying the stack with De Havilland booms or space inflatables. A possible connection arrangement is illustrated in Figure 7. Releasing compression on the stack and supplying two booms which slowly pull ribbon terminations A and A^1 in opposite directions, yields the configuration of Figure 8. Supplying a second set of booms to separate points B and B^1 yields the configuration of Figure 9. The booms, under weak compression, hold the various ribbons under weak tension.

Consider the connecting ribbons in Figure 9 which run between any four adjacent corners of four sensors. If one

Fig. 7

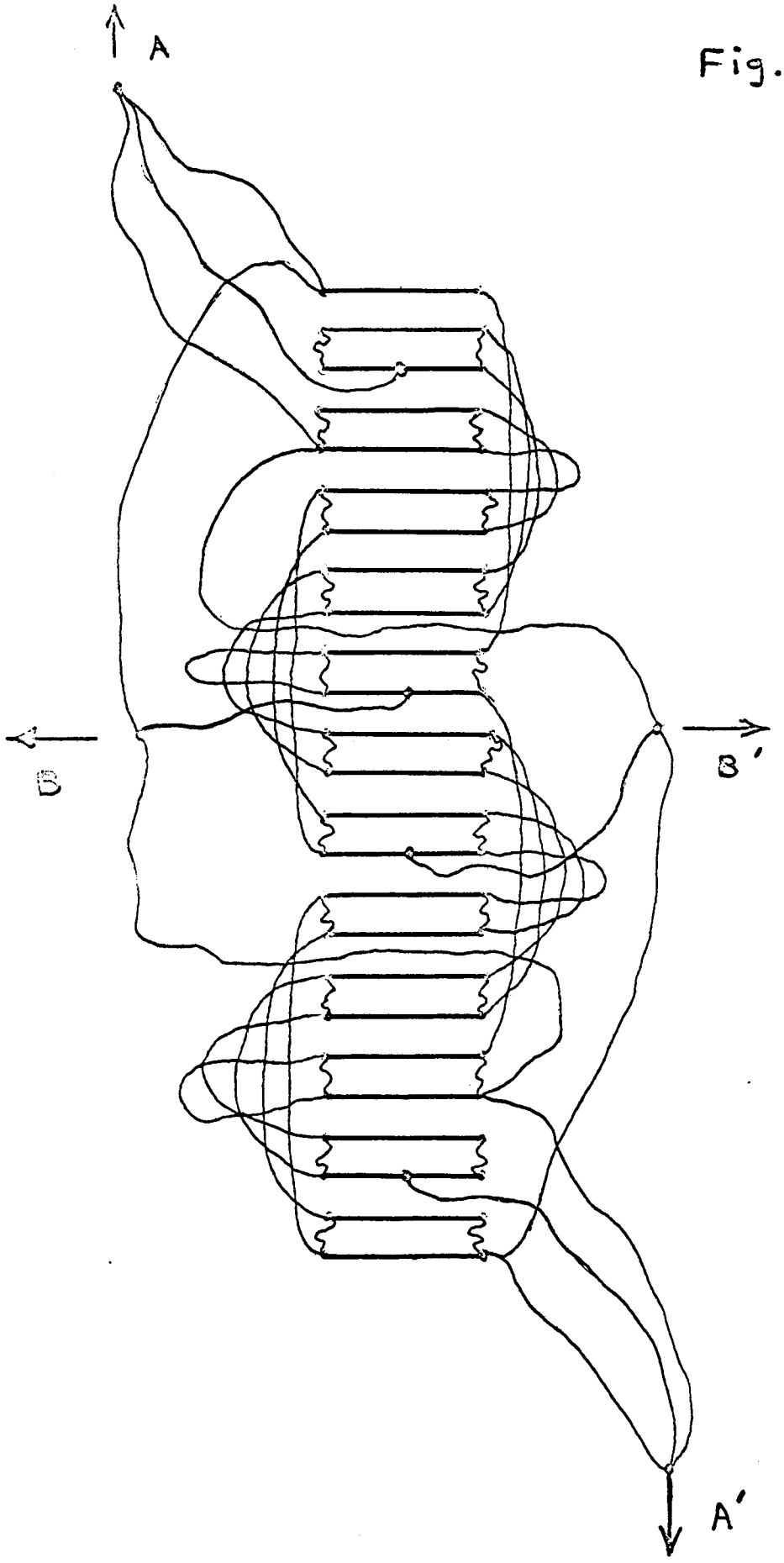

FIGURE 7 SENSOR STACK INTERCONNECTIONS
25 UNITS ER 13700-III

Fig. 8

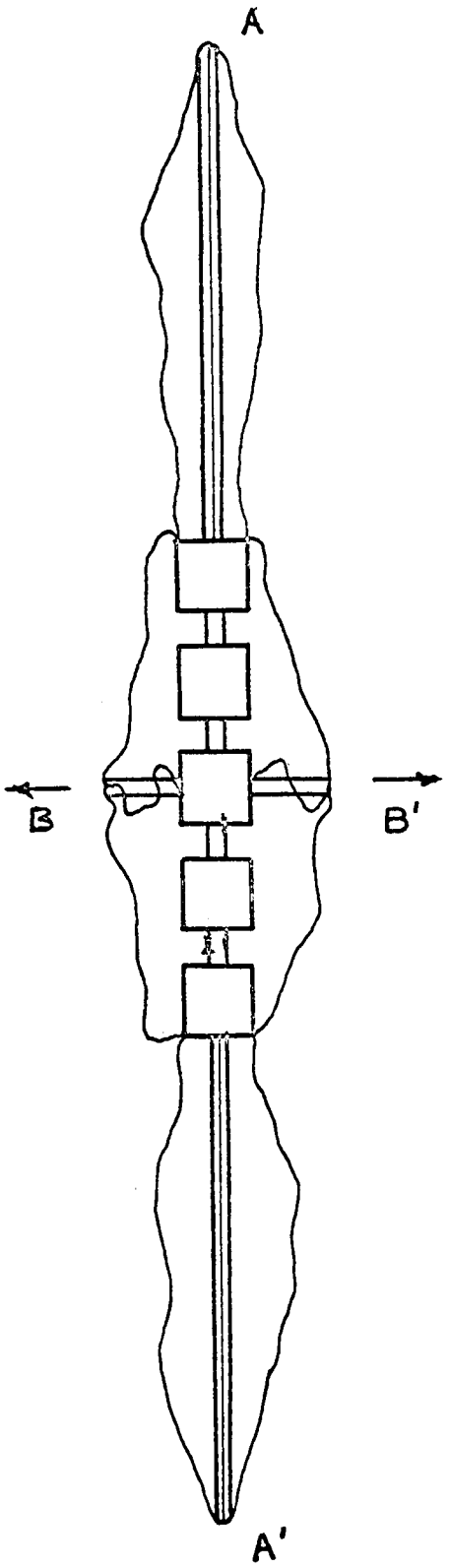

FIGURE 8 SENSOR STACK - PARTIALLY DEPLOYED

ER 13700-III

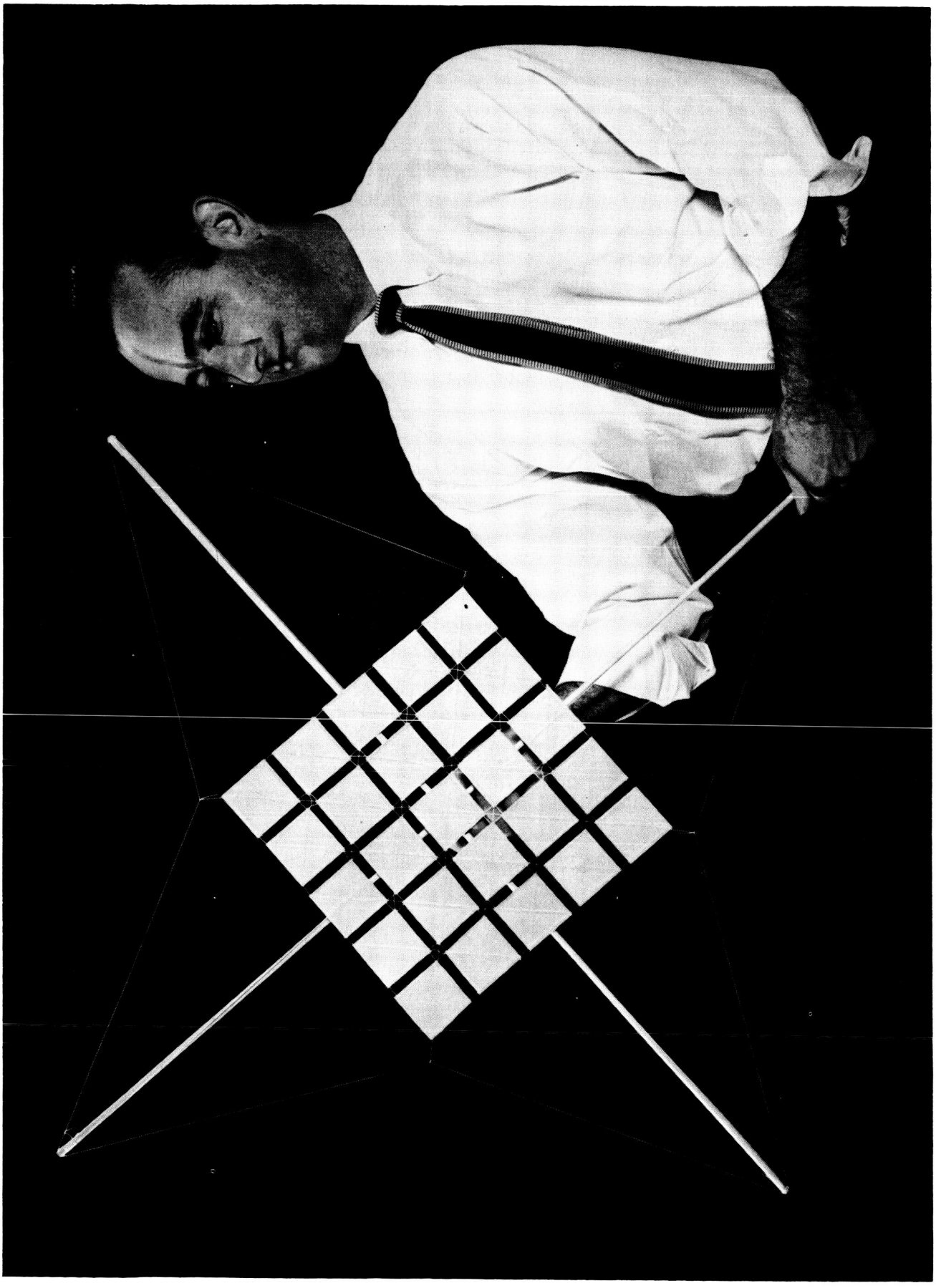

FIGURE 9 SENSOR STACK - FULLY DEPLOYED
ER 13700-III

choses to eliminate either the diagonal cords, or the cords lying on a square, in the latter case, cementing diagonal cords together at their point of crossover, the probability of clogging during deployment is greatly enhanced. This became evident after constructing model like that of Figure 9 except for having omitted cords lying along a square. The cord arrangement of Figure 9 did not lead to clogging in the several times this model was experimentally deployed.

Relying on ribbons under weak tension to position sensors rather than a rigid structural framework saves weight. The De Havilland booms can be deployed arbitrarily slowly so that Coriolis loading and "jerk" occurring at deployment termination will not clog or injure the system. Deploying sensors over either a circle or a square means that large sensor areas can be realized with minimum spatial extent.

Certain disadvantages exist. At deployment, compression will have to be taken off the stack slowly. Figure 7 reveals that a 25-unit set of one-inch thick sensors deployed as in Figure 9 requires at least a 10-inch separation between sensors. From a manufacturing point of view, square sensors of the order of 3 by 3 feet are feasible. To deploy 20,000 square feet of sensor surface approximately 1000 sensors will

be required, there being about 32 sensors along each side of a square. Here at least a 64-inch separation is required between sensors, whereas the sensor dimension length is only 36 inches.

Referring again to Figures 7 and 9 one notes that a partial solution to the problem is to reduce all column separation to 2 inches, keeping the row separation at 10 inches. From a manufacturing point of view it is desirable to make rectangular capacitors rather than square ones. Figure 10 illustrates the deployment of eight sensors incorporating these suggestions. When packing such a configuration into the spacecraft, two stacks of four sensors each would be laid side by side so as to utilize the spacecraft base plate area most effectively. (Figure 3)

Ideally when folding sensors which deploy as in Figure 9 the folds should be in the same direction. This, of course, can be accomplished by deploying a single long line of sensors - each separated from the adjacent sensor by about twice the sensor thickness. The large spatial extent of such a system would create problems in many areas. The problems can be eliminated, however, by bending the line into a circle as shown in Figure 11. De Havilland booms can no longer be used. Deployment can be achieved by an

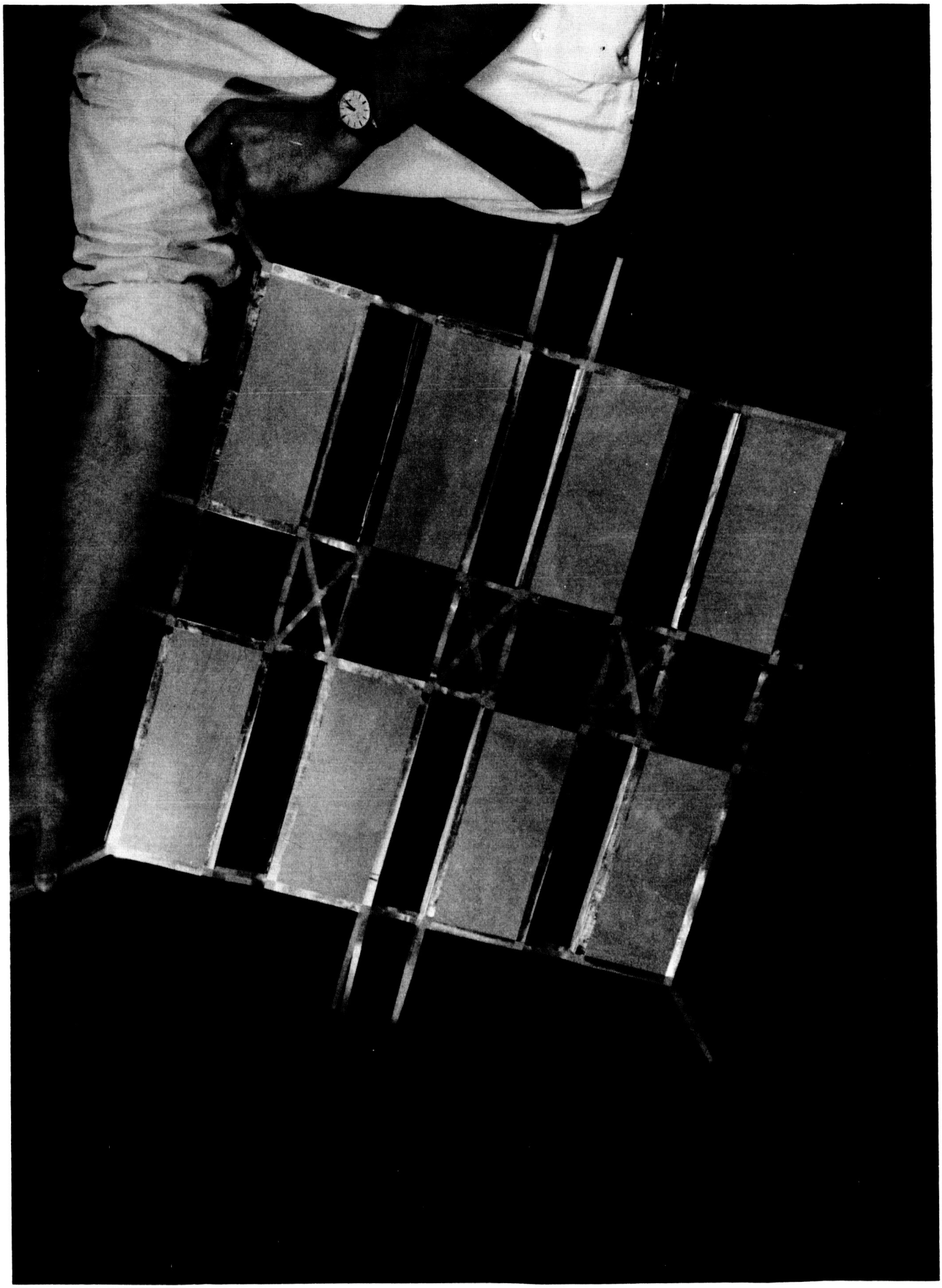

FIGURE 10 EIGHT UNIT SENSOR STACK - DEPLOYED

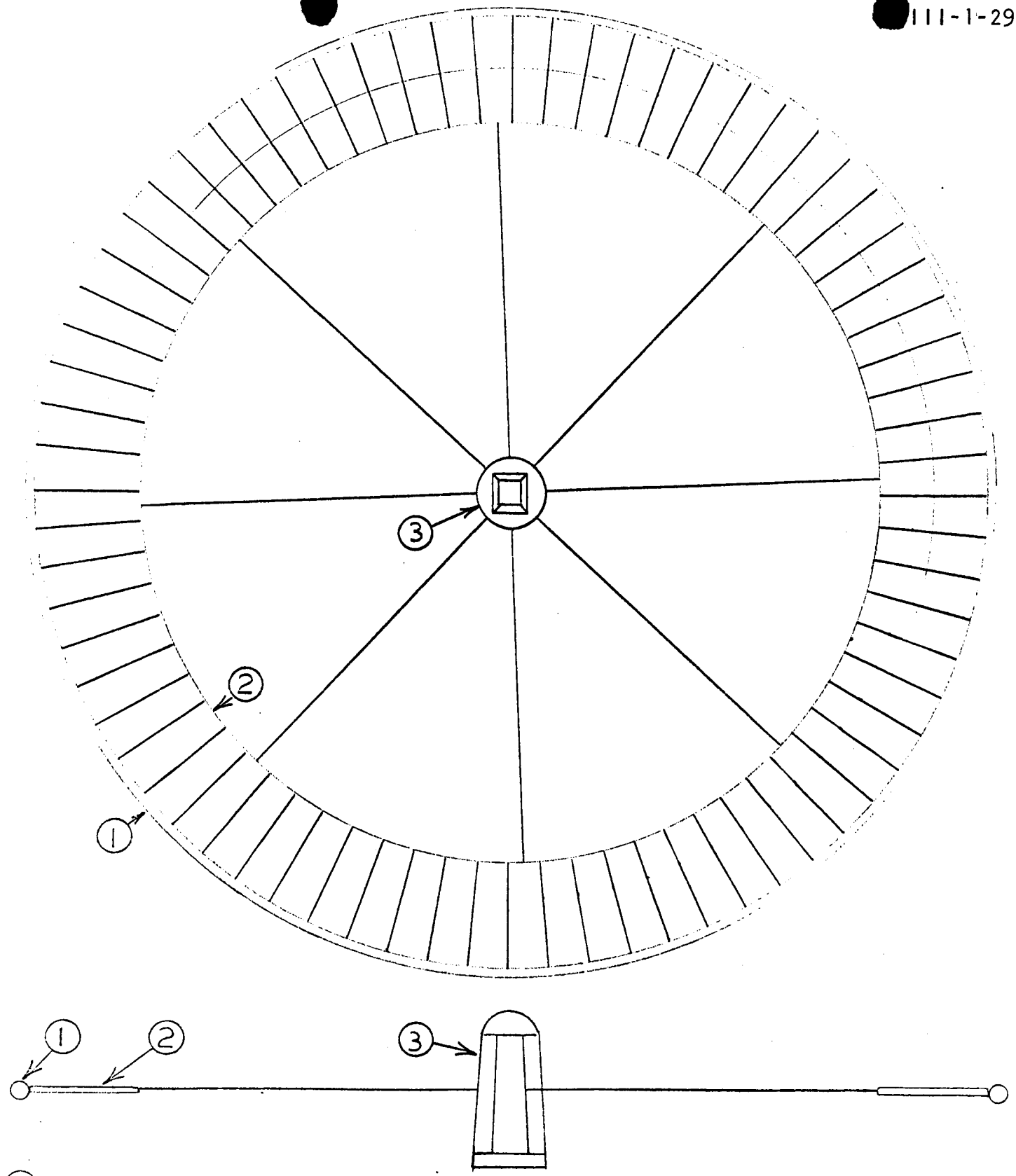

FIG. 11. CIRCULAR DEPLOYMENT

inflatable torus extending around the periphery of the system. Figure 12 is a working model of such a system folded for storage. The model can be folded in several different ways. Only one has been illustrated. Figure 13 shows the model partially deployed and Figure 14 fully deployed. Ribbons would connect the sensors to a central control console. The expansive forces exerted by the torus on the sensor plane would decrease to small values upon inflatant loss. By making the torus of strain rigidizing material like that used in Echo II structural strength remaining after inflatant loss would be of the order of fifty times that required to prevent sunlight from buckling the torus. Having the deployed system rotate slowly about an axis perpendicular to the sensor plane would insure the system's structural integrity.

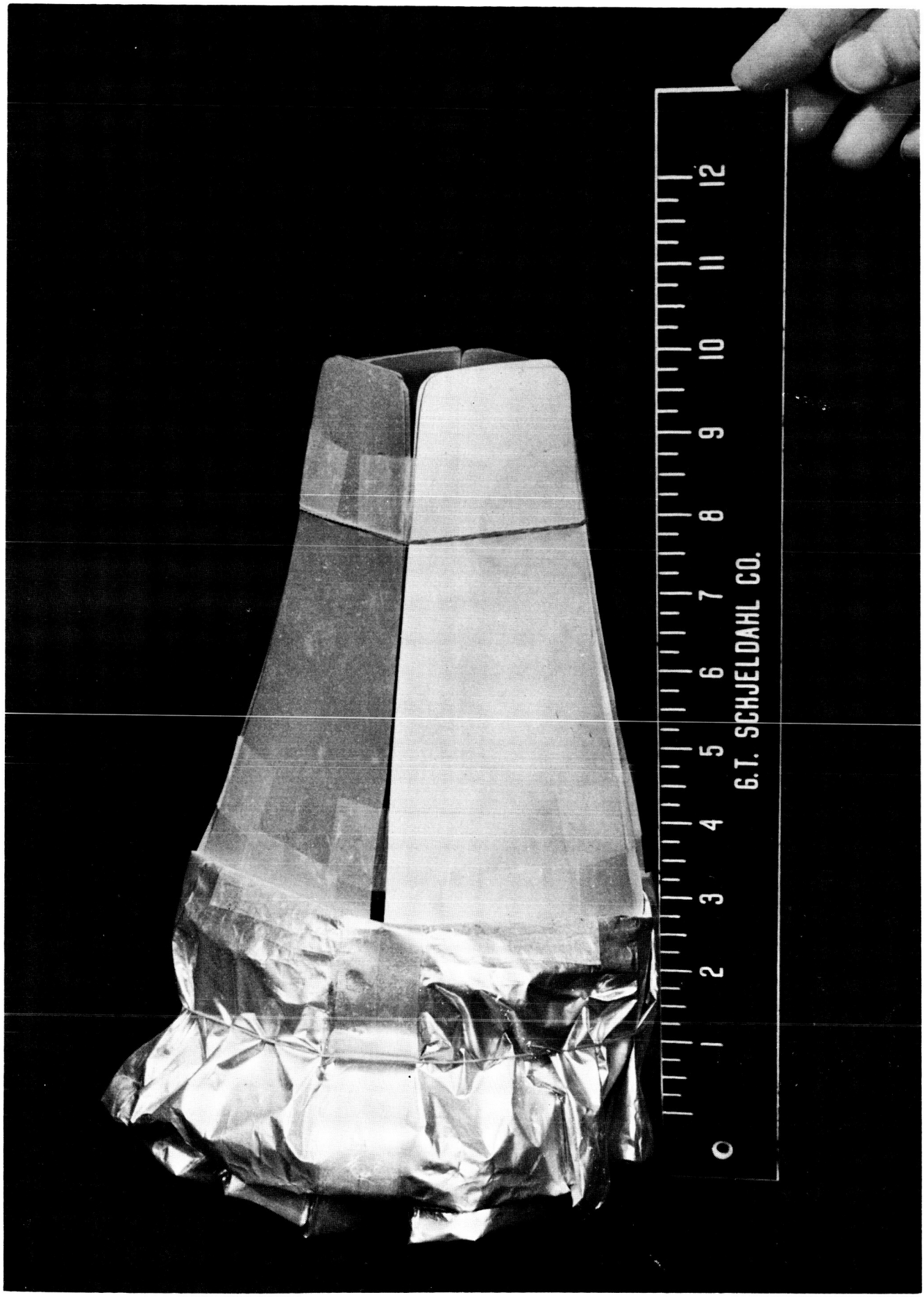

FIGURE 12 CIRCULAR MODEL - STORED
ER 13700-III

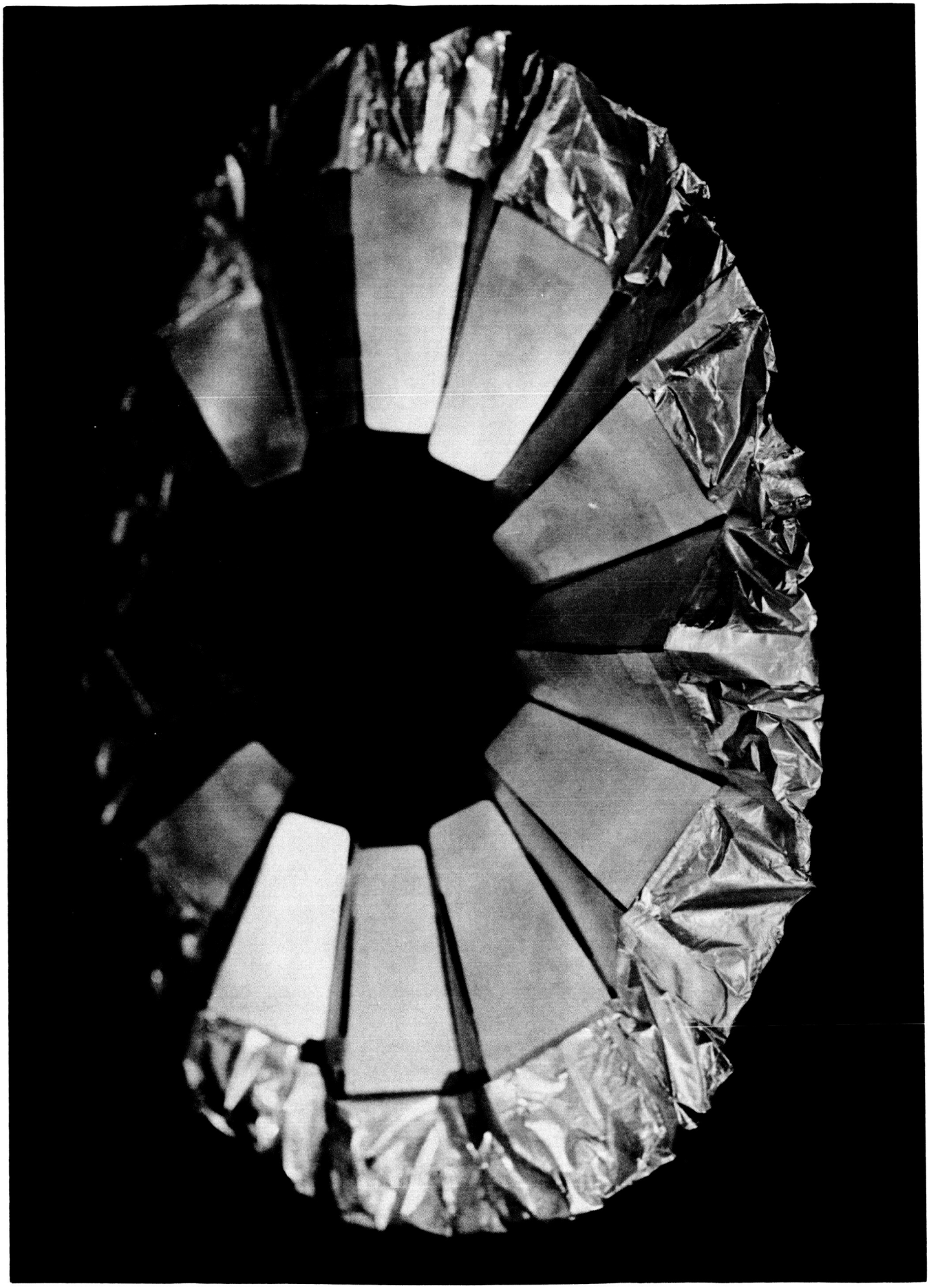

FIGURE 13 CIRCULAR MODEL - PARTIALLY DEPLOYED

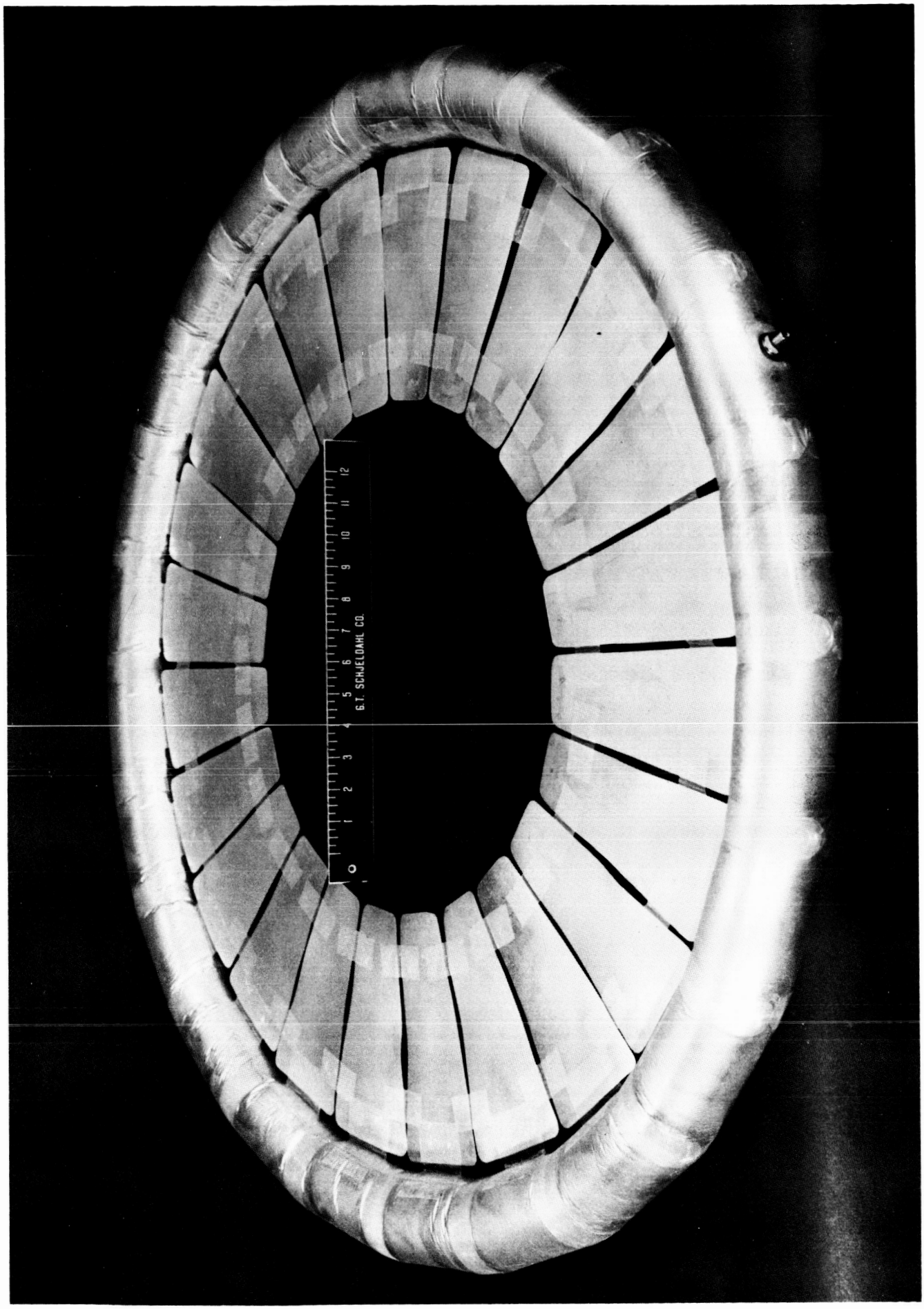

FIGURE 14 CIRCULAR MODEL - FULLY DEPLOYED
ER 13700-III

V. RECOMMENDATIONS

1. If capacitance gauge detectors are orbited, it would be well to include provisions for healing shorted capacitors, as well as capacitors on the verge of shorting.
2. If a compressible core is used, and if the material chosen cannot stand the high compressive forces during acceleration, the sensor stack could perhaps be stored on one of its sides, with weak compressive forces ($\cong$ 1 pound/inch^2) being applied to the stack perpendicular to the line of acceleration.
3. If a compressible core is used it would be of interest to know its stopping power relative to a conventional core. For constant core mass, a thick, low-density core appears to be a more effective stopper than a thin,high-density one. Perhaps weight savings can be realized.
4. Whatever core is used, radiation tests should be made on a sensor unit using this core at an early date.
5. If knowing which capacitor of a two-capacitor unit has been punctured turns out to be unnecessary, the

core can be eliminated. Development work could begin on an aluminum-dielectric-copper-aluminum configuration.

IV. THERMAL CONTROL

W. Coleman Guthrie
Thomas L. Winn
Morton J. Rosenberg

IV. THERMAL CONTROL

The principal design goal for the thermal control system was to devise a simple passive system which did not depend on devices such as shutters and thermal switches. This goal was established based primarily on reliability considerations. The passive design was achieved with the maximum equipment (except for transmitters) temperature variation from 88° to 19° F, well within the allowable operating limit of 0° to 120° F. The 19° F-temperature occurs after 4 hr in the shadow of the earth. The primary transmitter temperature is -7° F after 4 hr in the shadow. The temperature range of the capacitance sensors is from 140° to -380° F with the -380° F occurring after the 4 hr in the earth shadow. This temperature range is outside the presently allowed range of -300° to 220° F.

The major mission influences on the thermal design are the earth shadow period of four hours and the intermittent shadowing on the system module by the capacitance sensors. To limit temperature decay of the equipment during the shadow period, the heat storing capacity of the equipment is used. In the case of the primary and secondary redundant transmitter, 2.5 lb of mass is attached to each transmitter to limit the temperature decay. The thermal influence of the capacitance sensor arrays is mitigated by gravity and solar pressure, both of which cause angular rates about the vehicle x and y axes (see Fig. IV-1), thus thermally the design is based on the vehicle rotating about these axes.

The basic thermal control system tradeoff was between a completely passive system and a semipassive one using thermal control shutters. This tradeoff showed that the passive system, while more reliable, resulted in a 5 lb increase in the system module weight.

The analytical techniques used in the design analysis were both steady-state and transient thermal analysis. Due to the thermal complexity of the vehicle, digital computers were employed for the solution of the steady-state and transient equations. In both analyses, an exact solution was employed to account for the infrared and solar radiation exchange between the sensor arrays and the system module.

A. CONCLUSIONS AND RECOMMENDATIONS

A description of the recommended thermal control system is presented here.

An isometric view of the system module is shown in Fig. IV-2 and a layout is shown in Fig. III-9. The module consists of three 1/2-in. aluminum honeycomb equipment shelves with the upper and lower shelf

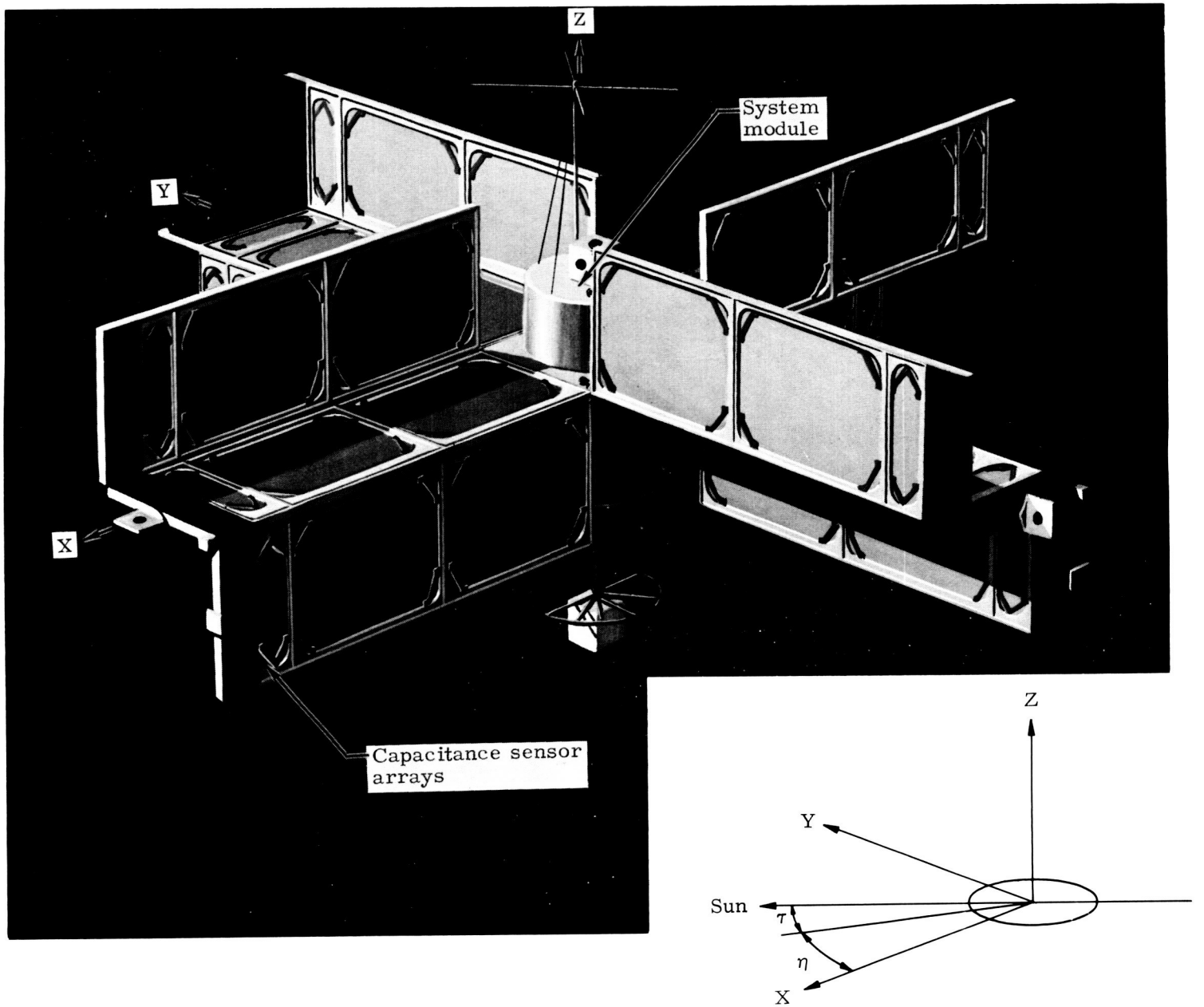

Fig. IV-1. MDSS Configuration

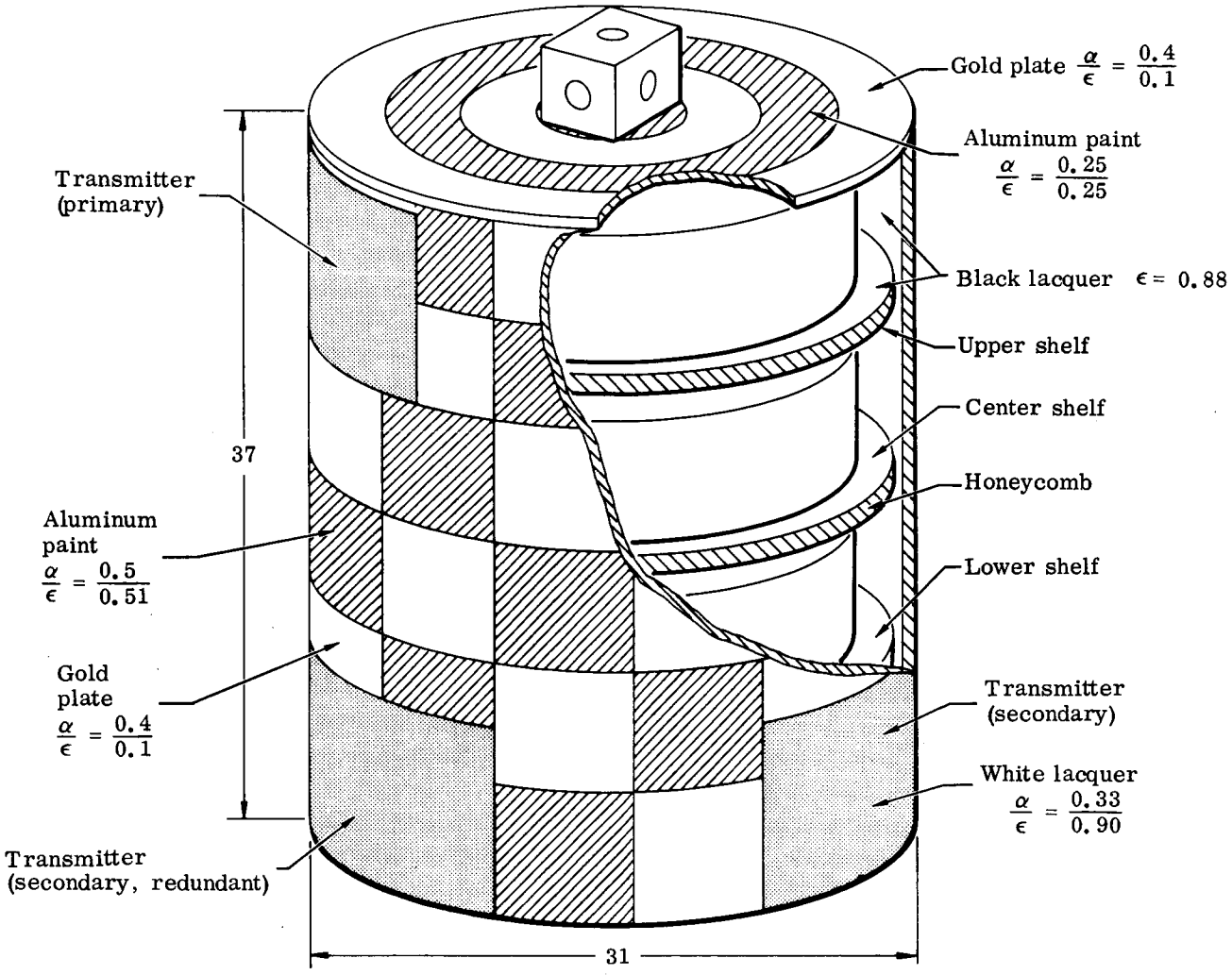

Fig. IV-2. Systems Module Thermal Design

supported from the center shelf. The exterior cover is constructed in 2 halves and is made of 1/4-in. aluminum honeycomb. Each half of the cover attaches to the center shelf. The system module location, relative to the sensor arrays, is shown in Fig. IV-1. The module is attached to the center vehicle truss at four points, so designed as to reduce the heat transfer from the module. The telemetry, sensor and power system electronics are mounted on the equipment shelves as shown in Fig. III-9. The primary and secondary transmitters are attached to the lateral surface of the exterior cover. This method is used to conduct the transmitter's thermal energy to the outer surface and then dissipate it by thermal radiation. To limit the temperature decay of the primary and redundant secondary transmitter when in the earth's shadow, mass is added as shown in Fig. IV-3. The mass consists of a 2.5-lb water-glycol aluminum container attached to the transmitter. To assure high thermal conductivity between the surfaces, Dow Corning 340 heat sink compound is applied to the interfaces.

The interior surfaces of the module are painted with a black lacquer ($\epsilon = 0.88$) to assure an even temperature distribution across the module and to thermally couple the equipment to the exterior cover. The exterior lateral surface is coated with a pattern of aluminum paint ($\alpha/\epsilon = 0.5/0.5$) and gold plate ($\alpha/\epsilon = 0.4/0.1$) to achieve the desired α/ϵ ratio of $0.436/221 = 1.96$. The exterior top and bottom surface is coated with a pattern of aluminum paint ($\alpha/\epsilon = 0.25/0.25$) and gold plate ($\alpha/\epsilon = 0.4/0.1$) with the resulting α/ϵ ratio of $0.2/0.08$. The exterior surfaces in contact with the transmitters are coated with a white lacquer ($\alpha/\epsilon = 0.33/0.90$).

The study has resulted in a simple, passive thermal control system. Although a slight weight penalty is incurred, a higher level of reliability (over a semiactive control system) was realized.

Based on this study, the following thermal control system recommendations are made:

(1) Increase the upper operating temperature of the primary transmitter in order to limit the minimum temperature in the earth shadow to 0° F. Another approach would be to increase the heat storage capacity of the water-glycol container.

(2) Conduct tests on the capacitance sensor to determine its performance at the -380° F temperature level.

(3) Conduct additional vehicle dynamic analysis to determine more accurate angular rates about the vehicle x, y and z axes.

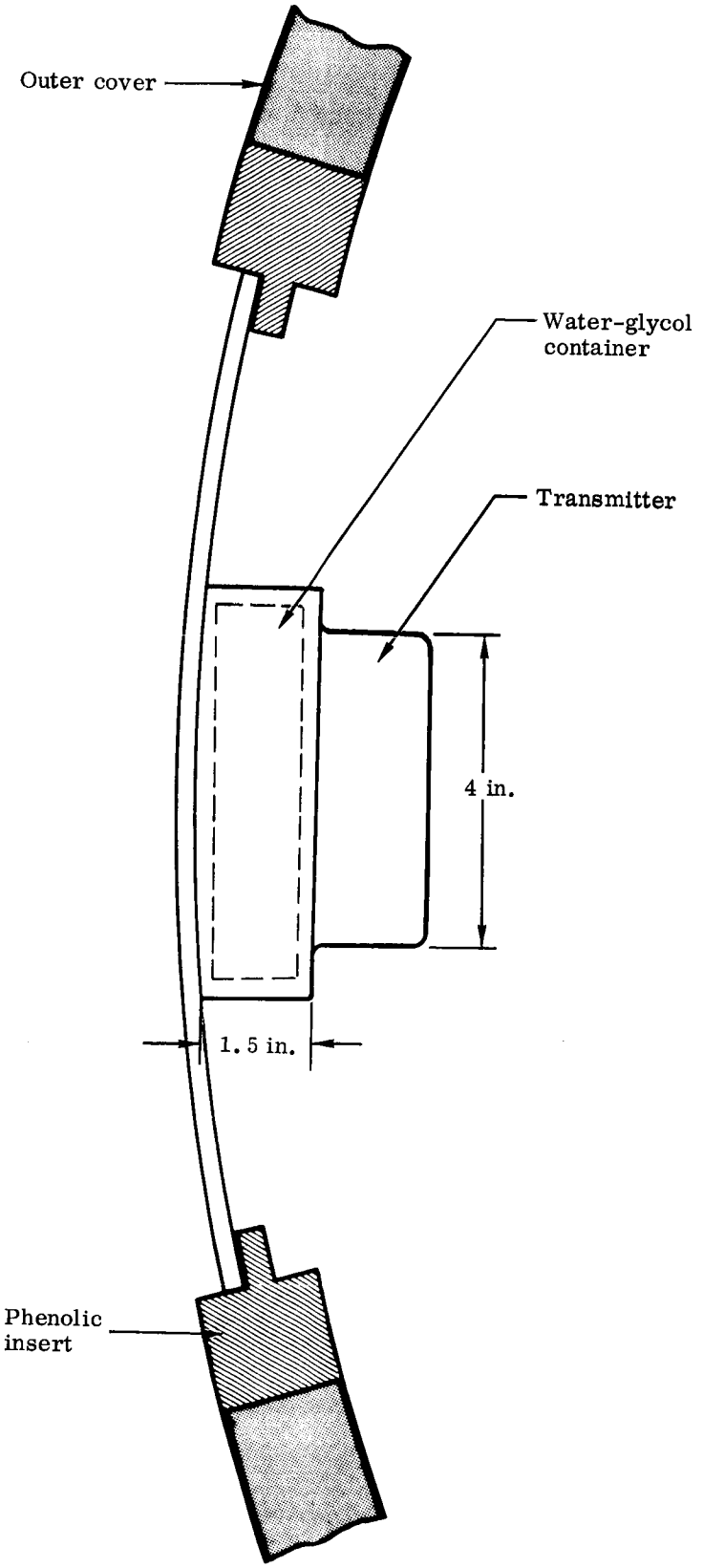

Fig. IV-3. Transmitter Installation

B. TECHNICAL DISCUSSION

1. Major Design Problems

The major influences on the thermal design of the MDSS are earth shadow periods of up to 4 hr and an unpredictable vehicle solar aspect angle. The long shadow periods are a result of the orbit eccentricity (nominal 200-mi perigee 150,000-mi apogee). The unpredictable solar aspect angle is a result of letting the vehicle tumble rather then providing attitude control.

The shadow periods that can be encountered during a 6-mo period for various launch times on a particular day are presented in Fig. IV-4. The maximum shadow period is 6.5 hr and occurs at an 8-hr UT launch. The shadow period can be reduced by establishing launch windows. The time in shadow selected for the vehicle design was 4 hr. Since the orbit period is 146 hr (compared to the shadow period), the thermal balance of the vehicle is determined by the incident solar and IR radiation during the sunlight portion of the orbit. When entering the shadow, the result will be a decrease in the incident thermal radiation and internal heat dissipated. Thus, a decrease in the spacecraft's temperature will occur unless active methods are employed to control the thermal balance.

The decrease in internal heat dissipated during the shadow is a result of the solar cells electrical power system being used exclusively on the primary telecommunication system. The secondary system uses solar cells plus a battery. The battery is used to supply power during the shadow period. Table IV-1 presents the electrical power dissipated within the system for both the primary and secondary power systems. The distribution of this energy is shown in Fig. IV-5.

The vehicle attitude during the mission will be influenced by gravity, solar pressure and aerodynamic drag as discussed in the attitude sensing and determination section. The analysis presented there shows that continuous angular rates exist about the x and y axis (see Fig. IV-1). Typical plots of these rates in terms of solar aspect angle are shown in Fig. IV-6. The angle η is measured from the x axis in the x-y plane and the angle τ is measured from the x-y plane.

Since the preliminary vehicle dynamic analysis shows that τ and η rates exist, the thermal design was based upon these dynamic conditions. From a thermal design standpoint, the worst condition that can occur for a vehicle based on τ and η rates is: (1) $\tau = 90°$ and $\dot{\tau} = 0$; and (2) $\tau = 0$, $\dot{\tau} = 0$, $\eta = 0$ and $\dot{\eta} = 0$. While the dynamic analysis indicate that the likelihood of these conditions occurring is very small, a study was made to determine the influence of these conditions. It is discussed in the following.

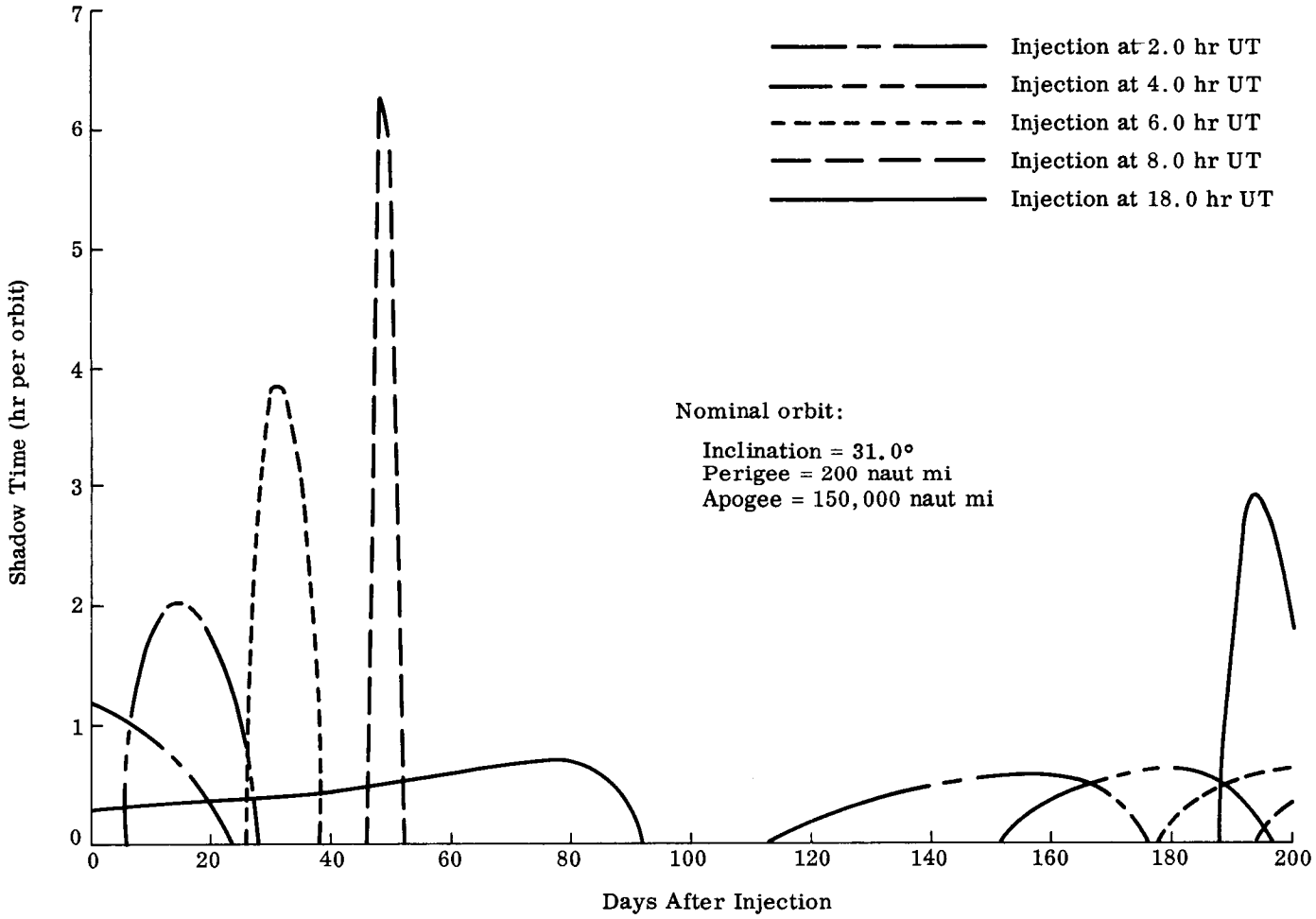

Fig. IV-4. Shadow Time History: Inject Epoch = 10/1/64

TABLE IV-1
Watts Dissipated in Equipment

Primary Power Supply

	Continuous (watts)
Hit count transmitter	18.0
	0.1
Subcarrier oscillator and modulator	0.10
Counters	0.14
Clock, commutator, formatter	0.46
1-mil capacitance sensors	0.60
2-mil capacitance sensors	0.75
Killer timer	0.05
Subtotal	18.75
Primary junction box	1.01
Total	19.76

Secondary Power Supply

	Continuous (watts)
VHF transmitter	18.0
	0.1
Range, range rate and command receiver	0.32
Subcarrier oscillator	0.10
Command decoder	0.01
Command logic	0.01
1-mil capacitance sensors	0.60
2-mil capacitance sensors	0.75
Exotech sensors	7.00
Capacitance and Exotech data unit	1.01
Mariner gauges	0.60
Velocity gauges	0.36
Mariner and velocity data unit	1.56
Magnetometer	--
Solar aspect and earth sensors	--
Attitude data unit: hourly	1.31 (1)
full	1.28 (2)
Diagnostic system	5 (3)
Diagnostic data unit: critical	--
full	--
Memory units	0.02
Killer timer	0.05
Master clock and divider	0.32
Primary system counters	0.14
Memory system overflow	0.46
Subtotal	22.1
Secondary junction box	5.07
Battery	1.72
Total	28.99 watt

(1) 3 min/hr
(2) 5 hr/orbit
(3) 1 hr/orbit

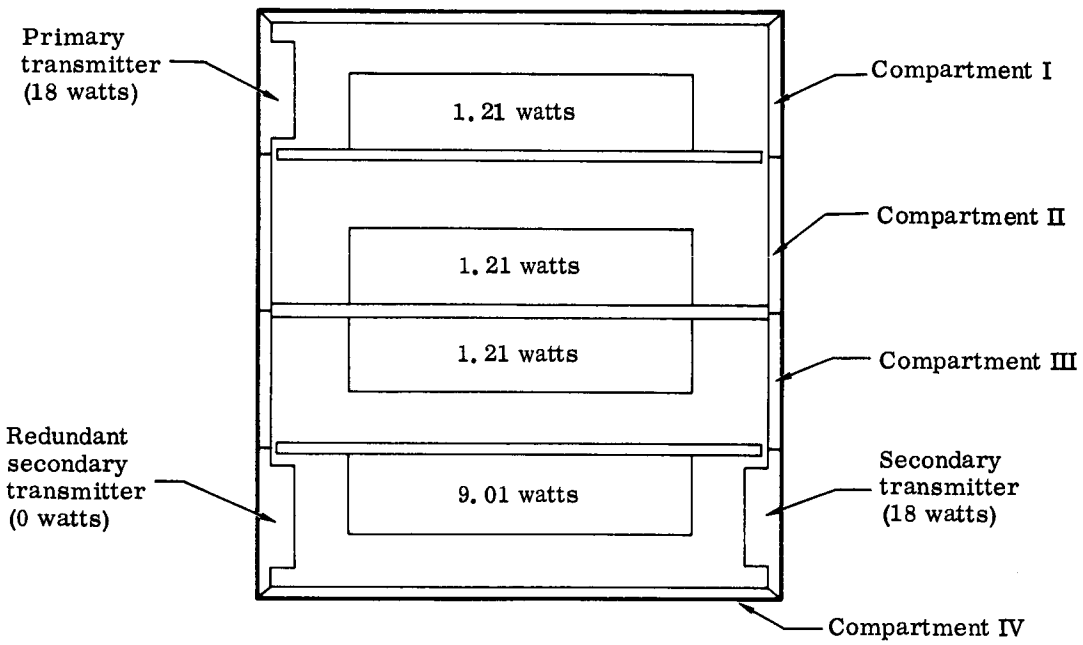

Fig. IV-5. Watts Dissipated Within Systems Module

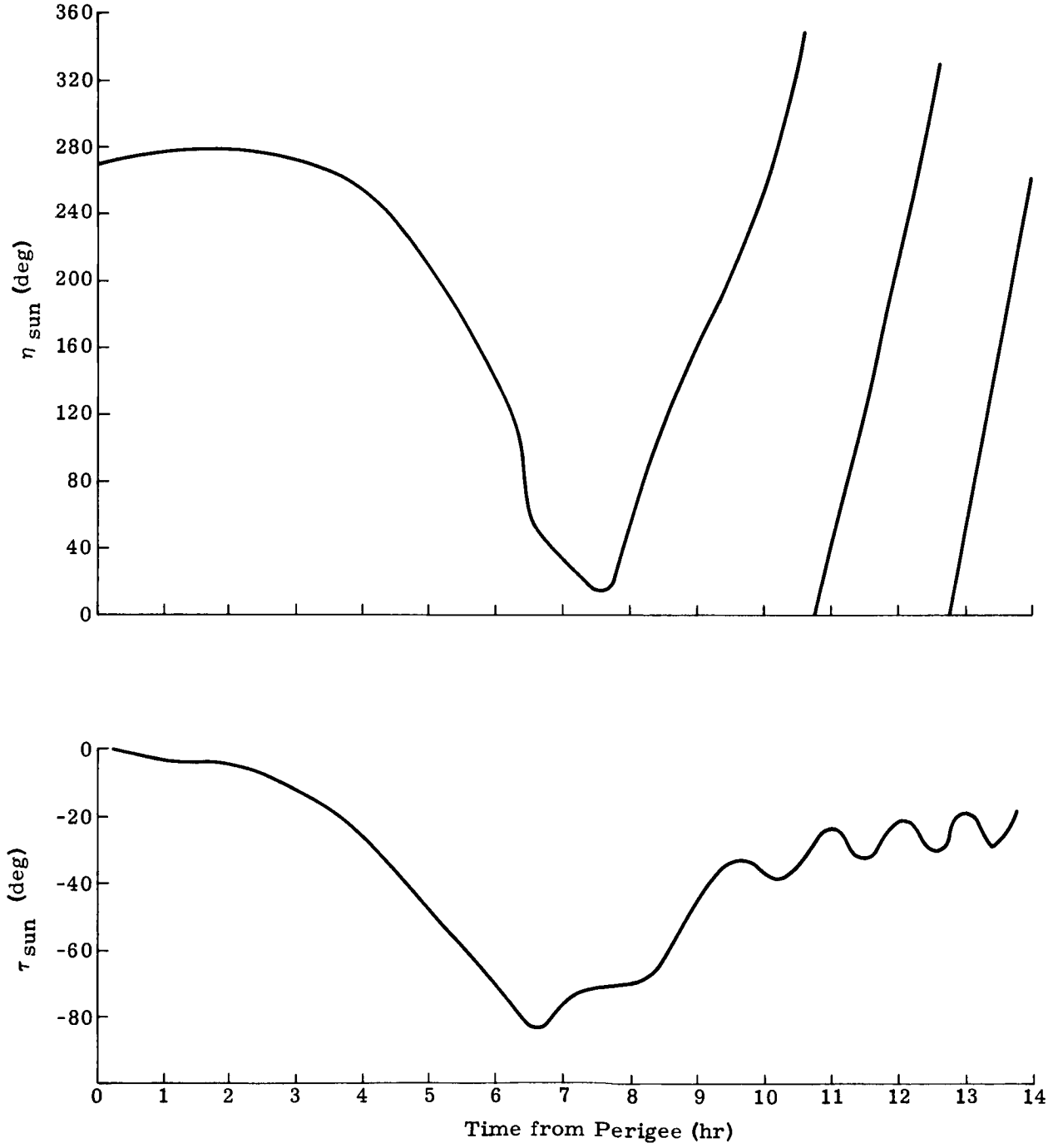

Fig. IV-6. Sun Angles η and τ: Sun Line Normal to Orbit Plane

2. System Module Analysis

The analytical model used to conduct the system module design and analysis is shown in Fig. IV-7. To compute the total thermal radiation incident to the exterior surface of the systems module, an exact solution, employing the equations discussed in Appendix IV-1A were used. To apply the equations, the solar radiation incident to each sensor array and the systems module were computed assuming the vehicle to be rotating about some given axis, say in the x-y plane. The total incident solar radiation to all the capacitance sensor arrays and the system module plus the optical properties and view factors are inserted into the equations and the temperature of the arrays plus the solar and infrared absorption factors are then computed. From the sensor array temperature and absorption factors, one can then compute that fraction of infrared radiation absorbed by the system module that is emitted by each sensor array by applying the following calculation.

$$q_{(\text{IR absorbed})} = \sigma \epsilon_S T_S^4 A_S B_{(S\text{-}SM)_{IR}}$$

where:

A_S = area of sensor array

$B_{(S\text{-}SM)_{IR}}$ = IR absorption factor--that part of the total energy emitted by the sensor array (S) that is absorbed by the system module (SM) considering all reflections in the system.

ϵ_S = emissivity of sensor array

T_S = temperature of sensor array

σ = Stefan-Boltzmann constant

In a like manner, the solar energy reflected from the sensor arrays that is absorbed by the system module can be computed with the following calculation:

$$q_{(\text{solar reflected absorbed})} = Q_S (1 - \alpha_S) A_S B_{(S\text{-}SM)_S}$$

where:

A_S = area of sensor array

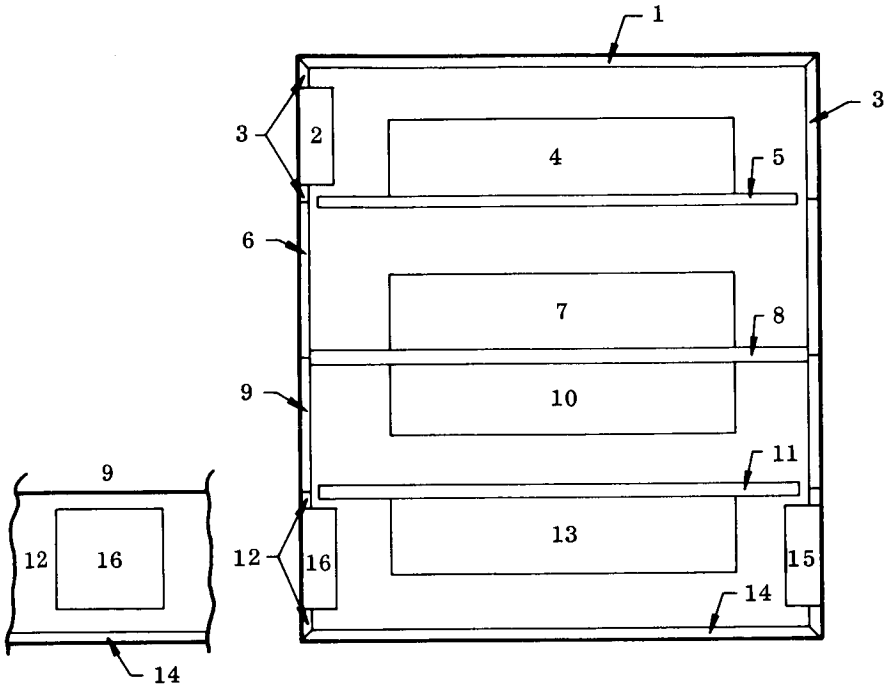

Typical
of transmitter
noding

Node	
1	Top of system module
2	Primary transmitter
3, 6, 9, 12	Lateral surface of system module
4, 7, 10, 13	Equipment
14	Bottom of system module
15	Secondary transmitter
16	Secondary transmitter (redundant)

Fig. IV-7. Thermal Analytical Model

$B_{(S\text{-}SM)_S}$ = solar reflected absorbtion factor--that part of the total solar energy reflected by the sensor array (S) that is absorbed by the system module (SM) considering all reflections in the system.

The solar, infrared and solar reflected energy absorbed by the system module is shown in Table IV-2 for a typical mode of rotation. The importance of accurately computing the solar reflected and infrared energy is obvious. For instance, on the lateral surfaces of the systems module the solar reflected and infrared energy is 37.9% of the total energy absorbed.

TABLE IV-2

Incident Absorbed Thermal Radiation Rotation About x Axis

System Module Surface	Direct Solar (Btu/hr-ft^2)	Reflected Solar (Btu/hr-ft^2)	IR from Sensor Arrays (Btu/hr-ft^2)
Top and bottom	28.2	0.42	0.53
Lateral surface	22.4	8.54	5.17
Transmitters	12.6	13.1	24.1

Referring again to Fig. IV-7 where nodes are shown in contact with adjacent nodes, conductive heat transfer was included in the analysis. The lateral heat transfer in the honeycomb structure was based on an equivalent aluminum sheet having a thickness of the honeycomb faces plus the mass of the core. The face thickness for the 1/2-in. shelves is 0.01 in. and for the exterior cover, it is 0.02 in. The value of thermal contact resistance between the equipment and equipment shelves was assumed to be 45 Btu/hr-ft^2-°F which, according to Atkins and Fried,* should be easily attained with a contact pressure in the order of 10 to 20 psi.

To compute the radiation heat transfer, the view factors between nodes and the emissivity of the nodes were substituted into the Appendix A equations and the absorption factors computed. These absorption factors, the incident radiation and nodel description were then substituted into the Appendix IV-1B equations and the temperature of all the nodes computed versus time. The IBM 7094 was used for the solution of the equations.

*Atkins and Fried, "Thermal Interface Conductance in a Vacuum," AIAA Paper No. 64-253.

Figure IV-8 presents the temperature of the system module with the vehicle rotating about an axis in the x-y plane or $\tau = 0$ and $\dot{\eta}$ is nonzero. The temperature entering the shadow represents the vehicle temperature for 0 eclipse time. This dynamic stabilization will occur approximately 30 hr after launch or exiting the shadow. The temperature variation of the equipment mounted on the shelves is between 88° and 85° F on entering the shadow. After 4 hr in the shadow, the temperature is from 19° F for Compartment I to 66° F for Compartment IV, the two other compartments being between these. Compartment IV decreases in temperature less than the other compartments because the batteries are located in Compartment IV. Thus, the heat capacity is higher here than in the others. When in the earth shadow, only the secondary telecommunication system is functioning, and it obtains its electrical power from the batteries. The primary telecommunication system is inoperative in the shadow since its only source of electrical power is from solar cells. The results of the different primary and secondary telecommunications systems modes of operation can be seen by comparing the temperature excursions of the primary and secondary system transmitters during the shadow period. The primary transmitter decreases from 73° to -7° F; the secondary from 73° to 47° F; and, the redundant secondary from 29° to -30° F. To prevent an even further decrease in temperature of the primary and redundant secondary transmitters, a heat storage device consisting of a water-glycol container was added to the primary and redundant secondary transmitters. The container is constructed of welded 1/4-in. aluminum plates containing 2 lb of water-glycol solution which has a freezing point of -40° F. It is installed as shown in Fig. IV-4. Figure IV-9 presents the temperature time history of the transmitters in the earth shadow with the heat capacity of the transmitter as the parameter. The figure shows that a heat capacity of 2.5 Btu/° F, or greater, is required to prevent the primary transmitter, which is passive in the shadow, from decaying below -7° F. The basic transmitter heat capacity is approximately 0.5 Btu/° F. Ten pounds of aluminum would be required to provide the 2.5 Btu/° F. Therefore, 2 lb of water-glycol (heat capacity of 1.6 Btu/° F) plus a 1.7 lb container (heat capacity of 0.4 Btu/° F) was selected as the heat sink material. The probability of a micrometeoroid penetrating the water-glycol container is essentially zero.

Figure IV-10 presents the temperature of the systems module entering and exiting the shadow, assuming the primary transmitter has failed. The temperatures of all the equipment in the compartments are still within the allowable range 0° to 120° F. The influence of the primary transmitter on the temperatures in Compartment I can be seen by comparing the entering temperature of the compartment for the normal system (Fig. IV-8) and the failed system (Fig. IV-11). The entering temperatures are 87° and 67° F, respectively. The temperatures computed in Figs. IV-8 and IV-11

4-hr shadow period

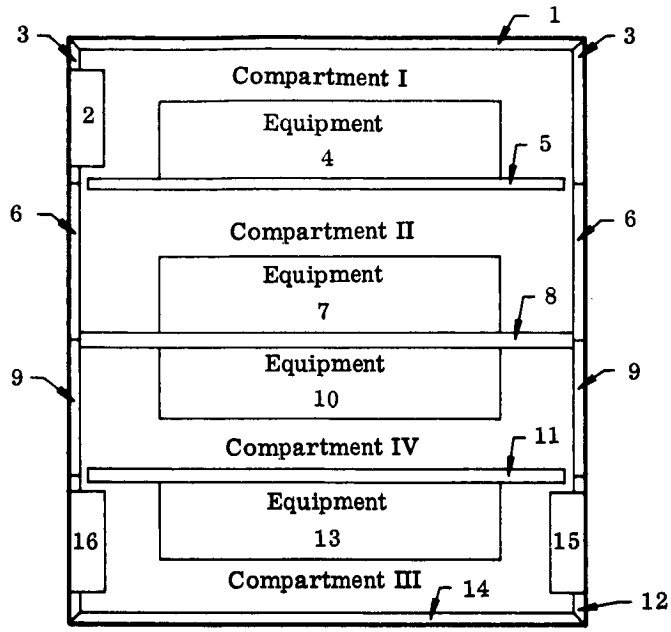

Temperature (^{o}F)

Node	Enter Shadow	Leave Shadow	Node	Enter Shadow	Leave Shadow
1	89	-3	11	85	40
2	73	-7	12	85	13
3	84	-10	13	88	66
4	87	19	14	88	26
5	86	15	15	73	-47
6	83	-5	16	29	-30
7	88	42			
8	85	31			
9	87	3			
10	85	47			

Fig. IV-8. Temperature of System Module Tumbling About X-Axis

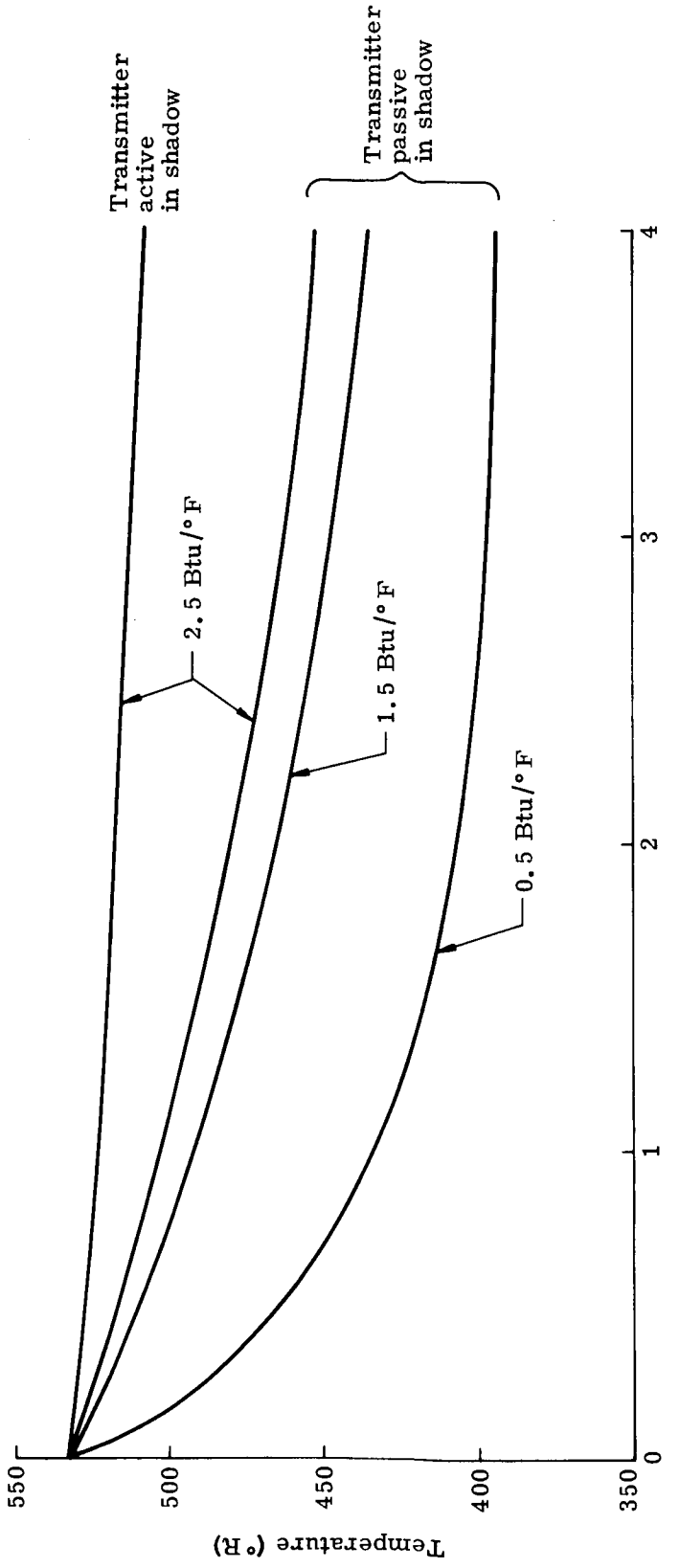

Fig. IV-9. Temperature Time History of Transmitters in Earth Shadow with Heat Capacity as Parameter

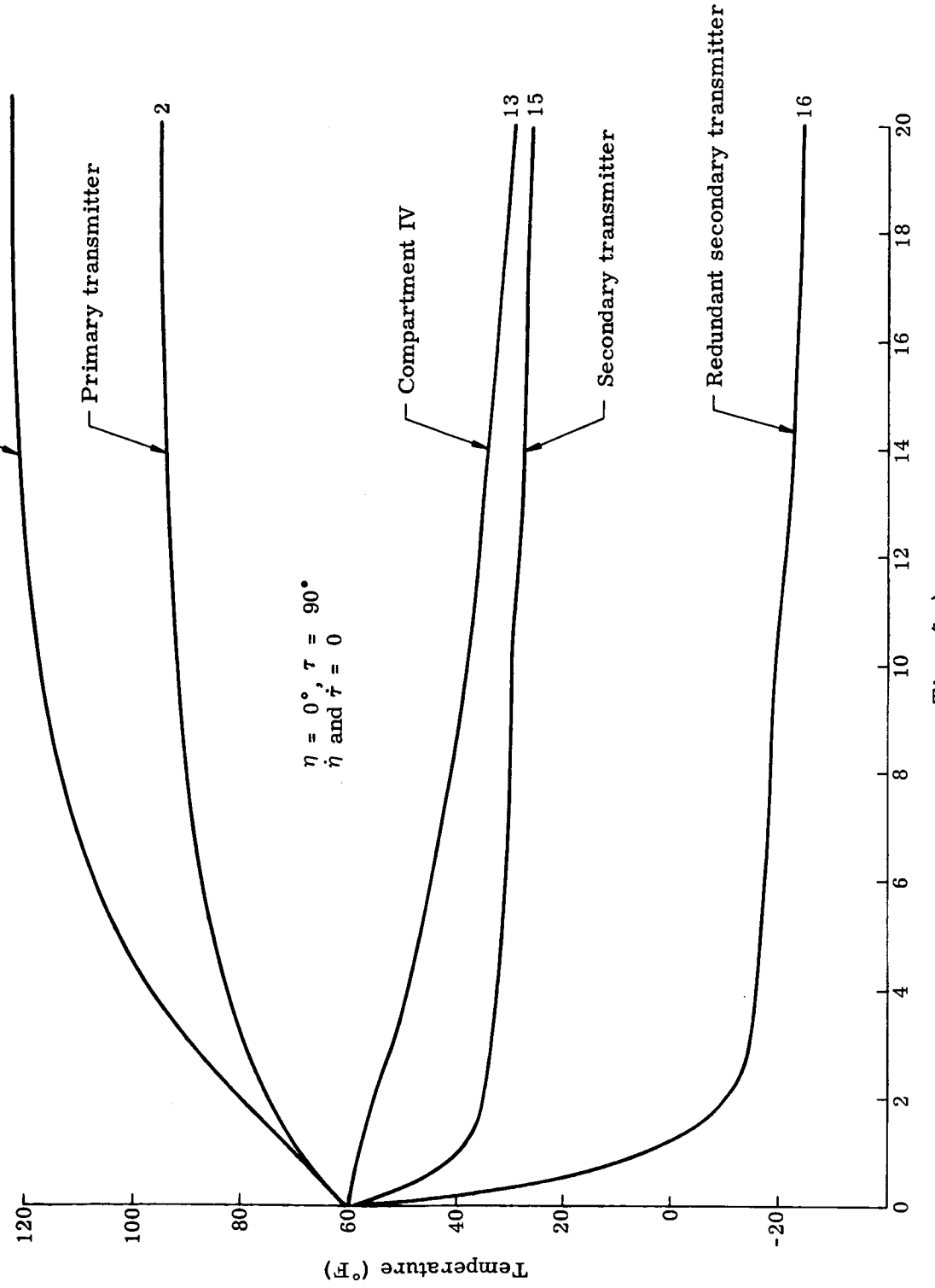

Fig. IV-10. System Module Temperature Time History-- $\eta = 0^{\circ}$, $\tau = 90^{\circ}$; $\dot{\eta}$ and $\dot{\tau} = 0$

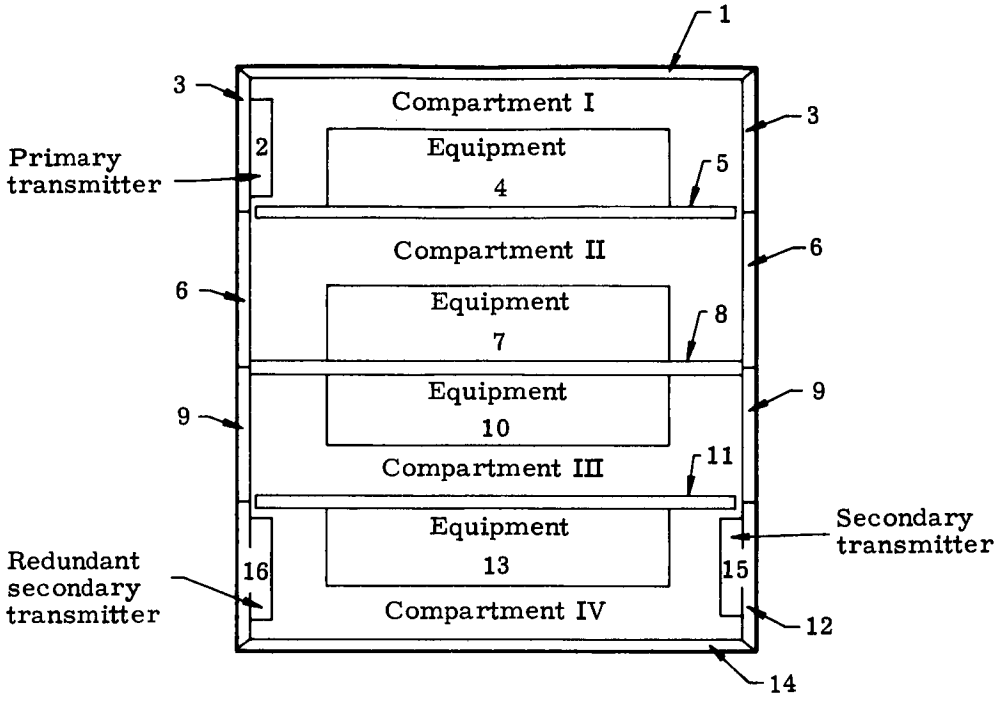

Temperature (°F)

Node	Enter Shadow	Leave Shadow	Node	Enter Shadow	Leave Shadow
1	75	-11	11	82	36
2	12	-40	12	86	10
3	74	-17	13	83	64
4	67	10	14	87	24
5	72	7	15	72	47
6	77	-10	16	27	-30
7	75	35			
8	79	26			
9	83	-1			
10	81	43			

Fig. IV-11. Temperature of System Module Tumbling About Axis in X-Y Plane: Four Hour Shadow Period, Primary Transmitter Failed

are the results of transient analyses. A typical temperature time history during and after the shadow period is presented in Fig. IV-12.

To investigate the influence on the vehicle temperatures of angular rates being damped out, two conditions were assumed. One with $\tau = 0°$ and $\dot{\tau} = 0$; the other, $\eta = 0°$, $\dot{\eta} = 0$, $\tau = 0°$ and $\dot{\tau} = 0$. Figure IV-11 presents the temperature time history for the condition $\eta = 0°$, $\tau = 90°$. It can be seen that Compartment I becomes the critical item. It exceeds the 120° F upper temperature limit after 12 hr. But from the vehicle attitude calculations the rates about the axes in the x-y plane are on the order of 16° F/hr at values of τ above 45° . Thus, an adequate margin exists to prevent excessive system module temperature based on the calculated rates of the x-y plane (i.e., τ). Figure IV-13 presents the case of $\eta = 0$, $\tau = 0$, $\dot{\eta} = 0$ and $\dot{\tau} = 0$. Here the maximum temperature limit is exceeded by Compartment III at the end of 4 hr. But again from the vehicle attitude calculations $\dot{\eta}$ appears to build up and become constant. Although at $\eta = 280°$, $\dot{\eta}$ is very low, the average rate is 20°/hr, providing an adequate margin for temperature control.

To show the influence of system module construction, an analysis of a typical system module was made with and without conductive paths from the equipment to the outer skin of the vehicle. The primary interest was to show the influence of module construction on the temperature decay of the module equipment when the vehicle enters the earth shadow. Figure IV-14 presents the case of the equipment installed with conductive paths to the exterior surface of the module. The temperature change at the end of 4 hr is 85° F. This is where the total cross section area of the conductive path is only 1 in.^{2} compared to the total module surface area of 1808 in.^{2}. Figure IV-14 also shows the identical module but without conductive paths between the equipment and outer surface of the module. Here the temperature decay at the end of 4 hr is only 22° F. The conclusion here is to minimize the conductive paths from the equipment to the exterior surface of the system module on vehicles where extended shadow periods are encountered This approach was taken on the design of the MDSS system module.

During the study, two modes of operation were considered for the telemetry transmitters. The two modes were: (1) to operate the transmitter continuously; and (2) to operate them on command. The continuous mode of operation is illustrated in Fig. IV-8. This type design is based on establishing a thermal balance with the transmitter operating. Mission requirements such as shadow periods can only be tolerated on a transient basis where the mass of the transmitter is used to maintain the required temperature limits. Figure IV-15 shows the comparisons of two types of thermal control systems for a transmitter operated on command. For the case shown, the transmitter is operated for a 2-hr period on command. When the transmitter is

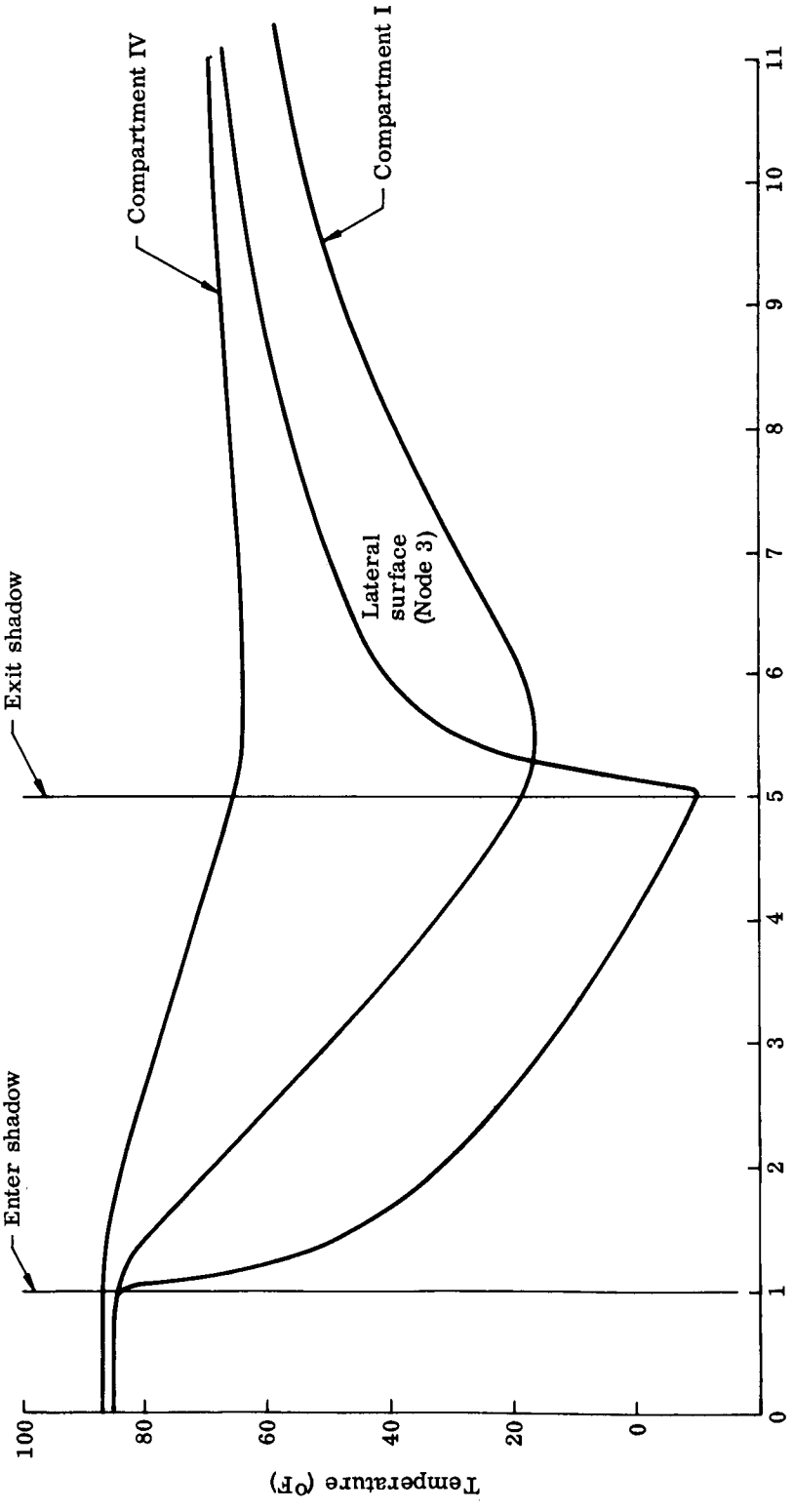

Fig. IV-12. Temperature Time History of System Module Entering and Leaving Shadow--Tumbling About X and Y Axis

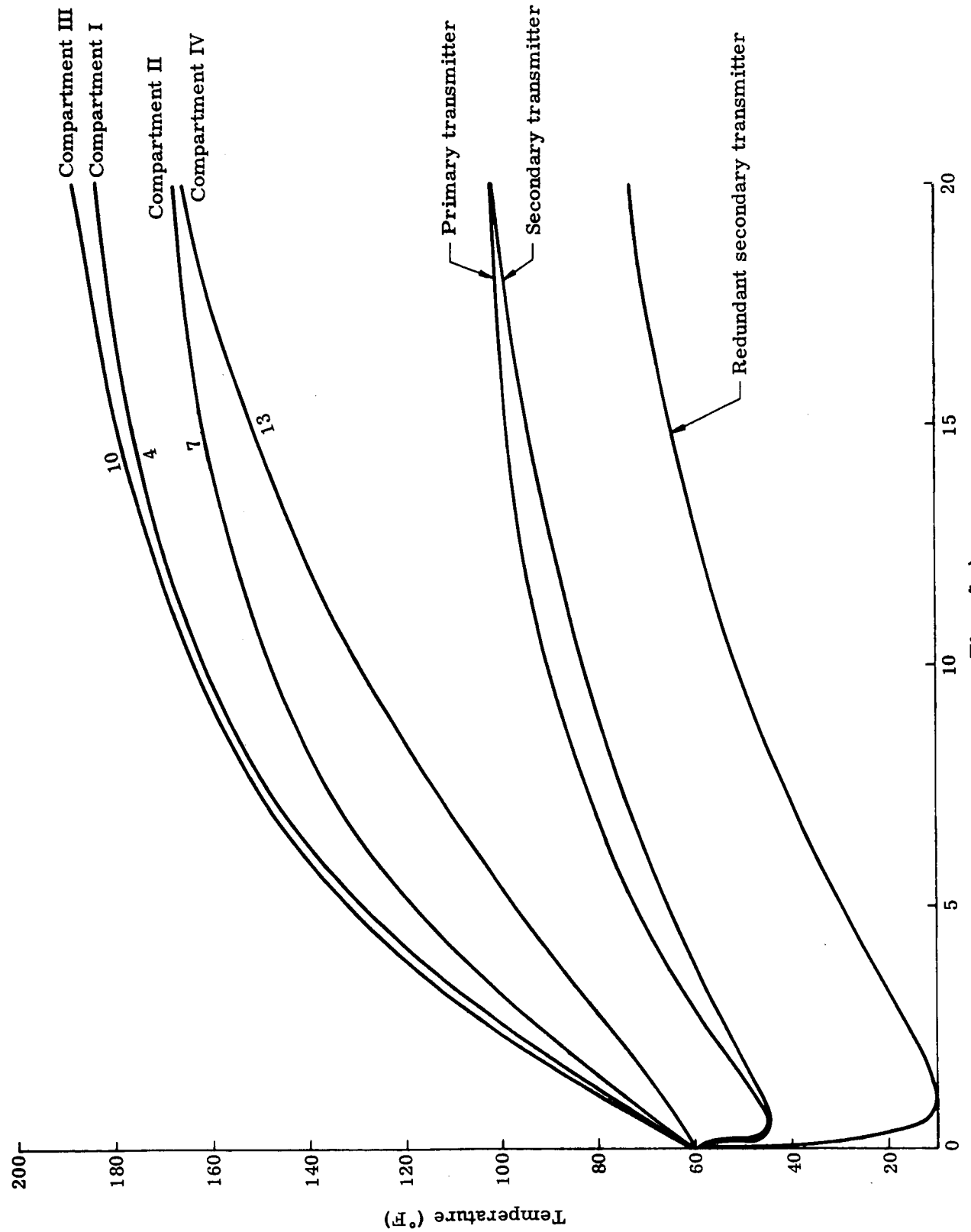

Fig. IV-13. System Module Temperature Time History-- $\eta = 0^{o}$, $\tau = 0$; $\dot{\eta}$ and $\dot{\tau} = 0$

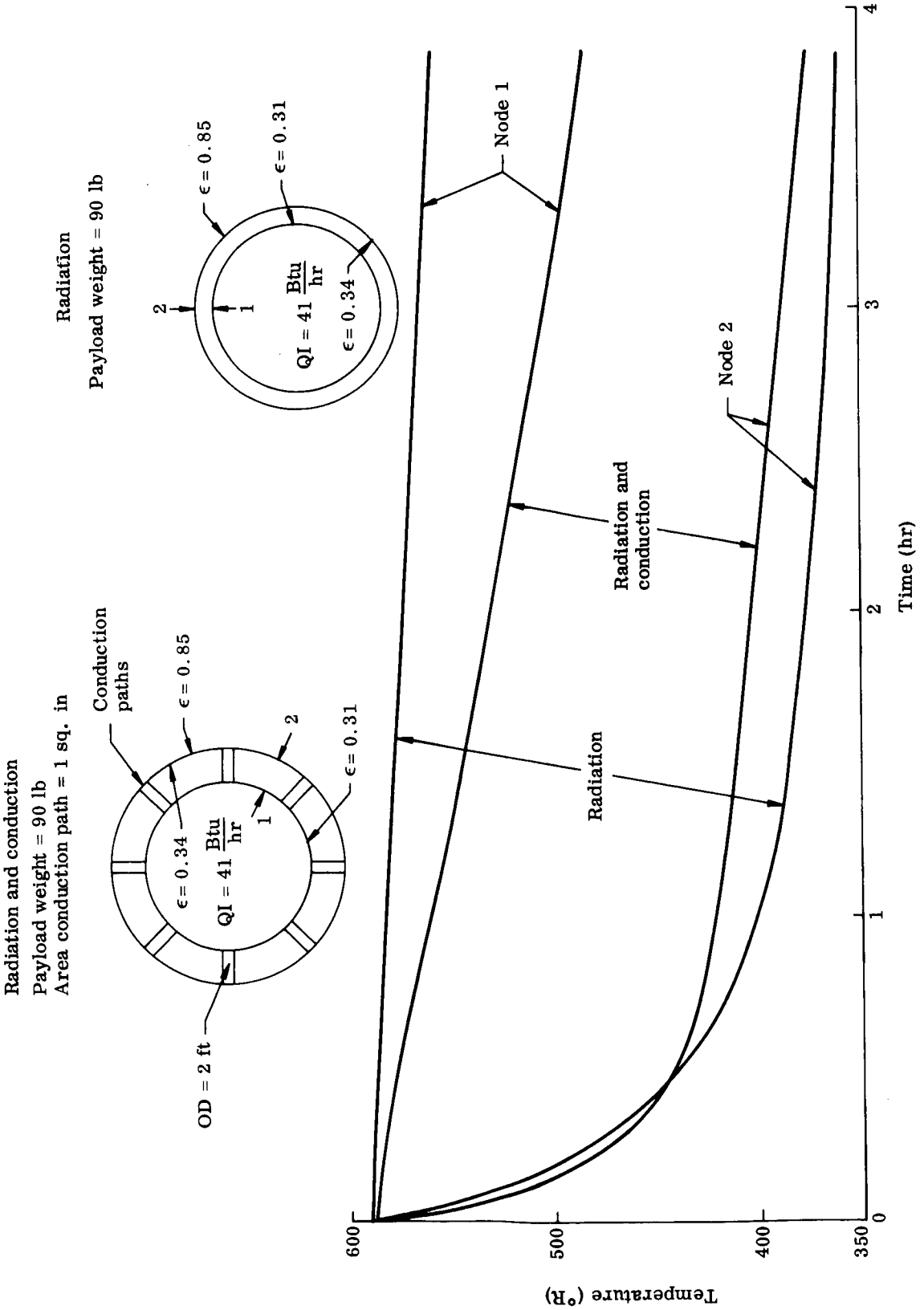

Fig. IV-14. Systems Module Temperature Decay Versus Time in Shadow

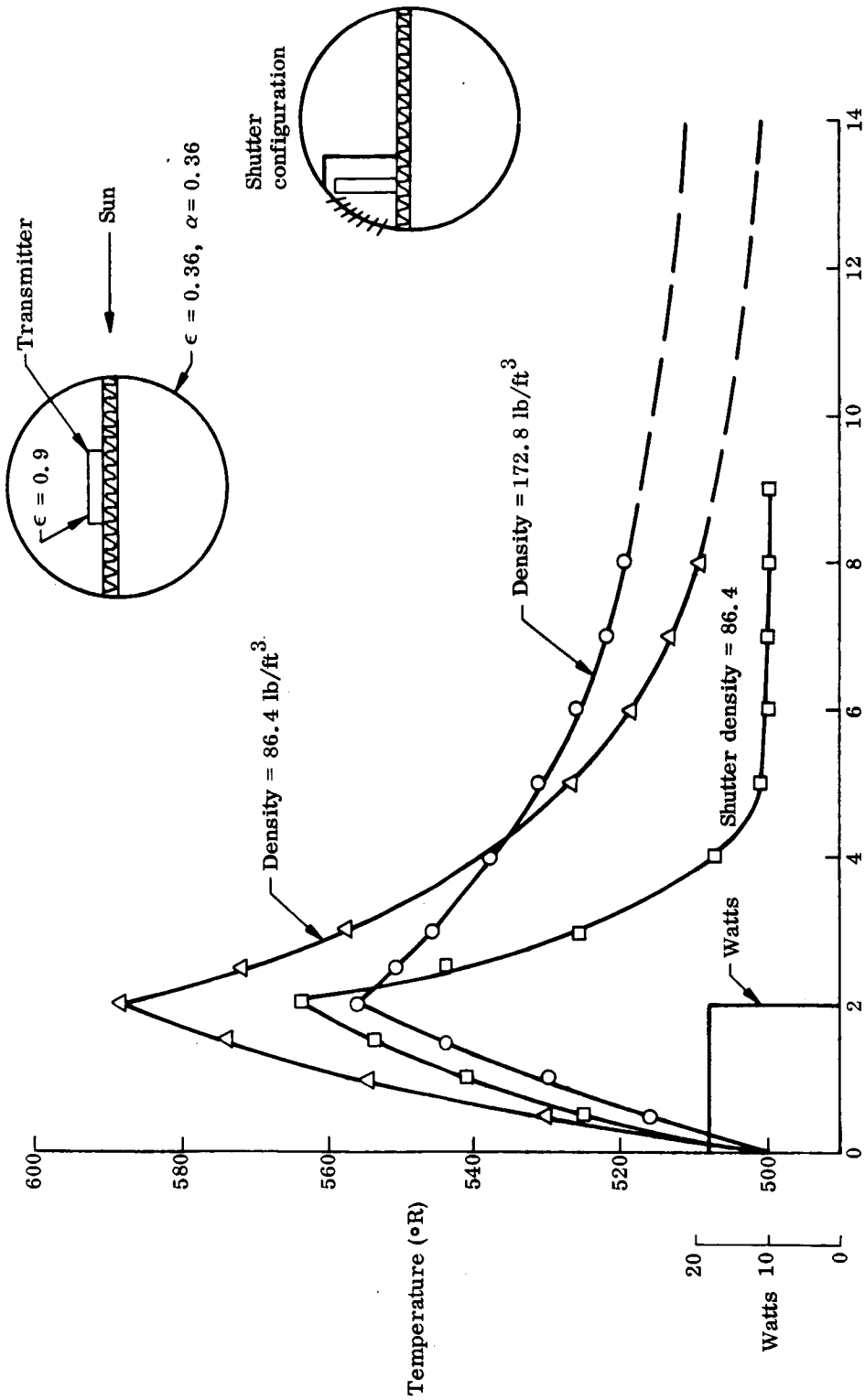

Fig. IV-15. Temperature-Time History of Transmitter Mounted Internally and Operated in Cyclic Mode

inoperative, the thermal coupling with the spacecraft is designed to maintain the transmitter at 40° F. The curves labeled density = 86.4 and 172.8 lb/ft^3 are cases where the transmitters mass is used to limit temperature increases during the operating periods. The density of 86.4 lb/ft^3 is typical of electronic components. The density of 172.8 lb/ft^3 has assumed that mass has been added to the transmitter. The upper temperature limit of 580° R (120° F) is exceeded at approximately 1.85 hr of operation, and by the mass addition (density = 172.8 lb/ft^3), the temperature is 556° R (94° F) after 2 hr. While the 94° F upper temperature limit is acceptable, the temperature decay is so slow that the period between transmissions would be 15 to 20 hr. The addition of a thermal control shutter to control the transmitter temperature results in the upper temperature limit being 564° R (104° F) after 2 hr of operation and the period of operation between transmissions is now on the order of 5 hr.

As previously stated, the vehicle design is based on the primary and secondary transmitters operating continuously. If it is desired to go to a command telemetry system with the same electrical power available as with the continuous system then an electrical heater may be added to the transmitter to maintain the transmitter's temperature. This system will require electrical circuits and logic to turn the heater off when the transmitter is operating and on when it is passive.

Figure IV-16 presents the analysis of the radiating fin attached to the transmitter. The primary interest here was to determine the typical effectiveness of such a fin. The temperature decay from the fin root (x = 0) to the edge of the fin (x = 7) is 15° F. This results in a fin effectiveness of 0.94%. The total heat radiated by the fin then becomes,

$$\sigma \epsilon T^4 (A_x + A_{fin}\, \Omega)$$

where

A_x = face area of the transmitter (ft^2)

A_{fin} = total fin area (ft^2)

Ω = fin effectiveness

T = temperature (° R)

ϵ = emissivity

σ = Stefan-Boltzmann constant

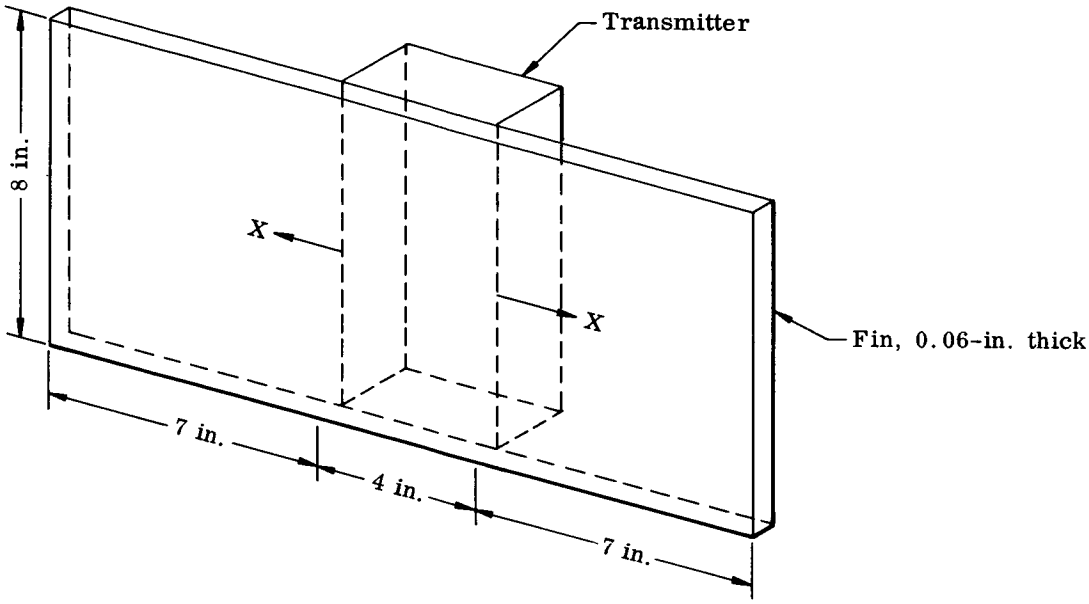

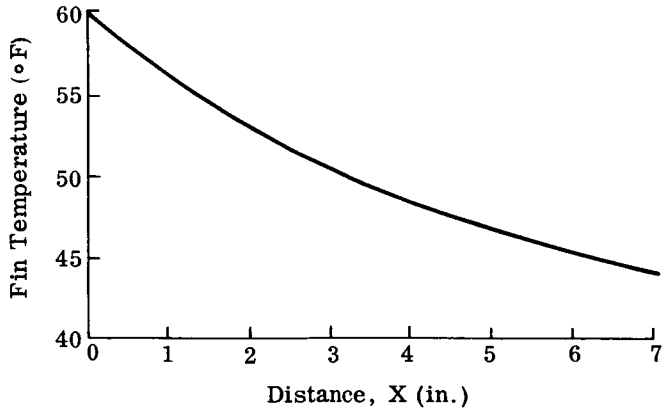

Fig. IV-16. Transmitter Thermal Radiating Fin

For the case shown with an emissivity of 0.9, the total radiated energy is 109 Btu/hr (31.8 watts). The thermal balance is more complicated than shown since the incident thermal radiation must be considered, which in turn influences the fin effectiveness. This analysis was conducted primarily to show feasibility.

C. CAPACITANCE SENSOR ARRAY

Three types of capacitance sensor arrays were analyzed during this study. They were:

(1) The solid core type

(2) Two independently supported sensors with a baffle plate

(3) Two independently supported sensor without a baffle plate.

The primary effort was directed toward the latter type sensor. The allowable temperature range of the capacitance sensor was established as 220° to -300° F. This is based on the upper temperature limit of mylar and on tests conducted by the G. T. Schjeldahl Company at -300° F. At the -300° F temperature, the sensor maintained electrical performance.

Figure IV-17 shows the influence of the sensors inner surface (vacuum-deposited copper) emissivity on the sensor temperatures. Using an emissivity of 0.15 for vacuum-deposited copper, the sensor temperature difference is 210° F. It was felt that a minimum temperature difference would be desirable to reduce differential expansion. Therefore an emissivity of 0.9 was investigated. This can be achieved by the application of India ink (similar to ECHO). The 0.9 emissivity resulted in reducing the temperature difference to 70° F and also reducing the upper temperature from 310° F to 230° F. The α/ϵ ratio used for this analysis was 0.6/0.375. Later data from the G. T. Schjeldahl Company shows that by proper control on α/ϵ ratio of 0.51/0.5 can be achieved with the alodine finish process applied to the sensors.

Since the sensor array temperatures are strongly influenced by the vehicle configuration, the array temperatures were computed for various values of η and τ and for two values of α/ϵ ratio as shown in Fig. IV-18. The α/ϵ ratio of 0.51/0.5 was selected for the mission. The maximum and minimum temperatures of the arrays for the 0.51/0.5 α/ϵ ratio are 140° and -100° F, respectively for in-the-sun operation. Figure IV-19 shows the temperature decay of the sensor and supporting frames during the shadow period. Since the arrays consist of little mass and have a large radiating surface the temperature, decay is very rapid. At the

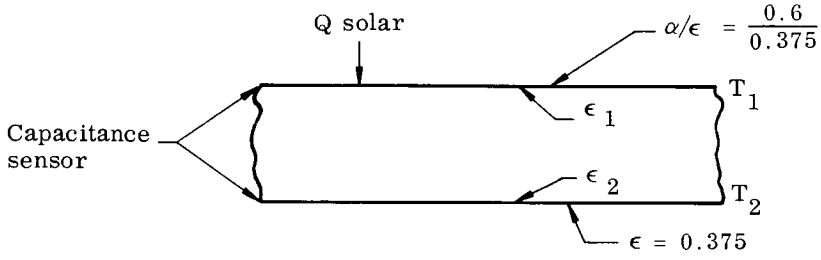

Temperature (°F)	ϵ_1 and ϵ_2	
	0.15	0.9
T_1	310	230
T_2	100	160

Fig. IV-17. Temperature of Capacitance Sensor Without Baffle

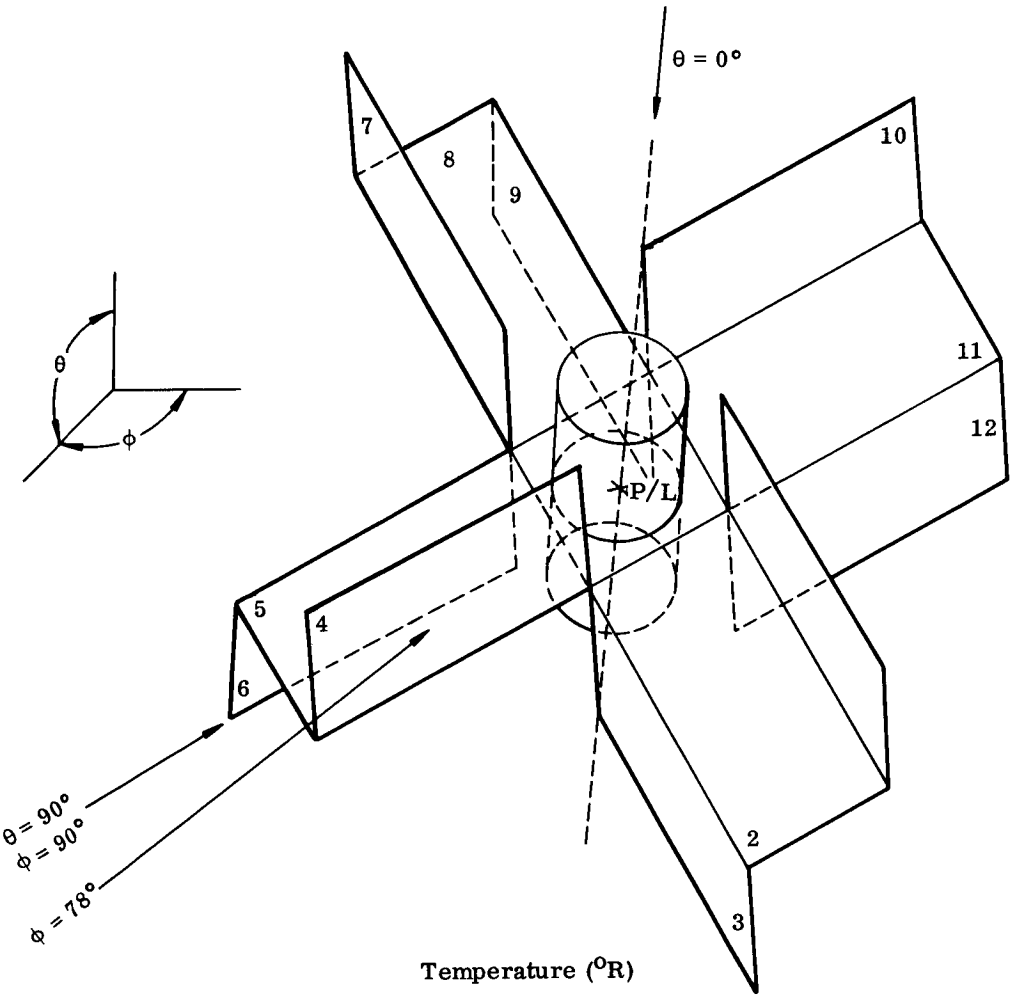

Temperature (°R)

α/ϵ = 0.60/0.375

	θ	ϕ	T_1	T_2	T_3	T_4	T_5	T_6	T_7	T_8	T_9	T_{10}	T_{11}	T_{12}
Spin	0	--	405	676	311	405	676	311	405	676	311	405	676	311
Spin	90	90	575	361	575	575	361	575	575	361	575	575	361	575
Spin	180	--	314	676	400	314	676	400	314	676	400	314	676	400
Tumble	90	90	379	610	378	587	560	587	384	611	382	587	562	587
Lower half of payload in shadow	90	78	658	386	648	301	251	281	551	344	648	509	369	509

α/ϵ = 0.5/0.5

Spin	0	--	384	602	300	384	602	300	384	602	300	384	602	300
Spin	90	90	516	343	516	516	343	516	516	343	516	516	343	516
Spin	180	--	302	602	379	302	602	379	302	602	379	302	602	379
Tumble	90	90	360	545	359	526	504	526	365	546	364	526	505	526
Lower half of payload in shadow	90	78	587	367	577	289	242	270	492	327	576	464	352	465

NOTE:

All values in °R.

Fig. IV-18. Capacitance Sensor Array Temperatures

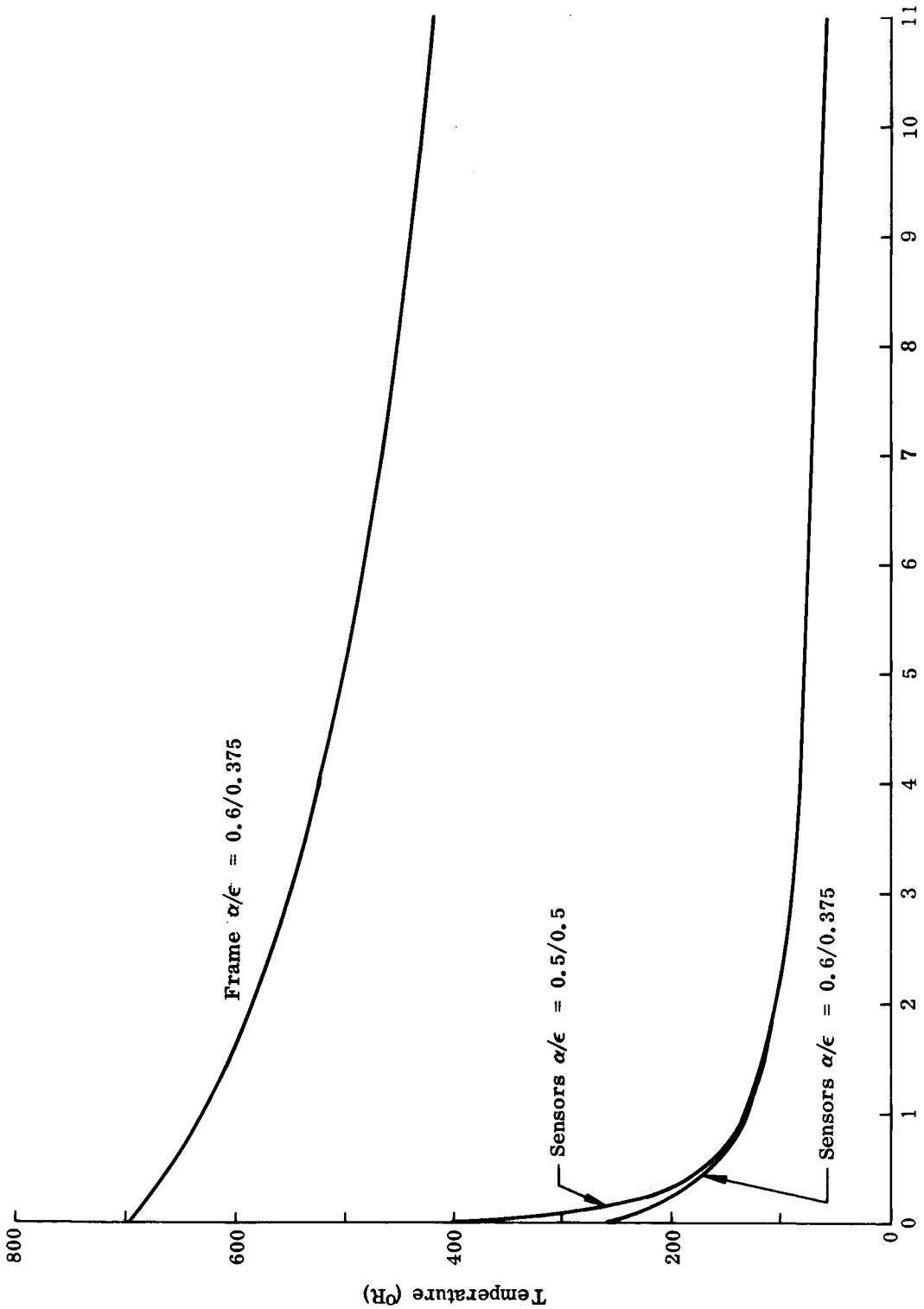

Fig. IV-19. Sensor Array and Frame Temperature Decay Versus Time in Shadow

end of 4 hr all the arrays have decreased to -380° F while the sensor array frame has decreased only 170° F. The -380° F is beyond the range of sensors that have been tested but it is felt the -380° F will not affect the sensor performance. The springs which attach the sensor arrays to the frames prevent the differential expansion between the sensor and frame from causing structural failures. Figure IV-20 presents the results of a detailed analysis to determine the temperature distribution of the sensor array frame. As shown the temperature gradient in the box beam is only a maximum of 1° F. The temperature of the frame opposite the incident solar radiation is approximately 20° F lower than the sensor array for both values of the α/ϵ ratio investigated.

Figure IV-21 presents the results of the ascent heating analysis for the separately supported sensor arrays. At the end of 250 sec where the ascent shroud is jettisoned, the maximum sensor temperature is 614° R (154° F)--well within the allowable temperature. Figure IV-22 presents the solid core-type capacitance sensor during ascent. As would be expected, its temperature increase is much less than that of the separately supported sensor. Its maximum temperature during ascent is 550° R (90° F).

An analysis of the sensor array with the baffle plate is shown in Fig. IV-23. The temperature distribution through the sensors and baffle is shown for two values of the ratio of k/x thermal conductivity/ baffle thickness. The k/x value of 4.0 is equivalent to a 1/4-in. thick baffle of polyurathane foam.

The temperature time history of the solar cell array is shown in Fig. IV-24 for the maximum and minimum temperatures entering the earth shadow. After 4 hr in the shadow, the minimum temperature is 185° R (-275° F) which is considered within the operating range of the solar cell array.

A detailed analysis of the secondary sensors was not made during this study primarily because detailed physical characteristics of these sensors were not available.

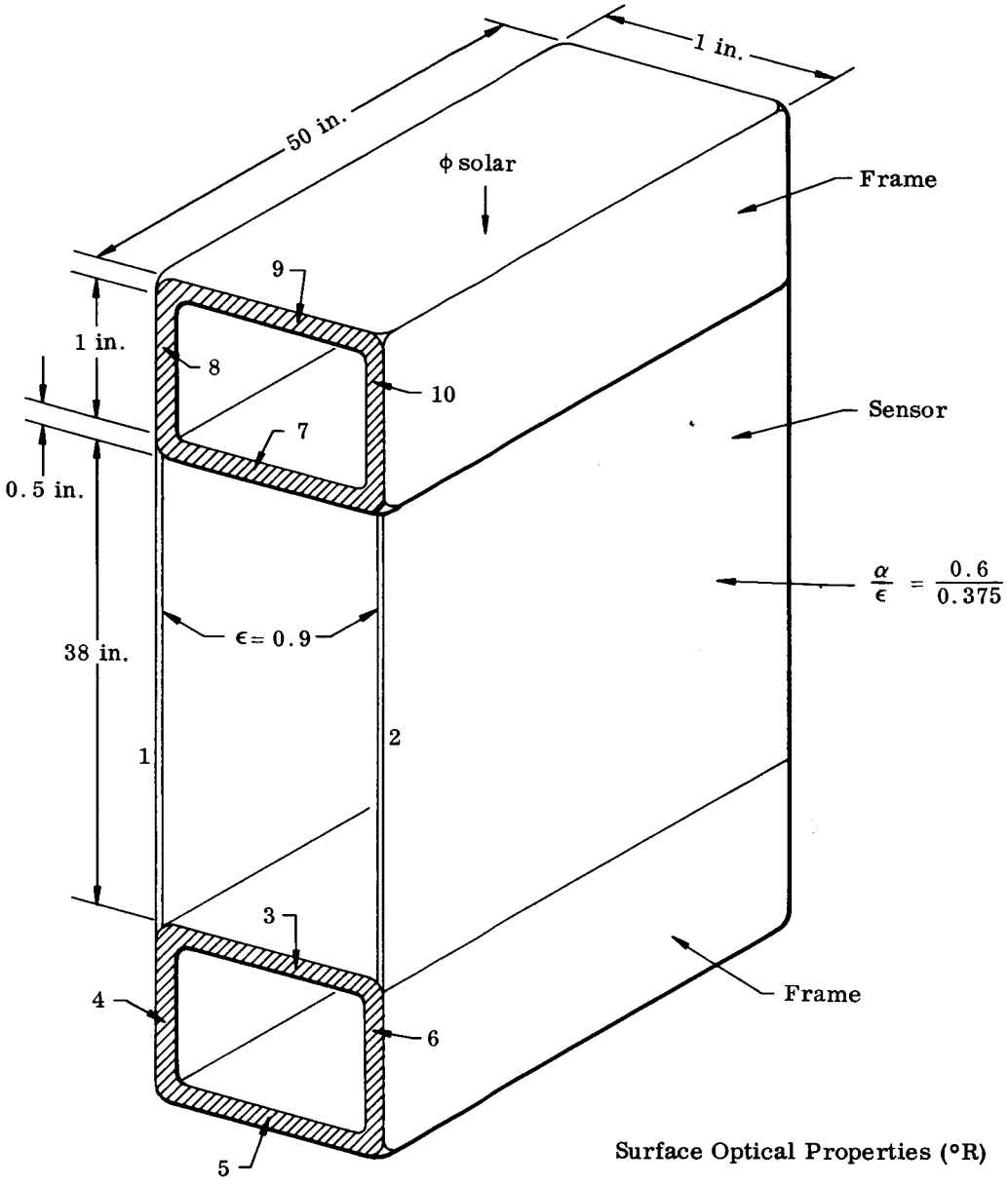

Surface Optical Properties (°R)

	$\left(\frac{\alpha}{\epsilon}\right)_n = \frac{0.6}{0.375}$ n = 3 to 10	$\left(\frac{\alpha}{\epsilon}\right)_n = \frac{0.4}{0.05}$ n = 3 to 10
(1)	300	300
(2)	300	300
(3)	282	279
(4)	282	279
(5)	282	279
(6)	282	279
(7)	620	714
(8)	620	714
(9)	621	715
(10)	620	714

Fig. IV-20. Temperature of Capacitance Sensor Frames

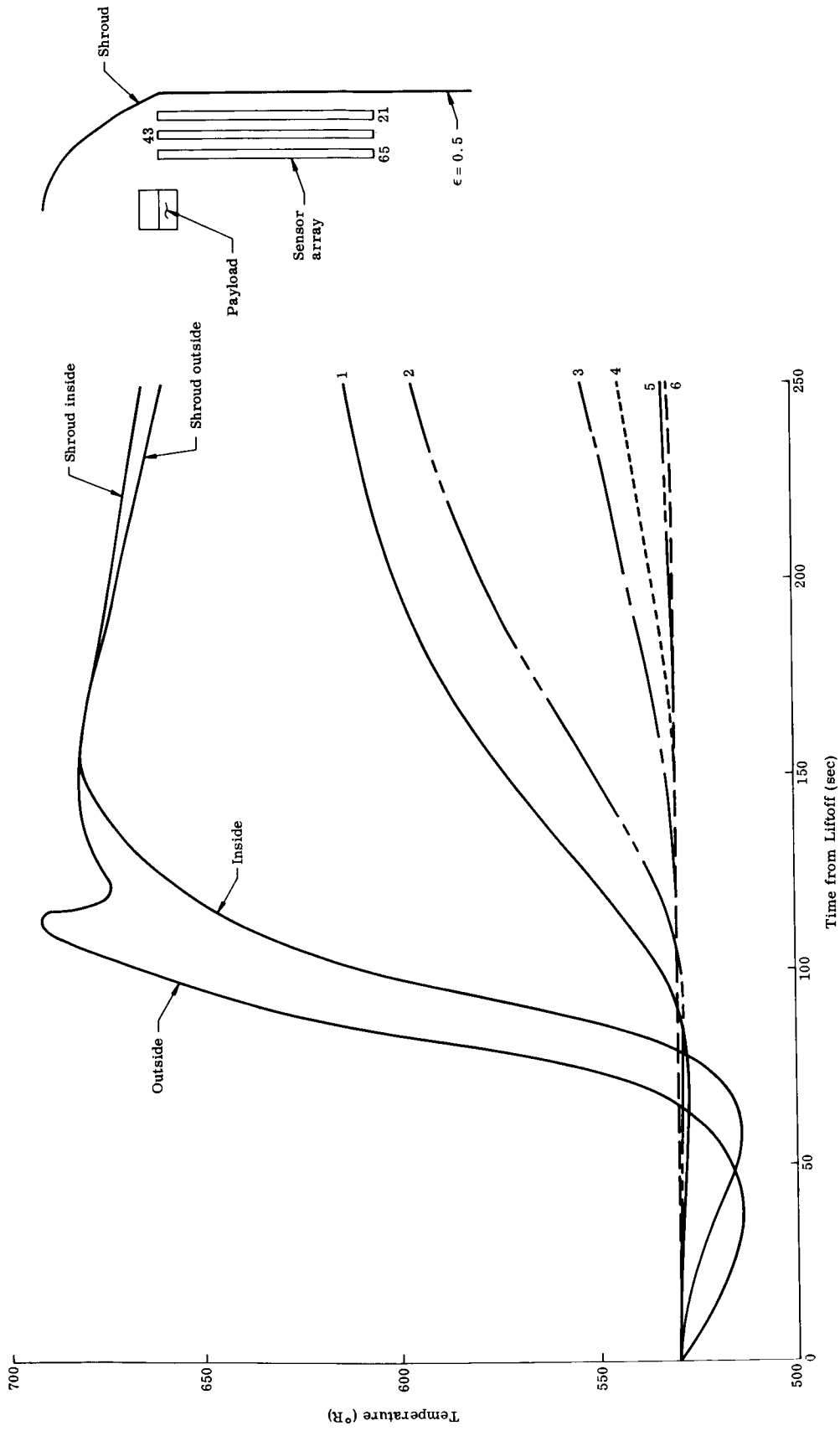

Fig. IV-21. Sensor Array and Shroud Temperature Versus Time From Liftoff: Without Baffle

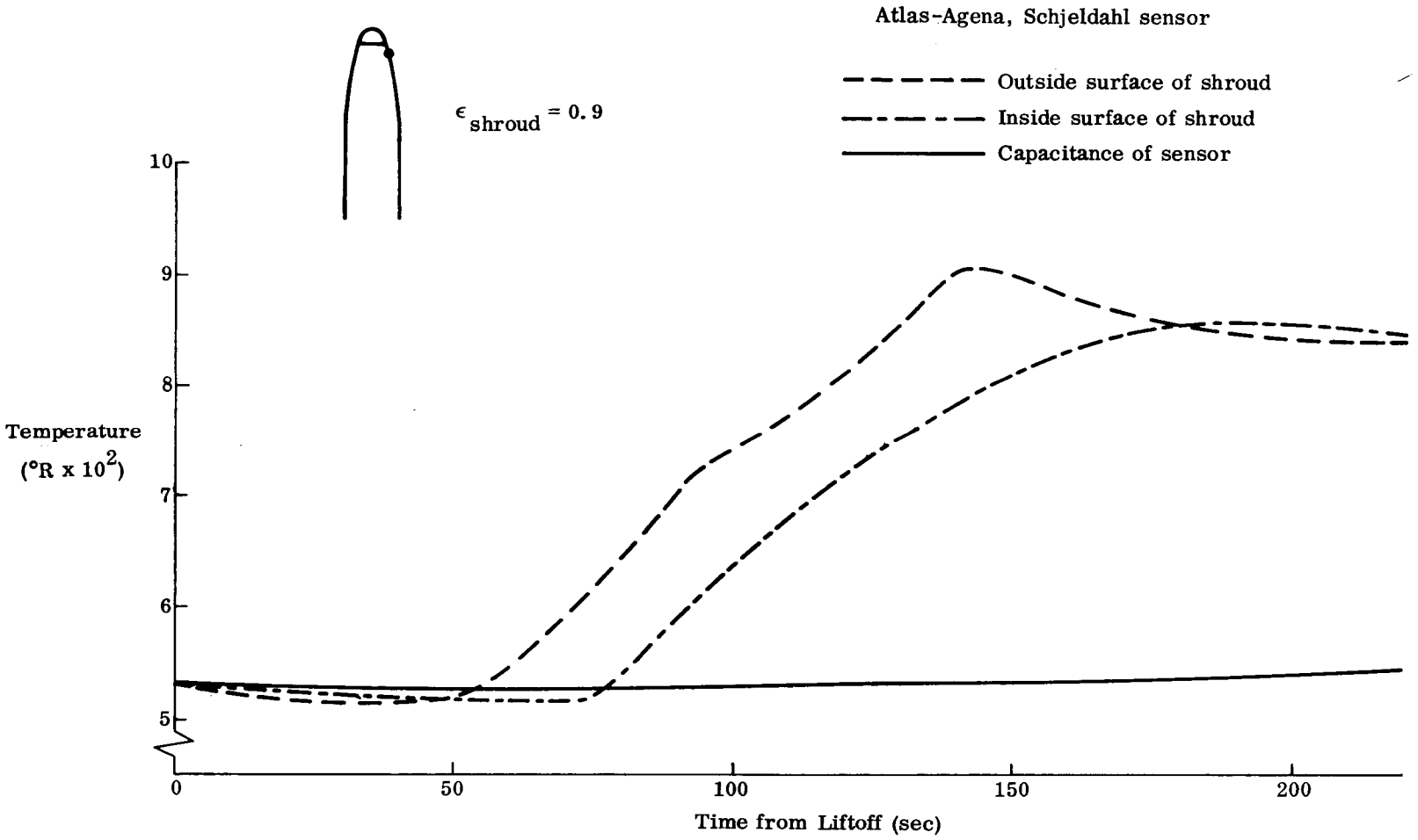

Fig. IV-22. Sensor Array and Shroud Temperature Versus Time from Liftoff

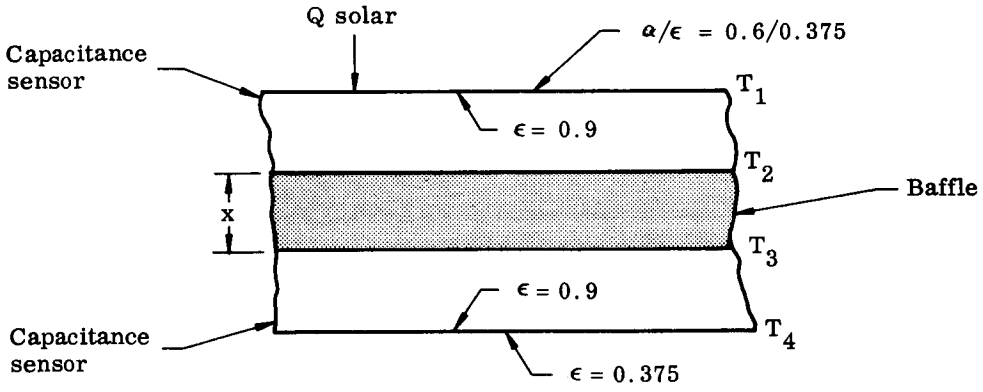

Temperature (°F)	k/x of Baffle 4.0	0.4
T_1	266	281
T_2	222	248
T_3	204	173
T_4	144	116

Fig. IV-23. Temperature of Capacitance Sensor with Baffle

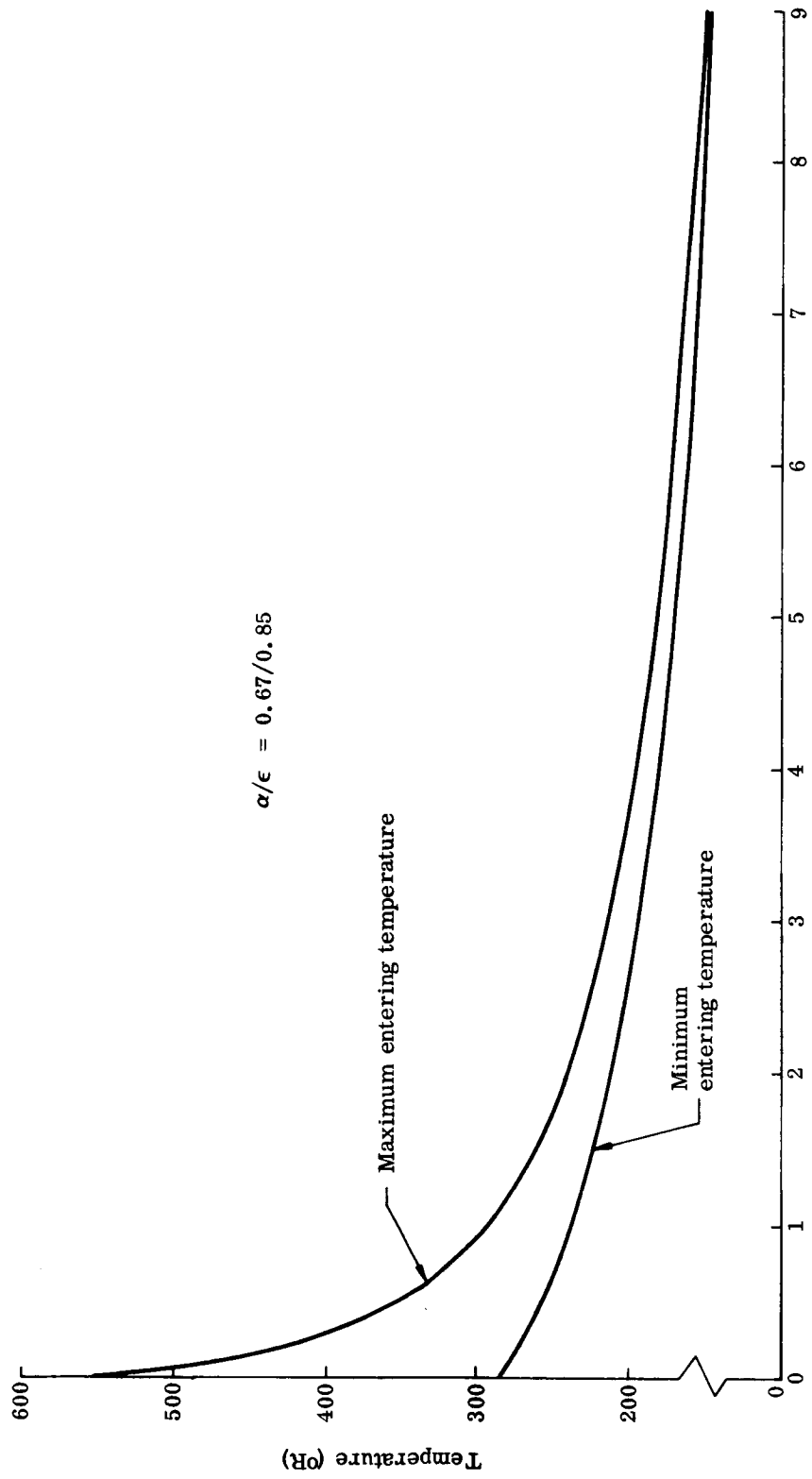

Fig. IV-24. Solar Cell Temperature Decay Versus Time in Shadow

APPENDIX IV-1

A. IBM 7094 COMPUTER PROGRAM, "SOLUTION OF STEADY-STATE SURFACE TEMPERATURES AND ABSORPTION FACTORS WITH REFLECTED THERMAL RADIATION"

This program computes the temperature of 70, or less, surfaces, considering reflected solar and IR radiation between all surfaces. The basic equations used for the solution are:

$$q_j = \sigma \epsilon_j A_j T_j^4 - \sum_{j=1}^{n} \sigma \epsilon_i A_i T_i^4 B_{ij} \qquad \text{(IV-1)}$$

$$B_{nj} = F_{nj} \epsilon_j + F_{n1} \rho_1 B_{1j} + F_{n2} \rho_2 B_{2j} \cdots F_{nn} \rho_n B_{nj} \qquad \text{(IV-2)}$$

where

q = net heat absorbed or emitted by the surface

A = area of surface

T = temperature of surface

B_{nj} = that fraction of radiant heat leaving surface (n) that is absorbed at surface (j) after all reflections

F_{nj} = view factor from (n) to (j)

ϵ = emissivity

ρ = $(1 - \epsilon)$

σ = Stefan-Boltzmann constant

B. IBM 7094 COMPUTER PROGRAM, "SPACE VEHICLE THERMAL ANALYSIS"

This program computes the transient and steady-state temperature of 140 elements, or less, considering conduction, radiation and convection heat transfer.

The equation used for the solution of conduction and radiation is:

$$\frac{MC_p}{\Delta t} T_{E_f} = \frac{MC_p}{\Delta t} T_{E_i} + \frac{1}{2} \left[q_{L_i} + q_{R_i} + q_{T_i} + q_{U_i} + q_{F_i} + q_{B_i} + q_{C_i} - q_{rad} + q_{rad\ in_i} + q_{A_{1_i}} + q_{A_{2_i}} + q_{K_i} \right] + \frac{1}{2} \left[\begin{array}{l} \text{same terms but at final time (f)} \\ \text{during computing interval} \end{array} \right]$$

where

M = mass

C_p = specific heat

T_E = temperature of element

Δt = computing interval

q_L, q_R, q_T, q_U, q_F and q_B = the conduction heat transfer to the element in the form $q_L = A_L U_L (T_L - T_E)$

q_{rad} = radiation from the element to space, $\sigma \epsilon T^4 A$

$q_{rad\ in}$ = incident radiation from the sun, albedo and parent body emitted

q_{A_1}, q_{A_2} = radiant energy exchange with other elements in the form $q_{A_1} = A_1 B_{EN} \epsilon_1 (T_n^4 - T_E^4)$ where B_{EN} is absorption factor

q_C = convective heat transfer to fluid, $q_C = h_L A_C (T_L - T_E)$

q_K = heat generated within the element

Subscripts

L = element on left

R = element on right

T = element on top

U = element on bottom

F = element on front

B = element on back

i = initial time

f = final time

V. ATTITUDE SENSING AND DETERMINATION

James J. Hinson
John C. Donohue

V. ATTITUDE SENSING AND DETERMINATION

The primary mission of the Micrometeoroid Deep Space Satellite (MDSS) is to obtain micrometeoroid penetration rate data as a function of altitude from the earth. Attitude sensing and determination is not required in accomplishing the primary mission. As a secondary objective, micrometeoroid velocity and directionality data is desired, particularly for those particles captured by the velocity gage. To accomplish this, orientation of the vehicle with respect to celestial space must be known.

The sensing system used for determining vehicle attitude is dependent upon vehicle motion expected during the mission, orientation requirements during the mission, orbit characteristics and desired orientation sensing accuracy. In some missions, for example, it may be desired to maintain a sun or earth orientation during most of the mission and, therefore, the attitude sensing system would probably employ a null-type sun sensor and, perhaps, a solar pressure control system. There is no requirement to maintain a selected space orientation nor to perform any specified re-orientations. From a vehicle dynamics point of view, the main requirement is for the vehicle not to have a preferred orientation or axis of rotation. Among approaches considered for attitude determination in the early phases of the study were: to employ a spin-stabilized vehicle, to provide an active control system for either providing a selected space orientation or controlled tumble, and to allow the vehicle to be uncontrolled in its rotational motion. From an attitude determination standpoint, the spinning configuration offers the simplest approach, while the uncontrolled vehicle presents the most challenging problem. All approaches were investigated and the uncontrolled approach selected primarily on the basis of constraints established as ground rules early in the study.

The design philosophy has been based on using off-the-shelf components, minimum system redundancy to ensure the success of obtaining attitude information and use of passive attitude sensing devices at the expense of performance degradation.

Dynamic analysis of the motions of several configurations has been conducted using an IBM 7094 digital computer program developed during the study. This portion of the study was undertaken in an effort to understand the effect of the field forces--such as differential gravity, solar pressure, aerodynamics and magnetic forces--on body motion. The particular configuration used in the analysis influences the resultant motion, since inertia ratios, vehicle magnetic dipole, and center of pressure-center of gravity locations influence the magnitude and direction of the applied torque from the force fields. Although the extent

of the analysis on the "Z" configuration was limited because of time and budget restrictions, certain conclusions were drawn. The cp-cg distance for the "Z" and the projected area vary with look angle, which, in effect, causes solar pressure torques and aerodynamic torques to vary. As a result, the "Z" configuration under certain conditions has a tendency to develop a spin rate about the longitudinal axis. This fact has been demonstrated in limited computer runs and, therefore, the maximum spin rate over the mission lifetime has not been determined. This must be further investigated to define the bounds of the spin and to evaluate the effect of this spin on other subsystems.

1. System Requirements

Attitude determination requirements are imposed by two of the secondary MDSS mission objectives, which are: to determine general directionality of meteoroid impacts on the penetration gages, and determine the micrometeoroid velocity and direction as a function of altitude.

General orientation requirement established by the directionality objective in connection with the penetration gages has been estimated to be 25° to 30°. The source of this requirement is based on obtaining a sufficient number of impacts during the mission. Using the attitude data, a statistical analysis can be conducted to determine the directionality of the impact.

The velocity sensor planned for the MDSS is the GSFC velocity tube which has three orthogonally mounted sensors. Geometrical construction of the tubes is such that an acceptance angle of $\pm 5°$ is generated, which is the inherent directionality accuracy of the unit. This instrument has a 2-mc oscillator for timing the meteoroid during the period from tube entrance to impact of the capacitance gage 10 cm away. Expected velocities of the micrometeoroids are between earth escape speed and 70 km/sec. Using the relative velocity of 11 km/sec at perigee, the time to traverse the tube is 0.909×10^{-5} seconds. Since the timer is capable of timing to 0.5×10^{-6} sec, the equivalent velocity error for this condition is approximately 1920 fps.

The velocity measurements are sensitive to sensor space orientation with respect to the vehicle orbital velocity at time of measurement. Satellite velocity at perigee, typically, is approximately 35,000 fps, while the anticipated minimum velocity of the meteoroids at perigee is 36,000 fps. It is imperative, to measure meteoroid velocity, to know the component of vehicle velocity in the sensor direction.

An examination of the GSFC velocity tube inherent accuracy, with respect to acceptance angle and oscillator limitations, has been conducted at perigee and apogee of a typical MDSS orbit. It was found,

using escape speed for meteoroid velocity, that the timer was the limiting factor on velocity accuracy. The equivalent velocity error of the timer, a function of the angle between the vehicle velocity direction and the sensor axis, has been converted into an equivalent attitude accuracy. A plot of the attitude accuracy required for both perigee and apogee is shown in Fig. V-1. Depending on the orbital condition and the angle between vehicle velocity and sensor axis, the required attitude accuracy varies between 0° and 36°. Since no absolute meteoroid velocity accuracy requirement has been generated in the study, a companion plot is shown in Fig. V-1 for the attitude accuracy required to give a 10% accuracy on meteoroid velocity. It should be noted that these curves apply to meteoroid velocities at escape speeds. If the meteoroids have higher velocities (the more probable case) the attitude accuracy requirements are reduced, allowing increased errors in the attitude determination system.

2. Possible Solutions

Unique attitude determinations at the time of micrometeoroid impact requires knowledge of two distinct space vectors. For a spinning vehicle, the angular momentum vector is intrinsically defined and, hence, measurement of the sun vector satisfies the necessary requirements for attitude determination. However, for a randomly tumbling vehicle, knowledge of another vector--such as the line of sight to earth or moon--is required. Practical solution of this task is further complicated due to a large orbit eccentricity which produces large variation in the earth subtense angle. With a controlled vehicle, either space fixed or employing a controlled tumble, narrow field of view sensors are feasible and attitude is known within a very good accuracy at all times but the system is more complex and has a weight penalty. The recommended approach from attitude determination considerations alone would be a spinning vehicle. Table V-1 indicates the advantages and disadvantages of the spinning, and uncontrolled and controlled tumbling approaches.

3. Constraints

Ground rules were established, during the course of the study, in joint meetings between Martin and NASA-LRC personnel, which influenced attitude determination system design. Since the requirement for attitude sensing is imposed by experiments which are of secondary importance in terms of mission objectives, the following constraints were placed on system design.

(1) Spinning vehicle not to be used unless required by subsystems other than attitude sensing.

(2) Passive techniques are preferred; if feasible, instrumentation with no moving parts should be used at the risk of performance degradation.

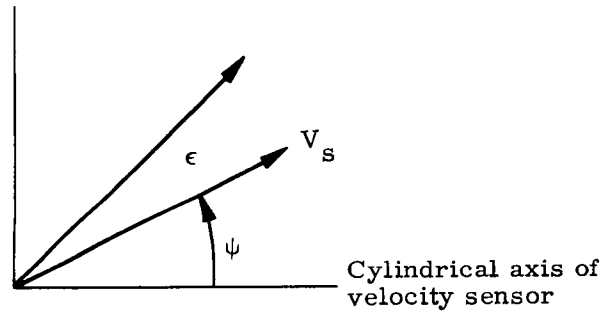

Equivalent attitude error of velocity tube accuracy versus ψ

Velocity of Micrometeoroid--escape speed

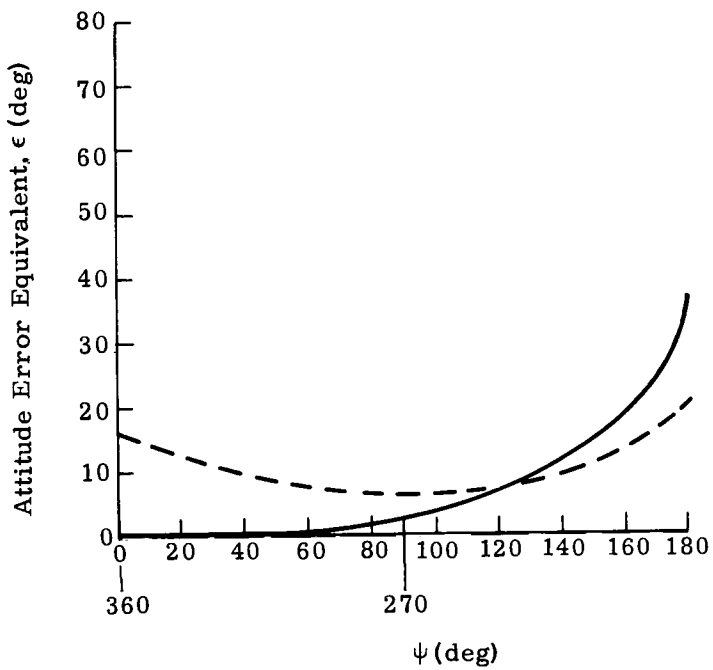

Equivalent attitude error allowing a 10% error in Micrometeoroid velocity

Velocity of Micrometeoroid - escape speed

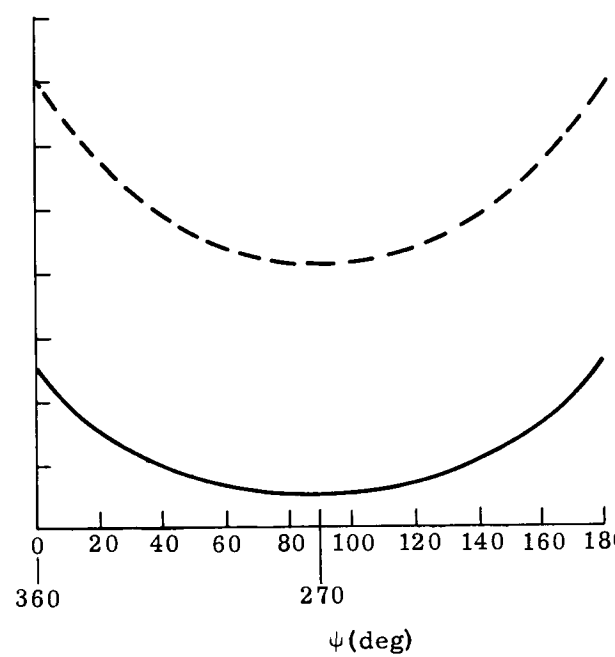

Fig. V-1. Attitude Determination Requirements

(3) Active control system should not be used.

(4) Redundancy should not be used to gain confidence in systems capability to obtain attitude data. Weight increase from this redundancy would be better utilized in other systems of the spacecraft--e.g., in increased sensor area.

(5) Completely independent attitude loops shall be used in the data handling and communication systems, including the memory storage unit.

With the above constraints and after evaluating the advantages and disadvantages of a spinning versus a tumbling vehicle on the performance of other subsystems, such as thermal and electrical power, the tumbling or uncontrolled approach was selected.

TABLE V-1

In-Orbit Attitude Sensing and Control

Spinning
- Eases sensing problem and telemetry requirements
- Guarantees stable attitude
- Antenna tracking problem eased
- Thermal control problem
- Data gathering deficiency

Uncontrolled tumbling
- Data gathering enhanced
- Thermal control problem eased
- Attitude sensing difficult
- Attitude motion (tumble rate and direction) unpredictable
- Antenna tracking difficult

Controlled tumbling
- Data gathering assured (proper orientation)
- Thermal control problem eliminated
- Requires semiactive system
- Antenna tracking difficult

4. Study Approach--Design Philosophy

The uncontrolled vehicle design selection as a result of the constraints enumerated in the preceding paragraph generated a difficult attitude sensing requirement. It was decided early in the program to use the sun as one of the basic reference sources and, further, to use one of the solar aspect sensing systems which had been demonstrated in space. Since the uncontrolled vehicle approach was to be used, answers to two basic questions were required:

(1) What is the dynamic motion of the vehicle in orbit?

(2) What reference other than the sun would be used and how would it be sensed?

To answer the first of these questions, an IBM 7094 computer program development was initiated which, in its final form, included effects of the known sources of disturbing torques, characteristics of the selected vehicle configuration, and characteristics of the orbit which the vehicle would traverse. Motion dynamics would be studied by examining the effects of each disturbing torque and, later, by including all disturbance sources. Such a program is complex and, by necessity, uses a great deal of computer running time. Therefore, restrictions had to be placed on the total number of runs made to investigate vehicle motion. It was felt that, since the booster and vehicle configurations were not finalized, a complete parametric study using the developed program was not justified. The approach was to make illustrative runs to understand the course of the vehicle motion and to develop typical vehicle motion time histories over the early part of the mission.

To answer the second question, a review of available literature was conducted and sensor manufacturers such as Barnes Engineering, Advanced Technology Laboratories and Adcole were contacted and the sensor problem discussed. The earth was selected as the second basic attitude reference source, and attempts were made to sense its source of radiation both in the optical and infrared regions. After extensive review of the requirements, it was concluded that achievement of 4π steradian coverage was beyond the state of the art in earth sensors. This coverage was desired in order to be able to sense attitude data at the time of a micrometeoroid hit on the vehicle. Several approaches, consisting of modifications to present sensors and a developmental program, were suggested by both Barnes and ATL to meet coverage requirements. In most of the approaches, moving parts were involved and some basic technical questions would have to be answered through tests in the development program. Other approaches, which included use of inertial components, use of a selected antenna pattern and viewing it from the receiving station, and use of the earth magnetic field, were under parallel consideration. Inertial components when applied to an uncontrolled vehicle, generally become complex, with multiple gimbals required. Use of relatively new concepts, such as all-axis air-bearing suspension sphere systems, were considered but found to be operational beyond the time period required. Determination of vehicle attitude by viewing a selected antenna pattern (used on Explorer II) was eliminated from consideration, since antenna requirements do not lend themselves to this form of mechanization. The magnetic field of the earth has been measured at the surface, in selected areas, on many occasions. Recent measurements by Vanguard, Explorer X and IMP satellites have been successfully compared to the various analytic models of the earth's field, at least out to seven to

ten earth radii. After considerable study and review of their comparisons, it was concluded that the earth's magnetic field could be used as a source of measurement from which vehicle attitude could be determined. Because of the limited region over which satellite measurements had successfully compared with calculated values, some other technique would be required for the remainder of the orbit.

Since obtaining 4π steradian coverage at any point in the orbit, using earth sensors, involved development programs and the probable use of moving parts, consideration was given to use of a predictive technique. This approach would make rapid attitude measurements over portions of the orbit, determine the torques causing this motion, then use a computer program to determine the attitude time history in portions of the orbit in which sensor data is not available.

Previous satellite motion and attitude sensing. Most unmanned satellites have, to date, employed some form of spin stabilization. Some of these, such as Explorer XI, were initially spinning about their axis of minimum inertia and began to tumble as a result of dissipated energy losses. Spin rates have varied from 10 to 150 rpm, depending on satellite requirements. The rate of spin usually decays in time, and the vehicles usually develop a spin axis precession, or wobble, due to disturbing torques (TIROS precesses about 4° per day). Spin-stabilized satellites have employed solar aspect sensors, earth IR sensors and antenna pattern recognition for sensing vehicle attitude. Several of the spin-stabilized vehicles employ either jets or magnetic coils (Telstar, Relay, TIROS) to maintain control over the spin axis orientation.

Many of the more recent satellite programs are employing some form of three-axis control through use of reaction jets or reaction wheels and their combination (OGO, OAO, Mariner, Discoverer). Motion of these satellites is usually highly restricted to either a celestial or earth orientation. Sensors used have included coarse and fine eye sun sensors, IR earth scanners, rate integrating gyros, optical earth sensors and star trackers.

Motion prediction experience. References V-1 and V-2 present some of the experience which exists in predicting the causes and results of angular rotations of satellites. Naumann (Ref. V-1) has determined the torques acting on several Explorer satellites by observing the change in orientation of the satellite. In those satellites observed, the permanent magnetic moments were primarily responsible for the motion observed. However, gravitational torques were also found to be significant. In Explorer IV, VII and XI, recorded radio strength patterns were used to obtain the observed attitude data. Observed data were fitted in segments by polynomials which were differentiated in time to yield the torques causing the motion. The gravitational torques were subtracted from these, and the resulting torques were fitted with both permanent and induced magnetic moments.

Fig. V-2 presents a comparison between the observed motion and the predicted motion, obtained by determining the torques acting on the vehicle. Excellent agreement is obtained from day 26 through day 90. Similar techniques were applied to Explorer IV, although the amount of observed data is limited. Again, it was found that the permanent magnetic moment was primarily responsible for the observed motion. Explorer VIII utilized a solar aspect angle measuring device and an earth sensor. The solar aspect data were checked again by assuming a certain magnetic torque and the effects of the gravitational torques on the integrated motion. Results over a period of 30 days compared extremely well with the observed data.

With the experience gained by Naumann and others, and using particular care in determining the moments of inertia, magnetic moments, center of gravity and center of pressure locations prior to flight, it is felt that the rotational behavior of satellites can be predicted. Using onboard measurements made in certain regions of the orbit, the torques acting on the vehicle can be determined and integrated over the mission to predict the attitude time history. The accuracy of this approach depends on obtaining data spread over the orbit such that the torques primarily responsible for vehicle motion can be determined.

Attitude sensors. After considering the problem associated with earth IR and optical sensors, and reviewing the success of satellite rotational motion prediction, the following design approach was selected. Three-axis magnetometers were investigated to ascertain the accuracy with which vehicle attitude could be determined between perigee and seven to ten earth radii. The simplest form of earth sensor would be used to obtain additional data during other portions of the orbit, depending on vehicle dynamics to scan space. Solar aspect sensors would be used throughout the orbit. This sensor complement, along with prediction techniques, provides the simplest possible approach to attitude determination for the MDSS.

A parallel effort was followed on more elaborate earth sensors, which would be capable of providing full orbit coverage and greater accuracy in attitude determination. Addition or substitution of these sensors into the baseline system, with a minimum effect on other subsystems, was a design goal.

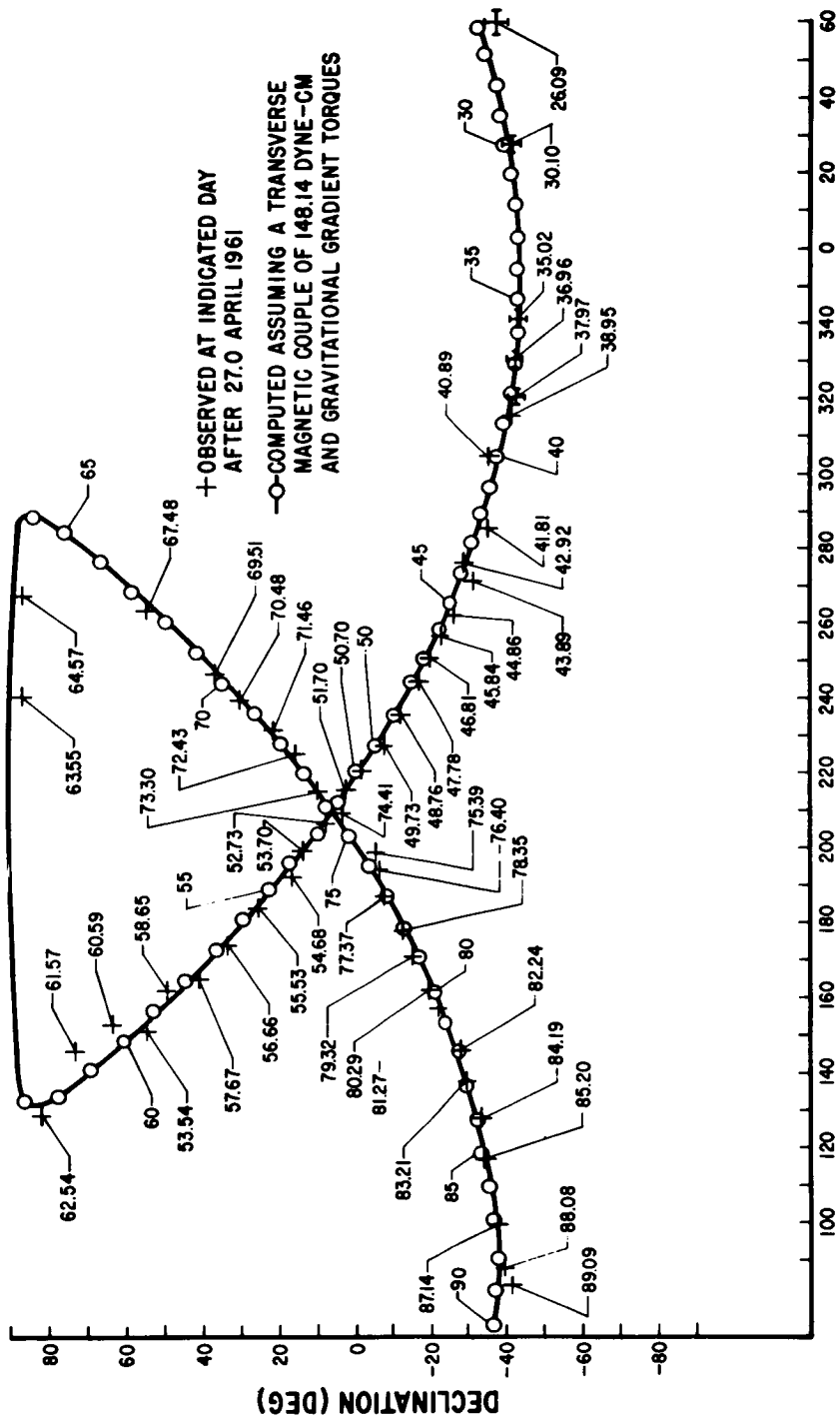

Fig. V-2. Computed Orientation of Explorer XI Compared to Observations for Day 26 to 90

A. RECOMMENDED SYSTEM AND CONCLUSIONS

The recommended system of sensing the attitude of the micrometeoroid deep space satellite consists of sun aspect sensors, 3 axis magnetometers, IR earth sensors, and appropriate electronics. All components are either space proven or will be prior to the operational date of the MDSS. This system offers the best compromise, using existing sensors, between attitude determination accuracy and system simplicity of all the systems studied. The basic concept depends on obtaining sensor data during portions of the orbit and at discrete points along the orbit, then using this data along with a ground-based computer to determine the attitude at any time. The computer program will simulate vehicle dynamics, and adjust various parameters in the program until the attitude time history matches the sensor data.

There are two modes of operation: a full attitude mode near perigee, and an hourly attitude mode for the remaining orbital period. Data during both modes are transmitted on the secondary telecommunication system.

Magnetometer readings are obtained during the full attitude modes along three mutually perpendicular axes. An error analysis of the effects of the residual magnetic characteristics of the vehicle has been conducted to examine the accuracy limitation. This analysis indicates that, to obtain vehicle attitude in an accuracy of ± 5 degrees, the residual equivalent magnetic dipole of the vehicle must be less than 10 gamma.

1. System Description

A functional block diagram of the attitude sensing subsystem is shown in Fig. V-3.

Attitude sensors--description and operation. Digital solar aspect sensors consist of the Adcole Model 133E operating in conjunction with the Adcole Model 233C shift register and solar aspect sensor processing electronics. The sun sensor field of view is $\pm 64°$ in two mutually perpendicular axes. The sensor determines two angles which define two planes, each containing the sun. The intersection of the two planes defines the line pointing at the sun. A total of five sensors are required for 4π steradian coverage. A functional schematic of the operation of this aspect sensor is shown in Fig. V-4. Basic components of this unit consist of the slit, reticle, gray-coded pattern, silicon photocells, amplifiers and a buffer storage unit. The gray-coded pattern and the seven photo cells provide 2^7 (128) unique combinations of "zeros" and "ones" covering the 128° field of view in one-degree increments. From Fig. V-4, it can be seen that the angle of incidence of the sun determines the position of the slit image on the gray-coded pattern and, thus, which photocells are illuminated. Illuminated photocell outputs are amplified

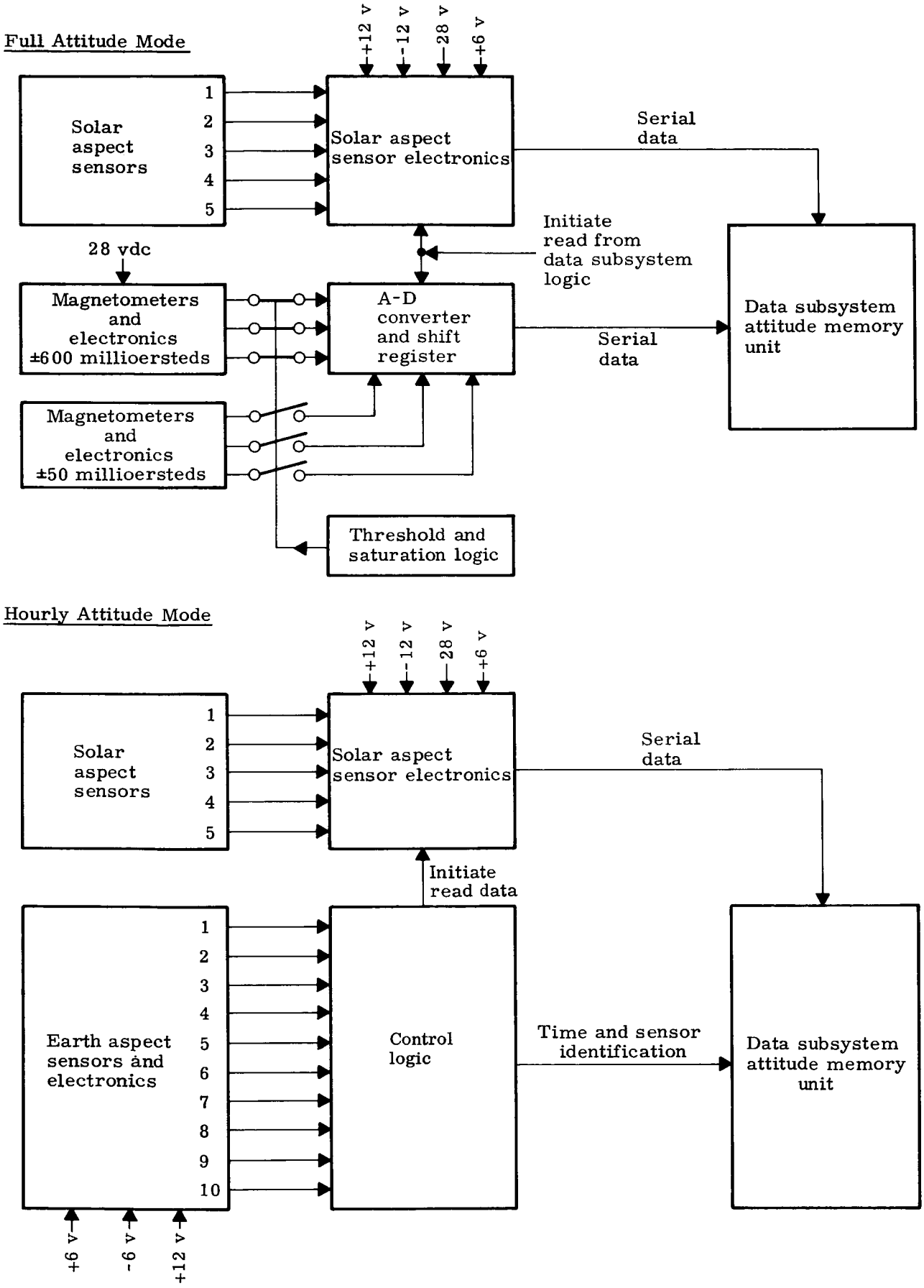

Fig. V-3. Functional Block Diagram

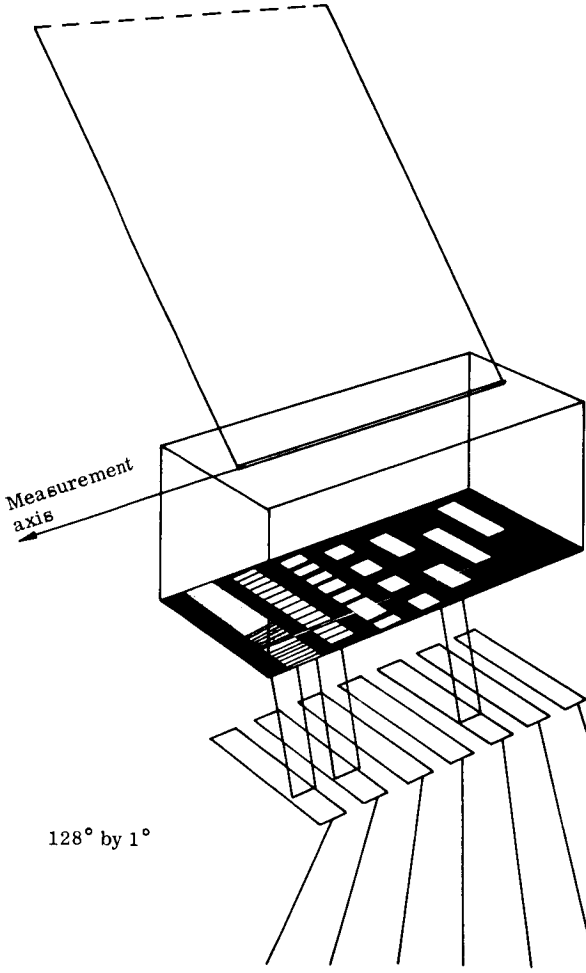

Decimal	Binary	Gray	
0	00000	00000	128°
1	00001	00001	127°
2	00010	00011	126°
3	00011	00010	125°
4	00100	00110	124°
5	00101	00111	
6	00110	00101	

Fig. V-4. Sun Sensor Operation

and sent as a "one" to buffer storage. The seven-bit digital word uniquely defines the aspect angle. Two such slits, mutually perpendicular for ± 64° coverage in two planes, are incorporated in the Adcole Model 233C. The five sensors are located on the vehicle with two sensors viewing perpendicular to a plane containing the remaining three and in opposite directions. The three sensors in the plane are accented such that the centers of their fields of view are 120° apart. Figure III-2 shows the installation of these sensors on the MDSS configuration. A block diagram of the sun sensors and electronics is shown in Fig. V-5. Solar aspect data are processed by the solar aspect electronics unit. For the five-sensor configuration, switches are used for each bit on each sensor. After receiving a read command, these bits are sequentially scanned until the illuminated sensor is identified. Outputs of the solar cells of the illuminated sensor are amplified and stored in the sun sensor shift register as either "zeros" or "ones." These data are then read out serially into the data subsystem attitude memory unit upon command from the data subsystem.

The three-axis magnetometers consist of two sets of the type RAM 5-C manufactured by Schoenstedt Company. Each set contains three orthogonally-mounted flux gate sensors, with a separate electronics package required to drive the sensors and convert the sensor output to an analog voltage proportional to the magnetic field input signal. Each sensing element is a Permalloy core surrounded by primary and secondary winding. A 5-kc alternating current, sufficient to saturate the magnetic core material, is applied to the primary winding. In the presence of an ambient magnetic field with a component parallel to the axes of the core, an AC voltage rich in even harmonics (particularly the second harmonic) of the signal impressed on the primary winding is generated on one secondary winding of each sensor. The amplitude of this voltage is proportional to the magnitude of the magnetic field intensity applied to the flux gate sensor core and the phase of this signal, when compared to a fixed reference, depends on the angle between the magnetic field vector and the sensor positive magnetic axis. The output voltage for a ± 600 millioersted range sensor is defined by:

$$E = 2.40 + 0.004 H \cos\phi$$

where

E = output in volts

H = ambient field in millioersteds

ϕ = angle between the magnetic field vector and the sensor positive magnetic axes.

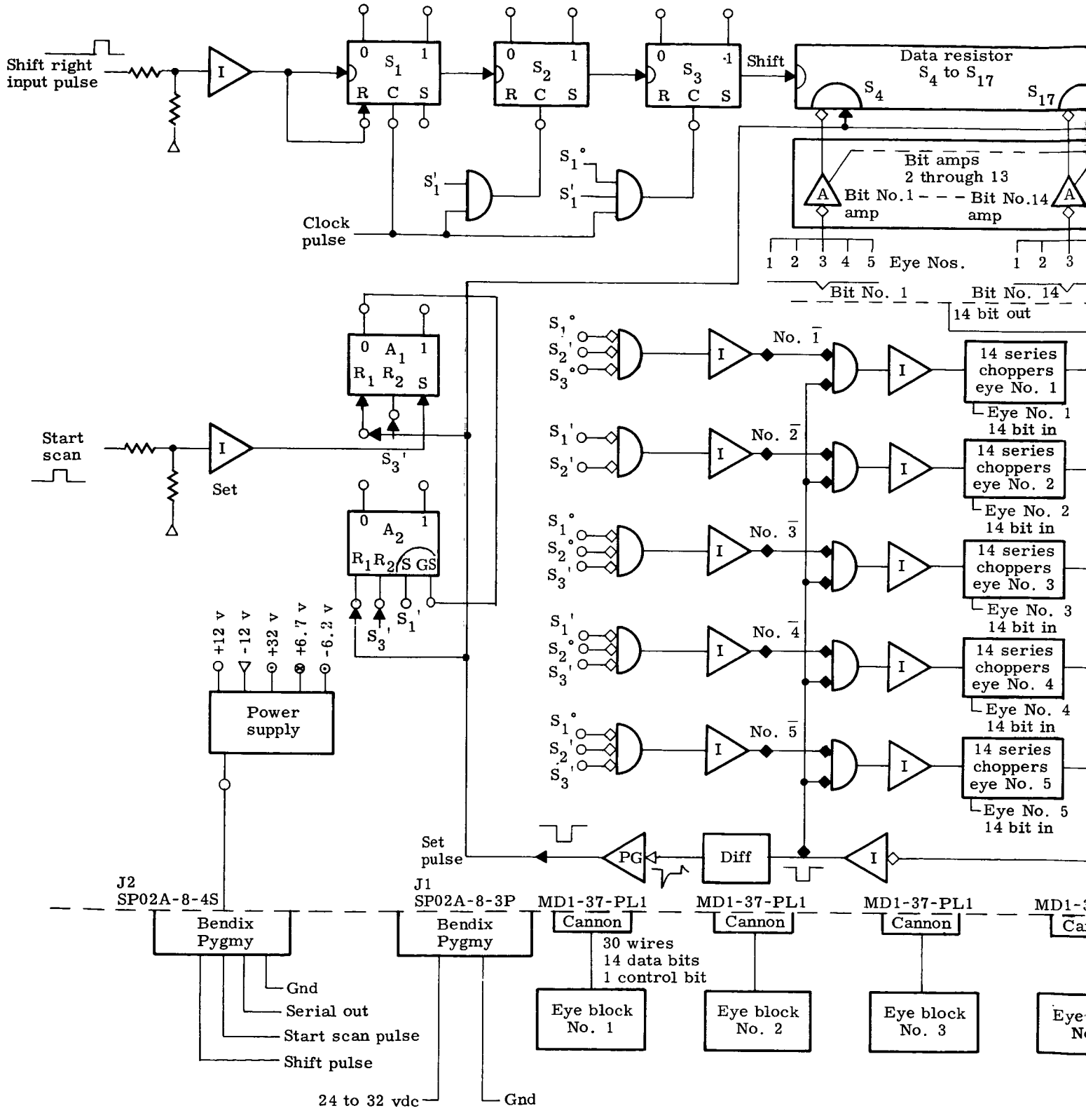
Shift right input pulse
I
0 S1 1
R C S
0 S2 1
R C S
0 S3 1
R C S
Shift
Data resistor
S4 to S17
S4
S17
Bit amps
2 through 13
A
Bit No.1 amp
Bit No.14 amp
A
Clock pulse
S1'
S1°
S1'
1 2 3 4 5 Eye Nos. 1 2 3
Bit No. 1
Bit No. 14
14 bit out
0 A1 1
R1 R2 S
Start scan
I
Set
S3'
0 A2 1
R1 R2 S GS
S3'
S1'
+12 v
-12 v
+32 v
+6.7 v
-6.2 v
Power supply
S1°
S2'
S3°
No. 1
No. 2
No. 3
No. 4
No. 5
14 series choppers eye No. 1
14 series choppers eye No. 2
14 series choppers eye No. 3
14 series choppers eye No. 4
14 series choppers eye No. 5
Eye No. 1 14 bit in
Eye No. 2 14 bit in
Eye No. 3 14 bit in
Eye No. 4 14 bit in
Eye No. 5 14 bit in
Set pulse
PG
Diff
J2
SP02A-8-4S
Bendix Pygmy
J1
SP02A-8-3P
Bendix Pygmy
MD1-37-PL1
Cannon
30 wires
14 data bits
1 control bit
Eye block No. 1
Eye block No. 2
Eye block No. 3
Gnd
Serial out
Start scan pulse
Shift pulse
24 to 32 vdc
Gnd

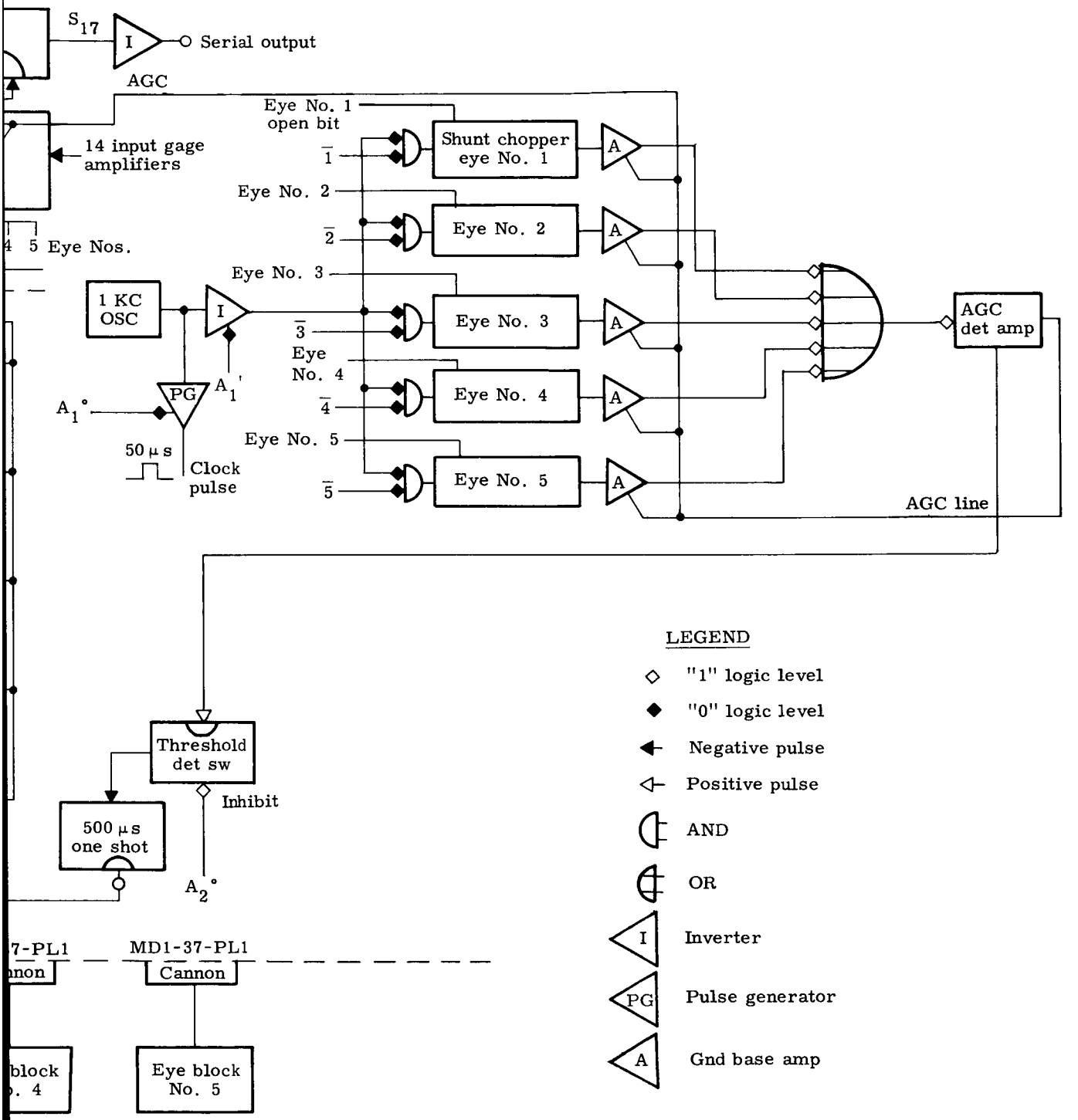

Fig. V-5. Solar Aspect System Logic Diagram

A block diagram of the magnetometer is shown in Fig. V-6. The output of the 5-kc oscillator is amplified and used to excite the primary coil of the sensor. The oscillator output, after being doubled, is also processed through a filtering, phase shifting and amplifying network, and used as the phase reference in the phase-sensitive rectifier. The output from the secondary winding is amplified, filtered and fed to the phase-sensitive rectifier. The signal output of the phase-sensitive rectifier is biased within the electronic unit at 2.4 volts, and is proportional to the input magnetic field.

An auxiliary coil is wound around each sensor core to compensate for permanent vehicle magnetic fields and to provide a means for in-flight calibration. The cancellation will be accomplished prior to launch by input current into the auxiliary coil after determining the vehicle field. The magnetometer will be checked during flight each time the attitude memory is read out and each time the data handling and communications system is on real time. This calibration is accomplished by applying a known current to the auxiliary coil and checking the sensitivity of the output.

The technical discussion on the magnetometer electronics has been reduced to one channel of one of the units. The remaining channels and the second unit are identical. Common channel electronics include the current regulator for ambient field cancellation, the 5-kc excitation and 10-kc demodulation reference voltage.

Based on determining attitude, to an accuracy of ± 10 degrees, from perigee out to seven earth radii, two sets of magnetometers are required, one with a ± 600 millioersted range and the other with ± 50 millioersted.

Model	Sensitivity (mv/millioersted)	Maximum Linearity Error 3% Full Scale (gamma)	DC Null Error Zero Field ± 0.02vdc (gamma)
MND-5C-50	48	150	42
MND-5C-600	4	1800	500

The above specifications are characteristic of each axis of the three-axis sets. The magnetometers are located on the outboard edges of the capacitance sensor panels as far removed as possible from any ferromagnetic material on the vehicle. Installation is shown in Fig. III-2.

Earth sensors consist of ten narrow field-of-view infrared sensors. The sensors are thermopile devices which make a DC differential meas-

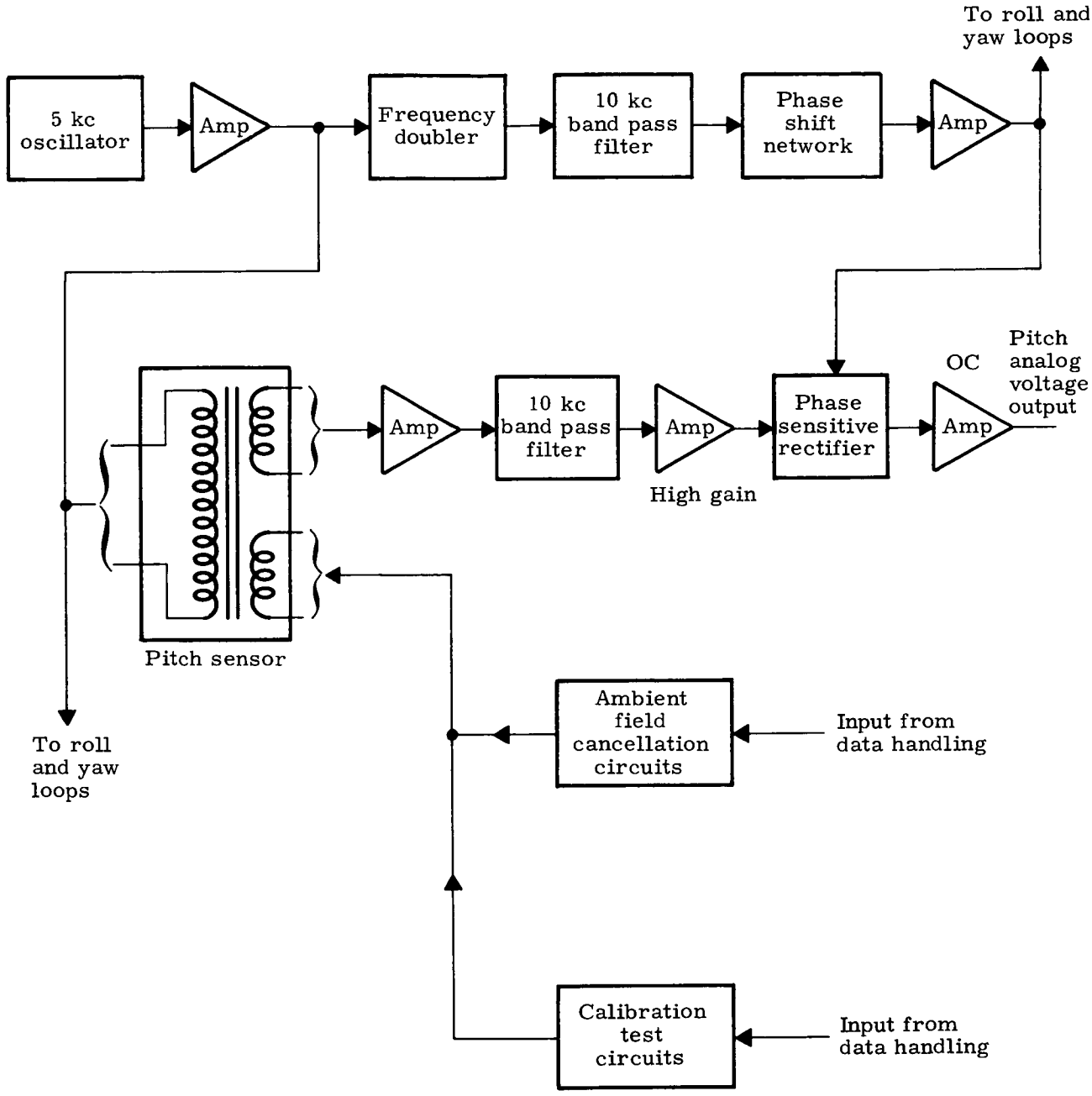

Fig. V-6. Magnetometer Sensing System

urement between opposing optical axes. The five units which incorporate the ten sensors are installed as shown in Fig. III-2. The detector output is a DC voltage in the microvolt range which must be amplified to usable levels. Figure V-7 is a block diagram of the earth sensor electronics. The photomodulator consists of a pair of NE-2 neon bulbs connected as a relaxation oscillator. Two photosensitive resistors (cadmium solenoid photocells) are bonded to each lamp. These elements undergo a resistance change of several orders of magnitude upon illumination. As the cells oscillate, they modulate the detector signal converting the low level DC signal from the thermopiles to an AC signal. This signal is then amplified through a high gain, low noise, AC amplifier, demodulated and filtered. The output of the demodulator activates signal detector logic circuitry which indicates that the sensor has seen earth. The output of this circuitry is then sent to the data handling and storage subsystem.

Prediction approach. The recommended system can uniquely determine the attitude of the spacecraft near perigee and out to approximately seven earth radii by use of the magnetometers and solar aspect sensors. Due to lack of correlation between the experimentally measured earth magnetic field and that based on prediction beyond seven earth radii, use of magnetometer data will be restricted to this region. Three-axis magnetometer readings alone do not uniquely determine attitude in all cases. An illustration of this is the vehicle tumbling about an axis parallel to the magnetic field direction; in this case, the magnetometer would have no change in output. Solar aspect sensors are used to provide the additional required reference direction for ambiguous magnetometer cases, and to provide a reference direction for use in other periods of the orbit with earth sensor data.

Because mission requirements impose a highly elliptical orbit and, thus, wide variation of the earth subtense angle, using the earth as a source of reference becomes very difficult. A very large number of fixed narrow beam sensors are required to obtain 4π steradian coverage when the earth subtends a small angle (Fig. V-8). The approach has been to use a minimum number, for the sake of simplicity, and to obtain data using vehicle dynamics to provide the scanning mechanisms. From motion studies completed to date, it appears reasonably conservative to be able to see the earth at least once per hour in the region of the orbit in which the magnetometer cannot be used.

Attitude and attitude rates as a function of orbit time will be determined using the magnetometer-solar aspect data obtained near perigee, orbit tracking data and ground-based computer programs. The following prediction technique will then be used to determine attitude at any later time in the orbit.

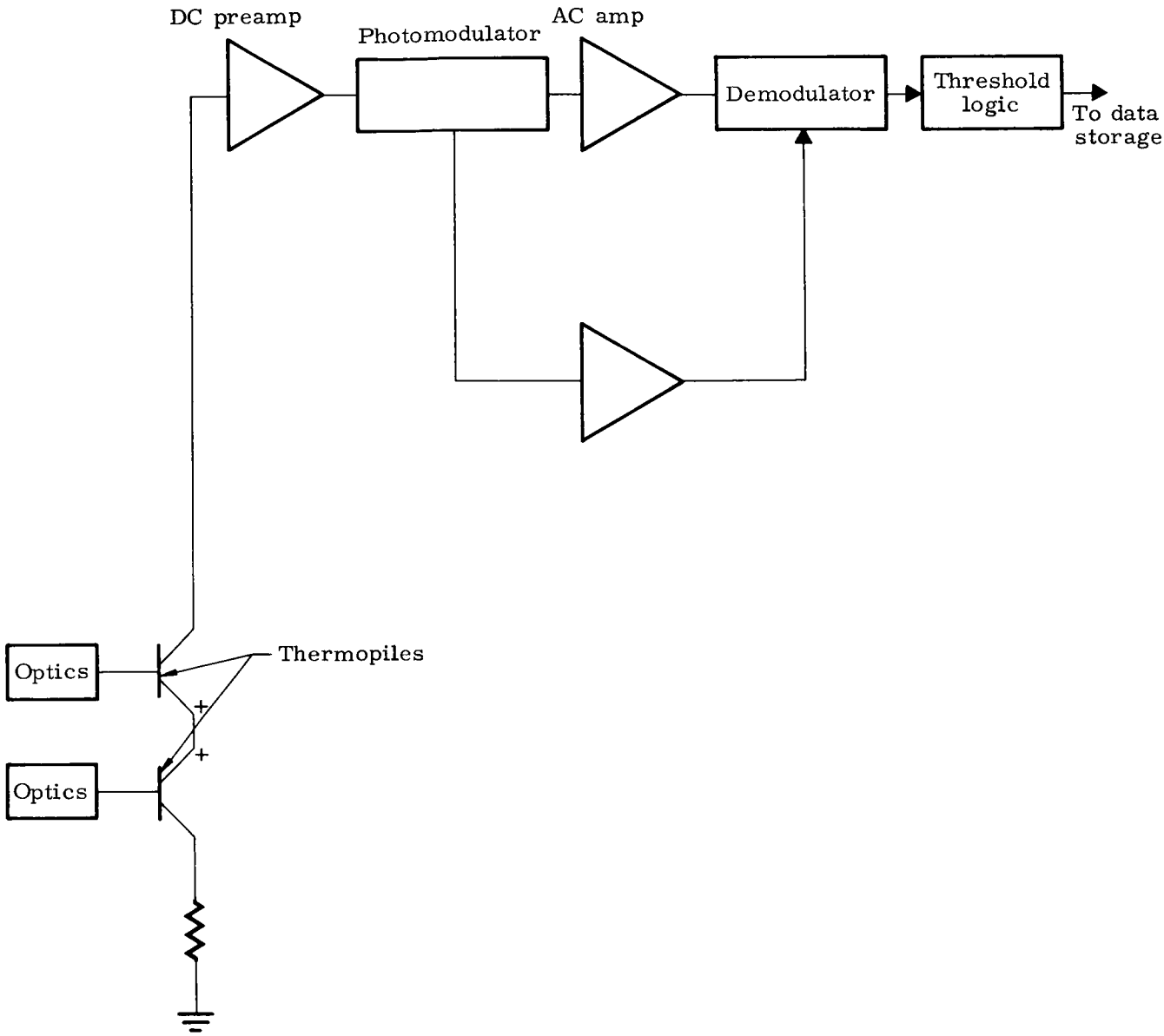

Fig. V-7. Earth Sensor Electronics

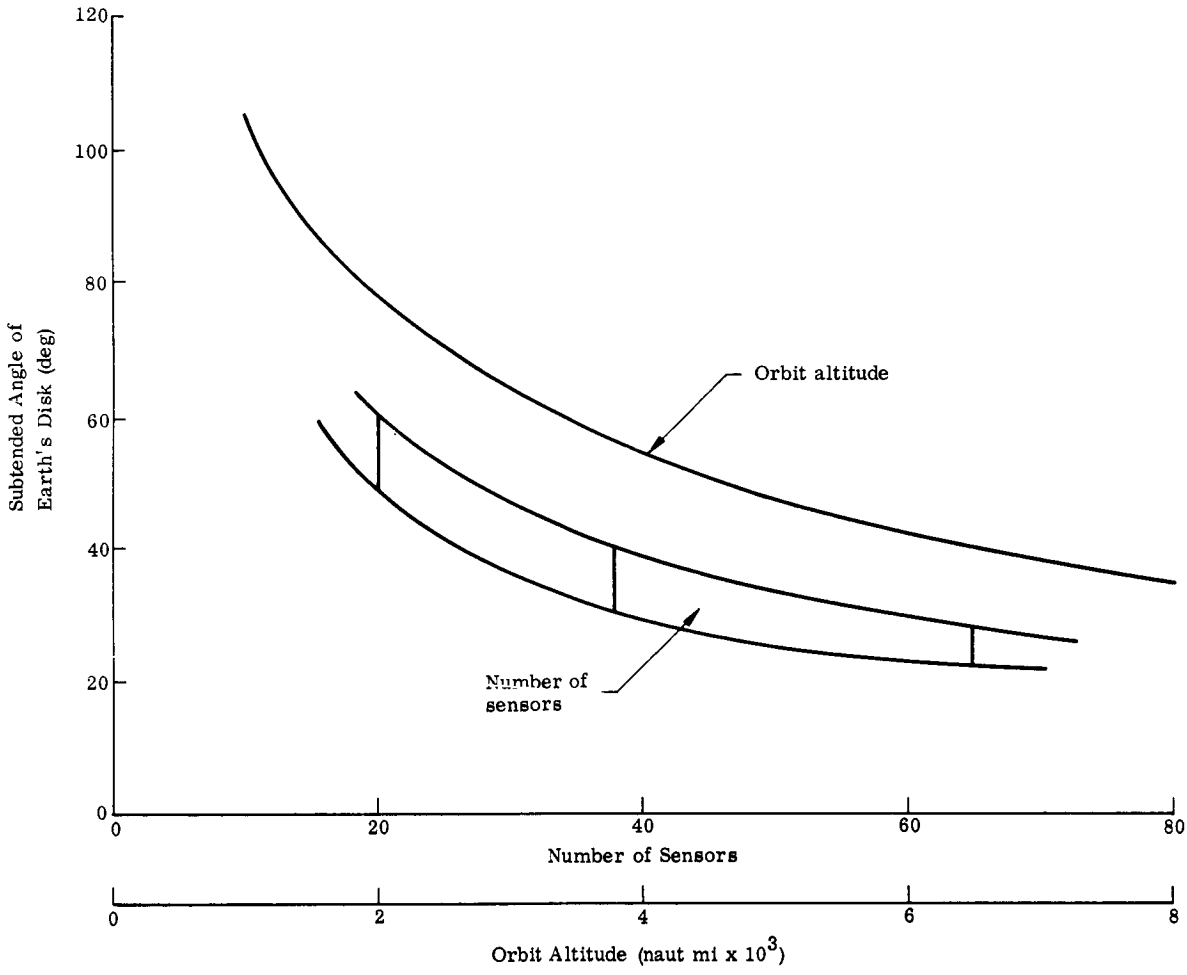

Fig. V-8. Earth Sensor Requirement

Several prediction techniques can be applied. The first, discussed earlier and employed on the Explorer series motion studies, determines the torques acting on the vehicle which would produce the motion as given by the sensed data. The gravitational torque is subtracted from the total torque, and the residual torque is matched against other possible sources such as magnetic (resulting from both induced and/or permanent magnetic moments), aerodynamic and solar pressure. Assuming various values for the most significant torques, the time variation of the torque is matched against that determined from the observed data. This process is continued until calculated torques agree with those observed. Motion is then predicted using these torques, and checked against observed motions for the remainder of the mission time. This approach assumes rather good knowledge of vehicle inertias and, therefore, inertia ratios. Without this assumption, neither the torques producing the observed motion nor the gravitational torque initially subtracted could have been determined. A second approach to the prediction is to determine vehicle attitude using the computer program which simulates attitude motion with the best estimate of inertias, center of pressure and center of gravity locations, initial conditions, aerodynamic drag, and solar pressure constants. Results from this simulation would be compared with the observed data over a selected time interval and modifications made to each of the variables until the motion is matched. Using these selected values for pertinent variables, the motion or would be continuously checked against observed data.

Either of these techniques can be employed and, probably, a combination will be used with perhaps some statistical approach added to the second technique to increase the probability of obtaining the best combination of values for the variables to reproduce the observed motion. As with any prediction technique, the more frequent and accurate the observed data, the more confident one can be in the prediction of motion during periods when observed data are not available.

The recommended system was selected on the basis that a large amount of data would be obtained during periods of high torques--near perigee. These data would continue to be collected until the primary torque acting on the system would be solar pressure. Earth sensors were added to collect some data during the long mission time in which solar pressure only is acting on the vehicle. The predicted motion resulting from magnetometer readings near their altitude limitation will be compared with the earth-solar aspect data.

2. System Operation

The recommended attitude sensing system has two modes of operation: full and hourly. The full attitude mode is used in the region of the orbit in which the magnetometers are effective for measuring the di-

rection of the earth's magnetic field with respect to the body axis, while the hourly attitude mode is based on obtaining data from the earth sensors. In both modes, data from the solar aspect sensors are obtained. Sampling frequency in both modes has been determined after considering the anticipated body motion, data storage requirements, sensor capability, attitude accuracy requirements and the relative importance of attitude orientation data in the overall mission objective. Attitude data are processed by the secondary data handling and communication system. Storage and processing units are completely independent of other secondary sensors and the entire attitude sensing system could be removed or modified with only minor effects on the secondary data handling and communication system, and without any effects on the primary system.

Full attitude mode. The full attitude mode is activated on command from the communication system. In this mode, solar aspect sensor and magnetometer outputs are sampled every 2 min and stored in the attitude memory unit. Based on a saturation and threshold logic switching circuit, either the ±50-millioersted or ±600-millioersted units are recorded. The total magnetic field vector magnitude is determined by combining the components measured along the X, Y and Z axes of the magnetometer units. This magnitude is compared to the saturation level of the ±50-millioersted unit and against a threshold value of ±45 millioersted in the ±600-millioersted unit. If the low range unit is saturated, the ±600 millioersted unit outputs are recorded until the total field vector falls below the threshold, at which time the readout is switched back to the low range unit. Each time the magnetometer readings are recorded, the five solar aspect sensors are scanned until a unit is located with aspect data stored in the shift register. This unit is then identified and read into memory, serially. Based on the error analysis given in Section A.3, the total time of data gathering in the full mode will be 4 to 5 hr. During this time, a total of 150 readings will be made which consist of 10 words of 8 bits for full attitude information, including sensor identification, sensor reading and time of reading. Total storage required is 12,000 bits.

Hourly attitude mode. The hourly attitude mode is used to obtain data points throughout the remainder of the orbit once per hour. Solar aspect and earth sensors are used in this mode. Since only five fixed mounted narrow beam (± 2°) earth sensors are used in the recommended system, the earth will not necessarily be within the field of view of a sensor for long periods of time. Dynamic analysis of vehicle motion suggests that there is a high probability that the earth will be viewed by at least one sensor during a period of one hour. When the earth sweeps through its field of view, earth sensor electronics will generate a pulse which activates a signal to store both time and sensor identification, and to initiate a readout of solar aspect sensor data. Solar aspect electronics scan the five solar aspect sensors, selecting and iden-

tifying the sensor which is illuminated. Solar aspect sensor electronics store the sun angles in a 17-bit storage register until a readout command is received from the data handling system. This shift register, along with earth sensor identification and time, is read serially into the attitude memory unit once per hour. The system has an inhibit circuit such that only one reading is accepted from the earth sensor until the hold register is read into memory. Using threshold and saturation logic circuits in the earth sensor electronics prevents a false reading from occurring because of the presence of the moon or sun in the field of view. Memory requirements for this mode are based on 139 readings of ten 8-bit words--11, 120 bits. Transmission of these data is commanded prior to command of the full attitude mode.

3. Error Analysis

An attempt has been made to evaluate quantitatively the accuracy to which the attitude of the vehicle can be determined in each of the two operational modes (full and hourly). From this measured data and the vehicle dynamics program, along with previous prediction results, one can qualitatively predict the accuracy of attitude at any time in the mission. Particular emphasis has been placed on the general considerations of using magnetometers and the effects of uncertainty in the earth field, magnetometer instrument errors, and vehicle residual magnetic characteristics. Only primary sources of error are considered at this time. Other sources, such as mechanical alignment of sensors, telemetry and data reduction errors, etc., are left for later analysis.

Magnetic measuring system. Knowledge of the earth's magnetic field at orbit altitudes has been discussed at length in the literature. Numerous models of this field at the earth's surface have been constructed using harmonic analysis. These models usually differ, not only in the values of the coefficients, but also in the number of harmonic terms used to describe the field. The accuracy of these models, when compared to observed satellite data, is dependent upon: the epoch upon which the coefficients are determined, the elimination of observed data points which are obtained during magnetic disturbances, the spread in both time and geographical location of the data upon which the coefficients are based, the accuracy of the orbit determination (since the predicted field is based on the observed orbit), and the contribution of the fields of origin external to the earth. Reports by Cain, et al. (Ref. V-3), Heppner, et al. (Ref. V-4) and Heuring (Ref. V-5) furnish data on the comparison of the observed data and that calculated using one or more of the various models, with discussions on the effects of various factors influencing the differences. Discussions by Cain, et al., on measurements obtained from Explorer X indicated errors in the scalar magnetic intensity over a range of altitudes from two to seven earth radii that vary from -45 to +23 gammas (Fig. V-9). These results are

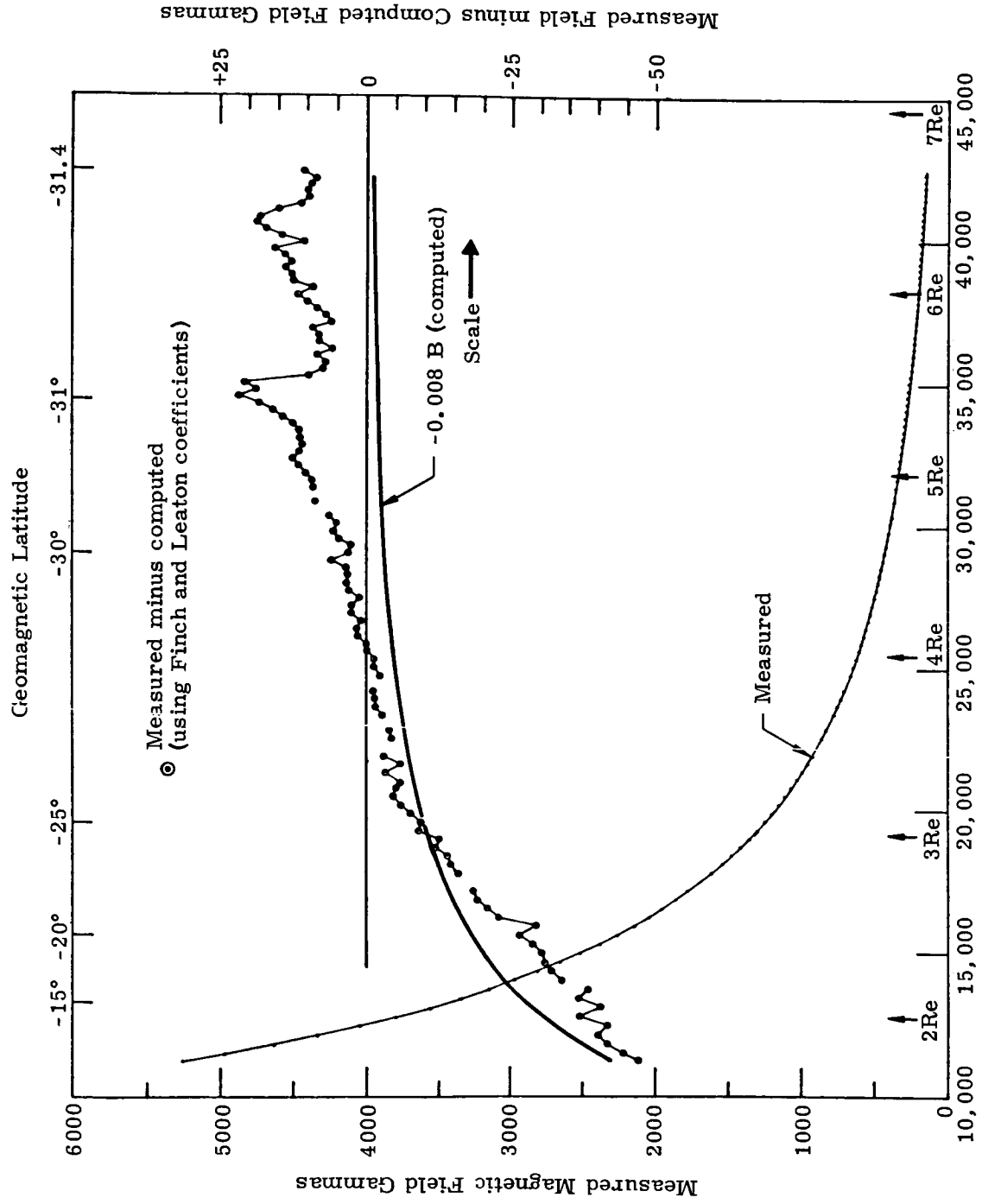

Fig. V-9. Measured minus Computed (using Finch and Leaton coefficients)

based on using Finch and Leaton 1957 coefficients. The observed data were obtained with a rubidium magnetometer. Flux gate magnetometers on Explorer X obtained data on the direction of the field from 4 to 12 earth radii. Accuracy in measuring the field was determined to be ±3°, with isolated points good only to 5° to 10°. When measured values were compared to the Finch and Leaton prediction, errors in direction of the field generally increased with earth radii; near 4 Re, this value was approximately 8°, at 7 Re had increased to 18°, and at 10 to 11 Re had increased to approximately 39° (Fig. V-10).

It would appear from this data that the altitude limitation on using magnetometers for attitude sensing, except for extremely crude estimates, should be in the range of 7 Re. The field determined by Finch and Leaton coefficients was found to have average errors of about -0.8% when compared to the Vanguard 3 data in Ref. V-3. Assuming this same average error applied to Explorer X data (Fig. V-9) shows that the error in the scalar measurements would vary between -10 and +25 gammas over 2 to 7 Re. Further improvement could be obtained by considering the effect of latitude on the average error as determined in Ref. V-3. Using these same corrections on the angular data, one could expect to reduce the 18° uncertainty at 7 Re to perhaps on the order of 5° to 8°. Orbit uncertainties alone have been estimated (Ref. V-3) to contribute rms values of 9 gamma, with maximum values of 51 gamma in the case of Vanguard 3 data. Heuring (Ref. V-5) has presented comparisons of some of the models and the Vanguard 3 data for the scalar field, emphasizing the effects of the number of coefficients required in the models and the differences between the models. It is shown in Fig. V-11 that, for altitude ranges between 2500 to 4000 km and higher, whereas Finch and Leaton coefficients give results which are 0.8% in error, the model of Jensen and Cain, using about 41 coefficients, yields only about 0.3% error. When considering the error as a function of both latitude and altitude, the Jensen and Cain model shows a reduction to less then 0.1% in the latitude band of 34° to 10° north. In the equivalent south latitudes, the errors are approximately 0.4%. Heuring suggests that this is probably because of the higher data density in the northern hemisphere for surface measurements from which the model coefficients are derived. If one compares this 0.1% value in gammas which is on the order of 13 to the value given in Ref. V-3 due to orbit uncertainty of 9 gamma, he can see that the Jensen and Cain model is extremely good for the Vanguard 3 orbit. Heuring further suggests that, by using all 512 coefficients of the Jensen and Whitaker model rather than only 63, the error could be further reduced by 0.2% from the value given--0.9%.

These results would indicate that the uncertainty in the knowledge of the earth's field intensity would be about 0.1% and the uncertainty in direction would be an angular error of from 2° to 8° in the range from 2 to 7 Re. Further justification for restricting the measurements

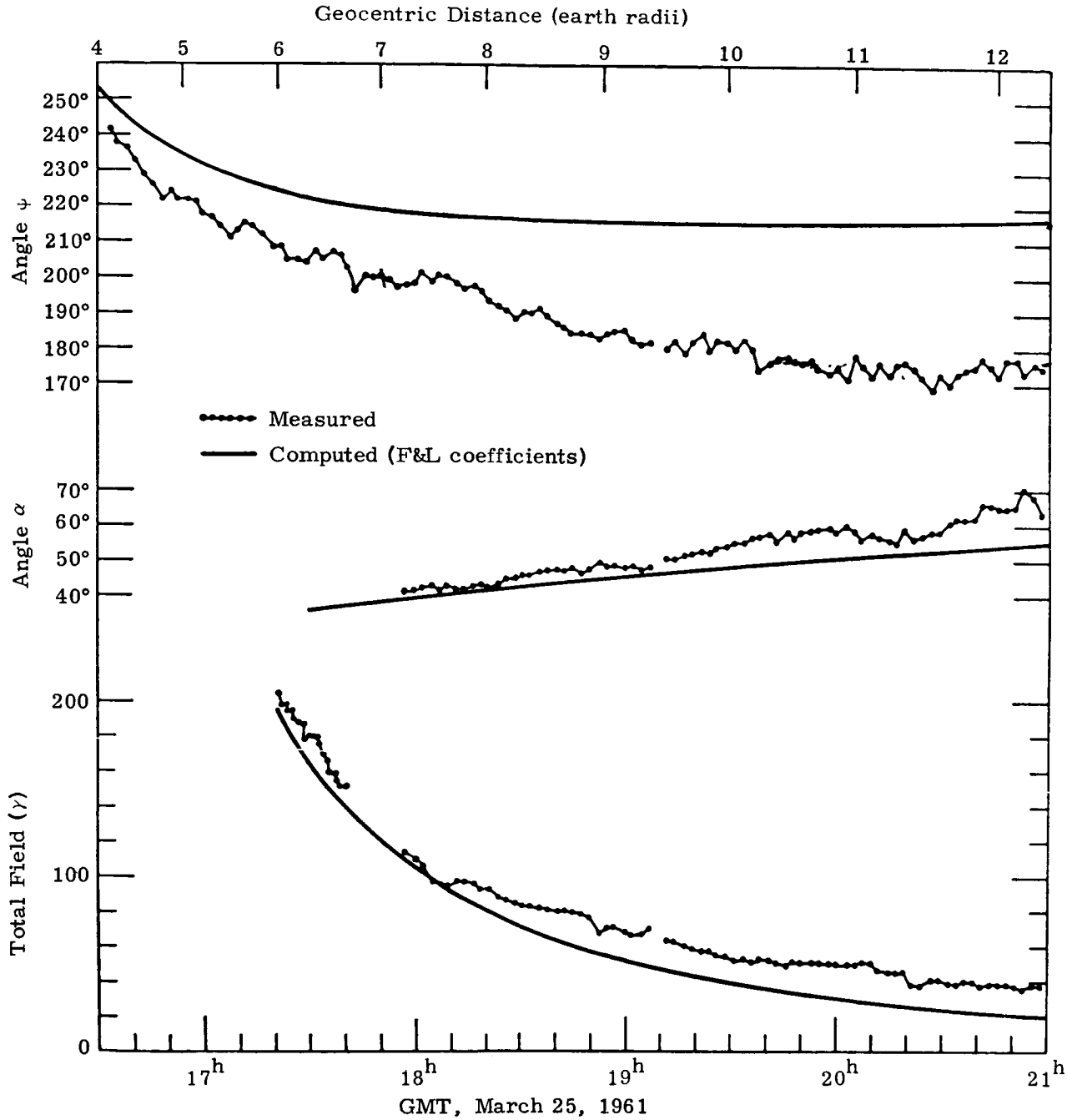

Fig. V-10. Field Measurements and a Computed Field (Finch and Leaton coefficients) in Payload Coordinates.

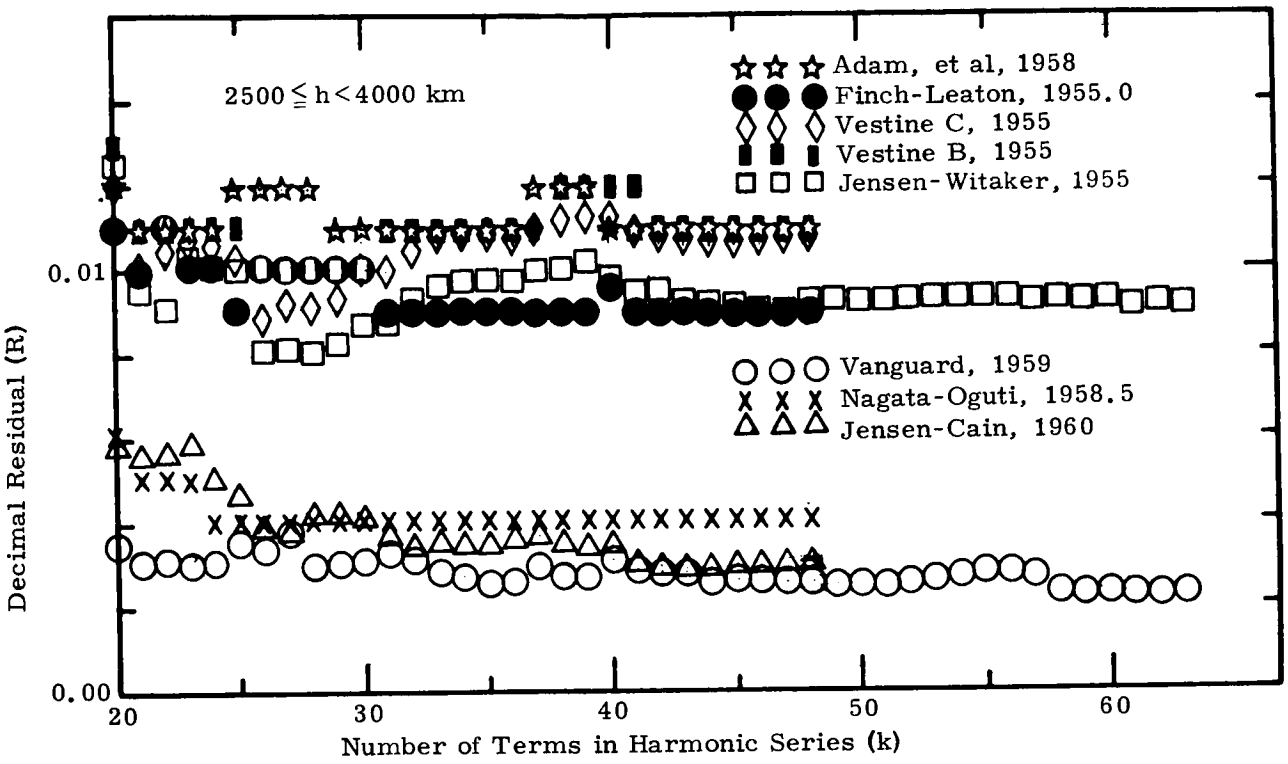

Fig. V-11. The Decimal Residual R (ratio of the rms of computed scalar magnetic intensity, less observed to rms of observed) as a Function of the Number of Terms k in the Quasi-plateau Region i. e., starting at k = 20 for Altitudes 2500-4000 km

to 7 Re are given in Ref. V-6, which discusses the results of measurements obtained with the IMP-1 satellite. Large variations between predicted and measured values are shown to occur beyond 7 to 10 Re.

Use of magnetometers to determine vehicle attitude presupposes a knowledge of the space orientation of the earth's magnetic field intensity vector ($\vec{H}$). Onboard sensing of the body axis component of this vector can be obtained through a three-axis flux gate magnetometer unit. The output of this unit defines the relative orientations of the vehicle body axes to the intensity vector. Having examined the possible errors in the knowledge of the earth's field, the next area of concern is instrument errors. The primary sources of error in the flux gate magnetometer are the maximum linearity error of 3% full scale and the dc null error for a zero field. Using these errors and examining the magnitude of the earth's intensity over the region of altitude to 7 Re with the objective of keeping the maximum error from these sources to between 4° to 8°, the number and range of magnetometers were selected. Figure V-12 depicts a typical altitude real time history, along with the dipole representation of the earth's magnetic field intensity magnitude. The time encountered in the region up to 7 to 10 Re is quite small compared to the orbital period (~ 144 hr). Using a 600-millioersted sensor range, a maximum error of 5.8° would occur when the magnetic field magnitude was 50 millioersted. This error would arise if one axis were colinear with $\vec{H}$ vector and possessing a linearity error of 75 gamma. The other sensor axes would be normal to the $\vec{H}$ vector and possessing the maximum zero field null error of 500 gamma:

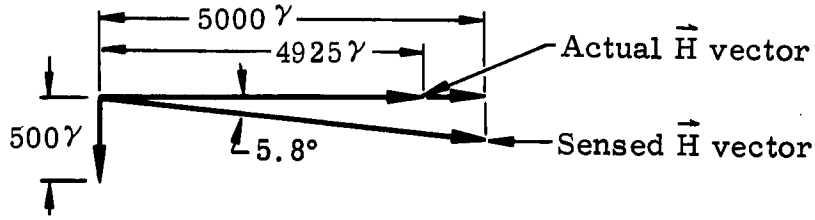

It was decided, based on this error, to use ±600 and ±50 millioersted sensors, switching between these based on the magnitude of the intensity vector. The resolution error and field strength as a function of sampling time for the ±600 and the ±50 millioersted sensors are shown in Figs. V-13 and V-14, respectively.

The third source of error in the magnetometer sensing system is due to the effect on the magnetometers of vehicle ferromagnetic material. In the present configuration, the most serious effect would seem to be caused by the 144 high carbon (1%) steel springs used in the micrometeoriod sensor panels. In general, the magnetic field disturbance can be expressed by the relationship:

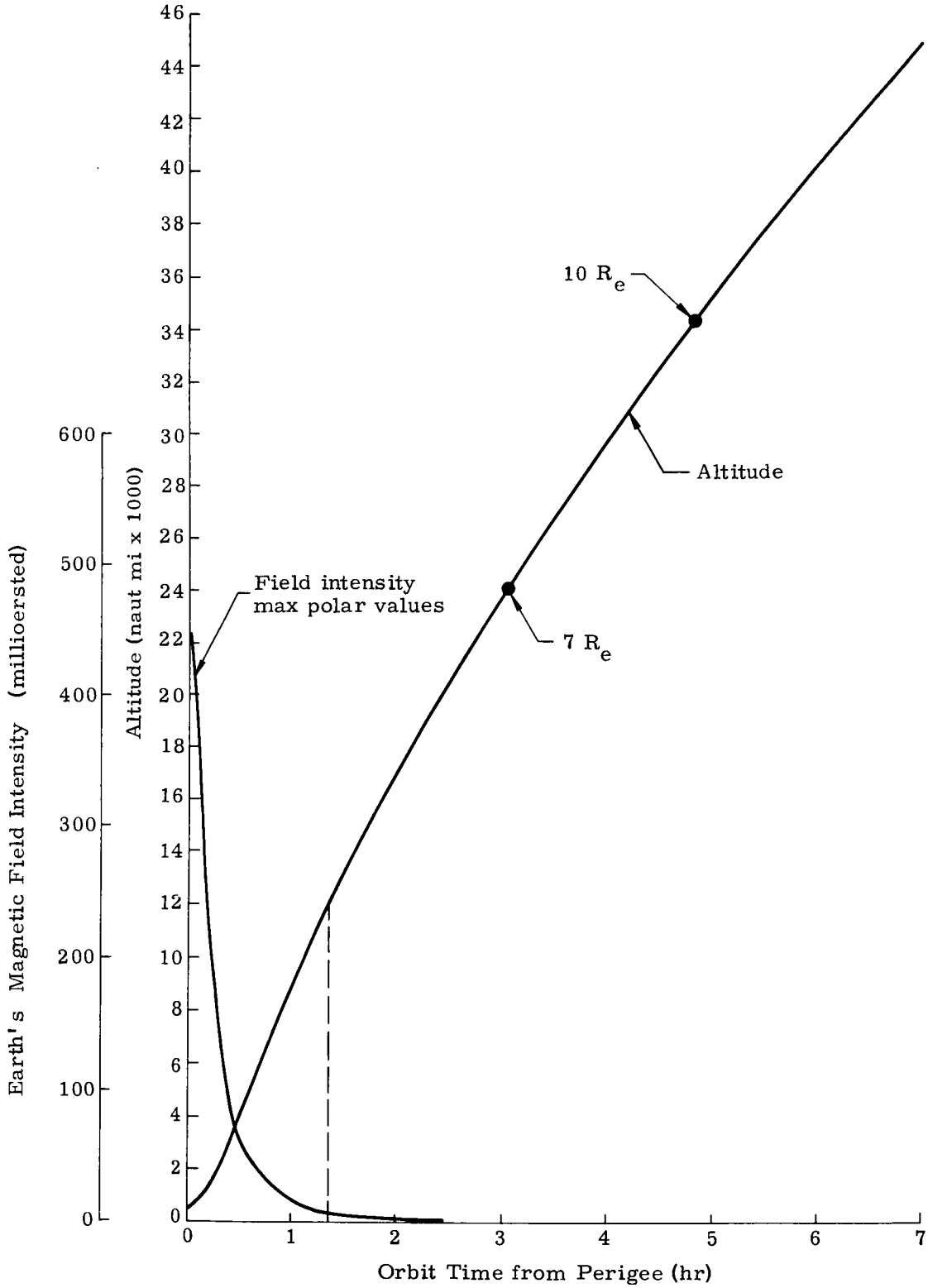

Fig. V-12. Earth's Magnetic Field Magnitude

$$\theta_e = \tan^{-1}\left(\frac{\text{Null error}}{\text{Field strength} - \text{Sensitivity error}}\right)$$

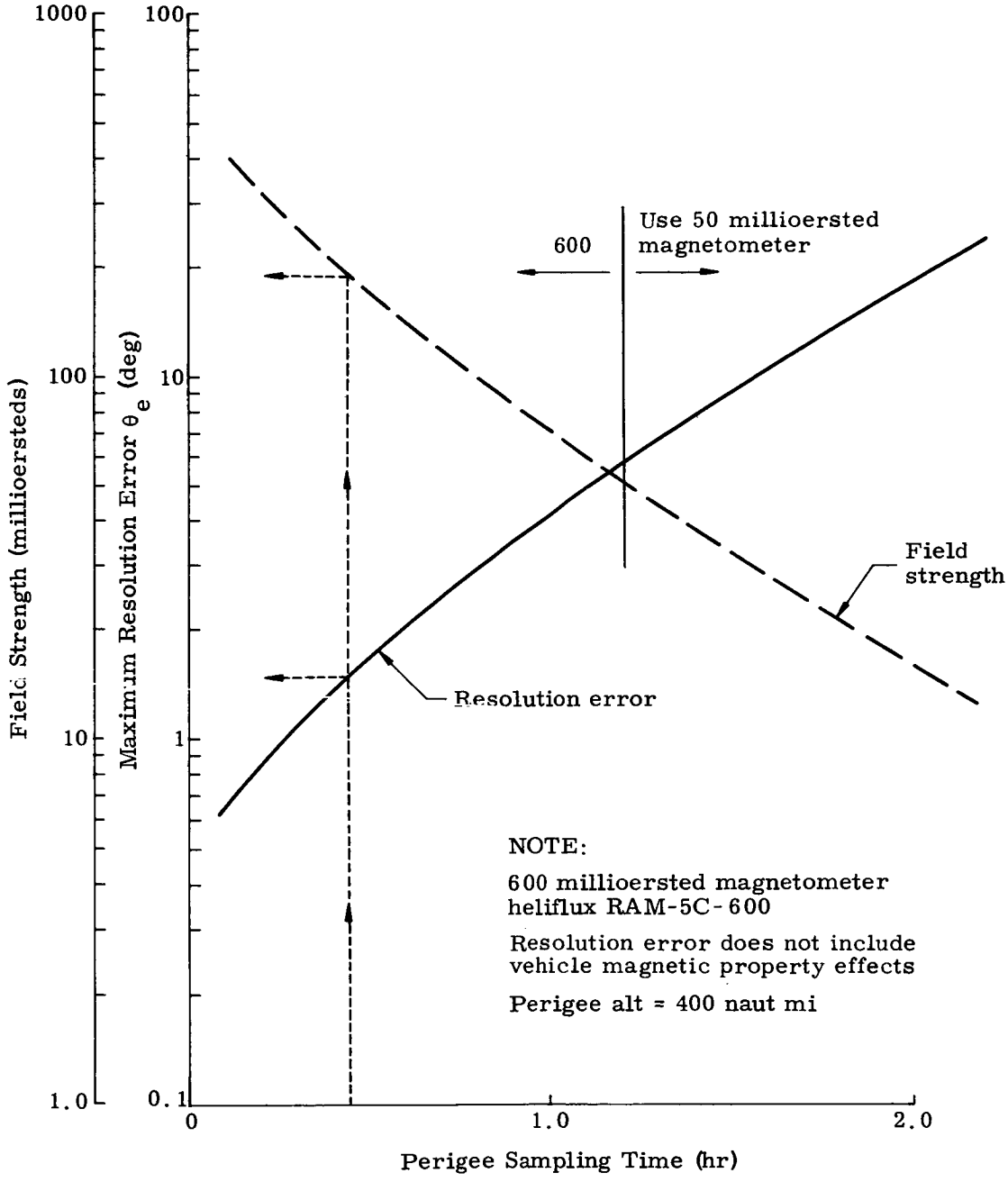

Fig. V-13. Resolution Error and Field Strength Versus Sampling Time

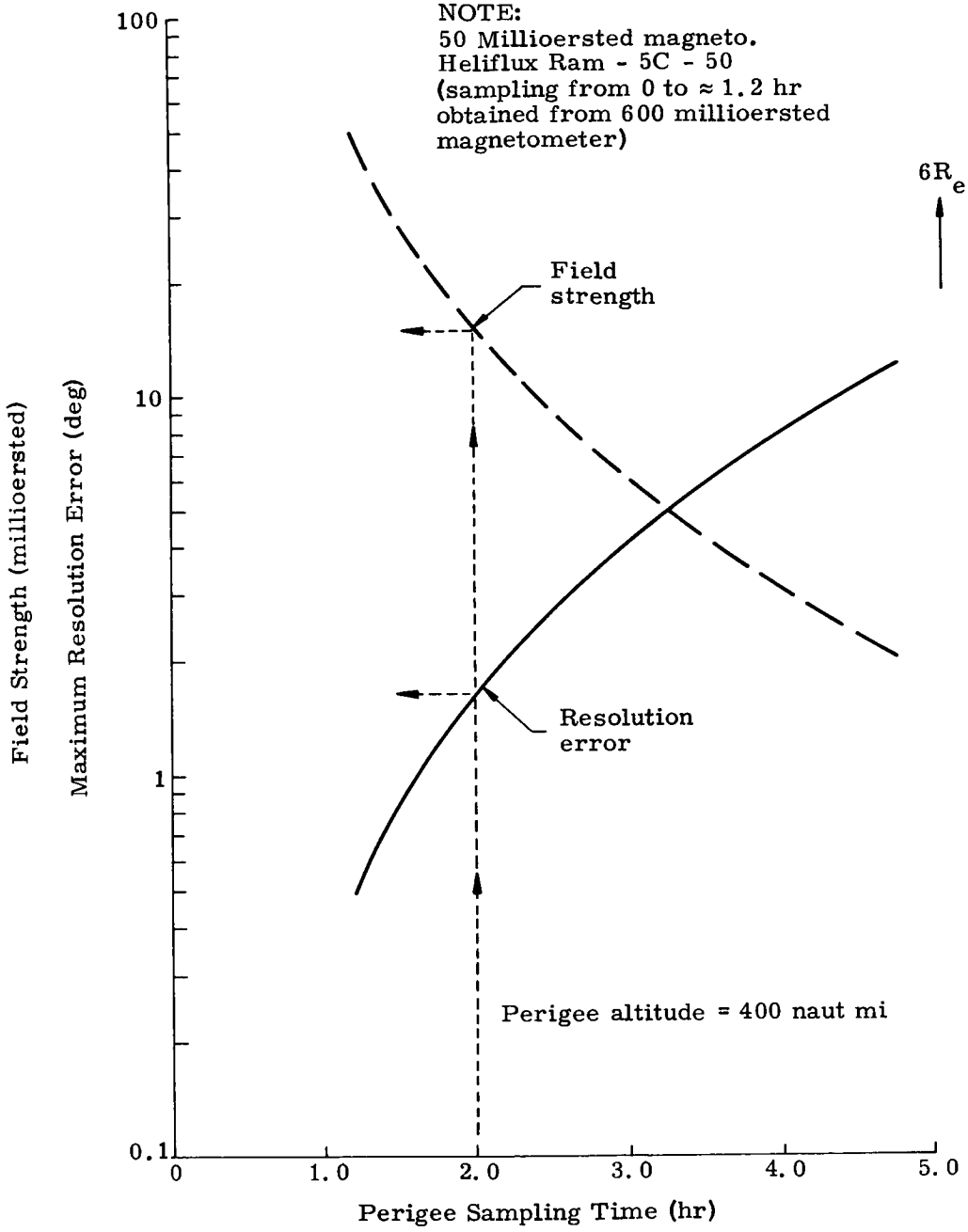

Fig. V-14. Resolution Error and Field Strength Versus Sampling Time

$$\Delta H = \frac{(B-H)^{\nu}}{4\pi r^3} \sqrt{3\cos^2\theta + 1}$$

where:

ΔH = disturbance in the magnetic field

r = distance from ferromagnetic material to the sensor location

$\frac{(B-H)^{\nu}}{4\pi}$ = effective magnetic moment of the ferromagnetic material, assuming it is essentially dipole

θ = angle between a line connecting the center of the dipole and the magnetometer, and the dipole axis

B = volume of ferromagnetic material

H = field strength (magnetic force)

Considering all 144 springs to be concentrated as one mass results in a volume of 870 cubic centimeters. For a completely degaussed spring placed in the earth's magnetic field, the magnetic induction is:

$$B = \mu_0 H_{earth}$$

where μ_0 is the relative permeability. Based on experimental data addition of 1% carbon in a quenched process significantly reduces μ_0 for steel to approximately 50 gauss/oersted. This value results in a magnetic induction at the earth's surface of 20 gauss.

The disturbance in the magnetic field (ΔH) becomes

$$\Delta H_{max} = \frac{9478}{V^3 \text{ (ft)}} \quad \text{(gamma)}$$

for all 144 springs. Considering the actual location of the springs relative to the magnetometer (Fig. III-2), it is realistic to compute field disturbances by super position as follows:

No. of Springs	r (ft)	Volume Ratio	ΔH (γ)
6	1	0.043	407.6
6	2.5	0.043	26.0
6	6.66	0.043	1.4
			435.0 Total

The practical minimum field sampling for the 50-millioersted sensor corresponding to the computed field disturbance error and allowable earth aspect sensor error of 10° is:

$$H_{50} = \frac{\left(42^2 + 435^2\right)^{1/2}}{\tan 10} + 435 \qquad \text{(gamma's)}$$

$$= 29.13 \text{ millioersteds}$$

When the magnetic characteristics of the satellite are better defined, appropriate sensor locations will be determined to reduce the field disturbances to a point where $H_{50} \approx 40$ gamma.

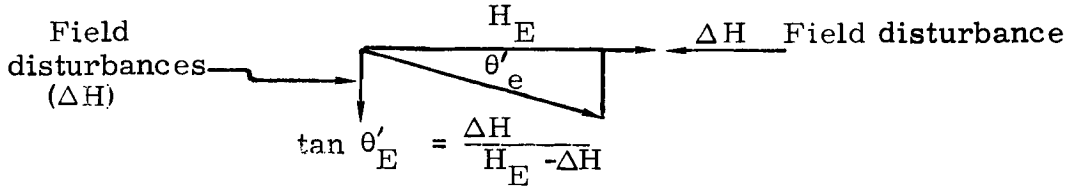

$$\theta_E \text{ total} = \left[\theta'^2_E + E^2 \text{ (resolution)}\right]^{1/2}$$

For θ_E total = 15° in 240 gamma earth's field, θ_E resolution equals 10° as can be seen from Fig. V-14.

$$\Delta H = 0.165\, H_E$$

To obtain 4.5 hours of sampling time H_E (minimum) = 240 gamma and, therefore, $\Delta H \approx 40$ gamma. For times less than 4.5 hr, the total θ_E due to a 40 gamma disturbance is less than 15°.

These preliminary calculations indicate that a 1- to 2-ft boom magnetometer installation may be imperative. Figure V-15 shows the variation in sampling time as a function of vehicle magnetic disturbance. The errors shown (5°and 15°) are based on the maximum error which occurs at the end of the given sampling time. The error due to the same magnitude of disturbance is smaller within this sampling time.

Solar aspect measuring system. The solar aspect sensors proposed for use on the MDSS have an accuracy of sun angle measurement in two perpendicular planes of ±1°. The system is a digital readout system; similar systems have been used in a number of satellite applications.

NOTE:

50 millioersted magnetometer

$$\Delta H = \frac{\tan(K)\, H_{\epsilon}}{1 + \tan(K)}$$

H_{ϵ} = earth's intensity

$$K = \sqrt{\theta^2_{E_{total}} - \theta^2_{res}}$$

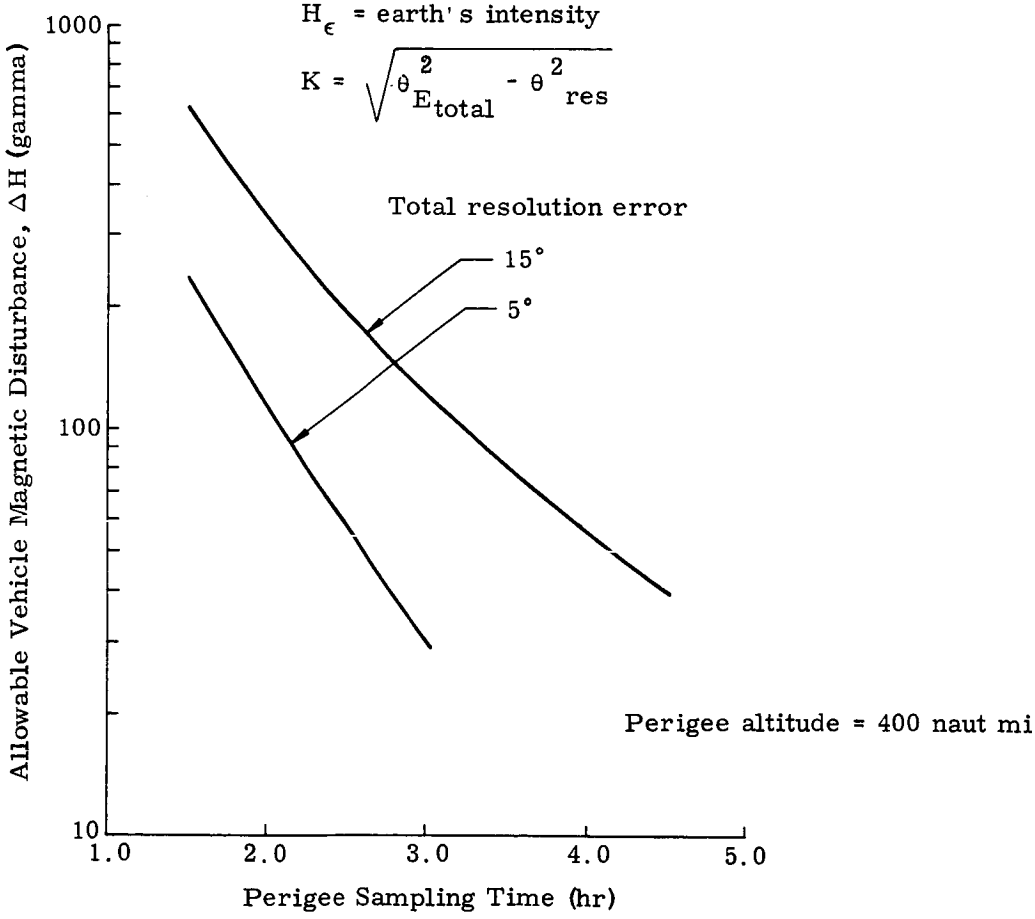

Fig. V-15. Allowable Vehicle Magnetic Disturbance Versus Sampling Time for Total Resolution Error

Earth aspect measuring system. This system is used at 7 to 10 Re and greater, along with the solar aspect sensors in the hourly attitude mode. With the limited number of sensors proposed (5), one might not expect accurate attitude determination, since these sensors are narrow beam IR types and sense only the presence of the earth in their field. Actually, the problem is more one of assurance of gathering any data from these sensors rather than accuracy. If one of the five sensors sees earth, the error in actual direction to earth is approximately one-half the subtended earth angle at that point in the orbit. Since, for most of the hourly attitude mode, this angle will be less than 10°, one can readily see that the accuracy with this system approaches that of the full attitude mode.

Summary. Solar aspect sensing in both the full and hourly attitude modes can be expected to be obtained to an accuracy of ±1°, with the exception of when the sun is occulted.

In the full attitude mode, using the magnetometers, three primary sources of error are considered: knowledge of the magnitude and direction of earth's magnetic intensity vector, inherent sensor resolution errors, and the effects of the residual magnetic characteristics of the vehicle. The analysis indicates that, with proper mounting of the magnetometers, selection of two sets of magnetometers to be used in the proper range of the orbit and limiting the measurements to an altitude range between 7 and 10 earth radii, the rms error in attitude can be held below 10° at the time the measurements are made.

In the hourly attitude mode, using the thermopile earth sensors, one can expect errors of one-half the subtended angle of the earth at the time of measurement; in general, less than 10°.

Based on previous experience in predicting vehicle rotational motions during portions of the orbit where measurements are not available, it is expected that attitude can be obtained to an accuracy of approximately 10° at any time. More detailed error analyses, along with dynamic analysis of the motion of the vehicle, are required to justify this approximation. For example, one could use a given set of initial conditions, vehicle characteristics and given orbit in a computer program and obtain the sensor outputs based on these assumptions. This data would then be used to obtain attitude observations as a function of orbit time. A second experimenter would start with the best estimate of initial conditions based on tracking accuracy, the best estimate of vehicle characteristics and orbit tracking attempting to fit the vehicle motion to the original data. In such a program, one would develop confidence in the number and accuracy of data points and the frequency required to obtain the desired vehicle attitude accuracy.

4. Physical Characteristics

Physical properties of the various pieces of equipment making up the attitude sensing system of the MDSS are listed in Table V-2. All selected components have either successfully flown on satellite programs or are planned for programs where flight data precedes the MDSS. The Shonstedt type RAM-5C magnetometer in a single axis configuration and a saturation level of ±30 gamma were flown successfully on Explorer X. Adcole solar aspect sensors similar to the proposed units have been qualified for the TIROS weather satellite, the MDS. The Barnes IR earth sensors are similar to units planned for the MDS for MSFC, the Apollo command capsule antenna positioning system and a small countermeasures missile made by Raytheon.

TABLE V-2

Item	No. of Units	Weight (lb)	Power (watts)	Package Dimensions (in.)
Magnetometers and electronics	6	4.7	0.6	4 x 1.5 x 5/8 4 x 6 x 6
Earth sensors	5	0.5	0.5	2.5 x 2 x 2
Sun sensors	5	1.0	--	2-1/4 x 2-1/4 x 1/2
Sun sensor electronics	1	6.0	1.5	7-3/4 x 4-1/2 x 3-7/8

B. STUDY RESULTS

1. Vehicle Dynamics

A five-degree-of-freedom digital micrometeoroid dynamics simulation program was generated in the course of this study. Basically, this program accounts for all significant disturbing torque sources which would be expected in the cislunar environment. The purpose of this program is to define the expected attitude motion for a tumbling vehicle and thereby relate this motion to the attitude determination system requirements as well as to thermal and electrical power systems design.

a. Disturbing torques

Basic disturbing torque sources are:

(1) Differential gravity

(2) Solar pressure

(3) Aerodynamic

(4) Magnetic

(5) Elastic vibration energy dissipation.

The latter source was not considered for the tumbling vehicle, since it is essentially a problem in cone angle buildup associated with a vehicle possessing large body rates about an axis of minimum moment of inertia. Magnetic torques caused by the interaction of inherent vehicle dipole characteristics with the earth's magnetic field were also neglected, based on a conference with the NASA-Pegasus Program Office personnel at MSFC, who determined that the relative ratio of ferromagnetic material to nonferrous material in a micrometeoroid satellite is quite small and will not produce a significant vehicle dipole. Remaining torques were accounted for in the digital program and will be defined in the following discussion. Table V-3 shows the relative magnitudes of these torques at orbit perigee and apogee.

b. Description of computer program

Five degrees of freedom were mechanized into the digital program; i. e., rotational motion about the X, Y and Z body axes, in-orbit plane tangential and radial position vector motion. Motion out of the orbit plane was neglected, since it is quite small and insignificantly affects the rotational dynamics of primary concern. The choice of a fixed or variable integration interval exists; however, the variable technique has

TABLE V-3

"Z" Configuration Torques

Torque Source	Orbit Position	Magnitude (ft-lb)
Differential gravity	Perigee	6.63×10^{-4}
	Apogee	1.00×10^{-8}
Solar pressure	Perigee	4.15×10^{-5}
	Apogee	4.15×10^{-5}
Aerodynamic	Perigee	73.9×10^{-4}
	Apogee	0

proven more desirable, since it automatically adjusts the interval to the changing orbital and rotational rates. Using this technique requires a nominal interval as an input parameter. The program will reduce this interval as necessary. However, under normal conditions, it will not increase the interval. For this reason the program was designed such that several nominal intervals, defined as a function of orbital radius, can be inputed. The present real time to machine time ratio is 5000 for small body rate conditions. Derivations of the significant torques and their mechanization follow.

(1) Frames of reference

In deriving the mathematical expressions for the torques acting about the vehicle body axes, five frames of reference were used:

(1) Body fixed--principal axes rotating with vehicle (Fig. V-16).

(2) Local vertical--rotates in orbit plane, with one axis collinear with radius vector and one axis normal to radius vector and in-orbit plane.

(3) Inertial--fixed in space with origin at earth's center.

(4) Earth fixed--fixed to earth with origin at earth's center: X and Y axes in equatorial plane; Z axis through geometric North Pole.

(5) Earth magnetic frame--fixed to earth but rotated about Z and X earth-fixed axes.

Each reference frame is defined, along with the major transformations between frames.

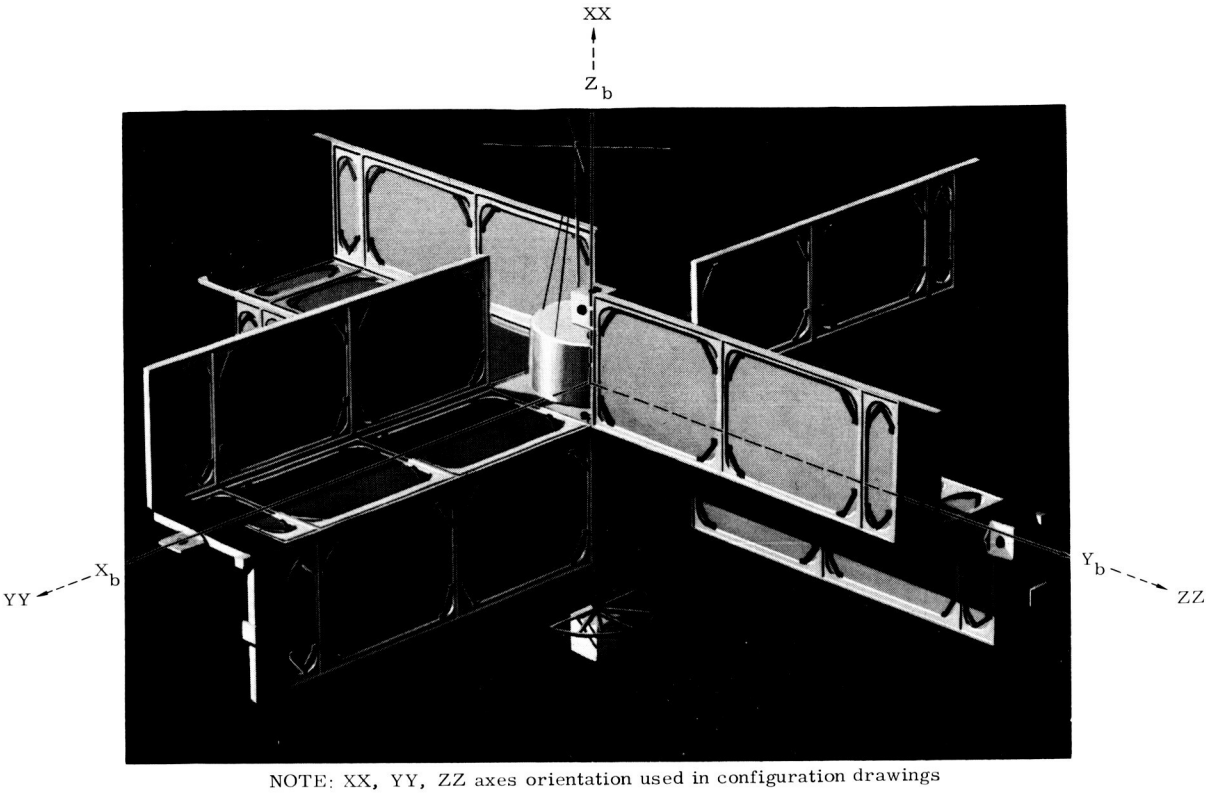

NOTE: XX, YY, ZZ axes orientation used in configuration drawings

Fig. V-16. Body Axis Orientation Used for Dynamics Simulation Study

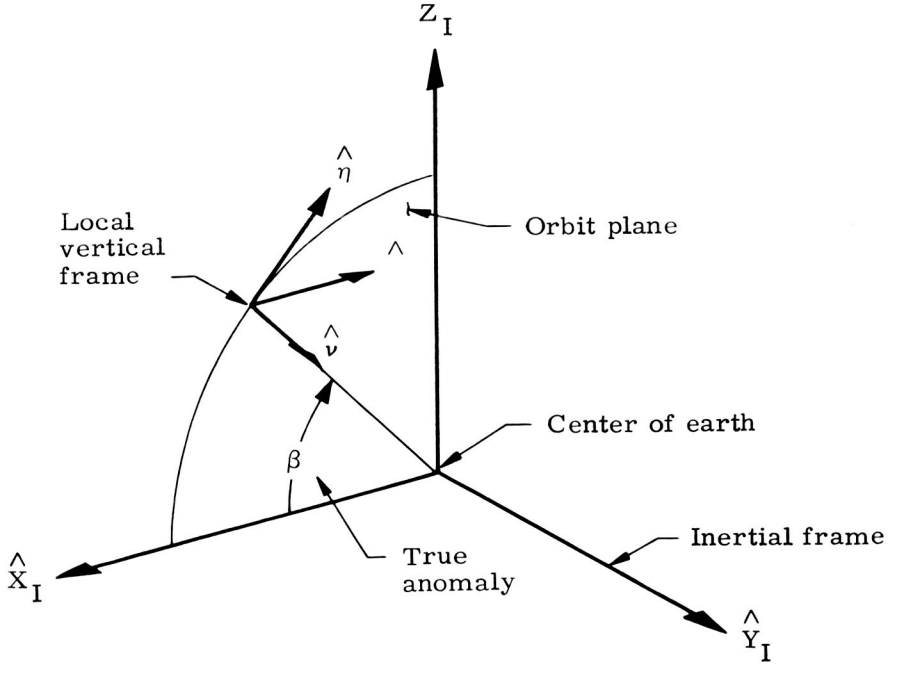

Fig. V-17. Local Vertical and Inertial Frames

Figure V-17 shows the relationship between the local vertical and inertial frames. The transformation between these frames is:

$$\begin{bmatrix} \hat{X}_I \\ \hat{Y}_I \\ \hat{Z}_I \end{bmatrix} = \begin{bmatrix} -\sin\beta & 0 & -\cos\beta \\ 0 & 1 & 0 \\ \cos\beta & 0 & -\sin\beta \end{bmatrix} \begin{bmatrix} \hat{n} \\ \hat{e} \\ \hat{v} \end{bmatrix} = [T_{IV}] \begin{bmatrix} \hat{n} \\ \hat{e} \\ \hat{v} \end{bmatrix}$$

The vertical to body frame is related through Eulerian angles ψ, θ, ϕ rotations (Fig. V-18).

$$\begin{bmatrix} \hat{X}_b \\ \hat{Y}_b \\ \hat{Z}_b \end{bmatrix} = \begin{bmatrix} \ell_{11} & \ell_{12} & \ell_{13} \\ m_{11} & m_{12} & m_{13} \\ n_{11} & n_{12} & n_{13} \end{bmatrix} \begin{bmatrix} \hat{n} \\ \hat{e} \\ \hat{v} \end{bmatrix} = [T_{BV}] \begin{bmatrix} \hat{n} \\ \hat{e} \\ \hat{v} \end{bmatrix}$$

where

$$\ell_{11} = \cos\theta \cos\psi$$

$$m_{11} = -\cos\theta\sin\psi + \sin\phi \sin\theta \cos\psi$$

$$n_{11} = \sin\phi \sin\psi + \cos\phi \sin\theta \cos\psi$$

$$\ell_{12} = \cos\theta \sin\psi$$

$$m_{12} = \cos\phi \cos\psi + \sin\phi \sin\theta \sin\psi$$

$$n_{12} = -\sin\phi \cos\psi + \cos\phi \sin\theta \sin\psi$$

$$\ell_{13} = -\sin\theta$$

$$m_{13} = \sin\phi \cos\theta$$

$$n_{13} = \cos\theta \cos\phi$$

The resulting inertial to body frame transformation becomes:

$$\begin{bmatrix} \hat{X}_I \\ \hat{Y}_I \\ \hat{Z}_I \end{bmatrix} = [T_{IV}] [T_{VB}] \begin{bmatrix} \hat{X}_b \\ \hat{Y}_b \\ \hat{Z}_b \end{bmatrix} = [T_{IB}] \begin{bmatrix} \hat{X}_b \\ \hat{Y}_b \\ \hat{Z}_b \end{bmatrix}$$

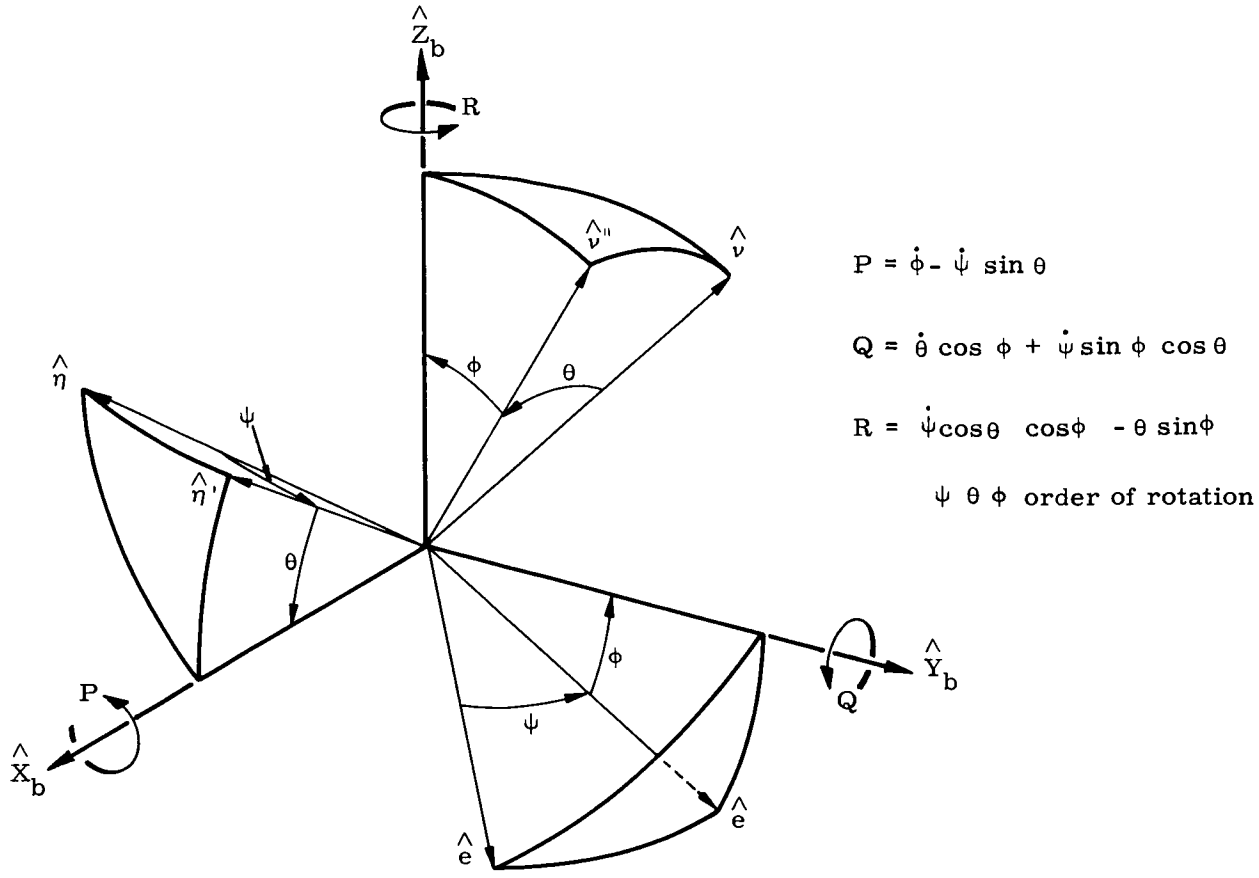

Fig. V-18. Local Vertical and Body Frames

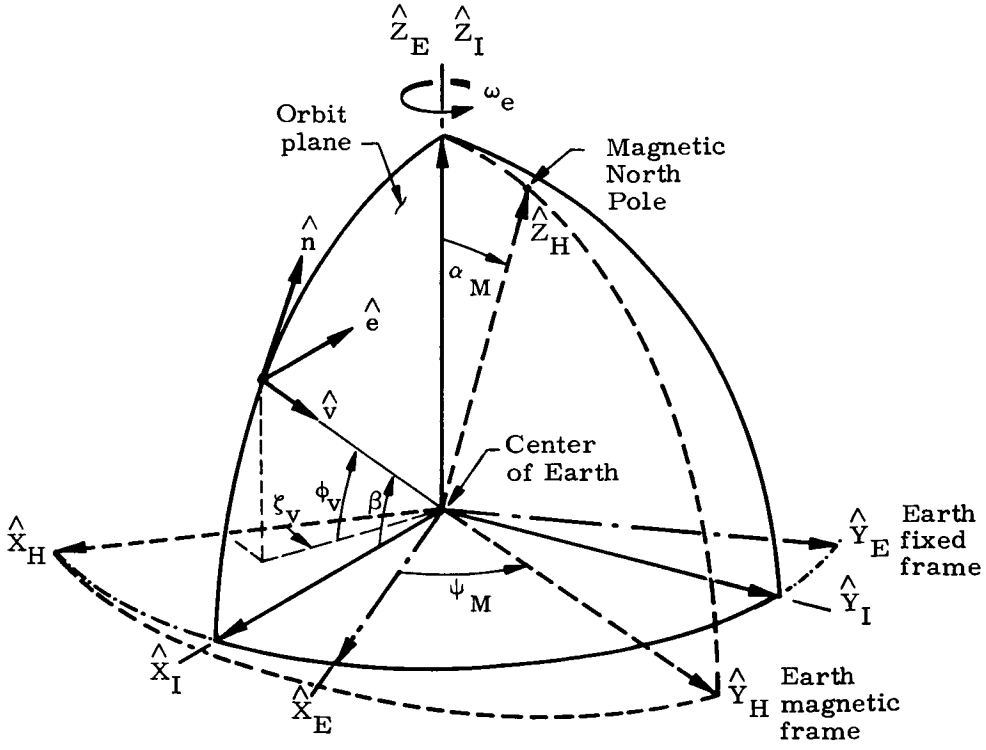

Fig. V-19. Earth Fixed Magnetic and Inertial Frame Relationship

$$[T_{IB}] = \begin{bmatrix} -\sin\beta\,\ell_{11} - \cos\beta\,\ell_{13} & -\sin\beta\,m_{11} - \cos\beta\,m_{13} & -\sin\beta\,n_{11} - \cos\beta\,n_{13} \\ \ell_{12} & m_{12} & n_{12} \\ \cos\beta\,\ell_{11} - \sin\beta\,\ell_{13} & \cos\beta\,m_{11} - \sin\beta\,m_{13} & \cos\beta\,n_{11} - \sin\beta\,n_{13} \end{bmatrix} \begin{bmatrix} \hat{X}_b \\ \hat{Y}_b \\ \hat{Z}_b \end{bmatrix}$$

In defining the magnetic torques in the body axes, it is necessary to define the earth's magnetic intensity vector in them. This operation is accomplished by defining a magnetic frame fixed to the earth and rotated away from the conventional fixed earth frame (Fig. V-19)

ϕ_ν = Vehicle magnetic latitude

ξ_ν = Vehicle magnetic longitude

ω_e = Earth's rotation rate

α_M = Colatitude of magnetic North Pole relative to earth fixed frame

ψ_M = Longitude of magnetic North Pole relative to earth fixed frame

$$\begin{bmatrix} \hat{X}_E \\ \hat{Y}_E \\ \hat{Z}_E \end{bmatrix} = \begin{bmatrix} \sin\psi_M & \cos\psi_M \cos\alpha_M & \cos\psi_M \sin\alpha_M \\ -\cos\psi_M & \sin\psi_M \cos\alpha_M & \sin\psi_M \sin\alpha_M \\ 0 & -\sin\alpha_M & \cos\alpha_M \end{bmatrix} \begin{bmatrix} \hat{X}_H \\ \hat{Y}_H \\ \hat{Z}_H \end{bmatrix} = [T_{EH}] \begin{bmatrix} \hat{X}_H \\ \hat{Y}_H \\ \hat{Z}_H \end{bmatrix}$$

$$\begin{bmatrix} \hat{X}_I \\ \hat{Y}_I \\ \hat{Z}_I \end{bmatrix} = \begin{bmatrix} \cos\omega_e t & -\sin\omega_e t & 0 \\ \sin\omega_e t & \cos\omega_e t & 0 \\ 0 & 0 & 1 \end{bmatrix} \begin{bmatrix} \hat{X}_E \\ \hat{Y}_E \\ \hat{Z}_E \end{bmatrix} = [T_{IE}] \begin{bmatrix} \hat{X}_E \\ \hat{Y}_E \\ \hat{Z}_E \end{bmatrix}$$

$$\begin{bmatrix} \hat{X}_H \\ \hat{Y}_H \\ \hat{Z}_H \end{bmatrix} = [T_{HE}]\,[T_{EI}]\,[T_{IB}] \begin{bmatrix} \hat{X}_b \\ \hat{Y}_b \\ \hat{Z}_b \end{bmatrix} = [T_{HB}] \begin{bmatrix} \hat{X}_b \\ \hat{Y}_b \\ \hat{Z}_b \end{bmatrix}$$

(2) Equations of motion

Orbital equations

$$\ddot{r} = \frac{-\mu}{r^2} + \frac{C_I^2}{r^3}$$

$$\dot{\beta} = -\frac{C_I}{r^2}$$

where

μ = gravitational constant

C_I = orbital angular momentum; constant for particular orbit

r = orbital radius

Rotational equations. The "Z" symmetrical panel axes are considered the body axes. For all practical purposes, this axis set is also the principal axes.

$$\dot{P} = \underbrace{\left[\frac{3\mu}{r^3}\left(\frac{I_Z - I_Y}{I_X}\right) n_{13}\, m_{13}\right]}_{\text{differential gravity}} + \underbrace{\left[\frac{F_{N_Z}\,\Delta C_{P_Y} - F_{N_Y}\,\Delta C_{P_Z}}{I_X}\right]}_{\text{solar pressure}}$$

$$+ \underbrace{\left[\frac{F_{N_Z}\,\Delta C_{P_Y} - F_{N_Y}\,\Delta C_{P_Z}}{I_X}\right]}_{\text{aerodynamics}}$$

$$+ \left[\frac{M_X}{I_X}\right]_{\text{magnetic}} - \left[\frac{I_Z - I_Y}{I_X}\right] RQ$$

$$\dot{Q} = \underbrace{\left[\frac{3\mu}{r^3}\left(\frac{I_X - I_Z}{I_Y}\right) \ell_{13}\, n_{13}\right]}_{\text{differential gravity}} + \underbrace{\left[\frac{F_{N_X}\,\Delta C_{P_Z} - F_{N_Z}\,\Delta C_{P_X}}{I_Y}\right]}_{\text{solar pressure}}$$

$$+ \underbrace{\left[\frac{F_{N_X}\,\Delta C_{P_Z} - F_{N_Z}\,\Delta C_{P_X}}{I_Y}\right]}_{\text{aerodynamics}}$$

$$+ \left[\frac{M_Y}{I_Y}\right]_{\text{magnetic}} - \left[\frac{I_X - I_Z}{I_Y}\right] PR$$

$$\dot{R} = \left[\frac{3\mu}{r^3}\left(\frac{I_Y - I_X}{I_Z}\right)\right] m_{13}\,\ell_{13} + \left[\frac{F_{N_Y}\,\Delta C_{P_X} - F_{N_X}\,\Delta C_{P_Y}}{I_Z}\right]$$

differential gravity — solar pressure

$$+ \left[\frac{F_{N_Y}\,\Delta C_{P_X} - F_{N_X}\,\Delta C_{P_Y}}{I_Z}\right]$$

aerodynamics

$$+ \left[\frac{M_Z}{I_Z}\right]_{\text{magnetic}} - \left[\frac{I_Y - I_X}{I_Z}\right] QP$$

where $\dot{P}$, $\dot{Q}$ and $\dot{R}$ are accelerations about the X, Y and Z body axes, respectively. P, Q and R are the rates

The component differential gravity, solar pressure, magnetic and aerodynamic accelerations are defined in the following paragraphs. Figure V-20 is a flow diagram of the mechanization of the equation of motion.

(3) Differential gravity torque

Figure V-21 relates the vector relationships involved in the action of a central force on an extended body. $\vec{r}$ is the radius vector from the center of the earth to the center of mass of the body. $\vec{r}_P$ is the vector from the center of mass to an elemental mass, dm, of the body. $\vec{\rho}$ is the vector from the center of earth to this element. The differential force exerted on dm by the gravitational field can be expressed as,

$$d\vec{F} = \frac{-\mu\, dm}{\rho^3}\,\vec{\rho}$$

By inspection of Fig. V-21, the following relationships can be stated.

$$\vec{\rho} = \vec{r} + r_P = r\hat{v} + \vec{r}_P$$

$$\hat{r} = -\hat{v} = -\ell_{13}\,\hat{X}_b - m_{13}\,\hat{Y}_b - n_{13}\,\hat{Z}_b$$

$$\vec{r}_P = X\,\hat{X}_b + Y\,\hat{Y}_b + Z\,\hat{Z}_b$$

$$\vec{\rho} = (-r\ell_{13} + X)\,\hat{X}_b + (-r\,m_{13} + Y)\,\hat{Y}_b + (-r\,n_{13} + Z)\,\hat{Z}_b$$

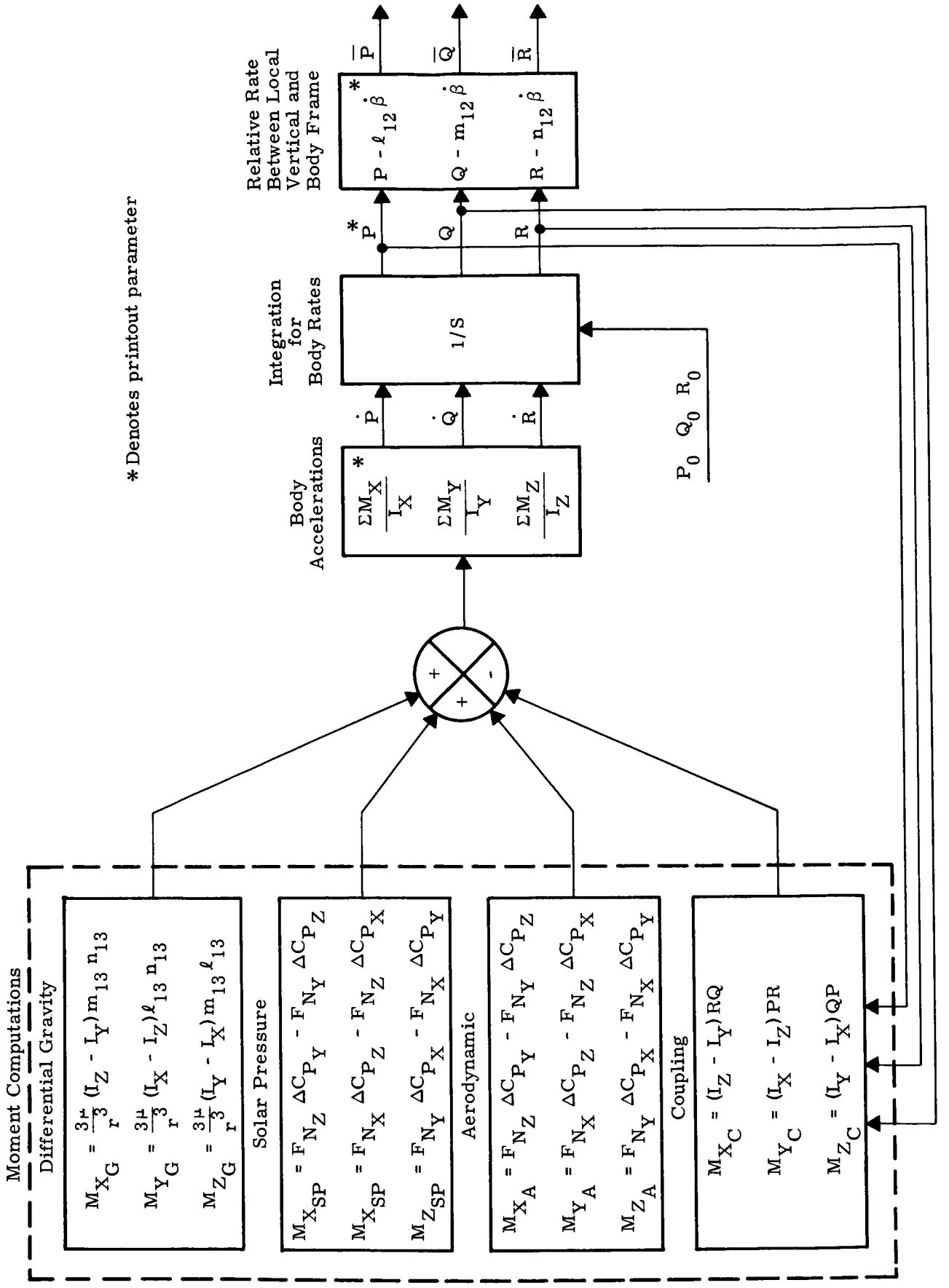

Fig. V-20a. Flow Chart of Micrometeoroid Digital Dynamics Simulation Program

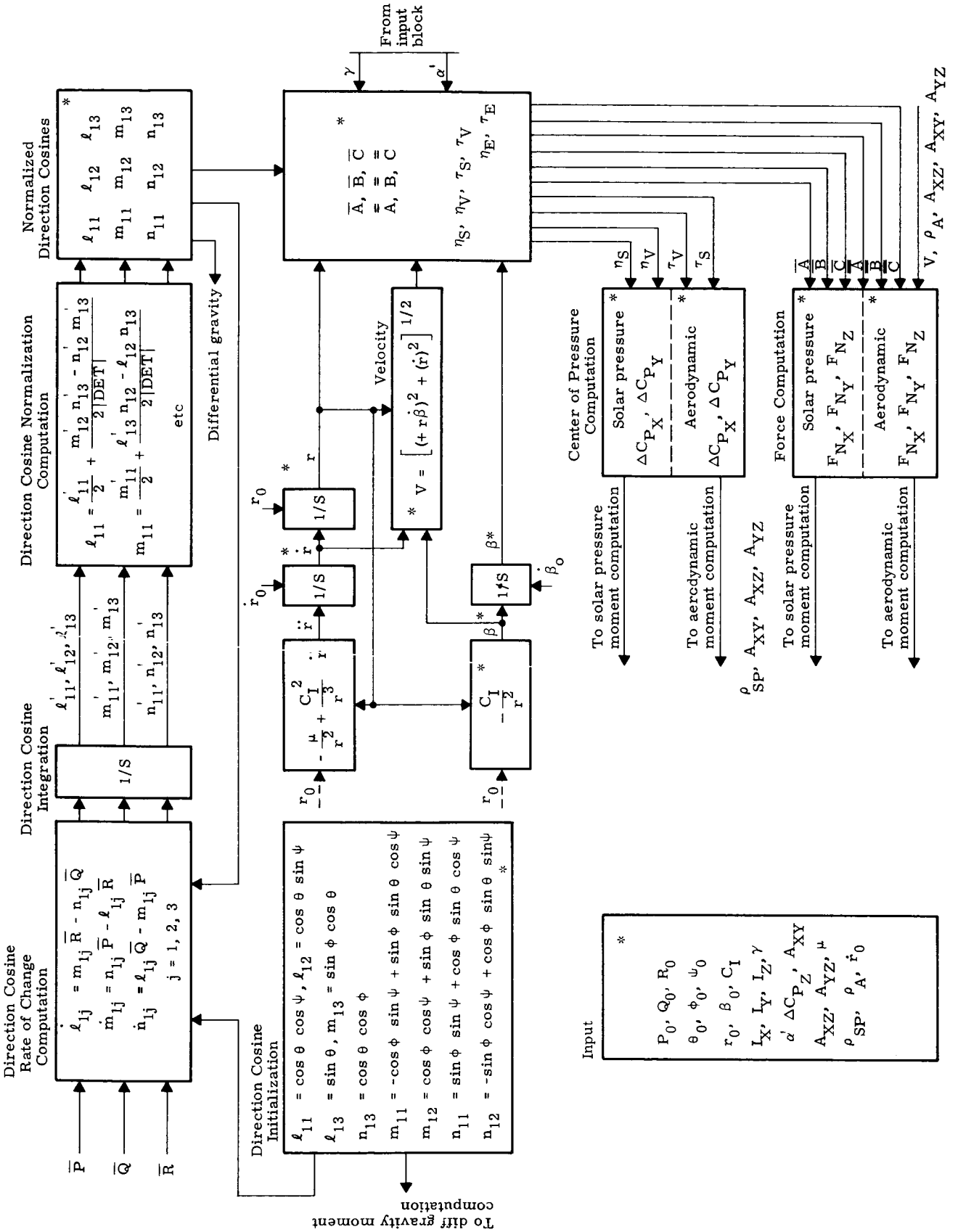

Fig. V-20b. Flow Chart of Micrometeoroid Digital Dynamics Simulation Program

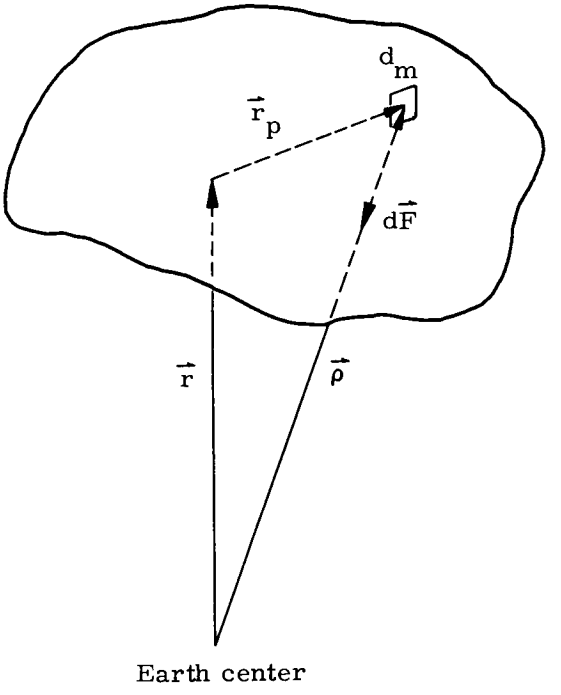

Fig. V-21. Action of a Central Force on an Extended Body

Therefore,

$$d\vec{F} = \frac{\mu dm}{\rho^3} \left[(-r\,\ell_{13} + X)\,\hat{X}_b + (-r\,m_{13} + Y)\,\hat{Y}_b + (-r\,n_{13} + Z)\,\hat{Z}_b \right]$$

we know that

$$\rho^2 = r^2 + r_P^2 + 2\,r\,(\vec{r}_P \cdot \hat{r})$$

$$\therefore\ \rho^3 = \frac{1}{r^3} \left[1 + \left(\frac{r_P}{r}\right)^2 + \frac{2}{r}\,(\vec{r}_P \cdot \hat{r}) \right]^{-3/2}$$

By neglecting $\left(\frac{r_P}{r}\right)^2$, and expanding using first two terms of the binomial theorem:

$$\rho^3 = \frac{1}{r^3} \left[1 - \frac{3}{r}\,(\vec{r}_P \cdot \hat{r}) \right]$$

The differential moment, due to differential force $d\vec{F}$, about the center of mass is:

$$d\vec{M} = \vec{r}_P \times d\vec{F}$$

$$d\vec{M} = \frac{-\mu dm}{r^3} \left[1 - \frac{3}{r}\,(\vec{r}_P \cdot \hat{r}) \right] \begin{bmatrix} \hat{X}_b & \hat{Y}_b & \hat{Z}_b \\ X & Y & Z \\ -r\,\ell_{13} + X & -r\,m_{13} + Y & -r\,n_{13} + Z \end{bmatrix}$$

The differential moment component about the X_b axis becomes:

$$d\vec{M}_{X_b} = \frac{-\mu}{r^2} \left[1 - \frac{3}{r}\,(\vec{r}_P \cdot \hat{r}) \right] \left[Z\,m_{13} - Y\,n_{13} \right] dm$$

$$\vec{r}_P \cdot \hat{r} = -\ell_{13}\,X - m_{13}\,Y - n_{13}\,Z$$

Substituting and integrating yields

$$\vec{M}_{X_b} = \frac{-\mu}{r^2} \left[m_{13} \int Z\,dm - n_{13} \int Y\,dm \right] - \frac{3\mu}{r^3} \left[\ell_{13}\,n_{13} \int XZ\,dm + \right.$$

$$+ m_{13}^2 \int Z\,Y\,dm + m_{13}\,n_{13} \int Z^2\,dm - n_{13}\,\ell_{13} \int X\,Y\,dm$$
$$- n_{13}\,m_{13} \int Y^2\,dm - n_{13}^2 \int Y\,Z\,dm \Big]$$

Since $\vec{r}_P$ originates at the center of mass

$$\int X\,dm = \int Y\,dm = \int Z\,dm = 0$$

Also, since the body axes are principal axes,

$$\int XY\,dm = \int XZ\,dm = \int YZ\,dm = 0$$

Therefore,

$$\vec{M}_{X_b} = \frac{-3\mu}{r^3} \left[m_{13}\,n_{13} \int (Z^2 - Y^2)\,dm \right]$$

Hence,

$$\vec{M}_{X_b} = \frac{3\mu}{r^3} (I_Z - I_Y)\,m_{13}\,n_{13}$$

Similarly,

$$\vec{M}_{Y_b} = \frac{3\mu}{r^3} (I_X - I_Z)\,\ell_{13}\,n_{13}$$
$$\vec{M}_{Z_b} = \frac{3\mu}{r^3} (I_Y - I_X)\,m_{13}\,\ell_{13}$$

The preceding derivation is similarly presented in Ref. V-7.

(4) Solar pressure torque

The direction vector of the solar rays from the sun with respect to the inertial axes is shown in Fig. V-22a. The first step in determining solar pressure moments is to define this unit vector in body coordinates. By inspection:

$$\hat{S} = \left[-\cos\gamma\cos\alpha',\ -\cos\gamma\sin\alpha',\ -\sin\gamma\right] \begin{bmatrix} \hat{X}_I \\ \hat{Y}_I \\ \hat{Z}_I \end{bmatrix}$$

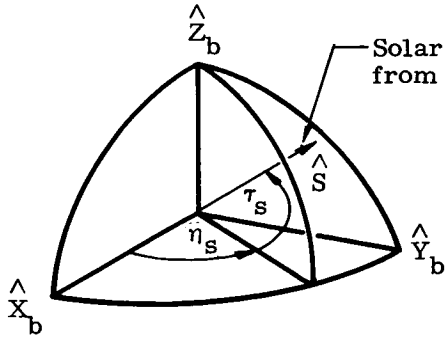

$$\hat{S} = \bar{A}\,\hat{X}_b + \bar{B}\,\hat{Y}_b + \bar{C}\,\hat{Z}_b$$

$$\tau_s = \sin^{-1}\bar{C}$$

$$\eta_s = \tan^{-1}\frac{\bar{B}}{\bar{A}}$$

a. Solar Ray Unit Vector

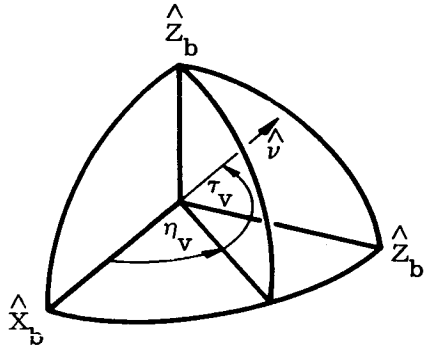

$$\hat{V} = \bar{\bar{A}}\,\hat{X}_b + \bar{\bar{B}}\,\hat{Y}_b + \bar{\bar{C}}\,\hat{Z}_b$$

$$\tau_v = \sin^{-1}\bar{\bar{C}}$$

$$\eta_v = \tan^{-1}\frac{\bar{\bar{B}}}{\bar{\bar{A}}}$$

b. Velocity Unit Vector

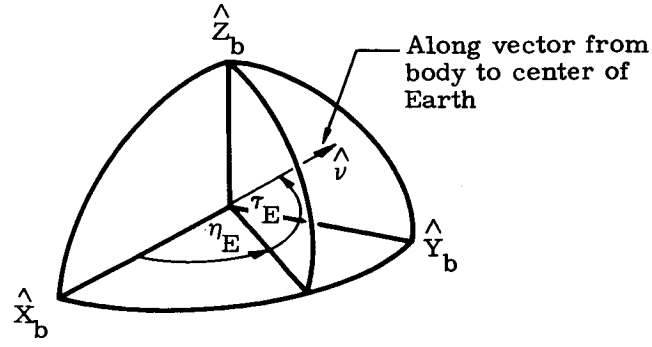

$$\hat{\nu} = \ell_{13}\,\hat{X}_b + m_{13}\,\hat{Y}_b + M_{13}\,\hat{Z}_b$$

$$\tau_E = \sin^{-1} n_{13}$$

$$\eta_E = \tan^{-1}\frac{m_{13}}{\ell_{13}}$$

c. Local Vertical Unit Vector

Fig. V-22. Definition of Pertinent Unit Vectors in Body Axes

$$\therefore \hat{S} = \left[-\cos\gamma\cos\alpha',\ -\cos\gamma\sin\alpha',\ -\sin\gamma\right]\left[T_{IB}\right]\begin{bmatrix}\hat{X}_b\\ \hat{Y}_b\\ \hat{Z}_b\end{bmatrix}$$

Expanding this matrix yields.

$$\begin{aligned}\hat{S} = {} & (\cos\gamma\cos\alpha'\sin\beta\ell_{11} + \cos\gamma\cos\alpha'\cos\beta\ell_{13} \\ & - \cos\gamma\sin\alpha'\ell_{12} - \sin\gamma\cos\beta\ell_{11} + \sin\gamma\sin\beta\ell_{13})\hat{X}_b \\ & + (\cos\gamma\cos\alpha'\sin\beta m_{11} + \cos\gamma\cos\alpha'\cos\beta m_{13} \\ & - \cos\gamma\sin\alpha' m_{12} - \sin\gamma\sin\beta m_{11} + \sin\gamma\sin\beta m_{13})\hat{Y}_b \\ & + (\cos\gamma\cos\alpha'\sin\beta n_{11} + \cos\gamma\cos\alpha'\cos\beta n_{13} \\ & - \cos\gamma\sin\alpha' n_{12} - \sin\gamma\sin\beta n_{11} + \sin\gamma\sin\beta n_{13})\hat{Z}_b\end{aligned}$$

or

$$\hat{S} = \bar{A}\,\hat{X}_b + \bar{B}\hat{Y}_b + \bar{C}\,\hat{Z}_b$$

Now, a photon of momentum δ, striking a surface ΔA is either completely absorbed or completely reflected. The resulting force on the surface is due to the change in momentum of the photon per unit time. Now, considering the surface characteristics to be such as to completely reflect all photons, the change of momentum per collision is:

$$\vec{\sigma}_N = 2\delta\cos i\,\hat{e}_N$$

where

i = angle of incidence

$\hat{e}_N$ = unit vector normal to surface.

If N is the number of photons incident upon a surface per unit time, the magnitude of force acting normal to the surface is:

$$F_N = 2N\delta\cos i\,A$$

Now if N_0 is the number of particles incident upon a unit surface per unit time at normal incidence,

$$N = N_0 \cos i$$

$$\therefore F_N = 2 N_0 \delta \cos^2 i A = 2 \rho_{SP} \cos^2 i A$$

ρ_{SP} = solar pressure constant

The assumption of all photons being reflected off the surfaces was made since it was felt that this is worst-case situation. However, in practice, the reflectivity coefficient will be much less than one. As discussed in Section B.1.c, it appears that a spin-up condition for the configuration is possible. Therefore, it is suggested that, if a further investigation is pursued, the surface absorption characteristics be considered as presented in Ref. V-8.

$$F_{NX_{SP}} = 2 \rho_{SP} A_{YZ} \bar{A}^2 \text{ for } \bar{A} > 0$$

$$F_{NX_{SP}} = -2 \rho_{SP} A_{YZ} \bar{A}^2 \text{ for } \bar{A} < 0$$

$$F_{NY_{SP}} = 2 \rho_{SP} A_{XZ} \bar{B}^2 \text{ for } \bar{B} > 0$$

$$F_{NY_{SP}} = 2 \rho_{SP} A_{XZ} \bar{B}^2 \text{ for } \bar{B} < 0$$

$$F_{NZ_{SP}} = 2 \rho_{SP} A_{XY} \bar{C}^2 \text{ for } \bar{C} > 0$$

$$F_{NZ_{SP}} = -2 \rho_{SP} A_{XY} \bar{C}^2 \text{ for } \bar{C} < 0$$

Solar pressure moments are generated through center of gravity and center of pressure differences

$$\vec{M}_{SP} = \left(\vec{\Delta C}_P \times \vec{F}\right)_{SP} = \left(F_{NZ} \Delta C_{P_Y} - F_{N_Y} \Delta C_{P_Z}\right)_{SP} \hat{X}_b + \left(F_{NX} \Delta C_{P_Z} - F_{NZ} \Delta C_{P_X}\right)_{SP} \hat{Y}_b + \left(F_{NY} \Delta C_{P_X} - F_{NX} \Delta C_{P_Y}\right)_{SP} \hat{Z}_b$$

where

$$\overrightarrow{\Delta C_P} = \Delta C_{P_X} \hat{X}_b + \Delta C_{P_Y} \hat{Y}_b + \Delta C_{P_Z} \hat{Z}_b$$

Geometric analysis of the "Z" configuration yielded the following center of pressure variation relationships. See Fig. V-22 for definition of η_S and τ_S.

$$\Delta C_{P_X} = 3.4 \sin \eta_S \sin \tau_S \text{ (for } |\bar{C}| \leq 0.707) \text{ and } \Delta C_{P_X} = 3.4 \sin \eta_S \cos \tau_S \frac{\bar{C}}{|\bar{C}|} \text{ (for } |\bar{C}| > 0.707)$$

$$\Delta C_{P_Y} = -3.4 \cos \eta_S \sin \tau_S \text{ (for } |\bar{C}| \leq 0.707) \text{ and } \Delta C_{P_Y} = -3.4 \cos \eta_S \cos \tau_S \frac{\bar{C}}{|\bar{C}|} \text{ (for } |\bar{C}| > 0.707)$$

$$\Delta C_{P_Z} = \text{constant}$$

(5) Aerodynamic torque

The first step in determining this torque is to define the velocity unit vector in body coordinates. Solution of the orbital equations of motion will generate r, $\dot{r}$, β, $\dot{\beta}$ and V, which are shown vectorially in Fig. V-23. By inspection, the following velocity vector equation can be stated.

$$\vec{V} = \left[-r\dot{\beta},\ 0,\ -\dot{r}\right] \begin{bmatrix} \hat{n} \\ \hat{e} \\ \hat{v} \end{bmatrix} = \left[-r\dot{\beta},\ 0,\ -\dot{r}\right] \left[T_{VB}\right] \begin{bmatrix} \hat{n} \\ \hat{e} \\ \hat{v} \end{bmatrix}$$

The velocity unit vector becomes

$$\hat{V} = \frac{1}{|\vec{V}|} \left[-r\dot{\beta},\ 0,\ -\dot{r}\right] \left[T_{VB}\right] \begin{bmatrix} \hat{n} \\ \hat{e} \\ \hat{v} \end{bmatrix}$$

or

$$\hat{V} = \bar{\bar{A}} \hat{X}_b + \bar{\bar{B}} \hat{Y}_b + \bar{\bar{C}} Z_b$$

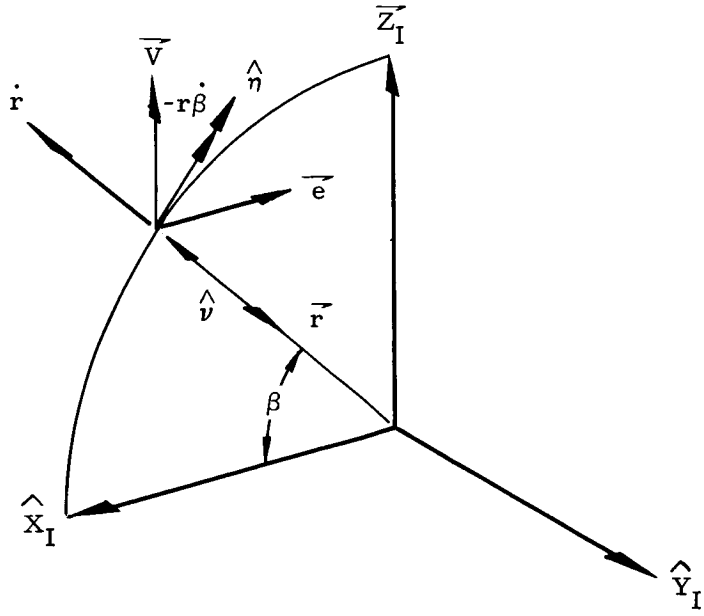

Fig. V-23. Orbital Velocity Parameters in Local Vertical Frame

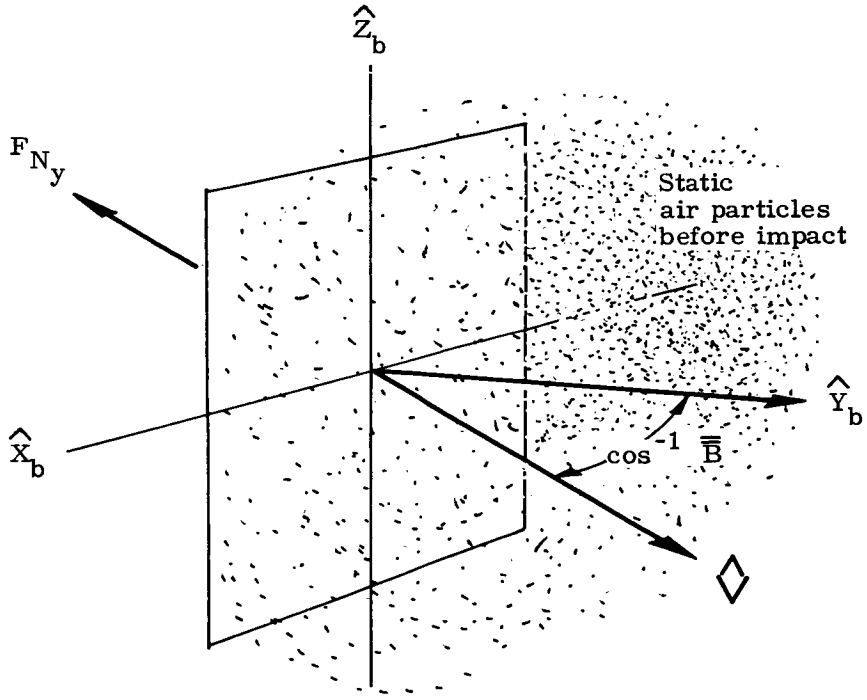

Fig. V-24. Illustration of Mechanics Involved in Aerodynamic Force

where

$$\bar{\bar{A}} = \frac{-r\dot{\beta}\,\ell_{11} - \dot{r}\,\ell_{13}}{|V|} \qquad \bar{\bar{B}} = \frac{-r\dot{\beta}\,m_{11} - \dot{r}\,m_{13}}{|V|} \qquad \bar{\bar{C}} = \frac{-r\dot{\beta}\,n_{11} - \dot{r}\,n_{13}}{|V|}$$

Referring to Fig. V-24 and considering a completely elastic impact of static air particles on area A_{XZ}, it is clear that

$$\overrightarrow{F_{NY}} = -\rho_a V^2 \bar{\bar{B}}^2 A_{XZ} \text{ for } \bar{\bar{B}} > 0$$

where

ρ_A = atmospheric density

Also,

$$\overrightarrow{F_{NY}} = +\rho_A V^2 \bar{\bar{B}}^2 A_{XZ} \text{ for } \bar{\bar{B}} < 0$$

Similarily, for the forces along the $\hat{X}_b$ and $\hat{Z}_b$ directions

$$\overrightarrow{F_{NX}} = -\rho_A V^2 \bar{\bar{A}}^2 A_{YZ} \text{ for } \bar{\bar{A}} > 0$$

$$\overrightarrow{F_{NX}} = +\rho_A V^2 \bar{\bar{A}}^2 A_{YZ} \text{ for } \bar{\bar{A}} < 0$$

Also

$$\overrightarrow{F_{NZ}} = -\rho_A V^2 \bar{\bar{C}}^2 A_{XY} \text{ for } \bar{\bar{C}} > 0$$

$$\overrightarrow{F_{NZ}} = +\rho_A V^2 \bar{\bar{C}}^2 A_{XY} \text{ for } \bar{\bar{C}} < 0$$

The aerodynamics moment form is identical to the solar pressure form. However, since, in general, the velocity direction with respect to the body axes will differ from the solar ray direction, the center of pressure calculations are referenced to the velocity unit vector terms (Fig. V-22b).

$$\Delta C_{P_X} = 3.4 \sin\eta_v \sin\tau_v \text{ for } |\bar{\bar{C}}| \leq 0.707$$

$$\Delta C_{P_X} = +3.4 \sin\eta_v \cos\tau_v \frac{\bar{\bar{C}}}{|\bar{\bar{C}}|} \text{ for } |\bar{\bar{C}}| > 0.707$$

$$\Delta C_{P_Y} = -3.4 \cos\eta_v \sin\tau_v \text{ for } |\bar{\bar{C}}| \leq 0.707$$

$$\Delta C_{P_Y} = -3.4 \cos\eta_v \cos\tau_v \frac{\bar{\bar{C}}}{|\bar{\bar{C}}|} \text{ for } |\bar{\bar{C}}| > 0.707$$

$$\Delta C_{P_Z} = \text{constant.}$$

$$\therefore \vec{M}_A = \left(F_{NZ}\,\Delta C_{P_Y} - F_{NY}\,\Delta C_{P_Z}\right)_A \hat{X}_b + \left(F_{NX}\,C_{P_Z} - F_{NZ}\,\Delta C_{P_X}\right)_A \hat{Y}_b + \left(F_{NY}\Delta C_{P_X} - F_{NX}\Delta C_{P_Y}\right)_A \hat{Z}_b$$

(6) Magnetic field torque

Assuming a dipole representation for the earth's magnetic field, the magnetic intensity vector can be defined in the magnetic frame as follows (Fig. V-19).

$$\vec{H}_E = \left[H_X,\ H_Y,\ H_Z\right] \begin{bmatrix} \hat{X}_H \\ \hat{Y}_H \\ \hat{Z}_H \end{bmatrix}$$

where:

$$H_X = \frac{M_E}{r^3}\left(-3 \sin\phi_\nu \cos\phi_\nu \cos\zeta_\nu\right)$$

$$H_Y = \frac{M_E}{r^3}\left(-3 \sin\phi_\nu \cos\phi_\nu \sin\zeta_\nu\right)$$

$$H_Z = \frac{M_E}{r^3}\left(-2 \sin^2\phi_\nu + \cos^2\phi_\nu\right)$$

M_E - geomagnetic moment

$$\therefore \vec{H}_E = \left[H_X,\ H_Y,\ H_Z\right]\left[T_{HE}\right]\left[T_{EI}\right]\left[T_{IB}\right] \begin{bmatrix} \hat{X}_b \\ \hat{Y}_b \\ \hat{Z}_b \end{bmatrix}$$

or

$$\vec{H}_E = \left[D,\ E,\ F\right] \begin{bmatrix} \hat{X}_b \\ \hat{Y}_b \\ \hat{Z}_b \end{bmatrix}$$

To calculate the scalar components of the intensity vector, the vehicle geomagnetic latitude (ϕ_ν) and longitude (ζ_ν) need be determined.

$$\vec{r} = \left[r\cos\beta,\ O,\ r\sin\beta\right] \begin{bmatrix} \hat{X}_I \\ \hat{Y}_I \\ \hat{Z}_I \end{bmatrix} = \left[r\cos\beta,\ O,\ r\sin\beta\right]\left[T_{IE}\right]\left[T_{EH}\right] \begin{bmatrix} \hat{X}_H \\ \hat{Y}_H \\ \hat{Z}_H \end{bmatrix}$$

$$\sin\phi_\nu = \frac{\vec{r} \cdot \hat{Z}_H}{|r|} = \cos\beta \cos\omega_e t \cos\psi_M \sin\alpha_M - \cos\beta \sin\omega_e t \sin\psi_M$$

$$\sin\alpha_M + \sin\beta \cos\alpha_M$$

Rewriting the radius vector:

$$\vec{r} = \left[r_X, r_Y, r_Z\right] \begin{bmatrix} \hat{X}_H \\ \hat{Y}_H \\ \hat{Z}_H \end{bmatrix}$$

$$\cos\zeta_\nu = \frac{r_X}{\left(r_X^2 + r_Y^2\right)^{1/2}} \quad \sin\zeta_\nu = \frac{r_Y}{\left(r_X^2 + r_Y^2\right)^{1/2}}$$

Now, if the vehicle has a permanent magnetic moment with components A, B and C along the X, Y, Z body axes respectively, an interaction torque will arise from the geomagnetic field.

$$\vec{M}_M = (A\hat{X}_b + B\hat{Y}_b + C\hat{Z}_b) \times \vec{H}_E$$

$$\vec{M}_M = \left[(BF - CE), (CD - AF), (AE - BD)\right] \begin{bmatrix} \hat{X}_b \\ \hat{Y}_b \\ \hat{Z}_b \end{bmatrix}$$

SYMBOLS

A, B, C	Permanent vehicle magnetic moments along $\hat{X}_b$, $\hat{Y}_b$, $\hat{Z}_b$
$\bar{A}$, $\bar{B}$, $\bar{C}$	Direction cosines of solar ray unit vector from sun in body frame
$\bar{\bar{A}}$, $\bar{\bar{B}}$, $\bar{\bar{C}}$	Direction cosines of velocity vector and body frame
C_I	Orbital angular momentum
D, E, F	Scalar components of earth magnetic intensity vector along $\hat{X}_b$, $\hat{Y}_b$, $\hat{Z}_b$
F_{N_X}, F_{N_Y}, F_{N_Z}	Normal forces along $\hat{X}_b$, $\hat{Y}_b$, $\hat{Z}_b$

α'	Longitude of solar ray unit vector in inertial
β	Orbital true anomaly
$\dot{\beta}$	Orbital true anomaly rate
γ	Latitude of solar ray unit vector in inertial frame
n_E	Longitude of local vertical unit vector in body frame
n_S	Longitude of solar ray unit vector in body frame
n_V	Longitude of velocity unit vector in body frame
$\hat{n}$, $\hat{e}$, $\hat{v}$	Local vertical frame unit vectors
μ	Gravitational constant
H_X, H_Y, H_Z	Scalar components of earth magnetic intensity vector along $\hat{X}_H$, $\hat{Y}_H$, $\hat{Z}_H$
I_X, I_Y, I_Z	Principal moments of inertia of vehicle
ℓ_{11}, m_{11}, n_{11}	Direction cosines of $\hat{n}$ unit vector in body frame
ℓ_{12}, m_{12}, n_{12}	Direction cosines of $\hat{e}$ unit vector in body frame
ℓ_{13}, m_{13}, n_{13}	Direction cosines of $\hat{v}$ unit vector in body frame
M_E	Geomagnetic moment
P, Q, R	Angular rates about $\hat{X}_b$, $\hat{Y}_b$, $\hat{Z}_b$, respectively
$\dot{P}$, $\dot{Q}$, $\dot{R}$	Angular accelerations about $\hat{X}_b$, $\hat{Y}_b$, $\hat{Z}_b$, respectively
$\vec{r}$	Orbital radius vector
$\dot{\vec{r}}$	Orbital radius vector rate
$\vec{V}$	Orbital velocity vector
$\hat{X}_b$, $\hat{Y}_b$, $\hat{Z}_b$	Body axes unit vectors
$\hat{X}_I$, $\hat{Y}_I$, $\hat{Z}_I$	Inertial axes unit vectors
α_M	Colatitude of magnetic North Pole relative to earth fixed frame

ξ_ν	Vehicle magnetic longitude
$\vec{\rho}$	Vector from center of earth to elemental mass, d_m
ρ_A	Atmospheric density
ρ_{SP}	Solar pressure constant
τ_E	Latitude of local vertical unit vector in body frame
τ_S	Latitude of solar ray unit vector in body frame
τ_v	Latitude of velocity unit vector in body frame
ϕ_ν	Vehicle magnetic latitude
ψ_M	Longitude of magnetic North Pole relative to earth fixed frame
ψ, θ, ϕ	Eulerian angles
ω_e	Earth's sideral rate

(7) Special considerations

Direction cosine orthogonality. A problem intrinsically associated with any digital integration program involving generation of a direction cosine matrix is matrix orthogonality. Nonorthogonality creeps into the computations due to such items as computer roundoff error. This problem has been alleviated in two ways. First, a double precision integration technique is used, and secondly, the computed direction cosine matrix is adjusted to reduce a bias type error in the following manner.

$$[A'] = \begin{bmatrix} \ell_{11}' & \ell_{12}' & \ell_{13}' \\ m_{11}' & m_{12}' & m_{13}' \\ n_{11}' & n_{12}' & n_{13}' \end{bmatrix}$$

then

$$\ell_{11} = \frac{\ell_{11}'}{2} + \frac{m_{12}' n_{13}' - n_{12}' m_{13}'}{|2 \text{ DET } A'|}$$

$$m_{11} = \frac{m_{11}'}{2} + \frac{n_{12} \ell_{13} - \ell_{12} n_{13}}{|2 \text{ DET } A'|}, \text{ etc.}$$

Angular output data. Integration of the equation of motion as shown in Section B.1.b directly produces the designed body rates, P, Q and R. However, to realize the vehicle orientation associated with these rates in inertial space, the angular position of the body axes with respect to the sun line is computed. This attitude information is presented as sun ray longitude and latitude in the body axes (Fig. V-22a). These parameters do not uniquely define vehicle attitude orientation to the sun. However, their rate of change does determine whether a preferred inertial orientation is being obtained. Also, they are of direct concern in designing the thermal and electrical power systems. The orientation of local earth vertical to the body axes is computed in the same manner as the sun vector (Fig. V-22c). It is apparent that knowing the latitude and longitude of these two unit vectors, plus the ephemeris data, allows for unique attitude orientation with respect to any defined frame of reference. However, the main reason for computing the local vertical parameters is to evaluate the effects of vehicle dynamics as it pertains to the number and sampling frequency of the earth sensors.

c. Typical vehicle dynamics

Evolution of the digital simulation program was stepwise continuous in mechanizing the torques as defined in the preceding section. During the early phases of the study, the program was essentially geared for a flat plate configuration. Hence, the "Z" configuration solar pressure torque (as defined in Section B.1.b) was the last item to be incorporated. Due to a time limitation, only a preliminary analysis of the effects of this torque on the dynamics of the "Z" configuration was possible. The following text will attempt to uncover the relationships of these torques on vehicle dynamics. However, it is felt that to fully evaluate the dynamic behavior of the "Z" and/or flat plate tumbling configurations, a separate evaluation is necessary to encompass a more complete matrix of initial conditions, orbit degradation, sun orientation variations and moment of inertia tolerances.

The following statements can be made from the analysis effort to date.

(1) Differential gravity torques are significant and act for approximately 3 to 4 hr about the low perigee altitude point.

(2) Dynamic motion variations due to differential gravity torques are related to the phasing of vehicle orientation to local vertical. Rotational energy can be gained or lost due to this phasing.

(3) Aerodynamic torques are impulse-like about perigee. Due to high altitude rate of change about perigee, this torque acts for a maximum time of 0.2 hr at the 200-naut mi perigee orbit.

(4) The net rotational energy added or dissipated due to the aerodynamic torque is related to the phasing of vehicle orientation with respect to the velocity vector.

(5) For the "Z" configurations, the nominal acceleration about the "Z" body axis is due to aerodynamic and solar pressure torques.

(6) A flat plate, with an aspect ratio of one and no center of gravity-center of pressure displacement, has vehicle dynamic characteristics which, for all practical purposes, are constant rates about the X and Y body axis or constant cyclic rotational energy exchange between the two axes if the initial "Z" body tip-off rate is other than zero.

(7) Preliminary results indicate the possibility of a spin rate developing for the "Z" configuration. This condition is primarily caused by solar pressure torques. The magnitude and direction are a function of initial conditions, including the sun orientation to the orbit plane. Long term effects of the variation in the sun orientation plus perigee perturbations in vehicle orientation to the sun, have not been evaluated. As a result, a limit on the spin rate, which would be realized over an extended mission life time, can not be determined without further study.

(1) Detailed discussion

Considering only differential gravity torques to act on the vehicle, the equations of motion reduce to:

$$\dot{P} = \frac{3\mu}{r^3}\left(\frac{I_Z - I_Y}{I_X}\right) n_{13}\, m_{13} - \left(\frac{I_Z - I_Y}{I_X}\right) RQ$$

$$\dot{Q} = \frac{3\mu}{r^3}\left(\frac{I_X - I_Z}{I_Y}\right) \ell_{13}\, n_{13} - \left(\frac{I_X - I_Z}{I_Y}\right) PR$$

$$\dot{R} = \frac{3\mu}{r^3}\left(\frac{I_Y - I_X}{I_Z}\right) m_{13}\, \ell_{13} - \left(\frac{I_Y - I_X}{I_Z}\right) QP$$

For a symmetrical flat plate or the "Z" vehicle, $I_X = I_Y$ and $I_Z > I_X$. For this situation, the "Z" body acceleration equation reduces to:

$$\dot{R} = 0$$

$$\therefore\ R = R_0$$

where R_0 is the tip-off rate about the "Z" body axis for a tumbling vehicle or spin rate for a spin vehicle.

Now, examining the condition where the initial orientation and tip-off rates are zero, R equals zero for all time. Moreover, the cross-coupling terms in the $\dot{P}$ and $\dot{Q}$ equations are zero. Also, since $\phi_0 = \psi_0 = \theta_0 = 0$.

$$n_{13}\, m_{13} = \sin\phi \cos\phi \cos^2\theta = 0$$

and

$$\ell_{13}\, m_{13} = -\cos\theta \cos\phi \sin\theta = 0$$

Therefore, at t = 0, no torques are acting on the vehicle. The resulting motion for this condition is shown in Fig. V-25. As can be seen, the X and Z body rates are zero while, for all practical purposes, the Y body rate maintains an average value of 5.2×10^{-4} rad/sec. Pertubations in this rate occur in the three perigee regions. The manner in which the initial rate builds up can be explained by referring to Fig. V-26. As mentioned earlier, the torque at t = 0 is zero. However, a short time later, the orbital motion causes the radius vector to rotate relative to the vehicle frame and a pitch angle is developed. As a result, $\ell_{13}\, n_{13}$ obtains a value which produces a positive acceleration about the Y body axes. This acceleration produces a positive rate which, coupled with the radius vector direction change produces a situation where the radius vector crosses the X_b axis, the pitch angle changes sign and a deceleration occurs. Due to the radius magnitude change, the deceleration torque magnitude is reduced such that the

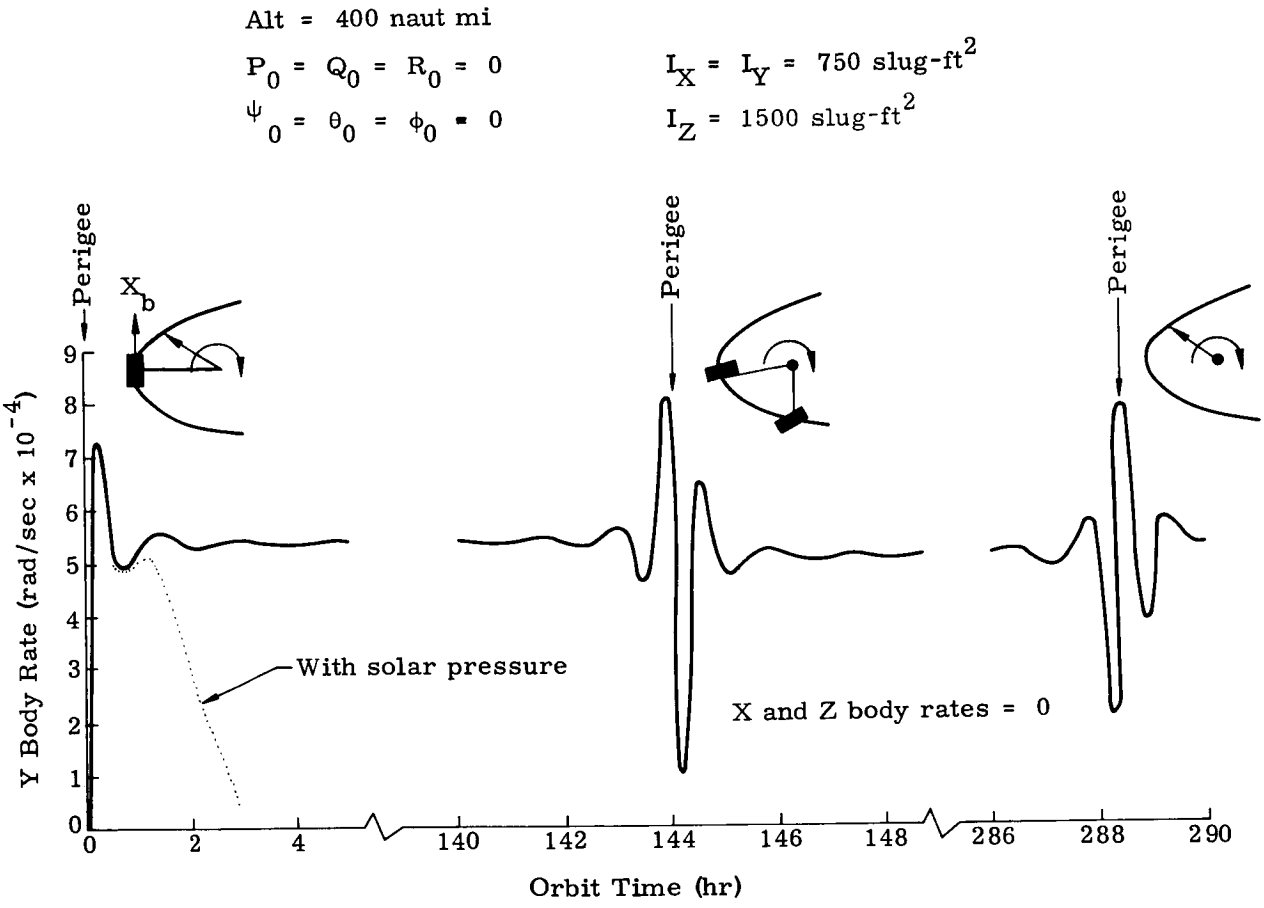

Fig. V-25. Dynamic Behavior Due to Differential Gravity--Zero Initial Conditions

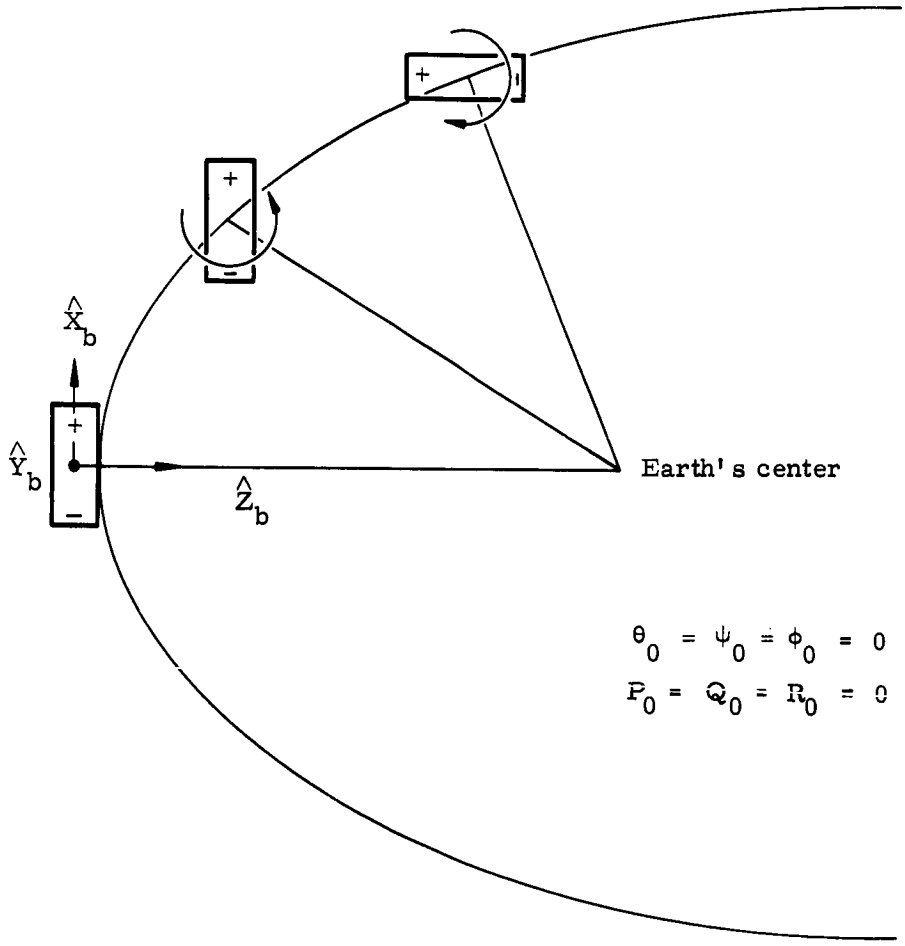

Fig. V-26. Illustration of Vehicle Differential Gravity Torque

initial induced rate is not cancelled out. A positive rate results. As the vehicle tumbles, it undergoes acceleration and deceleration torques but, due to the differential force magnitude reduction, each torque change is smaller and an acceleration damped system is realized, resulting in a steady-state positive rate handoff. The same type of torque action takes place on the succeeding perigee points. The X body rate remains zero, since no out-of-plane orientation is produced and the roll angle (ϕ) remains zero.

Considering next a case where the initial pitch angle is 90° and the pitch tip-off rate is 5.236×10^{-4} rad/sec, the vehicle behaves as shown in Fig. V-27. This motion is caused by differential gravity torques. Again, at $t = 0$, no accelerations are present. The initial positive pitch rate (Q_0) and the relative direction change of the radius vector, causes a negative pitch angle at Δt. This orientation produces a negative Y body acceleration which cancels out the tip-off rate and results in a negative Y body rate (Fig. V-28). The initial action is primarily one of deceleration since, during this time, the pitch angle remains negative.

During the second perigee period, the pitch angle phasing is such that continued acceleration in the negative sense is obtained, with approximately a -14×10^{-4} rad/sec rate resulting. This rate is maintained until the third perigee point. At this time, the pitch angle phasing produces a positive acceleration. A near zero rate is produced at the end of this perigee period. The aforementioned rate variations encountered during the perigee regions is a clear example of the pitch angle phasing effect.

The next condition of interest is one in which a small Z body tip-off rate (R_0) exists. For this case, the crosscoupling terms significantly enter into the resulting dynamic behavior, producing a quite different characteristic motion then thus far experienced. Figure V-29 depicts this motion, where R_0 equals 5.236×10^{-4} rad/sec. The resulting cyclic motion of the X and Y body rates is easily explained. Writing the equations representative of that point in the orbit where the differential gravity torque is insignificant yields:

$$\dot{P} + \left(\frac{I_Z - I_Y}{I_X}\right) R_0 Q = 0$$

$$\dot{Q} - \left(\frac{I_Z - I_X}{I_Y}\right) R_0 P = 0$$

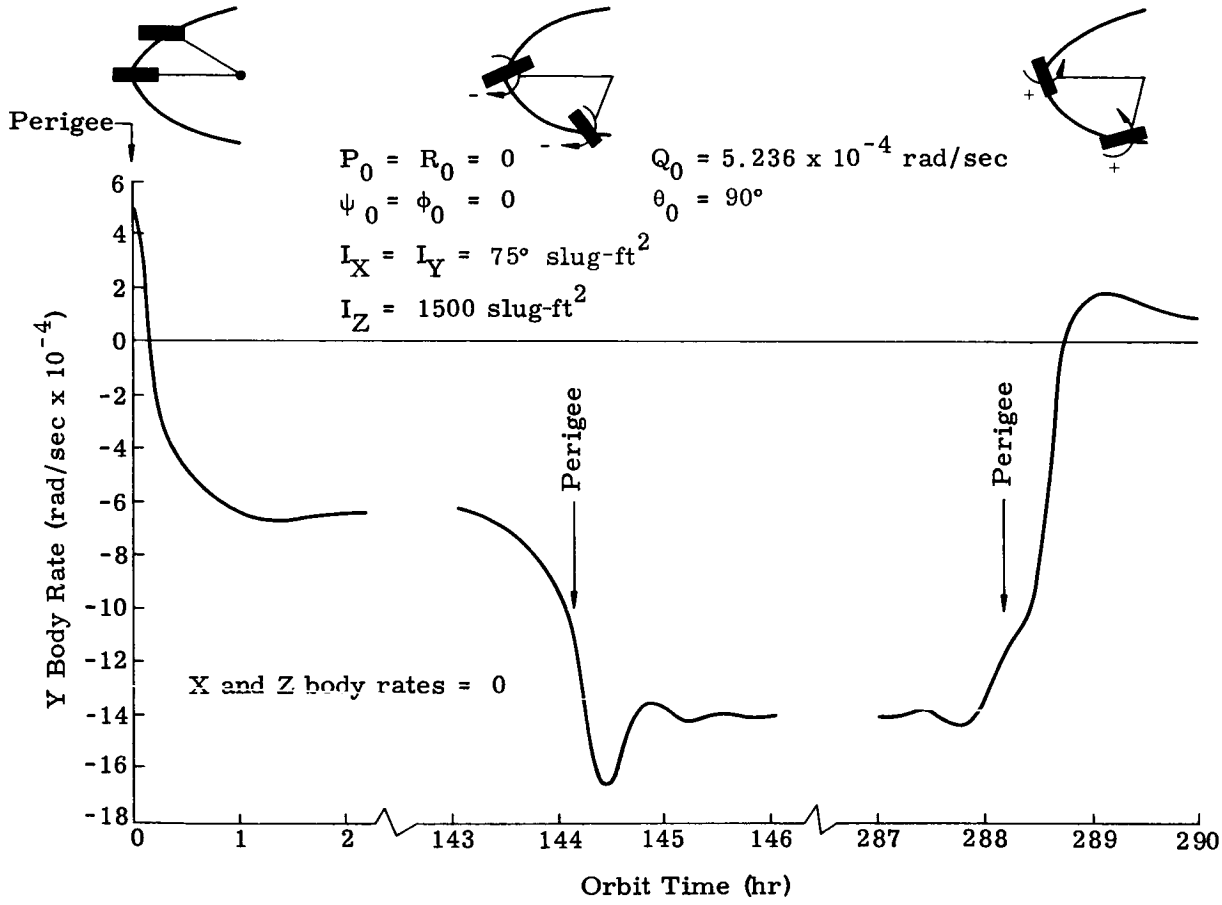

Fig. V-27. Dynamic Behavior Due to Differential Gravity Torques--Initial Pitch Offset and Rate

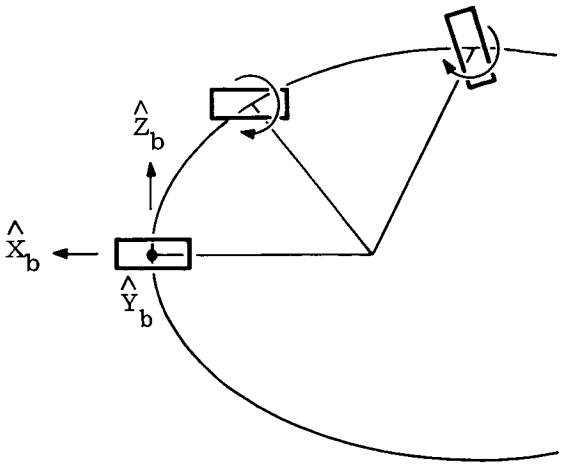

a. Injection Perigee

$\psi_0 = \phi_0 = 0$

$\theta_0 = 90°$

$Q_0 = 5.236 \times 10^{-4} \frac{\text{rad}}{\text{sec}}$

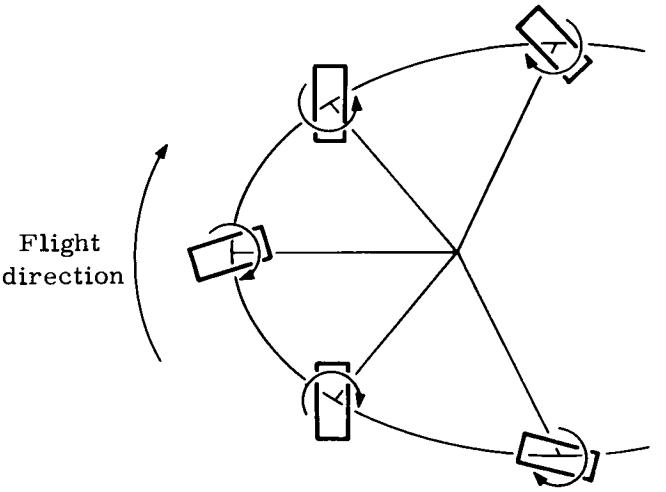

b. Second Perigee

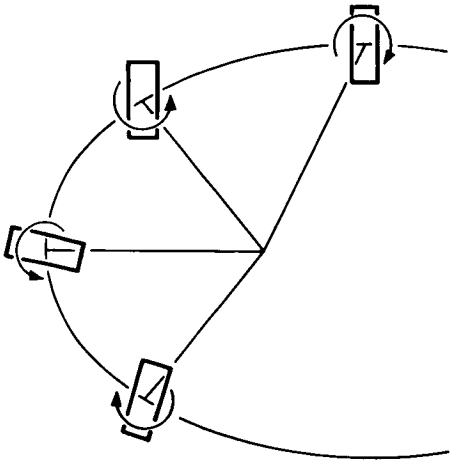

c. Third Perigee

NOTE:
Arrows indicate differential gravity acceleration direction

Fig. V-28. Illustration of Vehicle Differential Gravity Torque

$P_0 = Q_0 = 0$ $R_0 = 5.236 \times 10^{-4}$ rad/sec

$\psi_0 = \phi_0 = 0$ $\theta_0 = 90°$

R_B = constant = 5.236×10^{-4} rad/sec

$I_Z = 1500$ slug-ft^2

$I_X = I_Y = 750$ slug-ft^2

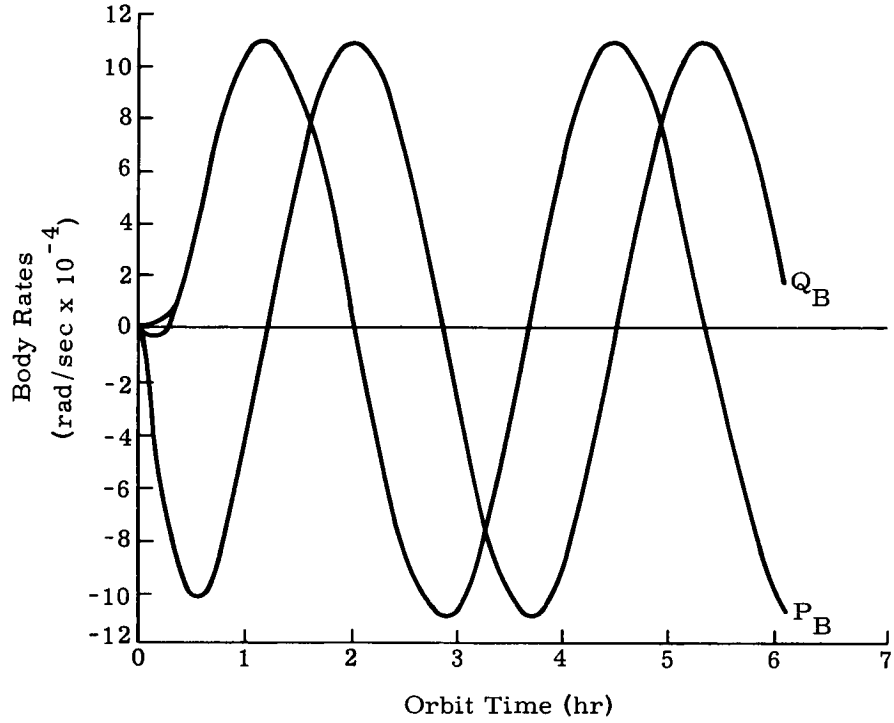

Fig. V-29. Dynamic Behavior Due to Differential Gravity Torques--Initial Pitch Offset and Yaw Rate

R_B = constant = 5.236×10^{-4} rad/sec

$P_0 = Q_0 = 0$ $R_0 = 5.236 \times 10^{-4}$ rad/sec

$\psi_0 = \phi_0 = 0$ $\theta_0 = 90°$

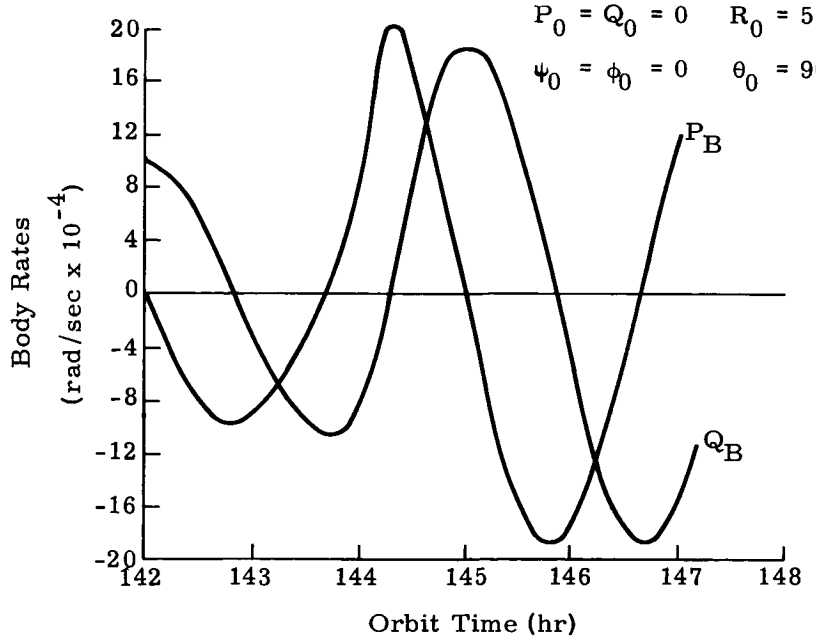

Fig. V-30. Dynamic Behavior Due to Differential Gravity Torques--Initial Pitch Offset and Yaw Rate

Differentiating the first equation, substituting from the second, and remembering $I_X = I_Y = I$.

$$\ddot{P} + R_0^2 \left(\frac{I_Z - I}{I}\right)^2 P = 0$$

This differential equation represents simple harmonic motion.

$$P = P_0 \cos \lambda t + \frac{\dot{P}_0}{\lambda} \sin \lambda t$$

$$\lambda = R_0 \left(\frac{I_Z - I}{I}\right)$$

Also, from these equations

$$Q = -\frac{\dot{P}}{\lambda} = P_0 \sin \lambda t - \frac{\dot{P}_0}{\lambda} \cos \lambda t$$

From this equation we obtain for $t = 0$

$$Q_0 = -\frac{\dot{P}_0}{\lambda}$$

These equations determine the Q and P rates to be cyclic with a frequence of

$$\lambda = R_0 \left(\frac{I_Z - I}{I}\right)$$

Also by multiplying the first acceleration equation by $\dot{Q}$ and the second by $-\dot{P}$, and adding gives:

$$Q\dot{Q} + P\dot{P} = 0$$

upon integration

$$Q^2 + P^2 = \text{constant} = \omega_{XY}$$

ω_{XY} is the resultant rate vector magnitude in the XY body axis plane and is constant in magnitude. These characteristics are seen to be present in Figs. V-29 and V-30 before and after the perigee points.

An understanding of these dynamic characteristics with respect to inertial space can be realized by referring to Fig. V-31. Consider the dimensions of the paper to be some inertial reference frame. Since no torques are present,

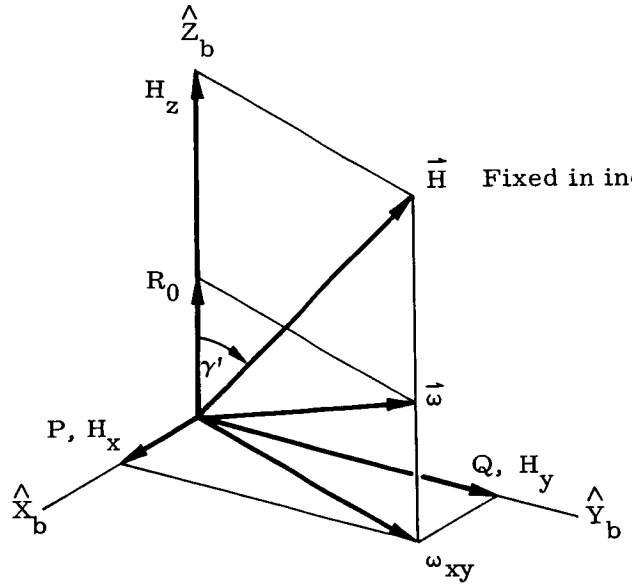

Rate vectors at t_1

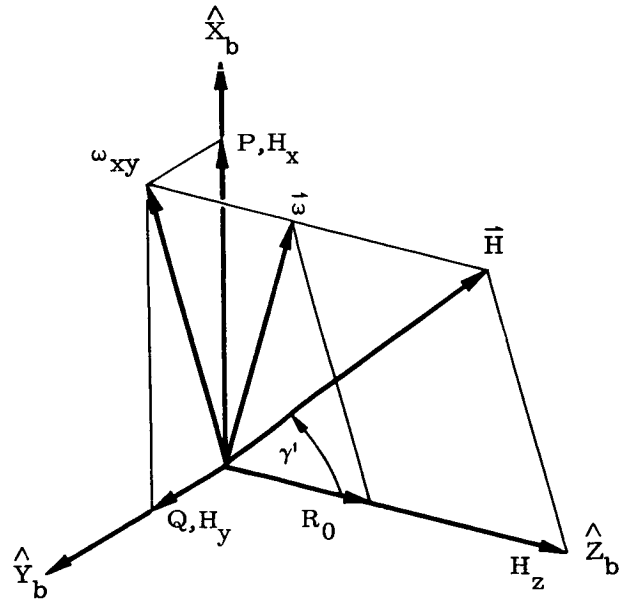

Rate vectors at t_2

Fig. V-31. Illustration of Vehicle Space Orientation

$$M = \dot{\vec{H}} = 0$$

This means that the angular momentum vector is fixed with respect to inertial space as shown at sometime, t_1. The XY components of this vector in the body frame varies with time whereas the $\hat{Z}_b$ component is constant, since R_0 is constant. The angle γ' between the $\hat{Z}_b$ and $\vec{H}$ is the familiar cone angle.

$$\tan \gamma' = \frac{I \omega_{XY}}{I_Z R_0}$$

This angle is constant.

At a later time, t_2, the body rates produce a different body axis inertial orientation. However, this orientation is constrained by the cone angle consistency and might be as shown in Fig. V-31. Refer to Ref. V-9 for more detail.

Referring back to Fig. V-29, the cone angle for the first orbit is 46.5° . During the second perigee region (Fig. V-30) differential gravity torques act and increase ω_{XY} by 100%. The cone angle increases to 61.5° but, since R_0 has not changed, the frequency (λ) remains fixed.

The manner in which the initial X and Y body rates are obtained during the first perigee regions is as follows. At time zero, all torques are zero. The radius vector change produces a negative Y body rate. This rate produces a positive X body rate through the crosscoupling term, also due to pitch, roll and yaw angle changes a negative X body rate is obtained through the differential gravity term. At 0.05 hr, the net X body acceleration is negative and accounts for the small initial negative rate in Fig. V-29. At 0.2 hr, the net X body acceleration becomes positive, due to the Y body rate buildup which increases the crosscoupling acceleration term to a point where it overrides the differential gravity acceleration. The Y body acceleration remains negative during this period since the crosscoupling is small and the pitch and roll angles have not changed the sign of $\ell_{13}\, m_{13}$. At 0.6 hr, the differential gravity accelerations in both axes have become insignificant with respect to the crosscoupling terms and the motion continues from this point until the next perigee region in the manner discussed earlier.

Another condition considered was one in which a 1-ft (CP-CG) offset along the Z axis was assumed and solar pressure and differential gravity forces were present. Specific initial conditions are identical to the previously discussed case where $R_0 = 5.236 \times 10^{-4}$ rad/sec. Figures V-32 and V-33 give a comparative description of these cases. Since there is no offset in the X or Y body directions, no torques act about the Z body, and R_0 remains constant as in the preceding case. However, solar pressure torques do act about the X and Y body axes. As a result, the frequency of rate variation remains constant and an amplitude change takes place. The initial perigee region is not shown, since the solar pressure torques only produced a time lag with little amplitude change. However, the second perigee point shows, very clearly, the possible effects in amplitude when both differential gravity and solar pressure torques are present. Just prior to approximately 144.13 hr, the solar pressure and differential X body torques are opposing each other and, suddenly, due to vehicle pitch angle, the sign of the differential gravity torque changes and, at the same time, the solar pressure torque increases and both are acting in the same direction. This torque combination produced the discontinuity shown in Fig. V-33. The same sequence occurred in the Y body accelerations, but to a lesser degree (Fig. V-32). The main effect of both perturbations is to decrease the rotational energy or, putting it another way, the cone angle does not significantly change as was true when only differential gravity torques were present. During the remainder of this orbit, the X and Y body rates are slightly affected by the relatively small solar pressure torques and phased such that a near sine wave type rate motion prevails.

The final case investigated included variable X and Y center of pressure offsets for solar pressure and aerodynamic torque calculations. A constant 1-ft displacement was assumed along the Z axis. This representation is relatively close to the actual "Z" configuration. The initial orientation angles and tip-off rates were considered zero. The sun is normal to the orbit plane which, at t = 0, puts its direction along the vehicle Y body axis ($\alpha' = 90$, $\gamma = 0$). The velocity vector is along the X body axis. The resulting dynamics for the first 14 hr are shown in Fig. V-34.

At time zero, a Y body aerodynamic torque and an X axis solar pressure torque are present. The aerodynamic torque lasts for only 0.05 hr, causing a step change of -12×10^{-4} rad/sec in the Y body rate. After this time, the differential gravity torque tends to reduce this rate. The leveling out of this rate between 1.5 and 3.5 is caused by net zero acceleration being produced from solar pressure, differential gravity and crosscoupling. After 3.5 hr the rate reduced due to a change in the crosscoupling term caused by increased X and Z body rates.

$P_0 = Q_0 = 0$ $R_0 = 5.236 \times 10^{-4}$ rad/sec

$\psi_0 = \phi_0 = 0$ $\theta_0 = +90°$

Constant (cp-cg) offset
along Z-body axis

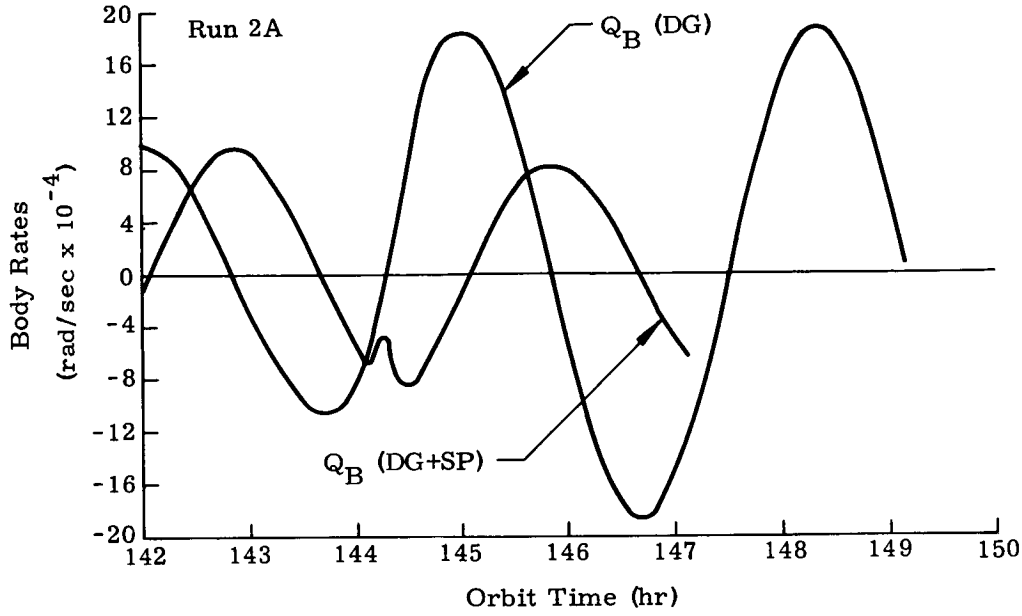

Fig. V-32. Effects of Solar Pressure on Dynamic Behavior

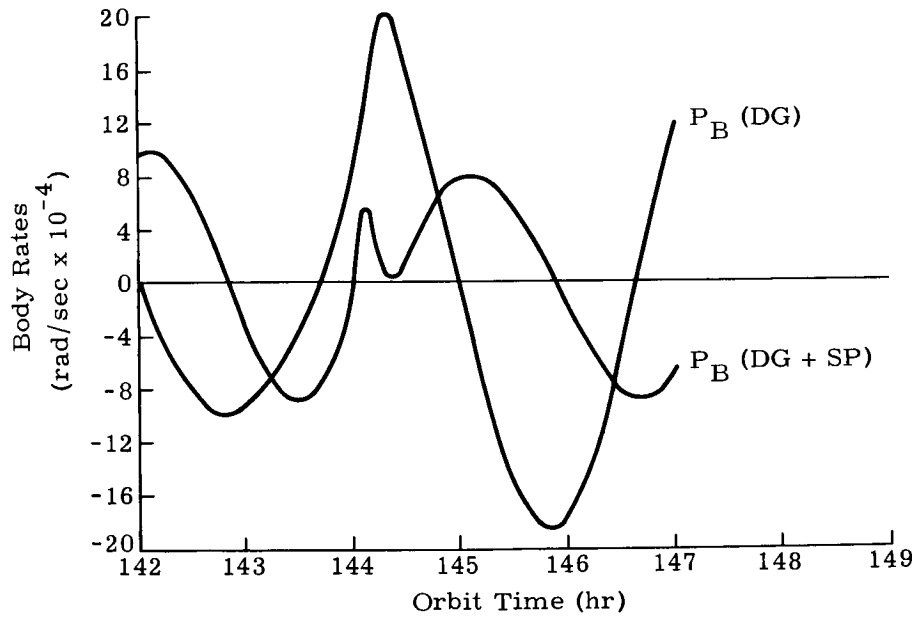

Fig. V-33. Effects of Solar Pressure on Dynamic Behavior

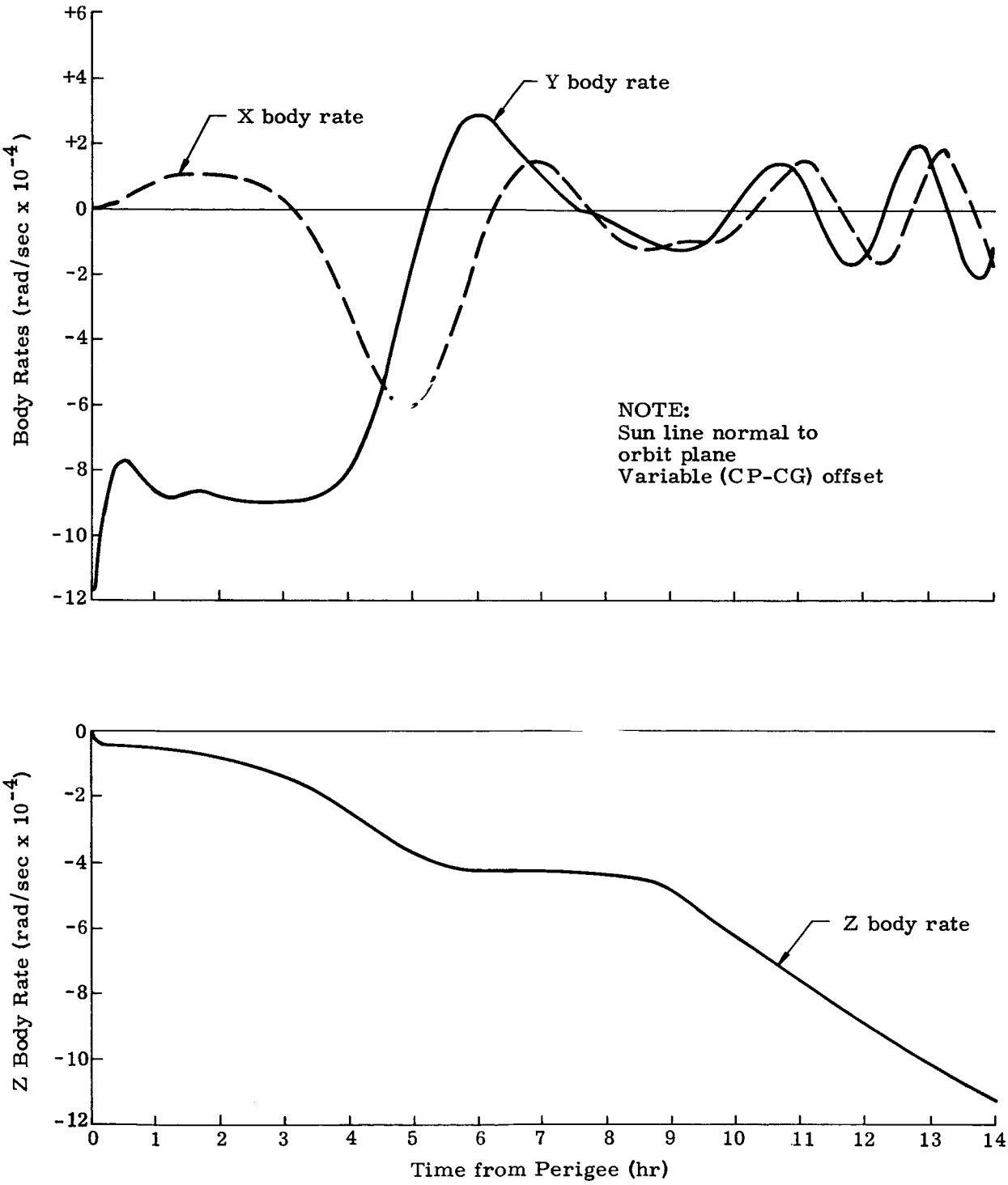

Fig. V-34. Z Configuration Dynamic Behavior

Due to the initial solar pressure torque, the X body rate builds up to a small positive value, and levels out due to acceleration equilibrium. At 2.5 hr, the differential gravity torque diminishes and the cross-coupling torque increases negatively due to the Z body rate buildup. After the initial small step in the Z body rate contributed by the aerodynamic torque, this rate is completely governed by solar pressure torques.

Figure V-35 shows the latitude (τ_S) and longitude (η_S) of the sun direction with respect to the body axis. The solar pressure cp offsets are derived in a manner such that a negative τ_S, yields negative Z body torques, and positive τ_S values yield positive torques. During the first 14 hr, τ_S is negative and accounts for the negative body rate buildup. Variations in this rate are expected since the magnitude of the cp offset is also a function of η_S. It should be stated that τ_S appears to be approaching a positive value, which would reverse the Z body acceleration and slow this body rate down. However, the increased machine time requirements, as well as the time and scope limitations of this study did not permit further evaluation. Another item of importance is that the present digital mechanization does not directly consider variations of sun angle to orbit frame. On a short term basis, this variation would not affect the dynamics, but on a long term basis it would. A study to evaluate this effect would be in order. This same line of reasoning warrants the inclusion of a study of an initial condition matrix for the "Z" and/or flat plate configurations. It is also felt worthwhile to evaluate use of an analog computer due to economic considerations. The main problem with this approach would be noise generation due to large variable ranges which might cause significant errors.

2. Earth Sensor Investigation

Attitude determination in a direct sense requires a knowledge of the direction in vehicle coordinates of some celestial body besides the sun. The body chosen in this study is the earth. This choice was made due to the relatively close proximity of the vehicle to the earth. Also, more characteristic data about this planet is available which, since the beginning of the space age, has resulted in the development of numerous space-qualified detector designs. Based on a passive system design, the earth detectors considered are those sensitive to the earth's magnetic and radiative characteristics. Magnetic detectors are discussed in Chapter VA Vol. III. The optical spectrum sensors were excluded due to their inadequacy to detect earth during occulted periods of the orbit and other factors. Major emphasis was devoted to investigating infrared earth detector systems. The long lifetime requirement further reduced this investigation to a system containing no bearings or sliding surfaces.

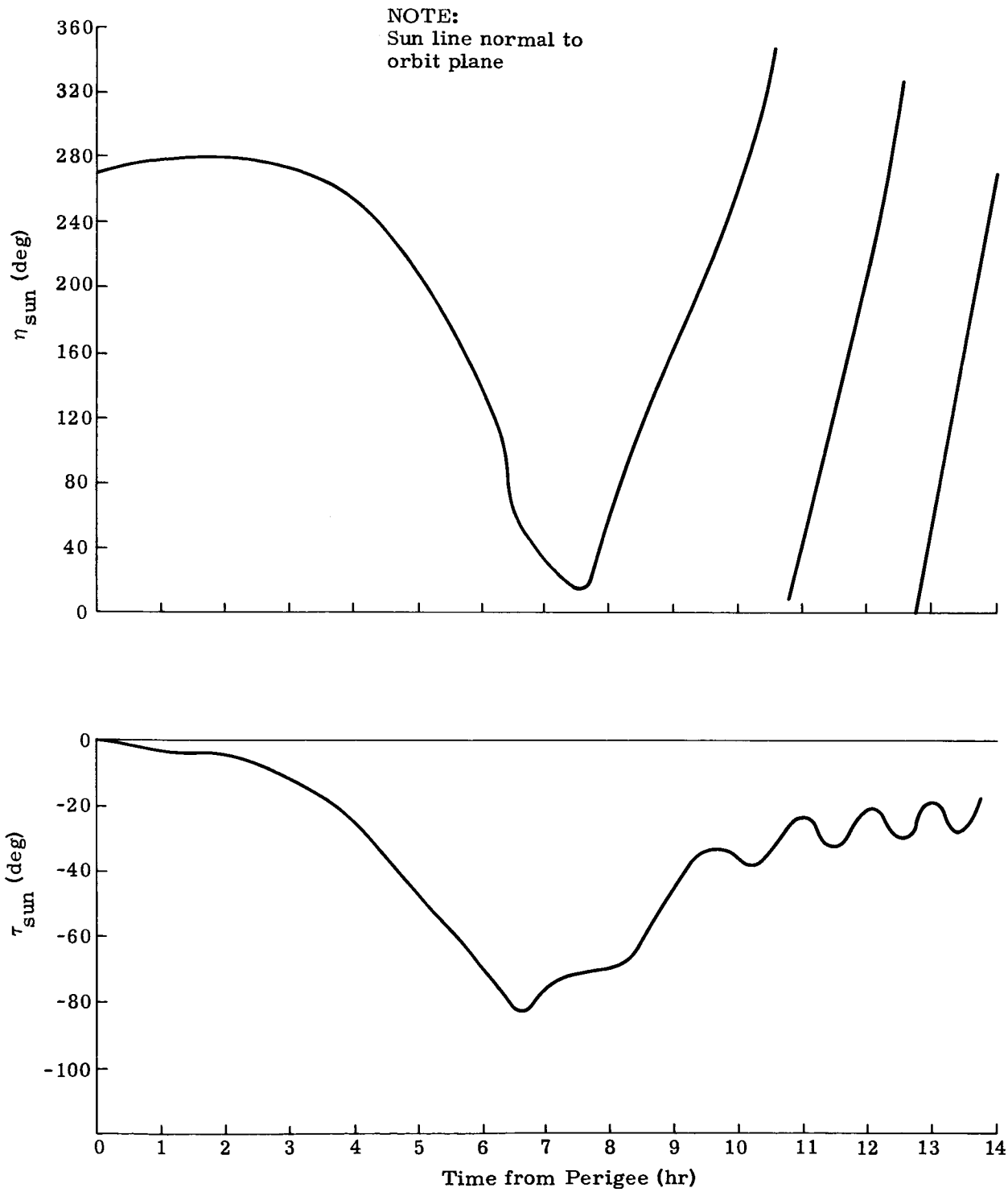

Fig. V-35. Sun Angles η_s, τ_s

Orbital paramaters of the MDSS are such as to produce large variations in the earth's subtense angle. At minimum perigee altitude, this angle is approximately 86°, reducing to 2° at apogee. This large subtense angle variation, coupled with a desired accuracy of approximately 8° to 15°, imposes the most stringent requirement on the attitude determination system. An appreciation for the tradeoffs between the number of sensors with fixed fields of view, earth's subtense angle and maximum sensing error is presented in Fig. V-36. Considering that during 80% of the orbital period, the disc size is smaller then 5°, it becomes quite obvious that the desired accuracy would require an enormous number of sensors. For instance the desired accuracy it would take 97 sensors with a 22° field of view to know the earth's direction to within 12° when the earth's subtense angle is 5°. A square field of view was used for ease of mathematical calculations of the number of sensors, but is certainly representative. Another way of presenting the problem is that the sensor field of view determines the number of sensors necessary to encompass 4π steradian coverage of a celestial sphere about the vehicle, while the earth's minimum subtense angle specifies the maximum error. That could be expected. This number of sensor and accuracy relationship, plus the desire to maintain a simple non-span system using off-the-shelf hardware leads to the present attitude determination predictive system. Included in this system are ten Pegasus-type small field of view IR earth sensors. More detail on this system is presented in Vol. III Chapter VA. The purpose of this section is to document other sensor system designs investigated which show potential for sensing earth during the small subtense angle regions but are either more complex, in that an "on-off" earth sensing signal is not produced, or they incorporate some type of space scan. These IR systems can be classified by detector types into two classes: thermopile or thermister bolometer systems.

a. Thermopile detector systems

A solid-backed thermocouple radiation detector consists essentially of a pair of metallic junctions deposited onto a heat sink, one junction being in good thermal contact with the sink by conduction while the other is thermally isolated by a thin insulating layer. An idealized detector of this type is shown in Fig. V-37. The area of the active junction is considered to be the portion over the insulator and is blackened, while the "cold" or reference junction is formed by the opposite ends of the metal strips which are in good conductive thermal contact with the sink. Assume that the surface is irradiated with a radiation density H (watts/cm^2). The junction will rise in temperature until the rate of heat loss by all processes equals the total radiant power incident. In the solid-backed configuration, conduction losses to the heat sink through the insulating layer and the junction metals will be much greater than radiation or convection losses. The steady-state thermoelectric voltage generated by the junction will be:

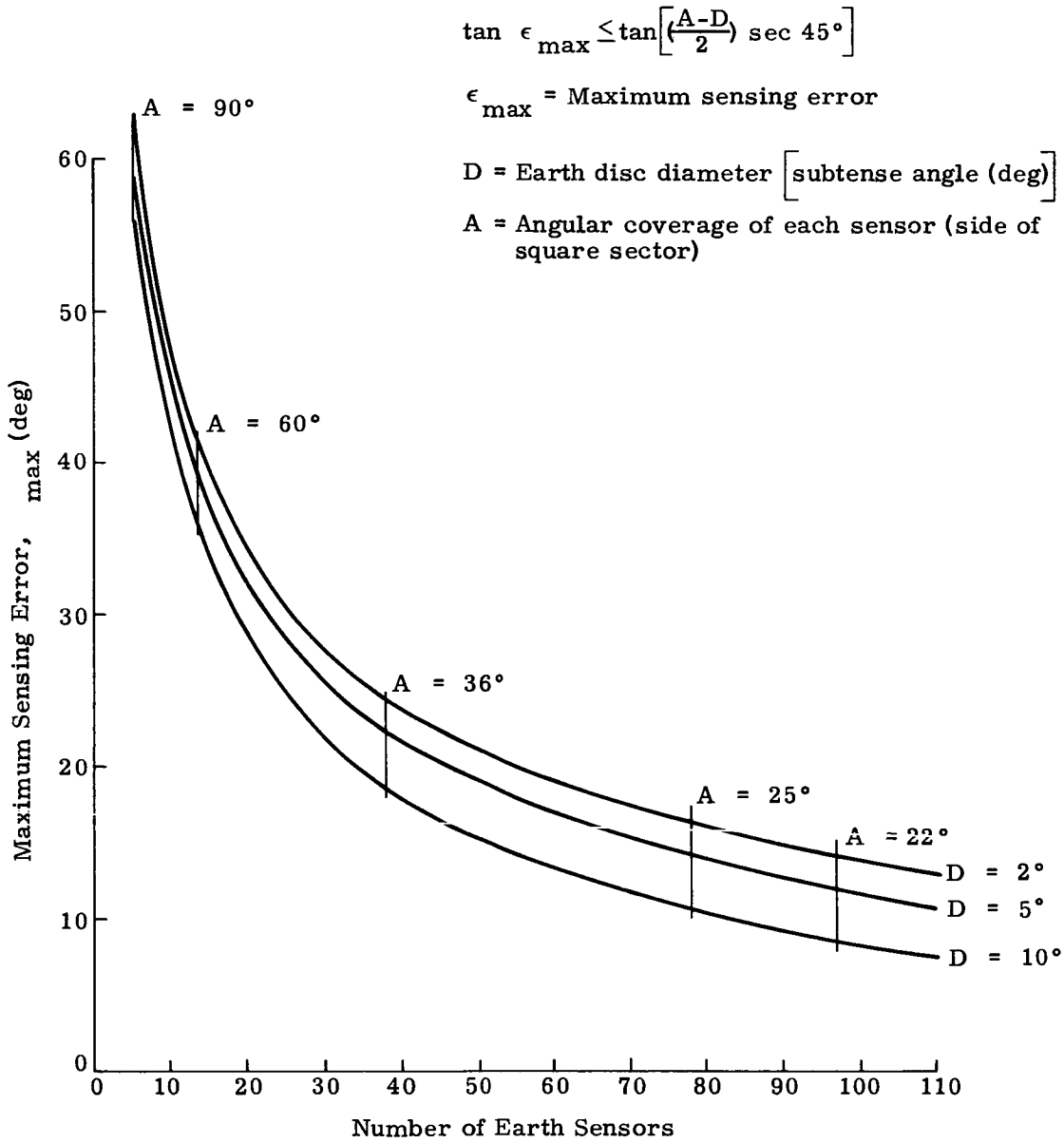

Fig. V-36. Maximum Error in Sensing Earth Direction

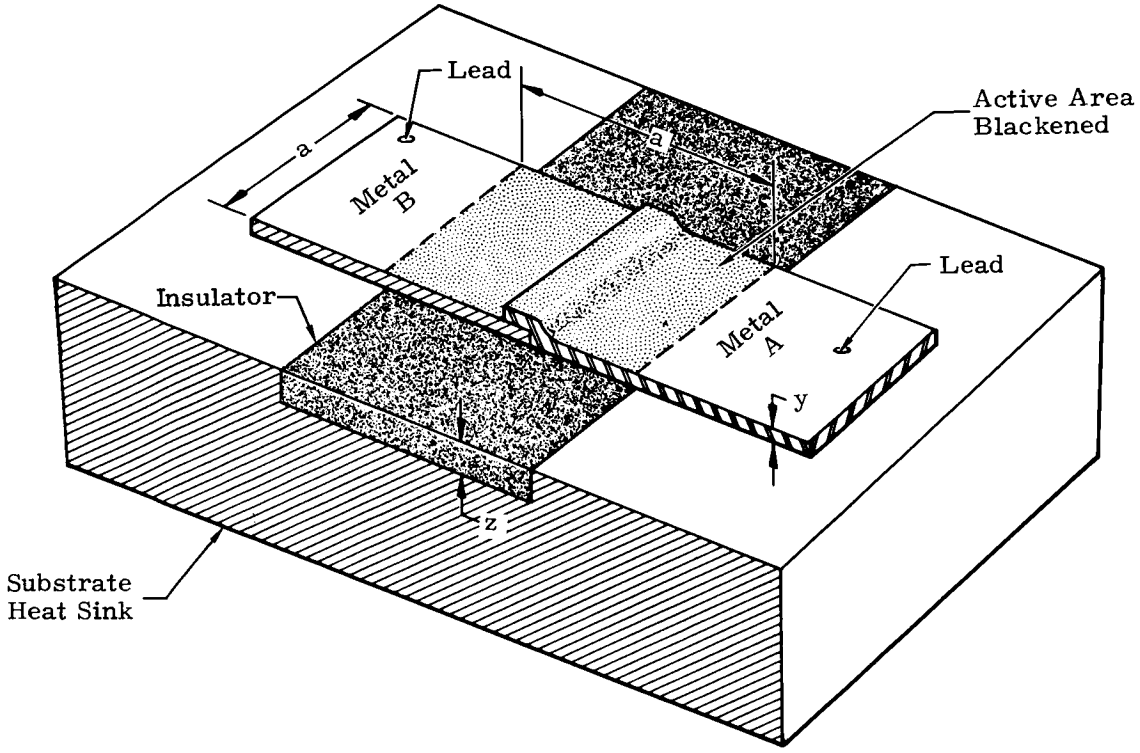

Fig. V-37. Solid-backed Thermocouple Detector

$$V_S = \psi \Delta T = \psi Z H a^2$$

where:

ΔT = temperature rise of the active junction above the sink temperature

ψ = combined thermoelectric power of the junction metals A and B

a^2 = area of the detector (a x a)

Z = thermal resistance of the active junction.

This voltage output is thermovoltaic, so that no bias supply is required and when the two junctions are at the same temperature (whatever that temperature may be), there is no output voltage. These detectors have been developed rugged enough for use in space application. In applying these thermopiles to earth sensors without moving parts, a microvolt level DC amplifier had to be designed having a drift equivalent to less than 1 microvolt at the output. This has been accomplished through use of a photomodulator technique in which the thermopile microvolt level DC output is electronically chopped by a cadmium selenide photoswitch actuated by a neon bulb as discussed in Vol. III, Chapter VA.

The Barnes Engineering Company has been developing the solid-backed thermopile detectors since 1961. Two basis design configurations developed by Barnes using these detectors are radiation balance and electronic scan types. Programs presently employing the radiation balance series are Pegasus as small field of view earth detectors for attitude determination, the Apollo command capsule antenna positioning system, and a small missile made by Raytheon. A system is presently under development for JPL which employs electronically scanned arrays of thermopile detectors. In the electronic scanning horizon sensor, several thermopiles are arranged in a closely adjacent array situated at the focus of an optical system (Fig. V-38). When this array brackets the horizon edge, the thermopiles viewing the planet below the horizon will produce a higher DC signal than those viewing cold space above the horizon. The sequential closing of a light-source illuminated cadmium selenide photoconductive switch connected in series with each of these thermopiles thus effectively samples the signal output of each thermopile at the detector level (Fig. V-39). This effectively causes an instantaneous field of view defined by each thermopile. By increasing the number of thermopile detectors, it can readily be seen that relatively large fields can be electronically scanned with an angular resolution determined by thermopile size and spacing. By grouping the thermopiles in an optical head which would define a large field of view, several

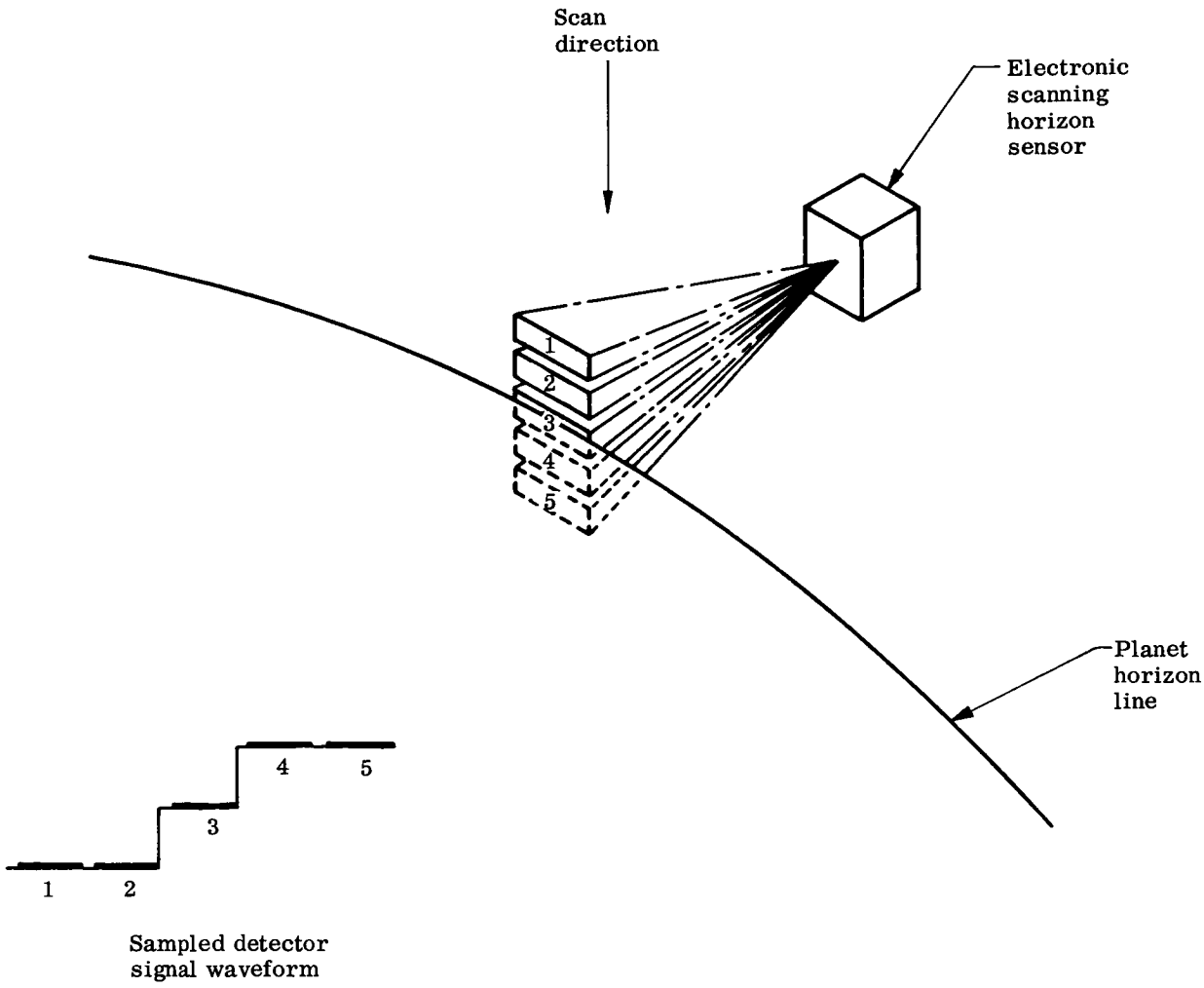

Fig. V-38. Tracking Signal Generation in Electronic Scanning Horizon Sensor

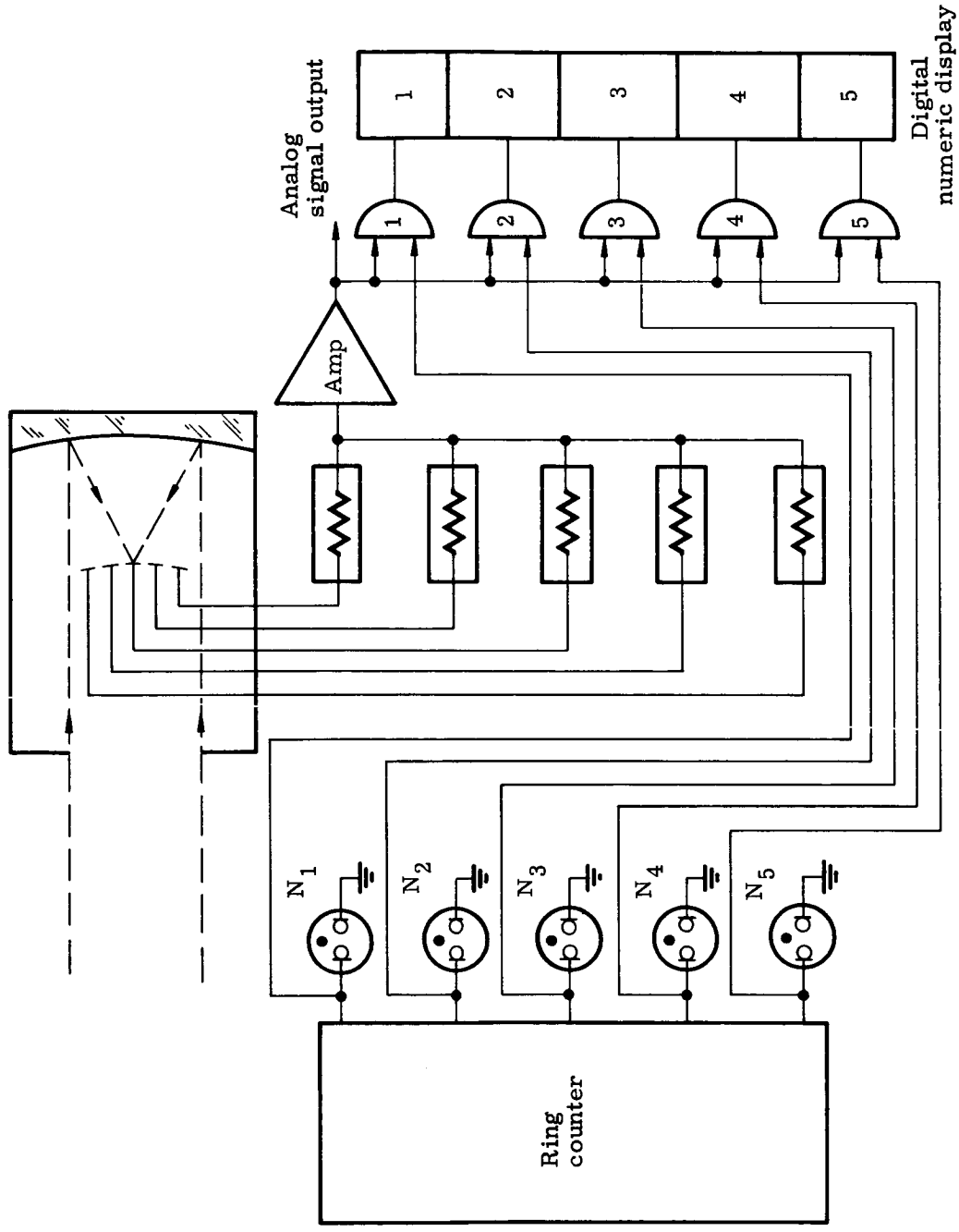

Fig. V-39. Electronic Scanning Demodulation System

of these heads could be positioned on the vehicle to cover 4π steradians. At the time of micrometeoroid impact, the heads could simultaneously be sampled and the thermopiles seeing earth recorded. However, a recent visit to the Barnes Company tentatively dismissed this idea for earth subtense angles below 10° due to signal to noise problems.

The Barnes Company suggested that a system of triangular thermopile arrays, defining a certain field of view of, for instance, 35° covering 4π steradians be used as shown in Fig. V-40. The total output voltage of each array would be sampled and recorded for a period of time when attitude data is desired. By assuming that the vehicle motion will move the earth through three of these arrays in a somewhat linear fashion during the sampling period, ground reduction interpolation techniques using the pulse widths of the array voltage outputs would define the earth direction at whatever time one would choose during the sampling interval. This technique has merit insofar as the linear motion assumption is true. Further analysis of vehicle dynamics would be necessary to define the optimum field of view and, therefore, the number of arrays for which such an assumption would be adequate. In effect this is saying that one is depending on vehicle motion to scan space.

b. Thermistor bolometer detector systems

The thermistor bolometer has been used exclusively in infrared horizon sensors having moving parts since, in an optically chopped operation, it has achieved a higher sensitivity than other detectors. It can be fabricated in small sizes and obtain relatively short time constants required for scanning sensors. As can be seen (Fig. V-41), the thermistor bolometer's output signal in a simple radiometric balance horizon sensor configuration is derived from a temperature-differential-caused resistance unbalance in the two flakes making up the bolometer bridge. This temperature results from an infrared irradiance differential between the bolometer flakes. For DC radiometric operation, the resistance of the bolometer flakes must "track" so that the maximum mismatch is equivalent to less than the minimum expected signal. Over the wide ambient temperature ranges normally experienced by space instrumentation, this high degree of resistance match is not achievable. This is inherently due to the fact that the temperature coefficients of resistivity for the thermistor varies with ambient temperature and from flake to flake. Therefore, unless the infrared irradiance is coded by some means such as chopping or scanning, the temperature difference between the active and compensating flakes due to irradiance cannot be distinguished from the one due to a resistance mismatch caused by an ambient temperature shift.

The micrometeoroid deep space satellite requirements were presented to the Advanced Technology Laboratories (ATL) and two possi-

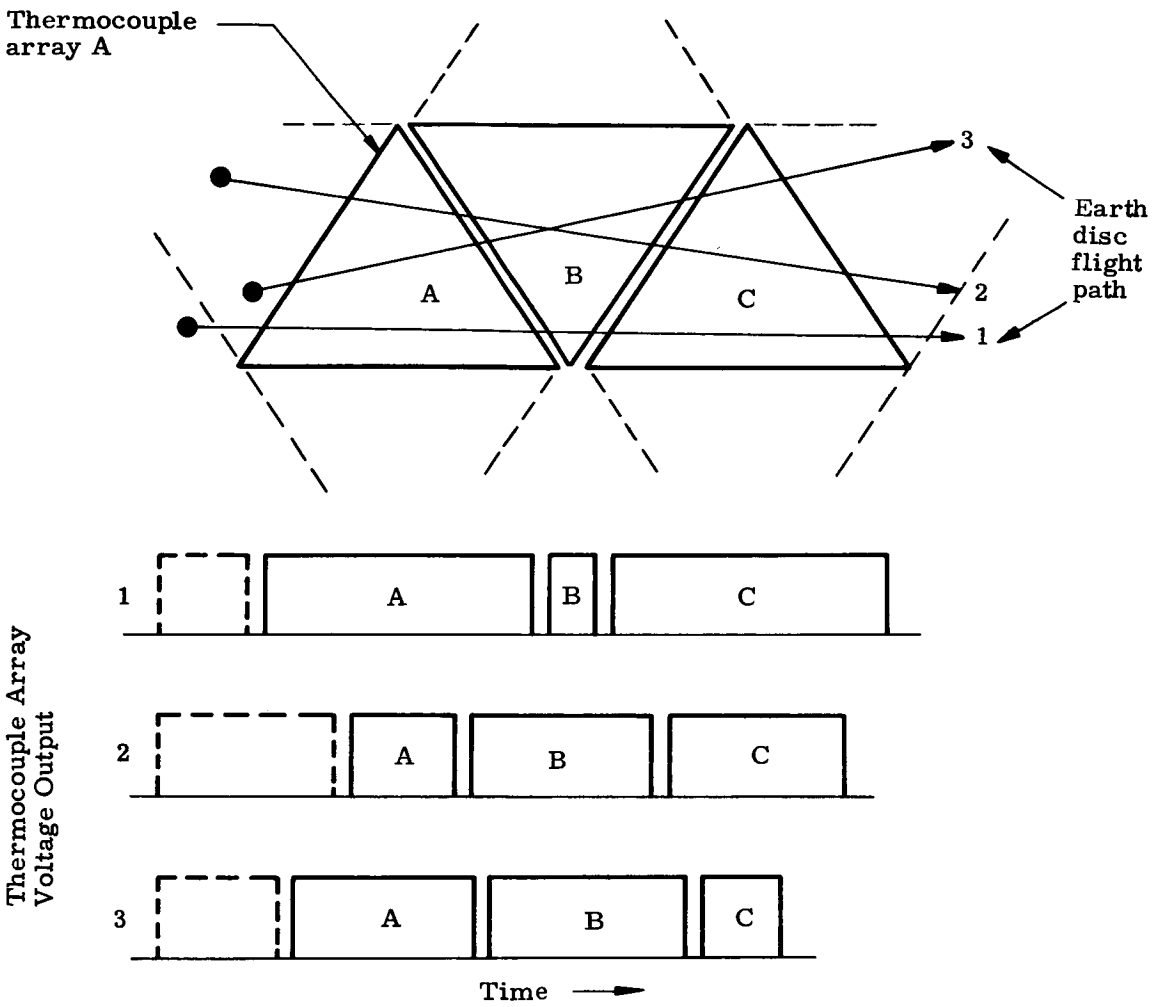

Fig. V-40. Triangular Thermopile Array Earth Sensors

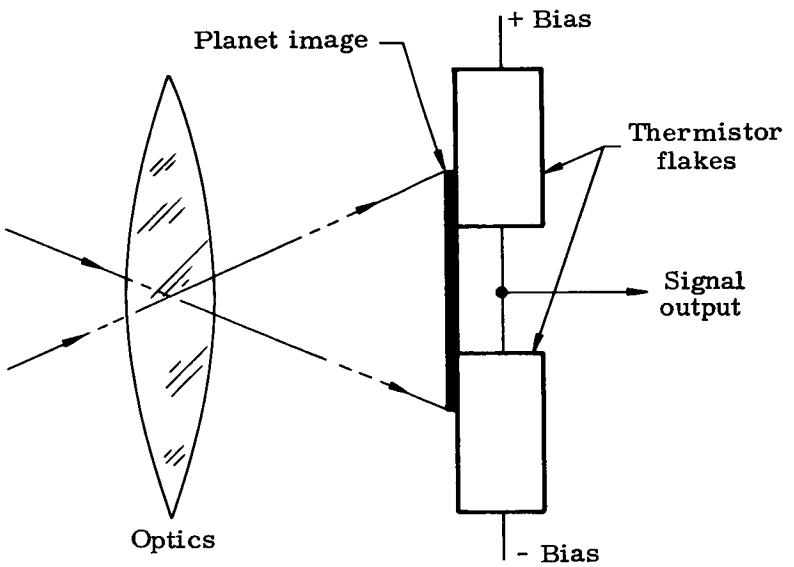

Fig. V-41. Thermistor Bolometer Horizon Sensor

ble designs were proposed. Both designs use their positor unit to scan space in an elevation sense. The major difference between the designs is, in one case, a motor-bearing drive unit is used to obtain the required azimuth scan, while the other design simply relies on vehicle motion for azimuth coverage. The heart of both systems is the positor unit, a device which can produce rapid optical motion beyond 50 cps without the use of bearings or any sliding surfaces. Basically optical motion is accomplished by a mirror mounted on the rotor of a permanent magnetic-type torque (Fig. V-42). Also connected to the rotor are two coils that can move in a cylindrical air gap. A pair of flexure pivots connect the rotor to the base structure. Each pivot consists of a set of two flat springs attached to the rotor and to the base in such a way as to form an X. The flat sides of the springs are perpendicular to the plane of the X and passing through its center point. Electrical connections to the rotor coils are made through the flexure pivots.

Figure V-43 shows, schematically, the electrical operation of the positor. A permanent magnet, located in the base, supplies a steady magnetic flux (shown by solid lines in the sketch) in the cylindrical air gap. Two field coils mounted on the ends of the fixed assembly are energized with high-frequency (from 2 to 5 kc) AC and furnish an alternating flux superimposed on the steady flux in the gap. If current is passed through the series-connected drive coils, a torque is produced which rotates the coils and the attached mirror against the flexure-pivot springs. At the same time, an AC EMF is induced in each coil. This EMF is linearly proportional to the angular position of the drive coils and mirror. The series connection of the two drive coils is phased so that a current passing through the two coils produces adding torques in the coils. This same phasing causes the induced high frequency voltages to oppose. This high frequency phase-reversing AC EMF, which appears at the series drive-coil terminals, is a linear indication of mirror angle. This signal will be independent of such variables as flexure-pivot-spring constant and permanent-magnetic field strength. Positors currently in manufacture at ATL can move an optical line of sight through 90°. They have been satisfactorily tested to 35g sinusoidal vibration. Stresses in the flexure-pivot assembly have been set so that the pivots have essentially unlimited lifetimes in horizon scanning applications. ATL was awarded contracts for the development of the horizon sensors for the Orbiting Geophysical Observatory, the Gemini two-man spacecraft, and the Advanced Agena spacecraft, which employ the positor device. The OGO and Gemini horizon sensors are now in production.

Infrared radiation from the earth is reflected from the positor mirror into an infrared telescope, containing a thermistor bolometer detector in its focal plane. The field of view of the telescope is quite narrow (about 1° in present systems) but the motion of the positor mir-

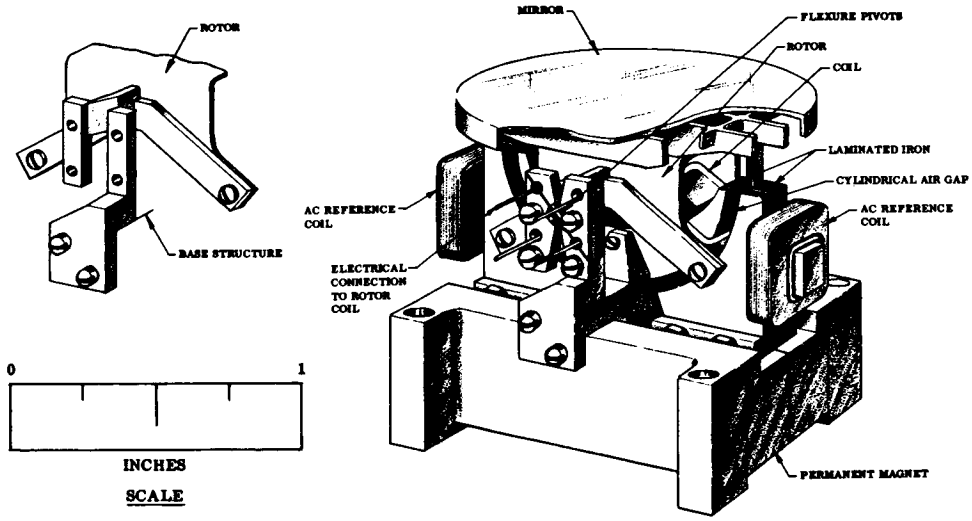

Fig. V-42. ATL Positor

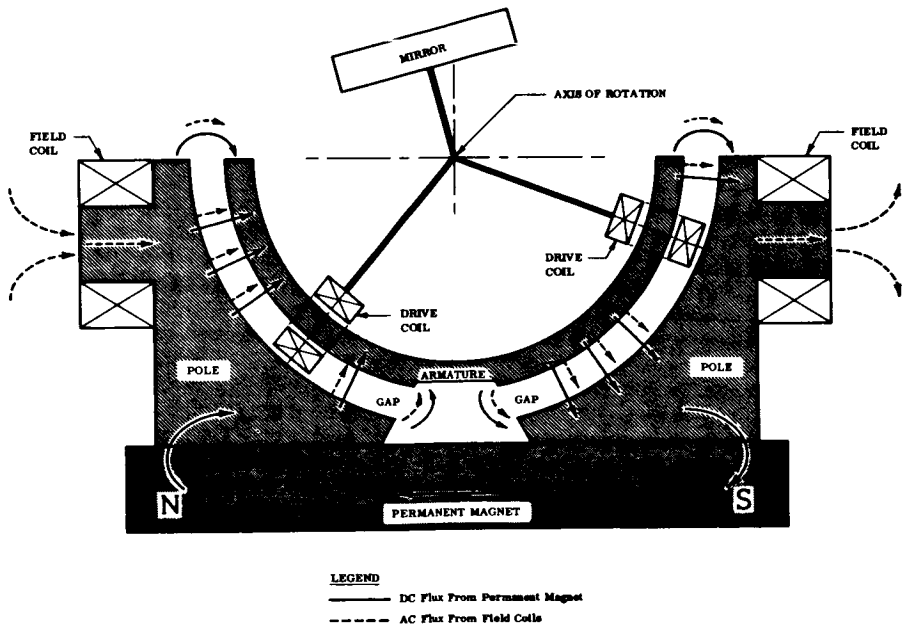

Fig. V-43. Positor Schematic

ror allows this narrow field to be deflected through 90°. A 90° x 1° band of the celestial sphere is effectively scanned by one unit. When earth detection is desired, a number of these horizon sensor units would scan space. By recording the bolometer outputs and positor elevation angle, ground reduction would determine the earth's direction in vehicle coordinates when the earth is in the system field of view. The one ATL design would simply mount several of these units evenly distributed on the vehicle and depend on vehicle motion to place the earth within the field of view during the sampling interval. This approach is analogous to the Barnes thermopile array design in as far as the scanning of the celestial sphere coverage depends on vehicle motion. More study into the practicality of such an assumption is needed.

The second ATL design eliminates dependence on vehicle motion for scanning and obtains this objective by designing an azimuth drive unit, which rotates the positor system 360° in azimuth. By using two such systems the entire celestial sphere can be scanned. The azimuth drive rate (about 15 rpm) will be relatively small as compared to the positor elevation scan rate. A development program by ATL would be necessary to ensure sufficient unit lifetime of the azimuth drive which will contain at least one bearing per unit. In both of these designs it is probable that earth, moon and sun will be detected during the sampling interval. Analysis of the bolometer signal level will in some cases identify the respective bodies. When this is not possible, ephemeris data relating the sun-vehicle-earth and sun-vehicle-moon angles will be relied upon. The major disadvantage of the azimuth drive design is the unit's questionable lifetime capability for a one-year operational period.

C. REFERENCES

V-1. Naumann, R. J., "Observed Torque-Producing Forces Acting on Satellites," NASA TR R-183, December 1963.

V-2. Naumann, R. J., Fields, S. A., Holland, R. L., "Analysis of Explorer 11 Orientation," Journal of Geophysical Research, August 1962, Vol. 67, No. 9, pp 3619 to 3623.

V-3. Cain, J. C., Shapiro, I. R., Stolarik, J. D., Heppner, J. P., "Measurements of the Geomagnetic Field by the Vanguard Satellite," NASA TMO-1418, October 1962.

V-4. Heppner, J. P., Ness, N. F., Scearce, C. S., Skillman, T. L., "Explorer 10 Magnetic Field Measurements," Journal of Geophysical Research, January 1963, Vol. 68, No. 1, pp 1 to 46.

V-5. Heuring, F. T., "The Analytic Description of the Geomagnetic Field at Satellite Altitudes," Journal of Geophysical Research, December 1964, Vol. 69, No. 23, pp 4959 to 4968.

V-6. Ness, N. F., Scearce, C. S., Seek, J. B., "Initial Results of the IMP-1 Magnetic Field Experiment," NASA X-612-64-95, April 1964.

V-7. Frick, R. H., Garber, T. B., "General Equations of Motion of a Satellite in a Gravitational Gradient Field," Rand Report RM-2527, December 1959.

V-8. McElvain, R. J., "Solar Radiation Torques Acting on an Earth-Sun Oriented Satellite," STL-TR-60-0000-04164, June 1960.

V-9. Thompson, W. T., "Introduction to Space Dynamics," John Wiley & Sons, 1963.